8.4 Inertance and the Linearized Euler Equation

Just as we did with the calculation of the compliance of a small lumped element in Sect. 8.2.3, we will begin our calculation of the inertance of a small lumped element by linearizing the relevant hydrodynamic equation. In this case, we ignore viscous and gravitational forces in Eq. (7.34) and begin with the Euler equation (7.42), reproduced below.

$$\frac{D\vec{v}}{Dt} = \frac{\partial \vec{v}}{\partial t} + \left(\vec{v} \cdot \vec{\nabla}\right)\vec{v} = -\frac{\vec{\nabla} p}{\rho} \tag{8.33}$$

8.4.1 The Venturi Tube

Some students find the convective contribution to the acceleration term, $\left(\vec{v} \bullet \vec{\nabla}\right)\vec{v}$, in the total derivative, $D\vec{v}/Dt$, of Eq. (8.8) and the Euler equation (8.33), to be a bit mysterious. This mystery might be cleared up if we look at a situation where $\partial v/\partial t = 0$ everywhere in the fluid, but the fluid's acceleration is non-zero. The Venturi tube flow meter,[7] shown schematically in Fig. 8.6, is a simple case that will be easy to analyze [5].

If we assume the drawing in Fig. 8.6 depicts a rectangular duct of constant width but the linearly varying cross-section between $x = 0$ and $x = L$, reducing the cross-sectional area by a factor of two, which is filled with an incompressible fluid, ($\partial \rho/\partial t = 0$), then conservation of mass (7.32) guarantees that the velocity, $\vec{v}$, must increase linearly within the constriction between $x = 0$ and $x = L$.

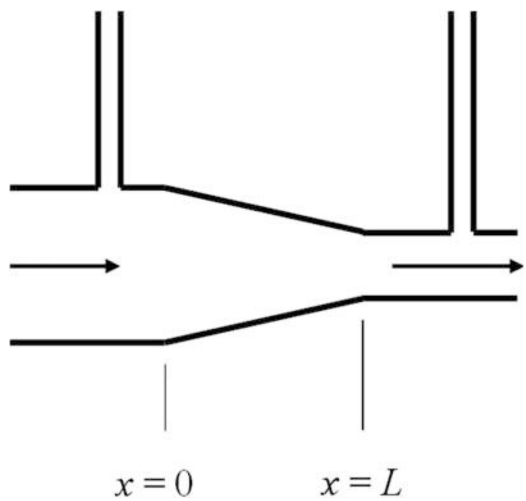

Fig. 8.6 An incompressible fluid flowing through the Venturi must accelerate from a lower velocity at the left of the constriction to a higher velocity at the right of the constriction. Although it is obvious that the fluid must be accelerating, the time derivative of the velocity at any fixed location within the fluid is zero. The height of the fluid in the two standpipes will be different because the pressure at the left must be higher than the pressure at the right to create the fluid's acceleration required by the Euler equation (8.33) under our assumption of the fluid's incompressibility

[7] Named after Italian physicist Giovanni Battista Venturi (1746–1822)

$$\vec{v}(x) = v_{left}\left(1 + \frac{x}{L}\right)\hat{e}_x \quad \text{for} \quad 0 \geq x \geq L \tag{8.34}$$

As a function of time, $\partial \vec{v}(t)/\partial t = 0$, but since the velocity depends upon position, the convective acceleration is non-zero.

$$\left(\vec{v} \cdot \vec{\nabla}\right)\vec{v} = v_x \frac{\partial v_x}{\partial x}\hat{e}_x + v_y \frac{\partial v_y}{\partial y}\hat{e}_y + v_z \frac{\partial v_z}{\partial z}\hat{e}_z \tag{8.35}$$

Since $\vec{v}$ along the center line is only a function of x, only the first term on the right-hand side of Eq. (8.35) is non-zero. This convective acceleration can be related to the pressure gradient, $\vec{\nabla} p \cong \left(p_{left} - p_{right}\right)/L$, by substitution into the Euler equation (8.33).

$$\rho\left(v_x \frac{\partial v_x}{\partial x}\right) = -\frac{\partial p}{\partial x} \tag{8.36}$$

The above version can be integrated to produce the pressure difference, $\Delta p = p_{left} - p_{right}$, that would lead to a height difference, $\Delta h = \Delta p/\rho g$, in the two standpipes shown at $x < 0$ and $x > L$ in Fig. 8.6.

$$-\int_{left}^{right} dp = \rho \int_{left}^{right} v_x \, dv_x \quad \Rightarrow \quad \Delta p = \frac{\rho}{2}\left(v_{right}^2 - v_{left}^2\right) \tag{8.37}$$

This result is a manifestation of the Bernoulli equation that is very important in nonlinear acoustics for understanding radiation pressure [6] and acoustical levitation [8]. For our purposes here, it illustrates that there can be accelerations and pressure gradients in fluids where $\partial \vec{v}(t)/\partial t = 0$ everywhere within the fluid.

8.4.2 The Linearized Euler Equation

The convective term in the acceleration is manifestly second order (in the absence of steady flow) since it is proportional to the product of two first-order quantities, $\vec{v}_1 \cdot \vec{v}_1$. We can use the same technique of harmonic analysis as used previously in Eq. (8.19), this time to determine the conditions that justify neglect of the convective acceleration term, using sound speed, $c = \omega/k$.

$$\left|\frac{\left(\vec{v} \cdot \vec{\nabla}\right)\vec{v}}{\partial \vec{v}/\partial t}\right| = \left|\frac{jk\hat{\mathbf{v}}^2}{j\omega\hat{\mathbf{v}}}\right| = \frac{|\hat{\mathbf{v}}|}{c} \quad \Rightarrow \quad \frac{|\hat{\mathbf{v}}|}{c} = M_{ac} << 1 \tag{8.38}$$

We can neglect the second-order term in Eq. (8.33), $\left(\vec{v} \cdot \vec{\nabla}\right)\vec{v}$, compared to the first-order term, $\partial \vec{v}/\partial t$, if the velocity amplitudes are within the acoustic approximation: $M_{ac} \ll 1$.

As before, when we eject a particular term from the fundamental governing equations, it takes along with it many interesting phenomena. In this case, the loss of the convective acceleration term, $\left(\vec{v} \cdot \vec{\nabla}\right)\vec{v}$, removes our ability to understand the formation of shock waves and sonic booms. It also eliminates any non-zero time-averaged acoustic forces that are related to the Bernoulli pressure, $\langle p_2 \rangle_t = (\rho_m/2)v^2$ [7]. These forces include radiation pressure [6], the levitation of solid objects in

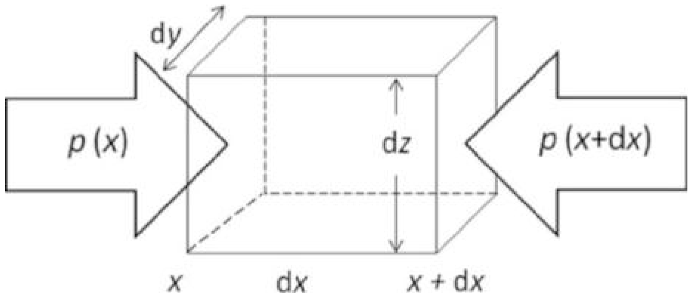

Fig. 8.7 A Eulerian volume element in a Cartesian coordinate system in the presence of a pressure gradient

intense standing wave fields,[8] and the manipulation of such levitated objects to cause rotations (acoustic torques) and vibrations [8].

To linearize the part of the Euler equation that remains after removal of the convective acceleration, the density can be expanded into its mean value, ρ_m, plus the first-order variation, ρ_1, as shown in Eq. (8.2).

$$\frac{\partial \vec{v}_1}{\partial t} = -\frac{\vec{\nabla} p_1}{\rho_m (1 + \rho_1/\rho_m)} \tag{8.39}$$

The acoustic approximation guarantees that $\rho_1/\rho_m = M_{ac} \ll 1$, so it can also be removed from Eqs. (8.33) and (8.39) to produce the linearized Euler equation that we will use to derive an expression for the lumped inertance of the small fluid element with all dimensions much less than the wavelength of sound.

$$\frac{\partial \vec{v}_1}{\partial t} = -\frac{\vec{\nabla} p_1}{\rho_m} \tag{8.40}$$

Before doing so, we can interpret Eq. (8.40) again using the Eulerian fluid particle shown in Fig. 8.7.

The force exerted on the left side of the differential volume, dV, is $p(x) dy\ dz$. The force exerted on the right side is $p(x + dx) dy\ \ dz$. The net force, F_{net}, is their difference.

$$F_{net} = [p(x) - p(x + dx)]\ \ dy\ \ dz \tag{8.41}$$

$p\ (x + dx)$ can be expanded in a Taylor series about x, as indicated by the subscript on the partial derivative.

$$p(x + dx) = p(x) + \left(\frac{\partial p}{\partial x}\right) dx \tag{8.42}$$

Using this result, the net force on the Eulerian volume element can be expressed in terms of the pressure gradient in the x-direction: $\nabla_x p = (\partial p/\partial x)$.

$$F_{net} = [p(x) - p(x + dx)]\ \ dy\,dz = -\left(\frac{\partial p}{\partial x}\right) dx\,dy\,dz = -\left(\frac{\partial p}{\partial x}\right) dV \tag{8.43}$$

[8] A nice acoustic levitation chamber video demonstration is available on *YouTube*, http://www.youtube.com/watch?v=94KzmB2bI7s. In a truly bizarre application, Wenjun Xie, at a university in Xi'an, China, used acoustics to levitate live insects, spiders, and fish as shown in Fig. 15.19.

Newton's Second Law of Motion states that this net force must be equal to the mass of fluid contained within dV times its acceleration. Since we have assumed a pressure gradient only in the x direction, we will again express the vector velocity in Cartesian components:

$$(\rho\, dV)\frac{\partial u}{\partial t} = -\left(\frac{\partial p}{\partial x}\right)dV \quad \Rightarrow \quad \rho\frac{\partial u}{\partial t} = -\left(\frac{\partial p}{\partial x}\right) \tag{8.44}$$

This is just the one-dimensional version of the linearized Euler equation that was derived in Eq. (8.40) from the hydrodynamic equation (8.33).

8.4.3 Acoustical Inertance

Consider a short pipe of constant cross-sectional area, A, filled with an incompressible fluid. For oscillations at a single frequency, we again let $\widehat{\mathbf{U}}$ be the complex amplitude of the oscillatory volume velocity through the element as shown in Fig. 8.8. We can apply the one-dimensional linearized Euler equation (8.44) to the element, assume time-harmonic variables, and make a finite-difference approximation to the one-dimensional pressure gradient, $\nabla_x p \cong -\Delta\mathfrak{Re}[\widehat{\mathbf{p}}e^{j\omega t}]/\Delta x$.

$$j\omega\frac{\widehat{\mathbf{U}}}{A} = \frac{1}{\rho_m}\frac{\Delta\widehat{\mathbf{p}}}{\Delta x} \tag{8.45}$$

The inertance, L, can be obtained by rearranging Eq. (8.45) to take the form of an acoustical impedance, $\boldsymbol{Z_{ac}}$, as was done previously for acoustical compliance, C, in Eq. (8.25).

$$\mathbf{Z_{ac}} \equiv \frac{\Delta\widehat{\mathbf{p}}}{\widehat{\mathbf{U}}} = j\omega\rho_m\frac{\Delta x}{A} \tag{8.46}$$

As with our derivation of the acoustical compliance, the acoustical inertance can be identified by analogy to the *inductive reactance* of AC circuit theory: $X_L = \omega L$.

$$L = \frac{\rho_m \Delta x}{A} \tag{8.47}$$

Just as with the compliance, C, the inertance, L, can be represented by an electrical circuit element (inductor) as shown in Fig. 8.9.

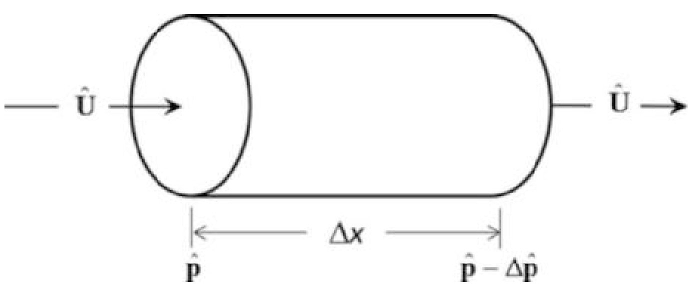

Fig. 8.8 As in Fig. 8.3, this figure depicts a fluid element that is a short section of pipe with length, $\Delta x \ll \lambda$, and cross-sectional area, A, corresponding to a diameter, $d = (4A/\pi)^{1/2} \ll \lambda$. Fluid enters the pipe at the left with a volume velocity amplitude, $\widehat{\mathbf{U}} = \widehat{\mathbf{u}}A$, at a pressure amplitude, $\widehat{\mathbf{p}}$. Since the fluid is assumed incompressible, it also exits at the right with volume velocity amplitude, $\widehat{\mathbf{U}}$, but at a different pressure amplitude, $\widehat{\mathbf{p}} - \Delta\widehat{\mathbf{p}}$, due to the fluid's inertia

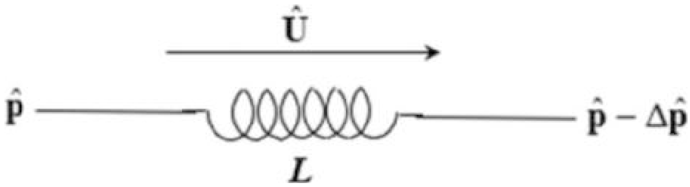

Fig. 8.9 An equivalent circuit diagram of the lumped inertance shown in Fig. 8.8. The volume velocity amplitude, $\widehat{\mathbf{U}} = \widehat{\mathbf{u}}A$, is a "current" passing through the element, and the pressure difference between the ends (like a potential difference, analogous to a voltage drop across the inductor) is responsible for the acceleration of the incompressible fluid

8.4.4 Acoustical Mass

As with the equivalent gas stiffness, K_{gas}, of an acoustical compliance expressed in Eq. (8.28), we can interpret our expression for acoustical inertance in Eq. (8.47) as the inertial mass of incompressible fluid, oscillating within the inertance element, due to the time-harmonic pressure gradient across it. We use Newton's Second Law of Motion since it represents the dynamical equivalent of the fluid-mechanical Euler equation: $F = ma$. The mass of fluid, m, contained within the short inertance element is the incompressible fluid's density times the volume, $m = \rho_m\,(\Delta x\, A)$, and its acceleration amplitude is $\widehat{\mathbf{a}} = \left(j\omega\widehat{\mathbf{U}}/A\right)$.

$$\begin{aligned} &\widehat{\mathbf{F}} = \Delta\widehat{\mathbf{p}}A = (\rho_m \Delta x A)\frac{j\omega\widehat{\mathbf{U}}}{A} \\ &\Rightarrow \frac{\widehat{\mathbf{p}}}{\widehat{\mathbf{U}}} = \frac{\left(\widehat{\mathbf{F}}/A\right)}{\widehat{\mathbf{U}}} \equiv j\omega L = (\rho_m \Delta x A)\frac{j\omega}{A^2} \quad \Rightarrow \quad L = \frac{\rho_m \Delta x}{A} \end{aligned} \tag{8.48}$$

At this point, it could be legitimate to complain that we were able to obtain expressions for the acoustical inertance, L, and the acoustical compliance, C, of a "lumped element" directly from Newton's Second Law and the Adiabatic Gas Law. Why were we forced to spend so much time working through the hydrodynamic equations? Of course, the answer is that the goal of the hydrodynamic derivations of both L and C was to familiarize you with those equations, as well as to define parameters that will be useful in acoustical network analyses, since they will be applied throughout this textbook to a variety of acoustical problems.

Nondissipative, linearized lumped-element analysis was only our first and our simplest application of hydrodynamics. Their utility will now be demonstrated in the analysis of Helmholtz resonators, which are important in a variety of applications (e.g., noise control, musical acoustics, and optimization of loudspeaker enclosure performance).

8.5 The Helmholtz Resonance Frequency

Having derived expressions (in two different ways!) for the acoustical inertance and acoustical compliance of elements whose dimensions are all small compared to the wavelength of sound, we are now in a position to join those "lumped elements" together to form an *acoustical network*. To do so, we need to know the *joining conditions*. What are the quantities that are continuous at the interface between any two elements?

In this case, the answer will be simple because the variables, p and U, were chosen in our definitions of the acoustical inertance of Eq. (8.47) and the acoustical compliance of Eq. (8.26), specifically to make it easy to join the elements of differing cross-sectional areas to each other. We know that p is

Stretched membranes of this kind are very convenient for these and similar experiments on the partials of compound tones. They have the great advantage of being independent of the ear, but they are not very sensitive for the fainter simple tones. Their sensitiveness is far inferior to that of the *res'onātors* which I have introduced. These are hollow spheres of glass or metal, or tubes, with two openings as shewn in figs. 16 a and 16 b. One opening (a) has sharp edges, the other (b) is funnel-shaped, and adapted for insertion into the ear. This smaller end I usually coat with melted sealing wax, and when the wax has cooled down enough not to hurt the finger on being touched, but is still soft, I press the opening into the entrance of my ear. The sealing wax thus moulds itself to the shape of the inner surface of this opening, and when I subsequently use the resonator, it fits easily and is air-tight.

FIG. 16 a.

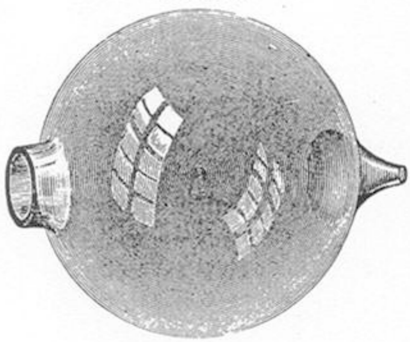

a b

Fig. 8.10 Excerpt from *On the Sensation of Tones* (Dover, 1954), showing the (apparently glass) resonator developed by Helmholtz for frequency analysis. (*a*) is the neck of the resonator and (*b*) is a funnel-shaped tube that is intended for insertion into the ear canal

continuous across an interface, both because of Pascal's law and because the linearized Euler equation (8.40) would lead to infinite accelerations if there were non-zero pressure differences across the interfacial boundary of infinitesimal thickness.

The continuity equation requires that fluid cannot accumulate at the interface between elements (which has no volume), therefore the mass flux must also be continuous. As before, the mass flux and the volume velocity are intimately related, $\dot{m} = \rho U$, so an equivalent requirement is that the volume velocity also be continuous across the interface if the density is continuous, which usually implies that the temperature is the same on both sides of the interface (Fig. 8.10).

Our first application of this "lumped-element" model will be to an acoustical network that has both historical and contemporary significance: the Helmholtz resonator. It was introduced by H. L. F. Helmholtz (1821–1894) in his classic book *On the Sensations of Tone*, published in 1862, in Chapter III, titled "Analysis of Musical Tones by Sympathetic Resonance."

If we examine Fig. 8.11, it is clear that continuity of volume velocity, U, is quite different from continuity of particle velocity, v. To conserve mass, the velocity of fluid flow in the neck of the Helmholtz resonator, v_{neck}, will be much larger than the velocities of the fluid near the neck either inside the volume, v_{volume}, of the resonator or in front of the neck. The streamlines for the flow transition will be bent [9], but if the amplitude of the oscillation is sufficiently small, the transition will be smooth.[9] At higher amplitudes, there could be all kinds of turbulent effects, such as vortex shedding and jetting, which will be irreversible and thus dissipative. These effects can be very important in high-amplitude resonators, but for the present linearized analyses, we are restricting our attention to

[9] The "smallness" criterion for the amplitude of oscillation is somewhat arbitrary, depending upon the desired accuracy of any particular calculation, but a reasonable rule of thumb is to require that the peak-to-peak displacement of the gas in the neck, $2\left|\hat{\boldsymbol{\xi}}\right|$, is at least ten times smaller than the length of the neck: $2\left|\hat{\boldsymbol{\xi}}\right| = 2\left(\left|\hat{\mathbf{U}}\right|/A\right)/\omega < (\Delta x_{neck}/10)$.

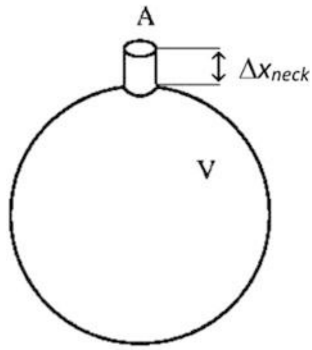

Fig. 8.11 Schematic representation of a gas-filled Helmholtz resonator consisting of a neck (inertance) of cross-sectional area, A, and length, Δx_{neck}, connected to volume, V (compliance), that is assumed to have perfectly rigid walls

Fig. 8.12 This very large set of 22 Helmholtz resonators is in the Garland Collection of Classic Physics Apparatus at Vanderbilt University. They were purchased to outfit the Vanderbilt physics department for the opening of the university in 1875. The tiny funnel-shaped tubes emerging from the tops of the spheres were placed in the experimentalist's ear canal; they are not the "necks" of the resonators. The necks of the resonators fit over wooden pegs in the wooden base that supports the collection

acoustical networks that oscillate by an infinitesimal amount away from their equilibrium state. At this point in our investigations, if such high-amplitude effects occur, then we would just simply decrease the excitation amplitude until they disappear.

In the days before the advent of electroacoustic transducers and amplifiers that could convert sound waves into electrical signals whose frequency content could be determined by electronic filters, spectrum analyzers, and FFT signal analyzers, acousticians could use Helmholtz resonators placed in their ears to determine the frequency of sounds. (Another option was to compare the observed tone to the frequencies of a set of tuning forks, like those shown in Fig. 5.11). Figure 8.12 shows a set of Helmholtz resonators that were used in an acoustic laboratory near the end of the nineteenth century.

As long as 12,000 years ago, Helmholtz resonators were used as musical instruments (e.g., ocarinas) in Asia and Mesoamerica [11]. Another early use of the Helmholtz resonator was as whistles, one version of such a whistle is shown in Fig. 8.13. Peruvian whistling bottles were made in pre-Columbian Peru from 500 BCE (Salinar and Gallinazo cultures along Peru's North Coast) until the Spanish conquest of the Incas (1150 AD) [12]. Today, Helmholtz resonators are used extensively as sound absorbers in architectural applications and as tuned "sound traps" in recording studios, ducts, and engine mufflers. A hollow brick that is used as a resonant absorber in rooms is shown in Fig. 8.14 [13].

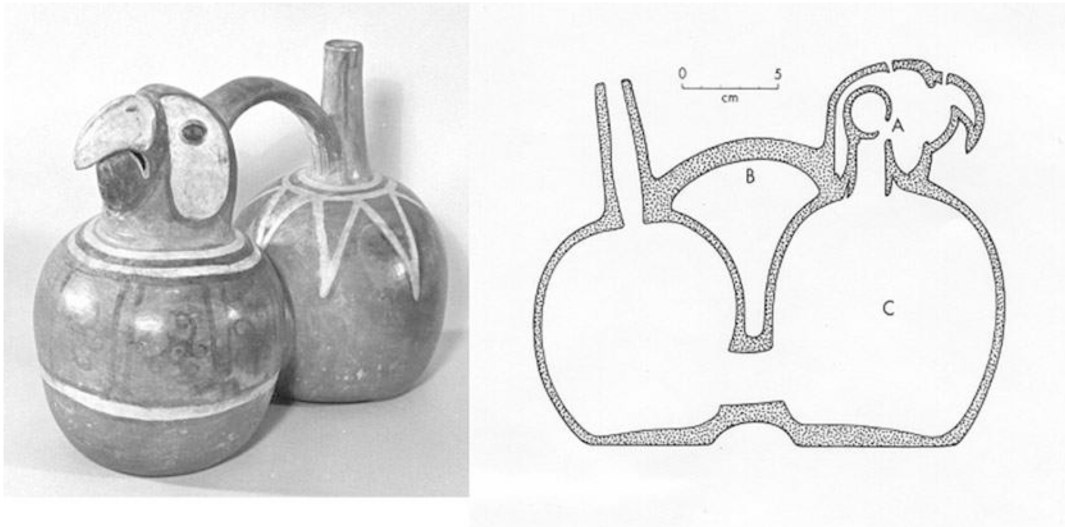

Fig. 8.13 (*Left*) Photograph of a double-chambered Peruvian whistling bottle. (*Right*) Cross-sectional diagram of that bottle [11]. The whistle, enclosed within the bird's head, is made from the Helmholtz resonator (*A*). The bridge handle (*B*) joins the body and the neck. The function of the larger volumes (*C*) is still a matter of controversy after 2500 years. Some say the larger volumes were intended for the storage of fluids, and others claim the vessels were used exclusively as whistles for ceremonial purposes, possibly in conjunction with psychotropic drugs [10]

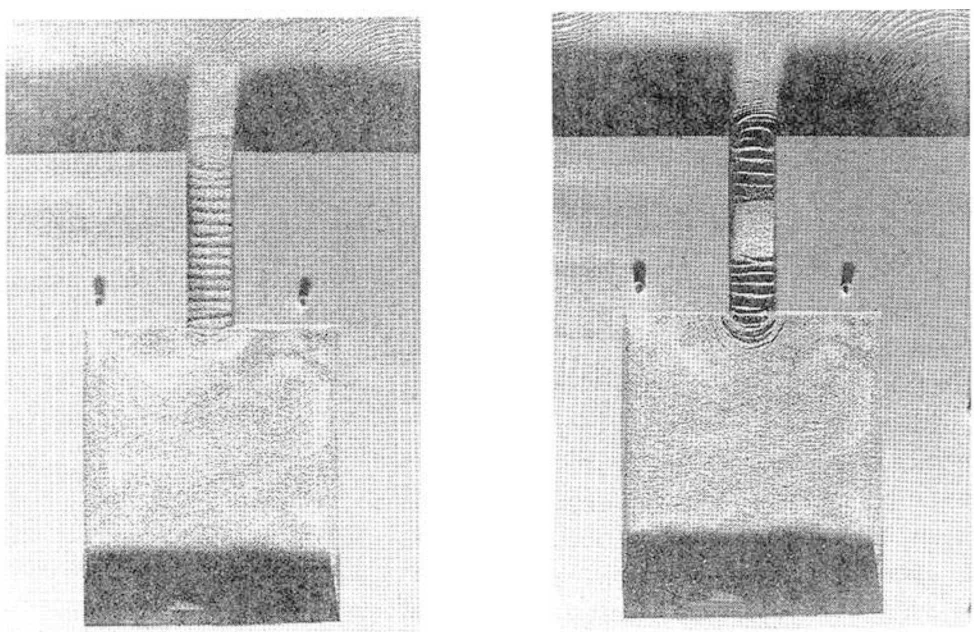

Fig. 9 Helmholtz resonance of the resonator. Fig. 10 Open-pipe resonance of the resonator.

Fig. 8.14 Photographs of two hollow bricks used as low-frequency "tuned absorbers" for reverberation control in buildings. The top of each brick has been removed and replaced with a transparent cover. (*Left*) The brick is being driven at its Helmholtz frequency, $f_o = 210$ Hz. The uniformly spaced striations of the cork dust indicate that the gas is oscillating within the neck with uniform velocity amplitude. (*Right*) The brick is driven at a frequency corresponding to the first open-open standing wave mode of the neck, $f_1 = 1240$ Hz. The absence of striations around the center of the neck indicates that it is the location of a velocity node, while the striations near the neck's ends indicate velocity anti-nodes at those ends [13]

8.5.1 Helmholtz Resonator Network Analysis

We can analyze the response of our Helmholtz resonator by drawing the equivalent circuit shown schematically in Fig. 8.15. For this analysis, we will assume that the resonator is placed in an externally generated sound field with pressure amplitude, $|\widehat{\mathbf{p}}|$, and with angular frequency, ω, so that outside the neck of the resonator, $p(t) = \Re e[\widehat{\mathbf{p}}e^{j\omega t}]$. Since the end of the compliance that is not joined to the neck is sealed, that pressure can only be applied to the compliance through the neck (inertance). For that reason, the "high" end of the voltage generator, representing the externally imposed pressure, is connected to the one end of the neck but is "grounded" to the closed end of the compliance (compare Fig. 8.11 with Fig. 8.15).

The volume velocity that is able to enter the compliance through the resonator's neck represents the resonator's response to the oscillating pressure imposed beyond the neck. Before calculating the amplitude and phase of the (complex) amplitude of the volume velocity as a function of the frequency, $\widehat{\mathbf{U}}(\omega)$, it is useful to consider the limits of the response at frequencies well above and below the resonance frequency of the resonator, ω_o, where the impedance of the inertance, $\boldsymbol{Z_L} = j\omega L$, and the impedance of the compliance, $\boldsymbol{Z_C} = 1/j\omega C$, exactly cancel each other.

From DC to frequencies less than ω_o, the gas flows easily through the neck into the compliance, and the volume velocity amplitude, $\widehat{\mathbf{U}}$, is controlled by the compliance, in accordance with the definition of compliance in Eq. (8.26): $\widehat{\mathbf{U}}(\omega < \omega_o) \cong j\omega C\widehat{\mathbf{p}}$. In this case, because the reactance of the inertance, $X_L = \omega L$, is much smaller than that of the reactance of the compliance, $X_C = (\omega C)^{-1}$, the amplitude of the pressure difference between the ends of the neck, $\Delta\widehat{\mathbf{p}}$ (see Figs. 8.11 and 8.15), is negligible for small ω and $|\widehat{\mathbf{p}}| \geq |\widehat{\mathbf{p}}_{cav}|$.

At frequencies above resonance, ω_o, the inertance of the neck controls how much gas can flow into the compliance: $\widehat{\mathbf{U}}(\omega > \omega_o) \cong \widehat{\mathbf{p}}/(j\omega L)$. At sufficiently high frequencies, the neck blocks flow into the compliance so $|\widehat{\mathbf{p}}_{cav}(\omega \gg \omega_o)| \ll |\widehat{\mathbf{p}}|$, as long as the frequency is still well below that for excitation of the first standing wave mode of the neck, $\omega_{1,}$ shown on the right-hand side of Fig. 8.14, or the resonance frequencies of the volume (see Chap. 13 and particularly Sect. 13.4 if the volume is spherical).

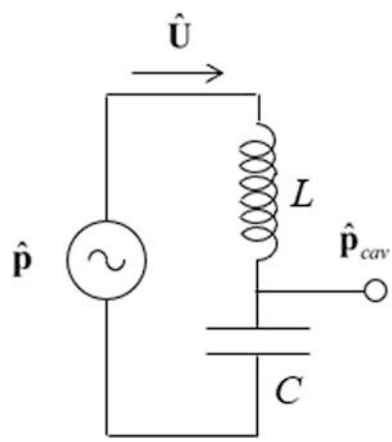

Fig. 8.15 This is an electrical equivalent circuit diagram of the Helmholtz resonator shown in Fig. 8.11. The volume velocity amplitude, $\widehat{\mathbf{U}} = \widehat{\mathbf{u}}A$, is a "current" passing through the neck (inertance) and into the cavity (compliance). That current is driven by an oscillating pressure, $p(t) = \Re e[\widehat{\mathbf{p}}e^{j\omega t}]$, imposed on the end of the neck that is not joined to the cavity (compliance) and is represented by a voltage generator. The voltage that appears at the junction of the inertance and compliance represents the pressure amplitude inside the compliance, $\widehat{\mathbf{p}}_{cav}$. As long as the wavelength of sound is small compared to the characteristic dimensions of the volume, $V^{1/3} \ll \lambda$, then $\widehat{\mathbf{p}}_{cav}$ will be uniform within the compliance

With those frequency limits in mind, we can write down the general expression for the amplitude of the volume velocity that enters the compliance through the neck: $\widehat{\mathbf{U}}(\omega) = \widehat{\mathbf{p}}/\mathbf{Z}(\omega)$. With L and C "in series," the total acoustical impedance, $\mathbf{Z}(\omega)$, is just the sum of the neck's acoustical impedance, $j\omega L$, and the volume's acoustical impedance, $j\omega C$.

$$\mathbf{Z}(\omega) = \mathbf{Z_L} + \mathbf{Z_C} = j\omega L + \frac{1}{j\omega C} \tag{8.49}$$

The acoustical impedance, as written in Eq. (8.25), determines the amplitude of the oscillating component of the pressure, $\widehat{\mathbf{p}}_{cav}$, inside the compliance, based on the control of the amplitude of the volume velocity, $\widehat{\mathbf{U}}(\omega)$, that is imposed by the acoustical impedance in Eq. (8.49).

$$\widehat{\mathbf{p}}_{cav} = \frac{\widehat{\mathbf{U}}}{j\omega C} = \frac{1}{j\omega C}\left[\frac{\widehat{\mathbf{p}}}{j\omega L + (j\omega C)^{-1}}\right] \tag{8.50}$$

The term within the square brackets in Eq. (8.50) incorporates the substitution $\widehat{\mathbf{U}}(\omega) = \widehat{\mathbf{p}}/\mathbf{Z}(\omega)$. When the denominator within the square brackets vanishes, the theory (in its current dissipationless form!) predicts that the pressure inside the compliance will become infinite, since $\mathbf{Z}\,(\omega_o) = 0$ at the Helmholtz resonance frequency.

$$\omega_o = \frac{1}{\sqrt{LC}} = c\sqrt{\frac{A}{V\Delta x_{neck}}} \tag{8.51}$$

The divergence of $|\widehat{\mathbf{p}}_{\mathbf{cav}}|$ as ω approaches ω_o will be eliminated when we add dissipation to our lumped-element model using DeltaEC in Sects. 8.6.7 and 8.6.8 and in the analyses provided in Sect. 9.4.4 that apply the thermoviscous boundary layer losses. The acoustic pressure amplitude in the compliance is "amplified" by the resonance near ω_o and attenuated far above ω_o.

$$\frac{\widehat{\mathbf{p}}_{cav}}{\widehat{\mathbf{p}}} \cong \frac{\mathbf{Z_C}}{\mathbf{Z_C} + \mathbf{Z_L}} = \frac{\omega_o^2}{\omega_o^2 - \omega^2} \quad \text{if} \quad \omega \neq \omega_o \tag{8.52}$$

It is also important to consider the phase of $\widehat{\mathbf{p}}_{cav}/\widehat{\mathbf{p}}$ at low and at high frequencies compared to ω_o, based on the right-hand term in Eq. (8.50). At $\omega \ll \omega_o$, fluid easily enters the compliance, and both $p\,(t)$ and $p_{cav}\,(t)$ are in-phase; when the pressure outside the volume is high, the pressure inside the volume is high also. For $\omega \gg \omega_o$, the sign in the denominator in Eq. (8.50) becomes negative indicating that $p\,(t)$ and $p_{cav}\,(t)$ are 180 degrees (π radians) out-of-phase. That phase reversal is exploited to invert the phase of the radiation from the rear of a loudspeaker cone in a bass-reflex loudspeaker enclosure so it will add to the pressure produced by the front of the loudspeaker, as discussed in Sect. 8.7. In that case, the Helmholtz resonator is used to enhance the low-frequency output of a loudspeaker.

8.5.2 A 500-mL Boiling Flask

With Eq. (8.51), we are now in a position to calculate the frequency of a Helmholtz resonator and compare measured results to the theory. Substitution of the resonator dimension and sound speed, provided in the caption of Fig. 8.16, into Eq. (8.51) predicts $f_o = \omega_o/2\pi = 245.3$ Hz. The experimentally determined frequency is $f_{exp} = 213.8$ Hz. The measured frequency is nearly 13% lower than the calculated result. That discrepancy is far greater than expected based on our ability to accurately determine the flask's physical dimensions or our ability to measure the resonance frequency (about ±1.5 Hz out of 214 Hz or approximately ±0.7%).

Fig. 8.16 Photograph of a 500 ml boiling flask and a B&K 1″ microphone (Type 4144; S/N 473976) mounted on a ring stand. The resonance frequency was determined by blowing over the neck to excite the Helmholtz resonance and measuring the frequency of the microphone signal using an HP 3561A Spectrum Analyzer. The nominal volume of the flask is 500×10^{-6} m^3. The diameter of the neck is $D_{neck} = 25.0 \pm 0.1$ mm, so the neck's cross-sectional area is $A = \pi(D_{neck})^2/4 = 490.9 \times 10^{-6}$ m^2. The length of the neck, as measured from the top of the lip to the first flare into the volume, is $\Delta x_{neck} = 49.2$ mm. The temperature in the laboratory during measurements tabulated in Fig. 8.17 was 22.5 °C, corresponding to a speed of sound, $c = 345$ m/sec. To the right and left of the ring stand are the graduated cylinder and the syringe used to measure the water added to the flask that varied the volume producing the data plotted in Fig. 8.17

As we will see later, this discrepancy is mostly a result of the fact that the oscillating gas flow does not stop abruptly neither at the lip of the neck nor at the neck's entrance into the spherical volume of the boiling flask.[10] The gradual transition of the flow from the oscillations within the neck to the stagnant gas surrounding the exterior of the resonator and inside of the volume is usually represented by a "radiation mass," which we will calculate when we study the radiation from a baffled piston (e.g., loudspeaker) in Sect. 12.8.3 and an unbaffled piston in Sect. 12.9. That additional mass increases the inertance of the neck and is usually incorporated into Eq. (8.51) by defining an "effective length," $\Delta x_{eff} > \Delta x_{neck}$, that is the sum of the physical length (in this case, $\Delta x_{neck} = 49.2$ mm) plus some constant times the radius of the neck.[11]

[10] The frequency is also lowered to a lesser degree by the fact that some of the gas in the spherical volume is being compressed and expanded isothermally in regions close to the boundary and the viscous drag of the gas adjacent to the walls of the neck increase its effective inertance. These effects will be included in the DeltaEC model in Sects. 8.6.10 and 8.6.11. The theory of these thermoviscous boundary layer effects is covered in Chap. 9 and calculated explicitly for a Helmholtz resonator in Sects. 9.4.3 and 9.4.4.

[11] As we will see, the standard "recommended effective length correction" improves the agreement between the measurement and the theory of Eq. (8.51), although it is not exact, since the flow transition between the neck and volume is somewhat shape-dependent as discussed by J. B. Mehl, "Greenspan acoustic viscometer: Numerical calculations of fields and duct-end effects," *Journal of the Acoustical Society of America* **106**(1), 73–82 (1999).

ΔV_i (ml)	Freq. (Hz)
0	213.8
46	225.6
96	236.8
146	252.3
196	273.0
246	301.7
296	333.6

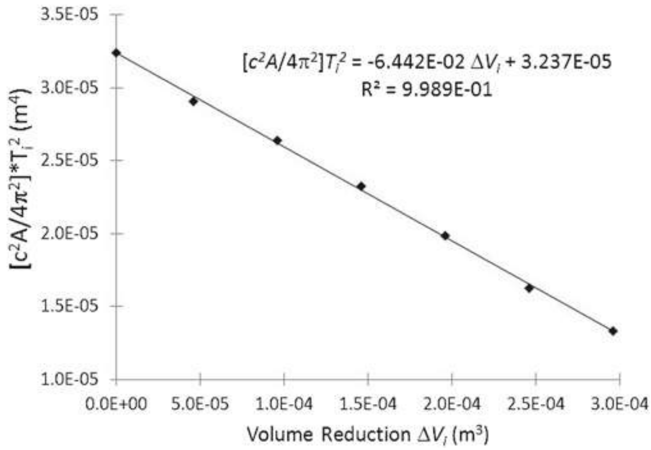

Fig. 8.17 The data in the table at the left is plotted on the graph at the right based on the linearized least-squares expression in Eq. (8.54). The scaled period squared, $[c^2A/4\pi^2]*T_i^2$, is plotted against the added volume of water, ΔV_i. Based on the slope and intercept of the best-fit line (see Sect. 1.9), $\Delta x_{eff} = 64.4 \pm 1.0$ mm, and $V_o = 502.4$ ml

Although we are not ready to make a theoretical calculation of an effective length correction for the neck in our example, we can use Eq. (8.51), and the measured frequency, to make an experimental determination of the neck's effective length based on the measured Helmholtz resonance frequency, f_{exp}.

$$\Delta x_{eff} = \left(\frac{c}{2\pi f_{\text{exp}}}\right)^2 \frac{A}{V} \tag{8.53}$$

Substitution of the measured value for $\Delta V = 0$ in Fig. 8.17 into Eq. (8.53) produces a value of $\Delta x_{eff} = 64.7$ mm, corresponding to a length correction of $\Delta x_{eff} - \Delta x_{neck} = 15.5$ mm $= 1.24a$, where $a = D_{neck}/2$ is the radius of the neck.

In principle, the effective length is independent of the volume of the Helmholtz resonator, as long as the flow contours representing the streamlines from the neck are not perturbed by interactions with the closed end of the volume. We can test this assumption by changing the volume, V, of the resonator. This can be accomplished by injecting measured quantities of water (assumed to be incompressible) into the boiling flask using the apparatus in Fig. 8.16. Neither the sound speed, c, the neck area, A, nor the neck length, Δx_{neck}, would be affected by these incremental changes in volume, ΔV_i.

Equation (8.51) can be rearranged to allow the square of the measured period, $T_i^2 = f_i^{-2}$, to be plotted against the added volume of water, ΔV_i.

$$\left[\frac{c^2}{4\pi^2}A\right]T_i^2 = \Delta x_{eff}(V_o - \Delta V_i) \tag{8.54}$$

The slope of the best-fit line in Fig. 8.17 will determine Δx_{eff}. The empty volume of the resonator, V_o, will also be determined by the fit: $V_o = -$(intercept)/(slope).

It is visually apparent from the quality of the least-squares straight-line fit to the data in Fig. 8.17 that Eq. (8.51) and Eq. (8.54) do an excellent job of representing the behavior of the Helmholtz resonator. The relative uncertainty in the slope can be related to the square of the correlation coefficient for the fit, $R^2 = 0.9989$ (see Sect. 1.9.2), producing a relative uncertainty in the effective length of $\pm 1.5\%$. That is a little better than what would be predicted based on a relative uncertainty in the resonant frequency measurement ($\pm 0.7\%$) and an estimate of the relative uncertainty in the volume changes of about 1 ml $\div$ 50 ml $= 2\%$. It is also encouraging that the ratio of the intercept to the slope produced an effective empty volume for the resonator of 502.4 ml.

8.6 DeltaEC Software

To this point, we have not yet exploited the power of digital computation beyond the generic spreadsheet and curve-fitting programs provided by mass-marketed commercial software packages. Several software packages have been developed specifically to serve the acoustic community. In underwater acoustics, ray-tracing programs are very popular, as are commercial packages such as LMS Sysnoise [14] used for modeling sound in three-dimensional spaces, BassBox Pro [15] for designing loudspeaker enclosures, or X-OverPro for designing loudspeaker crossovers.

The program that has become an important tool for thermoacousticians [16] since 1985 is the *Design Environment for Low-amplitude Thermoacoustic Energy Conversion* (DeltaEC). Drs. G. W. Swift and W. W. Ward developed it at Los Alamos National Laboratory for design and analysis of thermoacoustic engines, refrigerators, and gas mixture separators. It was updated in 2013 to provide an improved user interface with the help of John Clark [17]. Although it has the capability to model heat exchangers and porous media used in such thermoacoustic systems, DeltaEC is also well-suited to the design and/or analysis of any quasi-one-dimensional acoustical network consisting of ducts, horns, waveguides, compliances, branches, flow impedances, and loudspeakers in a variety of fluid media bounded by a variety of solids.[12]

Its results have been tested extensively in laboratories worldwide, and it executes calculations very quickly. This high computational speed is accomplished by using analytical results for the transverse variation in the complex pressure and velocity fields. For example, in a CONE segment, solutions to the Webster horn equation [18] provide the pressure as a function of position even through the cross-sectional area is changing and there are non-zero radial components of the fluid's velocity.

DeltaEC numerically integrates along one spatial dimension using a low-amplitude, acoustic approximation[13] assuming sinusoidal time dependence, $e^{j\omega t}$. It simultaneously integrates the continuity equation (7.32), the Navier-Stokes equation (7.34), and other equations, such as the energy equation, in a geometry specified by the user's choice of a sequence of "segments," such as ducts, compliances, transducers, heat exchangers, and thermoacoustic stacks or Stirling regenerators. DeltaEC always assumes steady-state conditions and harmonic time dependence of all acoustic variables.

We will use DeltaEC initially to revisit the 500 ml flask used as a Helmholtz resonator in the example of Sect. 8.5.2. Since DeltaEC includes the dissipative effects that we have ignored thus far, it

[12] The current version of DeltaEC includes the thermophysical properties of the following gases and liquids: nitrogen, dry air, humid air, carbon dioxide, hydrogen, deuterium, helium, neon, He/Ar and He/Xe gas mixtures, natural gas combustion products, liquid sodium, and sodium/potassium eutectic (NaK). Solids include an "ideal" solid with infinite heat capacity and infinite thermal conductivity, copper, nickel, stainless steel, tungsten, molybdenum, Kapton®, Mylar®, and Celcor® (a porous ceramic matrix). It also allows the user to create their own $*$.tpf file to represent the temperature and pressure-varying thermophysical properties of user-specified fluids and solids.

[13] DeltaEC also supports some nonlinear (i.e., high-amplitude) acoustical effect such as boundary layer turbulence, "minor loss," and amplitude-dependent interfacial discontinuities.

will provide some additional performance information, as well as serve as a familiarization exercise for the software.

8.6.1 Download DeltaEC

The latest version of DeltaEC is freely available on the web. Before downloading the software, the *DeltaEC User's Guide*, and sample DeltaEC files, it is a good idea to create a DeltaEC "folder" in your computer's main directory. The following link would take you close to the download site:

http://www.lanl.gov/thermoacoustics/DeltaEC.html
The DeltaEC software installer is also available at the Springer web site for this textbook and the Springer site for Swift's textbook *Thermoacoustics: A Unifying Perspective for Some Engines and Refrigerators*. [21].

You will have to unzip (Mac) or execute (Windows) the file. That process also installs a copy of the *DeltaEC User's Guide*. The manual is in ∗.pdf format and contains searchable hyperlinked text. We will only be concerned with the first four chapters of the *Guide*, but the Reference Sections (Chaps. 8, 9, 10, 11 and 12) are very useful once you have learned the basics. The Reference Sections also contain the equations that are implemented in the software.

This textbook will employ a "two-pronged approach" to familiarize you with some of the elementary acoustical functions that are provided by DeltaEC. The primary sources of information are the first four chapters of the *User's Guide*. The first chapter provides some background on the software and how it functions. The second chapter introduces the user interface by modeling the 1992 Penn State Championship Bottle both as a Helmholtz resonator and as an open-closed standing wave resonator of variable cross-section (see Problem 6 at the end of this chapter). The plotting features of DeltaEC are covered in the third chapter, and the reverse Polish notation (RPN) segment, which lets the user perform customized calculations within a model, is covered in the fourth chapter and introduced here (briefly) toward the end of Sect. 8.6.8.

Although the *DeltaEC User's Guide* should be your primary reference for exploitation of DeltaEC software, the *Guide* will be augmented in this textbook by providing several examples in the remainder of this section and the next. These examples are directly related to acoustical networks that have already been analyzed and will apply DeltaEC to model a standing wave resonator, the 500 ml Helmholtz resonator from Sect. 8.5.1, three coupled Helmholtz resonators in Sect. 8.7, and a bass-reflex loudspeaker enclosure based on the Helmholtz resonator model in Sect. 8.8.

8.6.2 Getting Started with DeltaEC (Thermophysical Properties)

After installing the DeltaEC software on all of your computers, a DeltaEC icon should appear on each computer's desktop near the lower left corner of the screen. You can open DeltaEC by double-clicking on the icon. The design of that icon is motivated by the thermal core of a traveling-wave thermoacoustic engine developed at Los Alamos National Laboratory [19].

DeltaEC usually requires the thermophysical properties of both the fluid supporting the wave and the properties of the solid that contains the fluid in each segment to execute the integrations. We can access this feature directly to have DeltaEC provide these data. When you open DeltaEC by clicking on the icon (instead of opening an existing ∗.out file), you will be presented with a "window" that is blank but has pull-down menus at the top. Under the "Help" menu, you can access the *User's Guide*. Under the "Tools" menu, you can access the ThemoPhys(ical) Prop(erties) window shown in Fig. 8.18.

Fig. 8.18 Screenshot of the DeltaEC Thermophysical Properties window. The default material parameters are for 1 bar (100,000 Pa) helium gas at 300 K and an acoustic excitation at 100.0 Hz

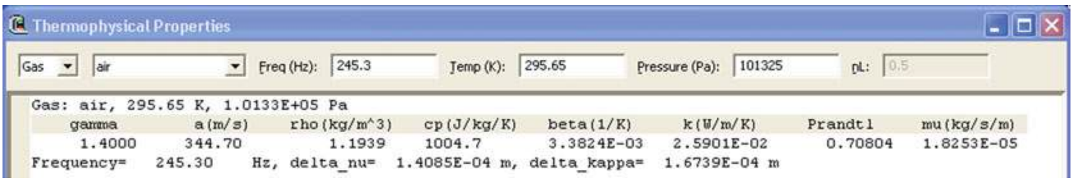

Fig. 8.19 Screenshot of the thermophysical values for the air used in the 500 ml Helmholtz resonator of the example in Sect. 8.5.2

That window can also be opened from the keyboard by typing "t" when the computer's attention is on the main DeltaEC window.

As our first example, we'll use the environmental conditions under which the algebraic results for the 500 ml Helmholtz resonator (Figs. 8.16 and 8.17) were calculated to provide the equilibrium fluid parameters for the air inside that resonator. In the Thermophysical Properties window, modify the gas type to be "air" using the pull-down arrow, the frequency to be 245.3 Hz, and the pressure to be standard atmospheric pressure of 101,325 Pa. Since DeltaEC variables are specified exclusively in MKS units, the temperature must be input in absolute [kelvin] units. The data for our 500 ml example was taken at 22.5 °C, so input the absolute temperature, $T_m = (22.5 + 273.15)$ K $= 295.65$ K, into the "Temp(K)" window.

With all of those values appearing in their appropriate location, use your mouse to click on "Show." This should instantly generate the requested thermophysical properties of air under the specified conditions as shown in Fig. 8.19.

The thermophysical property file header in Fig. 8.19 includes the fluid type (air), the mean temperature ($T_m = 295.65$ K), and the mean pressure ($p_m = 101{,}325$ Pa). The second line contains the frequency-independent fluid properties and their associated units. The first four parameters in the top line are the ratio of specific heats "`gamma`," sound speed "`a(m/s)`,"[14] density "`rho(kg/m^3)`," and specific heat at constant pressure "`cp (J/kg/K)`." These parameters should already be familiar.

The subsequent transport parameters will be discussed in Chap. 9, where the dissipative terms in Eqs. (7.34) and (7.43) are analyzed. The isobaric coefficient of thermal expansion, $\beta_p = -(1/\rho)(\partial\rho/\partial T)_p$, "`beta (1/K)`," is just the reciprocal of the absolute temperature, T_m, for an ideal gas. In our case, $\beta_p = (1/T_m) = 0.33824 \times 10^{-2}\ \text{K}^{-1}$, agreeing with the DeltaEC output to the five decimal places displayed. Next in line are the thermal conductivity, "`k(W/m/K)`"; the dimensionless Prandtl number (see Sect. 9.5.4), "`Prandtl`"; and the shear viscosity, "`mu(kg/s/m)`."

The bottom data line in Fig. 8.19 lists the frequency, "`frequency=`," and two frequency-dependent results: the viscous boundary layer thickness, "`delta_nu=`," also known as the viscous

[14] The Los Alamos Thermoacoustics Group uses Rayleigh's traditional notation for sound speed, a, instead of the more contemporary choice of c to represent sound speed. This is because c is used quite frequently in thermoacoustics to designate specific heats.

penetration depth, δ_ν, and the thermal boundary layer thickness, "delta_kappa=," aka the thermal penetration depth, δ_κ, which will be derived and discussed thoroughly in Chap. 9.

8.6.3 Creating planewave.out

There are several ways to create a DeltaEC model of an acoustical network. The result of such a model is a ∗.out file that consists of a sequence of segments like those shown in Fig. 8.21. One can start "from scratch," but I generally prefer to modify an existing file using the file editing commands in DeltaEC.

We will start by creating a file "from scratch" that represents a simple plane wave resonator of constant cross-section that is shown schematically in Fig. 8.22 and will result in the DeltaEC model shown in Figs. 8.20 and 8.21. Once we gain some experience with the way DeltaEC expects you to insert segments and input the parameters contained within each segment, we will modify planewave.out to create a DeltaEC model of the Helmholtz resonator example based on the 500 mL boiling flask in Sect. 8.5.2. To begin creating "planewave.out," you should have already downloaded DeltaEC from the Los Alamos Lab's "Thermoacoustics Home Page."

If DeltaEC is still open (because you were working on the thermophysical example), you can go to the "File" pull-down menu tab, and click "New." That action will produce a file with a single BEGIN segment and title the model "NewModel." Next to "NewModel" is "Change Me" in a blue font. By double-clicking on an item in a blue font, you are able to change it. Double-click on "Change Me" and type in "Planewave Resonator." There will also be a box that will let you add comments, but we won't put in any comments, so just click the "OK" button.

Before going further, now would be a good time to save the file. This is done by going to the "File" drop-down menu and selecting "Save As." Chose the directory in your computer where you would like to save this file (a convenient choice is the same folder that holds the DeltaEC program), and then title the file "planewave.out." You will see that the "tab" at the top of the DeltaEC model will change its name from "NewModel" to "planewave." As we add segments, it is a good idea to "Save" the file at regular intervals or before quitting.

BEGIN Segment. All DeltaEC models start with a BEGIN segment that specifies the "global" features of the model, like the gas or liquid type (e.g., helium, air, humid air, sodium, etc.); the mean fluid pressure, p_m; the mean temperature of the fluid at the start of the model, T_m; and the acoustic frequency, f. You can see these parameters when you click on the "+" sign at the left of BEGIN. This will "unpack" the segment and let you see the parameters it specifies. For very long models, being able to unpack individual segments with the "+" or "compact" with the "−" can be convenient.

In the unpacked form, you see seven parameters in blue font that we are free to modify. For this example, we'll accept the default values for (0a) = Mean P = 100 kPa, (0b) = Freq = 100 Hz, and the beginning temperature, (0c) = TBeg = 300 K. We'll also accept the default Gas Type as helium. We can ignore the "Optional Parameters" for now. The use of the segment number and

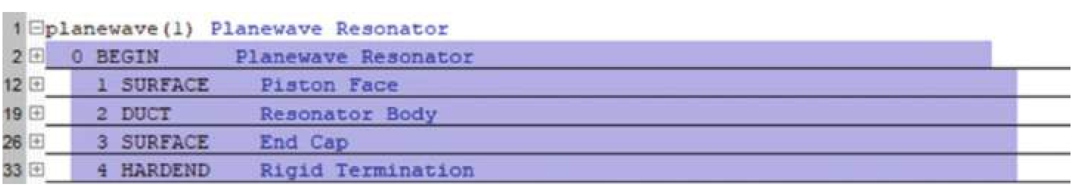

Fig. 8.20 Screenshot of the file "planewave(1).out" is shown before the individual segments are expanded. At the left are the line numbers that you will notice are not consecutive. That is because several lines are suppressed and only the segment numbers and their titles are shown

```
⊟planewave(1)  Planewave Resonator
 ⊟  0 BEGIN          Planewave Resonator
                  1.0000E+5 a Mean P Pa
                     100.00 b Freq   Hz
                     300.00 c TBeg   K
 Gues                1000.0 d |p|    Pa
 Gues                0.0000 e Ph(p)  deg
                  1.0000E-2 f |U|    m^3/s
                     0.0000 g Ph(U)  deg
 Optional Parameters
 helium          Gas type
 ⊟    1 SURFACE       Piston Face
                  1.0000E-2 a Area   m^2                   0.0000 A |p|    Pa
                                                           0.0000 B Ph(p)  deg
                                                           0.0000 C |U|    m^3/s
                                                           0.0000 D Ph(U)  deg
                                                           0.0000 E Htot   W
 ideal           Solid type                                0.0000 F Edot   W
 ⊟    2 DUCT          Resonator Body
        Same   1a 1.0000E-2 a Area   m^2      Mstr         0.0000 A |p|    Pa
                    0.35449 b Perim  m        2a           0.0000 B Ph(p)  deg
                     5.0000 c Length m                     0.0000 C |U|    m^3/s
 Master-Slave Links                                        0.0000 D Ph(U)  deg
 Optional Parameters                                       0.0000 E Htot   W
 ideal           Solid type                                0.0000 F Edot   W
 ⊟    3 SURFACE       End Cap
        Same   2a 1.0000E-2 a Area   m^2                   0.0000 A |p|    Pa
                                                           0.0000 B Ph(p)  deg
                                                           0.0000 C |U|    m^3/s
                                                           0.0000 D Ph(U)  deg
                                                           0.0000 E Htot   W
 ideal           Solid type                                0.0000 F Edot   W
 ⊟    4 HARDEND       Rigid Termination
 Targ                0.0000 a R(1/z)                       0.0000 A |p|    Pa
 Targ                0.0000 b I(1/z)                       0.0000 B Ph(p)  deg
                                                           0.0000 C |U|    m^3/s
                                                           0.0000 D Ph(U)  deg
 Possible targets                                          0.0000 E Htot   W
                                                           0.0000 F Edot   W
```

Fig. 8.21 Screenshot of the fully expanded file "planewave(1).out" before running the program. Since the file has not yet run, all of the results contained in the right-hand column are *red*. These "results," which are designated with capital letters, contain only *red zeros*. The highlighted "Gues(ses)" on lines 0d and 0e indicate the pressure magnitude, and phase, `|p|` and `Ph(p)`, are the "guesses." Their values are also red because the program has not yet modified those guesses to satisfy the "targets." The highlighted "Targ(ets)" on line (4a) and line (4b) indicate that those values are "targets." DeltaEC will attempt to adjust the values of the guesses to meet the targets when the program is run

parameter in parentheses is a convenient way to identify parameters in the model. Notice again that all parameters are specified in MKS units.

Our intention will be to drive this resonator with a sinusoidally varying volume velocity. We'll set the initial volume velocity magnitude, (0f) = |U| = 0.010 m^3/s, by clicking on the blue 0.0000 in the (0f) position. Doing so should bring up the "Parameter Edit: 0f |U|" window. Type 0.01 into the "Value" line and then click "OK." That should assign 1.0000*E* − 2 m^3/s as the value for (0f). By leaving (0 g) = `Ph (U)` = 0, we define all other phases in the model with respect to the phase of the driving volume velocity.

Since we are specifying the volume velocity that will drive the resonator, we will rely on DeltaEC to calculate the resulting acoustic pressure magnitude, `|p|`, and the phase of that pressure, `Ph (p)`, with respect to `Ph (U)` = 0 `deg.` at any frequency, `Freq` = (0b). To impose this choice, we can double-click on 100 that is the default value in (0d) to open the "Parameter Edit: 0d |p|" window. Type in 1000 for the Value, check the "Set as Guess" box, and click "OK." This brings up a Gues label to the left of (0d) to remind us that DeltaEC will be allowed to modify this value of $|\hat{\mathbf{p}}|$ to satisfy the model and its boundary conditions. It also puts our guess for pressure in red font to warn us that its value is not based on a solution of the model: (0d) = `|p|` = 1000.0 Pa. Since we don't know the phase of the pressure with respect to volume velocity, we also need to make (0e) = `Ph (p)` a guess. Just click on the default value 0.0000 to bring up the "Parameter Edit: 0e Ph(p)," check the "Set as Guess" box, and click "OK."

This indicates that the values are only "guesses" and DeltaEC's "shooting method" has been given "permission" to change those values to satisfy constraints placed on the model by the quantities that have been designated "targets." In this file, those "targets" will be the rigid (infinite) impedances specified in the final HARDEND segment, (4a) and (4b). That completes the BEGIN segment.

SURFACE Segment. Now we can specify the area of the "piston" that will produce the volume velocity we specified in (0f). Although we could just let the BEGIN segment produce that volume velocity, since the end of the resonator has some surface area, including a SURFACE segment after the BEGIN segment will mean that any dissipation on that "end cap," acting as a piston, will be included in our model. To add this next segment, just "right click" in the model, and an "Append" option will appear with a list of possible segments listed alphabetically. You may have to use the arrow to scroll down to see SURFACE. When it appears, just click on it, and DeltaEC will add the new SURFACE segment to your model.

It is useful to name the segment, so click on "`Change Me`" that is to the right of SURFACE, type in "Piston Face," and then click "OK." Again, we will not include any comments. SURFACE has only one parameter and we'll set it to (1a) = `Area` = 0.01 m^2. Just click on 0.0000 to bring up the "Parameter Edit: 1a Area" window, enter a "Value" of 0.01, and then click "OK." SURFACE is a solid, so the segment allows specification of "`Solid Type`." Accept the default value of "`ideal`." "Ideal" just means that we want DeltaEC to assume the solid has infinite heat capacity and infinite thermal conductivity, resulting in a surface that holds the gas isothermal at the gas-solid interface.[15] If you double-click on "`ideal`," it will bring up the menu of other built-in solid materials (e.g., stainless steel, copper, mylar, etc.). All physical segments in DeltaEC require specification of the gas type and/or solid type.

Unlike the BEGIN segment, the SURFACE segment has a list of six "Results," from (0A) = `|p|` to (0F) = `Edot`, at the right-hand side of the segment. All of the numerical results are in red font to warn us that the model has not run and that the current values are only placeholders. After the program has run successfully, all of the results that are currently shown in red will change to green, indicating the upgrade in the model status to actual "results."

The results will be discussed once the model is complete and has run successfully in Sect. 8.6.4. Now might be a good time to "Save" the file to include the newest segment either by using the "File"

---

[15] The ability of a solid to hold the temperature of the gas constant at the solid-gas interface is quantified by the ε_s parameter discussed in G. W. Swift, "Thermoacoustic engines," *Journal of the Acoustical Society of America* **84**(4), 1145–1180 (1988), Eq. (59). For most solids in contact with ideal gases at "ordinary" pressures, $\varepsilon_s \cong 0$, although if a sound wave is propagating through a liquid metal it is impossible to specify any solid material with sufficient heat capacity and thermal conductivity to hold the liquid isothermal at the liquid-solid interface.

drop-down menu or by simply clicking on the "floppy disk" icon on the banner beneath the drop-down menus.

DUCT Segment. We now add the resonator, a tube of circular cross-section. "Right click" in the model to activate the "Append" option and choose DUCT. Click on "Change Me" that is to the right of DUCT, name this segment "Resonator Body," and then click "OK." To specify the DUCT's cross-sectional area (2a), click on the default value to bring up the "Parameter Edit: 2a Area" window. This time we will not enter a value but instead click on the "SameAs" button. Since the only other parameter in our model with units of area is (1a), DeltaEC has guessed that (1a) might be a good choice. This is correct, so just click "OK." That will make the area of the DUCT the same as the area of the SURFACE (piston) segment. Choosing to link those areas makes it easy to change the cross-sectional area of the entire model by just changing the cross-sectional area of the piston.

DeltaEC has also chosen to make a "Master-Slave" linkage. It automatically chose the DUCT's `Perimeter` (2b) to be equal to 0.35449 m. DeltaEC guessed that our DUCT was circular and made the `Perimeter`, $\Pi = \sqrt{4\pi A}$. It also placed a notice to the right of (2a) and (2b) to remind us of that link with "`Mstr 2a`" to indicate that the value of (2a) is controlling the value of (2b). Again, if we chose to modify the cross-sectional area of the DUCT, then that Master-Slave link would keep the DUCT's cross-section circular. To accommodate ducts of different shape, the perimeter of the duct (2b) can be specified independently from its area (2a). You can see that choice if you double-click on Master-Slave Links to bring up the dialog box that has made the default choice: "Maintain constant perimeter as area changes." Double-click on the `Length` (2c) and make the length of the DUCT be 5.00 m.

Although DeltaEC claims to work for "low-amplitude" acoustics, there are features that allow models to incorporate some nonlinear fluid dynamics to accommodate higher amplitudes. Double-click on the `Optional Parameters` to open a dialog box that will let you choose low-amplitude (laminar) flow or high-amplitude (turbulent) flow. Click on the "Laminar" button. For turbulent flow, you would also have to specify a surface roughness factor.

SURFACE Segment. Append another SURFACE segment to represent the other end of the resonator. Name that segment "End Cap," then double-click on the `Area`, and make it "SameAs" (2a).

HARDEND Segment. The final HARDEND segment is a "logical" segment that is required to complete the file. It is one of only two possible choices, the other being SOFTEND. Use "Append" to add the final HARDEND segment and rename it as "Rigid Termination."

In a SOFTEND segment, the real and imaginary parts of the impedance are specified by the user. If the SOFTEND is infinitely "soft," then both the real part of the impedance, R (4a), and the imaginary part, I (4b), are zero. Of course, there are other choices that would make sense in other situations. For example, the real part of the SOFTEND impedance could be made equal to $\rho_m c/A$ for a duct to create an anechoic termination that would make the solution a traveling wave instead of a standing wave, as discussed in Sect. 3.6.3 for a string with a resistive termination.

For an ideal HARDEND, the impedance is infinite. Since ∞ is a difficult concept for a computer, HARDEND requires specification of the real and imaginary parts of the complex admittance, which is the (complex) reciprocal of the impedance. For an infinitely rigid and lossless HARDEND condition, $\Re e\,[1/z] = \Im m\,[1/z] = 0.0000$, as shown in lines (4a) and (4b) of Fig. 8.21.

We will make each of those rigid boundary conditions a "Target" that DeltaEC will attempt to satisfy. This is done by double-clicking on "`Possible Targets`." That will bring up a dialog box that allows us to select the first two of three possible targets. Check the box next to (4a) to make the real (i.e., dissipative) part of the admittance a target, `R(1/z)` $= 0$, and check the second box (4b) to make the imaginary (i.e., reactive) part of the admittance, `I(1/z)` $= 0$, also a target. To the left of both of those entries is "Targ." If you double-click on zero in either (4a) or (4b), you will open the dialog box that shows that the "Set Target" box has been checked. This now designates the values

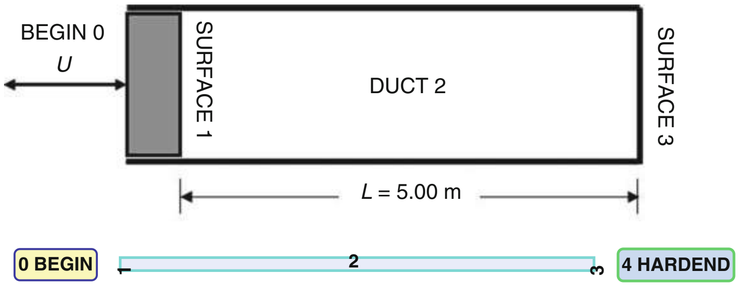

Fig. 8.22 (*Above*) A schematic diagram (not to scale) of the helium-filled plane-wave resonator modeled by planewave. out. The cross-sectional areas of the two SURFACE segments and the DUCT are all 0.010 m^2. (*Below*) This drawing is generated by DeltaEC's "View Schematic" function available under the "Display" pull-down menu. It preserves the physical shape of this long, slender resonator. The numbers in the drawing generated by DeltaEC correspond to the segment numbers in the model displayed in Fig. 8.20 (collapsed) and Fig. 8.21 (expanded)

specified in (4a) and (4b) as "targets" that DeltaEC's "shooting method" will try to make the results in 4G and 4H equal to those targets by modifying the values of guesses, 0d and 0e.

At this point, you should be sure to "Save" the model and then compare it to the screenshot in Fig. 8.21. If you click the "⊞/⊟" icon in the banner, the entire model should collapse to just the segment titles as shown in the screenshot in Fig. 8.20. Click on that icon again and all of the segments for the entire model should "unpack."

Figure 8.22 provides a schematic diagram of the physical resonator's parts that are modeled in the planewave.out file shown above the "schematic" generated by DeltaEC's "View Schematic" function available under the "Display" pull-down menu. I like to check the schematic view since it is drawn to scale. If I've entered a geometrical parameter incorrectly (e.g., a length in centimeters instead of meters), then the schematic view will look incorrect.

8.6.4 Running planewave.out

There are two ways to run DeltaEC. One way is to just let the program integrate its way through a file starting at the BEGIN statement. If complex $\widehat{\mathbf{p}}$ and $\widehat{\mathbf{U}}$ are specified in the BEGIN segment, then DeltaEC just integrates its way through the model, matching the complex values (both magnitude and phase) of $\widehat{\mathbf{p}}$ and $\widehat{\mathbf{U}}$ at the interfaces between segments of the model. I find that I rarely use that mode because most models have constraints that are not specified in the BEGIN segment and those constraints determine the values of $\widehat{\mathbf{p}}$ and $\widehat{\mathbf{U}}$ in all of the segments, including BEGIN, as was the case with the HARDEND condition in segment (#4) that dictated the complex pressure in the BEGIN segment (#0), given the amplitude of the excitation by the assumed volume velocity of magnitude, $|U| = 0.01$ m^3/s, in (0f).

Most of the time, I use the "equation solver" mode that lets DeltaEC adjust the "guesses" in an attempt to achieve the "targeted" values. The "shooting method" requires that there be an equal number of guesses and targets.[16] They can be viewed at any time by going to the "Display" pull-down menu and selecting "Guesses Targets." You can also access this display from the keyboard by typing "g" while the computer's focus is on the main DeltaEC window.

[16] In using DeltaEC, choosing the guesses and targets will require that the user have a reasonably good understanding of the network that is being modeled. For example, targeting the frequency while guessing the pressure would make no sense, since the sound speed of an ideal gas is pressure-independent, as demonstrated in Sect. 10.3.2.

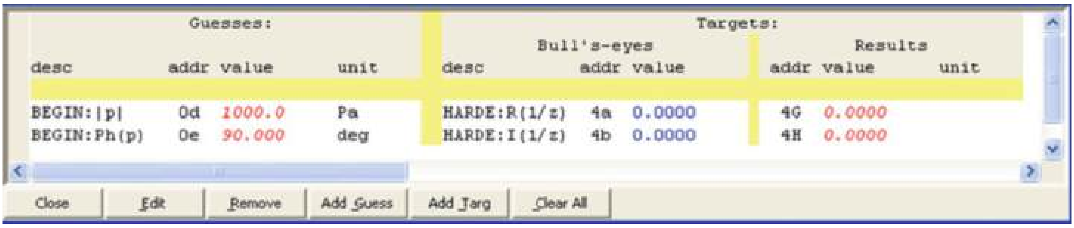

Fig. 8.23 Screenshot of the "Guesses and Targets" window shows the current choices of guesses that the solver will modify to reach the targets. The targeted values are in *blue*, but the guesses and the results are still in *red*, since the program has not yet been run. The *red* values of `|p|` and `Ph(p)` are the values that were input to the file. Since these are designated "guesses," DeltaEC will change them in an attempt to force the real part of the admittance, `R(1/z)` in (4a), and the imaginary part, `I(1/z)` in (4b), to both simultaneously be zero

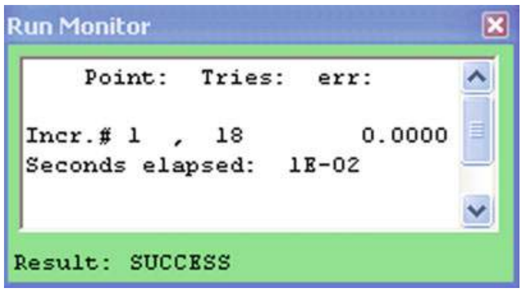

Fig. 8.24 Screenshot of the Run Monitor window after running planewave.out once. The Run Monitor says that a successful result was achieved after 18 iterations in the span of only 10 milliseconds. The "error" = 0.0000 is a measure of how close to the targeted values the program was able to reach by adjusting the guesses. (The "error" is the length of a vector that DeltaEC creates to represent the distance between the results and the targets. The user is free to provide weights for the components of the error vector that may differ from the DeltaEC defaults)

The particular choice of targets and guesses shown in Fig. 8.23 implies that we will be asking DeltaEC to determine the response of the modeled system to a volume velocity of 0.010 m^3/s imposed on one end of the resonator at a frequency of 100 Hz.

The time has come to run planewave.out. The run starts either (*i*) by clicking on the blue run arrowhead at the top of the DeltaEC window, (*ii*) by going to the "Tools" pull-down menu and selecting run, or (*iii*) by typing "r." DeltaEC responds by generating a "Run Monitor" window that is shown in Fig. 8.24. We can view the Guesses Targets window again and see how the guesses have changed. We see that under the specified conditions ($|U|$ = 0.010 m^3/sec and *Freq.* = 100 Hz), the pressure at the piston location (0d) is 3,853.2 Pa and the phase difference between $\widehat{\mathbf{U}}$ and $\widehat{\mathbf{p}}$ at that location is 41.520°.

Looking back at the expanded planewave.out file, we see that all of the results in the right-hand column and both guesses, (0d) and (0e), have changed from red to green indicating that the solver has found a self-consistent solution.

8.6.5 Finding the Resonance Frequencies of planewave.out

As we might imagine, there is nothing special about operation at 100 Hz. We could ask DeltaEC's solver to find the fundamental half-wavelength, $\lambda/2$, resonance frequency, f_1. Before doing so, let's run

Thermophysical Properties to get the speed of sound under the current conditions within the resonator: c (or a) = 1019.2 m/s. Simple nondissipative acoustical theory suggests that the fundamental frequency, $f_1 = c/2\,L = 101.92$ Hz, much like the fundamental frequency of the fixed-fixed string in Sect. 3.3.1. If we remove the phase of the pressure (0e) from the guess vector and instead make frequency (0b) a guess, we can have DeltaEC's solver find the resonance frequency. ***By setting the phase of the pressure (0e) to be the same as the phase of the volume velocity (0 g), the power delivered to the resonator from the piston is maximized.*** This is exactly the same result that determined the resonance of the damped, driven simple harmonic oscillator in Sect. 2.5.

We make the changes suggested above by returning to the "Guesses Targets" window or the expanded planewave.out file, clicking on the BEGIN:Ph(p) entry, then pressing the "Delete" button, and confirming the choice by pressing the "Yes" button in the "Clear Guess" window. Now we must add frequency as a guess. This is done by clicking the "Add Guess" button command and responding with 0b, the address of frequency in the BEGIN segment. We must also make the pressure be in-phase with the volume velocity by forcing 0e = 0°. This is easily accomplished by simply clicking on the value of 0e in the planewave.out file and changing its value from 43.6° to 0°.

Alternatively, the previous changes to the guesses and the reset of pressure phase (0e) to zero could have been accomplished by going directly to the expanded version of the BEGIN segment (#0) and double-clicking on 43.6°, which will bring up a "Parameter Edit: 0e Ph(p)" dialog box. Typing "0" into the value and unchecking "Set as Guess" will have the same effect as the procedure using the "Guesses Targets" window. Double-clicking on the frequency will again bring up the "Parameter Edit: 0b Freq" dialog box, and clicking on "Set as Guess" will make (0b) the second "Guess."

Now run the program again. This time the Run Monitor tells us that DeltaEC made 10 runs in 10 msec. The frequency (0b) has changed to 100.91 Hz (just a bit lower than our estimate of 101.92 Hz, because our half-wavelength calculation ignored dissipation), and $|p|$ has increased to 5,132.8 Pa from 3853.2 Pa, which was its value when we were near resonance at 100 Hz, but not at resonance.

To demonstrate the versatility of the DeltaEC solver, let's change the frequency back to 100 Hz, and ask DeltaEC to "tune" the length of the resonator to put the fundamental resonance exactly at 100 Hz at the specified value of the mean gas temperature. We return to the "Guesses Targets" window to "Delete" (0b) from the guess vector and make its value 100.0 Hz. This time, click on the value of the duct length (2c). When the Parameter Edit window opens, you will have the option of checking a box which says "Set as Guess." Check the box. If you look at the "Guesses Targets" window, you will see that the DUCT: Length (2c) is now a guess.

Run the program again to now calculate the length that the DUCT segment would be required to make 100.0 Hz the resonance frequency. As expected, to lower the frequency by just under 1%, the length has grown by just under 1% to 5.0453 m.

In a lossless plane wave resonator with rigid ends and uniform cross-sectional area, the higher resonances corresponding to integer numbers of half-wavelengths fitting between the ends to produce a harmonic series of resonance frequencies, $f_n = nf_1$, where $n = 1, 2, 3, \ldots\infty$, just as we observed with the fixed-fixed string in Sect. 3.3.1. To have DeltaEC calculate a few of these overtones, remove DUCT: Length (2c) from the guesses, replace it with BEGIN: Freq (0b) as the "guess," and then change the value of (0b) in the file to 200 Hz. If you run again, DeltaEC finds $f_2 = 200.80$ Hz. Modify frequency (0b) again to be 300 Hz to look for $f_3 = 302.68$ Hz. The reason the sequence of harmonics is not exactly in integer ratios is that there is dissipation and dispersion within the resonator. We will be able to understand (calculate!) these effects from the acoustic solutions of the hydrodynamic equations once dissipation has been introduced in Chap. 9 and the plane wave solutions to those equations are covered in Chap. 10.

8.6.6 State Variable Plots (∗.sp)

We can convince ourselves that DeltaEC has found the fundamental resonance frequency by using another valuable feature of the software. DeltaEC will display plots of the acoustic variables throughout the model by selecting "Plot SP file" from the "Display" pull-down menu. To improve the resolution of those plots, click on "Edit," and choose "Options" from the drop-down menu. Increase the number of Runge-Kutta steps in the "Nint" box from 10 to 50 and click "OK." Now "run" again and select "Plot SP file" from the "Display" drop-down menu. In the "header" shown in Fig. 8.25, uncheck `Im[p]` and check `Im[U]` to display the acoustic pressure and acoustic volume velocity for the $n = 3$ mode of this plane wave resonator. As expected, there are three half-wavelengths with the volume velocity being zero at both ends and the acoustic pressure being maximum at both ends.

Figure 8.25 shows that the real component of pressure, `Re[p]`; the imaginary component of the volume velocity, `Im[U]`; and acoustic power flow, `Edot`, have been selected for plotting. Figure 8.26 shows the plots of those selected variables for both the fundamental (half-wavelength) with $f_1 = 100$ Hz and the second mode (two half-wavelengths) with $f_2 = 200.8$ Hz.

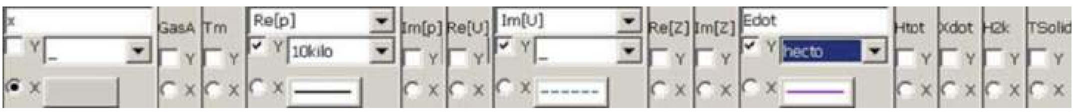

Fig. 8.25 Screenshot of the state variable plot variable selection window that allows the user to specify which variables should be plotted, as well as the color and line type (e.g., solid, dashed). For the state variable plots shown in Fig. 8.26, I have chosen to plot the real part of the pressure, $\Re$`e[p]`; the imaginary part of the volume velocity, $\Im$`m[U]`; and the magnitude of the acoustic power flow, `Edot`, by clicking the corresponding boxes. The *x* axis of the graph is selected as the *x* position along the resonator. Since all plots share a common vertical axis, DeltaEC has plotted the pressure in units of `10kilo(Pa)`, the volume velocity unscaled (m^3/sec), and the power in `hecto(W)`. Other choices could have been made with the pull-down menus, and other variables could have been plotted by checking other boxes (e.g., `Tm`, `Re[Z]`, etc.)

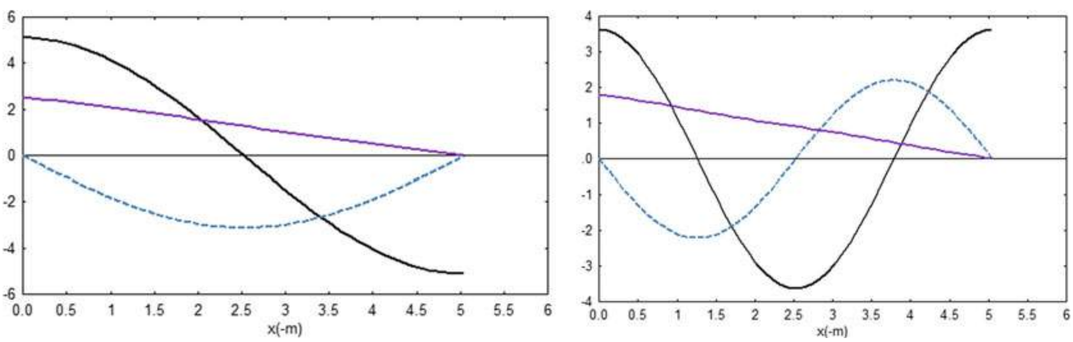

Fig. 8.26 Screenshot of the state variable plots for the fundamental (*left*) $f_1 = 100.0$ Hz and second harmonic (*Right*) $f_2 = 200.8$ Hz modes of the helium-filled resonator of length 5.0453 m. Since the pressure and volume velocity in a standing wave are approximately 90° out-of-phase, I have plotted $\Re$`e[p]` (*black solid line*) and $\Im$`m[U]` (*blue dashed line*), as well as the power (*solid purple line*) vs. position along the resonator from the source ($x = 0$) to the rigid end ($x = 5.0453$ m). To allow all of my chosen variables to be clearly visible on a single plot, DeltaEC has scaled those variables. In the above plots, the pressure has been divided by 10,000 and plotted in unit of 10 kPa, the volume velocity is plotted as [m^3/s], and the power has been divided by 100 and plotted as hectowatts

8.6.7 Modifying planewave.out to Create Flask500.out

We will modify planewave.out to represent the Helmholtz resonator of Sect. 8.5.2 by removing the two SURFACE segments, changing the gas from helium to air, changing the dimensions of the DUCT to represent the length and cross-sectional area of the neck of the 500 ml flask in Fig. 8.16, and placing a COMPLIANCE segment between the DUCT and the HARDEND to represent the boiling flask's 500 ml volume.

Start by clicking on the blue title above the BEGIN statement and changing it to "500 ml Boiling Flask (Helmholtz Resonator)" After changing the title, select "Save As" from the "Edit" pull-down menu, and save the file as "500mlFlask.out."

Under the "Edit" pull-down menu, select "Kill Segment," then select "1 SURFACE," and watch it disappear from the file. Now that the first SURFACE is gone, DUCT becomes Segment #1. Double-click on the value of area (1a), change it to 490.9e-6 m^2, and then click "OK." The neck cross-section is circular, so the perimeter should be $\Pi = 2(\pi A_{duct})^{1/2} =$ 0.07854 m. The Master-Slave link should have done that for you. We will use the physical length of the neck as our DUCT length (1c) = 49.2e-3 m. Finally, click on the title of the segment DUCT and change it to "Neck" It might be a good idea to save your changes at this point. There is a save icon near the top left of the model.

Some of the variables in the BEGIN Segment #0 also need modification. Again, by clicking on helium, air can be selected from the menu of gases. Modify `Mean P` (0a) to be the standard value of 101,325 Pa and the beginning temperature `TBeg` (0c) = 295.65°K. Based on the analysis in Sect. 8.5.2, the Helmholtz frequency is expected to be about 250 Hz, so modify (0b) to reflect that. In the schematic representation of Fig. 8.15, we let the flask be pressure-driven at the open end of the neck. Modify (0d) to be 1.0 Pa,[17] and uncheck the "Set as Guess" box. Set the magnitude of the volume velocity, $|U|$ at (0f), as a guess, after clearing (0d) from the guess vector. Put $|U|$ "in the correct ballpark" by modifying (0f) to be 0.001 m^3/sec.

Now all that is left is to "Kill" the other SURFACE that is now in Segment #2, and then insert a COMPLIANCE ahead of HARDEND, which became Segment #2 after the last SURFACE was deleted from the file. Under the "Edit" pull-down menu, select "Insert," use the dialog box pull-down to select COMPLIANCE, and place it before Segment #2 HARDEND.

Renaming the COMPLIANCE from "`Change Me`" to "500 ml sphere" would be an appropriate choice. Since the 500 ml volume is spherical, the surface area is $A_{sphere} = 4\pi(3V/4\pi)^{2/3} = 3.0465 \times 10^{-2}$ m^2. We should really also subtract the neck area, since that part of the sphere has no surface, so put 2.9974e-2 m^2 in "2a." The volume is 500 ml = 5e-4 m^3. The solid type can remain "`ideal`."

Segment #3 can be left as HARDEND, since we do not want any gas to flow out of the end of the volume that is opposite the neck represented by the DUCT in segment #1. Before going further, it would be wise to save this file again. Look over the file to see if you have made any obvious data entry errors (e.g., volume should be 5e-4 and not 5e4), and then hit the "Run" arrow.

8.6.8 Interpreting the ∗.out File

The results of running 500mlFlask.out are shown in Fig. 8.27. In the BEGIN segment (#0), the inputs that were "guesses" have been changed to the values that produced the best agreement with the

[17] Since this is a linear system, the frequency will be amplitude-independent. By choosing the pressure amplitude to be unity at the entrance to the neck (0d), the numerical value of the pressure amplitude at resonance in the Helmholtz resonator's volume will correspond to the quality factor of the resonance as expressed in Eq. C.1.

```
500 mlFlask 500 ml Boiling Flask (Helmholtz resonator)
  0 BEGIN      Initial
            1.0133E+05 a Mean P Pa
Gues            241.73 b Freq   Hz
                295.65 c TBeg   K
                1.0000 d |p|    Pa
                0.0000 e Ph(p)  deg
Gues        4.0777E-04 f |U|    m^3/s
                0.0000 g Ph(U)  deg
Optional Parameters
air           Gas type
    1 DUCT       Neck
            4.9090E-04 a Area   m^2                    74.355 A |p|    Pa
            7.8540E-02 b Perim  m                     -89.898 B Ph(p)  deg
            4.9200E-02 c Length m                  3.9806E-04 C |U|    m^3/s
Master-Slave Links                                -1.3686E-02 D Ph(U)  deg
Optional Parameters                                2.0388E-04 E Htot   W
ideal         Solid type                           2.9919E-05 F Edot   W
    2 COMPLIANCE 500 ml sphere
            2.9974E-02 a SurfAr m^2                    74.355 A |p|    Pa
            5.0000E-04 b Volume m^3                   -89.898 B Ph(p)  deg
Master-Slave Links                                 1.0843E-19 C |U|    m^3/s
                                                       179.30 D Ph(U)  deg
                                                   2.0388E-04 E Htot   W
ideal         Solid type                          -5.6390E-20 F Edot   W
    3 HARDEND    Final
Targ            0.0000 a R(1/z)                        74.355 A |p|    Pa
Targ            0.0000 b I(1/z)                       -89.898 B Ph(p)  deg
                                                   1.0843E-19 C |U|    m^3/s
                                                       179.30 D Ph(U)  deg
```

Fig. 8.27 Screenshot of the output file for 500mlFlask.out. Input parameters are displayed in the left-hand INPUT column in *blue* with the results in *green*. Calculated results show up in the right-hand "OUTPUT" column, also in *green*. The source (in the BEGIN segment) delivers 203.9 μW (1E), and only 29.9 μW leaves the neck (1F), indicating that the neck dissipated 174 μW. The power that left the neck was dissipated by thermal relaxation effects at the surface of the COMPLIANCE (see Sect. 9.3.2 and Fig. 9.10)

"targets." We see that the resonance frequency, defined as the frequency where $\widehat{\mathbf{U}}$ and $\widehat{\mathbf{p}}$ were in-phase (specified by 0e = 0 g = 0°), is 241.73 Hz. This is close to the result of $f_o = 245.3$ Hz calculated previously using Eq. (8.51).[18] At resonance, the magnitude of the volume velocity (0f) that enters the neck, driven by a 1.0 Pa (peak) pressure amplitude in front of the neck, is given in (0d) as 407.8 cm^3/s.

The first four results in the right-hand column of the next three segments will always be the complex pressure and volume velocity at the ***exit*** from the segment. At the exit of Segment #1 (where it joins the COMPLIANCE), the magnitude of the pressure is $|p| = 74.353$ Pa. It retains that value throughout the

[18] The fact that the resonance frequency found by DeltaEC is lower than the calculation based on Eq. (8.51) reflects the fact that DeltaEC includes the additional inertance of the fluid in the viscous boundary layer "attached" to the surface of the resonator's neck and the isothermal compressibility of the gas in the thermal boundary layer on the surface of the cavity. These dissipative boundary layer effects will be the focus of Chap. 9.

remaining two segments. This is a new result that we could not obtain from our nondissipative analysis of this network in Sect. 8.5.1, and it is important!

In our nondissipative analysis of Eq. (8.52), the ratio of the pressure in the cavity to that in front of the neck diverged at resonance: $|\widehat{\mathbf{p}}_{cav}/\widehat{\mathbf{p}}| = \infty$. Since DeltaEC includes the viscous dissipation caused by the drag of the oscillatory air flow within the neck, and the thermal relaxation losses due to thermal conduction between gases undergoing adiabatic temperature changes, derived in Eq. (7.25), within the volume, the pressure amplitude is now finite. In fact, the "gain" is the quality factor of the Helmholtz resonator, $Q = |\widehat{\mathbf{p}}_{cav}/\widehat{\mathbf{p}}| =$ (2A)/(0d) $\cong$ 74 (or + 37.4 dB). This pressure increase over a narrow frequency band is just what Helmholtz sought by "plugging" the resonators that share his name into his own ear.

The amplitude of the gas displacement in the neck, ξ_1, can be determined by "integrating" the volume velocity divided by the product of the neck area times the angular frequency: $\left|\widehat{\boldsymbol{\xi}}\right| = \left|\widehat{\mathbf{U}}\right|/(2\pi f A_{neck}) = 0.547$ mm. That is about 1.1% of the total neck length, so our assumption of a 1.0 Pa excitation in (0d) was well within our assumption of linear behavior.[9]

8.6.9 The RPN Segment

One of the most powerful features of DeltaEC is its ability to perform user-defined calculations within any model using the variable values calculated by the program. Such calculations can be done automatically within the program using the RPN segment available in DeltaEC. The serious student is referred to the *DeltaEC User's Guide* for a detailed discussion of the RPN segment, including tables that summarize the wide variety of accessible variables, convenient variable abbreviations for thermophysical properties and state variables (e.g., frequency, mean temperature, power flows, pressure, volume velocity, etc.) included in Table 11.2 of the *User's Manual*, and executable mathematical functions (e.g., square roots and other real and complex algebraic operations, circular and hyperbolic trigonometric functions, Bessel functions, logs, and exponentials) also included in Tables 11.3 through 11.7 of the *User's Manual*.

To illustrate, an RPN segment has been added to 500mlFlask.out and the file saved as 500mlRPN.out. That RPN segment, shown in Fig. 8.28, automatically calculates the peak-to-peak displacement,

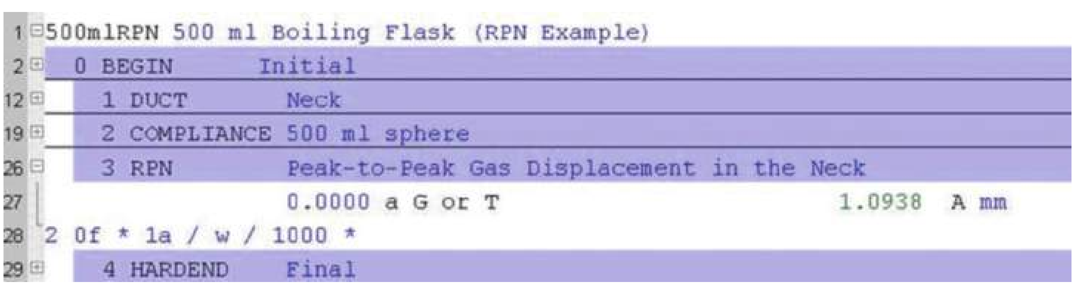

Fig. 8.28 Screenshot of a modified version of 500 mlFlask.out, shown in Fig. 8.27, which now includes an RPN segment (#3) that calculates the peak-to-peak gas displacement in the neck of the 500 ml boiling flask automatically and reports the result (3A) in millimeters

$2|\hat{\xi}|$, of the gas in the resonator's neck. To eliminate the need for parentheses, the RPN segment uses Reverse Polish Notation:[19] variables are "declared," and then an operation on the variable (e.g., taking the cosine of an angle) is executed. If an operation requires two variables (e.g., multiplying one variable by another), then both variables appear before the operation.[20]

For example, the magnitude of the volume velocity entering the neck, $|\hat{\mathbf{U}}|$, that is provided in (0f), must be divided by the cross-sectional area of the neck in (1a), to obtain the average gas velocity in the neck. That velocity then needs to be integrated, so that peak gas velocity must be by divided by ω to obtain the peak gas displacement, $|\hat{\xi}|$. Since the desired result is the peak-to-peak displacement, $2|\hat{\xi}|$, the result of the integration must be multiplied by two. In algebraic notation, $2\xi =$ `2*(0f)/[w*(1a)]`.[21] If the result is to be displayed in millimeters, the entire expression must be multiplied by 1000.

In RPN, that same calculation is written, $2\xi =$ `2 (0f) * (1a) /w/1000 *` or $2\xi =$ `2000 0f * 1a / w /`, to provide the result in millimeters. In the first version, the number "2" and (0f) are multiplied (∗), and then (1a) divides (/) the previous result. The RPN abbreviation for ω, which is "w," divides (/) that result, followed by "1000" and a multiplication (∗). For that RPN segment shown in Fig. 8.28, "ChngeMe" has been replaced by "mm," representing millimeters in the "units" column as a reminder that the result is given in (3A) as millimeters.

That RPN segment (#3) is shown along with the other "collapsed" segments of the model in Fig. 8.28. The RPN segment result (3A) is exactly twice what was calculated for $|\hat{\xi}|$ "by hand" from the results in the ∗.out file in Fig. 8.27.

[19] Reverse Polish notation (RPN) is a system where the "operator" follows the variable(s). The "Polish" designation is in honor of its inventor, Jan Łukasiewicz (1878–1956). That form of data entry and calculation was used in the scientific calculators made by Hewlett-Packard since the introduction the HP-35 in 1972, the first handheld scientific calculator. RPN is used in HP calculators to the present day. It is preferred by most scientists and engineers of my generation because it takes fewer key strokes and because operations are unambiguous without requiring parentheses.

[20] If you prefer parentheses, DeltaEC can display an RPN formula in that notation. Double-click on the RPN result, and then click "List Linkages" to show the formula using parentheses.

[21] DeltaEC will show an RPN result using "algebraic notation," using parentheses if you click on the RPN result then choose "List Linkages."

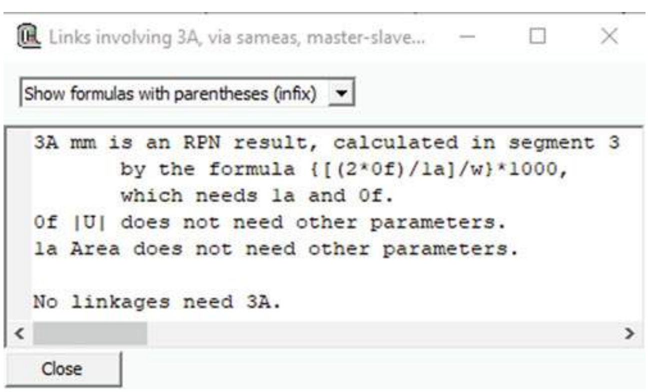

8.6.10 Power Flow and Dissipation in the 500 Ml Boiling Flask

The magnitude of the volume velocity, $\left|\widehat{\mathbf{U}}\right|$, that leaves the neck (1C = 398.06 cm^3/s) is slightly reduced from the value that entered the neck (1f = 407.77 cm^3/s) due to the compliance of the gas in the neck itself. It is worth noticing that in the compliance, $\widehat{\mathbf{U}}$ and $\widehat{\mathbf{p}}_{cav}$ are almost exactly 90° out-of-phase (1B), as they should be for a compliance described in Eq. (8.25). Of course, the volume velocity exiting the compliance is zero ($\left|\widehat{\mathbf{U}}\right|$ < 1.08 x 10^{-19} m^3/s) to satisfy the HARDEND condition in Segment #3 of Fig. 8.27 and Segment #4 in Fig. 8.28.

The next two results shown in Fig. 8.27 are `Htot` (1E) and `Edot` (1F). `Edot` is the acoustic (mechanical) power that exits the segment, and `Htot` is the total power (effectively the sum of the acoustical power plus thermal power converted from acoustical power by dissipation) leaving the segment.[22] Following Sect. 1.5.4, the acoustic power is one-half of the product of the acoustic pressure magnitude, $|\widehat{\mathbf{p}}|$, times the volume velocity magnitude, $\left|\widehat{\mathbf{U}}\right|$, times the cosine of the phase angle between those quantities. Since $\widehat{\mathbf{U}}$ and $\widehat{\mathbf{p}}$ are in-phase, the input acoustical power is $\langle \Pi_{in} \rangle_t = |\widehat{\mathbf{p}}|\left|\widehat{\mathbf{U}}\right|/2 =$ `(0d)` $*$ `(0f)/2` $=$ 203.88 μW. Energy is conserved so the total power, `Htot`, that moves through our resonator is fixed, hence (1E) = (2E) = (3E) = 203.89 μW. That total power cannot exit the model, but at the end of the model has been converted entirely to heat by thermoviscous dissipative processes.

The power dissipated in the neck is the difference between the acoustic power that entered from the BEGIN segment (1E = 203.88 μW) and what exited from the neck (1F = 29.919 μW) and entered the COMPLIANCE. Therefore, those viscous losses in the neck dissipated 173.96 μW, and that power was deposited on the neck as heat and/or swept away and dumped elsewhere by thermoacoustic boundary layer processes [20], which are beyond the scope of this textbook. Since the walls of the neck are "ideal" and have infinite heat capacity, the temperature of the neck did not increase. Thermoacoustic heat transport can actually cause portions of the duct to cool even in the presence of viscous heating [21].

The thermal relaxation dissipation in the compliance can be determined by subtracting `Edot` that leaves the compliance (2F) from `Edot` that enters (1F): 29.919 μW − 5.94 x 10^{-20} W = 29.919 μW. That heat is deposited on the walls of the COMPLIANCE.

Apparently, for this Helmholtz resonator, 85% of the dissipation in the model is due to the viscous losses produced by the oscillatory gas motion in the neck. At this point, radiation losses from the neck of the resonator have not been calculated.[23]

8.6.11 An "Effective Length" Correction

At this point, you should be able to try a few things with DeltaEC on your own (or with the few prompts that follow). Let's have DeltaEC adjust the length of the neck so that the resonance frequency becomes the measured value, $f_{exp} = 213.8$ Hz. This can be accomplished by opening 500mlFlask.out,

[22] See G. W. Swift, *Thermoacoustics: A Unifying Perspective for Some Engines and Refrigerators*, 2nd edn. (Springer/Acoust. Soc. Am., 2017); ISBN 978-3-319-66932-8, Chapter 5.2, for a discussion of the difference between total power and acoustic power.

[23] The radiation efficiency will be calculated later in this textbook (see Sect. 12.2.1). For those who can't wait, $\langle \Pi_{rad} \rangle_t = \left(\pi \rho_m f^2/2c\right)\left|\widehat{\mathbf{U}}\right|^2$. DeltaEC could have calculated those automatically, as well, if a PISTBRANCH or OPNBRANCH segment were placed before the neck that models a flanged open end or unflanged open end.

then inserting another DUCT of zero length ahead of the existing DUCT segment representing the neck, and naming that new segment "Effective Length Correction." It would also be a good time to rename the title of the model (Line #1) as "500 ml Boiling Flask (Effective Length)." Use "SaveAs" in the "File" drop-down menu to save the file as "FlaskEffLength.out."

As a convenience, DeltaEC will add a "Master-Slave Link" to the relationship between area and perimeter to keep the shape of the inserted duct circular. We do not want that link because we do not want the "effective length duct" to add any thermoviscous dissipation. To sever the link, just click on Master-Slave Links and select "none."[24]

In the new file, make the new effective length DUCT's area (1a) be "sameas 2a" by double-clicking on the value of (1a). This will bring up the "Parameter Edit" window for (1a). Click on the "SameAs" button and place "2a" in the window. The "SameAs" feature is very convenient, since various segments of a model whose dimension should be linked can be changed by changing only one variable in one segment. Set the perimeter to an arbitrarily small value, (1b) = 0.0001 m, since the effective length correction is not a "physical" duct that would introduce additional thermoviscous loss.[25] Change the value of frequency in (0b) to 213.8 Hz, and remove frequency (0b) from the guess vector. Let the length of the "effective length" duct (1c) be a "guess." Just double-click on the value of (1c) and check the "Set as Guess" box when the "Parameter Edit" window opens. Figure 8.29 shows the ∗.out file produced after that model has run successfully.

The resulting effective length correction, (1c) = 13.54 mm, slightly less than the value (15.5 mm) obtained when we used the expression in Eq. (8.53), which ignored dissipation. Again, less "effective length" was required to obtain the experimentally measured frequency since some of the necessary frequency reduction was provided by gas compliance and viscous dissipation in the neck and thermal-relaxation effects within the 500 ml volume. We will calculate the effective length correction in Sects. 12.8 and 12.9.

8.6.12 Incremental Plotting and the ∗.ip File

Our initial exploration of DeltaEC's capabilities will conclude by using the software to create a plot of the pressure magnitude and phase within the 500 ml volume as a function of frequency. DeltaEC produces two types of plots: One is the "State Plot," introduced in Sect. 8.6.6, that allows all of the different results for an individual run to be plotted, usually as a function of position along the apparatus (e.g., real and imaginary pressure magnitude, `Edot`, etc.). The State Plot is particularly useful for models that are complicated and contain branching and thermoacoustic elements, such as heat exchangers, that change energy flows and temperatures throughout the apparatus being modeled. They also provide essential confirmation of the normal mode shapes for standing waves in complex networks (see Fig. 8.26).

The other plot type is the "Incremental Plot." An incremental plot lets the user to choose two variables (called the "outer" and "inner" plotting variables) that can be incremented or decremented over a range of equally spaced values. One choice might be a range of static pressures (outer plot

[24] As with many items in this section, DeltaEC supports a lot more capabilities that we have space to explore in an introduction. If you want to know more about Master-Slave links or any other feature, you are referred to the *User's Guide*.

[25] There is also some dissipation due to the fluid shear which accompanies the divergence of the streamlines at both ends of the neck. A detailed analysis of this dissipation mechanism and the effective length correction is provided in K. A. Gillis, J. B. Mehl, and M. R. Moldover, "Theory of the Greenspan viscometer," *Journal of the Acoustical Society of America* **114**(1), 166–173 (2003).

```
FlaskEffLength 500 ml Boiling Flask (Effective Length)
  0 BEGIN        Initial
               1.0133E+05 a Mean P Pa
                   213.80 b Freq   Hz
                   295.65 c TBeg   K
                   1.0000 d |p|    Pa
                   0.0000 e Ph(p)  deg
Gues           4.1866E-04 f |U|    m^3/s
                   0.0000 g Ph(U)  deg
Optional Parameters
air            Gas type
  1 DUCT          Flask Neck Effective Length Correction
    Same   2a  4.9090E-04 a Area   m^2            18.539 A |p|    Pa
               1.0000E-04 b Perim  m             -86.913 B Ph(p)  deg
Gues           1.3539E-02 c Length m          4.1808E-04 C |U|    m^3/s
               5.0000E-04 d Srough           -8.6197E-03 D Ph(U)  deg
Master-Slave Links                            2.0933E-04 E Htot   W
Optional Parameters                           2.0927E-04 F Edot   W
ideal          Solid type
  2 DUCT          Neck
  3 COMPLIANCE 500 ml sphere
               2.9974E-02 a SurfAr m^2            85.759 A |p|    Pa
               5.0000E-04 b Volume m^3           -89.895 B Ph(p)  deg
Master-Slave Links                                0.0000 C |U|    m^3/s
                                                  0.0000 D Ph(U)  deg
                                              2.0933E-04 E Htot   W
ideal          Solid type                         0.0000 F Edot   W
  4 HARDEND       Final
```

Fig. 8.29 Screenshot of the output file for "FlaskEffLength.out." DeltaEC has adjusted the length of an additional duct so that the frequency (0b) is the measured value, $f_{exp} = 213.8$ Hz, taken from Fig. 8.17. Notice that the quality factor, based on the magnitude of the pressure in the COMPLIANCE, $|p| = (1A)$, has increased to produce $Q = 85.8$, which is larger than $Q = 74.4$, in Fig. 8.27. This increase is due to the additional stored kinetic energy produced by the velocity of the flow in the effective length correction, which introduced no additional dissipation, since the "perimeter" of that duct (1b) was set to be negligibly tiny

variable) that are used to generate plots over a specified range of frequencies (inner plot variable) for each pressure. In the following example, only one (outer) plot variable, the frequency (0b), will be incremented (or decremented) to generate a resonance response curve similar to Fig. 2.12 for the damped simple harmonic oscillator.

The magnitude (2A) and phase (2B) of the pressure inside the compliance of the 500mlFlask.out file in Fig. 8.27 will now be set up to be plotted as a function of frequency (0b). The magnitude of the pressure in front of the neck (0d) will remain constant at 1.0 Pa as the frequency is being swept below and above the resonance frequency. Since the resonance occurs around 240 Hz, the plot will be set up to go from 230 Hz to 250 Hz, placing the Helmholtz resonance frequency roughly in the middle of the plotting range.

It is a good idea to have a model that is converged at the starting point before attempting an incremental plot. Since the plot will start at 230 Hz, click on (0b) and set it to 230 Hz and be sure it is *not* designated as a "Guess." The phase could be positive or negative or any phase value that is modulo an integer multiple of 360°, but the phase, though correct, may be inconvenient for display of the plotting results. To avoid phases that exceed +360° or are less than −360°, click on (0 g), and set it to zero degrees. Then run the model to be sure that it converges at the starting point (230 Hz) for the plot. Seeing that the model converged and produced an initial phase between the pressure in front of the neck and the volume velocity at the neck's entrance of about 82.3°, the model is ready to begin plotting.

To set up the plot, make the magnitude (0f) and phase (0 g) of the volume velocity "guesses." Then double-click on the 230 Hz (0b). In the "Parameter Edit" window, check the "Incr Plot" box. That choice will launch the "Incr(emental) Plot Editor" window. Since the last run of the model was at 230 Hz, DeltaEC will assume that the initial value of the frequency plotting range is 230 Hz, so that frequency will automatically appear in the "From" window. To set the plotting range between 230 Hz and 250 Hz, put 250 Hz in the "To" window, and then set the number of plotting points (#Points) to 81. By specifying 81 points, a step size of 0.25 Hz/point is automatically displayed. An "OPlt" designator will appear to the right of (0b) in the ∗.out file to indicate that frequency is now an independent (outer) plotting variable. Save this new model as 500 mlFlask(Plot).out to distinguish it from previous models.

DeltaEC will automatically include the guesses in the plot file and will tabulate the results in a text file that will be automatically designated 500 mlFlask(Plot).ip. In this case, those guesses are the magnitude (0f) and phase (0 g) of the volume velocity driven through the neck by the externally applied 1.0 Pa pressure. Since we want to plot the magnitude (2A) and phase (2B) of the pressure within the compliance, we click on those results, and check the "Plot(Dependent)" box in the "O(uter) Par(ameter) edit" dialog box. This should produce a "P" to the left of (2A) and (2B) indicating that these results will now also be contained in the incremental plot file.

To check the plotting setup, go to the "Display" pull-down menu, and select "Incremental Plot Sum (mary)." That will produce the Incremental Plot Summary window reproduced in Fig. 8.30.

When you click on the run arrow, DeltaEC will run itself 81 times in about one-half second, ending at 250 Hz, and will have created a new incremental plot file and named it 500mlFlask(Plot).ip. You can examine the content of this plot file in a variety of ways. It can be "opened" in your favorite commercial plotting program (e.g., Excel™) or text editor (e.g., WordPad or NotePad), or it can be examined within DeltaEC using the native DeltaEC plotting software by clicking on "Display" and selecting the "Plot IP file" from the pull-down menu. Figure 8.31 shows a portion of the ∗.ip file, opened with a text editor, containing the first 13 results between 230 and 233 Hz.

If you repeat the plot or if you have plotted the file previously, DeltaEC will provide the option of "overwriting" the existing ∗.ip file, or you can choose to "append" this new run to the previous file (a useful option if you are spanning a large frequency range that you have broken up into shorter runs). If you want to keep the original file, DeltaEC will provide the option to "Rename" the new file.

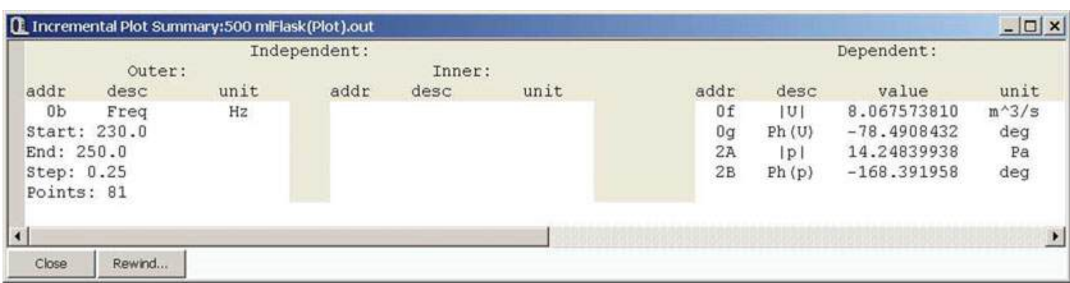

Fig. 8.30 Screenshot of the Incremental Plot Summary window shows that we have selected frequency (0b) as our independent plotting variable and that variable will range from 230 Hz to 250 Hz in 81 steps of 0.25 Hz. It will generate a plot file (∗.ip) that will contain the independent plotting variable (0b) and the dependent "guess" variables, $|U|$ (0f) and Ph (U) (0 g), as well as the pressure magnitude, $|p|$ (2A), and phase, Ph (p) (2B), in the COMPLIANCE

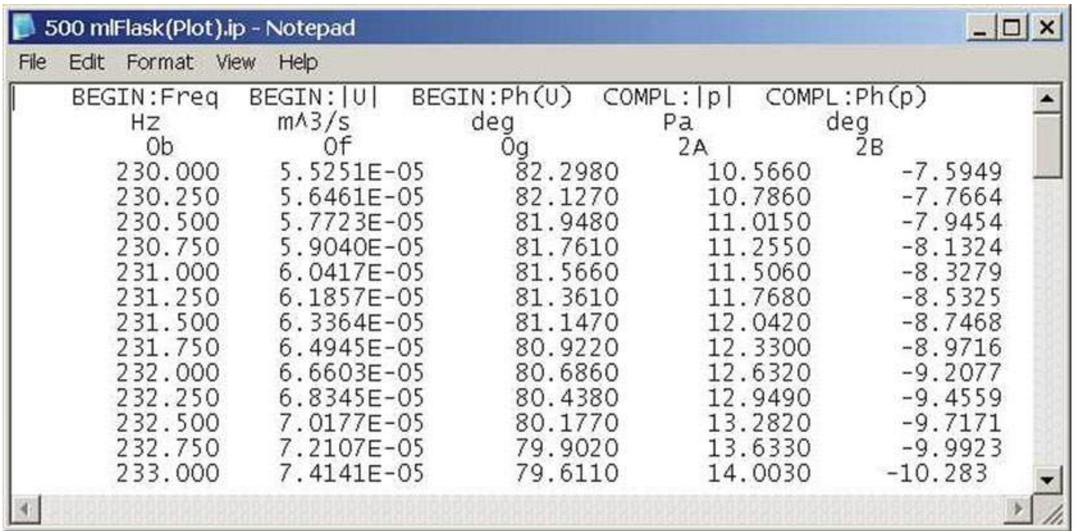

500 mlFlask(Plot).ip - Notepad

File Edit Format View Help

BEGIN:Freq	BEGIN:|U|	BEGIN:Ph(U)	COMPL:|p|	COMPL:Ph(p)
Hz	m^3/s	deg	Pa	deg
0b	0f	0g	2A	2B
230.000	5.5251E-05	82.2980	10.5660	-7.5949
230.250	5.6461E-05	82.1270	10.7860	-7.7664
230.500	5.7723E-05	81.9480	11.0150	-7.9454
230.750	5.9040E-05	81.7610	11.2550	-8.1324
231.000	6.0417E-05	81.5660	11.5060	-8.3279
231.250	6.1857E-05	81.3610	11.7680	-8.5325
231.500	6.3364E-05	81.1470	12.0420	-8.7468
231.750	6.4945E-05	80.9220	12.3300	-8.9716
232.000	6.6603E-05	80.6860	12.6320	-9.2077
232.250	6.8345E-05	80.4380	12.9490	-9.4559
232.500	7.0177E-05	80.1770	13.2820	-9.7171
232.750	7.2107E-05	79.9020	13.6330	-9.9923
233.000	7.4141E-05	79.6110	14.0030	-10.283

Fig. 8.31 Screenshot of the first 13 results produced by DeltaEC's incremental plotting function and placed in the ∗.ip file, for the response of the 500 ml boiling flask, is shown using a simple text editor. The file also includes a "header" with the "variable" (e.g., BEGIN: Freq), its units (e.g., Hz), and its "address" in the model (e.g., 0b)

Checking the file using DeltaEC's built-in plotter is convenient, since it is a faster way to examine the plot than to export the file to another spreadsheet or mathematics software package. I always check the plotted data with DeltaEC's indigenous plotting function to make sure that I have plotted the data that I wanted over my range of interest. A DeltaEC-generated incremental plot from the example just run is shown in Fig. 8.32. That incremental plotting window lists the plot variables that can be selected for plotting by checking the desired boxes. In this example, `BEGIN:Freq@0b` has been selected as the x axis for the plot. `COMPL|p|@2A` and `COMP:Ph(p)@2B` are chosen as the y axis variables.

The "windows" below the variables provide a variety of options for scaling the plot. In all three cases, the variable values in Fig. 8.32 are not scaled, hence the "_" symbol in that window. The window below the y axis variables allows selection of the shape, the size, and the color of the plotted points, as well as the options for a line to connect the points. The line color and style (e.g., solid, dashed, dotted, dash-dot) and line width can also be selected by the user. Under the "Options" drop-down menu, "Enable Legend" has been selected to produce the legend in the upper-right corner of the plot in Fig. 8.32. The legend identifies the plotted dependent variables as well as their units and scaling.

Since DeltaEC automatically includes thermoviscous dissipation, the 180° phase shift from below to above the resonance frequency is no longer discontinuous as predicted by the nondissipative result in Eq. (8.52). As shown in Fig. 8.32, the phase changes smoothly through resonance with the largest rate of change of phase as a function of frequency occurring at the resonance frequency. This is demonstrated in Fig. 8.33, where the phase of the plotted frequency closest to the resonance (241.75 Hz) and the phases of the two adjacent frequencies calculated in 500mlFlask(Plot).ip are fit to a straight line.

Agreement between the quality factor based on the amplitude gain and the quality factor based on the slope of the phase vs. frequency would be improved if smaller frequency increments around resonance were selected in the DeltaEC plotting file.

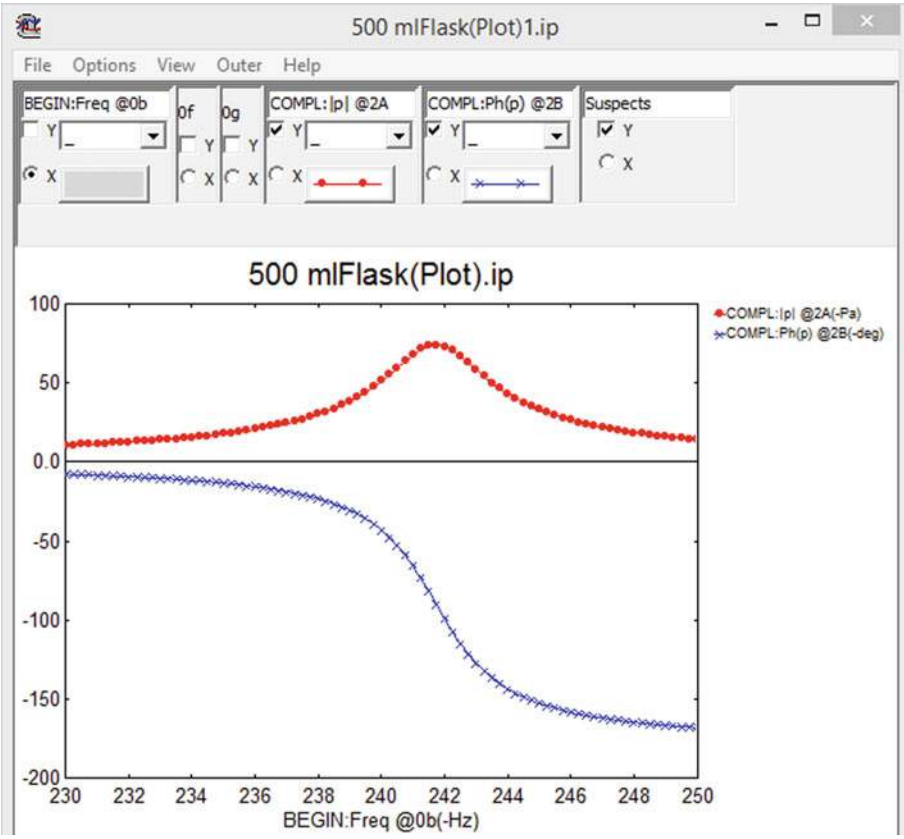

Fig. 8.32 Screenshot of the output window generated by DeltaEC for the incremental plot file 500mlFlask(Plot).ip. The pressure magnitude (2A) (*red circles*) and phase (2B) (*blue crosses*) in the COMPLIANCE segment were selected for plotting against frequency. The label for the *x* axis was also generated by DeltaEC. The legend is generated automatically and shows that the units for pressure are [Pa] and for phase is [deg]

8.6.13 So Much More Utility in DeltaEC

DeltaEC is a very versatile and powerful (and free!) computational tool that is provided with extensive documentation. This introduction could not really demonstrate the full power of the software, but it should have provided the minimum background for its further exploitation in this textbook and in your careers as acousticians. Students are encouraged to download and print parts of *DeltaEC User's Guide*, such as the Reference Section, which describes the use of the various segments and the section on the RPN Segment (*User's Guide* Chap. 4).

The RPN segment permitted the user great flexibility in calculating quantities of interest automatically within a DeltaEC model every time it is run. It also produces potential targets (e.g., phase differences) that might be more appropriate targets for the solver to use in making the model conform more closely to the behavior of the physical apparatus.

The next two sections will use DeltaEC to analyze two more "lumped-element" networks. They were chosen because they employ inertances and compliances and because they would be rather tedious to analyze without the assistance of DeltaEC.

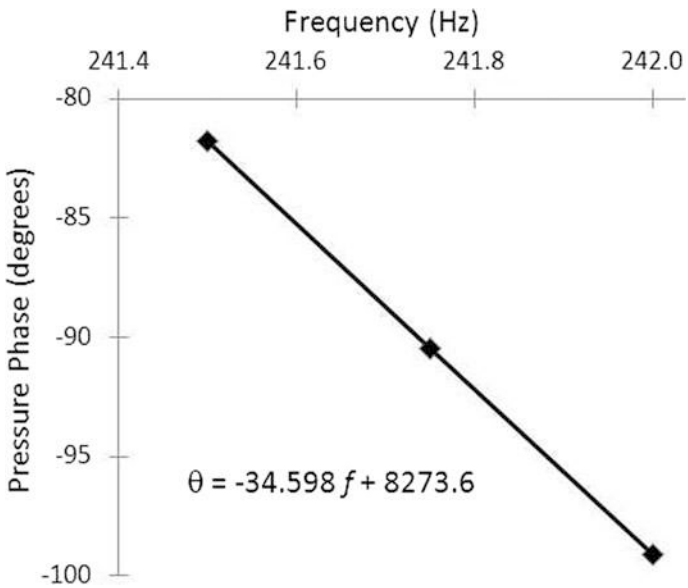

Fig. 8.33 The rate of change of phase around the resonance frequency of the 500 ml boiling flask is fit by a straight line with the slope, $(d\theta/df)_{f_o} = -34.6^\circ/\text{Hz}$. That slope is related to the quality factor, Q, of the resonance. The relation from Eq. 2.76 is reproduced as $Q = \left|\frac{\pi f_o}{360^\circ}\frac{d\phi}{df}\right|_{f_o} = \left|\frac{f_o}{114.6^\circ}\frac{d\phi}{df}\right|_{f_o}$ The slope suggests that $Q = 72.1$, in reasonable agreement with $Q = |p_{cav}/p_1| = 74.3$ calculated at resonance in Fig. 8.27, since the slope of the best-fit line is necessarily less than the slope evaluated exactly at f_o.

8.7 Coupled Helmholtz Resonators

The Helmholtz resonator is the fluid analogy of the mass-spring simple harmonic oscillator. The mass of the gas in the neck (see Sect. 8.4.4) is acted upon by the gas in the volume which provides a restoring force as a gas spring (see Sect. 8.2.4). After treating single degree-of-freedom harmonic oscillators in Chap. 2, we went on to analyze coupled oscillators with j masses connected to $j + 1$ springs in Sect. 2.6. We can do the same with coupled Helmholtz resonators. A simple physical example, built by Anthony Atchley, that has three necks (masses) and four volumes (gas springs) is shown in Fig. 8.34.

To obtain an approximate idea of what frequencies to expect, we can analyze a double-Helmholtz resonator that is created when one neck is connected to two identical volumes [22, 23]. That network is equivalent to a single (gas) mass restored by two mechanically parallel (gas) springs (see Sect. 2.2.1). Since two springs of equal stiffness provide a stiffness that is twice that of each individual spring, Eq. (8.51) can be modified to calculate the resonance frequency, ω_{Double}.

$$\omega_{Double} = \frac{1}{\sqrt{LC}} = c\sqrt{\frac{2A}{\Delta x_{neck} V}} \tag{8.55}$$

Using parameter values taken from the caption below Fig. 8.34, the volume of a single compliance is $V = 2.04 \times 10^{-5}$ m^3. The neck has a length, $\Delta x_{neck} = 19$ mm, and cross-sectional area, $A = 4.6 \times 10^{-5}$ m^2. If the air temperature is 23 °C, then $c = 345$ m/s, and $f_{Double} = \omega_{Double}/2\pi = 846$ Hz.

With three necks and four gas springs, the triple-Helmholtz resonator has three degrees of freedom and therefore will possess three lumped-element normal mode frequencies. The DeltaEC model,

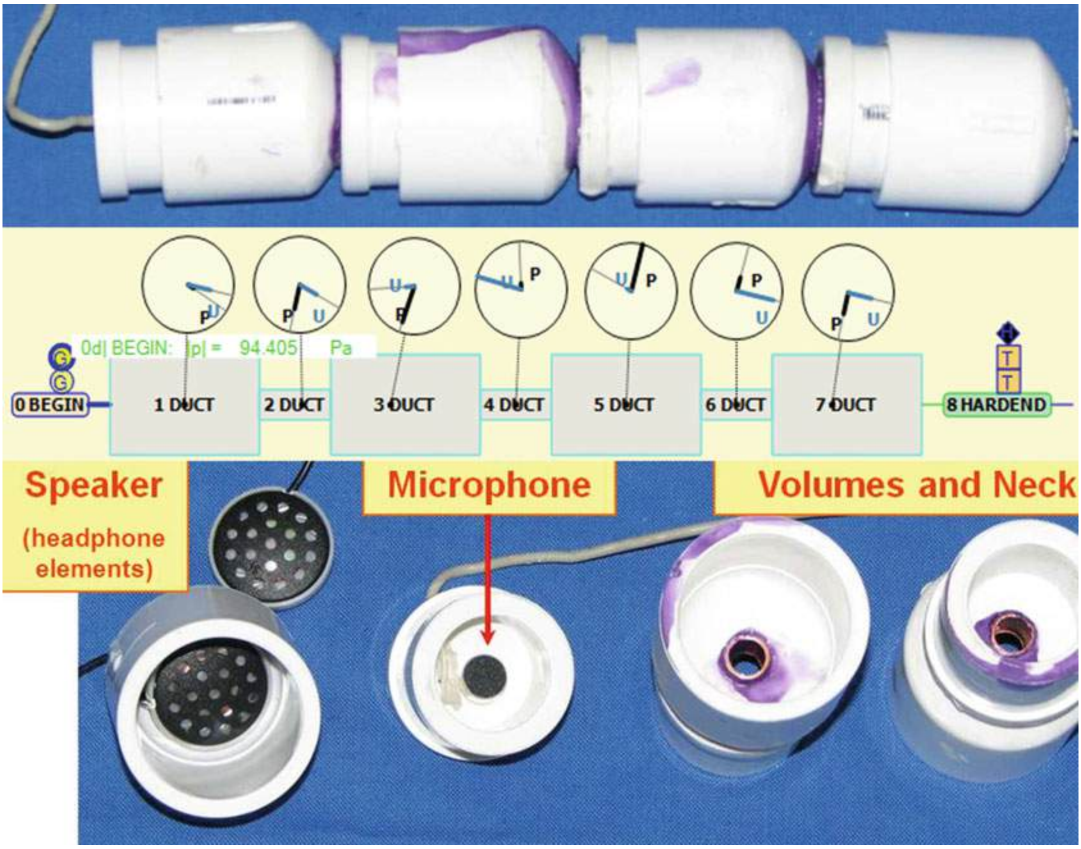

Fig. 8.34 Coupled Helmholtz resonators made from copper tubing (necks) and PVC plumbing caps (volumes), built by Anthony Atchley. (*Top*) An assembly of three necks and four volumes that create a table-top triple-Helmholtz resonator. Each neck is 19 mm long with an inner diameter of 7.6 mm. Each volume is 4.0 cm long with an inner diameter of 25.4 mm. (*Middle*) DeltaEC's "Schematic View" of TripleHelmholtz.out. As shown, it is possible to place a "phasor gauge" in any (or all) segment to show the relative phase of the pressure and volume velocity. To activate this feature, it is necessary to hold down the "alt" button and click your mouse on the segment of interest. In this illustration, the schematic view was produced for the third normal mode at 1010.9 Hz. In DUCT 1, acoustic pressure and volume velocity are nearly in-phase indicating that there is a large component of energy in the traveling wave near the BEGIN segment of the model. By the end of the model, the pressure and volume velocity in DUCT 5, DUCT 6, and DUCT 7 are nearly 90° out-of-phase, indicating that the energy is primarily due to the standing wave. (*Bottom*) A small loudspeaker is located at the end of the first volume, and a small microphone is located at the end of the fourth volume. The PVC volumes and necks are also disassembled for visual inspection

shown in "Schematic View" in Fig. 8.34, can be run to determine the three resonance frequencies, and three ∗.sp. files (see Sect. 8.6.6) can be generated showing the gas's volume velocity magnitudes corresponding to the three normal modes. Those normal modes are shown in Fig. 8.35, along with the analogous displacements of three discrete masses connected together by strings.

Although the second normal mode is similar to two double-Helmholtz resonators, oscillating 180° out-of-phase, with the gas in the central neck at rest, examination of the ∗.sp. file for that mode, in Fig. 8.36, shows that in such a small network, with a high ratio of surface area to volume, the thermoviscous losses are significant. The previous lossless analysis of the double-Helmholtz resonator shows that in such a network, the normal mode frequency should be 846 Hz. The DeltaEC model

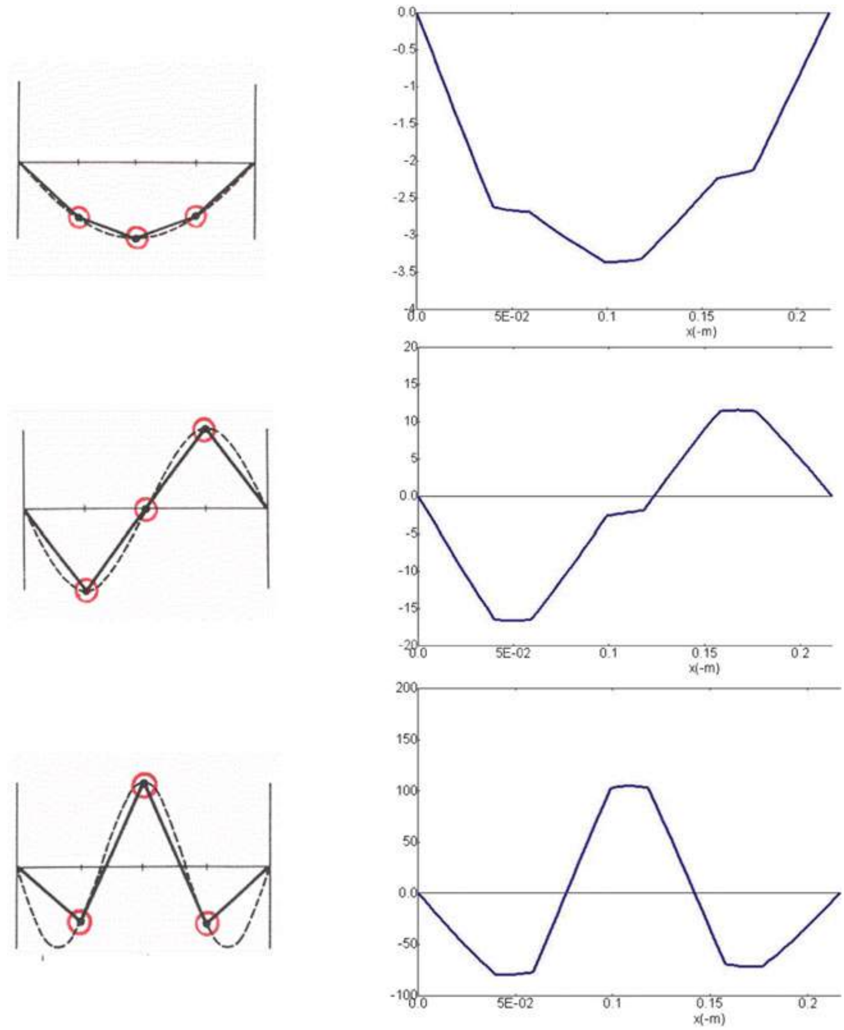

Fig. 8.35 Mode shapes for the three normal modes of the triple-Helmholtz resonator are plotted vs. position for the network shown in Fig. 8.34. Normal mode frequencies, determined from the DeltaEC model, are 231.4 Hz for the mode at the *top*, 670.8 Hz for the mode at the *middle*, and 1010.9 Hz for the mode at the bottom. The *left column* represents the displacements of the modes if discrete masses (*circles*) were mounted on a string, as discussed in Sect. 2.7.7, with the *dashed lines* representing the analogous normal modes for a continuous fixed-fixed string. The *right column* represents the magnitude of the volume velocity of the gas as it moves through the triple-Helmholtz resonator as plotted by three DeltaEC ∗.sp. files (see Sect. 8.6.6). For the lowest-frequency mode (231.4 Hz), all of the gas is moving in the same direction during any phase of the cycle. The highest velocity occurs in the central neck. In the second normal mode (670.8 Hz), the gas in the central neck is nearly stationary. Further detail for this mode is provided in Fig. 8.36. The highest-frequency mode has the gas motion of adjacent necks vibrating 180 degrees out-of-phase

places that normal mode resonance frequency at 671 Hz. It is clear from this state variable plot in Fig. 8.36 that the gas in the central neck is not at rest and the pressure on opposite ends of the left pair of volumes, which would be equal and opposite for the lossless case, is unequal in magnitude (28.8 Pa vs. 22.5 Pa). The same is true for the right pair of volumes (21.0 Pa vs. 18.2 Pa).

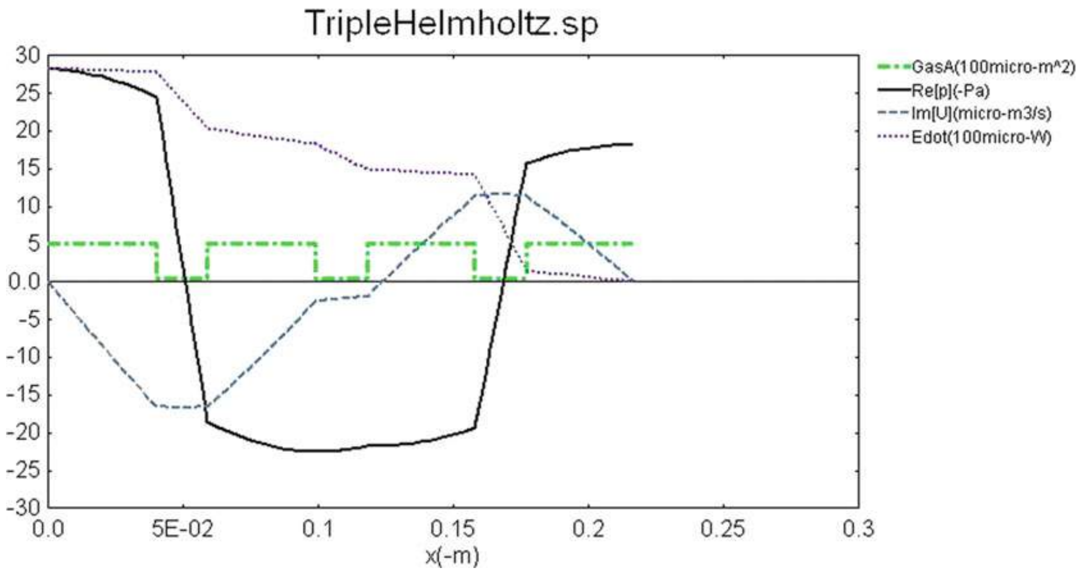

Fig. 8.36 State variable plot for the second normal mode of the triple-Helmholtz resonator shown in Fig. 8.34, with a resonance frequency of 670.8 Hz. The green *dash-dot line* represents the gas-filled cross-sectional area for the model (in cm^2). The *black solid line* represents the real component of the pressure (in Pa), $\mathfrak{Re}[p]$. The blue *dashed line* represents the imaginary component of the volume velocity (in cm^3/s), $\mathfrak{Im}[U]$. The purple *dotted line* represents the 2.83 mW of acoustic power that flows from the loudspeaker and is entirely dissipated when it reaches the end of the fourth volume, as it must, for a system in steady-state operation. This result differs from the approximation that assumes that the mode is equivalent to two lossless double-Helmholtz resonators oscillating 180 degrees out-of-phase with a resonance frequency of 846 Hz. It is clear from this state variable plot that the gas in the central neck is not at rest and the pressure on opposite ends of the left pair of volumes, which would be equal and opposite for the lossless double-Helmholtz case, is unequal in magnitude (28.8 Pa vs. 22.5 Pa). The same is true for the right pair of volumes (21.0 Pa vs. 18.2 Pa)

8.8 The Bass-Reflex Loudspeaker Enclosure

As will be shown in greater detail later (see Sect. 12.5.1), a moving-coil electrodynamic loudspeaker is a very inefficient source of sound at low frequencies if it is not surrounded by a rigid enclosure. Such an enclosure allows only the front surface of the speaker's cone to radiate into the listening space and suppresses the out-of-phase volume velocity produced by the rear of the speaker that would otherwise have cancelled the volume velocity created by the front of the speaker. This strategy is illustrated on the left-hand side of Fig. 8.37. One unfortunate consequence of such strategies is that the volume velocity produced by the back of the loudspeaker, though just as large as that produced by the front, is "wasted."

The phase reversal produced when a Helmholtz resonator is driven above its resonance frequency, ω_o, shown in Eq. (8.52) and plotted in Fig. 8.32, can productively utilize the volume velocity produced by the back of the loudspeaker. Such a *bass-reflex loudspeaker enclosure*, shown on the right-hand side of Fig. 8.37, exploits this phase reversal by taking the volume velocity generated from the rear of the loudspeaker's cone and inverting its phase, so the motion of the gas oscillating in the port (i.e., the neck of the Helmholtz resonator) adds (nearly in-phase) to the gas being driven by the front of the loudspeaker cone. At low frequencies, the separation of the cone's center and the vent is much less than one-half wavelength, so the volume velocity exiting the port will combine (using vector algebra to incorporate the phase differences) with the volume velocity produced by the front of the speaker to

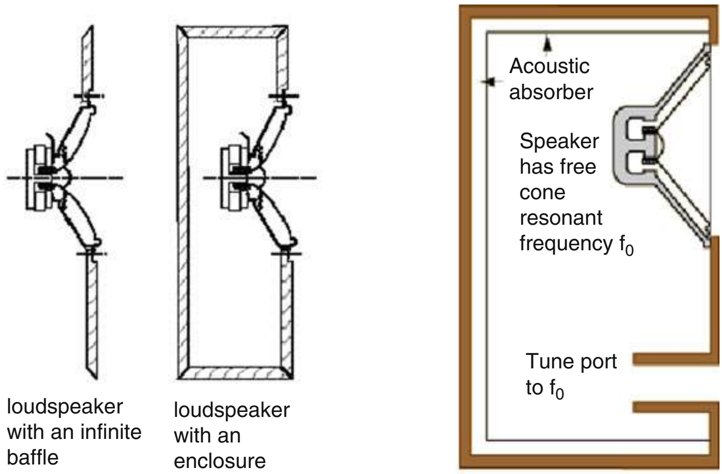

Fig. 8.37 The two sketches at the left show a loudspeaker mounted in an infinite baffle and in a sealed enclosure. Both strategies prevent the sound radiated from the back surface of the loudspeaker cone from cancelling the sound radiated from the front. At the right, the speaker is mounted in a Helmholtz resonator, with volume, V, which is commonly called a bass-reflex enclosure or a vented box enclosure. The "vent" (or port) is shown as an inertance of length, L, and cross-sectional area, A. The "acoustic absorber" is a porous medium (e.g., fiberglass) that is intended to attenuate standing waves within the rectangular enclosure (see Sect. 13.1.1)

produce the net volume velocity magnitude, $|U_{net}|$, that can exceed the volume velocity produced by the front of the loudspeaker.

There are several other technical issues that need to be considered for successful design of a bass-reflex loudspeaker enclosure that will not be addressed here. For example, the free-cone resonance of the speaker is strongly coupled to the Helmholtz resonance, and inclusion of damping material in the port can be useful in smoothing the overall response. (DeltaEC will automatically incorporate those effects for us if we specify the flow resistance of the damping material in the port as shown in Segment #3 of Fig. 8.39.) Since the volume velocity through the port can be substantial at frequencies close to the (strongly coupled) Helmholtz resonance frequency, flow noise generated by turbulence in the port and jetting caused by the high-speed gas flow in the port can be annoying. That flow noise is referred to by audio component manufacturers as the "port noise complaint" [24].

8.8.1 Beranek's Box Driven by a Constant Volume Velocity

It will be worthwhile to pursue this application a little further because it is an example of a Helmholtz resonator that is driven in a way that is different from the external pressure drive of our first example, shown schematically in Fig. 8.15 and modeled by DeltaEC in Figs. 8.27 and 8.29. A schematic diagram of a Helmholtz resonator being driven by a volume velocity source feeding the interior of the compliance is shown in Fig. 8.38. This configuration places the compliance of the volume and the inertance of the port acoustically in parallel. The volume velocity, $|U|$, provided by the rear of the speaker cone, goes simultaneously toward compressing the gas in the volume and driving gas through the neck (port).

To illustrate a Helmholtz resonator driven by a volume velocity source located within the compliance, a crude DeltaEC model of the bass-reflex enclosure is developed to represent the example in

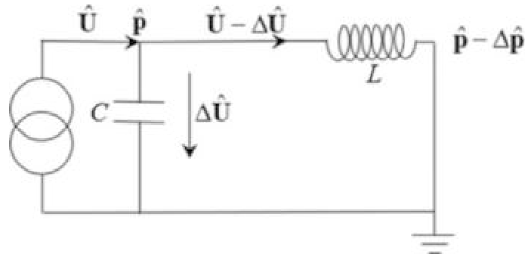

Fig. 8.38 This equivalent circuit diagram of a Helmholtz resonator driven by a current source (*overlapped circles*) represents the volume velocity magnitude, $\left|\widehat{\mathbf{U}}\right| = \omega A_{cone}\left|\widehat{\boldsymbol{\xi}}\right|$, created by the motion of the rear of a loudspeaker's cone, having an area, A_{cone}, moving sinusoidally with peak displacement amplitude, $\left|\widehat{\boldsymbol{\xi}}\right|$. Part of that volume velocity amplitude, $\Delta\widehat{\mathbf{U}}$, goes into compressing the air in the enclosure of compliance, C; the remainder, $\widehat{\mathbf{U}} - \Delta\widehat{\mathbf{U}}$, exits the port that has an inertance, L

Beranek's *Acoustics* textbook [25]. It's crude because it assumes that the loudspeaker produces a constant volume velocity of 0.040 m^3/s, which is independent of frequency. In fact, the volume velocity of the loudspeaker is frequency-dependent, due to the mass, stiffness, and damping (mechanical impedance) of the loudspeaker (see Sect. 2.5.5). The frequency dependence of the complex input electrical impedance of the loudspeaker's voice coil and associated magnet structure also modifies the current, hence the resulting force, if the coil is driven by a source of constant voltage. These effects will be ignored initially to demonstrate the phase-inversion effect of the bass-reflex approach. In the next section, a real loudspeaker (JBL 2242 PHL, S/N: J033N-51645), easily modeled using DeltaEC, will be used to excite the same enclosure in a more realistic way from a "constant voltage" source.

This example will also ignore any damping material (e.g., fiberglass) that might be used to line the interior surface of the compliance. Such material is designated in Fig. 8.37 (Right) as "acoustic absorber." That material is used to suppress standing waves within the enclosure (see Sect. 13.1), which occur at frequencies much higher than those which we consider here for the bass-reflex enclosure's behavior.

Beranek's speaker example has an effective piston area, $A_{cone} = 8.03 \times 10^{-2}$ m^2, and his enclosure has an internal volume, $V = 0.31$ m^3 ($30'' \times 35'' \times 18''$). The surface area of this acoustical compliance is 2.86 m^2. (This surface area could be increased in a DeltaEC model to represent the "acoustic absorber" that is included to suppress standing waves within the enclosure that occur at frequencies that are much higher than those of interest in the analysis of the bass-reflex behavior.) Beranek's port area, $S_p = 0.055$ m^2, corresponding to a port diameter of about 8 cm (3.14″). The port has a length of 0.25 m (9.8″), neglecting any end corrections. An acoustic flow resistance of 500 Pa-s/m^3 (see Segment #3) has been added to the port to control the behavior at resonance.[26] These parameter choices are reflected by the output file, BeranekBox(U-drive).out, shown in Fig. 8.39.

Care must be taken to understand the phase differences between the volume velocity of the source (set at 0° in BEGIN), $\widehat{\mathbf{U}}_{\mathbf{drive}}$, and the volume velocity produced by the front of the loudspeaker. The front of the loudspeaker is moving in the direction opposite that of the back side that produces $\widehat{\mathbf{U}}_{\mathbf{drive}}$. The net volume velocity, U_{net}, must be the vector sum of the volume velocity from the ***front*** of the loudspeaker plus the volume velocity of the gas moving through the port. The magnitude of the net velocity can be calculated using the Law of Cosines.

[26] Using these box parameters and neglecting damping, the Helmholtz frequency for the box containing air with a sound speed of 347 m/sec is 43.6 Hz, using Eq. (8.51) and adding one flanged end correction to create an effective length for the port, $L_{eff} = 28.4$ cm.

```
⊟BeranekBox(U-source)-Fig. 38 Beranek's 15" Base-Reflex Enclosure
⊟  0 BEGIN        Initial
                  1.0000E+05 a Mean P Pa
                      10.000 b Freq   Hz
                      300.00 c TBeg   K
 Gues                -25.201 d |p|    Pa
 Gues                 209.24 e Ph(p)  deg
                  4.0000E-02 f |U|    m^3/s
                      0.0000 g Ph(U)  deg
 Optional Parameters
 air             Gas type
⊞    1 COMPLIANCE Beranek's enclosure volume  (30"x35"x18")
⊞    2 DUCT       Bass Reflex Port
⊟    3 IMPEDANCE  Flow resistance in the port
                      500.00 a Re(Zs)  Pa-s/m^3           3.8033E-13 A |p|     Pa
                      0.0000 b Im(Zs)  Pa-s/m^3              -92.677 B Ph(p)   deg
 Master-Slave Links                                       4.1863E-02 C |U|     m^3/s
                                                             -4.3766 D Ph(U)   deg
                                                             0.43978 E Htot    W
                                                          2.3611E-16 F Edot    W
⊟    4 SOFTEND    Exit from the port
 Targ                 0.0000 a Re(z)                      3.8033E-13 A |p|     Pa
 Targ                 0.0000 b Im(z)                         -92.677 B Ph(p)   deg
                                                          4.1863E-02 C |U|     m^3/s
                                                             -4.3766 D Ph(U)   deg
                                                             0.43978 E Htot    W
 Possible targets                                         2.3611E-16 F Edot    W
                                                          3.6757E-17 G Re(z)
                                                         -1.2388E-15 H Im(z)
                                                              300.00 I T       K
⊟  5 RPN          Net volume velocity (A) and degrees phase differnce (B)
                      0.0000 a G or T                      3.6382E-03 A m^3/s
                                                              184.38  B Degrees
 180 4D - # cos 0f 2C * * 2 * 0f 0f * + 2C 2C * + sqrt
```

Fig. 8.39 Screenshot of the DeltaEC model of Beranek's bass-reflex loudspeaker enclosure that is driven by a constant amplitude volume velocity source (0f) located in the compliance that produces $\left|\widehat{\mathbf{U}}_{\mathbf{drive}}\right| = 4.0 \times 10^{-4}$ m³/s. Segment #3 places some damping material (e.g., fiberglass) in the port to control the amplitude at resonance. Segment #5 is an RPN target that calculates the phase difference between the volume velocity from the front of the loudspeaker (180° - 1e) and within the port (2D), to calculate the net volume velocity (5A) using Eq. (8.56). Note the RPN Segment #5 calculates and displays two quantities, $|U_{net}|$ and ϕ. The graph in Fig. 8.40 is based on this file. The blue highlight of the drive frequency (0b) and the result of the vector sum (5A) and (5B) indicates that the frequency, $|U_{net}|$, and ϕ will appear in the "Highlighted Parameters" window available under the "Display" pull-down menu

$$c^2 = a^2 + b^2 - 2ab\cos\phi \quad \Rightarrow \quad U_{net}^2 = U_{drive}^2 + U_{port}^2 - 2|U_{drive}|\left|U_{port}\right|\cos\phi \tag{8.56}$$

To calculate the phase of the volume velocity through the port, U_{port}, relative to the volume velocity from the front of the loudspeaker, $U_{speaker} = -U_{drive}$, it is helpful to recognize that U_{drive} and U_{port} will be in-phase at frequencies well below ω_o. Therefore, the phase difference between $U_{speaker}$ and U_{port} at any frequency, $\phi(f) = \phi_{drive} + 180° - \phi_{port} = 180° - \phi_{port}$, since $\phi_{drive} = 0°$, by definition in the BEGIN segment (0 g). The full calculation is executed by DeltaEC from the file BeranekBox (U-source).out, shown in Fig. 8.39. The results of those calculations are plotted in Fig. 8.40.

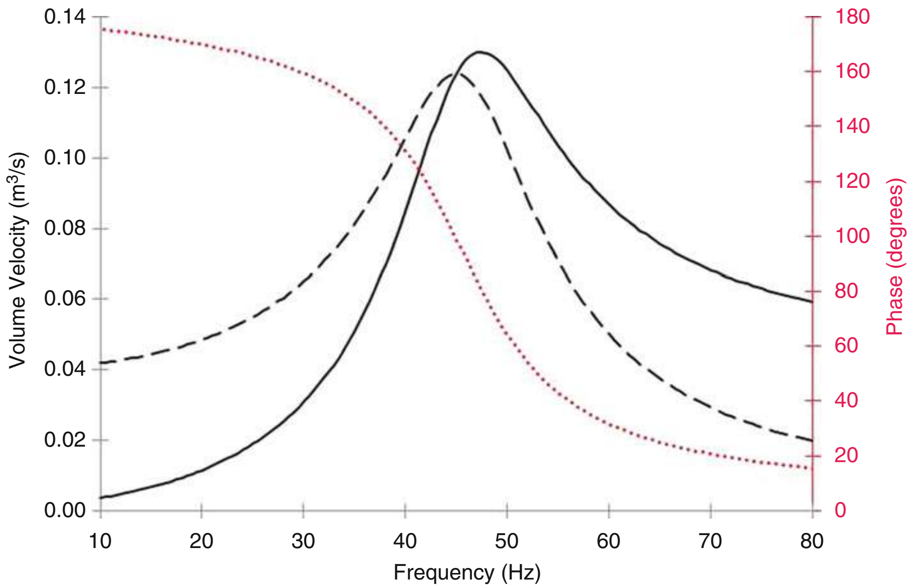

Fig. 8.40 Plot of the response of Beranek's bass-reflex loudspeaker enclosure, driven by a constant volume velocity source, $\left|\hat{\mathbf{U}}_{\mathbf{drive}}\right| = 4.0 \text{ x } 10^{-4}$ $\mathbf{m^3}$/s, located in the compliance. If a loudspeaker were producing that volume velocity, its motion would be 180 degrees out-of-phase with the volume velocity source. The phase difference between the volume velocity generated by a loudspeaker and the volume velocity through the port, $\phi(f)$, is represented by the *dotted line* whose value should be read from the right-hand axis labeled "Phase (degrees)." The magnitude of the volume velocity through the port, $|U_{port}|$, is shown as the *dashed line* and is referenced to the left-hand axis labeled "Volume Velocity ($\mathbf{m^3}$/s)." The magnitude of the vector sum of the port velocity and the loudspeaker velocity, $|U_{net}|$, is shown by the *solid line* that is also scaled by the left axis. At low frequencies, the magnitude of the net volume velocity, $|U_{net}|$, is less than the volume velocity of the source, $|U_{drive}|$, due to phase cancellation, and approaches zero as the frequency goes to zero. Note that above 32.5 Hz, the net volume velocity is larger than the volume velocity source, $|U_{drive}|$. For that reason, it is very rare to see small loudspeaker enclosures that do not use the bass-reflex (Helmholtz resonator) approach to enhance their low-frequency output

The enhancement of the bass response, shown by the fact that net volume velocity exceeds the volume velocity from the front of the speaker's cone at frequencies above about 35 Hz, helps compensate for the decrease in the sensitivity of human hearing at low frequencies (see Fig. 10.5).

8.8.2 Loudspeaker-Driven Bass-Reflex Enclosure*

It will be worthwhile to place a real loudspeaker in Beranek's bass-reflex loudspeaker enclosure as the last example in this chapter. Techniques for measurement of electrodynamic loudspeaker parameters were demonstrated in Sect. 2.5.5. DeltaEC provides a selection of segments that easily incorporate a loudspeaker into a DeltaEC model. The resulting combination of an electromechanical harmonic oscillator and a fluidic Helmholtz resonator presents challenges if approached algebraically. We will see that incorporation of a loudspeaker in a Helmholtz resonator within DeltaEC is no more difficulty than the model of Beranek's bass-reflex enclosure that was run with a constant amplitude volume velocity source in the BEGIN statement of the model shown in Fig. 8.39. Although the use of such a DeltaEC model for optimization of the system's performance can be more complicated, just "plugging in" the appropriate DeltaEC segment to represent the loudspeaker is simple.

```
2nd BeranekJBL-VSpeaker(Plot) JBL 2242 in Beranek's Bass-Reflex
  0 BEGIN        Initial
    1 VSPEAKER     JBL 2242 PHL (S/N: J033N-51645)
                   0.1300 a Area    m^2                 34.432 A |p|      Pa
                   4.8424 b R       ohms                70.976 B Ph(p)    deg
                1.2500E-3 c L       H          P     3.8022E-2 C |U|      m^3/s
                   32.200 d BLProd  T-m                 158.51 D Ph(U)    deg
                   0.1780 e M       kg                  1.8078 E Htot     W
                   9410.0 f K       N/m              2.8191E-2 F Edot     W
                   10.000 g Rm      N-s/m               1.8078 G WorkIn   W
                   10.000 h |V|     V                   10.000 H Volts    V
                                                       0.74724 I Amps     A
                                                       -61.062 J Ph(V/I)  deg
                                                     3.8022E-2 K |Ux|     m^3/s
ideal          Solid type                               158.51 L Ph(-Ux)  deg
    2 RPN          Speaker Input Impedance (Magnitude)
                   0.0000 a G or T    P                13.383   A Ohms
1H 1I /
    3 COMPLIANCE Beranek's enclosure volume (30"x35"x18")
    4 DUCT         Bass Reflex Port
    5 IMPEDANCE    Flow resistance in the port
    6 SOFTEND      Exit from the port
  7 RPN          Net volume velocity (A) and degrees phase differnce (B)
                   0.0000 a G or T    P             4.8371E-2   A m^3/sec
                                      P               -10.429   B Degrees
-180 1D + 6D - # cos 2 * 1C * 6C * 1C 1C * + 6C 6C * + sqrt
```

Fig. 8.41 Screenshot of the output file for a JBL 2242 PHL electrodynamic loudspeaker driving Beranek's bass-reflex enclosure modeled in Fig. 8.40. In this DeltaEC file, the enclosure is driven by a constant voltage source of amplitude 10.0 V_{pk} (0h) corresponding to a root-mean-squared voltage of 7.07 V_{rms} applied across the speaker's voice coil. An RPN segment (#2) has been added to calculate the magnitude of the driver's electrical input impedance, $Z_{el} = V/I = (1G)/(1H)$. All of the collapsed segments are identical to those in Fig. 8.39

In this example, the measured parameters of a JBL Model 2242 PHL (S/N: J033N-51645) will characterize the loudspeaker in the VSPEAKER segment that is included in BarenekBox-VSpeaker. out, shown in Fig. 8.41. Because modern solid-state audio amplifiers produce a nearly constant voltage replica of the audio signal (at least until the current limit is exceeded), a VSPEAKER segment is used to represent the speaker and amplifier combination. As shown in Fig. 8.41, the loudspeaker is specified entirely by the parametric inputs to Segment #1.[27] The user must provide the radiating area of the

[27] The particular choice of parameters used in the DeltaEC electrodynamic speaker specification is not unique. Within the loudspeaker design community, the Thiele-Small parameters are far more common, especially in catalog descriptions of commercial drivers (see Fig. 2.42), although the DeltaEC parameter choice is more general, since DeltaEC must accommodate a variety of gases, pressures, and temperatures.

Of course, there is a one-to-one correspondence between the parameters required by DeltaEC and the Thiele-Small parameters [A. N. Thiele, "Loudspeakers in vented boxes," J. Audio Eng. Soc. **19**, 382–392 (May 1971) and 471–483 (June 1971)]. For example, instead of specifying K, m, and R_m, the stiffness, K, will be expressed as the equivalent volume stiffness of air, V_{AS} [m^3], if the speaker's radiating area, S_D [m^2], is known (see Fig. 7.5). The moving mass, m, can be extracted from the free-cone resonance frequency, f_s [Hz], and the mechanical damping, R_m [kg/s], will be related to the dimensionless mechanical quality factor, Q_{MS}.

$\mathrm{K} = \gamma\, p_m\, S_D^2/V_{AS}$

$m = \mathrm{K}/4\pi^2 f_s^2$

$R_m = 2\pi\, f_s\, m/Q_{MS}$

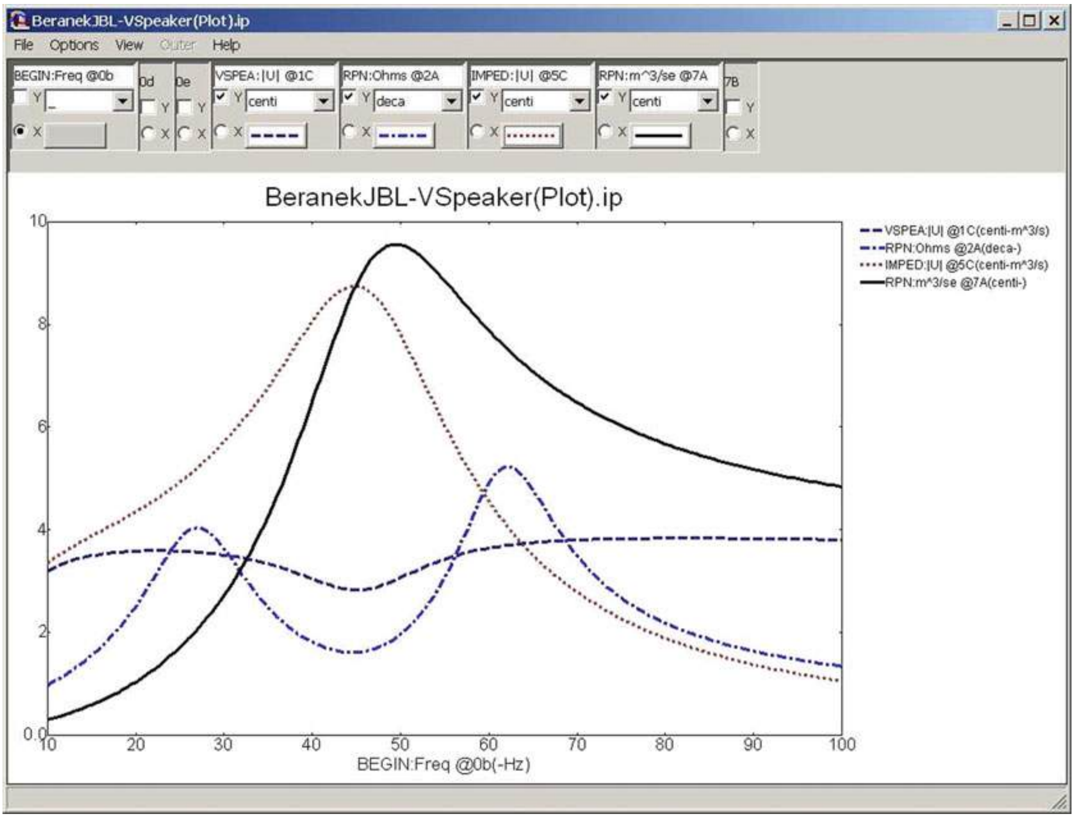

Fig. 8.42 Screenshot of the frequency response of the JBL 2242 PHL driving Beranek's bass-reflex enclosure that is modeled in Fig. 8.41. This graph shows the magnitudes of the speaker's input electrical impedance (*blue dash-dotted line*), the volume velocity of the air oscillating in the port (*brown dotted line*), the magnitude of the volume velocity produced by the loudspeaker cone (*dashed line*), and the magnitude of the net volume velocity produced by the vector sum of the volume velocities, $|U_{net}|$, produced by the port and the loudspeaker (*black solid line*). At frequencies above 33 Hz, the net volume velocity (*black solid line*) exceeds the volume velocity from the front of the loudspeaker alone (*blue dashed line*), demonstrating the enhancement provided by the Helmholtz resonance as a consequence of its ability to invert phase above resonance

speaker (1a), the DC resistance of the voice coil (1b), the inductance of the voice coil (1c), and the force factor, also known as the $B\ell$-product (1d). The moving mass of the cone plus voice coil plus suspension surround and spider (1e) is also required, along with the suspension stiffness (1f) and the mechanical resistance (1g), as well as the amplitude of the driving voltage (1h). Of course, all of the input parameters must be provided to DeltaEC in SI units.

Figure 8.42 provides a graph that includes the speaker's input electrical impedance (2A) and the magnitude of the volume velocity produced by the front side of the speaker's cone (1C) when driven by an input voltage of 7.07 V_{rms} applied to the voice coil that is independent of frequency. The net volume velocity, $|U_{net}|$, is produced by the vector sum of the speaker's cone and the gas oscillating within the enclosure's port.

The loudspeaker's mechanical (free-cone) resonance frequency, $f_s = \sqrt{K/m}/2\pi \cong 36.6\ Hz$, if it were measured in a vacuum. The Helmholtz resonance of the enclosure without the loudspeaker ($f_o = 43.6$ Hz) can be determined from BeranekBox(U-source).out in Fig. 8.39. A first approximation to a bass-reflex loudspeaker enclosure design usually makes the Helmholtz frequency of the enclosure (with the loudspeaker immobilized) roughly equal to the speaker's free-cone resonance frequency. No attempt was made to "tune" the enclosure, possibly by modifying the port's dimensions or its damping, to enhance the loudspeaker's performance, but it is obvious from inspection of Fig. 8.42 that above 33 Hz, the net volume velocity produced by the speaker/enclosure combination is greater than that produced by the front radiating surface of the loudspeaker only, without any (conscious) optimization effort.

The dash-dotted curve in Fig. 8.42, representing the magnitude of the input electrical impedance, $|Z_{in}|$, of the loudspeaker's voice coil, shows two peaks corresponding to the two normal mode frequencies of a two degree-of-freedom coupled harmonic oscillator (see Sect. 2.7). The two independent resonance frequencies of the Helmholtz resonator alone, f_o, and the free-cone resonance frequency of loudspeaker alone, f_s, differ by $\Delta f_{independent} = |f_o - f_s| = |43.6–36.6|$ Hz = 7.0 Hz. The separation of the two peaks in the electrical impedance of the loudspeaker, $\Delta f_{coupled} = (62–27)$ Hz = 35 Hz. This is a clear manifestation of the "level repulsion" exhibited by two strongly coupled harmonic oscillators that was discussed in Sect. 2.7.6.

The peak in the magnitude of the volume velocity through the port, which occurs at about 45 Hz, corresponds to the dip in the volume velocity provided by the front surface of the loudspeaker, demonstrating that the energy dissipated in the port produces a perceptible additional load on the loudspeaker's motor mechanism. This loading, of course, was not evident in the DeltaEC model of Fig. 8.39, which assumed a constant value for the driver's volume velocity.

8.9 Lumped Elements

This (rather long) chapter was intended to accomplish two major goals: First, it provided the initial application of the equations of hydrodynamics to acoustical problems of interest by linearizing the continuity equation and linearizing the Euler equation to produce the acoustical compliance and acoustical inertance of small acoustical elements. The decision to define acoustical impedance as the ratio of the acoustic pressure to volume velocity facilitated the combination of inertances and compliances, since volume velocity is continuous across the junction between lumped elements that typically can have different cross-sectional areas. Though it is true that these elements were small compared to the acoustic wavelength, at the frequencies of interest, as was demonstrated at the end of Chap. 2, combinations of many such elements provide a logical transition to wave motion in distributed systems with dimensions comparable to (or greater than) the wavelength of sound (see Fig. 10.1). Of course, the lumped elements have significant utility within their own domain of applicability.

Second, this chapter also introduced DeltaEC software that could be used to predict the behavior of network of such "lumped elements," focusing first on the combination of an inertance and a compliance to produce a Helmholtz resonator, driven by external oscillating pressure or by an internal source of volume velocity. DeltaEC provided a computational structure that could be applied to networks of lumped elements and included the effects of thermoviscous dissipation on the surfaces of those elements. Application of DeltaEC to a 500 ml boiling flask provided a "benchmark" problem that we will be able to use to test the hydrodynamic models for dissipative process that will be the subject of the next chapter.

The comparison between our nondissipative model, which produced an expression for a Helmholtz resonator's resonance frequency, and some simple (but sufficiently accurate) measurements of that frequency exposed a substantial discrepancy between theory and experiment. That discrepancy was removed by postulating an "effective length correction," since the dependence of the frequency on the volume of the resonator seemed to follow the behavior dictated by the simple nondissipative network calculation. Only "hand-waving" plausibility arguments, appealing to effects of flow adjacent to the resonator's neck, were provided as "justification." That is not science! We will need to create a legitimate theory that produces a quantitative "end correction" that can be related to the neck's radius and the specific geometrical constraints on the flow of fluid into and out of the neck in the vicinity of the neck's openings. Such a theory will be forthcoming when the radiation from circular pistons is developed in Chap. 12.

Talk like an Acoustician

Lumped element	Fluid particle or fluid parcel
Acoustical compliance	Lagrangian description
Acoustical inertance	Eulerian volume
Helmholtz resonator	Nonlinear effect
Harmonic analysis	Streaming
Isotropic fluid	Adiabatic sound speed
Mean value	Acoustical impedance
Instantaneous value	Capacitive reactance
Acoustic approximation	Atmospheric lapse rate
Acoustic Mach number	Inductive reactance
Fourier's theorem	Acoustical network
Laboratory frame of reference	Joining conditions
Eulerian coordinate system	Bass-reflex loudspeaker enclosure

Exercises

1. **Atmospheric lapse rate**. Commercial jet aircraft typically cruise at altitudes around 36,000 feet.
   (a) *Temperature*. What would be the temperature of air at that altitude if we assume a dry adiabatic gas and a sea-level pressure of 100 kPa and sea-level temperature of 15 °C?
   (b) *Density*. Assuming an isothermal atmosphere with a temperature that is the average of 15 °C and the temperature calculated in part (a), what would be the density and pressure of the air at cruising altitude?
2. **Bobbing Hydrophone**. Suppose a hydrophone is suspended some distance below a buoy that is floating at the surface of a body of water as shown in Fig. 8.43. If there are waves on the surface that

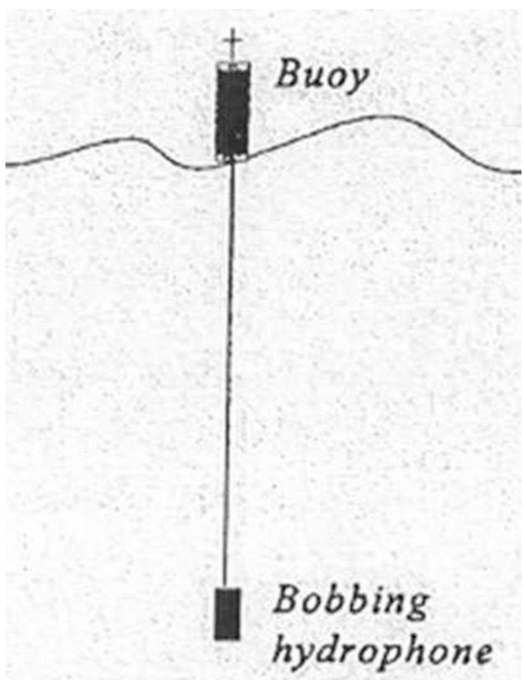

Fig. 8.43 Hydrophone suspended from a floating buoy

cause the buoy to move in the vertical direction by an amount, $z(t) = \Re e\left[\widehat{\mathbf{A}} e^{j\omega t}\right]$, where $\left|\widehat{\mathbf{A}}\right| = 0.20\ m$, determine the amplitude of the pressure signal detected by the hydrophone at the same frequency, ω, if we assume that the separation between the hydrophone and the buoy is constant and the water is incompressible.

3. **Up, up, and away.** A thin rigid spherical shell that is 1.00 m in diameter has a mass of 0.50 kg when evacuated. At "sea level" ($h = 0$) on the surface of the Earth, under typical atmospheric conditions ($T = 15.0\ °C$, $P = 101{,}325$ Pa), such a sphere would displace 0.641 kg of air; therefore it is buoyant and would rise. If we assume conditions specified by the *1976 Standard US Atmosphere* [4], then the density of air, $\rho(h)$, would decay exponentially, as described in Eq. (8.31), as a function of height, h, above the Earth's surface. The density of air at sea level is $\rho_o = 1.225$ Kg/m^3. The characteristic exponential decay length, $\mu \equiv \Re T/gM = 8435$ m.
   (a) *Altitude*. What is the equilibrium height above the Earth, h_o, to which the hollow sphere will rise?
   (b) *Väisälä-Brunt frequency*. Since the equilibrium is stable, if the sphere is displaced from its equilibrium position, its height will oscillate about equilibrium. The effective mass of the oscillating sphere will include a contribution from the motion of the surrounding air. That additional "hydrodynamic mass" is equal to one-half of the mass of air that the sphere displaces (see Sect. 12.5.1) [26]. Assuming negligible damping, what is the period of free oscillation of the sphere when it is displaced (vertically) from its equilibrium position and released if the additional "hydrodynamic mass" of the surrounding fluid is added to the mass of the sphere? The acceleration due to gravity at the equilibrium position can be taken as 9.8 m/s^2.
   (c) *Damping*. The drag force on a sphere in a viscous fluid is given (at low Reynolds numbers) by $F_{vis} = 6\pi\eta r v$, where r is the radius of the sphere, v is its velocity, and $\eta = 1.72 \times 10^{-5}$ N-sec/m^2 is the viscosity of air at the equilibrium height. Determine the decay time, τ, for the oscillations of the sphere to decay to $1/e$ of their initial amplitude.
   (d) *Spherical shell strength*. The spherical shell is not really rigid. It is made of a carbon fiber composite with density, $\rho = 1.6$ gm/cm^3; Young's modulus, E = 70 GPa; Poisson's ratio, $\nu = 0.1$; and ultimate compressive strength of 500 MPa. Can such a shell survive at sea level without imploding? If so, what change in radius occurs as it goes from sea-level pressure to the pressure calculated at the equilibrium height calculated in part (a)?
4. **Pistonphone microphone calibrator**. A pistonphone is a handheld instrument commonly used to calibrate microphone systems. As shown in Fig. 8.44, it is essentially a rigid-walled cavity driven at a single frequency by two horizontally opposed pistons that ride on a rotating cam so that each

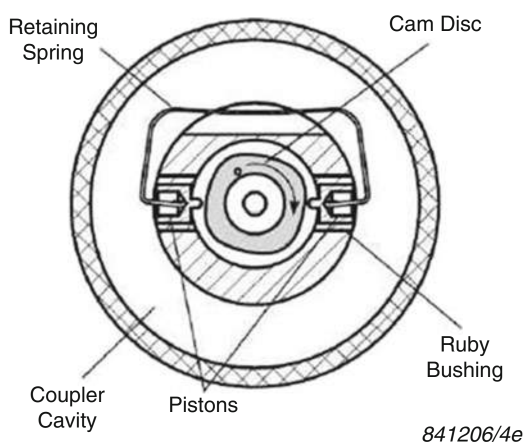

Fig. 8.44 Pistonphone microphone calibrator. (Drawing courtesy of Brüel and Kjær)

piston has known displacement amplitude. The dimensions of the cavity are all much smaller than the wavelength of sound at the operating frequency. For the purpose of this problem, assume the cavity is cylindrical with a height of 1.50 cm and a radius of 1.80 cm. Let the volume of the cavity be 3.8 cm^3, and ignore the space taken by the piston-cam system. Assume the mean pressure in the cavity, $p_m = 101$ kPa, $c_{air} = 343$ m/sec, and that $\gamma_{\text{air}} = 1.403$.

(a) *Piston volume velocity*. Treating the cavity as a lossless compliance, what must be the magnitude of the peak (not effective) volume velocity produced by the pistons for the peak sound pressure within the cavity to be 44.8 Pa_{peak} (equivalent to a sound pressure level of 124 dB_{SPL} *re:* 20 $\mu\text{Pa}_{\text{rms}}$) when driven at 250 Hz?

(b) *Phase*. What is the approximate (to within $\pm 5°$) phase difference between the pressure in the cavity and the volume velocity of the piston?

(c) *Piston motion*. What is the peak-to-peak displacement of each piston if there are two pistons (as shown in Fig. 8.44) and each piston has a diameter of 3 mm, assuming that both pistons have the same displacement amplitudes?

5. **1.0 liter flask**. In Sect. 8.5.2, we used Eq. (8.54) to determine the empty resonator volume, V_o, and the effective neck length, Δx_{eff}, by adding known amounts of water to a flask and measuring the corresponding resonance frequency using a microphone inside the flask. [Note: The mic volume was 6 cm^3.] Now you can enjoy doing this on your own for this larger flask with the data provided in Table 8.1. The diameter of the neck is 33.85 mm and its physical length is 85 mm.

(a) *Effective length*. Calculate V_o and Δx_{eff}.

(b) *Effective length correction*. Calculate the additional length that had to be added to the physical length to produce Δx_{eff}, and also express this length in terms of the radius of the neck.

(c) *Water compressibility*. Is the compressibility of the water in the flask negligible in comparison to the compressibility of the air? Assume the flask contains 400 mL of water for your calculations.

6. **The Penn State commemorative bottle**. The bottle shown in Fig. 8.45 can be modeled in DeltaEC with a DUCT as a neck, a CONE as the transition between the neck and the volume, and another DUCT that has the volume of the end of the bottle closed with a SURFACE segment followed by a HARDEND segment.

(a) *Helmholtz resonance frequency*. Determine the resonance frequency of the resonator in Fig. 8.45 if the bottle is filled with air at 101,325 Pa at a temperature of 20 °C.

(b) *Quality factor*. Use the results of the DeltaEC model to find the Q of the Helmholtz resonance (neglecting radiation losses).

(c) *Standing waves*. Use your DeltaEC model to calculate the frequencies of the three lowest-frequency standing wave resonances of the bottle.

(d) *$*$.sp plots*. Plot the cross-sectional area, *GasA*; the in-phase pressure magnitude, $\Re\text{e}\,[p]$; and the out-of-phase volume velocity, $\Im\text{m}\,[U]$, for the Helmholtz mode and the two lowest-frequency standing wave modes.

Table 8.1 Resonance frequencies for the 1.0 liter flask

Injection (Hz)	Frequency (ml)
6	149.1
106	156.8
206	165.5
306	175.8
406	188.2
506	203.1

Fig. 8.45 The neck length for this bottle is 17.8 mm and its inner radius is 8.26 mm. The volume is a cylinder that is 12.7 cm long with an inner radius of 24.4 mm. The length of the conical section that joins the neck to the volume is 10.0 cm

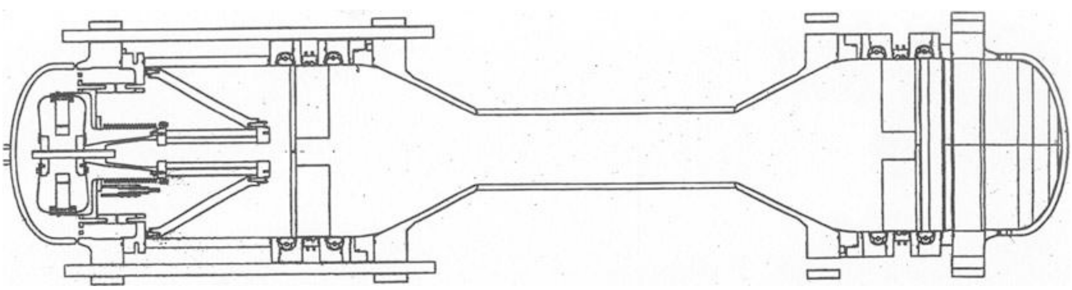

Fig. 8.46 This double-Helmholtz resonator is about 2.0 m long and contains a moving-magnet electrodynamic loudspeaker in the left-hand volume that can produce as much as 6 kW of acoustical power at an electroacoustic efficiency, $\eta_{ac} \cong 90\%$ [28]. The loudspeaker and part of the resonator are shown in the photograph in Fig. 4.21 (*Right*). The left-hand volume, $V_{left} = 0.145$ m^3, and the right-hand volume, $V_{right} = 0.125$ m^3. These volumes include the conical transitions. The neck that connects the two volumes is 0.711 m long and has an inner radius of 9.68 cm

7. **Double-Helmholtz resonator**. The double-Helmholtz resonator shown in Fig. 8.46 was used as a thermoacoustic refrigerator [27].
   (a) *Density*. The resonator is pressurized with 88% helium and 12% xenon at 3.0 MPa and is at a temperature of 20 °C. Calculate the mean atomic weight of the noble gas mixture, $M_{mix} = x\, M_{Xe} + (1 - x)\, M_{He}$, were x is the xenon concentration. Use the mean atomic weight to determine the mixture's density. [Note: You must provide your calculation, but you are welcome to check your answer using the DeltaEC ThermoPhysical Properties.]
   (b) *Resonance frequency*. As a double-Helmholtz resonator with unequal volume compliances, calculate the resonance frequency of the resonator in Fig. 8.46 that is filled with an 88/12 mixture of helium and xenon at 3.0 MPa.

(c) *Gas velocity*. In this resonator, the pressure ratio, $|\widehat{\mathbf{p}}|/p_m$, in the right-hand volume was 5.5%. What is the amplitude of the particle velocity of the gas in the neck? Also report that velocity amplitude in miles per hour and as a percentage of the sound speed.

(d) *DELTAEC model*. Make a DELTAEC model of this double-Helmholtz resonator that is driven by a piston in the left-hand volume with volume velocity 0.010 m^3/sec. The surface areas of the compliances are $A_{left} = 2.3\ m^2$ and $A_{right} = 1.6\ m^2$. [Note: The imposed volume velocity will not produce the full 6 kW mentioned in the caption to Fig. 8.46.]

8. **Helmholtz resonator**. In Sect. 8.5.2, the effective length correction for the neck of a Helmholtz resonator and the volume of the resonator were determined by measured variations in the resonator's volume, a procedure that you were asked to repeat in Problem 5. In this problem, you will do the same, but by substitution of differing necks with carefully measured physical lengths. Figure 8.47 shows a Helmholtz resonator that is constructed from plumbing fixtures that include 6″ (nominal) Schedule-40 PVC pipe and a 6″ PVC 90° elbow. One end of the resonator is closed with a ¼″ thick PVC plate, and the base is medium-density fiberboard (MDF). The inside diameter of the pipe (1.5″ nominal) used for the necks is $D_{neck} = 40.8$ mm. Assume a room temperature sound speed of 343 m/s.

(a) *Enclosure volume and effective length correction*. Using the data in Table 8.2, determine the volume of the Helmholtz resonator's compliance and the effective length correction and their relative uncertainties.

Fig. 8.47 (*Left*) PVC Helmholtz resonator that includes a piston that can be removed rapidly from the neck to excite a free-decay of the Helmholtz resonance. At the bottom of the enclosure is a BNC connector that provides access to a microphone built into the enclosure volume. (*Right*) Several necks of different lengths can be inserted into the fixture near the MDF base of the Helmholtz resonator. Individual necks have lengths of 47.3 mm, 79.0 mm, 116.7 mm, 160.7 mm, and 213.9 mm as listed in Table 8.2. Also visible is a cap to seal the necks and the piston

Table 8.2 The neck lengths and measured free-decay periods in milliseconds, T_i, for the five necks shown in Fig. 8.47 when they are inserted into the volume produced by the 6" PVC pipe and 90° elbow

Neck (mm)	Period (ms)
47.3	14.98
79.0	17.29
116.7	19.65
160.7	21.85
213.9	24.50

Table 8.3 Zero-crossing-to-peak amplitude of the signal from a microphone located inside the Helmholtz resonator's compliance (volume). Each amplitude has been given a sign since the sign of the amplitude alternates each half-cycle. Since time is expressed in terms of the number of cycles, it is not necessary to know either the frequency or the period to calculate Q

Cycle #	0-to-Peak (mV)
0.0	+1306
0.5	-1219
1.0	+1175
1.5	-1100
2.0	+1050
2.5	−981
3.0	+944
3.5	−881
4.0	+850
4.5	−806
5.0	+775
5.5	−731
6.0	+700
6.5	−656
7.0	+625
7.5	−588
8.0	+569
8.5	−541
9.0	+516
9.5	−491
10.0	+472
10.5	−450
11.0	+431
11.5	−406
12.0	+384
12.5	−369
13.0	+353
13.5	−338
14.0	+319
14.5	−300

(b) *Quality factor*. Based on the peak-to-peak values of the free-decay amplitudes given in Table 8.3 for each half-cycle of vibration, determine the Q of the resonance.

References

1. C. E. Bradley, Acoustic streaming field structure: The influence of the radiator, J. Acoust. Soc. Am. **100**(3), 1399–1408 (1996). See Fig. 2.
2. D. Gedeon, DC gas flows in Stirling and pulse-tube cryocoolers, in *Cryocoolers 9*, R. G. Ross (ed.), pp. 385–392 (Plenum Press, 1997).
3. D. Fagen and W. Becker, Babylon Sisters, *Gaucho* (MCA, 1984), Roger Nichols, engineer, Gary Katz, producer.
4. *U. S. Standard Atmosphere, 1976* (National Oceanic and Atmospheric Administration, Report S/T 76-1562, 1976).

5. R. W. Fox and A. T. MacDonald, *Introduction to Fluid Mechanics,* 4th ed. (J. Wiley & Sons, 1992). See example problem 5.5, pp. 209–211; ISBN 0-471-54852-9
6. R.T. Beyer, Radiation pressure – the history of a mislabeled tensor. J. Acoust. Soc. Am. **63**(4), 1025–1038 (1978)
7. L. D. Landau and E. M. Lifshitz, *Fluid Mechanics*, 2nd ed. (Butterworth-Heinemann, 1987). See §5; ISBN 0 7506 2767 0
8. M. Barmatz, Overview of Containerless Processing Technologies, in *Materials Processing in the Reduced Gravity Environment of Space*, ed. by G. E. Ridone, (New York, Elsevier, 1982), pp. 25–37
9. J.B. Mehl, Greenspan acoustic viscometer: Numerical calculation of fields and duct-end effects. J. Acoust. Soc. Am. **106**(1), 73–82 (1999)
10. F. Hoffman, Aw, c'mon and take a hit, *Flash*, No. 2 (1977), pp. 30–33.
11. C. C. Mann, *1491*, 2nd ed. (Vintage, 2011); ISBN 978-1-4000-3205-1.
12. S.L. Garrett, D.K. Stat, Peruvian whistling bottles. J. Acoust. Soc. Am. **62**(2), 449–453 (1977)
13. Mukai, et al., Experimental study on the absorption characteristics of resonance-type brick/block walls, J. Acoust. Soc. Japan (E) **20**(6), 433–438 (1999).
14. http://www.lmsintl.com/SYSNOISE.
15. http://www.ht-audio.com/bassbox.htm.
16. S. L. Garrett and S. Backhaus, The power of sound, *American Scientist* **88**(6), 516–525 (2000) is available at the *American Scientist Magazine* web site: http://www.americanscientist.org/issues/feature/2000/6/the-power-of-sound.
17. W. Ward, J. Clark, and G. Swift, *Design Environment for Low-amplitude Thermoacoustic Energy Conversion* (DeltaEC), Ver. 6.4b2.7, Los Alamos National Laboratory Report N° LA-CC-16-053 (4 Dec 2017).
18. P. M. Morse, *Vibration and Sound*, 2nd ed. (McGraw-Hill, 1948), Ch. VI, §24, pp. 265–288. This classic textbook has been reprinted by the Acoustical Society of America, 1981; ISBN 0-88318-876-7.
19. S. Backhaus, G.W. Swift, A thermoacoustic Stirling heat engine. Nature **399**, 335–338 (1999)
20. P. Merkli, H. Thomann, Thermoacoustic effects in resonant tubes. J. Fluid Mech. **70**, 161–177 (1975)
21. G. W. Swift, *Thermoacoustics: A Unifying Perspective for Some Engines and Refrigerators*, 2nd ed. (Springer/Acoust. Soc. Am., 2017); ISBN 978-3-319-66932-8.
22. J. Wilhelm, K.A. Gillis, J.B. Mehl, M.R. Moldover, An improved Greenspan acoustic viscometer. Int. J. Thermophys. **21**, 983–997 (2000)
23. K.A. Gillis, J.B. Mehl, M.R. Moldover, Theory of the Greenspan viscometer. J. Acoust. Soc. Am. **114**(1), 166–173 (2003)
24. P. Roth, *Portnoy's Complaint* (Random House, 1969); ISBN 978-0394441198-6.
25. L. L. Beranek, *Acoustics* (McGraw-Hill, 1954); ISBN 07-004835-5. This classic textbook has been reprinted by the Acoustical Society of America, 1996; ISBN 0-88318-494-X.
26. S. Garrett, The effect of "Kelvin Drag" on the oscillations of a neutrally buoyant sphere. Am. J. Phys. **49**, 807 (1981)
27. R.A. Johnson, S.L. Garrett, R.M. Keolian, Thermoacoustic cooling for surface combatants. Nav. Eng. J. **112**(4), 335–345 (2000)
28. J. F. Heake, "Characterization of a 10-kilowatt Motor/Alternator for Thermoacoustic Refrigeration," Master of Science in Acoustics, Penn State University, December 2001.

9 Dissipative Hydrodynamics

Contents

In the previous chapter, the resonance frequency, ω_o, of a Helmholtz resonator was calculated. When driven at that frequency, the predicted pressure amplitude inside the resonator's volume (compliance) became infinite. This was because the theory used to model that inertance and compliance network in Figs. 8.11 and 8.15, and in Eq. (8.50), did not include any dissipation. By introducing DeltaEC, we were able to calculate the amount of power dissipated in the neck (inertance) and volume (compliance) of a 500 ml boiling flask. In this chapter, those losses will be calculated from hydrodynamic "first principles."

Just as we used lumped acoustical elements in Chap. 8 to begin our exploration of the linearized, nondissipative forms of the hydrodynamic equations, we will again use lumped elements to introduce thermal and viscous dissipative effects, restricting our attention (temporarily) to thermoviscous effects

S. L. Garrett, *Understanding Acoustics*, Graduate Texts in Physics,
https://doi.org/10.1007/978-3-030-44787-8_9

at solid-fluid boundaries. Later, in Chap. 14, those dissipative mechanisms will be generalized to include dissipative effects (attenuation), with the addition of molecular relaxation effects (see Sect. 4.4), which will be incorporated by the introduction of a "bulk viscosity," to account for dissipation of sound waves propagating in spaces that are far from any boundaries.

9.1 The Loss of Time Reversal Invariance

There are certain phenomena that can be "played backward" in a movie or video that do not look different than when played forward. If we took a video of a wavelike pulse propagating on a string or a slinky, like the Gaussian pulses in Figs. 3.2, 3.3, and 3.4, it would be very difficult to tell whether the video was being played forward or backward. This indifference to the "arrow-of-time" is called *time reversal invariance*.

On the other hand, there are certain things that do not look right played backward. An egg dropping to the floor and cracking does not make sense played backward—a yellow slimy mess that self-organizes into an unbroken shell and then levitates. The murder at the start of *Memento* [1] shows the bullet case reentering the gun and a Polaroid™ photo fading out and then reentering its camera.

When dissipation is included in our hydrodynamic equations, time reversal invariance must be abandoned. This can be demonstrated mathematically by focusing on a traveling wave moving to the right, along the x axis, as described in Eq. (1.9), which represented complex exponential form.

$$p(x,t) = p_m + \Re e\left[\widehat{\mathbf{p}}e^{j(\omega t - kx)}\right] \tag{9.1}$$

The complex amplitude of the wave, $\widehat{\mathbf{p}}$, can introduce an additional phase factor to compensate for some arbitrary choice of the time origin, $t = 0$. If we reverse the sign of the time, the phase factor changes from $j(\omega t - kx)$ to $-j(\omega t + kx)$, which is the equivalent of making the wave propagate in the negative x direction. When we change the direction of time, the sign of the velocity also changes (Figs. 9.1 and 9.2).

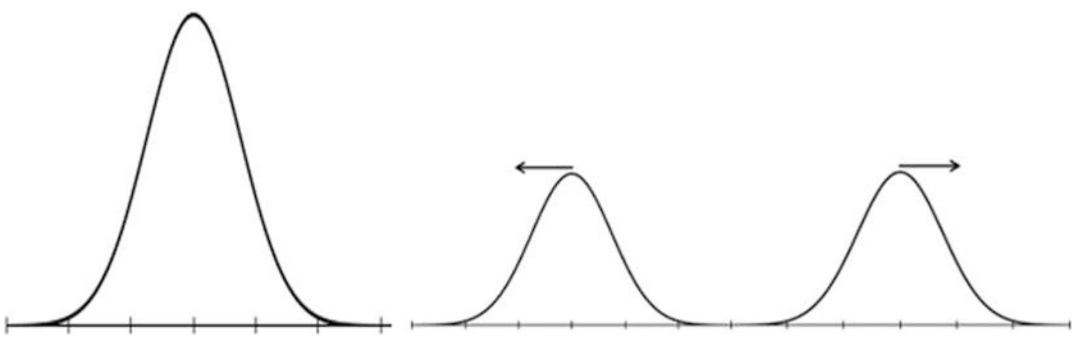

Fig. 9.1 Sketches of pulses in a nondissipative medium showing the (transverse) pulse amplitude propagating reversibly in time along one dimension. We could assume that the pulse started at $t = 0$, as the single lump shown on the *left*, and then became two pulses of the same width and shape having amplitudes equal to half the original pulse height, traveling in opposite directions. We could also assume that the arrows showing the direction of motion for the two pulses at the right could be reversed. Then the pulses are moving toward each other; they superimpose to form the larger pulse on the *left* and then pass through each other to become the two pulses shown at the *right* with their *arrows* (as drawn) again showing the direction of their subsequent motion after they had passed through each other

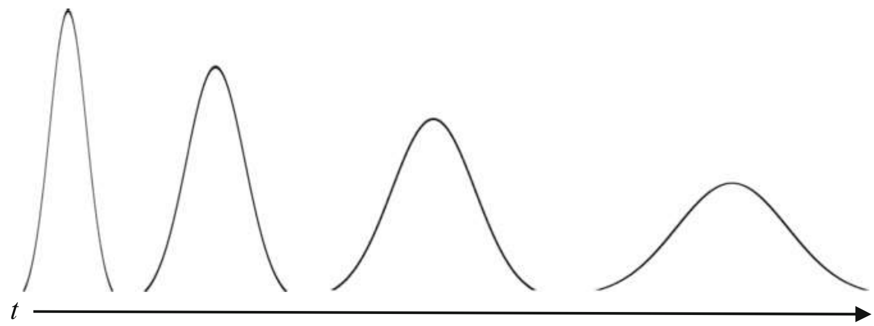

Fig. 9.2 Unlike Fig. 9.1, the time evolution of the pulse at the left can only proceed in the direction indicated by the *arrow*. The progression of the pulse is determined by a diffusion equation like Eq. (9.4). If the pulse at the *left* represents an initial temperature distribution in a fluid, over time the temperature would diffuse as shown due to the thermal conductivity of the medium. If the pulse represented the injection of dye into a stagnant fluid, the diffusion of the dye would be represented by the subsequent pulse shapes. The most diffuse pulse, shown at the *right*, would never spontaneously self-focus into the more concentrated temperature or dye distribution shown at the *left*

In the continuity equation (7.32), the reversal of time changes the sign of the time derivative, $\partial\rho/\partial t$. The term that includes the divergence, $\nabla\bullet\left(\rho\vec{v}\right)$, also has its sign reversed because the velocity changes sign. Both terms on both sides of the continuity equation are thus "negated" by the time reversal so the equation is unaffected; just multiply the whole equation by (-1) and we are back where we started.

This is not the case for the Navier-Stokes equation (7.34), even in its linearized form that discards the convective term, $\left(\vec{v}\bullet\nabla\right)\vec{v}$, and ignores gravity.

$$\rho\frac{\partial\vec{v}\left(\vec{x},t\right)}{\partial t}=-\vec{\nabla}p\left(\vec{x},t\right)+\mu\nabla^2\vec{v}\left(\vec{x},t\right)\tag{9.2}$$

Since both the velocity and the time change sign, the derivative, $\partial\vec{v}/\partial t$, does not change sign. On the right-hand side of Eq. (9.2), the pressure, $p\left(\vec{x},t\right)$, is a thermodynamic variable and therefore a Galilean invariant; its value is a property of the medium that is not a function of the reversal of time or of uniform motion of the coordinate system.

We'd be in fine shape with both the time derivative and the gradient of the pressure, since the sign of neither changes under time reversal (i.e., the Euler equation is time reversal invariant). But the Laplacian operator, ∇^2, that is multiplied the *shear viscosity*, μ, operates on the velocity, which does change sign when time is reversed. The Navier-Stokes equation, as written in Eq. (9.2), is therefore not time reversal invariant. Neither is the linearized entropy equation, as written in Eq. (7.43), even if the viscous entropy generation term is neglected and we assume that the *thermal conductivity*, κ, is independent of position, where s is the specific entropy (per unit mass) [J/K − kg] = [m^2/s^2 − K].

$$\rho T\frac{\partial s\left(\vec{x},t\right)}{\partial t}=\kappa\nabla^2T\left(\vec{x},t\right)\tag{9.3}$$

Here again, both $s\left(\vec{x},t\right)$ and $T\left(\vec{x},t\right)$ are Galilean invariant thermodynamic properties of the fluid that do not change under time reversal. The sign of $\partial s/\partial t$ does change since the sign of the time is reversed. Equation (9.3) can be transformed into the *Fourier Diffusion Equation* after substituting the relation between changes in heat per unit mass, dq, and changes in entropy per unit mass, ds. We have $dq = T\,ds$, from Eq. (7.5), and the relation between the addition of heat and the change in temperature at constant pressure, $dq = \rho c_p\, dT$, for a polytropic substance, from Eq. (7.14).

$$\frac{\partial T\left(\vec{x},t\right)}{\partial t} = \frac{\kappa}{\rho c_P}\nabla^2 T\left(\vec{x},t\right) \tag{9.4}$$

Equations that have the form of Eq. (9.2) and Eq. (9.4) are *diffusion equations*. They produce dissipation and they violate time reversal invariance. If those irreversible effects are present, then energy will be dissipated. We can clearly see a difference if the video is played forward or backward in the presence of dissipation.

9.2 Ohm's Law and Electrical Resistivity

We will start our investigation of dissipative hydrodynamics with thermal conduction. To do so, we will make an analogy to dissipation in direct current (dc) electrical circuit theory, since most students who go on to careers in engineering and science learn *Ohm's law* in high school.

Our previous representation of ideal compliances and inertances were analogous to ideal capacitors and inductors; energy could be stored as compressive (elastic) potential energy in a compliance or as kinetic energy in an inertance, but it would not be dissipated, as it could in an electrical circuit where the current flows through an electrical resistance, R_{dc}. The relationship between the current flowing through the resistance, I, and the voltage difference, ΔV, across the resistance is known as Ohm's law: $I = \Delta V/R_{dc}$. The electrical resistance is a (mathematically) real quantity (usually considered to be a constant that is independent of current[1]), so that the current and the voltage are in-phase; hence, $\phi = 0$.

The time-averaged electrical power, $\langle \Pi_{el} \rangle_t$, dissipated in the resistor is a positive-definite function of either the current or the voltage.

$$\langle \Pi_{el} \rangle_t = \frac{I\ \Delta V}{2}\cos\phi = \frac{I^2 R_{dc}}{2} = \frac{(\Delta V)^2}{2R_{dc}} \tag{9.5}$$

As we have done with our acoustical variables, ΔV and I are designated by their peak values, not the root-mean-squared values that would be displayed by an ac voltmeter. The phase angle between $I(t)$ and $\Delta V(t)$ is ϕ, but since $I(t)$ is in-phase with $\Delta V(t)$, $\cos\phi = 1$. It does not matter whether the current is flowing to the right or to the left; power will be dissipated in a resistor and entropy will be created by an irreversible process. This electrical power dissipation in a resistor is usually called *Joule heating*, after James Prescott Joule (1818–1889).

Considering a material, shown schematically in Fig. 9.3, having a constant electrical conductivity, σ, with units of $[(\Omega - \mathrm{m})^{-1}]$,[2] the electrical resistance measured across its length, R_{dc}, will depend

[1] William Hewlett, an electrical engineering student at Stanford University, used a current-dependent resistance (a flashlight bulb) to stabilize the amplitude of an audio oscillator circuit as his master's thesis. That oscillator subsequently became the HP-200. It was the first product developed commercially by the original Silicon Valley start-up: Hewlett-Packard. The first five of their "production" models were purchased by Walt Disney to produce sound effects in the animated feature film, *Fantasia*.

[2] Before the French-dominated *Le Système International d'Unités* was adopted, the unit of conductance was the mho (ohm spelled backward). They re-named the unit of electrical conductance the siemens [S]. These are the same folks, who, in their collective wisdom, re-named the unit of frequency from the obscure cycles-per-second (cps) to the hertz [Hz].

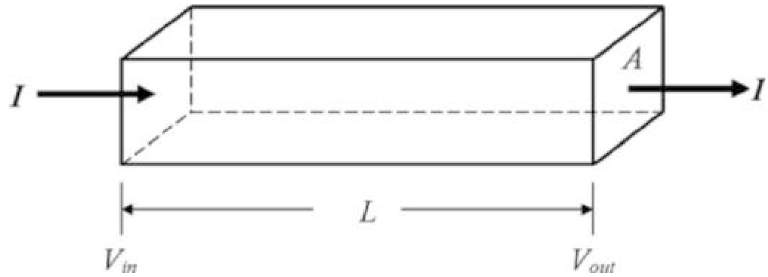

Fig. 9.3 Electrical current, I, flows through a conductor with electrical conductivity, σ, from a higher electrical potential, V_{in}, to a lower electrical potential, V_{out}. The electrical resistance, R_{dc}, of the resistor of length, L, and cross-sectional area, A, is $R_{dc} = L/\sigma A$

directly upon its length, L, and inversely upon its cross-sectional area, A. For that resistor, the current passing through the resistor, I, and the voltage difference, ΔV, across the resistor are related by the direct current (dc) version of Ohm's law.

$$I = \frac{\Delta V}{R_{dc}} = \frac{\sigma A}{L}(V_{in} - V_{out}) \tag{9.6}$$

If two identical pieces of the same material, like that shown in Fig. 9.3, were put side-by-side (in parallel), their areas would add, and the resistance would be cut in half. If $\Delta V = V_{in} - V_{out}$ remains constant, the current would double. If two pieces were placed end-to-end (in series), their lengths would add without changing their areas, and the resistance would be doubled. Again, if ΔV remained constant, the current would be reduced by half, relative to the single sample.

9.3 Thermal Conductivity and Newton's Law of Cooling

Newton's Law of Cooling has exactly the same form as Ohm's law, as written in Eq. (9.6), where we recognize I as the rate of electrical charge flow, with units of amperes [A] or coulombs/second [C/s]. By analogy, the rate of heat flow, $\dot{Q}$[J/s], is linearly related to the temperature difference, ΔT, across the length, L, of the sample. It is also proportional to the thermal conductivity of the material, κ, having units of [W/K-m] or [W/°C-m].

$$\dot{Q} = \frac{\Delta T}{R_{th}} = \frac{\kappa A}{L}(T_{in} - T_{out}) = \kappa A \frac{\Delta T}{L} \tag{9.7}$$

The SI units of heat flow are watts [W] or joules/second [J/s]. As expressed in the right-hand term of Eq. (9.7), the heat flow (thermal power flow) is proportional to the temperature gradient, $\Delta T/L$ (Fig. 9.4).

As shown in Fig. 9.5, analysis of the heat flow, $\dot{Q}$, through a sample like that in Fig. 9.4, but with length, dx, converts Newton's Law of Cooling in Eq. (9.7) into the Fourier Diffusion Equation (9.4). The heat flux, $\dot{q}_{in}$, with units of heat (energy) per unit area per unit time [W/m^2], enters the slab at x, and $\dot{q}_{out}$ exits at $x + dx$.

The thermal power, $\dot{Q}_{net}$, that is deposited in the slab results in an increase in the temperature of the slab with time. If we assume that the differential element of length, dx, has cross-sectional area, A, and the material has a specific heat per unit mass, c_p, that is independent of temperature, then the heat capacity of the differential element is the mass of the element, $\rho A\, dx$, times the specific heat (per unit mass). By Eq. (9.8), this net input of thermal power must result in a change in the temperature of the slab with time.

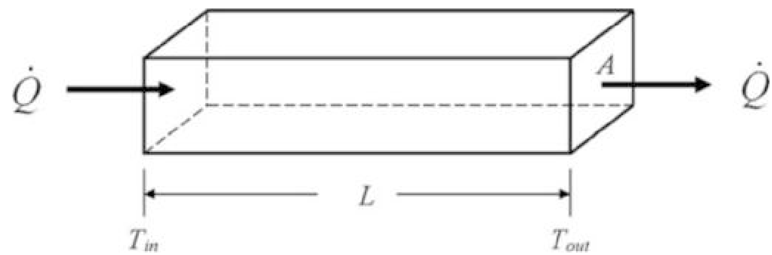

Fig. 9.4 Heat power, $\dot{Q}$, flows through a thermal conductor made from a material with constant thermal conductivity, κ, from a higher temperature, T_{in}, to a lower temperature, T_{out}. The thermal resistance, R_{th}, of the sample of length, L, and cross-sectional area, A, is $R_{th} = L/\kappa A$

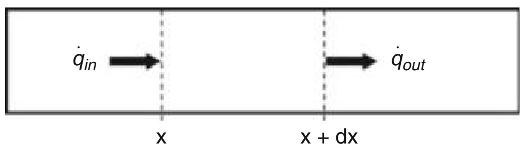

Fig. 9.5 A different heat flux, $\dot{q}_{in}$, flows into a differential "slab" of thickness, dx, and area, A, than flows out, $\dot{q}_{out}$, at $x + dx$. As a result, the heat that remains within the differential element, $\dot{Q}_{net}$, causes the temperature of that element to change in accordance with the definition of heat capacity, $C_P = (\partial Q/\partial T)_P$, where we assume the sample is held at constant pressure

$$\dot{Q}_{net} = \rho c_p A\, dx \frac{dT}{dt} = \dot{Q}(x) - \dot{Q}(x + dx) = A[\dot{q}(x) - \dot{q}(x + dx)] \tag{9.8}$$

Since the heat flows in response to a temperature gradient, as expressed by Newton's Law of Cooling (9.7), and Eq. (9.8) produces the net heat transport in terms of the (one-dimensional) temperature gradients, $\partial T/\partial x$, evaluated at x and $x + dx$.

$$\rho c_p A\, dx \frac{dT}{dt} = A\left[-\kappa\left(\frac{\partial T}{\partial x}\right)_x + \kappa\left(\frac{\partial T}{\partial x}\right)_{x+dx}\right] \tag{9.9}$$

At this point, we are only one Taylor series expansion away from Fourier's Diffusion Equation.

$$\begin{aligned}
&\left(\frac{\partial T}{\partial x}\right)_{x+dx} \cong \left(\frac{\partial T}{\partial x}\right)_x + \frac{\partial}{\partial x}\left(\frac{\partial T}{\partial x}\right)_x dx + \ldots \\
&\Rightarrow \left(\frac{\partial T}{\partial x}\right)_{x+dx} - \left(\frac{\partial T}{\partial x}\right)_x \cong \left(\frac{\partial^2 T}{\partial x^2}\right)_x dx
\end{aligned} \tag{9.10}$$

Since dx is a small quantity (compared to what?), we can neglect the terms containing higher powers $(dx)^n$ of dx and combine Eq. (9.9) and Eq. (9.10), while bringing the thermal conductivity, κ, outside the derivative, assuming that it is spatially uniform.

$$\frac{\partial T}{\partial t} = \frac{\kappa}{\rho c_p}\frac{\partial^2 T}{\partial x^2} = \frac{\kappa}{\rho c_p}\nabla^2 T = \alpha \nabla^2 T \tag{9.11}$$

The earlier expression is identical to the Fourier Heat Diffusion Equation that we derived from our linearization of the entropy equation (7.43) under the same assumption of a constant temperature-independent thermal conductivity. The new constant introduced in the right-hand term of (9.11), $\alpha = \kappa/\rho c_p$, is the *thermal diffusivity*.[3] Energy and temperature units cancel in this ratio, so α has units of length-squared divided by time [m^2/s] [2].

The thermal diffusivity is useful because it is a measure of the ability of a material to conduct thermal energy relative to its ability to store thermal energy. Materials with a large α will respond quickly to changes in their thermal environment, while materials with small α will respond more sluggishly, taking longer to reach a new equilibrium condition if the temperature of the surroundings is changed. The thermal diffusivity of most metallic solids and gases (near room temperature) is $\alpha \cong 10^{-5}$ m^2/s, while for insulating solids and many liquids, $\alpha \cong 10^{-8}$ to 10^{-7} m^2/s. Of course, if the fluid is in motion, the convective heat transport (e.g., "wind chill") can dominate conductive heat transport [3].

9.3.1 The Thermal Boundary Layer

As acousticians, we are interested in the acoustical solutions to Eq. (9.11) that involve time-harmonic temperature deviations, $T(t) = T_s \cos(\omega t)$, typically at a single frequency, ω, from some mean temperature, T_m. As claimed before, harmonic analysis is the acoustician's most powerful mathematical tool. We will begin by applying Eq. (9.11) to a semi-infinite wall defining a plane surface at $x = 0$ that has an oscillating temperature, $T(0, t) = T_m + T_s \cos(\omega t)$. By letting T_s be a scalar, we are defining the phase of the temperature response with respect to the oscillating temperature of the boundary. The wall is in contact with a fluid that has a thermal diffusivity, $\alpha = \kappa/\rho c_p$, as diagrammed in Fig. 9.6.

We will assume that the space-time behavior of the fluid at $x \geq 0$ is that of a wave traveling to the right, $T_{fluid}(x,t) = T_m + \Re e\left[\hat{\mathbf{T}} e^{j(\omega t - \mathbf{k}x)}\right]$, and substitute this expression into the one-dimensional version of Eq. (9.11) to convert the differential equation into an algebraic equation.

$$j\omega\hat{\mathbf{T}} = -\alpha\mathbf{k}^2\hat{\mathbf{T}} \tag{9.12}$$

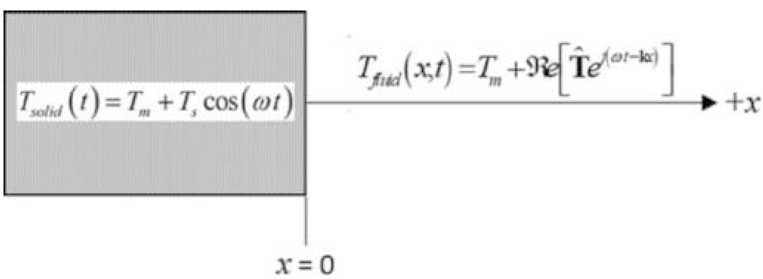

Fig. 9.6 A semi-infinite solid with an oscillatory surface temperature, $T_{solid}(0, t) = T_m + T_s \cos(\omega t)$, is in contact at the plane $x = 0$ with a fluid at the same mean temperature, T_m. Since there is only fluid at $x \geq 0$, we will assume a right-going wavelike space and time dependence for the oscillating component of the fluid's temperature, $T_{fluid}(x,t) = T_m + \Re e\left[\hat{\mathbf{T}} e^{j(\omega t - \mathbf{k}x)}\right]$

[3] This material parameter is also sometimes called the *thermometric conductivity* and abbreviated as χ. For instance see, L. D. Landau and E. M. Lifshitz, *Fluid Mechanics*, 2nd ed. (Butterworth-Heinemann, 1987); ISBN 0 7506 2767 0. See §50.

Cancelling the $\widehat{\mathbf{T}}$s and dividing both sides by $-\alpha$, Eq. (9.12) becomes $\mathbf{k^2} = -j\omega/\alpha = \omega/j\alpha$. Taking the square root[4] of $\mathbf{k^2}$ (see Sect. 1.5.2), we find that $\mathbf{k}$ is a complex number, having real and imaginary parts of equal magnitude.

$$\mathbf{k} = \sqrt{\frac{\omega}{j\alpha}} = \frac{1-j}{\sqrt{2}}\sqrt{\frac{\omega}{\alpha}} = (1-j)\sqrt{\frac{\omega}{2\alpha}} \equiv \frac{1-j}{\delta_\kappa} \tag{9.13}$$

It is convenient to define a real scalar physical length, δ_κ, based on the reciprocal wavenumber that is the (exponential) thickness of the oscillatory thermal boundary layer. The scale length of thermal diffusion, δ_κ, is very important in acoustics (see "`delta_kappa`" in Fig. 8.19) and is called the *thermal penetration depth.*

$$\delta_\kappa \equiv \sqrt{\frac{2\kappa}{\rho c_p \omega}} = \sqrt{\frac{2\alpha}{\omega}} = \sqrt{\frac{\alpha}{\pi f}} \tag{9.14}$$

The complex wave number, $\mathbf{k}$, has equal real and imaginary parts. In electromagnetism, this similar behavior occurs when an electromagnetic wave impinges on an electrically conducting (usually metallic) solid or the surface of an ionic solution (e.g., seawater). In that case, the equivalent to Eq. (9.14) is known as the "*skin depth*" (see Sect. 9.4.2).

This behavior is different from that which occurs at the interface between two optically transparent media when the angle of incidence exceeds the critical angle[5] or at the interface between two acoustical media with different specific acoustical impedances (see Sect. 11.2.1). For the case of total internal reflection, the wavenumber within the excluded medium is entirely imaginary and the disturbance is known as an *evanescent wave*.

The complex wavenumber, $\mathbf{k}$, in Eq. (9.13) still has the units of reciprocal length [m^{-1}]. Substitution of $\mathbf{k}$ from (9.13) back into the assumed solution, $T_{fluid}(x,t) = T_m + \Re e\left[\widehat{\mathbf{T}} e^{\,j(\omega t - \mathbf{k}x)}\right]$, shown in Fig. 9.6, and application of the boundary condition at $x = 0$, provides an explicit expression for the spatial distribution of temperature oscillations within the fluid.

$$T_1(x,t) = \Re e\left[\widehat{\mathbf{T}}_s e^{-x/\delta_\kappa} e^{\,j(\omega t - x/\delta_\kappa)}\right] \quad \text{for} \quad x \geq 0 \tag{9.15}$$

Expanding Eq. (9.15) in terms of real trigonometric functions, Euler's formula in Eq. (1.53) will facilitate plotting of the real and imaginary parts of the spatial dependence of $T_1(x)$, shown in Fig. 9.7.

[4] To take the square root of $-j = j^{-1}$, it is sometimes useful to draw a diagram on the complex plane by expressing j^{-1} as $-j$, drawn vertically downward at $-90°$ from the positive real axis. The square root operation divides that angle by two, resulting in a unit vector rotated only $-45°$ away from the real axis having a projection of $(2)^{-½}$ along the real axis and $-(2)^{-½}$ along the imaginary axis demonstrating that one root of $\sqrt{-j}$ is $(1-j)/\sqrt{2}$. Regarding $-90°$ as $+270°$, and again dividing by two, yields the other root, $(j-1)/\sqrt{2}$.

[5] Evolution has found these waves useful for the control of light reaching the optic nerve of insects with compound eyes. Did you ever notice that it is hard to swat a fly under a wide range of lighting conditions? How can you control the light levels when your eye has a thousand lenses? One iris for each lens is clearly out of the question, since each lens has a diameter of only about 30 μm. The mechanism employed by insects to control light levels makes each lens the entrance to an optical waveguide (called an ommatidium by the entomologists), much like an optical fiber used in telecommunications, that channels light from the lens down to the optic nerve (see Fig. 11.6). In bright light, a chemical change in the fluid surrounding the waveguides causes a precipitate to form that scatters the wave decaying (exponentially) beyond the waveguide into the fluid. Scattering of this diffusion wave reduces the light that makes it down the waveguide to the optic nerve. For further information on the physics of insect vision and some relevant graphics, see R. P. Feynman, *Lectures on Physics*, Vol. I (Addison-Wesley 1963), §36-4.

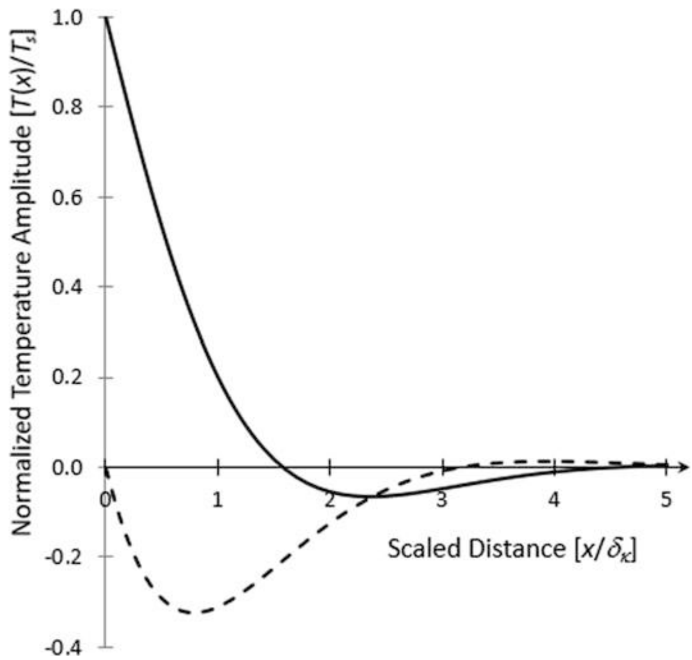

Fig. 9.7 The real (*solid*) and imaginary (*dashed*) components of the oscillatory portion of the temperature near a wall that has an oscillating temperature at its surface. The y axis is normalized so that $T_s = 1$. The x axis is scaled by the thermal penetration depth, δ_κ. The real part of Eq. (9.16) is in-phase with the temperature oscillations at the surface of the solid and is equal to the magnitude of those oscillations, thus satisfying the boundary condition at $x = 0$: $T_{fluid}(0, t) = T_{solid}(0, t)$ at all times. At a distance of $0.7854\delta_\kappa$ from the wall, the amplitudes of the real and imaginary parts have equal magnitude

$$T_1(x) = T_s e^{-x/\delta_\kappa}\left[\cos\left(\frac{x}{\delta_\kappa}\right) - j\sin\left(\frac{x}{\delta_\kappa}\right)\right] \quad \text{for} \quad x \geq 0 \tag{9.16}$$

It is clear from Fig. 9.7 that Eq. (9.15) and Eq. (9.16) satisfy the boundary condition requiring that the temperatures of the solid and the fluid, at their plane-of-contact, $x = 0$, are exactly equal, $\Re e[T_1(0, t)] = T_s$, and in-phase, $\Im m[T_1(0, t)] = 0$, at all times. If the adjacent temperatures were not equal, then the discontinuity would require Eq. (9.11) to produce infinite heat flows. The temperature disturbance in the fluid is localized quite near the wall. At distances greater than $x = 4\delta_\kappa$, the effects of the wall's oscillating temperature correspond to temperature oscillations in the fluid that are less than 2% of those at the interface between the wall and the fluid.

The situation encountered more commonly in acoustical systems is that the temperature of the fluid is oscillating while the wall temperature remains constant, typically due to the solid's higher thermal conductivity and heat capacity per unit volume. For example, in an ideal gas, the amplitude of adiabatic temperature oscillations, $T_{1,adiab}$, far from any solid boundaries, were given by Eq. (7.25): $T_{1,\ adiab} = T_m[(\gamma - 1)/\gamma](|\widehat{\mathbf{p}}|/p_m)$. Typically, a solid boundary will keep an ideal gas's temperature constant on the solid-gas interface plane, which is defined as $x = 0$ in Fig. 9.6. In that case, the boundary condition is that $T_1(0, t) = 0$.

$$T_1(x,t) = T_{1,\ adiab}\Re e\left[e^{j\omega t}\left(1 - e^{-(1+j)x/\delta_\kappa}\right)\right] \quad \text{for} \quad x \geq 0 \tag{9.17}$$

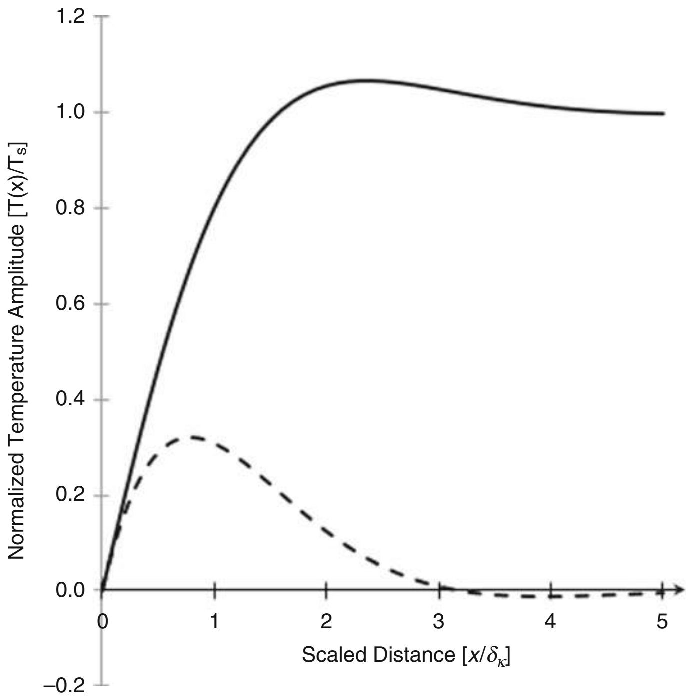

Fig. 9.8 The real (*solid line*) and imaginary (*dashed line*) parts of the oscillatory portion of the temperature near an isothermal surface are plotted for the situation where the fluid far from the wall has a normalized oscillating temperature magnitude, $|T_1(x/\delta_\kappa \gg 1)| = 1$, that might be caused by adiabatic expansion and compression of an ideal gas given by Eq. (7.25). The x axis is again scaled by the thermal penetration depth, δ_κ. The isothermal surface at $x = 0$ requires that both the real and imaginary parts of Eq. (9.18) vanish at the interface: $T_s(0, t) = 0$. The thermal influence of the wall extends only a distance of about four thermal penetration depths into the fluid

The real and imaginary parts of that solution, provided in Eq. (9.18), are plotted in Fig. 9.8.[6]

$$T_1(x,t) = T_{1,\ adiab}\Re e\left[e^{j\omega t}\left\{1 - e^{-x/\delta_\kappa}\cos\left(\frac{x}{\delta_\kappa}\right) + j\left[e^{-x/\delta_\kappa}\sin\left(\frac{x}{\delta_\kappa}\right)\right]\right\}\right] \text{ for } x \geq 0 \tag{9.18}$$

9.3.2 Adiabatic Compression Within a Bounded Volume

At various places in Chaps. 7 and 8, I have claimed that the acoustic compressions and expansions of an ideal gas take place adiabatically. Having produced an acoustical solution the Fourier Heat Diffusion Equation (9.11), and having defined the thermal penetration depth, δ_κ, in Eq. (9.14), we

[6] It is difficult for most people to visualize the spatial and temporal dependence of the temperature based only on plots of the real and imaginary parts of the solution as a function of position, such as those provided in Figs. 9.7 and 9.8. An animation of the temperature variation for an ideal gas near a solid (isothermal) wall is available at the Los Alamos National Laboratory Thermoacoustics Home Page: http://www.lanl.gov/thermoacoustics/Book/index.html. In the second paragraph on the page at that site, you have the option to download a zipped animation file. You can “unzip” the file and then run the DOS-executable animation THERMAL.EXE. The animation starts with the pressure and velocity in a standing wave and then zooms into the solid boundary to animate the temperature in the fluid as a function of space and time. The animation goes further to calculate the work done by an imaginary piston moving with the fluid to demonstrate that power is dissipated during the transition from adiabatic compressions far from the wall to isothermal compressions at the fluid-solid boundary.

```
Gas: air, 295.65 K, 1.0133E+05 Pa
    gamma       a(m/s)     rho(kg/m^3)   cp(J/kg-K)    beta(1/K)      k(W/m-K)       Prandtl      mu(kg/m-s)
     1.4000      344.70         1.1940      1004.7      3.3824E-03     2.5901E-02      0.70804     1.8253E-05
Frequency=   241.73     Hz, delta_nu=  1.4188E-04 m, delta_kappa=  1.6862E-04 m
```

Fig. 9.9 Screenshot of the thermophysical properties of dry air at $T_m = 295.65 = 22.5$ °C for the 500 ml boiling flask analyzed in Sect. 8.5.2 and modeled in DeltaEC in Fig. 8.27

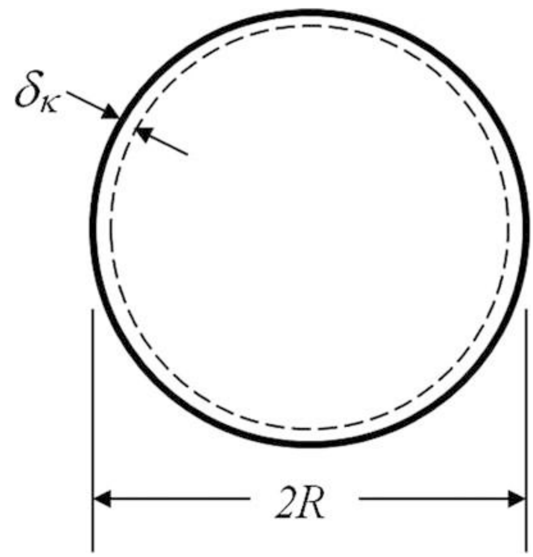

Fig. 9.10 Schematic representation of the spherical volume of radius, R, that forms the acoustical compliance of the Helmholtz resonator depicted in Fig. 8.16. Within a spherical shell of thickness, δ_κ, adjacent to the glass, the pressure oscillations of the gas are nearly isothermal. Throughout the remaining volume, the compressions and expansions of the gas are adiabatic

are now equipped to determine the circumstances that are necessary so that acoustic compressions and expansions occur nearly isothermally in the vicinity of solid surfaces.

Before addressing this question of adiabatic vs. isothermal in a more formal context, it might be useful to examine the effects of thermal conduction in an acoustical compliance, such as the air-filled 500 ml volume of the Helmholtz resonator, shown in the photograph of Fig. 8.16. As shown in Fig. 8.27, the resonance frequency of the empty resonator was (0b) = 241.7 Hz. Figure 9.9 shows the DeltaEC Thermophysical Property output for that case. The value of the thermal penetration depth is visible at the lower right-hand corner: `delta_kappa` $= \delta_\kappa = 168.62$ μm.

The radius of the 500 ml spherical volume, $R = (3\ V/4\pi)^{1/3} = 4.92$ cm. At the interface between the glass and the air, the gas must remain isothermal. The exaggerated boundary layer's thickness is shown schematically by the dashed spherical surface in Fig. 9.10.

At a distance of $2\delta_\kappa$ from the glass, the magnitude of the temperature oscillations of the gas (9.18) is 86.5% of their value far from that boundary, based on Eq. (9.18) as determined by the magnitude of the pressure oscillations within the volume, p_{cav}, according to Eq. (7.25). We can "split the difference" and approximate the effect of the wall by considering the gas a distance, δ_κ, or less from the glass as being compressed and expanded isothermally and the gas farther than δ_κ from the wall undergoing adiabatic compressions and expansions. The "isothermal region" of the 500 ml sphere has the volume of a spherical shell, $V_{isothermal} = 4\pi\delta_\kappa R^2$, with the shell radius, $R = 4.92$ cm, and a thickness, $\delta_\kappa = 168.6$ μm, for the conditions specified in Fig. 9.9. The ratio of the "isothermal" volume to the "adiabatic" volume can be calculated.

$$\frac{V_{isothermal}}{V_{adiabatic}} \cong \frac{4\pi R^2 \delta_\kappa}{(4\pi/3)R^3} = \frac{3\delta_\kappa}{R} \quad \text{if} \quad R >> \delta_\kappa \tag{9.19}$$

For our case, $\delta_\kappa / R = 3.43 \times 10^{-3}$, so the volumetric ratio in Eq. (9.19) is 1.0%. This shows that use of γ in the expression for the compliance of the volume, $C = V/\gamma p_m$, in Eq. (8.26), was justified. Since $\gamma_{air} \cong 7/5 = 1.40$, the isothermal compliance ($\gamma_{\text{iso}} \equiv 1$) is 40% larger than its adiabatic value, so we would expect the resonance frequency predicted by Eq. (8.51) to be lower by about 0.2%, due to the increased compressibility of the gas within the isothermal boundary layer.

9.3.3 Energy Loss in the Thermal Boundary Layer*

Heat is transferred from the compressed (hence, hotter) gas to the solid (isothermal) substrate during one-half of the acoustic cycle and is transferred from the solid substrate back to the expanded (hence, cooler) gas during the other half of the acoustic cycle. The entropy lost during these two heat transfers is non-zero even though the amount of heat transferred is nearly identical. The reason is that the change in entropy is related to the ratio of the heat transfer, dQ, to the absolute temperature at which that heat transfer takes place, T. Since the heat transferred from the substrate to the gas occurs at a lower average temperature, approximately $T_m - (T_1/2)$, than the heat transfer from the gas to the substrate, taking place at approximately $T_m + (T_1/2)$, where T_1 is the adiabatic temperature change far from the substrate's surface, derived previously in Sects. 1.1.3 and 7.1.3, there will be a net increase in the total entropy, $(\Delta S)_{net} > 0$, during the complete cycle.

Although an exact calculation of this acoustic energy loss per unit surface area per unit time, $\dot{e}_{th}$, occurring in the thermal boundary layer requires an integral over a complete cycle, that derivation is somewhat more complicated than the analogous calculation of the energy loss due to viscous shear stresses in the fluid, $\dot{e}_{vis}$, provided in Sect. 9.4.3. Instead of the exact calculation, we can use Newton's Law of Cooling to estimate the heat transferred per unit surface area during each half-cycle assuming a square-wave pressure change, $\pm p_1$, rather than a sinusoidal variation of pressure.

The heat transferred from the gas to the substrate, $dQ_{+½}$, per unit area, A, during one-half of an acoustic period, $(2f)^{-1}$, can be approximated, assuming T_1 is constant during the transfer and $\partial T / \partial x \cong T_1/\delta_\kappa$. The heat transfer from the substrate to the gas is $dQ_{-½}$.

$$\frac{dQ_{\pm ½}}{A} \cong \frac{\pm\kappa}{2} \frac{T_1}{f\delta_\kappa} \propto \frac{\pm\kappa}{2f\delta_\kappa}\left(\frac{|\hat{\mathbf{p}}|}{p_m}\right) \tag{9.20}$$

The entropy change, $dS_{\pm ½}$, for each half-cycle depends upon the temperature at which each heat transfer, $dQ_{\pm ½}$, takes place.

$$\frac{dS_{\pm ½}}{A} \cong \frac{dQ_{\pm ½}}{A}\left(\frac{1}{T_m \pm (T_1/2)}\right) = \frac{\pm\kappa}{2fT_m\delta_\kappa}\left(\frac{T_1}{1 \pm (T_1/2T_m)}\right) \tag{9.21}$$

The net increase in entropy, $(\Delta S)_{net} = dS_{+½} - dS_{-½}$, can be approximated by a binomial expansion of the factor in parentheses in Eq. (9.21), since $T_1/2T_m \ll 1$.

$$\frac{(\Delta S)_{net}}{A} \propto \frac{\kappa}{f\delta_\kappa}\frac{T_1}{2T_m}\left[\left(\frac{1}{1-(T_1/2T_m)}\right) - \left(\frac{1}{1+(T_1/2T_m)}\right)\right] \propto \left(\frac{T_1}{T_m}\right)^2 \propto \left(\frac{|\hat{\mathbf{p}}|}{p_m}\right)^2 \tag{9.22}$$

The conversion of this net entropy increase into a net energy dissipation per cycle per unit area simply requires multiplication by T_m. It should be clear that the thermal boundary layer's acoustic energy dissipation per unit area, per unit time, $\dot{e}_{th}$, is both positive-definite and proportional to $|\hat{\mathbf{p}}|^2$. An exact calculation [4], assuming the proper time averaging over a sinusoidal modulation of the acoustic pressure, is analogous to the calculation for $\dot{e}_{vis}$ that will result in Eq. (9.37).

$$\dot{e}_{th} = -\frac{(\gamma - 1)}{4\gamma}\frac{|\hat{\mathbf{p}}|^2}{p_m}\delta_\kappa \omega \tag{9.23}$$

As expected, $\dot{e}_{th}$ vanishes for an isothermal process where $\gamma = 1$.

9.3.4 Adiabatic vs. Isothermal Propagation in an Ideal Gas

Having introduced the thermal penetration depth as the real (exponential) length that characterizes the thickness of oscillatory thermal boundary layer, we can use δ_κ to show that sound waves in ideal gases are very nearly adiabatic. To do this, let us start with the assumption that sound propagation is adiabatic and calculate the frequency above which that assumption breaks down.

If we refer to the sinusoidal waves shown in Fig. 3.5, the crests (displacement maxima) correspond to a temperature, T_1, that is higher than T_m by the amount specified in Eq. (7.25): $T_1 = T_m[(\gamma - 1)/\gamma](p_1/p_m)$. Similarly, the temperature of the gas at the troughs (pressure minima) is lower than T_m by $-T_1$. The crests and troughs are separated in space by one-half wavelength, $\lambda/2$. Can heat diffuse between the warmer crests and the cooler troughs during a half-cycle? The diffusion distance is given by the thermal penetration depth. At 345 Hz, $\lambda/2 = 0.50$ m in air. At the same frequency, $\delta_\kappa = 141$ μm. During one half-cycle, $T/2 = 1.45$ ms, heat cannot diffuse far enough to equalize the temperatures of the peaks and troughs of the wave.

The above argument can be made more general by setting the wavenumber, $k = \omega/c$, for the adiabatic sound wave equal to the wavenumber for thermal diffusion, δ_κ^{-1}, and solving for the frequency, ω_{crit}, at which those two are equal. This is also equivalent to setting the adiabatic sound speed, $c_s = (\partial p/\partial \rho)_s = \omega/k$, equal to the "speed of heat," $c_{th} = \omega\delta_\kappa$.

$$\omega_{crit} = \frac{\rho_m c_p c^2}{2\kappa} \tag{9.24}$$

For air at 300 K and standard pressure, the critical frequency, $\omega_{crit} = 2.72 \times 10^9$ rad/s, or $f_{crit} = \omega_{crit}/2\pi = 432$ MHz. At that frequency, the wavelength of sound is less than one micron, so our assumption of adiabatic sound propagation is quite good for all frequencies of interest in gases.[7]

At f_{crit} for air, the half-wavelength of sound corresponds to only 11 times the average distance between molecules. At these frequencies, our hydrodynamical approach, which assumes that fluids can be represented as a continuum, is starting to break down and corpuscular effects start to become important.

Of course, at lower pressures, this effect occurs at lower frequencies, so our analysis has to transition from hydrodynamical to ballistic, where the individual particle collisions dominate the propagation.[8] It has recently been shown that ballistic propagation should be considered in the study

[7] In liquids, ω_{crit} is even higher. In water, $f_{crit} = 1210$ GHz, although this is less significant because the difference between the adiabatic and isothermal sound speeds are so small due to the smaller thermal expansion coefficient. At 4 °C, the density of water reaches its maximum value, so the thermal expansion coefficient vanishes and the isothermal and adiabatic sound speeds are equal. The existence of life on this planet probably owes much to the fact that ice is less dense than water.

[8] This transition from hydrodynamic to *ballistic propagation* is known as the "Knudsen limit." In that regime, the real and imaginary components of the wavenumber become equal. Based on M. Greenspan, "Propagation of Sound in Five Monatomic Gases," J. Acoust. Soc. Am. **28**(4), 644–648 (1956), the hydrodynamic results should not be used for frequencies above $\omega \cong c^2/10\alpha$. An excellent review article by Greenspan appears in *Physical Acoustics*, Vol. II A, edited by W. P. Mason and R. N. Thurston (Academic Press, 1964), pp. 1–45.

of sound propagation high in the Earth's atmosphere and in the atmospheres other planets in our solar system [5].

9.4 Viscosity

The irreversibility in the Navier-Stokes equation (7.34) arises from the term proportional to the shear viscosity, $\mu \nabla^2 \vec{v}$. The fundamental difference between a solid and a fluid (liquid or gas) is that shear deformations of a solid are restored elastically (see Sect. 4.2.3), while fluids cannot sustain a state of static shear indefinitely. Figure 9.11 depicts two parallel plates separated by a distance, d, that are in relative motion at a velocity, v_x, and contain a viscous fluid in between.

A "no-slip" boundary condition is applied to the viscous fluid at the interface between the fluid and the solid surface. The force, F_x, per unit area, A_y, of the plate, is given by the equivalent of Ohm's law for the relevant component of the shear stress, τ_{xy}, as a function of the velocity gradient.

$$\tau_{xy} = \frac{F_x}{A_y} = \mu \frac{\partial v_x}{\partial y} \tag{9.25}$$

We can take Eq. (9.25) to be our definition of the *shear viscosity*, μ, which has the units of [Pa-s].

This differs slightly from Ohm's law (9.6) and Newton's Law of Cooling (9.7) because the electrical potential difference (voltage) and the temperature difference are both real scalars. Velocity is a vector, so the shear stress, $\overleftrightarrow{\boldsymbol{\tau}}$, is a tensor. If the shear viscosity, μ, is not a function of the shear rate, then fluids that obey Eq. (9.25) are known as *Newtonian fluids*.[9]

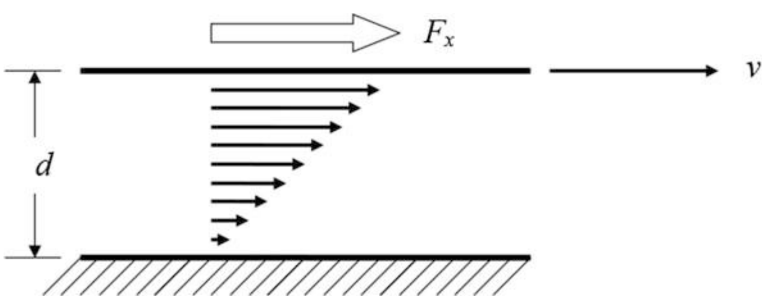

Fig. 9.11 Two-dimensional representation of a fluid that is being sheared by the relative motion of two parallel plates. The *lower plate* is shown as stationary and the *upper plate* is moving in the x direction at a uniform speed, v_x. The *outlined arrow* (⇒) represents the constant force, F_x, that is required to overcome the fluid's frictional drag. That force is applied in the x direction, on the plate with area, A_y, normal to the y axis. Due to the non-slip boundary condition at the interface between the viscous fluid and the plates, the velocity of the fluid is the same as that of the plates over the planes where the substrates and fluid are in contact

[9] The entire field of rheology is dedicated to the study of non-Newtonian fluids and plastic flows. Non-drip paints are thixotropic fluids; their viscosities decrease with increasing strain rate. You want a paint that has a low viscosity when it is being applied to reduce drag on the paint brush (and wrist of the painter), but a high viscosity once it is applied to a surface to keep it from dripping. Viscoelastic fluids like Silly Putty™ are also non-Newtonian fluids. A detailed discussion of viscosity and of non-Newtonian flow is provided by R. B. Bird, W. E. Steward, and E. N. Lightfoot, *Transport Phenomena* (J. Wiley & Sons, 1960); ISBN 0-471-07392-X, in Chapter 1.

The shear viscosity, μ, is also sometimes called the *dynamic viscosity* or *absolute viscosity* to distinguish it from the *kinematic viscosity*, $\nu \equiv \mu/\rho$. We will see in the next sub-section that the kinematic viscosity plays the same role for viscous flow as the thermal diffusivity, α, plays for heat transfer. Both ν and α are *diffusion constants* and have the SI units of [m^2/s].

9.4.1 Poiseuille Flow in a Pipe of Circular Cross-Section

When one plate moves parallel to a stationary plate, as shown in Fig. 9.11, the velocity of the fluid varies linearly across the gap (as symbolized by the arrows of different length) and the y component of the gradient of the velocity, $\nabla_y v_x = \partial v_x/\partial y$, is a constant. We can calculate the velocity profile for steady-state flow (i.e., $\partial v_x/\partial t = 0$) in a tube of circular cross-section, with radius, a, by solving the Navier-Stokes equation (7.34). Due to the cylindrical symmetry of the problem, the x component of the Navier-Stokes equation for a Newtonian fluid can be expressed in cylindrical coordinates [6]:[10]

$$\rho\left(\frac{\partial v_x}{\partial t} + v_r\frac{\partial v_x}{\partial r} + \frac{v_\theta}{r}\frac{\partial v_x}{\partial \theta} + v_x\frac{\partial v_x}{\partial x}\right) = \\ -\frac{\partial p}{\partial x} + \mu\left[\frac{1}{r}\frac{\partial}{\partial r}\left(r\frac{\partial v_x}{\partial r}\right) + \frac{1}{r^2}\frac{\partial^2 v_x}{\partial \theta^2} + \frac{\partial^2 v_x}{\partial x^2}\right] + \rho g_x \tag{9.26}$$

Although Eq. (9.26) looks rather intimidating,[11] in most applications many of the terms vanish. In the case of steady-state flow in a pipe, only two terms from Eq. (9.26) survive in Eq. (9.27).

$$\frac{\mu}{r}\frac{\partial}{\partial r}\left(r\frac{\partial v_x}{\partial r}\right) = \frac{\partial p}{\partial x} = \frac{\Delta p}{L} \tag{9.27}$$

The last term on the right-hand side of Eq. (9.27) assumes that the flow is in response to a pressure difference, Δp, in a pipe of length, L. The equation can be integrated twice to produce an expression for the velocity as a function of radius, $v_x(r)$.

$$v_x(r) = \frac{\Delta p}{4\mu L}r^2 + C_1 \ln[r] + C_2 \tag{9.28}$$

C_1 and C_2 are constants of integration. Since $v_x(0)$ must remain finite, $C_1 = 0$. (For flow in the annular space between two pipes, C_1 becomes useful for matching the boundary condition at the inner radius.[12]) The constant C_2 is determined from the non-slip boundary condition that requires $v_x(a) = 0$.

$$v_x(r) = \frac{\Delta p}{4\mu L}\left(a^2 - r^2\right) \tag{9.29}$$

[10] Any book on hydrodynamics or vector calculus will provide expressions for differential vector operators in at least cylindrical and spherical coordinates. Some examples are mentioned in Refs. [2, 3, 6], at the end of in this chapter, as well as most books on engineering mathematics.

[11] There are two more of these for the (radial) r component and the (azimuthal) θ component of Eq. (9.26) that are just as ugly!

[12] See Ref. [6], for solutions in tubes of other cross-sections, in §17, pp. 53–54 for (Problem 1) annular, (Problem 2) elliptical, and (Problem 3) triangular ducts.

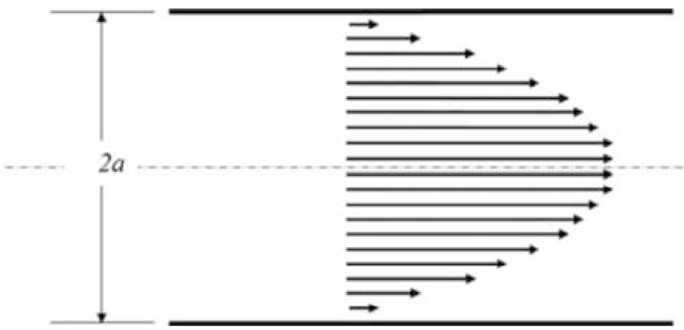

Fig. 9.12 Schematic representation of the velocity vectors for steady flow through a pipe of cylindrical cross-section with radius, a. The velocity profile, given in Eq. (9.29), is parabolic. This flow behavior is known as "Poiseuille flow." (Jean Léonard Marie Poiseuille (1797–1869) was a French physicist and physiologist who first published this result, in 1840, during his investigation of blood flow in narrow capillaries. The CGS unit of viscosity, the poise, was named in his honor.) When looking at this two-dimensional representation, it is important to keep its cylindrical symmetry in mind. Imagine the entire sketch rotated about the dashed centerline

The pipe's "discharge" (i.e., mass flow, $\dot{m}$, or volume velocity, $U = \dot{m}/\rho$) can be calculated by integrating the parabolic velocity profile of Eq. (9.29), shown in Fig. 9.12, over the pipe's cross-sectional area.

$$\dot{m} = \rho U = 2\pi\rho\int_0^a v_x(r)r\ dr = \frac{\pi\rho a^4}{8\mu}\frac{\Delta p}{L} \tag{9.30}$$

This result, known as *Poiseuille's formula*, is valid as long as the parabolic profile has been established[13] and the flow velocity in the pipe is slow enough that the flow remains laminar (like Fig. 9.12) and does not become turbulent.[14]

9.4.2 The Viscous Boundary Layer

Just as we used a surface with a time-dependent temperature in contact with a stagnant fluid to derive an expression for the thermal penetration depth, δ_κ, in Eq. (9.14), we can assume transverse oscillations of a solid surface, as shown in Fig. 9.13, to derive an expression for the oscillatory viscous boundary layer.

We will assume that the space-time behavior of the fluid for $x \geq 0$ is that of a wave traveling to the right, $v_y(x,t) = \Re e\left[\widehat{\mathbf{v}}_\mathbf{y}\ e^{j(\omega t - kx)}\right]$. We assume that the fluid is otherwise at rest so there is no mean flow: $\vec{v}_m = 0$. Since the transverse motion of the wall does not compress any fluid, the pressure is constant throughout the fluid, allowing us to ignore the $\vec{\nabla} p$ term in Eq. (9.2).

[13] When flow enters a smaller tube from a larger reservoir, it must travel some distance before the flow becomes "organized" into the parabolic profile shown in Figure 9.12. This distance is known as the "entrance length," L, and is usually expressed in terms of the tube's inner diameter, D, and the Reynolds number, Re (see the next footnote): $L/D \cong 0.06\ Re$.

[14] The criterion for the transition to turbulence in smooth-walled round pipes is usually given in terms of the nondimensional Reynolds number, $Re = \rho < v > D/\mu$, where $<v>$ is the flow velocity averaged over the pipe's area, $\pi D^2/4$. The transition from laminar (Fig. 9.12) to turbulent flow is usually taken to occur at a Reynolds number greater than 2200 ± 100 in circular pipes with a "smooth" surface finish. Further details regarding the transition to turbulence are given in most fluid dynamics textbooks, such as Refs. [2, 3, 6], and presented as a "Moody chart," where the nondimensional drag is plotted vs. Reynolds number for various values of surface roughness.

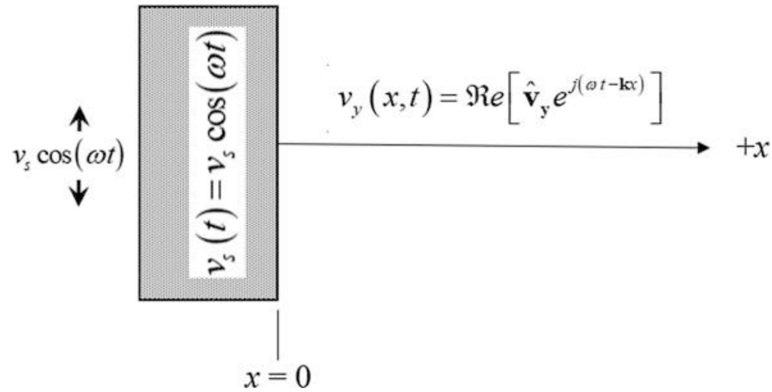

Fig. 9.13 A semi-infinite solid surface oscillates in the y direction with a transverse oscillatory velocity, $v_s \cos(\omega t)$. The surface is in contact with a fluid along the $x = 0$ plane. At that interface, the fluid moves with the same velocity as the solid due to the non-slip boundary condition at $x = 0$. Since there is only fluid at $x \geq 0$, we will assume a right-going wavelike space and time dependence for the oscillating component of the fluid velocity, $v_y(x, t)$, as we did for temperature oscillations in Fig. 9.6

$$\rho \frac{\partial v_y(x,t)}{\partial t} = \mu \nabla^2 v_y(x,t) \tag{9.31}$$

We can substitute the wavelike expression into the two remaining terms in this one-dimensional version of the linearized Navier-Stokes equation to again obtain the required relationship between ω and $\mathbf{k}$:

$$j\omega \hat{\mathbf{v}}_\mathbf{y} = -\frac{\mu}{\rho}\mathbf{k}^2 \hat{\mathbf{v}}_\mathbf{y} = -\nu \mathbf{k}^2 \hat{\mathbf{v}}_\mathbf{y} \tag{9.32}$$

We have again utilized ν, called the kinematic viscosity, which has the units of [m^2/s], just like the thermal diffusivity, α, which was introduced in Eq. (9.11). As before, we have solved Eq. (9.31) for the complex wavenumber, $\mathbf{k}$, and introduce a *viscous penetration depth*, δ_ν, to characterize the shear wave within the fluid.

$$\mathbf{k} = \sqrt{\frac{-j\omega}{\nu}} = \frac{1-j}{\sqrt{2}}\sqrt{\frac{\omega}{\nu}} = (1-j)\sqrt{\frac{\omega}{2\nu}} \equiv \frac{1-j}{\delta_\nu} \quad \Rightarrow \quad \delta_\nu = \sqrt{\frac{2\mu}{\rho\omega}} = \sqrt{\frac{2\nu}{\omega}} \tag{9.33}$$

From this point on, the results for $v_y\,(x,t)$ in the viscous fluid are identical to those already presented for $T_1\,(x,t)$.[15] Figure 9.7 would describe the velocity field in front of the transversely oscillating boundary of Fig. 9.13 if the x axis were scaled by δ_ν instead of by δ_κ. Similarly, if the boundary were stationary and the fluid far from the boundary were moving with an oscillatory velocity amplitude, v_y, then Fig. 9.8 would describe the motion of the fluid if the x axis were scaled by δ_ν instead of δ_κ.[16]

---

[15] Mathematicians would call the Fourier Heat Diffusion equation (9.11) and the Navier-Stokes equation (9.2) "isomorphic." The fact that T is the variable in Eq. (9.11) and v_y is the variable in Eq. (9.31) only bores most mathematicians. The forms of the solutions to both equations must be identical.

[16] For an animated visualization of the fluid in the oscillatory viscous boundary layer, we can again turn to the Los Alamos Thermoacoustics Home Page and run OSCWALL.EXE to see exactly the situation (rotated by 90°) that is diagrammed in Fig. 9.13. The reverse case of a stationary wall and fluid moving uniformly far from the wall is animated in VISCOUS.EXE. In that animation, a vibrating piston sets up the fundamental $\lambda/2 = L$ standing wave in a tube and then focuses in on a portion of the resonator's wall at the velocity anti-node near the center of the tube.

The solutions would be identical for Maxwell's equations governing the electric field, $\vec{E}$, due to an electromagnetic wave impinging on an electrically conducting medium.

$$\frac{\partial \vec{E}}{\partial t} = \frac{1}{\sigma\mu} \nabla^2 \vec{E} \tag{9.34}$$

In that case, $\delta = (2/\sigma\mu\omega)^{1/2}$ is known as the electromagnetic "*skin depth*." Here μ is the magnetic permeability (not viscosity), and σ is the same electrical conductivity as introduced earlier in Ohm's law (9.6).

9.4.3 Viscous Drag in the Neck of a Helmholtz Resonator

We now return once again to the example of our 500 ml flask in Fig. 8.16 and calculate the effects of viscosity on the flow through the neck of our Helmholtz resonator. From Fig. 9.9, we see that the viscous penetration depth for that example is $\delta_\nu = 141.9$ μm. Since the radius of the neck, $a = D_{neck}/2 = 12.5$ mm, the ratio, $\delta_\nu/a = 0.0114 << 1$, so the effect of the non-slip boundary condition at the stationary neck surface does not extend very far into the air that fills the neck. In that limit, we describe the motion of the fluid in the neck as *plug flow* that is diagrammed schematically in Fig. 9.14.

The relevant component of the shear stress on the surface of the neck, τ_{xy}, is determined by Eq. (9.25). In this case, the fluid near the neck's axis is moving with speed, v_x, in the axial direction, and the fluid in contact with the neck must be stationary to satisfy the non-slip boundary condition. Since $|\mathbf{k}| \propto |1/\delta_\nu|$, it is easy to evaluate the velocity gradient, $\partial v_x/\partial y \propto v_x/\delta_\nu$, where v_x is the peak fluid velocity in the neck far from surface of the neck and y is the radial direction normal to the surface of the neck.

$$\tau_{xy} = \frac{F_x}{A_y} = \mu \frac{\partial v_x(y,t)}{\partial y} = \mu \frac{|\hat{\mathbf{v}}_\mathbf{x}|}{\delta_\nu} \propto \mu \frac{v_x}{\delta_\nu} \tag{9.35}$$

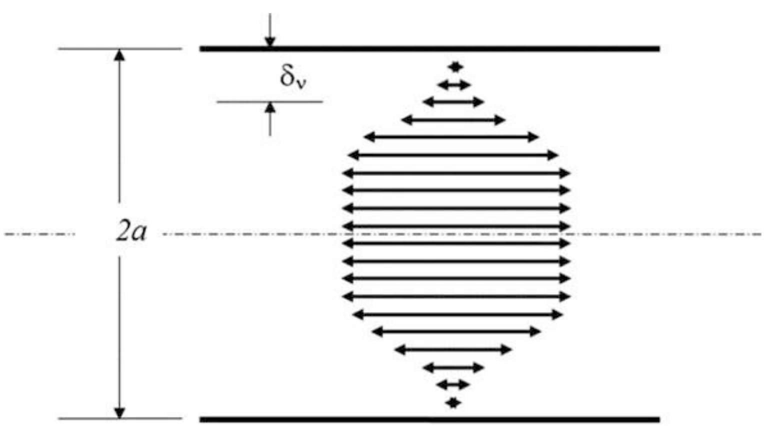

Fig. 9.14 Schematic representation of oscillatory "plug flow" in the cylindrical neck of a Helmholtz resonator with radius, $a \gg \delta_\nu$. In the region far from the walls, the velocity is independent of the radial distance from the central axis of the neck. The velocity decays exponentially over a characteristic exponential distance, δ_ν, to zero at the walls where it must vanish to satisfy the non-slip boundary condition for a viscous fluid. When looking at this drawing, it is important to keep the cylindrical symmetry in mind. Imagine the entire sketch rotated about the dashed centerline

In this application, A_y is the surface area on the inside of the neck. The wall and the fluid are in relative motion since the wall is stationery and the fluid is oscillating. Since the physical neck length, $L = 49.2$ mm, and the diameter, $D_{neck} = 25.0$ mm, $A_y = \pi D_{neck} L = 3.864 \text{ x } 10^{-3}\ \text{m}^2$. The time-averaged power dissipated, $\langle \Pi_{vis} \rangle_t$, per unit area by the viscous shear stress, $\dot{e}_{vis} = \langle \Pi_{vis} \rangle_t / A_y$, is one-half the time average of the product of the peak stress, τ_{xy}, times the peak velocity, v_x, where $T = f^{-1}$ is the period.

$$\dot{e}_{vis} = \frac{\langle \Pi_{vis} \rangle_t}{A_y} = \frac{1}{T}\int_0^T \left[\tau_{xy} \cdot v_x(t)\right] dt \propto \frac{\mu}{T}\int_0^T \frac{v_x^2(t)}{\delta_\nu}\, dt \tag{9.36}$$

The oscillatory flow velocity, $v_x(r, t)$, through the neck of the resonator is uniform (except in the thin viscous boundary layer). The sinusoidal time dependence of the velocity can be represented as $v_x(t) = v_x \cos(\omega t)$.

$$\dot{e}_{vis} = \frac{\langle \Pi_{vis} \rangle_t}{A_y} \propto \frac{\mu}{2}\frac{v_x^2}{\delta_\nu} = \frac{\rho_m}{4}\left|\frac{\widehat{\mathbf{U}}}{A_y}\right|^2 \delta_\nu \omega \tag{9.37}$$

The far right expression for $\dot{e}_{vis}$ is obtained by using the definition of the viscous penetration depth in Eq. (9.33) to substitute for the shear viscosity, $\mu = \left(\delta_\nu^2 \rho_m \omega\right)/2$, and by letting $\langle v_x \rangle = |\langle U_1 \rangle|/A$. As with any dissipative mechanism, like Joule heating in Eq. (9.5), $\dot{e}_{vis}$ is positive-definite and independent of the sign (direction) of v_x or U.

Although the result for $\dot{e}_{vis}$ in Eq. (9.37) is correct, the use of proportionalities instead of equalities was motivated by the fact that the actual expression for the viscous stress tensor is not the one provided in Eq. (9.35) but a complex phasor, $\widehat{\boldsymbol{\tau}}_{\mathbf{xy}}$, that lags $\widehat{\mathbf{v}}$ by 45° in time.[17]

$$\left|\widehat{\boldsymbol{\tau}}_{\mathbf{xy}}\right| = \frac{\sqrt{2}\mu v_x}{\delta_\nu} e^{-y/\delta_\nu} \tag{9.38}$$

By examining the DELTAEC model of the 500 ml flask shown in Fig. 8.27, we can calculate the average value of $\langle v_x \rangle = |\langle U_1 \rangle|/A$ based on input (2a), the cross-sectional area of the neck, $A = 4.909 \times 10^{-4}\ \text{m}^2$. The volume velocity entering the neck is given in Segment #0, where (0f) gives $|U_1| = 4.0777 \times 10^{-4}\ \text{m}^3/\text{s}$ at the open end of the neck. The volume velocity leaving the neck and entering the compliance is given in Segment #1, where result (1C) gives $|U_1| = 3.9806 \times 10^{-4}\ \text{m}^3/\text{s}$ for an average volume velocity $|\langle U_1 \rangle| = 4.0292 \times 10^{-4}\ \text{m}^3/\text{s}$, so $\langle v_x \rangle = |\langle U_1 \rangle|/A = 0.8208$ m/s. Using the viscosity from Fig. 9.9, $\mu = 1.835 \times 10^{-5}$ Pa$-$s, and $\delta_\nu = 141.9$ μm, Eq. (9.37) yields an average viscous power dissipation per unit area of $\dot{e}_{vis} = \langle \Pi_{vis} \rangle_t / A = 42.0\ \text{mW/m}^2$.

The surface area of the neck $A_y = \pi D_{neck} L = 3.86 \times 10^{-3}\ \text{m}^2$, so the time-averaged power dissipated in the neck due to viscous drag in the oscillatory boundary layer $\langle \Pi_{vis} \rangle_t = \dot{e}_{vis}(\pi D_{neck} L) = 167.4$ μW. This is quite close to the value in the DELTAEC model that provides for the dissipation in the neck (1E)–(1F) = 174 μW. The small discrepancy (about 3.7%) arises from the fact that we took an average of the flow velocity that was not weighted (i.e., integrated) to accommodate the v_x^2 dependence of $\dot{e}_{vis}$ in Eq. (9.37). DELTAEC is correct. Using the same results from the DELTAEC model of Fig. 8.27, to calculate the average of the squared velocity, $\langle v_x^2 \rangle = 0.6818\ \text{m}^2/\text{s}^2$, so $\langle \Pi_{vis} \rangle_t = \dot{e}_{vis}(\pi D_{neck} L) = 170.2$ μW. This result is even closer to the correct DELTAEC result. We

[17] A more rigorous general derivation of the viscous boundary layer dissipation and of the acoustic power is provided by Swift in his textbook, *Thermoacoustics* [10]. See §4.4.2 and Chap. 5.

have avoided evaluation of any integrals, but in the process have developed a fundamental understanding of dissipation in the viscous boundary layer.

Although we have not derived the corresponding power dissipation per unit area due to thermal conduction, $\dot{e}_{th}$, the strategy was presented in Sect. 9.3.3 and is illustrated in the THERMAL.EXE animation.[18]

$$\dot{e} = \dot{e}_{vis} + \dot{e}_{th} = -\frac{\rho_m}{4}\left|\frac{\widehat{\mathbf{U}}}{A}\right|^2 \delta_\nu \omega - \frac{(\gamma - 1)}{4\gamma}\frac{|\widehat{\mathbf{p}}|^2}{p_m}\delta_\kappa \omega \tag{9.39}$$

The second term in Eq. (9.39) can be applied to the 500 ml Helmholtz resonator of Fig. 8.16 to calculate the power dissipated by the irreversible thermal conduction between the (isothermal) walls of the compliance and the gas undergoing adiabatic expansions and compressions far from the walls.

Using Fig. 8.27, the DeltaEC result (2A) = (3A) gives $|p_{cav}| = 74.355$ Pa. Figure 9.9 provides the air's thermal conductivity, $\kappa = 2.59 \times 10^{-2}$ W/K-m, and the thermal penetration depth, $\delta_\kappa = 168.6$ μm, resulting in $\dot{e}_{th} = 9.98$ mW/m^2. The surface area of the spherical compliance is input (2a): $A_{sphere} = 2.9974 \times 10^{-2}$ m^2. The product gives the time-averaged power dissipated in on the surface of the spherical volume due to thermal relaxation loss in the oscillatory boundary layer $\langle \Pi_{th} \rangle_t = \dot{e}_{th} A_{sphere} = 29.91$ μW. This is exactly the value that the DeltaEC model provides as (1F)–(2F) = 29.92 μW.

9.4.4 Quality Factors for a Helmholtz Resonator

Having expressions for thermoviscous boundary layer dissipation, we can calculate the quality factor, Q, of the Helmholtz resonator shown in Fig. 8.16. Q is a dimensionless measure of the sharpness of the resonance (see Appendix B). Without dissipation, $Q = \infty$, as seen in Eq. (8.52). Based on the DeltaEC model in Fig. 8.28 and Eq. (C.1), the $Q = |p_{cav}/p|$ = result (3A)/input (0d) = 74.355.

Figure 8.32 displays the incremental plot file, ∗.ip, for the same resonator providing that amplitude and phase of $p_{cav}(f)$. We can approximate the derivative of the phase with respect to frequency at resonance by fitting the three phases (the one closest to resonance and the two above and below it) vs. frequency for an approximate value of $(\partial\theta/\partial f)_{f_o} \cong 34.6°$/Hz. Substitution into Eq. (B.4) gives $Q \cong 73.6$. Running DeltaEC over a finer frequency step size around f_o should produce a slightly greater value for the slope of the phase vs. frequency.

It will be instructive to calculate the Q for both the viscous and thermal losses individually since the final results will be simple and rather intuitively satisfying. To begin, recall the definition of Q based on the ratio of the energy stored in the system, E_{stored}, to the energy dissipated in one cycle, $E_{dissipated/cycle} = \langle \Pi_{dis} \rangle_t T = \langle \Pi_{dis} \rangle_t / f$. From Eq. (B.2),

$$Q = 2\pi \frac{E_{stored}}{E_{dissipated/cycle}} = \frac{\omega E_{stored}}{\langle \Pi_{dissipated} \rangle_t} \tag{9.40}$$

For our Helmholtz resonator, the quality factors for each dissipative process will be calculated individually. Since the energy dissipation is additive, the total quality factor, Q_{tot}, will be the reciprocal of the sum of the reciprocals of the quality factors for the viscous dissipation, Q_{vis}, for thermal

[18] A derivation of Eq. (9.39) is provided in G. W. Swift, *Thermoacoustics: A unifying perspective for some engines and refrigerators*, 2nd ed. (Acoust. Soc. Am., 2017); ISBN 978-3-319-66932-8, Chapter 5.1.

conduction, Q_{th}, and for radiation of sound, Q_{rad} (actually, an "accounting loss" as discussed in Sect. 3.7 for a string).

$$\frac{1}{Q_{tot}} = \frac{1}{Q_{vis}} + \frac{1}{Q_{th}} + \frac{1}{Q_{rad}} \tag{9.41}$$

Like any single-degree-of-freedom simple harmonic oscillator, the stored energy oscillates between its kinetic and potential forms with the sum being constant at steady state. As in Eq. (2.18), the maximum kinetic energy, $(KE)_{\max}$, can be used to represent the value of the stored energy. For the Helmholtz resonator, the kinetic energy is determined by the velocity of the fluid in the resonator's neck, with cross-sectional area, $A = \pi a^2$. Because the viscous penetration depth is much less that the radius of the neck, $\delta_\nu \ll a$, we will assume "plug flow," as shown schematically in Fig. 9.14, and approximate the moving mass of the gas in the neck of our Helmholtz resonator to be all of the mass, m, of the gas within the neck, as was done in Sect. 8.4.4.

$$m = \rho_m A L_{neck} = \rho_m \left(\pi a^2\right) L_{neck} \tag{9.42}$$

Just as the thin viscous boundary layer was neglected in the calculation of the moving mass, the gas velocity, $v_1 = |U_1|/A_{neck}$, will be assumed to be independent of the radial distance from the neck's center line (i.e., plug flow).

$$E_{stored} = (KE)_{\max} = \frac{1}{2} m v_1^2 = \frac{\rho_m A_{neck} L_{neck}}{2} \left|\frac{\widehat{\mathbf{U}}}{\pi a^2}\right|^2 \tag{9.43}$$

Since our results will be compared to the DeltaEC model of the 500 ml flask in Fig. 8.27, we will neglect the kinetic energy of the gas beyond the ends of the neck that produced the effective length correction necessary to match the theoretically calculated and experimentally determined resonance frequencies.

To calculate the energy dissipated by viscous shear on the surface of the neck of the resonator having surface area, $A_{neck} = 2\pi a L_{neck}$, and cross-sectional area, πa^2, the power dissipation per unit area, $\dot{e}_{vis}$, given in Eq. (9.37), will be used.

$$E_{dis/cycle} = \frac{\dot{e}_{vis} A_{neck}}{f_o} = \frac{\rho_m}{4 f_o} \left|\frac{\widehat{\mathbf{U}}}{\pi a^2}\right|^2 \delta_\nu \omega_o A_{neck} = \frac{\pi}{2} \left|\frac{\widehat{\mathbf{U}}}{\pi a^2}\right|^2 \rho_m \delta_\nu 2\pi a L_{neck} \tag{9.44}$$

When we take the ratio of Eq. (9.43) to Eq. (9.44) to calculate Q, using Eq. (9.40), the amplitude of the oscillation squared, proportional to $|U_1/A_{neck}|^2$, will cancel. This must be the case, since we are considering a linear system and linearity demands that the quality factor must be amplitude independent.

$$Q_{vis} = 2\pi \frac{E_{stored}}{E_{dis/cycle}} = 2\pi \frac{\left(\rho_m \pi a^2 L_{neck}\right)/2}{(\pi/2)\delta_\nu 2\pi a L_{neck}} = \frac{2\pi a^2 L_{neck}}{\delta_\nu 2\pi a L_{neck}} = \frac{a}{\delta_\nu} \tag{9.45}$$

This is a wonderfully simple and intuitively satisfying result: $Q_{vis} = a/\delta_\nu$. The quality factor due to viscous dissipation at the surface of the neck of a Helmholtz resonator is simply the dimensionless ratio of the neck's radius to the viscous penetration depth in the gas.

A numerical calculation for Q_{vis} in a cylindrical duct involves the integration of the flow field using a J_o Bessel function with a complex argument, $(j-1)r/\delta_\nu$, to represent the velocity, resulting in an approximation that is valid to within 0.3% for $a/\delta_\nu > 3$ [7].

$$Q_{vis} \cong \frac{a}{\delta_\nu} + \frac{\delta_\nu}{5a} - \frac{3}{4} \quad \text{for} \quad \frac{a}{\delta_\nu} \geq 3 \tag{9.46}$$

The same approach can be used to calculate the quality factor for thermal dissipation on the surface of the Helmholtz resonator's volume (i.e., compliance). Since the amplitude of the pressure oscillations within the volume is proportional to p_1, as shown in Eq. (9.39), it will be convenient to convert $|U_1/\pi a^2|$ in Eq. (9.43) to a pressure amplitude, since the quality factor for thermal losses, Q_{th}, must also be amplitude independent in the linear acoustics limit. From Eq. (8.25), the adiabatic compliance of a volume, V, can be used to relate pressure amplitude, $|\hat{\mathbf{p}}|$, to the volume velocity amplitude, $\left|\hat{\mathbf{U}}\right|$.

$$\hat{\mathbf{p}} = \frac{1}{j\omega}\frac{\gamma p_m}{V}\hat{\mathbf{U}} \quad \Rightarrow \quad E_{stored} = (KE)_{\max} = \frac{\rho_m L_{neck}}{2A_{neck}}\frac{\omega_o^2 V^2}{\gamma^2}\frac{|\hat{\mathbf{p}}|^2}{p_m^2} \tag{9.47}$$

Substitution of $\dot{e}_{th}$ from Eq. (9.39), times the surface area of the spherical compliance, $S_{Vol} = 4\pi R^2$, into Eq. (9.40) produces the expression for the thermal contribution to the quality factor, Q_{th}.

$$Q_{th} = \frac{2\pi \frac{\rho_m L_{neck}}{2A_{neck}}\frac{\omega_o^2 V^2}{\gamma^2}\frac{|\hat{\mathbf{p}}|^2}{p_m^2}}{\frac{(\gamma-1)}{4\gamma f_o}\frac{|\hat{\mathbf{p}}|^2}{p_m} S_{Vol}\delta_\kappa \omega_o} = \left[\omega_o^2 \frac{\rho_m}{\gamma p_m}\frac{L_{neck}V}{A_{neck}}\right]\frac{2(4\pi/3)R^3}{(\gamma-1)\delta_\kappa 4\pi R^2} \tag{9.48}$$

The Helmholtz resonance frequency, ω_o, is given in Eq. (8.51), and $c^2 = \gamma p_m / \rho_m$, so the term in Eq. (9.48) contained within the square brackets is just unity, proving again that "substitution is the most powerful technique in mathematics" (see Sect. 1.1).

$$Q_{th} = \frac{2}{3(\gamma-1)}\frac{R}{\delta_\kappa} \tag{9.49}$$

As expected, the thermal quality factor becomes infinite (i.e., lossless) if the expansions and compressions of the gas within the entire volume of the Helmholtz resonator are isothermal, $\gamma_{iso} = 1$. We also see again that the quality factor is proportional to the ratio of a length characterizing the size of the spherical volume, R, and the thermal penetration depth, δ_κ.

The results for Q_{vis} in Eq. (9.45) and Q_{th} in Eq. (9.49) can be used to estimate the quality factor for the 500 ml boiling flask example that was used to create the DeltaEC file in Fig. 8.27, using the penetration depths at $f_o = 241.73$ Hz, provided in Fig. 9.9, when combined as shown in Eq. (9.41). This results in a $Q_{vis} = 88$, and a $Q_{th} = 482$, for $Q_{tot} = 74.4$. The DeltaEC model also gives $Q = 74.4$.

Although the time-averaged radiated power, $\langle \Pi_{rad} \rangle_t$, will not be derived until Chap. 12 (see Eq. 12.18), it was mentioned in Footnote 24 in Chap. 8.

$$\langle \Pi_{rad} \rangle_t = \pi \frac{\rho_m f^2}{2c}\left|\hat{\mathbf{U}}\right|^2 \tag{9.50}$$

The dependence upon $|U_1|^2$ means that it is easy to calculate a contribution to the quality factor from the radiation "loss" using Eq. (9.43) to express the stored energy.

$$Q_{rad} = 2\pi \frac{\frac{\rho_m \pi a^2 L_{neck}}{2}\left|\frac{\hat{\mathbf{U}}}{\pi a^2}\right|^2}{\pi \frac{\rho_m f_o}{2c}\left|\hat{\mathbf{U}}\right|^2} = 2\frac{(\lambda L_{neck})}{\pi a^2} \tag{9.51}$$

The expression on the far right in Eq. (9.51) uses $c = \lambda f$ to express the quality factor as proportional to the ratio of two areas. For the 500 ml flask DeltaEC model in Fig. 8.27, where $\lambda = 1.426$ m at resonance, $Q_{rad} = 286$. This is more than three times greater than Q_{vis}, reinforcing the earlier result from the DeltaEC model that showed that viscous loss in the neck was the dominant loss mechanism in that example.

9.5 Kinetic Theory of Thermal and Viscous Transport

Thus far, in this chapter, we have taken a phenomenological approach to describe the dissipation caused by thermal conduction and viscous shear. Those mechanisms have been characterized by diffusion equations that introduced two phenomenological constants: the thermal conductivity, κ, and the shear viscosity, μ. Those constants are properties of the fluid that might depend upon pressure and/or temperature. By introducing a simple microscopic model for these diffusive processes, we can gain additional insight into the relationship between these constants and the microscopic properties of ideal gases.

The same microscopic model that was used in Chap. 7 to derive the Ideal Gas Law and to introduce the mean squared particle velocity and the Equipartition Theorem in Eq. (7.2) can be resurrected to calculate κ and μ for an ideal gas by adding the concept of a mean free path, $\overline{\ell}$, characterizing an average distance that an atom or molecule in a gas will travel before colliding with another of its own kind.[19]

For the following calculations, we assume that the gas is "dilute" [8]. This means that we will assume that each particle spends a relatively large fraction of its time at distances far from other particles so that the time between collisions is much greater than the time involved in a collision. We also assume that the probability of a simultaneous collision between more than two particles can be neglected. Finally, we assume de Broglie wavelength, $\lambda_B = h/mv$, for the particles with momentum, mv, is much shorter than the separation between particles so quantum-mechanical effects can be ignored: $\lambda_B \ll \overline{\ell}$.

9.5.1 Mean Free Path

If we assume that our "point particles" have a mass, m, and an effective hard sphere diameter, D, then two identical particles in the gas will collide if their centers are separated by a distance that is less than or equal to D. We focus our attention on a single particle that is moving with a mean velocity, $\overline{v}'$, determined by the Equipartition Theorem, as applied in Eq. (7.26), $\langle v^2 \rangle^{½} \equiv \overline{v}' = \sqrt{3k_B T/m}$. This mean thermal velocity is designated $\overline{v}'$ to remind us that we have assumed that all other particles are not moving. Assuming (temporarily) that all other particles are stationary, then the moving particle sweeps out a cylindrical volume, $V_{Swept} = \pi D^2 \overline{v}' t$, in a time, t.

The number of (stationary) particles within that swept volume depends upon the (number) density of the gas, $n = \rho/m$, where m is the mass of an individual particle. During the time interval, t, there will be $W = nV_{Swept}$ stationary gas particles within that cylinder. The collision rate, $\dot{n} = (W/t) = \pi D^2 \overline{v}' n$. The *mean free path*, $\overline{\ell}$, is the distance the particle travels between collisions that take place, on average, every $\overline{\tau} = \dot{n}^{-1}$ seconds.

[19] A more detailed and systematic discussion of these concepts is given by E. H. Kennard in his classic textbook, *Kinetic Theory of Gases with an Introduction to Statistical Mechanics* (McGraw-Hill, 1938).

Of course, all the other particles are not stationary but are moving with the same mean (thermal) velocity, $\overline{v}'$, so the actual velocity that we need in our expression for the mean free path is the mean relative particle velocity, $v_{rel} \equiv \overline{v}$. If two particles are traveling in exactly the same direction, their mean relative velocity would be zero. If they are moving directly toward each other, their mean relative velocity would be $2\overline{v}'$. Integration over all possible directions could determine the average relative velocity, but it is easier to utilized the "reduced mass," $\mu = m_1 m_2/(m_1 + m_2)$, to determine mean relative velocity. Placing the reduced mass into the Equipartition Theorem produces the mean relative velocity in the same way the reduced mass was used to determine the antisymmetric frequency of two otherwise free particles that were joined by a spring, as discussed in Sect. 4.3.1, then applied to the Tonpilz transducer.

Since the particles are assumed to be identical, $\mu = m/2$, so the value of the relative velocities of the particles,$\overline{v}_{rel}$, is given by the Equipartition Theorem.

$$\left\langle v_{rel}^2 \right\rangle^{½} \equiv \overline{v} = (3k_B T/\mu)^{½} = (6k_B T/m)^{½} = \overline{v}'\sqrt{2} \tag{9.52}$$

That result can be used to calculate the mean free path as introduced when we initially assumed that the other particles were stationary.

$$\overline{\ell} = \frac{\overline{v}}{\pi D^2 \overline{v}' n} = \frac{1}{\pi\sqrt{2}D^2 n} \tag{9.53}$$

It is useful to recognize that the mean free path is independent of $\overline{v}$ or $\overline{v}'$ and therefore independent of temperature. At higher temperatures, the particles are moving faster, but V_{Swept} is correspondingly larger.

Near room temperature, for air at atmospheric pressure, the number density can be calculated from the Ideal Gas Law or from the molar volume and Avogadro's number: $n = \rho/m = p_m/k_B T \cong 2.5 \times 10^{25}$ particles/m^3 $\cong N_A/(22.4 \times 10^{-3}$ m^3). For air, a typical molecular diameter, $D_{air} \cong 2 \times 10^{-10}$ m = 2 Å, so $\pi D^2 \cong 1.3 \times 10^{-19}$ m^2, making $\overline{\ell} \cong 2.2 \times 10^{-7}$ m = 0.22 microns. Using the same values, the time between collisions is $\overline{\ell}/\overline{v} \cong 6 \times 10^{-10}$ seconds, or the collision rate, $\dot{n}$, is 2×10^9/second = 2 GHz. Each molecule of air at atmospheric pressure and room temperature experiences about two billion collisions each second.

9.5.2 Thermal Conductivity of an Ideal Gas

With our understanding of the mean free path, we are now able to determine a value of the thermal conductivity of an ideal gas from the microscopic model. If we assume a linear temperature gradient in a gas, then the thermal energy that is transported by a gas particle will be based on the temperature that particle had at the position where it suffered its last collision. Figure 9.15 provides a suitable geometry for such a calculation by assuming that the temperature gradient, $\partial T/\partial z \neq 0$, exists in the z direction.

The number of particles crossing a unit area per unit time (i.e., the particle flux) in the z direction is determined by the particle density, n, and the mean particle velocity, $\overline{v}'$. If there are n particles per unit volume, roughly one-third of them have velocities in the z direction and half of those, or $n/6$ particles per unit volume, have mean velocities in the $(-z)$ direction.

Particles which cross the dashed line in Fig. 9.15 from below have, on average, experienced the last collision at a distance, $\overline{\ell}$, below that plane. But the mean energy per particle, $\overline{\varepsilon}$, is a function of T and,

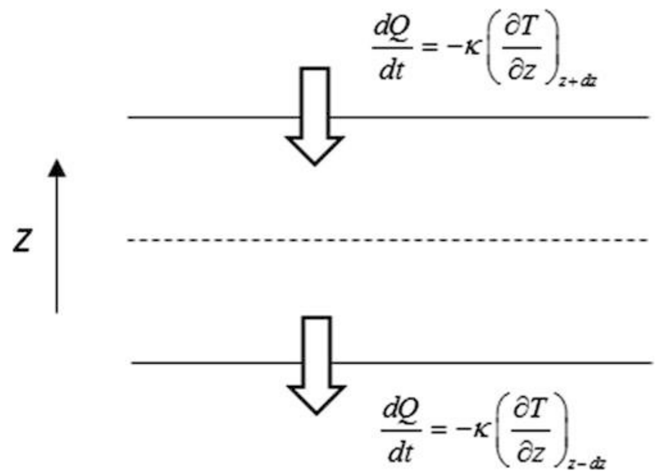

Fig. 9.15 Coordinate system for the calculation of the thermal conductivity, κ, of an ideal gas. The heat flux, represented by the arrows, is determined by number of particles crossing the line per unit time and the temperature of the particles that was determined by the last collision they suffered before crossing the line

since $T = T(z)$, the mean energy is also a function of z, $\overline{\varepsilon}(z)$. The particles crossing from below carry with them a mean energy, $\overline{\varepsilon}(z - \overline{\ell})$, and the ones above experienced the last collision at a distance, $\overline{\ell}$, above that plane, $\overline{\varepsilon}(z + \overline{\ell})$. Each "free particle," which has three degrees of freedom, carries an average kinetic energy of $\overline{\varepsilon} = 3k_BT/2$, corresponding to a heat capacity of $3k_B/2$ per particle (see Sect. 7.2.1).

$$\left(\frac{\partial Q}{\partial t}\right)_{above} = \frac{1}{6}n\overline{v}'\overline{\varepsilon}(z + \overline{\ell}) = \left(\frac{n\overline{v}'}{6}\right)\left[\frac{3k_B}{2}\left(T + \overline{\ell}\frac{\partial T}{\partial z}\right)\right] \tag{9.54}$$

Similarly, the heat flux going in the opposite direction from below, $\dot{q}_{below}$, is determined by the last collision that took place at a slightly lower temperature.

$$\left(\frac{\partial Q}{\partial t}\right)_{below} = \frac{1}{6}n\overline{v}'\overline{\varepsilon}(z - \overline{\ell}) = \left(\frac{n\overline{v}'}{6}\right)\left[\frac{3k_B}{2}\left(T - \overline{\ell}\frac{\partial T}{\partial z}\right)\right] \tag{9.55}$$

The net energy flux, $\dot{q}_{net}$, from hot to cold, is given by the difference of the fluxes calculated in Eqs. (9.54) and (9.55).

$$\left(\frac{\partial Q}{\partial t}\right)_{net} = \left(\frac{\partial Q}{\partial t}\right)_{below} - \left(\frac{\partial Q}{\partial t}\right)_{above} = -\left(\frac{n\overline{v}'\overline{\ell}k_B}{2}\right)\frac{\partial T}{\partial z} \tag{9.56}$$

As indicated in Fig. 9.15, the thermal conductivity of a gas, κ_{gas}, can be expressed in terms of the result in Eq. (9.56).

$$\frac{\partial Q}{\partial t} = -\kappa\frac{\partial T}{\partial z} \quad \Rightarrow \quad \kappa_{gas} = \frac{1}{2}n\overline{v}'\overline{\ell}k_B \tag{9.57}$$

A more rigorous kinetic theory for thermal conductivity of inert gases at low pressures was developed by Chapman in England and Enskog in Sweden. Their approach calculates the numerical pre-factor in Eq. (9.57) to be 0.37, rather than 0.5, since the particles that are not going straight up or down along the z direction experienced their last collision at a distance less than $\overline{\ell}$ [9]. Their calculations also describe the thermal conductivity of polyatomic molecules quite accurately.

Using the Equipartition Theorem to let $\langle v^2\rangle^{½} \equiv \overline{v}' = \sqrt{3k_BT/m}$ provides a microscopic expression for the thermal conductivity of an ideal gas, κ_{gas}.

$$\kappa_{gas} = 0.37 \frac{nk_B\overline{v}'}{\pi\sqrt{2}D^2 n} = 0.37 \frac{k_B}{2\pi D^2}\sqrt{\frac{3k_BT}{m}} \cong \frac{0.1}{D^2}\frac{k_B^{3/2}}{m^{1/2}}\sqrt{T} \tag{9.58}$$

Our application of a microscopic model, based on the collision of hard spheres, demonstrates that the thermal conductivity of an ideal gas is independent of the pressure or density of the gas (at least as long as the dimensions of the system are much larger than the mean free path) for most gases at pressures below 1 MPa and is inversely proportional to the square root of the particle's mass and inversely proportional to the particle's cross-sectional area.

The model also predicts that the thermal conductivity will be proportional to the square root of the absolute temperature, $\sqrt{T}$. For real gases, the observed temperature dependence of the thermal conductivity of ideal gases is closer to $T^{0.7}$ [10], due to the fact that the gas particles are not "hard spheres" but interact through a molecular force field like the Lennard-Jones potential shown in Fig. 2.39.

9.5.3 Viscosity of an Ideal Gas

A microscopic determination of the viscosity can be obtained in exactly the same way using the momentum transported by a particle of mass, m, across a plane. We can use an approach similar to that expressed in the geometry of Fig. 9.15. As before, we assume that the density of the gas is sufficiently low that the mean free path is much greater than the particle diameter but much less than the typical dimensions of the system (e.g., the spacing between the moving plates in Fig. 9.11 or the diameter of the tube in Figs. 9.12 and 9.14).

The mean shear velocity, v_x, is again determined by the last collision the particle suffered prior to crossing the plane from above or from below, and the momentum in the x direction transported by each particle is mv_x. The particle density can be used to calculate the momentum transported per unit area, per unit time, P.

$$P_{above} = \frac{n\overline{v}m}{6}\left[v_x + \frac{\partial v_x}{\partial z}\overline{\ell}\right] \quad \text{and} \quad P_{below} = \frac{n\overline{v}m}{6}\left[v_x - \frac{\partial v_x}{\partial z}\overline{\ell}\right] \tag{9.59}$$

The net momentum change per unit area is the difference of the two expressions in Eq. (9.59).

$$P_{above} - P_{below} = \tau_{xz} = \frac{n\overline{v}'m\overline{\ell}}{3}\left(\frac{\partial v_x}{\partial z}\right) \tag{9.60}$$

Comparison of Eq. (9.60) to the phenomenological expression for one component of shear stress, τ_{xy}, in Eq. (9.25), produces a microscopic expression for the shear viscosity of an ideal gas, μ_{gas}.

$$\mu_{gas} = \frac{n\overline{v}'m\overline{\ell}}{3} = \frac{\rho\overline{v}'\overline{\ell}}{3} = \frac{1}{\pi D^2}\left(\frac{mk_BT}{6}\right)^{1/2} = \frac{0.13}{D^2}k_B^{1/2}m^{1/2}T^{1/2} \tag{9.61}$$

Just like the thermal conductivity of an ideal gas, this estimate of the shear viscosity is independent of the pressure or density and proportional to the square root of the absolute temperature and to the square root of the particle mass. Like the ideal gas thermal conductivity, the actual temperature dependence of the viscosity for real gases is also closer to $T^{0.7}$ [10].

9.5.4 Prandtl Number of an Ideal Gas and Binary Gas Mixtures*

The relative importance of thermal conductivity and viscosity can be expressed in a dimensionless ratio that is known as the *Prandtl number*, $\mathrm{Pr} = \mu c_P/\kappa$, where c_P is the specific heat (per unit mass) at constant pressure. This ratio is particularly important for convective heat transfer where the viscosity determines the energy dissipation from imposed flow and the thermal conductivity determines the heat transport. Liquid metals, like mercury or sodium-potassium eutectic (NaK), have a very small Prandtl number because of their low viscosity (hence, the popular designation as "quicksilver," in the case of mercury) and high thermal conductivity, due to the efficient heat transport provided by the conduction electrons. On the other hand, viscous fluids with low thermal conductivity, like molasses, have large Prandtl numbers.

For monatomic ideal gases, the isobaric heat capacity per particle (see Sect. 7.2.1) is $(5k_B/2)$ so the isobaric specific heat per particle is $(5k_B/2m)$. In combination with the ideal gas viscosity in Eq. (9.61) and thermal conductivity in Eq. (9.58), it is easy to demonstrate that the Prandtl number for ideal gases should be a constant.

$$\mathrm{Pr}_{gas} \equiv \frac{\mu_{gas} c_P}{\kappa_{gas}} = \frac{\delta_\nu^2}{\delta_\kappa^2} = \frac{0.13}{0.37}\frac{5k_B}{2m}\frac{D^2}{D^2}\frac{k_B^{1/2} m^{1/2} T^{1/2}}{k_B^{3/2} T^{1/2}/m^{1/2}} \cong 0.9 \tag{9.62}$$

Measured values for the Prandtl number of monoatomic gases are not 0.9 but closer to ⅔. For other polyatomic gases, the Prandtl numbers are also constant and range from about 0.7 to 0.9 [11]. This is due to the fact that it is those "hard spheres" that are responsible for both the heat and the momentum transport.

A similar result, known as the Wiedemann-Franz Law [12], shows that the ratio of the thermal conductivity, κ, and the electrical conductivity, σ, of metallic solids is a constant, independent of the particular metal, that depends only upon temperature.

$$L \equiv \frac{\kappa}{\sigma T} = \frac{\pi^2}{3}\left(\frac{k_B}{e}\right)^2 \tag{9.63}$$

L is the Lorenz number and depends only upon fundamental constants (the charge on the electron, e, and Boltzmann's constant, k_B). Again, this is due to the fact that it is the electrons in metals that provide both heat transport and electrical conductivity.

For ideal gases, a more rigorous calculation was made by Eucken [13] that related the thermal conductivity of gases to their viscosity.

$$\kappa_{gas} = \left(c_P + \frac{5\Re}{4M}\right)\mu_{gas} \quad \Rightarrow \quad \mathrm{Pr}_{gas} = \frac{c_P}{c_P + 1.25(\Re/M)} \tag{9.64}$$

Eucken's formula gives the correct result for monatomic (noble) gases using the universal gas constant, $\Re \equiv 8.314462$ J/mol-K, and is a very good approximation for most polyatomic gases.

Although the Prandtl number for ideal gases is a constant, it is possible to reduce the Prandtl number for gas mixtures. In a mixture of a light and heavy gas, the light species can dominate the heat transfer while the heavier species dominates the momentum transfer. Swift has demonstrated this by a simple calculation for inert gas mixtures based on the results from the microscopic model, using the subscripts "1" and "2" to designate two different gases.

$$\begin{aligned} k_B T &\propto (½) m_1 \overline{v}_1^2 \propto (½) m_2 \overline{v}_2^2 \\ \mu_{mix} &\propto (n_1 \overline{v}_1 m_1 + n_2 \overline{v}_2 m_2)\overline{\ell} \propto n_1\sqrt{m_1} + n_2\sqrt{m_2} \\ \kappa_{mix} &\propto (n_1 \overline{v}_1 + n_2 \overline{v}_2) c_P \overline{\ell} \propto n_1/\sqrt{m_1} + n_2/\sqrt{m_2} \\ c_P &\propto \frac{\mathfrak{R}}{n_1 m_1 + n_2 m_2} \end{aligned} \tag{9.65}$$

These proportions can be used to form the ratio of a mixture's Prandtl number, Pr_{mix}, to the pure gas Prandtl number, Pr_{gas}, in terms of the molar concentration of species "1," $x_1 = n_1/(n_1 + n_2)$, and to the square root of their mass ratio, $\beta = \sqrt{m_1/m_2}$.

$$\frac{\mathrm{Pr}_{mix}}{\mathrm{Pr}_{gas}} = \frac{n_1\sqrt{m_1} + n_2\sqrt{m_2}}{\left(\frac{n}{\sqrt{m_1}} + \frac{n_2}{\sqrt{m_2}}\right)(n_1 m_1 + n_2 m_2)} = \frac{1 - (1-\beta)x_1}{\left[1 + \left(\frac{1}{\beta} - 1\right)x_1\right]\left[1 - \left(1 - \beta^2\right)x_1\right]} \tag{9.66}$$

Figure 9.16 plots the gas mixture Prandtl number as a function of the mole fraction of helium, x_1, for helium-argon mixtures with $\beta_{He/Ar} = 0.316$ and helium-xenon mixtures with $\beta_{He/Xe} = 0.175$. For pure gases (i.e., $x_1 = 0\%$ or $x_1 = 100\%$), $\mathrm{Pr}_{\mathrm{mix}} = 2/3$, but a mixture of a light and a heavy gas can produce lower Prandtl numbers. The results in Fig. 9.16 demonstrate that the Prandtl number of a helium-argon mixture can be reduced to a minimum value of $\mathrm{Pr}_{He/Ar} = 0.37$ and a helium-xenon mixture can produce a minimum Prandtl number as low as $\mathrm{Pr}_{He/Xe} = 0.20$. The lowest inert gas Prandtl number would be achieved with a mixture of ^{3}He and radon, $\mathrm{Pr}_{He/Rn} = 0.14$, although such a mixture would be highly radioactive. A more detailed kinetic theory calculation produces nearly identical results [14].

The use of gas mixtures that reduce Prandtl number have been shown to improve the performance of thermoacoustic engines and refrigerators [15], although it has also been shown that such high-amplitude sound waves can also introduce concentration gradients in mixtures [16].

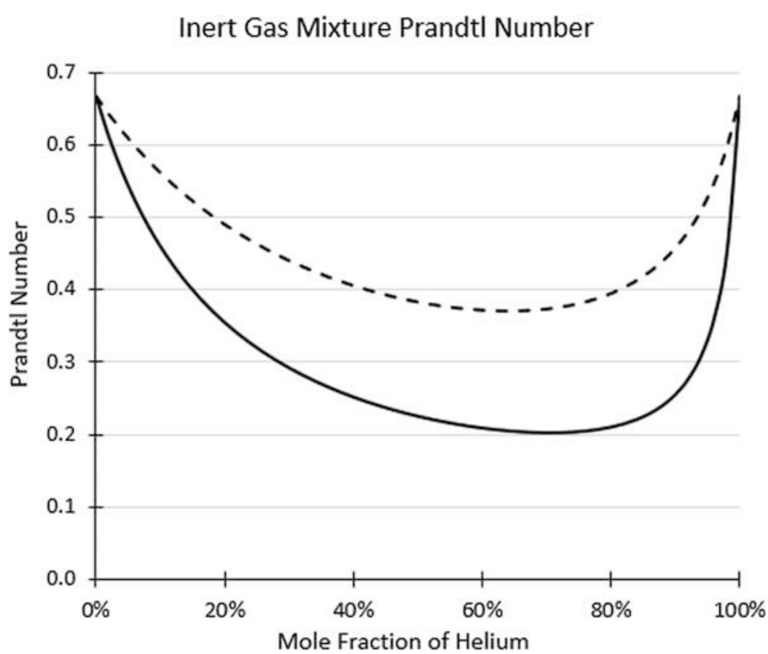

Fig. 9.16 The Prandtl number of inert gas mixtures as a function of the mole fraction of helium. The *dashed line* represents helium-argon mixtures and the *solid line* represents helium-xenon mixtures

9.6 Not a Total Loss

Just as we had examined the lossless equations of hydrodynamics in Chap. 8 by applying them to simple "lumped elements," this chapter has introduced the diffusion equations that govern dissipation in fluidic acoustical systems (thermal conduction also contributes to dissipation in solids) by applying them to a Helmholtz resonator that had been modeled by DeltaEC in the previous chapter. In doing so, two new length scales were introduced: the thermal and viscous penetration depths, δ_κ and δ_ν. Those length scales play the same critical role that wavelength and wavenumber played in the nondissipative equations. Comparison of the thermal penetration depth to the wavelength provided quantitative justification for the assumption we will exploit in the following chapter where sound waves are treated as being adiabatic oscillatory excursions away from equilibrium.

As in Chap. 7, the microscopic models and the phenomenological models of dissipative processes in ideal gases provided complementary insights into the behavior of the phenomenological constants, κ and μ, with respect to changes in density and temperature, as well as supplying an intuitive picture of the processes by which heat and momentum are transported. The simple kinetic theory, based on a "hard sphere" collision assumption, introduced an additional important length scale: the mean free path, $\bar{\ell}$. When $\bar{\ell} \ll \lambda$, our continuum model of diffusive processes provides an appropriate description.

With the thermodynamic, hydrodynamic, and microscopic analyses introduced in this chapter and in Chap. 7, the fundamentals necessary to understand wave propagation in fluids, and particularly in ideal gases, will be put to use in the remainder of this textbook.

Talk Like an Acoustician

Time reversal invariance	Ballistic propagation
Shear viscosity	Newtonian fluids
Dynamic (or absolute) viscosity	Diffusion constant
Fourier Diffusion Equation	Non-slip boundary condition
Ohm's law	Shear (or dynamic or absolute) viscosity
Joule heating	Kinematic viscosity
Newton's Law of Cooling	Poiseuille's formula
Thermal diffusivity	Oscillatory plug flow
Thermometric conductivity	Viscous penetration depth
Thermal penetration depth	Entrance length
Skin depth	Thermal velocity
Instantaneous value	Mean free path
Acoustic approximation	Prandtl number

Exercises

1. **Moon free path**. Atmospheric pressure on the moon is about 10^{-13} atm. = 10^{-8} Pa. Assume that the moon's atmosphere has the same chemical composition as Earth's and calculate the mean free path for molecules in our moon's atmosphere. Is the concept of pressure meaningful for such a long mean free path? Why or why not?
2. **Vacuum insulation**. As long as the characteristic dimensions of a gas-filled space are much greater than the mean free path of the gas particles, the thermal conductivity is independent of gas pressure. To reduce thermal conduction through a gas, the vacuum space gap, g, must be less than the mean free path, $\bar{\ell}$, of the gas molecules trapped in the vacuum insulation space.

The inverse relationship between number density, n, and mean free path, $\overline{\ell}$, illustrated in Eq. (9.53), is no longer valid when $\overline{\ell}$ becomes larger than g. Beyond that point, the thermal resistance of the insulation space will increase linearly in proportion to increase of the mean free path because there are fewer gas particles to transport heat and those particles are more likely to collide with the walls than they are to collide with each other.

How low must the gas pressure in the insulation space be so that the thermal resistance of the vacuum space is ten times smaller than the thermal resistance when $g \ll \overline{\ell}$ if $g = 10$ mm, assuming that the vacuum space contains some air?

3. **Relaxation frequency for a capacitive microphone**. The volume inside a condenser microphone that is behind the diaphragm (see Fig. 6.14) must be isolated from the acoustical pressure variations which drive the motion of the microphone's diaphragm. Because the microphone diaphragm must be able to withstand slow changes in pressure encountered during transportation (e.g., shipping by air), a capillary tube is provided so that changes in ambient gas pressure, p_m, can be relieved, but acoustical pressure variations at the frequencies of interest are not allowed to influence the gas pressure within the microphone's back volume.
   (a) *Poiseuille resistance.* Use Eq. (9.30) to write an expression for the acoustic flow resistance, $R_{ac} = \Delta p/U$, appropriate to steady gas flow in the Poiseuille regime.
   (b) *Relaxation time*. Using the result from part (a), write an expression for the exponential relaxation time, $\tau = R_{ac}C$, where the compliance, C, given in Eq. (8.26), is determined by the microphone's back volume, V_{back}, assuming that the compressions and expansions of the gas within that volume are adiabatic. Discuss whether or not the adiabatic assumption is valid.
   (c) *Viscous penetration depth.* For audio applications, the low-frequency cut-off is usually taken to be 20 Hz, corresponding to the nominal lower limit of human hearing [17]. Determine the viscous penetration depth at that frequency in air at 20 °C with $p_m = 100$ kPa.
   (d) *0.010″ diameter capillary*. If the back volume of the microphone is $V_{back} = 674$ mm^3 and it is connected to a capillary tube that has an inside diameter of 250 microns, and a length of 10.0 mm, determine the exponential relaxation time, τ, for pressure equilibration and corresponding cut-off frequency, $f_{\text{-}3dB} = (2\pi\tau)^{-1}$.
4. **Viscous damping of an oscillating spar buoy**. The spar buoy shown in Fig. 2.33 has a diameter of 25 cm. The bottom 3.0 m of the buoy is submerged. Its vertical oscillations have a period of 3.6 seconds. The buoy's effective moving mass, $m_o = 154$ kg.
   (a) *Viscous penetration depth.* If the water has a density, $\rho_{H_2O} = 1026$ kg/m^3, and a shear viscosity, $\mu_{H_2O} = 1.07 \times 10^{-3}$ Pa-s, how large is the viscous penetration depth at the buoy's natural frequency of vertical oscillations?
   (b) *Viscously entrained mass*. What is the additional mass of water trapped in the viscous boundary layer if we assume that mass is the mass of water within one viscous penetration depth? (The circular bottom of the buoy can be ignored since it is not applying any shear stresses on the water.)
   (c) *Viscous damping*. Determine the mechanical resistance, R_m, by calculating the viscous drag of the water on the buoy. Use your value of R_m to determine the exponential relaxation time, $\tau = 2m_o/ R_m$, if the only source of damping is the viscous drag provided by the surrounding water.
5. **Greenspan viscometer**. Shown in Fig. 9.17 is a schematic cross-section of a cylindrically symmetric (about the "Duct" axis) double-Helmholtz resonator that has been used by the National Institute of Standards and Technology (formerly, the Bureau of Standards) to make an acoustical determination of the viscosity of gases [18]. Both volumes, V, are identical and A is the total surface area of

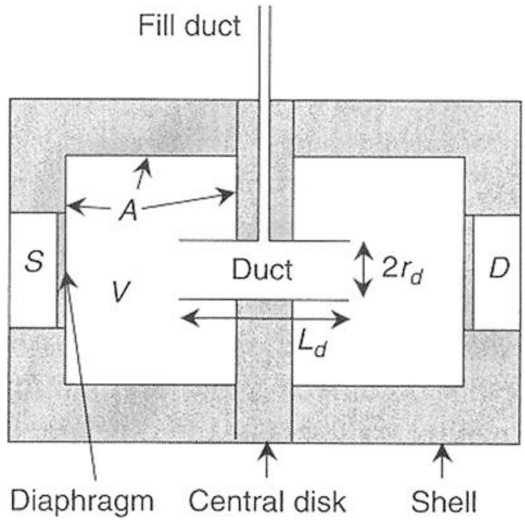

Fig. 9.17 Cross-sectional schematic representation of a Greenspan viscometer [19]

each volume. "S" and "D" are PZT stacks that act as the excitation and detection transducers that are covered by a "Diaphragm" which can be considered perfectly rigid.

For this problem, assume that the viscometer is filled with neon gas at a mean pressure, $p_m = 1.0$ MPa. Both compliances have the same volume, $V = 29$ cm^3, and the same surface area, $A = 55$ cm^2. The duct length, $L_d = 3.1$ cm, and the radius of the duct, $r_d = 2.3$ mm. This viscometer produced measurements of viscosity that differed from published results obtained by other methods by less than ±0.5% and sound speeds that differed by less than ±0.2% [18].

(a) *Helmholtz resonance frequency*. Assuming that the neon gas is lossless, calculate the resonance frequency of this dual Helmholtz resonator using a sound speed in neon of c_{Ne} (20 °C) = 449 m/s.

(b) *Gas displacement in the duct*. If the amplitude of the acoustic pressure in either volume is 10.0 Pa, what is the peak-to-peak displacement of the gas in the duct?

(c) *Viscous penetration depth*. Based on the resonance frequency, calculate the viscous penetration depth if the neon has a density, ρ_{Ne} (20 °C) = 8.28 kg/m^3, and a viscosity, μ_{Ne} (20 °C) = 3.13×10^{-5} Pa-s.

(d) *Quality factor*. Calculate the quality factor, Q, for this Helmholtz resonance.

(e) *Viscosity*. In the limit that $\delta_\nu \ll r_d$, express the gas viscosity, μ, in terms of the Helmholtz resonance frequency, f_o, the gas density, ρ, and the resonance quality factor, Q.

(f) *Thermal relaxation*. Investigate how negligible the thermal boundary layer losses are in the compliances.

References

1. C. Nolan, *Memento*, Newmarket Productions (Columbia TriStar, 2001).
2. F. M. White, *Mass and Heat Transfer* (Addison-Wesley, 1991). See §1.3.5; ISBN 0-201-17099-X.
3. F. P. Incropera and D. P. DeWitt, *Fundamentals of Heat and Mass Transfer*, 3rd ed. (J. Wiley & Sons, 1990). See Ch. 6; ISBN 0-471-61246-4.
4. G. W. Swift, *Thermoacoustics: A unifying perspective for some engines and refrigerators,* 2nd ed. (Acoust. Soc. Am., 2017); ISBN 978-3-319-66932-8. See Eq. (5.11).

5. A.D. Hanford, L.N. Long, The absorption of sound on Mars using the direct simulation Monte Carlo. J. Acoust. Soc. Am. **119**, 3264 (2006)
6. L. D. Landau and E. M. Lifshitz, *Fluid Mechanics*, 2nd ed. (Butterworth-Heinemann, 1987). See §15; ISBN 0 7506 2767 0.
7. J.R. Olson, G.W. Swift, Energy dissipation in oscillating flow through straight and coiled pipes. J. Acoust. Soc. Am. **100**(4), 2123–2131 (1996)
8. F. Reif, *Fundamentals of Statistical and Thermal Physics* (McGraw-Hill, 1965). See §12.4.
9. S. Chapman and T. G. Cowling, *Mathematical Theory of Non-Uniform Gases*, 2nd ed. (Cambridge Univ. Press, 1951).
10. G. W. Swift, *Thermoacoustics: A unifying perspective for some engines and refrigerators,* 2nd ed. (Acoust. Soc. Am., 2017). See §2.3.2, pg. 48–49; ISBN 978-3-319-66932-8.
11. R. B. Bird, W. E. Stewart, E. N. Lightfoot, *Transport Phenomena* (Wiley & Sons, 1960). See Table 8.3–1.
12. G. Wiedemann, R. Franz, Relative conductivity of solids. Ann. Phys. Chemie **89**, 497–531 (1853)
13. A. Eucken, On the thermal conductivity of several gases. Physik. Z. **14**, 324–332 (1913)
14. F.W. Giacobbe, Estimation of Prandtl numbers in binary mixtures of helium and other noble gases. J. Acoust. Soc. Am. **96**(6), 3538–3580 (1994)
15. S.L. Garrett, J.A. Adeff, T.J. Hofler, Thermoacoustic refrigerator for space applications. J. Thermophys. Heat Transf. (AIAA) **7**(4), 595–599 (1993)
16. G.W. Swift, D.A. Geller, S.N. Backhaus, High-purity thermoacoustic isotope separation. J. Acoust. Soc. Am. **136**(2), 638–648 (2014)
17. N. Fletcher, Condenser microphones – a tutorial. Acoust. Australia **30**(3), 109–113 (2002)
18. J. Wilhelm, K.A. Gillis, J.B. Mehl, M.R. Moldover, An improved Greenspan acoustic viscometer. Int. J. Thermophys. **21**, 983–999 (2000)
19. M. R. Moldover, K. A. Gillis, J. J. Hurly, J. B. Mehl and J. Wilhelm, "Acoustic Measurements in Gases," in *Experimental Methods in Physical Sciences*, Vol. 39 (Academic Press, 2001). See Chap. 10; ISBN 0-12-475986-6.

One-Dimensional Propagation

10

Contents

S. L. Garrett, *Understanding Acoustics*, Graduate Texts in Physics,
https://doi.org/10.1007/978-3-030-44787-8_10

Having already invested in understanding both the equation of state in Chap. 7 and in the hydrodynamic equations in Chap. 8, only straightforward algebraic manipulations will be required to derive the wave equation, justify its solutions, calculate the speed of sound in fluids, and derive the expressions for acoustic intensity and the acoustic kinetic and potential energy densities. The "machinery" developed to describe waves on strings will be sufficient to describe one-dimensional sound propagation in fluids, even though the waves on the string were transverse and the one-dimensional waves in fluids are longitudinal.

Most treatments of one-dimensional propagation in acoustics courses start their discussion of waves in fluids at this point (possibly treating lumped-element systems later), but with our understanding of the fundamental phenomenological equations already established for lumped elements, we will be able to take a more rigorous approach that will also allow incorporation of other effects that can be combined with the dissipative effects introduced in Chap. 9, particularly for calculation of the attenuation of sound in Chap. 14. Also, having examined combinations of inertances and compliances, the transition from lumped fluid elements to waves in fluids is philosophically identical to the transition from coupled simple harmonic oscillators to waves on strings.

10.1 The Transition from Lumped Elements to Waves in Fluids

The equation of state, as exemplified by the adiabatic gas law of Eq. (7.20), and the linearized versions of the continuity equation combined with the adiabatic gas law in Eq. (8.23) were used to create lumped compliances in Sect. 8.2.3. The linearized version of the Euler Eq. (8.40) was used to create lumped inertances, and then both inertance and compliance were applied to fluid elements that were small compared to the wavelength of sound in Sect. 8.4.3. Those equations can now be extended to continuous fluid media in systems that are substantial fractions of a wavelength or larger.

Since the lumped-element model was linear, we are free to combine solutions. Although the neck of our Helmholtz resonator in Sect. 8.5.2 was represented entirely by its inertance (gas mass) and the spherical volume was represented entirely by its compliance (gas stiffness), in general, a single "lumped" element could simultaneously exhibit both properties by linear superposition. If there are changes in the volume velocity of the fluid entering and leaving the element, ΔU, as well as a pressure difference, Δp, across an element, like those diagrammed schematically in Figs. 8.3 and 8.8, then the element would exhibit both inertance (due to Δp) and compliance (due to ΔU).

In this chapter, we will expand our focus to include acoustical systems with characteristic dimensions comparable to, or longer than, the wavelength of sound in the fluid. These can also be modeled using lumped parameters, if we employ enough elements. For instance, a resonator with diameter that is a small fraction of the wavelength, but a length that is equal to one-half of the wavelength of sound, can be modeled as a sequence of compliances and inertances as depicted schematically in Fig. 10.1.

As demonstrated in Sect. 2.7.7, the behavior of standing waves on strings can be approximated by identical discrete masses coupled by identical lengths of a massless string under uniform tension. The fundamental mode of nine such coupled oscillators is shown in Fig. 2.30 to be a good approximation to the half-sinewave mode of a string, like that shown in Fig. 3.6. This approach has some significant utility if you are interested in studying systems with changing cross-section. As shown in Fig. 10.2, a horn of finite length, analyzed in Sect. 10.9.3, can be approximated by a series of stepped ducts of increasing cross-section.

The broadband, omnidirectional sound source shown in Fig. 10.3 was designed to radiate sound uniformly in all directions and to give reproducible and reliable results for evaluation of building acoustics with a sufficient overall sound pressure level to provide adequate signal-to-noise ratios. The

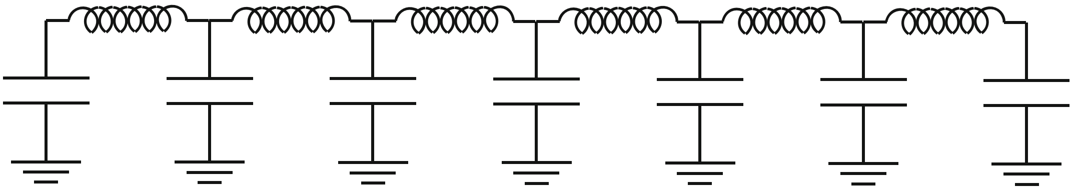

Fig. 10.1 A half-wavelength resonator (*above*) of constant cross-sectional area with rigid ends is approximated as a series of seven lumped compliances and six lumped inertances. The elements near the ends contribute primarily compliance since the longitudinal motion of the fluid must vanish at the boundary (velocity nodes). Most of the energy stored near the ends is compressive (potential). The central elements contribute mostly inertance since the fluid velocity at the center is largest (near the velocity anti-node). Most of the energy within the central pair of inertances is kinetic. In fact, the approximation is nearly as good if the central compliance is removed from the model (but only for the fundamental half-wavelength mode!). The two pairs of elements that are intermediate between the two end elements and the central elements must provide both significant inertance and compliance

Fig. 10.2 A stepwise approximation to a horn. The number of elements is chosen so the area change between elements is small [1]

Fig. 10.3 The Brüel & Kjær Type 4295 sound source was "carefully engineered to radiate sound evenly in all directions" by Dr. Jean-Dominique Polack. The source was designed to conform to the standard 1/3-octave band sound level and directionality requirements by using a resonator coupled to an electrodynamic loudspeaker. Although a resonator is about as far from a "broadband" sound source as one might possibly imagine, it does satisfy the standards as written

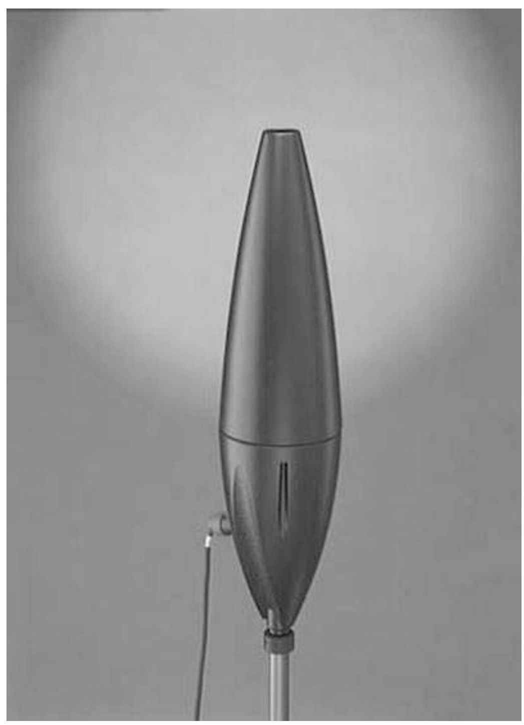

International Organization for Standardization (ISO) has published two standards for broadband sound sources that are used for architectural acoustical evaluations in buildings [2]. The standards require uniform levels, within a frequency-dependent number of decibels (see Sect. 10.5.1) in each of twenty-one 1/3-octave frequency bands (ISO 3382). The source must also radiate sound uniformly in all directions (ISO 140).

A very clever acoustician, Jean-Dominique Polack,[1] realized that he could design a very simple source consisting of a single loudspeaker radiating out of a small aperture (to ensure omnidirectionality, as shown in Fig. 12.32a) that would be very compact and efficient by making a resonator and "tuning" the resonances within each 1/3-octave band (though not necessarily at the band center frequency). He did this by writing a finite element code that incorporated 28 lumped elements and then adjusted those elements to place the resonances within the 1/3-octave bands specified by ISO 3382.[2]

At some point, it makes sense to model the entire resonator as a continuum just as it did in our transition from coupled simple harmonic oscillators to strings. We do that by specifying a continuous function that describes the pressure and fluid velocity at each point in space and time—a wave function.

10.2 The Wave Equation

Our study of the fundamental equations of hydrodynamics has provided us with a set of three Eqs. (7.32), (7.34), and (7.42) that describe the motion of any homogeneous, viscous, thermally conducting, and isotropic, single-component fluid. We supplemented those hydrodynamic equations by equations of state (7.49) and (7.50) that provide relationships among the mechanical variables (p and ρ) and thermodynamic variables (T and s) that appear in the hydrodynamic equations.

The linearized, one-dimensional, nondissipative versions of those equations are first-order partial differential equations that define relationships among different variables. For example, the continuity equation or mass conservation Eq. (8.17) relates changes in density to the divergence of the fluid velocity or mass flux. Similarly, the linearized one-dimensional Euler Eq. (8.40) relates changes in the velocity to gradients in the pressure. An equation of state, for example, (7.19), can relate changes in pressure to changes in density.

It is possible to combine those first-order partial differential equations to create a second-order partial differential equation for a single variable. To illustrate this process, let us start with a one-dimensional version of the linearized continuity Eq. (8.17), where we let $v_x = u = v_1$,

$$\frac{\partial \rho_1(x,t)}{\partial t} + \rho_m \frac{\partial v_1(x,t)}{\partial x} = 0, \tag{10.1}$$

and the linearized one-dimensional Euler equation, where again $v_x = u = v_1$,

[1] Prof. Polack was on the faculty at the Danish Technical University (less than a 10 min drive from Lyngby to the Brüel & Kjær Headquarters in Nærum, Denmark) when he made this design. He is currently a professor at Université Pierre et Marie Curie and the Head of Doctoral School of Mechanics, Acoustics, Electronics and Robotics (SMAER, ED 391).

[2] The resultant resonator was conical. It can be modeled easily in DeltaEC as a single CONE element (plus an electrodynamic driver VESPEAKER at one end and an OPNBRANCH radiation condition at the other end). This is a lot easier than 28 lumped elements once you accept that a cone will solve the problem.

$$\frac{\partial v_1(x,t)}{\partial t} + \frac{1}{\rho_m}\frac{\partial p_1(x,t)}{\partial x} = 0. \tag{10.2}$$

That set of two first-order coupled differential equations contains three (potentially complex) variables: ρ_1, v_1, and p_1. To "close" the system, we need one additional equation to eliminate either p_1 or ρ_1. Closure can be achieved by invoking an equation of state. In this case, we will choose to express density in terms of pressure, $\rho = \rho(p)$, which can be expanded in a Taylor series to eliminate ρ_1 in favor of p_1 in Eq. (10.1).

$$\rho_1 = \left(\frac{\partial \rho}{\partial p}\right)_s p_1 + \left(\frac{\partial^2 \rho}{\partial p^2}\right)_s \frac{(p_1)^2}{2!} + \left(\frac{\partial^3 \rho}{\partial p^3}\right)_s \frac{(p_1)^3}{3!}\cdots \tag{10.3}$$

As was demonstrated in Sect. 9.3.4, at nearly all frequencies of interest in gases or liquids, sound propagation is adiabatic. For that reason, we have taken the derivatives of the density with respect to pressure in Eq. (10.3) while holding entropy per unit mass constant, as indicated by the subscript, s, on the partial derivatives. Since we are interested in the linearized result, we retain only the first term in the Taylor series of Eq. (10.3). As we will see shortly, it is convenient to name that derivative[3] the reciprocal of the square of the speed of sound, c^{-2}.

$$\frac{1}{c^2} = \left(\frac{\partial \rho}{\partial p}\right)_s \tag{10.4}$$

Substituting Eq. (10.4) into Eq. (10.1), we obtain,

$$\frac{1}{c^2}\frac{\partial p_1(x,t)}{\partial t} + \rho_m \frac{\partial v_1(x,t)}{\partial x} = 0 \tag{10.5}$$

Now Eqs. (10.2) and (10.5) constitute a pair of homogeneous first-order coupled differential equations in two variables. Those equations can be combined to eliminate either p_1 or v_1. Let us start by eliminating v_1. That can be accomplished by multiplying the linearized Euler Eq. (10.2) by ρ_m and taking its derivative with respect to x.[4]

$$\rho_m \frac{\partial^2 v_1(x,t)}{\partial x \partial t} + \frac{\partial^2 p_1(x,t)}{\partial x^2} = 0 \tag{10.6}$$

We can then take the time derivative of the linearized continuity Eq. (10.5).

$$\frac{1}{c^2}\frac{\partial^2 p_1(x,t)}{\partial t^2} + \rho_m \frac{\partial^2 v_1(x,t)}{\partial t \partial x} = 0 \tag{10.7}$$

Since the order of differentiation is irrelevant, when Eq. (10.6) is subtracted from Eq. (10.7), we are left with a second-order, homogeneous, partial differential equation in only one variable.

[3] Some say thermodynamics is the field where every partial derivative has its own name.

[4] We assume that ρ_m is independent of x throughout most of this book. Many thermoacoustic phenomena, including engines and refrigerators, rely on the x dependence of T_m and ρ_m, so the fundamental equations of thermoacoustics are more complicated [8].

$$\frac{\partial^2 p_1(x,t)}{\partial t^2} - c^2 \frac{\partial^2 p_1(x,t)}{\partial x^2} = 0 \tag{10.8}$$

The result in Eq. (10.8) is the well-known one-dimensional *wave equation*. It provides us with an expression that can relate the time and space dependence of $p_1(x, t)$. Since pressure and density deviations from equilibrium are related by the square of the sound speed, then we would obtain the same wave equation for ρ_1.

$$\frac{\partial^2 \rho_1(x,t)}{\partial t^2} - c^2 \frac{\partial^2 \rho_1(x,t)}{\partial x^2} = 0 \tag{10.9}$$

If the combination process is reversed by taking the spatial derivative of the linearized continuity Eq. (10.5), we obtain,

$$\frac{\partial^2 p_1(x,t)}{\partial x \partial t} + \rho_m c^2 \frac{\partial^2 v_1(x,t)}{\partial x^2} = 0 \tag{10.10}$$

Similarly, the linearized Euler Eq. (10.2) can be multiplied by ρ_m, and then the time derivative can be taken.

$$\rho_m \frac{\partial^2 v_1(x,t)}{\partial t^2} + \frac{\partial^2 p_1(x,t)}{\partial t \partial x} = 0 \tag{10.11}$$

Once again, ignoring the order of differentiation, subtraction of Eq. (10.10) from Eq. (10.11) produces the wave equation for the linear contribution to the x component of the acoustic particle velocity, v_1.

$$\frac{\partial^2 v_1(x,t)}{\partial t^2} - c^2 \frac{\partial^2 v_1(x,t)}{\partial x^2} = 0 \tag{10.12}$$

10.2.1 General Solutions to the Wave Equation

The wave equation, as written in Eq. (10.8) or Eq. (10.12), is a second-order partial differential equation. As such, it must have two linearly independent solutions: y_a and y_b. Of course, any one-dimensional, linear, wave equation will be isomorphic to the version that appeared first as the equation for propagation of transverse waves on a string in Eq. (3.4).

As was demonstrated in Sect. 3.1, it is not difficult to show that any arbitrary function having $(ct \pm x)$ in its argument is a solution. Whether c is the speed of sound in a fluid, or the speed of transverse waves on a string, $f(ct \pm x)$ are the solutions to Eq. (3.4) as well as Eqs. (10.8), (10.9), and (10.12). If we choose pressure as the variable that characterizes the amplitude of the sound wave, then the excess acoustic pressure due to the sound wave, $p_1(x, t)$, can be expressed as the superposition of the right-going and left-going waves.

$$p_1(x,t) = p_1^{right}(ct - x) + p_1^{left}(ct + x) \tag{10.13}$$

As with our solutions for waves on strings, for purposes of computational convenience and conformity with physical reality for most acoustical systems, we employ the trigonometric functions, or complex exponential functions, or combinations of those functions as our solutions of choice for single-frequency waves, as we did for traveling waves.

$$p_1\left(\vec{x}, t\right) = \Re e\left[\widehat{\mathbf{p}}_{\mathbf{left}} e^{j\left(\omega t + \vec{k}\cdot\vec{x}\right)} + \widehat{\mathbf{p}}_{\mathbf{right}} e^{j\left(\omega t - \vec{k}\cdot\vec{x}\right)}\right] \tag{10.14}$$

Standing waves can be represented as the superposition of a right- and left-going traveling waves of equal amplitudes. Letting $\widehat{\mathbf{p}}_{\mathbf{left}} = Ae^{-j(\phi_t+\phi_x)}/2$ and $\widehat{\mathbf{p}}_{\mathbf{right}} = Ae^{-j(\phi_t-\phi_x)}/2$, with $\vec{k}\cdot\vec{x} = kx$, and making $\Im m[A] = \Im m[\phi_t] = \Im m[\phi_x] = 0$, Eq. (10.14) becomes,

$$p_1(x, t) = A\cos\left(kx - \phi_x\right)\cos\left(\omega t - \phi_t\right) \tag{10.15}$$

As before, the scaling of time by angular frequency, ω, and position by wavenumber, k, is a particularly useful choice that makes the argument of the functions dimensionless.

The same functions could just as well have been written for the linear variations in the density, $\rho_1(x, t)$, from its equilibrium value, ρ_m, or the variation in the particle velocity, $v_1(x, t)$, where we have assumed $v_m = 0$.

10.3 The Dispersion Relation (Phase Speed)

Once we have used the wave equation to demonstrate that the solutions for each variable that characterizes its linear deviation from equilibrium have wave-like space and time behavior, the wave equation does not provide any immediate additional utility. To demonstrate this fact, we can return to the coupled first-order linearized continuity Eq. (10.1) and Euler Eq. (10.2).

By using the complex notation of Eq. (10.14) with $\widehat{\mathbf{p}}_{\mathbf{left}} = 0$ to describe a single-frequency right-going propagating wave, differentiation with respect to time corresponds to a simple multiplication of p_1 by $+j\omega$ and differentiation with respect to position corresponds to a simple multiplication of p_1 by $-jk$. Application of this convenience (aka complex) transformation (harmonic analysis) to the linearized continuity Eq. (10.5) yields,

$$\frac{j\omega\widehat{p}_{right}}{c^2} - jk\rho_m\widehat{v}_{right} = 0. \tag{10.16}$$

Similarly, the linearized Euler Eq. (10.2) becomes,

$$j\omega\widehat{v}_{right} - \frac{jk\widehat{p}_{right}}{\rho_m} = 0. \tag{10.17}$$

This pair of linear coupled algebraic equations, (10.16) and (10.17), will only have a nontrivial solution if the determinant of their coefficients vanishes.

$$\begin{vmatrix} \dfrac{+j\omega}{c^2} & -jk\rho_m \\ \dfrac{-jk}{\rho_m} & +j\omega \end{vmatrix} = 0 \tag{10.18}$$

Evaluation of the determinant specified in Eq. (10.18) produces a relationship between ω and k that is known as a *dispersion relation*.

$$k^2 - \frac{\omega^2}{c^2} = 0 \tag{10.19}$$

This result provides the definition of the phase speed, $c \equiv \omega / k$, thus justifying the concepts of wavenumber, k; wavelength, λ; frequency, f; and period, T, that we have been using since Chap. 3: $c = f\lambda = \omega/k$.

10.3.1 Speed of Sound in Liquids

The square of the adiabatic speed of sound is expressed as the thermodynamic derivative of pressure with respect to density in Eq. (10.4). For fluids, that result is related to another thermodynamic derivative; the adiabatic bulk modulus, B_s, has the same units as pressure:

$$B_s = -V\left(\frac{\partial p}{\partial V}\right)_s = -\frac{1}{\rho}\left(\frac{\partial p}{\partial\left(1/\rho\right)}\right)_s = \rho\left(\frac{\partial p}{\partial \rho}\right)_s \tag{10.20}$$

In Sect. 4.2.1, the previous derivation for the bulk modulus in solids did not specify whether the modulus was evaluated under isothermal or adiabatic conditions since there is very little difference between those values for solids.

The adiabatic bulk modulus is the reciprocal of the adiabatic compressibility. By comparison of Eq. (10.20) to Eq. (10.4), we see that the adiabatic sound speed in a fluid can be expressed in terms of the adiabatic bulk modulus and the fluid's mass density.

$$c = \sqrt{\frac{B_s}{\rho_m}} \tag{10.21}$$

The form of Eq. (10.21) is typical of sound propagation speeds because it shows that the speed is determined by the ratio of a restoring "stiffness" to an inertial mass density.

The bulk modulus is an intensive material property. For most liquids, it is usually found in handbooks and can be a complicated function of both pressure and temperature. The expression for the speed of sound in seawater, given in Eq. (11.26), includes terms that are a function of salinity, as well as pressure [3]. Even a simple cryogenic liquid, such as liquid nitrogen (LN_2), exhibits complicated pressure dependence of its sound speed:

$$\begin{aligned} c(LN_2) = {} & 854.1 + 0.8370p - 0.9072 \times 10^{-3}p^2 \\ & + 0.9697 \times 10^{-6}p^3 - 0.4904 \times 10^{-9}p^4 \end{aligned}$$

where c is in [m/s] and p is in atmospheres (1 atm $\equiv$ 101,325 Pa) [4].

10.3.2 Speed of Sound in Ideal Gases and Gas Mixtures

For an ideal gas, the form of the sound speed is particularly simple and universal. Logarithmic differentiation of the ideal gas adiabatic equation of state, $p\rho^{-\gamma}$ = constant, immediately produces an expression for the speed of sound in an ideal gas, based on Eq. (10.4):

$$\frac{dp}{p_m} = \gamma \frac{d\rho}{\rho_m} \quad \Rightarrow \quad c = \left(\frac{\partial p}{\partial \rho}\right)_s^{1/2} = \sqrt{\frac{\gamma p_m}{\rho_m}} \tag{10.22}$$

The Ideal Gas Law (7.4) allows Eq. (10.22) to be expressed in terms of the molecular (or atomic) mass of the gas, M; its absolute [kelvin] temperature, T; and the universal gas constant, $\Re$:

$$c^2 = \frac{\gamma \Re T}{M} \tag{10.23}$$

It is worthwhile to reflect on the adiabatic sound speed for ideal gases as expressed in Eq. (10.23) for several reasons: First, it demonstrates that *the sound speed in an ideal gas is not a function of pressure*. This is not obvious from Eq. (10.22), which could (naïvely) be interpreted to imply that the sound speed increases with the square root of pressure. This is incorrect, because the ratio of pressure to density depends only upon absolute [kelvin] temperature, polytropic coefficient, and molecular weight.

Equation (10.23) also highlights the fact that the sound speed is proportional to the square root of absolute [kelvin] temperature. As of 20 May 2019, the international standard absolute temperature scale is based on sound speed measurements [5], just as the *exact* value of Boltzmann's constant, $k_B \equiv 1.380649 \times 10^{-23}$J/K, and the universal gas constant, $\Re \equiv k_B N_A \equiv 8.314462$ J/mole-K, has been tied to sound speed measurements since the mid-1980s [6].

The third reason that Eq. (10.23) is important is that it provides a means of calculating the speed of sound in gas mixtures. If we have a binary mixture of ideal gases with a concentration, x, of one species with molecular mass, M_1, and concentration, $(1 - x)$, of the second species with molecular mass, M_2, then the mean molecular mass of the gas mixture, M_{mix}, is simply their concentration-weighted average:

$$M_{mix} = xM_1 + (1 - x)M_2 \tag{10.24}$$

This expression can be generalized to mixtures, such as air, with more than two constituents (see Table 10.1).

Since the polytropic coefficient, $\gamma = c_p/c_V$, also known as the ratio of specific heats, is an intensive quantity, it is not correct to calculate γ_{mix} as a weighted average of the individual polytropic coefficients, although it is not too bad an approximation in some circumstances [7], since the range of γ is limited: $1 < \gamma \leq 5/3$. To calculate γ_{mix} correctly, the heat capacities are averaged:

$$\gamma_{mix}(x) = \frac{c_p}{c_V} = \frac{xc_{p,1} + (1 - x)c_{p,2}}{xc_{V,1} + (1 - x)c_{V,2}} \tag{10.25}$$

This result can be written in another form if the concentration weighting is applied to the reciprocals of $(\gamma - 1)$ [8].

$$\frac{1}{\gamma_{mix} - 1} = \frac{x}{\gamma_1 - 1} + \frac{1 - x}{\gamma_2 - 1} \tag{10.26}$$

A similar approach can be used to estimate the transport coefficients in gas mixtures: thermal conductivity, viscosity, and Prandtl number, as was done in Sect. 9.5.4 [9].

Since the sound speed is independent of pressure and the temperature dependence can be easily compensated, being proportional to the square root of absolute temperature,[5] it is possible to build sonic gas analyzers that determine the concentration of a contaminant quickly, accurately, and inexpensively [12, 13]. The helium contamination alarm, shown schematically in Fig. 10.4, uses the variation in sound speed to detect leakage of air into a helium gas recovery system [14]. Other more sophisticated systems have been developed that allow flow-through measurement with differential processing to increase common-mode rejection of flow and environmental noise [12, 15].

[5] Analog Devices, Inc. sells a wonderful temperature sensing integrated circuit (AD 592) that sources one microampere of current for each degree of absolute temperature, making electronic temperature compensation nearly trivial.

Table 10.1 Properties of the constituents of standard dry air at $T_m = 0$ °C [10] which produce a sound speed of 331.44 m/s [11]

Constituent	Molar mass [gm/mol]	Mole fraction	Contribution [gm/mol]	c_p [kJ/kg-K]	$\gamma = c_p/c_v$
N_2	28.013 4	0.780 84	21.873 983	1.0404	1.400
O_2	31.998 8	0.209 476	6.702 981	0.09187	1.395
Ar	39.948	0.009 34	0.373 114	0.5216	1.667
CO_2	44.009095	0.000 314	0.013 819	0.8460	1.289
Ne	20.183	1.818E-05	0.000 367	1.0299	1.667
Kr	83.80	1.14E-06	0.000 096	0.2480	1.667
CH_4	16.043 03	2.0E-06	0.000 032	2.2193	1.304
He	4.002 6	5.24E-06	0.000 021	5.1931	1.667
N_2O	44.012 8	2.70E-07	0.000 012	0.8721	1.27
Xe	131.30	8.7E-08	0.000 011	0.1583	1.667
CO	28.01	1.9E-07	0.000 006	1.0420	1.40
H_2	2.015 94	5.0E-07	0.000 001	14.3020	1.405
H_2O	18.015 34	0	0	1.8624	1.32

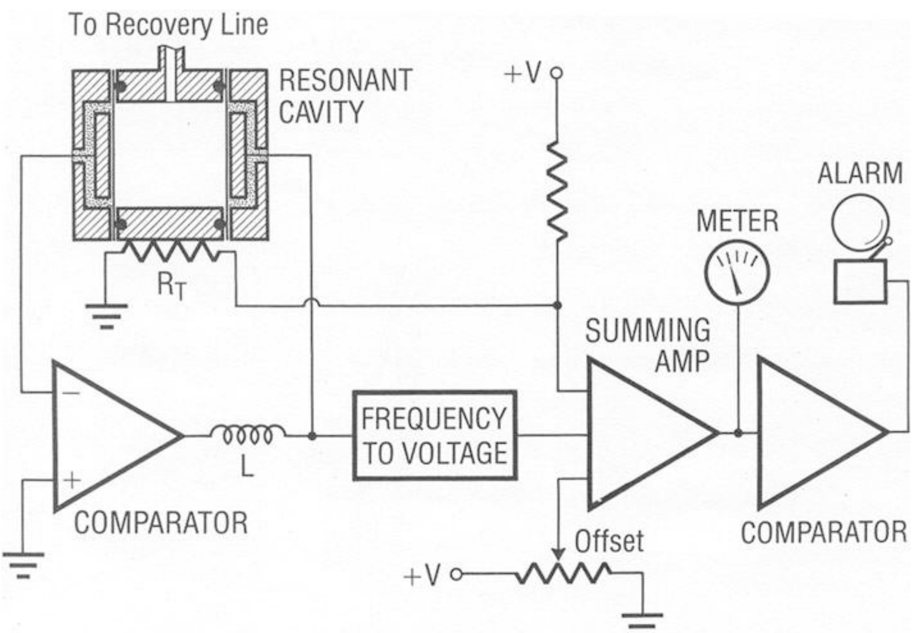

Fig. 10.4 The cylindrical plane wave resonator in the upper left corner of this block diagram is closed at each end by electret (12 μm thick aluminized Teflon®) transducers (see Sect. 6.3.3) [16]. One electret transducer is used as a microphone and the other as a speaker. A slot at the resonator's midplane allows the resonator to sample the helium gas flowing through the recovery line without degrading the resonator's quality factor. The system is maintained at its fundamental resonance frequency by applying the amplified microphone output to the speaker through an inductor tuned to the electret speaker's electrical capacitance. (In a public address system, this would be considered feedback squeal.) A 37 m coil of #44 copper wire ($R_T \cong 350\ \Omega$) is epoxied to the resonator and is used as a thermometer. A frequency-to-voltage conversion (tachometer) chip [17] produces a dc voltage proportional to the resonance frequency that is summed with the temperature-dependent voltage produced by R_T along with an offset voltage that is adjusted when pure helium gas is in the recovery line. If air enters the recovery line, the frequency decreases, and an alarm is activated and the recovery valve is closed [14]

10.4 Harmonic Plane Waves and Characteristic Impedance

The linearized first-order Euler Eq. (10.2) can be solved to relate the acoustic fluid (particle) velocity, v_1, to the acoustic pressure, p_1. For a harmonic, one-dimensional plane traveling wave, expressed in Eq. (10.14), the ratio of pressure to particle velocity is z, remembering that $c = \omega / k$.

$$z \equiv \left| \frac{p_1}{v_1} \right| = \rho_m c \tag{10.27}$$

This property of a fluid is sufficiently important to be given its own name: the *specific acoustic impedance* or the *characteristic impedance*. The units of specific acoustic impedance are Pa-s/m, also called the *rayl* (sometimes the MKS rayl to distinguish it from the cgs rayl), in honor of the third Lord Rayleigh (J. W. Strutt, 1842–1919).

Another short digression regarding the three impedances used in acoustics is beneficial at this point. We have previously encountered an impedance that we called the acoustic impedance. It was defined as the ratio of the pressure to the volume velocity at one location: $\mathbf{Z_{ac}} = \widehat{\mathbf{p}}/\widehat{\mathbf{U}}$. That impedance was particularly useful for describing systems that join elements with differing cross-sectional areas (e.g., Helmholtz resonator) to ensure the continuity of mass flow. We will also see that another version, the acoustic transfer impedance, $\mathbf{Z_{tr}}$, will be very useful in problems that involve acoustic radiation and transduction (see Sect. 10.7). The acoustic transfer impedance is given by the pressure at one location (the receiver) divided by the volume velocity produced at the source of sound.

In Eq. (10.27), we have just defined a specific acoustic impedance, the ratio of pressure to particle velocity, which is a property of the acoustic medium and is independent of geometry. It is especially useful in the description of plane waves, particularly when they impinge on boundaries between media with different properties, as will be addressed in detail in Chap. 11. The third impedance is the mechanical impedance, $\mathbf{Z_{mech}} = \widehat{\mathbf{F}}/\widehat{\mathbf{v}}$. The mechanical impedance is useful for determining the steady-state response of a vibro-mechanical network.

Frequently in acoustics, and particularly for problems involving transduction, these different complex impedances (as well as the electrical impedance, $\mathbf{Z_{el}} = \widehat{\mathbf{V}}/\widehat{\mathbf{I}}$) need to be combined to couple an electromechanical system to an acoustical medium. It is easy to relate the three impedances for a system with a characteristic cross-sectional area, A.

$$\mathbf{Z_{ac}} = \frac{\widehat{\mathbf{p}}}{\widehat{\mathbf{U}}} = \frac{\widehat{\mathbf{p}}}{A\widehat{\mathbf{v}}} = \frac{\widehat{\mathbf{F}}/A}{A\widehat{\mathbf{v}}} = \frac{\mathbf{Z_{mech}}}{A^2} \quad \text{and} \quad |\mathbf{Z_{ac}}| = \frac{z}{A} \tag{10.28}$$

In Eq. (10.28), the pressure amplitude, $\widehat{\mathbf{p}}$; volume velocity amplitude, $\widehat{\mathbf{U}}$; and particle velocity amplitude, $\widehat{\mathbf{v}}$, were all complex phasors to emphasize the fact that impedance is a concept that is based on linear acoustics and the assumption of a single-frequency wave-like disturbance from equilibrium.

The specific acoustic impedance, $z = \rho_m c$, is convenient for representing the space and time dependence of the acoustic fluid (particle) velocity, $v_1(x, t)$, for a traveling wave moving in the positive x direction. Below, Eq. (10.29) has $\pm\rho_m c$ in the denominator to remind us that a wave traveling in the minus x direction would have a negative specific acoustic impedance.

$$v_1\left(\vec{x}, t\right) = \frac{p_1\left(\vec{x}, t\right)}{\pm\rho_m c} = \Re e\left[\frac{\widehat{\mathbf{p}}}{\pm\rho_m c} e^{j\left(\omega t \mp \vec{k}\cdot\vec{x}\right)}\right] \tag{10.29}$$

The continuity equation can be used to relate density variations, $\rho_1(x, t)$, to the particle velocity, $v_1(x, t)$, of a plane wave with the final version restricted to a single-frequency wave.

$$\rho_1\left(\vec{x},t\right) = \rho_m \frac{v_1\left(\vec{x},t\right)}{c} = \frac{1}{c^2}\Re e\left[\widehat{\mathbf{p}}\, e^{\,j\left(\omega t \mp \vec{k}\cdot\vec{x}\right)}\right] \tag{10.30}$$

The dot product that appears in the spatial dependence within the argument of the exponential functions in Eqs. (10.14) and (10.29) can be expanded into its Cartesian components for an arbitrary choice of directions with respect to the Cartesian axes.

$$p_1\left(\vec{x},t\right) = \Re e\left[\widehat{\mathbf{p}} e^{\,j\left(\omega t - k_x x - k_y y - k_z z\right)}\right] \quad \text{where} \quad \left(\frac{\omega}{c}\right)^2 = k_x^2 + k_y^2 + k_z^2 \tag{10.31}$$

Normally, if a plane wave is propagating in an arbitrary direction, it is easier to re-orient the coordinate axes so that one axis is along the direction of propagation and the one-dimensional expressions will suffice. In an isotropic medium, the wave vector, $\vec{k}$, defines a direction that is perpendicular to the wave's planes of constant phase.

10.5 Acoustic Energy Density and Intensity

Since our hydrodynamic equations provide a complete description of the fluid, there should be no need to introduce any additional equations to account for the energy density of the fluid or for the acoustical energy transported by the waves. For the nondissipative case, that fact can be demonstrated by combining the continuity equation and the Euler equation in another way.

We start by writing the linearized three-dimensional vector form of the continuity Eq. (8.9), augmented by the equation of state (10.4), as expressed in the one-dimensional version in Eq. (10.5).

$$\frac{\partial \rho_1}{\partial t} + \rho_m \nabla \cdot \vec{v}_1 = \frac{1}{c^2}\frac{\partial p_1}{\partial t} + \rho_m \nabla \cdot \vec{v}_1 = 0 \tag{10.32}$$

The continuity equation can be combined with the linearized three-dimensional vector form of the Euler equation.

$$\rho_m \frac{\partial \vec{v}_1}{\partial t} + \vec{\nabla} p_1 = 0 \tag{10.33}$$

If we take the dot product of $\vec{v}_1$ with Eq. (10.33) and multiply Eq. (10.32) by p_1 and add the two equations together, we can collect terms if we notice that the product rule (see Sect. 1.1.2) produces the following identities:

$$\vec{v}_1 \cdot \frac{\partial \vec{v}_1}{\partial t} = \frac{1}{2}\frac{\partial v_1^2}{\partial t} \quad \text{and} \quad p_1 \frac{\partial p_1}{\partial t} = \frac{1}{2}\frac{\partial p_1^2}{\partial t} \tag{10.34}$$

We can also exploit the vector version of the product rule for differentiation (see Sect. 1.1.2).

$$\nabla \cdot \left(p_1 \vec{v}_1\right) = p_1 \nabla \cdot \vec{v}_1 + \vec{v}_1 \cdot \vec{\nabla} p_1 \tag{10.35}$$

The combination can be expressed as a conservation equation for acoustic energy.

$$\frac{\partial}{\partial t}\left[\frac{1}{2}\rho_m v_1^2 + \frac{1}{2}\frac{p_1^2}{\rho_m c^2}\right] + \nabla \cdot \left(p_1 \vec{v}_1\right) = 0 \tag{10.36}$$

As was established in Sect. 7.3.1, when the continuity Eq. (7.32) was first introduced, Eq. (10.36) has the form of a *conservation equation*: it is *the time derivative of a density plus the divergence of a flux*. It is easy to identify the (½)$\rho_m v_1^2$ term in Eq. (10.36) as the kinetic energy density of the sound wave; therefore (½)$p_1^2/\rho_m c^2$ must be the potential energy density. In this case, the corresponding flux is the *acoustic intensity*, *I*.

$$\vec{I} = p_1 \vec{v}_1 \tag{10.37}$$

The energy densities and the intensity are quadratic combinations of first-order acoustic variables. The two energy densities within the square brackets in Eq. (10.36) are positive-definite quantities. Why do we *not* neglect these second-order quantities when, up to this point, we have discarded all second-order quantities? In this case, this second-order quantity is the leading-order contribution. When we linearized other equations, there were linear terms that dominated second-order terms, typically by a factor of M_{ac}, for example, in Eqs. (8.18) and (8.19). For energetic variables (e.g., energy density, intensity, enthalpy flux), there are no first-order contributions in the absence of steady flow.

In the presence of dissipation, the acoustical energy is not conserved, and Eq. (10.36) would no longer be homogeneous, although it would have the same form:

$$\frac{\partial}{\partial t}E + \nabla \cdot \vec{I} = -D \tag{10.38}$$

In Eq. (10.38), E is the energy density, $\vec{I}$ is the (vector) intensity, and D is a dissipation factor [18].

$$D = \frac{1}{c^2}\left(\frac{4}{3}\mu + \zeta\right)\left|\frac{\partial \vec{v}}{\partial t}\right|^2 + \left(\frac{\gamma - 1}{\gamma}\right)\frac{\kappa}{\rho_m^2 c_p c^4}\left|\frac{\partial p}{\partial t}\right|^2 + \mu\left|\vec{\nabla} \times \vec{v}\right|^2 \tag{10.39}$$

The (irreversible) dissipation created by the shear viscosity, μ, and the thermal conductivity, κ, should be familiar from the expressions for boundary-layer losses provided in Eq. (9.34). The first term in Eq. (10.39) introduces a new "viscosity," ζ, which is called a "bulk viscosity" (or also called "second viscosity"). As will be discussed in Sect. 14.5, the bulk viscosity has been added to account for relaxation absorption (e.g., the fact that it takes some non-zero time for the Equipartition Theorem to distribute energy equitably between translational and rotational degrees of freedom) [19]. The second term in Eq. (10.39), proportional to the thermal conductivity, κ, is obviously thermal loss, since it contains $(\gamma - 1)/\gamma$ as a coefficient and is proportional to the square of the acoustic pressure. The final term arises from (rotational) flow with non-zero curl, such as the shear produced in the viscous boundary layer that was calculated in Sect. 9.4.3.

10.5.1 Decibel Scales

The Bell Telephone Laboratories developed much of the "modern" (twentieth-century) science of acoustics and its implementation in engineering practice. For almost a century, Bell Telephone (renamed AT&T in 1899) enjoyed a telecommunications monopoly within the United States. This allowed the company to recoup its investment in equipment and capital improvements like buildings, poles, purchased right-of-way, etc. Eventually (1913), the US Government put a cap on Bell's profits, limiting them to 10% after taxes. To operate under this lower margin, Bell invested "excess profits" by spending them on research and development within two of its subsidiaries: Bell Laboratories and Western Electric. Despite this cap on profits, Bell became one of the most successful companies in the history of the world. It was the largest US corporation until a forced divestiture was imposed by the US Congress in 1984.

Most of us are more familiar with the later Nobel Prize winning research accomplishments of Bell Labs. The best-known of these is the invention of the transistor (Bardeen, Brittan, and Shockley, 1947) and the invention of the laser (Schawlow and Townes, 1948). Also credited to Bell Lab scientists are the discovery of local electronic states in solids (Anderson Localization, 1977) and the discovery of the 4 K residual cosmic black-body background radiation left over from the "Big Bang" (Penzias and Wilson, 1978), as well as acoustical engineering advances that did not receive the Nobel, such as the electret microphone (Sessler and West 1964). More recent Nobel Prizes include optical trapping (Chu 1997)[6] and the quantum Hall effect (Stormer 1998).

During the interval between the two world wars, many of the engineering concepts we use today evolved from research at Bell Labs that were directed toward the commercialization of a worldwide telecommunication network. The later research involved major advances in digital electronics including the "sampling theorem" of Claude Shannon (1948), the concept of digital filters introduced by R. W. Hamming (1977), and the fast Fourier transform by John Tukey (1965), along with the development of the UNIX operating system (1971). Before the advent of digital electronics, Bell Labs did the systems engineering that started with the characterization of vocalization and auditory perception (Fletcher and Munson, see Fig. 10.5) and carried through with the competition between transmission loss and amplification[7] required to transmit human voices around the world. The focus on the competition between amplifier gain and transmission loss led to the introduction of the decibel.

The decibel (abbreviated dB) was introduced by Bell Labs engineers to quantify the reduction in audio level over a 1-mile length of standard telephone cable. It was originally called the transmission unit, or TU, but was renamed in 1923 or 1924 in honor of the laboratory's founder and telecommunications pioneer, A. G. Bell. Before the days of hand-held electronic calculators, it was easier to add or subtract logarithms than it was to multiply long strings of gain and loss factors.

Although there are periodic debates about whether or not to dispose of the decibel, in acoustics it is unlikely that the decibel will disappear during the span of your career [20]. One reason for the decibel's persistence into the age of digital electronics is physiological. The dynamic range of human hearing covers about 14 orders of magnitude in intensity. In some sense, sound pressure levels expressed in decibels provide a "centigrade scale" for sound levels that nicely matches human auditory experience; 0 dB_{SPL} is about the quietest sound a human can detect, and 100 dB_{SPL} is about as loud a sound as we can tolerate.

By far, the most important feature of the decibel is that *the decibel is always a base-10 logarithmic measure of a ratio, never a ratio itself.*

The intensity level, *IL*, is expressed in decibels.

[6] In acoustics, the equivalent of "optical trapping" is acoustical levitation superstability (see Sect. 15.4.7): M. Barmatz and S. L. Garrett, "Stabilization and oscillation of an acoustically levitated object," US Pat. No. 4,773,266 (Sept. 27, 1988).

[7] In my estimation, one of the most significant engineering breakthroughs of the twentieth century was the invention, by Harold S. Black (1989–1983) at Bell Labs, of the negative feedback amplifier in 1928. In Black's own words, "Our patent application was treated in the same manner as one for a perpetual-motion machine. In a climate where more gain was better, the concept that one would throw away gain to improve stability, bandwidth, etc., was inconceivable before that time."

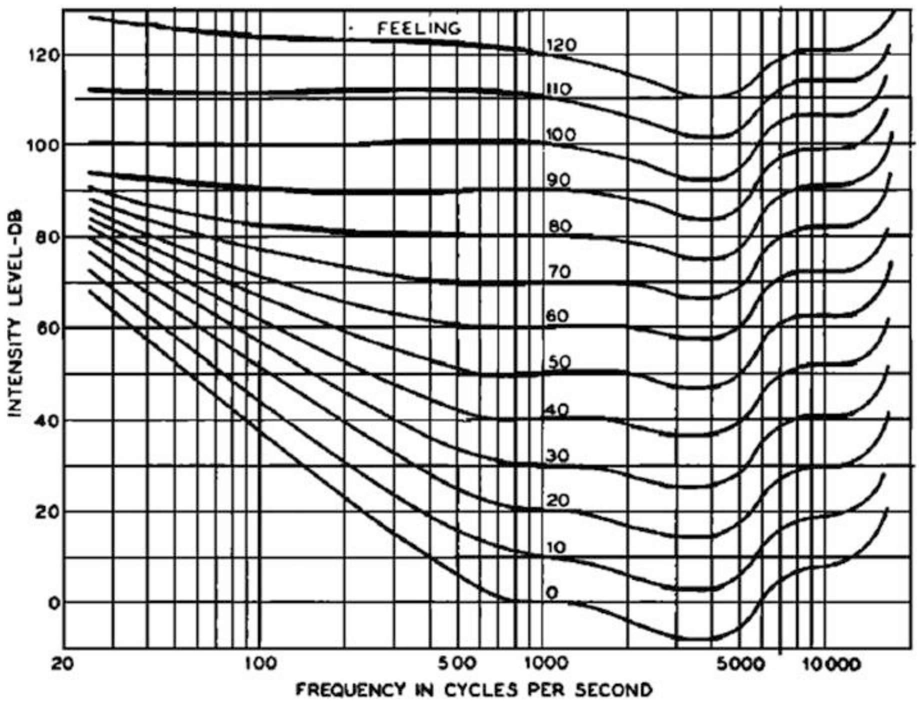

Fig. 10.5 The equal-loudness contours, known as the Fletcher-Munson curves, are taken from [21]. The *solid lines* correspond to the intensity of sound in air, in dB re: 1 pW/m^{2}, which is required to produce a perceived loudness equal to that of a 1.0 kHz tone with the same intensity level. That "loudness level" is called the "phon." To produce a loudness level of 60 phon, at 1.0 kHz, the sound pressure level would be 60 dB$_{SPL}$. The "0 dB" curve is often called the "threshold of hearing," and the "120 dB" curve is called the "the threshold of feeling"

$$IL = 10\log_{10}\left(\frac{I}{I_{ref}}\right) \tag{10.40}$$

The time-averaged acoustic intensity, $I = \langle p_1 v_1 \rangle_t$, is defined by the energy conservation Eq. (10.36). The time-averaged *reference intensity*, I_{ref}, used to define IL in Eq. (10.40), will depend upon the situation. For sound in air, $I_{ref} \equiv 10^{-12}$ W/m^2 = 1 pW/m^2. Using our definition of specific acoustic impedance for plane waves in Eq. (10.27), the value of the specific acoustic impedance in dry air is $z = \rho_m c = 413.3$ Pa-sec/m (rayls) at 20 °C, so I_{ref} can also be expressed in terms of the root-mean-squared pressure, p_{rms}, of sound.

$$I = \langle p_1 v_1 \rangle_{time} = \frac{1}{2} p_1 \frac{p_1}{\rho_m c} = \frac{p_{rms}^2}{\rho_m c} \tag{10.41}$$

In Eq. (10.41), we let $p_{rms} = p_1/\sqrt{2}$ by assuming that the pressure was varying sinusoidally in time.[8] If that is the case, then I_{ref} corresponds to a root-mean-squared pressure amplitude, $p_{rms} = 20.33$ μPa$_{\text{rms}}$. For convenience, the *reference sound pressure* in air is defined as $P_{ref} \equiv 20$ μPa$_{\text{rms}}$.

[8] The "true" definition of a root-mean-squared (rms) amplitude is always tied to the power associated with that amplitude. To account for non-sinusoidal waveforms, engineers introduce a dimensionless "*crest factor*," CF, that is defined as the ratio of the peak value of a waveform to its rms value. For a sine waveform, CF (sine) $= \sqrt{2}$, for a triangular waveform, CF (triangle) $= \sqrt{3}$, and for a half-wave rectified sinewave, CF (half-wave rectified) = 2. Most instruments that claim to measure the "true rms" value of a parameter (e.g., voltage) will exhibit an accuracy that decreases with increasing crest factor. For measurement of Gaussian noise, instruments that tolerate $3 < \text{CF} < 5$ are usually adequate.

The concept of sound pressure level, expressed in decibels, appeared in Chap. 7 to describe the amplitude of a dangerously loud sound: 115 dB_{SPL}.

$$dB_{SPL} = 20 \log_{10}\left(\frac{p_{rms}}{P_{ref}}\right) \tag{10.42}$$

The fact that the base-ten logarithm in Eq. (10.42) is multiplied by 20 instead of 10, as in Eq. (10.40), reflects the definition of *the decibel as the base-10 logarithm of a power or intensity ratio, even when its value is determined by the ratio of amplitudes*.

If the decibel is used to express an amplitude-independent ratio (like the gain of an amplifier or the attenuation of a filter), then a reference level is not required, but the ratio must still be the logarithm of a power or energy ratio. For example, if the voltage gain of an amplifier is ten, then that gain can be expressed as $20\log_{10}(10) = +20\ \text{dB}$.

When a decibel refers to an absolute measurement, then it is important to include the reference along with the reported value. That can be accomplished in several ways. One is the subscript used for 115 dB_{SPL} that implied that $P_{ref} = 20\ \mu Pa_{rms}$ for sound pressure levels (SPL). The preferred method is always to explicitly include the reference: 115 dB *re:* 20 μPa_{rms}.

There are several frequency-weighting schemes that are used to produce a dB level that reflects the (amplitude-dependent!) frequency response of human hearing that will be addressed in Sect. 10.5.3.[9] For example, an A-weighted sound pressure level (L_A) can be expressed as 115 dB(A) or 115 dB_A.

10.5.2 Superposition of Sound Levels (Rule for Adding Decibels)

As just mentioned, the decibel was introduced to turn a multiplicative string of gains and losses into an arithmetic sum. When it comes to the superposition of sound fields, the decibel must be employed with extreme care!

If we add two sound sources, each with a sound pressure level of 60 dB_{SPL}, the result is either 63 dB_{SPL} if the sources are *incoherent*, since their powers add, or as much as 66 dB_{SPL} if the sources are *coherent* (having the same frequency) and in-phase, since their pressures would add. If the sources are coherent and out-of-phase, there may be no sound at all. *In no case will the sum of two 60 dB_{SPL} sources ever result in 120 dB_{SPL}!*

10.5.3 Anthropomorphic Frequency Weighting of Sound Levels

It is common to assert that healthy humans can detect sound with frequencies ranging from 20 Hz to 20 kHz, but the sensitivity of human hearing is very dependent upon both frequency and amplitude, as well as on the listener's age, health, and prior exposure to loud sounds. The frequency dependence of human hearing is represented by *equal-loudness contours* that were first measured by Fletcher and Munson at Bell Labs in 1933 [21]. Subsequent determinations were made to produce equal-loudness contours that specified the auditory acuity of different age groups [22], and consensus contours have been codified in an international standard [23]. For our present purposes, the *Fletcher-Munson curves*, shown in Fig. 10.5, provide an illustration of the amplitude dependence of the normal frequency dependence of human hearing, although more recent determinations exist [24].

[9] The weighting of A, B, C, and D (no weighting) levels are specified in several international standards, for example, the International Standards Organization (ISO) 3746:2010, and are plotted in Fig. 10.6.

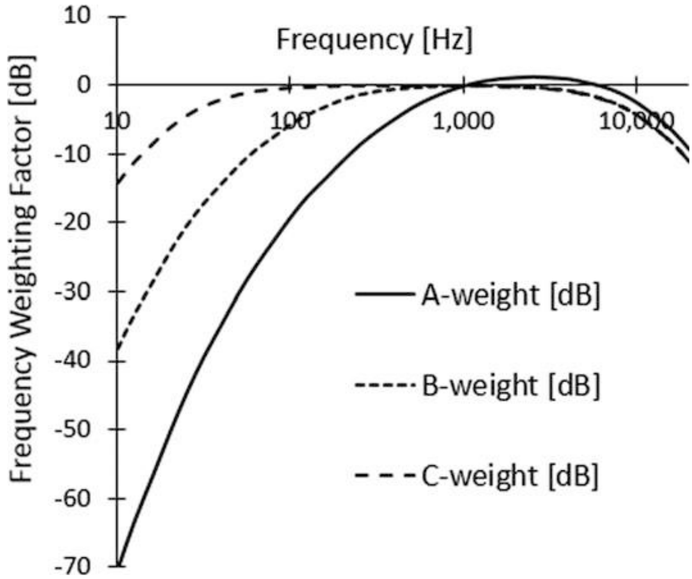

Fig. 10.6 Frequency-weighting factors for specification of sound level meter responses to simulate human loudness perception as specified in ANSI 1.4-1983. [25] The A-weighting was intended for sounds with intensities lower than 55 dB_{SPL} and the C-weighting for sounds with intensities above 85 dB_{SPL}. The B-weighting was intended for levels between the A and C limits but has been utilized very rarely

Examination of Fig. 10.5 suggests that "normal" human hearing is most sensitive at frequencies between 3 kHz and 4 kHz (near the $\lambda/4$ resonance of the ear canal[10]) and that sensitivity degrades at higher and lower frequencies. The curves also demonstrate that there is less frequency dependence at higher sound levels. We are nearly 60 dB less sensitive to a tone at 40 Hz as we are to a tone of the same intensity at 1 kHz near the threshold of hearing, but our sensitivity is nearly frequency independent between 20 Hz and 1.0 kHz if the intensity of the tone is 100 dB *re:* 20 μPa_{rms}.

The contours (i.e., solid lines) in Fig. 10.5 are labeled with the sound pressure level of a 1.0 kHz tone. Those contours define a loudness level with the unit of "phons." A 1.0 kHz tone with a sound pressure level of 60 dB *re:* 20 μPa_{rms} would be perceived as having a loudness equal to a 40 Hz tone with a sound pressure level of 80 dB *re:* 20 μPa_{rms}; both would have a loudness of 60 phons.

When attempting to quantify the perceived loudness of a tone, it would be convenient to have a way to express the loudness of a tone that takes human perception into account. Early attempts to create a metric that includes that frequency dependence, shown in Fig. 10.5, introduced three frequency-weighting schemes to simulate hearing acuity at three different levels. These weighting schemes were called A-weighted for levels below 55 dB_{SPL}, B-weighted for sounds greater than 55 dB_{SPL} but less than 85 dB_{SPL}, and C-weighted sound pressure levels for sounds with intensities in excess of 85 dB_{SPL}. These filter functions were standardized for the design of sound level meters [25] and are shown in Fig. 10.6.

The frequency-weighting standard [25] also includes tolerances for the levels that must be met by a Type-0 (laboratory quality), a Type-1 (field measurement), and a Type-2 (general purpose) sound level meter, as well as three exponential integration intervals: fast ($\tau = 125$ ms), slow ($\tau = 1.0$ s), and impulse (rise time, $\tau_{\uparrow} = 35$ ms and release time constant, $\tau_{\downarrow} = 1.5$ s.) As a practical matter, the standard also provides an implementation of the frequency weighting using passive R-C filter networks.

Such frequency-weighted metrics are usually designated dB(A) or dB_A and dB(C) or dB_C. Over time, the use of B-weighting has fallen out of favor, and frequently A-weighting is used regardless of

[10] The transfer function for sound pressure at the eardrum to the sound pressure presented to the outer ear is above 14 dB of gain from 2.5 to 3.2 kHz as shown in Table 2 of the ANSI-ASA S3.4 Standard.

the intensity of the sound being measured. In some instances, particularly with measurement of airport noise [26], the difference between the dB(A) and dB(C) levels are used to quantify the presence of low-frequency signals.

The frequency-weighting scheme used for sound level meters was just the first attempt to relate physical measurements to human auditory perception. In many cases, that metric is used to predict the level of annoyance produced by unwanted sounds (noise) [27] or the reduction in speech intelligibility in the presence of background noise [28]. Many other metrics have been established to correlate annoyance to the sound amplitude, frequency, and intermittency of noise sources, but almost all involve measurement of A-weighted levels. Sounds that may not be annoying during the day or at work might produce stress and interrupt sleep if they occur during the evening or nighttime. Various metrics provide algorithms for combining levels measured as a function of time.

Several metrics, in addition to the A-weighted level, have been adopted by the US Environmental Protection Agency (EPA) for annoyance assessment. The Equivalent Sound Level, L_{eq}, is just the time averaged, A-weighted sound pressure, p_A, using $P_{ref} = 20\ \mu\mathrm{Pa}_{\mathrm{rms}}$.

$$L_{eq} = 10\ \log_{10}\left[\frac{1}{T}\int_0^T \frac{p_A^2}{P_{ref}^2}\ \mathrm{d}t\right] \tag{10.43}$$

The time interval, T, for calculation of this average is not specified. For the Day-Night Sound Level, L_{dn}, the calculation period is 24 h, and an additional 10 dB is added to the measured L_{eq} for hours between 10:00 pm (22h00) and 7:00 am (07h00), to calculate L_{dn}.

$$L_{dn} = 10\ \log_{10}\left\{\frac{1}{24}\left[15\left(10^{L_d/10}\right)\right] + \left[9\left(10^{[(L_n+10)/10]}\right)\right]\right\} \tag{10.44}$$

A further refinement, which attempts to better predict the community response to noise [26], introduces a 5 dB boost to A-weighted levels measured in the evening between 7:00 pm (19 h00) and 10:00 pm (22 h00), resulting in a sum similar to Eq. (10.44) that produces the Community Noise Equivalent Level (CNEL), also known as the Day Evening Night Sound Level, L_{den}. For a continuous sound level of 60 $\mathrm{dB_A}$, $L_{eq} = 60$ dB, $L_{dn} = 64.4$ dB, and $L_{den} = 66.7$ dB.

A detailed investigation of such annoyance metrics is beyond the scope of this textbook, but an understanding of these frequency-weighted sound levels forms the basis for understanding most other metrics.

10.6 Standing Waves in Rigidly Terminated Tubes

Based on our experience describing standing waves on strings with idealized boundary conditions in Sect. 3.3.1, it is easy to calculate the standing wave modal frequencies for a tube of length, L, and cross-sectional area, A, if $(A)^{½} \ll \lambda$. Under such circumstances, all of the fluid motion within the tube will be longitudinal, thus parallel to the tube's axis.[11] When more than one of an enclosure's dimensions is comparable to the wavelength of sound, λ, then the sound within such an enclosure

[11] When we include thermoviscous dissipation on the walls of the tube, the velocity will not be constant throughout the tube's cross-section, since the no-slip boundary condition for a viscous fluid requires that the longitudinal velocity vanish at the tube's walls. In many cases, the ratio of the viscous penetration depth, δ_ν, to the tube's radius, a, is small, $\delta_\nu \ll a$, so the flow velocity is nearly uniform throughout most of the tube's cross-section. The thermal effects near the wall increase the compressibility of the gas (see Sect. 9.3.2), so they also create a small velocity perpendicular to the wall.

can no longer be considered "one-dimensional." Such three-dimensional enclosures will be analyzed systematically in Chap. 13.

For simplicity, this section will focus on a rigid tube that is circular in cross-section, so that $A = \pi a^2$, where a is the circular tube's radius. If the tube has rigid end caps at both ends, $x = 0$ and $x = L$, then the fluid cannot penetrate the ends so $v_1(0, t) = v_1(L, t) = 0$ for all times, t. Since $v_1 (x, t)$ will obey the wave Eq. (10.12), a standing wave solution, like that for $p_1(x, t)$in Eq. (10.15), can be written which automatically satisfies the boundary condition at $x = 0$.

$$v_1(x,t) = \Re e\left[\widehat{\mathbf{v}} \sin(kx) e^{j\omega t}\right] \tag{10.45}$$

Repeating our experience with the fixed-fixed string in Sect. 3.1.1, the acceptable values for the wavenumber, k_n, are quantized by imposition of the boundary condition at $x = L$.

$$\sin(k_n L) = 0 \quad \Rightarrow \quad k_n L = n\pi \quad \text{for} \quad n = 1, 2, 3, \ldots \tag{10.46}$$

The frequencies of the standing wave (normal) modes in the tube are therefore also restricted to discrete values, $f_n = n(c/2\,L)$.

$$2\pi f_n = \omega_n = k_n c = \frac{n\pi c}{L} \quad \Rightarrow \quad \lambda_n = \frac{2L}{n} \quad \text{or} \quad L = n\left(\frac{\lambda_n}{2}\right) \tag{10.47}$$

The physical interpretation of this result is identical to the one provided for the modes of a fixed-fixed string: the normal mode shapes correspond to placing n sinusoidal half-wavelengths within the overall length of the tube, L. Substitution of these normal mode frequencies, ω_n, and wavenumbers, k_n, into the functional form of Eq. (10.45) provides the description of the shapes,$\widehat{\mathbf{v}}_n(x)$, for each of the normal modes.

$$\widehat{\mathbf{v}}_n(x) = C_n \sin\left(n\frac{\pi x}{L}\right); \quad n = 1, 2, 3, \ldots \tag{10.48}$$

In this form, C_n is a real scalar velocity amplitude for each mode that will be determined by the amplitude of excitation for that mode. (We could let the C_n be complex if we are considering the superposition of several modes, each having its own time phase.)

Having the explicit solution of Eq. (10.48) for the space and time distribution of the longitudinal particle velocity of the fluid, the pressure distribution, $p_1(x, t)$, can be determined from Euler's equation.

$$\vec{\nabla} p_1 = \frac{\partial p_1}{\partial x} = -\rho_m \frac{\partial v_1}{\partial t} \quad \Rightarrow \quad \frac{\partial\,\widehat{\mathbf{p}}_\mathbf{n}}{\partial x} = -j\rho_m \omega_n C_n \sin(k_n x) \tag{10.49}$$

Integrating both sides of Eq. (10.49) over x produces the expressions for the distribution of pressure within the rigidly terminated tube.

$$\begin{aligned} \int \frac{\partial\,\widehat{\mathbf{p}}_\mathbf{n}}{\partial x}\,dx &= \widehat{\mathbf{p}}_\mathbf{n}(x) = -j\rho_m \omega_n C_n \int \sin(k_n x)\,dx \\ &= \frac{j\rho_m \omega_n C_n}{k_n} \cos(k_n x) \Rightarrow \quad \widehat{\mathbf{p}}_\mathbf{n}(x) = j(\rho_m c) C_n \cos(k_n x) \end{aligned} \tag{10.50}$$

The appearance of cos (k_n x) in this result for $\widehat{\mathbf{p}}_\mathbf{n}(x)$ indicates that there will be pressure maxima (anti-nodes) at both boundaries. The "j" indicates that the acoustic pressure will be 90° out of phase with the velocity, so that when the pressure reaches its maximum, the velocity will everywhere be zero, and vice versa; when the fluid's longitudinal particle velocity is the greatest, the acoustic pressure throughout the resonator will be zero.

For a tube that is open on both ends, the solutions to the wave equation produce resonance frequencies, f_n, that are identical to those for longitudinal waves in a free-free bar presented in Eq. (5.13), except it is $p_1\,(0, t) = p_1\,(L, t) = 0$.

$$\begin{aligned} \widehat{\mathbf{v}}_{\mathbf{n}}(x) &= C_n \cos(k_n x) \;\; \text{with} \;\; k_n = \frac{n\pi}{L} \;\; \Rightarrow \;\; f_n = n\frac{c}{2L}; \quad n = 1, 2, 3, \ldots \\ \widehat{\mathbf{p}}_{\mathbf{n}}(x) &= j(\rho_m c) C_n \sin(k_n x) \end{aligned} \tag{10.51}$$

In reality, the open-end condition is not exactly "pressure released." Thinking back to our investigations of the natural frequency of a Helmholtz resonator in Sect. 8.5, we needed to add an "effective length" to the open end of a tube. The same will be true for standing waves in narrow tubes for which $a \ll \lambda$. That effective length correction will be discussed in Sects. 12.8 and 12.9. For the moment, we could use a correction that extends the length of an open tube by $0.613a$, as given in Eq. (12.133), if there are no other constraints on the flows in, out, or around the "open end."

10.6.1 Quality Factor in a Standing Wave Resonator

Using the definitions of kinetic and potential energy density produced by the energy conservation Eq. (10.36), when the acoustic pressure is zero throughout the resonator, all of the energy will be kinetic, and when the velocity is zero everywhere, all the energy will be potential. The sum of the kinetic and potential energies at any instant will be constant. These facts can be exploited to calculate the quality factors, Q_n, for the *nth* plane wave mode of a resonator, based on the expression for thermoviscous boundary layer losses in Eq. (9.38).

The sum of the kinetic and potential energies, E_{tot}, at any instant will be constant: $E_{tot} = (KE)_{max} = (PE)_{max}$. To evaluate the Q due to viscous losses along the cylindrical surface of the resonator, it is convenient to calculate the maximum kinetic energy by integrating the maximum kinetic energy density throughout the volume of the resonator using the expression for the acoustic fluid velocity in Eq. (10.48).

$$(KE)_{\max} = \frac{\rho_m C_n^2 \pi a^2}{2} \int_0^L \sin^2\left(n\frac{\pi x}{L}\right) dx = \frac{\pi a^2 L \rho_m C_n^2}{4} \tag{10.52}$$

From Eq. (9.37), the power dissipated by viscous shear at the resonator's walls, with surface area, $S = 2\pi a L$, will also be given by an integral of the fluid's particle velocity from Eq. (10.48).

$$\langle \Pi_{vis} \rangle_t = \frac{\rho_m \delta_\nu \omega}{4} 2\pi a C_n^2 \int_0^L \sin^2\left(n\frac{\pi x}{L}\right) dx = \frac{\rho_m \delta_\nu \omega}{4} \pi a L C_n^2 \tag{10.53}$$

The viscous contribution to the quality factor, Q_{vis}, will just be the radian frequency, ω, times the ratio of the stored energy, given in Eq. (10.52), to the time-averaged power dissipation in Eq. (10.53), as expressed in Eq. (B.2).

$$Q_{vis} = \frac{\omega E_{\text{Stored}}}{\langle \Pi_{vis} \rangle_t} = \omega \left(\frac{\pi a^2 L \rho_m C_n^2}{4}\right) \left(\frac{\rho_m \delta_\nu \omega}{4} \pi a L C_n^2\right)^{-1} = \frac{a}{\delta_\nu} \tag{10.54}$$

As expected for a linear system, the excitation amplitude of the modes, C_n, cancels, and we are left with a very simple expression that is identical to the result for Q_{vis} due to viscous shear in the neck of a

Helmholtz resonator, given in Eq. (9.44). Based on the definition of the viscous penetration depth, $\delta_\nu = \sqrt{2\mu/\rho_m\omega}$, in Eq. (9.33), the viscous quality factor will increase with the square root of the modal frequency, $f_n = \omega_n/2\pi$.

The calculation can be repeated for the thermal relaxation losses on the resonator's surface. Assuming the resonator is made from a material that has a much higher "accessible" heat capacity than the ideal gas which fills it, Eq. (9.23) can be used to calculate the time-averaged thermal power dissipation on the resonator's cylindrical surface, $\langle\Pi_{th}\rangle_t$.

$$\begin{aligned}\langle\Pi_{th}\rangle_t &= \frac{(\gamma-1)}{4\gamma}\delta_\kappa\omega\frac{(\rho_m c)^2 C_n^2}{p_m}(2\pi a)\int_0^L \cos^2\left(n\frac{\pi x}{L}\right)dx \\ &= \frac{(\gamma-1)}{4\gamma}\frac{(\rho_m c)^2 C_n^2}{p_m}\delta_\kappa\omega\pi aL = \frac{(\gamma-1)}{4}\rho_m\delta_\kappa\omega C_n^2\pi aL\end{aligned} \tag{10.55}$$

The final version in Eq. (10.55) makes use of the fact that for adiabatic sound waves in ideal gases, $c^2 = \gamma p_m/\rho_m$. The expression for $E_{tot} = (KE)_{max}$ from Eq. (10.52) will serve nicely here for calculation of Q_{th}.

$$Q_{th} = \frac{\omega E_{\text{Stored}}}{\langle\Pi_{th}\rangle_t} = \omega\frac{\left(\frac{\pi a^2 L\rho_m C_n^2}{4}\right)}{\left(\frac{(\gamma-1)}{4}\rho_m\delta_\kappa\omega C_n^2\pi aL\right)} = \frac{1}{(\gamma-1)}\frac{a}{\delta_\kappa} \tag{10.56}$$

Although there is no viscous shear on the resonator's rigid end caps, since the fluid's particle velocity is normal to their surfaces, there are still thermal relaxation losses since both rigid ends are always pressure anti-nodes where the fluid will experience the maximum adiabatic temperature variations. The calculation for Q_{ends} is identical to Eq. (10.54) except that the pressure does not have to be averaged along the x direction.

$$\langle\Pi_{th}\rangle_{ends} = 2\frac{(\gamma-1)}{4\gamma}\delta_\kappa\omega\frac{(\rho_m c)^2 C_n^2}{p_m}\left(\pi a^2\right) = \frac{(\gamma-1)}{2}\rho_m\delta_\kappa\omega C_n^2\left(\pi a^2\right) \tag{10.57}$$

$$Q_{ends} = \omega\left(\frac{\pi a^2 L\rho_m C_n^2}{4}\right)\left(\frac{(\gamma-1)}{2}\rho_m\delta_\kappa\omega C_n^2\left(\pi a^2\right)\right)^{-1} = \frac{1}{2(\gamma-1)}\frac{L}{\delta_\kappa} \tag{10.58}$$

Since the dissipation is additive, the total quality factor, Q_{tot}, will require the parallel combination of the three individual contributions to the quality factor.

$$\frac{1}{Q_{tot}} = \frac{1}{Q_{vis}} + \frac{1}{Q_{th}} + \frac{1}{Q_{ends}} \tag{10.59}$$

In this derivation, it is assumed that the resonator's walls and end caps are made of a material that holds those surfaces strictly isothermal. The dimensionless ratio, $\varepsilon_s = \rho_m c_p\delta_\kappa/\rho_s c_s\delta_s$, determines how close the resonator's boundaries are to enforcing isothermality at the solid-fluid interface where ρ_s, c_s, and δ_s are the density, specific heat, and thermal penetration depths for the solid. If $\varepsilon_s \ll 1$, then the solid-fluid interface remains isothermal. If not, then the quality factor must include ε_s [29].

$$\frac{1}{Q} = \frac{\delta_\nu}{a} + \frac{(\gamma-1)}{(1+\varepsilon_s)}\frac{\delta_\kappa}{a} + \frac{(\gamma-1)}{(1+\varepsilon_s)}\frac{2\delta_\kappa}{L} \tag{10.60}$$

10.6.2 Resonance Frequency in Closed-Open Tubes

The resonance frequencies of a closed-open tube are analogous to those of the fixed-free string of Sect. 3.3.1. Again, ignoring the need to apply an effective length correction to the open end of the tube, the expression for the standing wave solutions is identical to Eq. (3.24) and results in successive modes corresponding to an odd-integer number of quarter wavelengths equal to the length of the resonator, L, if we assume that the rigid end of the resonator is located at $x = 0$ and the open end is at $x = L$.

$$\begin{aligned} &\hat{\mathbf{v}}_{\mathbf{n}}(x) = C_n \sin(k_n x) \\ &\hat{\mathbf{p}}_{\mathbf{n}}(x) = j(\rho_m c) C_n \cos(k_n x) \\ &k_n = \frac{(2n-1)\pi}{2L} \quad \Rightarrow \quad f_n = (2n-1)\frac{c}{4L}; \quad n = 1, 2, 3, \ldots \end{aligned} \tag{10.61}$$

For the closed-open tube, the expression for the quality factor in Eq. (10.59) requires an additional term to account for radiation losses (see footnote 24 in Chap. 8), Q_{rad}, and thermal relaxation loss only occurs at the closed end, Q_{end}.

$$\frac{1}{Q_{tot}} = \frac{1}{Q_{vis}} + \frac{1}{Q_{th}} + \frac{1}{Q_{end}} + \frac{1}{Q_{rad}} \tag{10.62}$$

10.7 Driven Plane Wave Resonators

As we have done throughout this textbook, after the normal modes have been calculated, our attention has shifted to the excitation of those modes. Once again, the steady-state response will be determined by an impedance. In this case, the appropriate impedance will be the *acoustic transfer impedance*, $\mathbf{Z_{tr}} = \hat{\mathbf{p}}_{\mathbf{M}}/\hat{\mathbf{U}}_{\mathbf{S}}$. The acoustic impedance, $\mathbf{Z_{ac}} = \hat{\mathbf{p}}/\hat{\mathbf{U}}$, was introduced in Chap. 8 during our investigation of lumped elements and the Helmholtz resonator because pressure and volume velocity were continuous across the junctions between lumped elements, even if their cross-sectional areas were different. The acoustic transfer impedance, $\mathbf{Z_{tr}}$, simply relates the pressure at one location (labeled the microphone location), $\hat{\mathbf{p}}_{\mathbf{M}}$, presumably a place where a microphone or other pressure transducer is located, to the volume velocity, $\hat{\mathbf{U}}_{\mathbf{S}}$, produced at a different (source) location, typically where the sound is being generated.

For a plane wave resonator of constant cross-sectional area, the acoustic transfer impedance at resonance can be calculated directly from the definition of the quality factor, Q_n, of the *nth* mode, given in Appendix B, used earlier in Eq. (10.54) and reproduced below.

$$Q = 2\pi \frac{E_{\text{stored}}}{E_{\text{dissipated/cycle}}} = \frac{\omega E_{\text{stored}}}{\langle \Pi_{\text{dissipated}} \rangle_t} \tag{10.63}$$

At steady state, the time-averaged power dissipation must be equal to the power produced by the driver. For simplicity, we will treat the driver as a source of volume velocity, located at $x = L$, as shown in Fig. 10.9, $\hat{\mathbf{U}}_{\mathbf{S}}(L) = \hat{\dot{\mathbf{x}}}(L) A_{pist} = \hat{\mathbf{v}}(L) A_{pist}$, where we have assumed that the volume velocity source is a rigid piston located at $x = L$, having area, A_{pist}, with the longitudinal speed, $\dot{x}(L)$, of that piston being everywhere uniform at its surface.

As before, at resonance, the phase angle, ϕ, between $\hat{\mathbf{p}}_{\mathbf{M}}$ and $\hat{\mathbf{U}}_{\mathbf{S}}$, will be zero, so the power produced by the piston working against the acoustic pressure is simply $\langle \Pi \rangle_t = (½)|\hat{\mathbf{p}}_{\mathbf{M}}|\left|\hat{\mathbf{U}}_{\mathbf{S}}\right|$, remembering that

$\widehat{\mathbf{p}}_{\mathbf{M}}$ and $\widehat{\mathbf{U}}_{\mathbf{S}}$ are peak amplitudes and that a sinusoidal time dependence has been assumed for both variables.[12]

The potential energy stored in the plane wave resonator can be calculated in the same way as the stored kinetic energy was calculated in Eq. (10.52), but in this case, we integrate the potential energy density, $(½)|\widehat{\mathbf{p}}(x)|^2/(\rho_m c^2)$, based on Eq. (10.36), over the resonator's volume, V_{res}. For simplicity, we will assume a cylindrical resonator with constant radius, a, and overall length, L.

$$(PE)_{\max} = \frac{\pi a^2}{2\rho_m c^2}|\widehat{\mathbf{p}}_{\mathbf{M}}|^2 \int_0^L \cos^2\left(n\frac{\pi x}{L}\right) dx = \frac{\pi a^2 L}{4\rho_m c^2}|\widehat{\mathbf{p}}_{\mathbf{M}}|^2 = \frac{V_{res}}{4\gamma p_m}|\widehat{\mathbf{p}}_{\mathbf{M}}|^2 \tag{10.64}$$

Substituting $|\widehat{\mathbf{p}}_{\mathbf{M}}| = |\widehat{\mathbf{p}}_{\mathbf{n}}| = (\rho_m c)C_n$ shows that Eq. (10.64) and Eq. (10.52) are identical, illustrating the fact that all of the energy stored in a standing wave changes back and forth between kinetic energy and potential energy.

The rightmost term in Eq. (10.64) assumes the resonator, having an internal volume, $V_{res} = \pi a^2 L$, is filled with an ideal gas, so that $c^2 = \gamma\, p_m/\rho_m$. Substitution into Eq. (10.63) produces an expression for the acoustic impedance at the driven end of the resonator at plane wave resonance frequencies, f_n, with quality factors, Q_n.

$$Q_n = \frac{\omega V_{res}|\widehat{\mathbf{p}}_{\mathbf{M}}|^2}{4\gamma p_m (½)|\widehat{\mathbf{p}}_{\mathbf{M}}|\left|\widehat{\mathbf{U}}_{\mathbf{S}}\right|} \quad \Rightarrow \quad \mathbf{Z}_{\mathbf{tr}} \equiv \frac{\widehat{\mathbf{p}}_{\mathbf{M}}}{\widehat{\mathbf{U}}_{\mathbf{S}}} = \pm\frac{Q_n}{\pi f_n}\frac{\gamma p_m}{V_{res}} \tag{10.65}$$

The "±" in the right-hand version of Eq. (10.65) accounts for the fact that the phase difference between $\widehat{\mathbf{p}}_{\mathbf{M}}$ and $\widehat{\mathbf{U}}_{\mathbf{S}}$ alternates by 180° between odd and even modes if the source and receiver are not located at the same end of the resonator.

For reasonably high values of Q_n, the acoustic pressure amplitudes, $\widehat{\mathbf{p}}_{\mathbf{M}}$, based on Eq. (10.50), at both ends of a plane wave resonator with rigid terminations (i.e., closed-closed) are equal: $|\widehat{\mathbf{p}}(0)| = |\widehat{\mathbf{p}}(L)| = |\widehat{\mathbf{p}}_{\mathbf{M}}|$. In that case, the acoustic transfer impedance and the acoustic impedance are equal: $\mathbf{Z}_{\mathbf{ac}} = \mathbf{Z}_{\mathbf{tr}}$. Equation (10.65) allows us to express the pressure at the ends of the resonator and, by Eq. (10.50), the pressure anywhere in the resonator, in terms of the volume velocity created by the source, $\widehat{\mathbf{U}}_{\mathbf{S}}(L)$.

$$|\widehat{\mathbf{p}}(0)| = |\widehat{\mathbf{p}}(L)| = |\widehat{\mathbf{p}}_{\mathbf{M}}| = \frac{Q_n}{\pi f_n}\frac{\gamma p_m}{V_{res}}\left|\widehat{\mathbf{U}}_{\mathbf{S}}(L)\right| \quad \text{for} \quad Q_n \gg 1 \tag{10.66}$$

It is possible to measure both the resonance frequencies, f_n, predicted by Eq. (10.47), and the quality factors, Q_n, predicted by Eq. (10.59), in conjunction with Eqs. (10.54) and (10.58), if the sound source and receiver are both fairly rigid themselves. Aluminized Teflon™ electret material (typically 6–12 microns thick) placed against a rigid backplate provides an excellent approximation to the rigid end conditions that were assumed in the calculations of Sect. 10.6. Such an electret transducer pair was used for measurement of air contamination in a helium recovery line that is shown in Fig. 10.4 [14], as well as a version used to detect the isotopic ratio of ^{3}He to ^{4}He [7]. Both of those resonators provided an almost ideal realization of a rigidly capped cylinder that incorporates an electret transducer (see Sect. 6.3.3) that functions as a volume velocity source (electrostatic loudspeaker) on one end and as a receiver (electret microphone) on the other.

[12] For simplicity, we can assume that the source and microphone are both located at the same end of the resonator. If they were at opposite ends, then their relative phase would shift by 180° degrees in going from an odd to an even mode of the resonator.

10.7.1 Electroacoustic Transducer Sensitivities

We can go one step further by introducing the transducer sensitivities that will allow us to model a resonator with its electroacoustic transducers as an electrical "black box" that can be represented as the linear passive four-pole networks shown schematically in Fig. 10.7.

Following MacLean [30], we can choose the following definitions for the microphone sensitivities, **M**, and the source strengths, **S**, for those electroacoustic transducers. These source strength and sensitivities are expressed as complex numbers because there can be frequency-dependent phase differences between the acoustic and electrical variables.

$$\mathbf{M_o} = \left(\frac{\partial V}{\partial p}\right)_{i=0} = \frac{\text{Open circuit mic output voltage}}{\text{Pressure at the mic}} \tag{10.67}$$

$$\mathbf{M_s} = \left(\frac{\partial i}{\partial p}\right)_{V=0} = \frac{\text{Short circuit mic output current}}{\text{Pressure at the mic}} \tag{10.68}$$

$$\mathbf{S_o} = \left(\frac{\partial p}{\partial i}\right) = \frac{\text{Pressure produced at the mic}}{\text{Current supplied to the source}} \tag{10.69}$$

$$\mathbf{S_s} = \left(\frac{\partial p}{\partial V}\right) = \frac{\text{Pressure produced at the mic}}{\text{Voltage applied to the source}} \tag{10.70}$$

The subscripts "*o*" and "*s*" on those microphone sensitivities refer to the transducer terminals being left open (infinite load electrical impedance) or short-circuited (zero load electrical impedance). Using those definitions, it is possible to write the transfer function, **H** (f), that provides the microphone's output voltage, $\hat{\mathbf{V}}_2$, in terms of the voltage applied across the speaker, $\hat{\mathbf{V}}_1$.

$$\hat{\mathbf{V}}_2 = \mathbf{M_o}\left(S_s\hat{\mathbf{V}}_1\right) \quad \Rightarrow \quad \mathbf{H}(f) = \frac{\hat{\mathbf{V}}_2}{\hat{\mathbf{V}}_1} = \mathbf{M_o}\mathbf{S_s} \tag{10.71}$$

Alternatively, the electrical transfer impedance, $\mathbf{Z_{el}}$ (f), could be written to relate the current into the source to the microphone's open-circuit output voltage.

$$\hat{\mathbf{V}}_2 = \mathbf{M_o}\left(\mathbf{S_o}\hat{\mathbf{i}}_1\right) \quad \Rightarrow \quad \mathbf{Z_{el}}(f) = \frac{\hat{\mathbf{V}}_2}{\hat{\mathbf{i}}_1} = \mathbf{M_o}\mathbf{S_o} \tag{10.72}$$

Either expression might be useful in the design of an electronic circuit, like the feedback circuit of Fig. 10.4 or a phase-locked-loop frequency tracker that was described in Sect. 2.5.3. Although

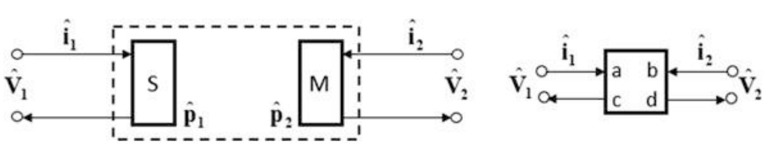

Fig. 10.7 (*Left*) The dashed box indicates an acoustic network that contains an electroacoustic source, S, and a microphone, M, that are coupled together through an acoustic medium that can be characterized by an acoustic transfer impedance, $\mathbf{Z_{tr}}$. Although this looks physically similar to a plane wave resonator, this schematic representation is generic and could represent any combination of a loudspeaker and a microphone that are coupled by an acoustical medium in an arbitrary geometry (see, e.g., Fig. 10.25). (*Right*) A generic linear, passive, four-pole electrical network that represents the transducers coupled by the acoustic medium with four matrix elements: *a*, *b*, *c*, and *d*, as represented in Eq. (10.73)

Eq. (10.65) provides a useful expression for a plane wave resonator's acoustic transfer impedance, $\mathbf{Z_{tr}}$, one would also need to know the sensitivities of the transducers for such a design.

Fortunately, the formalism that has just been introduced, using the electroacoustic networks diagrammed schematically in Fig. 10.7, provides a technique for obtaining the electroacoustic transducer's sensitivities from purely electrical measurements, if we know the acoustic transfer impedance of the medium coupling the source and the receiver and the boundary conditions.

10.7.2 The Principle of Reciprocity

The *Principle of Reciprocity* was first introduced into acoustics by Lord Rayleigh, in 1873, when he derived the reciprocity relation for a system of linear equations and gave "a few examples [to] promote the comprehension of a theorem which, on account of its extreme generality, may appear vague." [31] He cited physical examples in acoustics, optics, and electricity and then credited Helmholtz with a derivation of the result in a uniform, inviscid fluid in which may be immersed any number of rigid, fixed solids, pointing out the principle "will not be interfered with" even in the presence of damping.

The consequences of the reciprocity principle for the absolute calibration of microphones, without requiring the use of a "primary pressure standard," were not appreciated until 1940, when MacLean [30], and independently Cook [32], showed it was possible to determine the absolute sensitivity of an electroacoustic transducer by making only electrical measurements. Since that time, the reciprocity calibration method has been universally adopted by standards organizations worldwide as the method of choice for absolute determination of the sensitivity of microphones [33] and hydrophones [34].

The reciprocity calibration technique can be applied to any electroacoustic transducer that is **reversible** (i.e., can be operated as either a speaker or as a microphone in gas or as hydrophone or projector in liquid), **linear**, and **passive**. Passivity implies that the transducer does not contain an independent internal power source, amplifier, etc.

The four-pole electrical network shown in Fig. 10.7 (right) can be represented by two coupled linear algebraic equations. To simplify the following derivation, we will treat the constants as well as the electrical currents and voltages to be real scalars,

$$\begin{aligned} V_1 &= ai_1 + bi_2 \\ V_2 &= ci_1 + di_2 \end{aligned} \tag{10.73}$$

The reciprocity principle dictates that if a stimulus is applied on the left side of the network, producing a response on the right side, then when the same stimulus is applied to the right side, the response on the left side must be identical to the response when the situation was reversed.[13]

Reciprocity can be illustrated using the network in Fig. 10.7 with the corresponding representation as the coupled linear Eqs. (10.73): Driving the left side, ①, with a voltage, $V = V_1$, while an ammeter is attached across the terminals on the network's right side, ②, creating a "short circuit" (i.e., $V_2 = 0$), the ammeter would read a current, i_2. When the situation is reversed and the ammeter shorts the left side terminals, ①, so $V_1 = 0$, the same voltage is impressed across the network's right-side terminals, ②, so $V = V_2$. Then the reciprocity principle requires that i_2 produced in the first case is equal to i_1 produced in the second.

[13] The reciprocity principle also applies in vector form. If we applied a vector force at some location, ①, on a flexible structure, and the vector displacement is measured at some other location, ②, we would observe the same vector displacement at ① if the same vector force were applied at ②.

This reciprocal behavior imposes a constraint on the coefficients (matrix elements) of Eq. (10.73), which all have the units of electrical impedance. This constraint can be demonstrated by implementing the sequence described in the previous paragraph using primed variables to indicate the "reversed" situation.

$$\begin{aligned} &\text{Shorting } 2: \quad V_2 = 0 = ci_1 + di_2 \quad \Rightarrow \quad i_1 = \frac{-d}{c} i_2 \\ &\text{Shorting } 1: \quad V_1 = 0 = ai_1{}' + bi_2{}' \quad \Rightarrow \quad i_2{}' = \frac{-a}{b} i_1{}' \end{aligned} \tag{10.74}$$

Using these conditions, it is possible to calculate the voltages that appear across the terminals of the driven side of the network.

$$\begin{aligned} &\text{Driving } 1: \quad V = -\frac{ad}{c} i_2 + bi_2 \quad \Rightarrow \quad V = \left(b - \frac{ad}{c}\right) i_2 \\ &\text{Driving } 2: \quad V = ci_1{}' \; - \frac{da}{b} i_1{}' \quad \Rightarrow \quad V = \left(c - \frac{ad}{b}\right) i_1{}' \end{aligned} \tag{10.75}$$

Since we have driven the network with V on both sides, the reciprocity principle demands that the observed short circuit currents also be equal in both cases: $i_2 = i_1$'. Equating the two expressions for voltage in Eq. (10.75), the reciprocity principle requires that $b = c$.

$$b - \frac{ad}{c} = c - \frac{ad}{b} \tag{10.76}$$

These linear equations obey the reciprocity principle if the off-diagonal terms are equal: $b = c$ [35].

There has been a common misconception in most textbooks regarding the application of the reciprocity relations to electrodynamic transducers and others that incorporate magnetic fields (e.g., variable reluctance, magnetostrictive) [36]. This arises from the fact that the "reversibility" requirement must be applied to both the transducer and the coupling medium. For example, in the presence of steady flow, a volume velocity source at location ① will produce an acoustic pressure at location ② when that same volume velocity source was applied at location ② to produce acoustic pressure at location ① *only* if the steady flow was reversed. Since magnetic fields are the result of electrical currents (including the microscopic electrical currents in permanent magnetic materials [37]), those currents must be reversed, resulting in a sign change for the magnetic fields.

Starting in 1950 [38], this reversibility requirement was disguised by designating transducers that used magnets as "anti-reciprocal" making the off-diagonal terms have opposite signs in those cases: $b = -c$ [39]. Hunt's perspective has been perpetuated [40].

10.7.3 In Situ Reciprocity Calibration

If the first transducer in Fig. 10.7 (left) is driven, then using expressions like Eqs. (10.71) and (10.72), the voltage and current output of the second transducer can be calculated. If we reverse the roles, and drive the second transducer to calculate the voltage and current output of the first transducer, it is possible to show that the ratio of a transducer's strength as a source to its sensitivity as a microphone is entirely determined by the acoustic transfer impedance and is independent of the particular transducer or its transduction mechanism (e.g., electrodynamic, electrostatic, or piezoelectric), as long as the transducers are linear, passive, and reciprocal [30]. Let subscript 1 indicate the first case, and let subscript 2 indicate the role reversal.

$$\frac{\mathbf{S}_{o,\ 1}}{\mathbf{M}_{o,\ 1}} = \frac{\mathbf{S}_{o,\ 2}}{\mathbf{M}_{o,\ 2}} = \frac{\mathbf{S}_{s,\ 1}}{\mathbf{M}_{s,\ 1}} = \frac{\mathbf{S}_{s,\ 2}}{\mathbf{M}_{s,\ 2}} = \mathbf{Z}_{tr} = \frac{\widehat{\mathbf{p}}_1}{\widehat{\mathbf{U}}_2} = \frac{\widehat{\mathbf{p}}_2}{\widehat{\mathbf{U}}_1} \tag{10.77}$$

Using relationships in Eq. (10.77) to eliminate **M** in favor of **S** or vice versa in Eq. (10.71) or Eq. (10.72), it is possible determine the sensitivities of two identical, reversible, electroacoustic transducers.

$$\widehat{\mathbf{V}}_2 = \mathbf{M}_o\mathbf{S}_o\widehat{\mathbf{i}}_1 = \mathbf{M}_o^2\mathbf{Z}_{tr}\widehat{\mathbf{i}}_1 = \frac{\mathbf{S}_o^2}{\mathbf{Z}_{tr}}\widehat{\mathbf{i}}_1 \quad \Rightarrow \quad \mathbf{M}_o = \sqrt{\frac{\widehat{\mathbf{V}}_2}{\widehat{\mathbf{i}}_1\mathbf{Z}_{tr}}} \text{ and } \mathbf{S}_o = \sqrt{\frac{\widehat{\mathbf{V}}_2\mathbf{Z}_{tr}}{\widehat{\mathbf{i}}_1}} \tag{10.78}$$

Although we will show how this can be applied if the two transducers are not identical and if only one is reversible, it is impossible to overestimate the importance of the result of Eq. (10.78) for the progress of electroacoustics and for acoustic measurement and instrumentation in general. Equation (10.78) establishes the fact that the sensitivity of a transducer can be determined by knowing the properties of the acoustic medium (e.g., ρ_m and c) and its boundaries, calculating $\mathbf{Z}_{tr}$ and then making purely electrical measurements without the necessity of a primary pressure standard.[14]

We now need to remove the restriction that the two reversible transducers were identical that was imposed above to quickly move from Eq. (10.77) to Eq. (10.78) and demonstrate the plausibility of an absolute transducer calibration based only on electrical measurements. This is easily accomplished by introducing a third transducer that need not be reversible but that can act as a "signal strength monitor." In fact, only one transducer needs be reversible for the following procedure to produce absolute calibrations of all three transducers.

Once again, we will assume that we are placing all three transducers in a rigidly terminated standing wave resonator filled with an ideal gas so we can let Eq. (10.65) be used to provide the required $\mathbf{Z}_{tr}$. We also assume that the transducers are themselves sufficiently rigid that their presence in the resonator does not alter the sound field.[15]

Figure 10.8 is a schematic representation of such a resonator that has a source, S, at one end; a reversible transducer, R, at the opposite end; and an auxiliary microphone, M, also located at one end.

Fig. 10.8 Schematic representation of a gas-filled plane wave resonator that has a reversible transducer, R, at one end and a sound source, S, at the other end. A third transducer that functions only as a microphone, M, can be located at either end of the resonator

[14] The primary calibration of voltage is simpler (in principle, although it requires temperatures near absolute zero for the Josephson junction) since it is possible to relate the dc voltage across a superconducting Josephson junction to the resulting oscillation frequency, f, since their ratio is determined by Planck's constant, h, and the charge on an electron, e: $V \equiv nhf/2e$, where n is an integer. $2e/h = (483.5978)$ MHz/μV.

[15] This is equivalent to saying that the transducers are non-compliant in much the same way that the "constant displacement drive" for a string does not "feel" the load of the string and preserves the "fixed" boundary condition. For reciprocity calibration of transducers that behave as an ultracompliant driver (i.e., a constant force drive equivalent), see [43].

Although M and S could be reversible, it is not required for execution of the following procedure. An actual physical realization of this configuration is shown in Fig. 10.25, where both S and R are reversible but M can only function as a microphone. This procedure exploits the fact that all transducers are assumed to exhibit linear behavior and results in an absolute reciprocity calibration of R and a calibration relative to R for both S and M:

(a) We start by driving the reversible transducer with a current, i_2, and then measuring the output voltage, V_m, of the microphone, M.
(b) The source, S, is then driven with a current, i_1, that is sufficient to make the output of microphone, M, return to V_m. This recreates the sound field in the resonator produced when R was driven by i_2 in step (a).
(c) Having reproduced the sound field that the reversible transducer created in step (a), the reversible transducer's open-circuit output voltage, V_2, is measured.

These three measurements are now sufficient to calibrate all three transducers without requiring that any be "identical."

Since the first (reversible) transducer is obviously identical to itself, Eq. (10.78) can be used to determine its open-circuit sensitivity as a microphone, $\mathbf{M_o}$, and its source strength, $\mathbf{S_o}$, since we know $\mathbf{Z_{tr}}$ from Eq. (10.65). For the remainder of this sub-section, we will let the sinusoidal voltages and currents be represented their rms values.

$$|\mathbf{M_o}| = \sqrt{\frac{V_2}{i_2|\mathbf{Z_{tr}}|}} \quad \text{and} \quad |\mathbf{S_o}| = \sqrt{\frac{V_2|\mathbf{Z_{tr}}|}{i_2}} \tag{10.79}$$

Knowing the reversible microphone's sensitivity, the pressure at either end of the resonator is determined: $p_1 = V_2/|\mathbf{M_o}|$. Since that is the pressure that also appears at M, its sensitivity, $M_{o,aux}$, is determined by its voltage output, V_m.

$$|\mathbf{M_{o,aux}}| = |\mathbf{M_o}|\frac{V_m}{V_2} \tag{10.80}$$

Finally, the source strength of transducer S is determined, again because p_1 is known when i_1 was applied to S.

$$|\mathbf{S_{o,source}}| = \frac{V_2}{|\mathbf{M_o}|i_1} \tag{10.81}$$

Since the linearity of the transducers' response is required, it is not necessary to readjust the amplitude of the drive to re-create the sound field originally produced when the reversible transducer was used as the sound source. It would be equally valid to simply use the ratio of the voltage produced by the auxiliary microphone when the reversible transducer, R, was driven, $V_{M,1}$, in step (a) and the corresponding auxiliary microphone output voltage, $V_{M,2}$, when the source, S, was driven. The result for the reversible transducer's open-circuit sensitivity, $\mathbf{M_o}$, is given in Eq. (10.82) for calibration at a resonance frequency, f_n, with the corresponding quality factor, Q_n.

$$|\mathbf{M_{o,1}}(f_n)| = \left(\frac{\pi V_{res}}{\gamma p_m}\right)^{1/2}\left[\frac{V_2}{i_2}\frac{V_{M,1}}{V_{M,2}}\frac{f_n}{Q_n}\right]^{1/2} \tag{10.82}$$

Historically, other authors have referred to the reciprocal of the acoustic transfer impedance as the "reciprocity factor," $\mathbf{J} = (\mathbf{Z_{tr}})^{-1}$, but I see no reason to obscure the origin of this "factor" by giving it a separate designation. In fact, I contend that the reciprocity calibration method was limited to only small "couplers" (see Fig. 10.27) or free-field geometries until Rudnick's classic paper on reciprocity calibration in "unconventional geometries" appeared in 1978 [41].

The fact that an absolute calibration could be made in any electroacoustical system for which the acoustic transfer impedance could be calculated made it possible to perform in situ transducer calibrations in almost any apparatus and under actual conditions of use. One extreme example of the utility of this approach is demonstrated by the reciprocity calibration of electret microphones used to make an absolute determination of the sound pressures generated by resonant mode conversion in superfluid helium at temperatures within one degree of absolute zero (1 K = −272 °C = −458 °F) [42]. Not only was the sensitivity of such a transducer different from the same transducer calibrated in air, but the sensitivity could change after the apparatus was brought back to room temperature and then submerged again in liquid helium.

The reciprocity method was extended to force-driven transduction by Swift and Garrett in 1987 to allow reciprocity calibration of magnetohydrodynamic sound sources [43]. Such "ultracompliant" sources and receivers are the equivalent of what we called a "constant force" driver, which were contrasted to "constant displacement" or "constant velocity" drive mechanisms that were used to excite finite or semi-infinite strings in our investigations of the driven string in Sects. 3.7 and 3.8.

10.7.4 Reciprocity Calibration in Other Geometries

Most reciprocity calibrations for either hydrophones [44] or microphones [45] are executed in a coupler (cavity) that is small compared to the wavelength of sound at the calibration frequencies (see Fig. 10.24), or under free-field conditions, usually within an anechoic chamber (see Fig. 12.41) [46]. As before, the only requirement for such calibrations is knowledge of the appropriate acoustic transfer impedance. Until the radiation produced by small sources that create spherically spreading pressure waves in unbounded media are discussed Chap. 12, we will not be able to calculate the acoustic transfer function for free-field conditions. The acoustic transfer impedance for that case is included here for the reader's convenience. The distance separating the "acoustic centers"[16] of the source and the receiver is d.

$$\text{Free-field}: \quad |\mathbf{Z_{tr}}| = \frac{\rho_m c}{2d\lambda} \tag{10.83}$$

Free-field reciprocity calibrations of microphones in air have been demonstrated to frequencies as high as 100 kHz in 1948 [47] and more recently up to 150 kHz [48].

For a coupler with internal volume, V, and all internal dimensions much smaller than the wavelength, $V^{1/3} \ll \lambda$, the acoustic transfer impedance is given by the cavity's compliance in Eq. (8.26).

$$\text{Coupler}: \quad \mathbf{Z_{tr}} = \frac{\rho_m c^2}{j\omega V} = \frac{\gamma p_m}{j\omega V} \tag{10.84}$$

A schematic diagram of a typical commercial coupler used for reciprocity calibration systems, like the Brüel & Kjær Type 4143, is shown in Fig. 10.24 that is provided with two coupler volumes with nominal internal volume of 20 cm^3 and 3.4 cm^3 [49]. To perform a reciprocity calibration to high frequencies, the coupler must be rather small. In that case, it is sometimes necessary to modify the cavity's compliance to include the compliance of the transducers' diaphragms. Alternatively, higher-

[16] The acoustic center of a reversible microphone or a sound source under free-field conditions is defined as the extrapolated center of the spherically diverging wave field (see Problem 4 in Chap. 12).

frequency calibrations can be made by filling the coupler with a gas such as He or H_2 that have significantly higher sound speeds. Also, to reach the highest levels of precision, it may be necessary to determine an effective polytropic coefficient (i.e., ratio of specific heats), γ_{eff}, to take into account that the gas near the coupler's and the microphone's surfaces has an isothermal compressibility as discussed in Sect. 9.3.2. Since the coupler volume tends to be minimized to allow calibration at higher frequencies, the surface-to-volume ratio can introduce a significant correction to the coupler's compliance (i.e., acoustic transfer impedance), particularly at lower frequencies where the thermal penetration depth is longer and, hence, the isothermal volume is a larger fraction of the coupler's volume.

Recently, a reciprocity calibration was made using a coupler with a volume of 1.5 m^3 that included two 10″ sub-woofers as the reversible transducers and produced reciprocity calibrations of infrasound sensors used for monitoring compliance with the Comprehensive Nuclear-Test-Ban Treaty [50] for frequencies between 0.005 Hz $\leq f \leq$ 10 Hz [51].

For a double Helmholtz resonator, like that shown in Fig. 9.18, having equal volumes, V, on either side, joined by a duct of cross-sectional area, $A = \pi r_d^{\,2}$, with length, L_d, the transfer impedance depends upon the resonance frequency, $\omega_o = c\sqrt{2A/L_d V}$, and the quality factor, Q.

$$\text{Double Helmholtz resonator}: \quad |\mathbf{Z_{tr}}| = \frac{\rho_m c Q}{\sqrt{8AV/L_d}} \tag{10.85}$$

A plane wave tube of cross-sectional area, A, that may include an echoic termination to guarantee unidirectional wave propagation can also be a useful geometry for reciprocity calibrations, as long as the plane wave propagation is ensured by requiring that $A^{1/2} \ll \lambda$.

$$\text{Planewave tube}: \quad |Z_{\mathbf{tr}}| = \frac{\rho_m c}{A} \tag{10.86}$$

The result for a plane wave resonator from Eq. (10.65) of volume, V_{res}, operating in its *nth* mode, with resonance frequency, f_n, and quality factor, Q_n, filled with an ideal gas, is repeated below.

$$\text{Planewave resonator (gas-filled)}: \quad |\mathbf{Z_{tr}}| = \frac{Q_n}{\pi f_n} \frac{\gamma p_m}{V_{res}} \tag{10.87}$$

10.7.5 Resonator-Transducer Interaction

The coupling of two or more systems that possess their own individual resonance frequencies has been one focus of this textbook since coupled simple harmonic oscillators were introduced in Sect. 2.7. The topic of this section of Chap. 10 is the driven plane wave resonator, so it is natural that the coupling of an electrodynamic loudspeaker to such a resonator be examined. As introduced in Eq. (2.55) for a forced simple harmonic oscillator, we start by writing down Newton's Second Law of Motion to account for the net force, in this case being the force on the speaker's piston, which has an instantaneous velocity, $\dot{\xi}_1(t)$, with positive ξ toward the left in Fig. 10.9.

$$m_o \frac{d^2\xi_1}{dt^2} + R_m \frac{d\xi_1}{dt} + \mathrm{K}\xi_1 = f - A_{pist}p(t) \tag{10.88}$$

The speaker's moving mass, m_o; suspension stiffness, K; and mechanical resistance, R_m, were discussed in Sect. 2.5.5, as was the force, $f(t) = (B\ell)I(t)$, that the magnet and voice coil (i.e., motor mechanism) exert on the piston of area, A_{pist}. The situation is diagrammed schematically in Fig. 10.9.

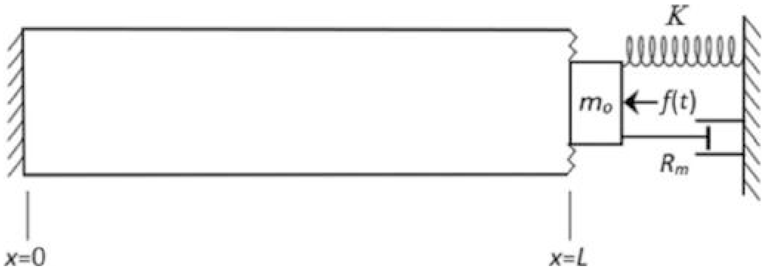

Fig. 10.9 Schematic representation of a plane wave resonator of uniform cross-sectional area, A_{res}, that is driven by an electrodynamic loudspeaker with a piston of area, A_{pist}, located at $x = L$. The *zig-zag lines* connecting the piston to the resonator at $x = L$ represent some flexure seal (e.g., the "surround" of the speaker shown in Fig. 2.16 right or the bellows in Fig. 4.14 and in Fig. 4.21 right). The piston's effective area, A_{pist}, will include some contribution from the flexure seal. In general, $A_{pist} \neq A_{res}$

In addition to Newton's Second Law in Eq. (10.88), the fluid in the resonator that is in contact with the piston must have the same volume velocity as that of the piston, $U_1(L) = -A_{pist}\dot{\xi}_1$. Under steady-state conditions for a single-frequency excitation, the reaction force, $A_{pist}\widehat{\mathbf{p}}$, on the piston produced by the acoustic pressure at its surface, $A_{pist}\widehat{\mathbf{p}}(L)$, can be expressed in terms of the acoustical impedance presented by the resonator. By placing the rigid end of the resonator at $x = 0$, Eq. (10.45) can be used to express the velocity of the gas, while Euler's equation determines the gas pressure as a function of position and time, (temporarily) neglecting any resonator dissipation.

$$\begin{gathered}\mathbf{Z_{ac}} \equiv \frac{\widehat{\mathbf{p}}}{\widehat{\mathbf{U}}} = \frac{j\rho_m c\widehat{\mathbf{v}}\cos(kx)}{A_{res}\widehat{\mathbf{v}}\sin(kx)} = j\frac{\rho_m c}{A_{res}}\cot(kx) \\ \Rightarrow \quad \widehat{\mathbf{p}}(L) = -\mathbf{Z_{ac}}(L)A_{pist}\widehat{\dot{\boldsymbol{\xi}}}\end{gathered} \tag{10.89}$$

If dissipation in the resonator is represented by an exponential decay constant, α, so the amplitude of a traveling plane wave decays in proportion to $e^{-\alpha x}$, and using Eq. (B.5) the quality factor of a plane wave resonance is $Q = (½)\, k/\alpha = \pi/(\alpha\lambda)$, then the acoustic impedance has a slightly more complicated dependence upon (kL), which reduces to Eq. (10.89) in the limit that $(\alpha L) \ll 1$ [52].

$$\mathbf{Z_{ac}}(kL) = \frac{\rho_m c}{A_{res}}\, \frac{\alpha L - j\cos(kL)\sin(kL)}{\sin^2(kL) + (\alpha L)^2\cos^2(kL)} \tag{10.90}$$

The motor mechanism (voice coil and magnet) must supply the force that displaces the piston's mass, damping, and stiffness and must also supply the force that the piston exerts on the fluid. However, we can easily investigate the resonance frequencies analytically by neglecting all dissipation (i.e., both R_m and α) and realizing that no external force is needed to maintain an oscillation on resonance with no dissipation. (The dissipative terms will be included in the DeltaEC model of Fig. 10.11.) Then, the moving mass of the speaker is just bouncing on the sum of the two elastic forces: $-j\omega\widehat{\boldsymbol{\xi}}\mathrm{K}$ from the speaker's suspension and $A_{pist}\widehat{\mathbf{p}}$ from the gas pressure oscillations. Since the fluid's effect is represented by the acoustic impedance, $Z_{tr} \equiv \widehat{\mathbf{p}}/\widehat{\mathbf{U}}$, in Eq. (10.89) or (10.90), and the speaker's components are represented by a mechanical impedance, $\mathbf{Z_{mech}} = \widehat{\mathbf{F}}/\widehat{\mathbf{v}}$, we can convert both to the mechanical domain using Eq. (10.28).

$$j\left(m_o\omega - \frac{\mathrm{K}}{\omega}\right) = jA_{pist}^2 \frac{\rho_m c}{A_{res}} \cot(kL) \tag{10.91}$$

The plotting of this equation is simplified if the driver parameters are nondimensionalized by taking the ratio of the speaker's moving mass, m_o, to the mass of gas contained within the resonator, m_{gas}.

$$m^* = \frac{m_o}{m_{gas}} = \frac{m_o}{\rho_m A_{res} L} \quad \Rightarrow \quad m_o = m^* \rho_m A_{res} L \tag{10.92}$$

The speaker's stiffness can be normalized by taking its ratio with respect to the zero-frequency stiffness of the gas as given in Eq. (8.28).

$$\mathrm{K}^* = \frac{\mathrm{K}}{\mathrm{K}_{gas}} = \frac{\mathrm{K}V}{\rho_m c^2 A_{res}^2} = \frac{\mathrm{K}A_{res}L}{\rho_m c^2 A_{res}^2} = \frac{\mathrm{K}L}{\rho_m c^2 A_{res}} \quad \Rightarrow \quad \mathrm{K} = \frac{\mathrm{K}^* \rho_m c^2 A_{res}}{L} \tag{10.93}$$

Equation (10.91) can be re-written as a function of the speaker's nondimensionalized parameters, m^* and K^*, and (kL), where the "k" in the parentheses is the wavenumber. The ratio of the piston area to the resonator area is $A^* = A_{pist}/A_{res}$.

$$\begin{aligned} m^* \frac{\omega}{c} \rho_m L A_{res} - \frac{\mathrm{K}^* \rho_m c A_{res}}{\omega L} &= \rho_m \frac{A_{pist}^2}{A_{res}} \cot(kL) \\ m^*(kL) - \frac{\mathrm{K}^*}{(kL)} &= (A^*)^2 \cot(kL) \end{aligned} \tag{10.94}$$

The driver-resonator interaction can be illustrated by coupling the speaker we evaluated in Chap. 2, Prob. 19, that was characterized using the techniques of Sect. 2.5.5, to a rigidly terminated cylindrical resonator. That speaker had a free-cone resonance frequency, $f_o = 55$ Hz, and an effective piston area, $A_{pist} = 125\ \mathrm{cm}^2$. For computational simplicity, let's connect that speaker to a 1.0-meter-long, air-filled cylinder with an inside diameter, $D = (4A_{\mathrm{pist}}/\pi)^{½}$, so $A* = 1$, and terminated at the other end, $x = 0$, by a rigid end cap. If the air is dry and at a mean pressure, $p_m = 101{,}325$ Pa, and temperature, $T_m = 20\ °\mathrm{C} = 293$ K, the speed of sound, $c = 343.2$ m/s. Using the results of Eq. (10.51) for such a resonator with both ends rigid, $f_1 = c/2\ L = 171.6$ Hz, with the subsequent harmonic series of longitudinal standing wave modes at $f_n = nf_1$, if both ends were rigid.

Using those speaker parameters, while neglecting dissipation in the speaker and the resonator, $m^* \cong ¾$ and $\mathrm{K}^* \cong ¾$. Letting $A^* = 1$, the graphical solution to Eq. (10.94) is shown in Fig. 10.10, where the solid line represents cot (kL) for the resonator and the short-dashed line represents the frequency dependence of the speaker's mechanical impedance. The lowest-frequency intersection at $(k_oL) = 0.397\pi$ is close to the speaker's free-cone resonance. Subsequent intersections correspond fairly closely to the closed-closed resonances of the resonator, $(k_nL) = n\pi$, for $n \geq 1$.

If the rear of the loudspeaker is enclosed by a rigid hemisphere, the additional gas stiffness, approximated in Eq. (10.95), raises the speaker's nondimensionalized stiffness, $\mathrm{K}^* \cong 23$. That case corresponds to the long-dashed line in Fig. 10.10. Now the speaker's resonance frequency corresponds to $(k_oL) = 1.654\pi$, placing it above the resonator's rigid-rigid $n = 1$ mode, as well as the free-cone resonance, and below the $n = 2$ mode. In both cases, the speaker's mechanical resonance "repels" the isolated resonator's harmonic standing wave modes. This *level repulsion* is also illustrated in Table 10.2.

To include dissipation in the speaker and the resonator, it is easier to model such a resonator and driver using the ISPEAKER segment in DeltaEC, as shown in Fig. 10.11. Segment #1 provides the values of the essential loudspeaker parameters in MKS units: A_{pist} (1a); voice coil resistance, R_{dc} (1b); voice coil inductance, L (1c); $B\ell$-product (1d); moving mass, m_o (1e); suspension stiffness, K (1f); and

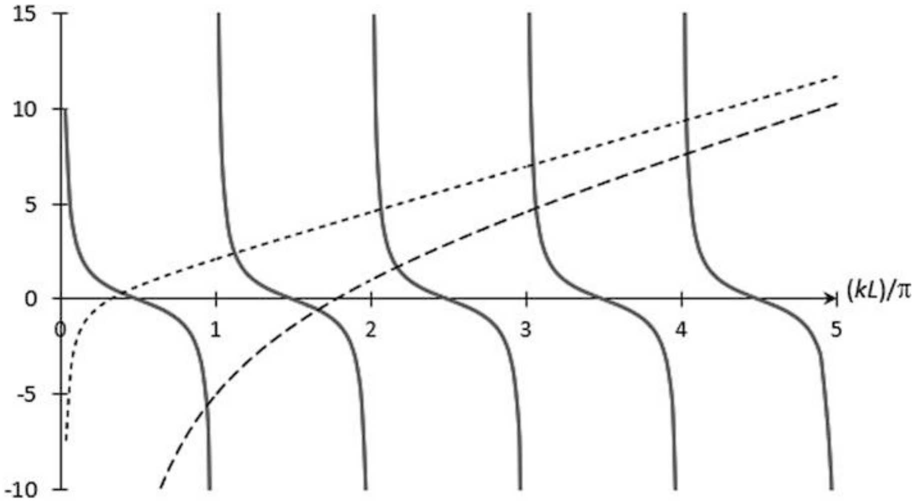

Fig. 10.10 Graphical method of solution to the transcendental Eq. (10.94) with $A* = 1$. The *solid curves* represent the right-hand side of that equation, and the *dashed curves* are the left-hand side. The values for the horizontal axis are $(kL)/\pi$. The short dashes represent the mechanical parameters ($m^* \cong$ ¾ and $K^* \cong$ ¾) of loudspeaker from Chap. 2, Prob. 19, that are included in the DeltaEC screenshot of Fig. 10.11. The *long dashes* represent the same loudspeaker but with the rear of the speaker enclosed by a hemispherical enclosure (see Fig. 10.13) that provides additional gas stiffness and makes $K^* \cong 23$

Table 10.2 Solutions to Eq. (10.94) for $m^* =$ ¾ with the speaker's mechanical resonance at 55 Hz

Mode	$K^* = 3/4$ (kL)/π	f_n [Hz]	$K^* = 23$ (kL)/π	f_n [Hz]
0	0.39718	68.2	1.65441	283.9
1	1.12399	192.9	0.94316	161.8
2	2.06602	354.5	2.16703	371.9
3	3.04457	522.4	3.06495	525.9
4	4.03358	692.2	4.04106	693.4

The left column corresponds to $K^* =$ ¾, and the right column corresponds to $K^* = 23$ and a speaker with enclosure resonance of 299 Hz. In both cases, the speaker's resonance "repels" the standing wave solutions for an ideal rigid-rigid plane wave resonator which would have $(k_n L) = n\pi$ for $n \geq 1$. Frequencies are based on $f_1 = c/2\,L = 171.6$ Hz

mechanical resistance, R_m (1f). The choice of drive current, I (1 h), is arbitrary but reasonable. The DeltaEC model lets us plot the coupled speaker-resonator response as a function of frequency, including dissipation in both the resonator and the driver, as shown in Fig. 10.12. Several interesting features can be seen clearly.

For reference, the dashed line represents the standing wave solutions for an isolated closed-closed resonator, $f_n = nf_1$, based on the results of Eq. (10.51). The spectrum for the coupled systems shows an additional resonance at about 68 Hz corresponding to the mechanical resonance of the speaker as already calculated for the lossless case in Table 10.2. At that frequency, the resonator is shorter than a half-wavelength so the "load" presented by the resonator behaves as a gas stiffness, K_{gas}, that adds to the speaker's mechanical suspension stiffness, K, raising the speaker's resonance frequency above its free-cone value, $f_o = 55$ Hz. The frequency of the speaker's resonance and those of the first five standing wave modes of the resonator that are produced by the DeltaEC model are listed in Table 10.3.

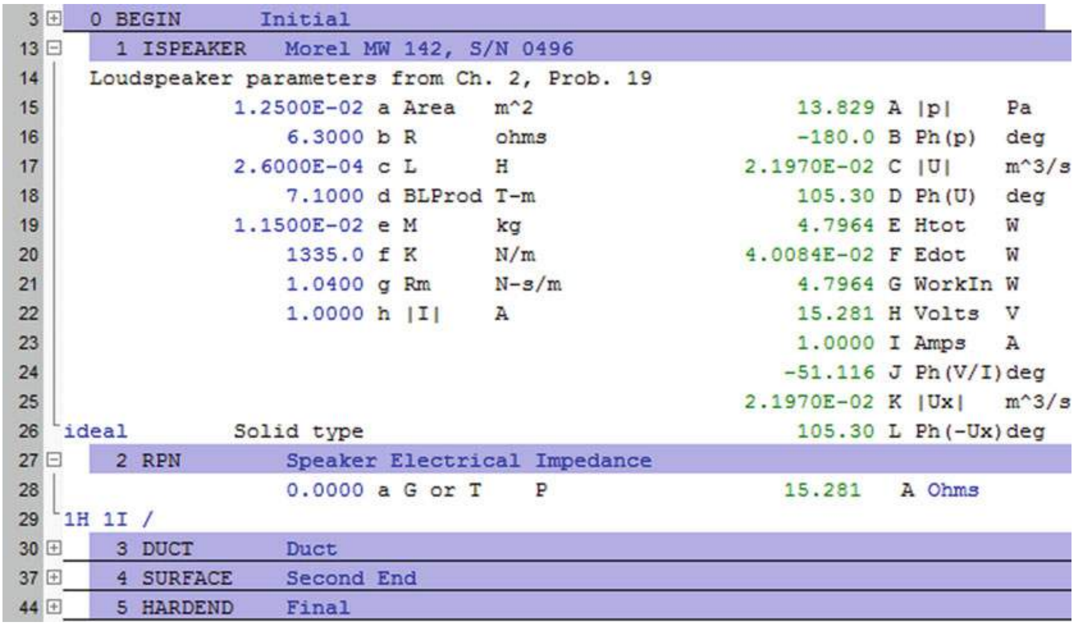

```
3  ⊞  0 BEGIN       Initial
13 ⊟   1 ISPEAKER   Morel MW 142, S/N 0496
14     Loudspeaker parameters from Ch. 2, Prob. 19
15               1.2500E-02 a Area   m^2            13.829 A |p|    Pa
16                   6.3000 b R      ohms           -180.0 B Ph(p)  deg
17               2.6000E-04 c L      H          2.1970E-02 C |U|    m^3/s
18                   7.1000 d BLProd T-m            105.30 D Ph(U)  deg
19               1.1500E-02 e M      kg             4.7964 E Htot   W
20                   1335.0 f K      N/m        4.0084E-02 F Edot   W
21                   1.0400 g Rm     N-s/m          4.7964 G WorkIn W
22                   1.0000 h |I|    A              15.281 H Volts  V
23                                                  1.0000 I Amps   A
24                                                 -51.116 J Ph(V/I)deg
25                                              2.1970E-02 K |Ux|   m^3/s
26   ideal       Solid type                         105.30 L Ph(-Ux)deg
27 ⊟   2 RPN      Speaker Electrical Impedance
28                   0.0000 a G or T   P           15.281   A Ohms
29   1H 1I /
30 ⊞   3 DUCT     Duct
37 ⊞   4 SURFACE  Second End
44 ⊞   5 HARDEND  Final
```

Fig. 10.11 Screenshot of a DeltaEC model with the ISPEAKER (#1) and the RPN (#2) segments expanded. The RPN calculates the magnitude of the speaker's electrical impedance and the ISPEAKER segment provides the speaker parameters in MKS units

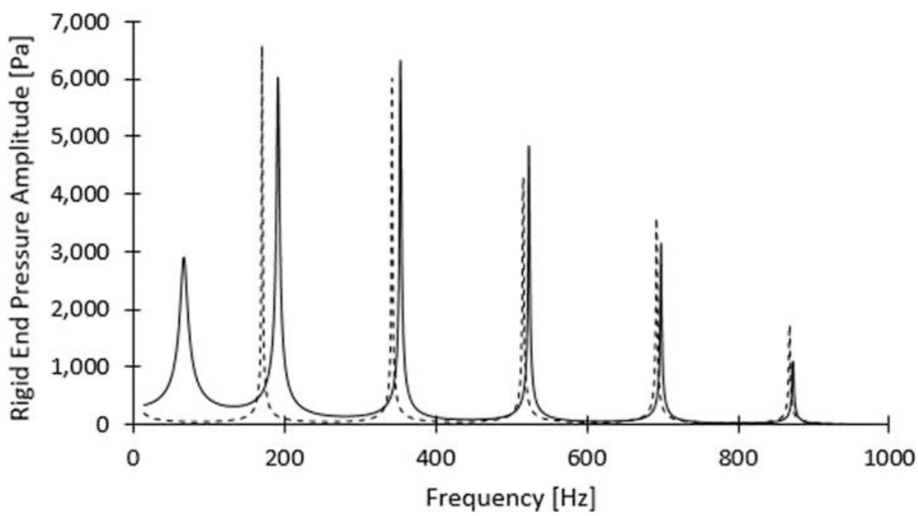

Fig. 10.12 The *solid line* represents the frequency response of the coupled speaker-resonator system that was generated by the DeltaEC model in Fig. 10.11 with $m^* = ¾$ and $K^* = ¾$. The *dashed line* is the frequency response created with rigid terminations at both ends and a boundary that excites the modes with a constant volume velocity. The *lowest-frequency peak* represents the resonance of the loudspeaker. The standing wave modes are shifted to higher frequencies due to the complex mechanical impedance of the loudspeaker

Figure 10.13 shows a DeltaEC model that uses the IESPEAKER segment to incorporate an enclosure behind the speaker that is a hemisphere with the same diameter as the piston that produced the $K^* = 23$ case. The acoustic pressure generated by that combination is shown in Fig. 10.14, and the frequencies of the peak are included in Table 10.3.

Table 10.3 Summary of the frequencies of the speaker's mechanical resonance ($n = 0$) and the frequencies of the first five modes of the resonator, f_n, that include dissipation

Mode	Rigid	$f_o = 55$ Hz	Enclosed
0	—	68	269
1	171	192	159
2	343	354	366
3	517	524	527
4	693	699	700
5	869	874	874

The modes of the closed-closed resonator (Rigid), given by Eq. (10.51), are provided for reference. These frequencies are in excellent agreement with the results of the nondissipative calculations summarized in Table 10.2

```
Enclosed 5 in Speaker Enclosed 5 in. WM 142
 0 BEGIN          Dry air at standard atmosphere and 20 deg C
  1 COMPLIANCE Rear Speaker Enclosure
 5" diameter hemisphere
             2.5300E-02 a SurfAr m^2             1.0032E+04 A |p|     Pa
             6.6300E-04 b Volume m^3                 -90.43 B Ph(p)   deg
Master-Slave Links                               7.9247E-02 C |U|     m^3/s
                                                     179.50 D Ph(U)   deg
                                                     0.0000 E Htot    W
ideal        Solid type                            -0.48083 F Edot    W
  2 IESPEAKER  Morel MW 142, S/N 0496
             1.2500E-02 a Area     m^2               580.56 A |p|     Pa
                 6.3000 b R        ohms             -92.742 B Ph(p)   deg
             2.6000E-04 c L        H             7.9247E-02 C |U|     m^3/s
                 7.1000 d BLProd T-m                 179.46 D Ph(U)   deg
             1.1500E-02 e M        kg                25.655 E Htot    W
                 1335.0 f K        N/m              0.88574 F Edot    W
                 1.0400 g Rm       N-s/m             25.655 G WorkIn  W
                 1.0000 h |I|      A                 51.311 H Volts   V
                 0.0000 i Ph(I)    deg               1.0000 I Amps    A
                                                 2.2671E-02 J Ph(V/I) deg
                                                     9452.3 K |Px|    Pa
ideal        Solid type                              89.712 L Ph(Px)  deg
  3 RPN          Speaker Electrical Impedance
  4 DUCT         Duct
  5 SURFACE      Second End
  6 HARDEND      Final
```

Fig. 10.13 Screenshot of the DeltaEC model with the "enclosed speaker" IESPEAKER (#2) segment expanded and the "enclosure back volume" COMPLIANCE (#1) segment expanded

The enclosure's small back volume contributes significantly more gas stiffness, K_{gas}, to the speaker's suspension than the speaker's own mechanical stiffness, K. Since the enclosure's dimensions are all much smaller than the wavelength of the sound at that frequency, the expression for gas stiffness in Eq. (8.28) can be employed to approximate the enclosed speaker's resonance frequency.

$$K_{gas} = \gamma p_m \frac{A_{pist}^2}{V} = 39{,}400 \ \text{N/m} \quad \Rightarrow \quad f_o = \frac{1}{2\pi}\sqrt{\frac{K + K_{gas}}{m_o}} = 299 \ \text{Hz} \tag{10.95}$$

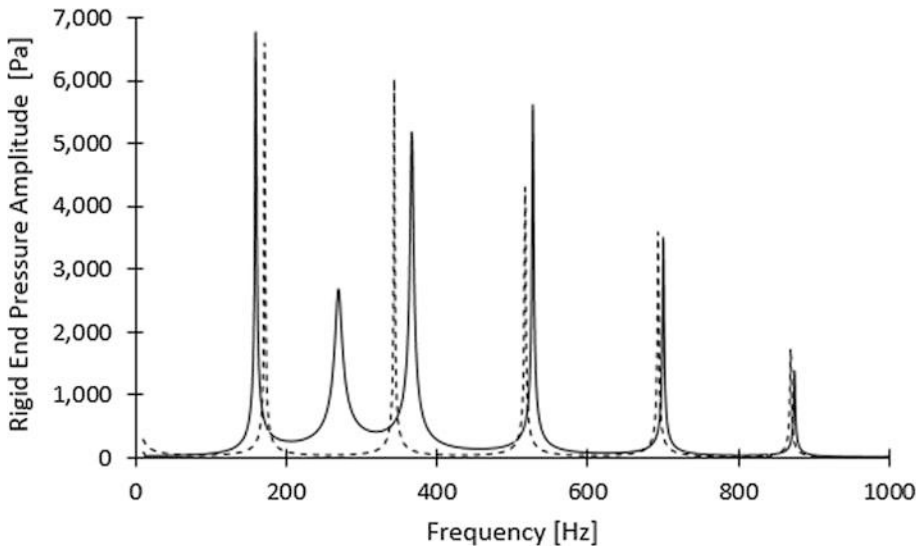

Fig. 10.14 The *solid line* represents the frequency response of the coupled "enclosed" speaker-resonator system that was generated by the DELTAEC model in Fig. 10.13 with $m^* = ¾$ and $K^* = 23$. The *dashed line* represents the frequency response created with a rigid termination at both ends and a boundary that provides a constant volume velocity, as it was in Fig. 10.12. The frequency peak produced by the mechanical resonance of the loudspeaker now appears between the $n = 1$ and the $n = 2$ standing wave resonances. The frequencies of the standing wave modes are "repelled" by the coupled loudspeaker resonance exhibiting the same "level repulsion" that appeared first when coupled harmonic oscillators were introduced in Sect. 2.7.6 and was also demonstrated in the bass-reflex loudspeaker enclosure's response in Fig. 8.42

This value is 30 Hz higher than the result in Table 10.2 because the "load," produced by the gas, on the front surface of the loudspeaker's piston is not included in the calculation of Eq. (10.95).

10.7.6 Electrodynamic Source Coupling Optimization*

In many applications where an electrodynamic loudspeaker is coupled with a resonator, it is advantageous to optimize the electroacoustic efficiency of the coupling. If it is assumed that the acoustical properties of the resonator have been determined by the application, then it is possible to demonstrate that the efficiency of the driver's excitation of that resonance will depend upon the area of the driver's piston, A_{pist}.

There are two sources of dissipation in an electrodynamic driver. One is related to the driver's mechanical damping, R_m, that is proportional to the square of the driver's piston velocity, $|\hat{\mathbf{v}}_\mathbf{d}|^2 = \left|\hat{\dot{\xi}}\right|^2 = \left(\left|\hat{\mathbf{U}}\right|/A_{pist}\right)^2$.

$$\langle \Pi_m \rangle_t = \frac{R_m}{2} |\hat{\mathbf{v}}_\mathbf{d}|^2 = \frac{R_m}{2} \frac{\left|\hat{\mathbf{U}}\right|^2}{A_{pist}^2} \equiv a \frac{\left|\hat{\mathbf{U}}\right|^2}{A_{pist}^2} \tag{10.96}$$

The other loss mechanism is due to the time-averaged electrical dissipation (i.e., Joule heating), $\langle \Pi_{dc} \rangle_t$, produced by the driving current's passage through the driver's voice coil, $\hat{\mathbf{I}}$, that has an electrical resistance, R_{dc}. The force, $\widehat{\mathbf{F}}$, that the driver must produce is related to the product of the acoustic pressure on the driver's face, $\widehat{\mathbf{p}}$, and the piston's area, A_{pist}.

$$\widehat{\mathbf{F}}\left(\widehat{\mathbf{I}}\right) = \widehat{\mathbf{p}}A_{pist} = (B\ell)\widehat{\mathbf{I}} \quad \Rightarrow \quad \widehat{\mathbf{I}} = \frac{\widehat{\mathbf{p}}A_{pist}}{(B\ell)} \tag{10.97}$$

At resonance, the pressure on the face of the piston, $\widehat{\mathbf{p}}$, and the volume velocity that the piston produces, $\widehat{\mathbf{U}}$, will be in-phase. Furthermore, since the resonant load is specified, their ratio must be the acoustical impedance of the resonator at the piston's location: $\mathbf{Z_{ac}} = \widehat{\mathbf{p}}/\widehat{\mathbf{U}}$.

$$\langle \Pi_{dc} \rangle_t = \frac{R_{dc}}{2}\left|\widehat{\mathbf{I}}\right|^2 = \frac{R_{dc}}{2}\left(\frac{\widehat{\mathbf{p}}A_{pist}}{(B\ell)}\right)^2 = \frac{R_{dc}}{2}\left(\frac{\mathbf{Z_{ac}}\widehat{\mathbf{U}}A_{pist}}{(B\ell)}\right)^2 \equiv bA_{pist}^2\left|\widehat{\mathbf{U}}\right|^2 \tag{10.98}$$

Inspection of Eqs. (10.96) and (10.98) reveals that those two dissipation mechanisms have a reciprocal dependence upon the square of the piston's area. As the area of the piston decreases, the piston's velocity must increase to provide the same amount of volume velocity. On the other hand, as the area of the piston increases, the force required to move the piston, hence the required current flow through the voice coil, must increase with the area of the piston.

The total time-averaged driver dissipation, $\langle \Pi_{driver} \rangle_t$, is the sum of Eq. (10.96) and Eq. (10.98). Since the volume velocity is common to both terms (and dictated by the power requirement of the application), the optimum piston area, A_{opt}, can be obtained by differentiating the total driver dissipation with respect to the piston's area.

$$\frac{\langle \Pi_{driver} \rangle}{\left|\widehat{\mathbf{U}}\right|^2} = \frac{a}{A_{pist}^2} + bA_{pist}^2 \quad \Rightarrow \quad \frac{\partial\left(\frac{\langle \Pi_{driver} \rangle}{\left|\widehat{\mathbf{U}}\right|^2}\right)}{\partial A_{pist}} = -\frac{2a}{A_{opt}^3} + 2bA_{opt} = 0 \tag{10.99}$$

Since both the acoustical impedance of the resonator at resonance, given by Eq. (10.65), and the mechanical resistance of the driver are real constants, they can be represented by a dimensionless constant, s, that relates the real component of the acoustical impedance times the resonator's cross-sectional area, A_{res}, to the mechanical resistance of the driver: $A_{res}^2|\mathbf{Z_{ac}}| = sR_m$.

For optimum efficiency, the driver must be operated at its mechanical resonance frequency, ω_o, making $\mathbf{X_m}(\omega_o) = j(\omega_o m_o - \mathrm{K}/\omega_o) = 0$, so that none of the electrodynamic force is wasted accelerating the driver's mass, m_o, at $\omega > \omega_o$ or deflecting the driver's suspension stiffness, K, at $\omega < \omega_o$. Also, by the maximum power transfer theorem, "load matching" requires that $s = 1$.

$$\left(\frac{A_{opt}}{A_{res}}\right)^4 = \frac{R_m(B\ell)^2}{R_{dc}Z_{ac}^2A_{res}^4} = \frac{R_m(B\ell)^2}{R_{dc}R_m^2} = \left[\frac{(B\ell)^2}{R_mR_{dc}}\right] \equiv \beta \tag{10.100}$$

The quantity in square brackets is a dimensionless number, β, known as the Wakeland number, that depends only upon the driver's parameters.

$$\frac{A_{opt}}{A_{res}} = \beta^{1/4} \cong \sqrt{\sigma} \tag{10.101}$$

In some cases, it may not be possible or practical to use this optimum piston area since there may be other constraints that limit the piston's excursion or the goal may be to deliver the maximum power to the load at some lower efficiency.

Table 10.4 Motor parameters for various electrodynamic drivers that have been used by thermoacoustics researchers [54]

Driver	$(B\ell)$ [N/A]	R_{dc} [Ω]	R_m [kg/s]	σ	η_{max} [%]	$\Pi_{electric}$ [W]
MW-142 [55]	7.5	5.1	1.9	2.6	44	150
JBL 2206H [56]	18.1	5.3	9.5	2.7	47	300
Altec 290-16 K [57]	21.5	10.6	2.8	4.1	61	10
STAR [58]	15.3	8.2	1.8	4.1	61	20
SETAC [59]	18	1.7	2.2	9.4	81	200
Bose LM-1 [60]	18.36	1.36	2.34	10.34	82.4	100
B-300 [61]	8.0	0.05	15	9.3	81	300
C-2 [61]	41	0.24	48	12	85	2000
C10 [61]	85	0.52	80	13	86	10,000

The first three entries are "off-the-shelf" commercial loudspeakers. The STAR and SETAC drivers are custom-designed and built moving-coil devices. The last four drivers are moving-magnet devices. The last three were designed for single-frequency transduction at high efficiency and high power by Q-Drive, located in Troy, NY

A more detailed analysis is provided by Wakeland who shows that the maximum efficiency, η_{max}, is related to that dimensionless driver parameter, $\beta \equiv (B\ell)^2/(R_m R_{dc})$, and introduces $\sigma = \sqrt{\beta + 1}$ [53]. Wakeland's more accurate determination of σ approaches the simpler result of Eq. (10.101) as the value of β increases. Typical values of β for high-power, high-efficiency electrodynamic drivers are usually above 5 and less than 200.

$$\eta_{\max} = \frac{\beta}{\beta + 2\sqrt{\beta + 1} + 2} = \frac{\sigma - 1}{\sigma + 1} \tag{10.102}$$

A summary of the optimum efficiencies for several electrodynamic loudspeakers is given in Table 10.4 [53]. For the MW-142 in Problem 19 of Chap. 2, $\beta = 5.8$ and $\eta_{max} = 44\%$. For a 10 kW moving-magnet electrodynamic driver, shown in Fig. 4.21, $\beta = 175$ and $\eta_{max} = 86\%$.

10.8 Junctions, Branches, and Filters

We now change our focus from one-dimensional plane wave resonators to one-dimensional traveling plane waves in tubes with diameters, D, that are again small compared to the wavelength, $D \cong \sqrt{A} \ll \lambda$. The behavior of such traveling waves will be examined when they impinge on a junction between tubes that have an abrupt change in cross-sectional area, A. The reflection and transmission of energy at such a junction will be determined by the discontinuity in the acoustical impedance (or acoustical admittance) on either side of such a junction that could be due to changes in mean density, ρ_m, times sound speed, c, in addition to changes in cross-sectional area. The analysis will be extended to branches that join one tube to several others or to other acoustical networks (e.g., to a Helmholtz resonator). In all of these cases, we will again impose continuity of mass flow (i.e., volume velocity) across the junction and where the pressure at the junction is necessarily single-valued.

10.8.1 Abrupt Discontinuities and the Acoustic Admittance

By this time, continuity of mass flow suggests that the tubes should be characterized by an acoustic impedance, although as we are about to demonstrate, the reciprocal of the acoustic impedance, known

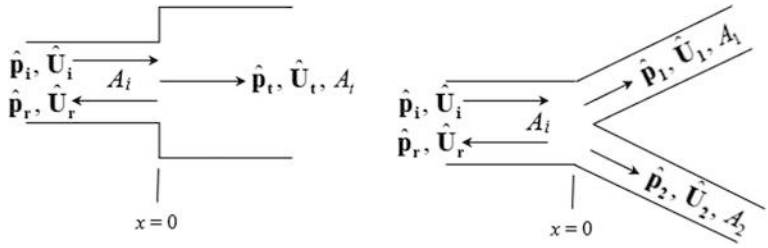

Fig. 10.15 (*Left*) Single-frequency traveling wave with amplitude, $\widehat{\mathbf{p}}_\mathbf{i}$, is incident on a junction between tubes of different cross-sectional areas. Some energy is transmitted and some reflected. (*Right*) Traveling wave impinges from a single tube on a junction with two tubes, all with different cross-sectional areas

as the *acoustic admittance*, $\mathbf{Y_{ac}}$, will provide a more convenient characterization. For the case of the right-going wave that encounters a discontinuity in cross-sectional area, as diagrammed in Fig. 10.15 (left), the boundary conditions at $x = 0$ can be expressed by forming the ratio of volume velocity to pressure.

$$\widehat{\mathbf{p}}_\mathbf{i} + \widehat{\mathbf{p}}_\mathbf{r} = \widehat{\mathbf{p}}_\mathbf{t} \quad \text{and} \quad \widehat{\mathbf{U}}_\mathbf{i} + \widehat{\mathbf{U}}_\mathbf{r} = \widehat{\mathbf{U}}_\mathbf{t} \quad \Rightarrow \quad \frac{\widehat{\mathbf{U}}_\mathbf{i} + \widehat{\mathbf{U}}_\mathbf{r}}{\widehat{\mathbf{p}}_\mathbf{i} + \widehat{\mathbf{p}}_\mathbf{r}} = \frac{\widehat{\mathbf{U}}_\mathbf{t}}{\widehat{\mathbf{p}}_\mathbf{t}} \tag{10.103}$$

Since all three waves are traveling waves, $\mathbf{Y_{ac}} = \mathbf{Z_{ac}^{-1}} \equiv \left(\widehat{\mathbf{U}}/\widehat{\mathbf{p}}\right) = \pm A/\rho_m c$, with the minus sign for the reflected wave because it will be traveling to the left. The continuity of volume velocity and the fact that the pressure at the junction is single-valued, shown in Eq. (10.103), can be expressed in terms of $\mathbf{Y_{ac}}$, which are real numbers.

$$Y_i(\widehat{\mathbf{p}}_\mathbf{i} - \widehat{\mathbf{p}}_\mathbf{r}) = Y_t\widehat{\mathbf{p}}_\mathbf{t} = Y_t(\widehat{\mathbf{p}}_\mathbf{i} + \widehat{\mathbf{p}}_\mathbf{r}) \quad \Rightarrow \quad Y_i\frac{\widehat{\mathbf{p}}_\mathbf{i} - \widehat{\mathbf{p}}_\mathbf{r}}{\widehat{\mathbf{p}}_\mathbf{i} + \widehat{\mathbf{p}}_\mathbf{r}} = Y_t \tag{10.104}$$

Equation (10.104) can be solved for the *amplitude reflection coefficient*, $R \equiv |\widehat{\mathbf{p}}_\mathbf{r}|/|\widehat{\mathbf{p}}_\mathbf{i}|$, and the *amplitude transmission coefficient*, $T \equiv |\widehat{\mathbf{p}}_\mathbf{t}|/\widehat{\mathbf{p}}_\mathbf{i}$.

$$R \equiv \frac{|\widehat{\mathbf{p}}_\mathbf{r}|}{|\widehat{\mathbf{p}}_\mathbf{i}|} = \frac{Y_i - Y_t}{Y_i + Y_t} \quad \text{and} \quad T \equiv \frac{|\widehat{\mathbf{p}}_\mathbf{t}|}{|\widehat{\mathbf{p}}_\mathbf{i}|} = \frac{2Y_i}{Y_i + Y_t} \tag{10.105}$$

These results seem sensible. If the properties of the tube do not change at $x = 0$, then $Y_i = Y_t$, so $R = 0$ and $T = 1$; the wave just keeps moving to the right, as it should through a uniform tube in the absence of dissipation. On the other hand, if $A_t \ll A_i$, and the same fluid medium fills both sections, then $Y_i \gg Y_t$, so the incident and reflected wave amplitudes are identical and the transmitted pressure, p_t, is doubled, though the volume flow rate moving past the junction is much smaller.

If the situation is reversed so if $A_t \gg A_i$, and the same fluid medium fills both sections, then $Y_i \ll Y_t$, so the incident and reflected waves have opposite phases since $R \cong -1$, and the transmitted pressure is very small, $T \ll 1$. This would be the case if the incident tube opened up to the atmosphere (i.e., $Y_t = \infty$). In that case, the volume flow rate would be unrestricted, but the transmitted acoustic pressure amplitude, $|\widehat{\mathbf{p}}_\mathbf{t}|$, would be very small since the cincident tube is effectively attached to an infinite fluid pressure reservoir.

Based on the intensities of the three waves, it is also possible to calculate a power reflection coefficient, R_Π, and power transmission coefficient, T_Π, that will be proportional to the squares of the pressures times the acoustic admittance, $\langle \Pi \rangle_t = |\widehat{\mathbf{p}}|^2 Y/2$.

$$R_\Pi = \frac{|\widehat{\mathbf{p}}_\mathbf{r}|^2}{|\widehat{\mathbf{p}}_\mathbf{i}|^2} = \frac{(Y_i - Y_t)^2}{(Y_i + Y_t)^2} \quad \text{and} \quad T_\Pi = \frac{Y_t}{Y_i}\frac{|\widehat{\mathbf{p}}_\mathbf{t}|^2}{|\widehat{\mathbf{p}}_\mathbf{i}|^2} = \frac{4Y_iY_t}{(Y_i + Y_t)^2} \tag{10.106}$$

Energy conservation is confirmed by the fact that $R_\Pi + T_\Pi = 1$; any power that is not reflected must be transmitted. If the admittances are closely matched, so $Y_2/Y_1 \cong 1$, and then there is almost perfect transmission of the energy since the reflected portion is roughly $(1/4)(Y_2/Y_1 - 1)^2$. This result provides justification for the stepwise approximation to a horn in Fig. 10.2, where the number of elements is chosen so the area change between adjacent elements is small so that reflections from the discontinuities can be ignored and the propagation can be considered to remain unidirectional.

Having identified the acoustic admittance as the physical quantity that determines the distribution of the incident, reflected, and transmitted energy, it is not difficult to generalize the previous results for a tube that branches into many tubes of differing acoustic admittance at the junction, such as the system diagrammed in Fig. 10.15 (right).

$$\begin{gathered} Y_i(\widehat{\mathbf{p}}_i - \widehat{\mathbf{p}}_r) = \left(\sum_{n=1}^{N} Y_n\right)\widehat{\mathbf{p}}_t \quad \text{where} \quad Y_n = \frac{A_n}{\rho_n c_n} \\ \text{and} \quad \widehat{\mathbf{p}}_t = \widehat{\mathbf{p}}_i + \widehat{\mathbf{p}}_r = \widehat{\mathbf{p}}_1 = \widehat{\mathbf{p}}_2 = \ldots = \widehat{\mathbf{p}}_n \end{gathered} \tag{10.107}$$

The amplitude reflection and transmission coefficients are the corresponding generalizations of Eq. (10.105).

$$R = \frac{\widehat{\mathbf{p}}_\mathbf{r}}{\widehat{\mathbf{p}}_\mathbf{i}} = \frac{Y_i - \sum_{n=1}^{N} Y_n}{Y_i + \sum_{n=1}^{N} Y_n} \quad \text{and} \quad T = \frac{\widehat{\mathbf{p}}_\mathbf{t}}{\widehat{\mathbf{p}}_\mathbf{i}} = \frac{2Y_i}{Y_i + \sum_{n=1}^{N} Y_n} \tag{10.108}$$

The power transmission coefficients must be different for different outlet tubes. For the *nth* outlet tube, $\langle \Pi_{t,n} \rangle_t = (1/2)\Re e\left[\widehat{\mathbf{p}}_\mathbf{n}\widehat{\mathbf{U}}_\mathbf{n}^*\right] = (1/2)Y_n|\mathbf{p}_\mathbf{t}|^2$. Meanwhile, $\langle \Pi_i \rangle_t = (1/2)Y_i|\widehat{\mathbf{p}}_\mathbf{i}|^2$. We can use $T = \widehat{\mathbf{p}}_\mathbf{t}/\widehat{\mathbf{p}}_\mathbf{i}$ in Eq. (10.108) to write the power transmission coefficient into the *nth* tube:

$$T_{\Pi,n} = \frac{\langle \Pi_n \rangle_t}{\langle \Pi_i \rangle_t} = \frac{Y_n}{Y_i}\frac{|\widehat{\mathbf{p}}_\mathbf{n}|^2}{|\widehat{\mathbf{p}}_\mathbf{i}|^2} = \frac{4Y_iY_n}{\left(Y_i + \sum_{n=1}^{N} Y_n\right)^2} \tag{10.109}$$

By using Eqs. (10.108) and (10.109), one can verify that energy is conserved to exhibit the reassuring result:

$$R_\Pi + \sum_{n=1}^{N} T_{\Pi,n} = R^2 + \sum_{n=1}^{N} T_{\Pi,n} = 1 \tag{10.110}$$

An interesting application of the pressures in branching systems to the human cardiovascular system, in particular the iliac bifurcation of the aorta, is discussed by Lighthill [1].

10.8.2 Tuned Band-Stop Filter

Based on the diagrams in Fig. 10.15, it appears that our interest is focused on the junction between semi-infinite pipes where we expect unidirectional propagation in the +x direction and an acoustic

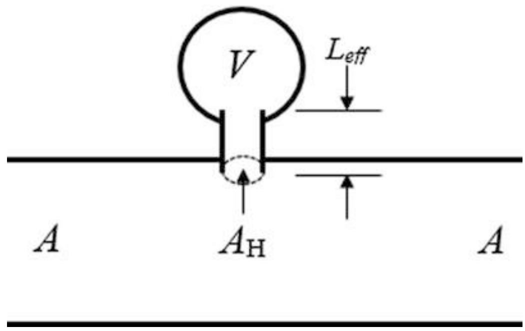

Fig. 10.16 Helmholtz resonator as a side branch on a duct of uniform cross-sectional area, A. The intrusion of the "neck" into the duct and into the volume represents the effective length of the neck, L_{eff}, which is greater than its physical length, as observed in Sect. 8.5.2

admittance for right-going traveling waves, as expressed in Eq. (10.86) or Eq. (10.107), so that $Y_n = A/\rho_m c$ for all $n \geq 1$. There is no such restriction on Y_n. In the following application, we will use the formalism of Eq. (10.109) to calculate the transmission coefficient for sound that propagates along a duct that uses a Helmholtz resonator as a side branch to produce a *band-stop filter* that is shown schematically in Fig. 10.16.

The lumped element approach of Chap. 8 can be exploited to analyze this band-stop filter, also known as a "trap," that can be useful for suppression of a single frequency in ducts, like those produced by a fan's blade-passage frequency.

As calculated in Sect. 8.5.1, the series combination of an inertance and a compliance can have a vanishingly small input acoustical impedance when X_C and X_L cancel each other at the Helmholtz frequency, ω_o. If a Helmholtz resonator is attached to a duct as a side branch, shown schematically in Fig. 10.16, all of the incident volume velocity is diverted to the branch leaving nothing to produce a transmitted pressure at the Helmholtz frequency through the duct beyond the branch to the right of the junction.

As shown in Fig. 10.16, a Helmholtz resonator that combines a compliance with internal volume, V, and a neck of cross-sectional area, A_H, with an effective length (see Sect. 8.5.2), L_{eff}, is connected to a duct of otherwise uniform cross-sectional area, A. This situation can be incorporated into Eq. (10.109) by letting N = 2, with $Y_i = Y_1 = Y_t = R_{ac}^{-1} = A/\rho_m c$ and $\mathbf{Y_2} = 1/jX_H$ where$X_H = X_L + X_C = \omega L - (1/\omega C)$ and $\omega_o = 1/\sqrt{LC}$.

$$X_H = \omega L - \frac{1}{\omega C} = \omega L\left(1 - \frac{\omega_o^2}{\omega^2}\right) = \omega_o L\left(\frac{\omega}{\omega_o} - \frac{\omega_o}{\omega}\right) \tag{10.111}$$

Substitution into Eq. (10.109) provides the power transmission coefficient.

$$\begin{aligned} T_{\Pi,1} &= \frac{4Y_iY_1}{|Y_i + Y_1 + \mathbf{Y}_2|^2} = \frac{4Y_i^2}{\left|2Y_i + \frac{1}{jX_H}\right|^2} \\ &= \frac{1}{1 + \frac{\overset{ac}{R}}{4X_H^2}} = \frac{1}{1 + \frac{1}{\frac{4\omega_o^2L^2}{R_{ac}^2}\left(\frac{\omega}{\omega_o} - \frac{\omega_o}{\omega}\right)^2}} \end{aligned} \tag{10.112}$$

Introduction of an exponential time constant, $\tau_{L/R} = L/R_{ac}$, can simplify and symmetrize the expression for the transmission coefficient.

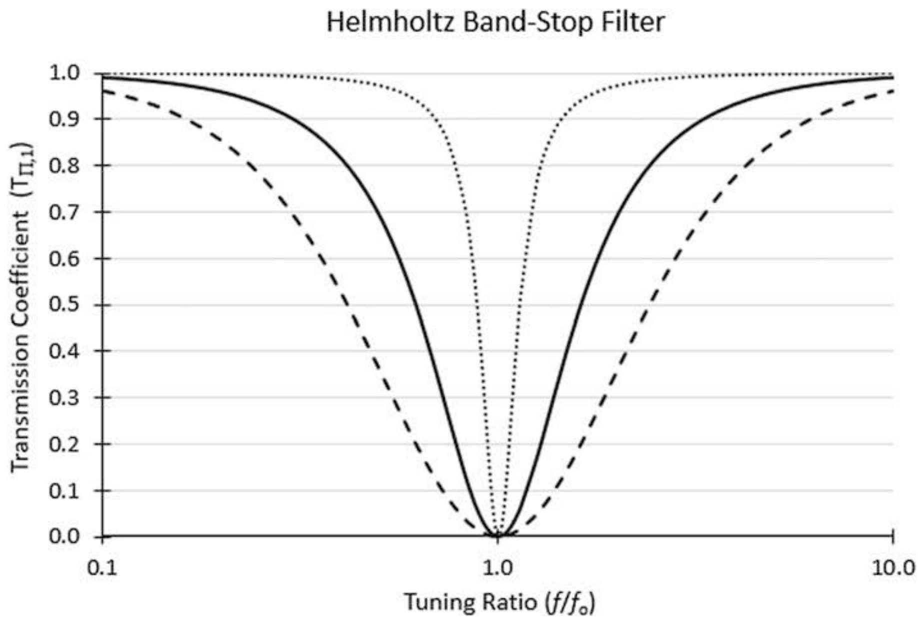

Fig. 10.17 Power transmission coefficient, $T_{\Pi,1}$, for a duct with a Helmholtz resonator as a side branch. The *solid line* corresponds to$(2\omega_o\tau_{L/R}) = 1.0$, with the *dashed line* for $(2\omega_o\tau_{L/R}) = 0.5$ and the *dotted line* for $(2\omega_o\tau_{L/R}) = 4.0$

$$T_{\Pi,1} = \frac{1}{1 + \frac{1}{(2\omega_o\tau_{L/R})^2}\left(\frac{\omega}{\omega_o} - \frac{\omega_o}{\omega}\right)^{-2}} = \frac{(2\omega_o\tau_{L/R})^2\left(\frac{\omega}{\omega_o} - \frac{\omega_o}{\omega}\right)^2}{(2\omega_o\tau_{L/R})^2\left(\frac{\omega}{\omega_o} - \frac{\omega_o}{\omega}\right)^2 + 1} \tag{10.113}$$

This transmission coefficient is plotted for three values of the dimensionless product of twice the Helmholtz resonance frequency times the exponential time constant, $0.5 \le (2\omega_o\tau_{L/R}) \le 4.0$, in Fig. 10.17, as a function of the frequency ratio, f/f_o, on a logarithmic axis.

If the frequency is either much lower or much higher than the Helmholtz frequency, then the squared frequency ratio difference term in Eq. (10.113), $[(\omega/\omega_o) - (\omega_o/\omega)]^2$, dominates, and nearly all of the power is transmitted past the branch: $T_\Pi \cong 1$. If $\omega = \omega_o$, then the frequency term in the numerator is zero, so no power is transmitted in the limit that the dissipation in the Helmholtz resonator can be neglected.

At the Helmholtz frequency, ω_o, the energy conservation condition in Eq. (10.110) requires that all of the power be reflected. With the admittance of the Helmholtz resonator at resonance being infinite (in the absence of dissipation), the phase-inverted reflection from the junction is what would be expected since, from the left, the situation would be indistinguishable from the case where $A_t \gg A_i$ in Eq. (10.105).

10.8.3 Stub Tuning

One final *high-pass filter* application can be very useful if steady flow needs to be removed from acoustic propagation through the duct. Sirens can have very high efficiency [62], but they require steady gas flow. That steady flow can be diverted from a duct while allowing the high-amplitude acoustic pressure wave to be transmitted through the duct if a thin membrane is placed across the duct and a vent tube that is one-quarter wavelength long is placed between the siren and the membrane.

If the membrane is sufficiently thin and flexible, the sound will pass through nearly unattenuated (see Sect. 11.1.1). If the "stub" is one-quarter wavelength long, at the siren's frequency, then it will act as a 1:$\pm\infty$ transformer (see Sect. 3.8.1 and Fig. 3.10), so the nearly zero low-frequency acoustical impedance of the open end will present a nearly infinite acoustical impedance at the duct end for sound at the siren's frequency; all the sound goes down the duct, and all the siren's gas flow goes out the stub.

10.9 Quasi-One-Dimensional Propagation (Horns)

Thus far, this chapter has examined propagating plane waves in ducts and standing plane waves in resonators, both having constant cross-sectional areas, A, that are assumed to have linear dimensions that are much smaller that the wavelength of sound, $\sqrt{A} \ll \lambda$. The spatial dependence of such waves has been specified by a single coordinate. In all cases, the evolution of the waves depended only upon the x coordinate, and all of the wave's acoustic variables (i.e., pressure, density, temperature, and particle velocity) have been uniform over planes that are perpendicular to the x axis. This geometry is responsible for the term "plane wave" that we use to designate such behavior.

In fact, the dependence on a single spatial coordinate is not unique to one-dimensional propagation. In Chap. 12, when the radiation of sound in a three-dimensional unbounded fluid medium is analyzed, spherically diverging sound waves are also characterized by a single spatial coordinate, the radial distance, r, from the omnidirectional source's acoustic center. In the nondissipative limit, energy is conserved so that the pressure amplitude at a distance, r, is inversely proportional to that distance. The integral of the time-averaged intensity, $\langle I \rangle_t = \langle [p^2(r,\, t)] \rangle_t / 2\rho_m c$, over any spherical surface of area, $A(r) = 4\pi r^2$, centered on the source, remains constant.

For such spherically symmetric wave propagation, all fluid particle motion is radial. There would be no fluid motion that would cross the boundary of any cone with its apex centered at the source. For that reason, any conical horn of infinite length, with rigid surfaces, would support identical wave motion within its constant apex angle.[17] This argument should be reminiscent of the analysis of nodes of standing waves on pendula in Sect. 3.6.2, as well as arguments regarding membrane mode shapes that exploited nodal lines and nodal circles to calculate the behavior of those modes in Sect. 6.2.4 and Prob. 2 in Chap. 6 for membrane shapes that are not bounded by a rectangle or circle.

10.9.1 Semi-infinite Exponential Horns

Bolstered by such arguments, it is attractive to extend the analysis of one-dimensional propagation in a duct of uniform cross-sectional area to horns that have a monotonic change in cross-sectional area with distance, $A(x)$, which is a function of only the x coordinate, if we assume that the area changes slowly over distances comparable to the wavelength of the sound wave propagating through the horn.

Long before the development of electroacoustics and before an acoustical theory for horns existed, horns were recognized as an apparatus for concentrating sound energy and for improving the coupling between vibrating surfaces to the surrounding fluid medium. Several (amusing?) historical implementations are shown in Fig. 10.18. In the early days of electroacoustics, when the power

[17] Within the cone, the pressure amplitudes would be larger than those of a spherically spreading wave if the source's volume velocity was the same in both cases. If the cone subtends a solid angle, Ω, then the pressures would be enhanced by a factor of $4\pi/\Omega$, assuming the additional load would not reduce the source's volume velocity.

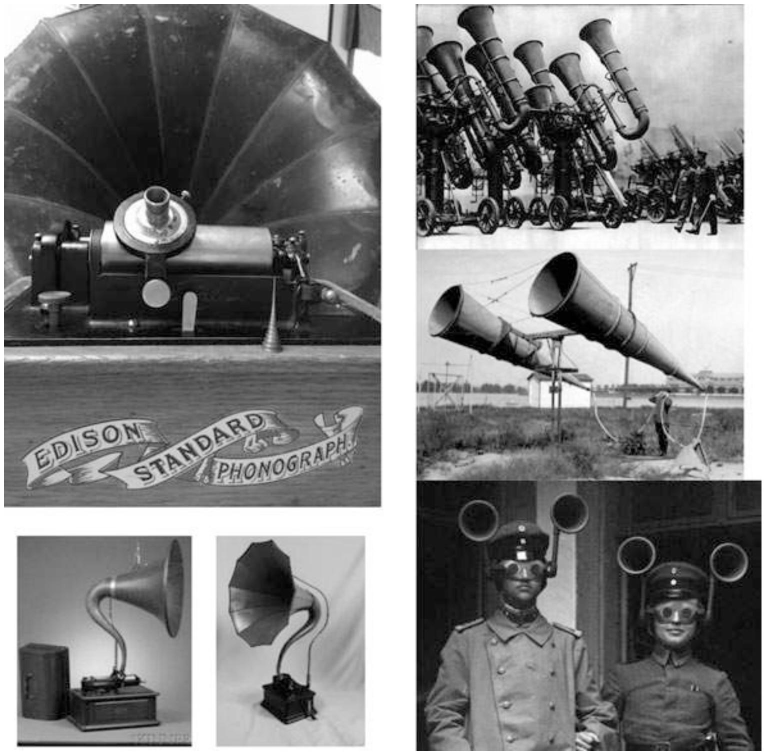

Fig. 10.18 (*Top left*) Two horns from the author's personal collection. The "Triumph" straight horn, located behind the Edison Standard Phonograph, has a 24″ (61 cm) diameter opening that reduces to a ½" (1.3 cm) diameter at the apex for an area ratio of 2300:1. That horn is 36″ (91 cm) long. Placed on that phonograph is a very small solid stepped exponential horn that is 1¾″ (5.5 cm) long that was used by Prof. W. L. Nyborg to concentrate ultrasonic energy for streaming [63] and cellular (biological) cavitation experiments in fluids (courtesy of Prof. Richard Packard, a former Nyborg master's student). (*Bottom left*) Two curved Edison phonograph horns. (*Top right*) A horn-based aircraft detection and localization system used by the Imperial Japanese Army in 1936, known as the "Wartuba." (*Center right*) Another aircraft system used for stereo localization, photographed at Bolling Air Force Base, near Washington, DC, in 1921. (*Bottom right*) Personal listening device worn by German soldiers in 1917 that is combined with binoculars so that the aircraft can be seen as well as heard

available using vacuum tube audio amplifiers was limited and motion pictures added sound tracks, horns were required to increase the efficiency of loudspeakers to ensonify the large volumes of theaters and auditoria [64].

To formulate a quasi-one-dimensional model of horns, it is necessary to modify the linearized one-dimensional continuity Eq. (10.1) that was derived in Sect. 8.2.1, based on the geometry specified in Fig. 8.2. In analogy with Eqs. (8.10)–(8.12), the change in the mass of fluid within a differential slab of volume, d$V = A(x)$ dx, will be due to the difference in mass of fluid that enters $A(x)$ with velocity along the x direction of $u(x)$ and the mass that exits through an area, $A(x +$ d$x)$, with velocity, $u(x +$ d$x)$, as shown in Fig. 10.19.

$$\begin{gathered}\dot{m} = (\rho_m uA)_x - (\rho_m uA)_{x+dx} = -\left(\frac{\partial(\rho_m uA)}{\partial x}\right)_x dx \\ \frac{\partial \rho_1}{\partial t} + \frac{\rho_m}{A(x)}\left(\frac{\partial(u_1 A)}{\partial x}\right) = \frac{\partial \rho_1}{\partial t} + \frac{\rho_m u_1}{A(x)}\left(\frac{\partial A}{\partial x}\right) + \rho_m\left(\frac{\partial u_1}{\partial x}\right) = 0\end{gathered} \tag{10.114}$$

The linearized Euler Eq. (10.2) remains unchanged. The linearized equation of state (10.4) still relates adiabatic pressure and density changes, but the square of the sound speed here will now be subscripted,

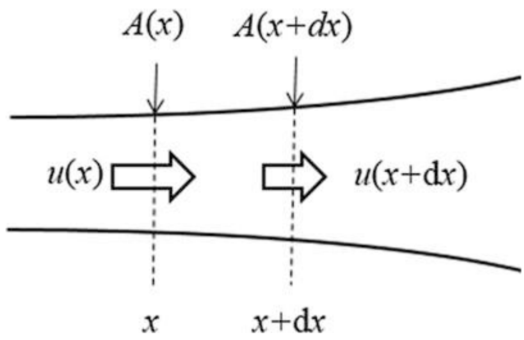

Fig. 10.19 This geometry can be used for the derivation of a continuity equation that applies to a duct of continuously varying cross-sectional area, $A(x)$. To conserve volume velocity, the x-component of the fluid particle velocity, $u(x)$, must decrease as the cross-sectional area of the horn increases

c_o, to remind us that it is the equilibrium thermodynamic sound speed, $c_o^2 = (\partial p/\partial \rho)_s$, as distinguished from the phase speed, $c_{ph} = \omega/k$, since those two speeds will not be the same, as they were for the truly one-dimensional problem in Eq. (10.19).

$$\rho_m \frac{\partial u}{\partial t} + \frac{\partial p}{\partial x} = \rho_m \frac{\partial u}{\partial t} + c_o^2 \frac{\partial \rho}{\partial x} = 0 \tag{10.115}$$

The second term in the continuity Eq. (10.114) involves the derivative, $(1/A)(\partial A/\partial x) = \partial \ln(A)/\partial x$ (see Sect. 1.1.3), suggesting that a particularly simple solution to these coupled first-order differential equations might exist if the cross-sectional area of the horn varied as an exponential function of distance, x, along the horn's axis.

$$A(x) = A_o e^{2x/h} \tag{10.116}$$

A *flare constant*, h, has been introduced to scale the rate of change in area from its initial area, $A_o \equiv A(0)$. Using the same nondissipative argument for energy conservation made in the previous discussion of the conical horn, the amplitude of the acoustic pressure variation along the horn's axis must also decrease exponentially since the product, $p^2(x)A(x)$, must remain constant. Since the horn is semi-infinite, we need only to consider wave motion that propagates in the $+x$ direction.

$$p_1(x,t) = \Re e\left[\widehat{\mathbf{p}}_{\mathbf{o}} e^{-x/h} e^{\,j(\omega t - \kappa x)}\right] \ \text{and}\, \rho_1(x,t) = \Re e\left[\frac{\widehat{\mathbf{p}}_{\mathbf{o}}}{c_o^2} e^{-x/h} e^{\,j(\omega t - \kappa x)}\right] \tag{10.117}$$

Our symbol for the wavenumber, κ, is chosen to remind ourselves that it has yet to be determined. The initial acoustic pressure phasor at the throat of the horn is $\widehat{\mathbf{p}}_{\mathbf{o}}$.

Substitution of Eqs. (10.116) and (10.117) into the coupled differential Eqs. (10.114) and (10.115) allows them to be converted to coupled algebraic equations.

$$\begin{aligned} j\omega\rho_m \widehat{\mathbf{u}} - c_o^2\left(\frac{1}{h} + j\kappa\right)\widehat{\boldsymbol{\rho}} &= 0 \\ \rho_m\left[\frac{2}{h} - \frac{1}{h} - j\kappa\right]\widehat{\mathbf{u}} + j\omega\widehat{\boldsymbol{\rho}} &= 0 \end{aligned} \tag{10.118}$$

As before, when seeking the dispersion relation, like that in Eq. (10.19), the determinant of the coefficients of the acoustic field variables, $\widehat{\boldsymbol{\rho}}$ and $\widehat{\mathbf{u}}$, must vanish if nontrivial solutions to Eq. (10.118) exist.

$$\begin{vmatrix} j\omega\rho_m & -\dfrac{c_o^2}{h}(1 + j\kappa h) \\ \dfrac{\rho_m}{h}(1 - j\kappa h) & j\omega \end{vmatrix} = 0 \tag{10.119}$$

We now can construct the necessary dispersion relation between wavenumber, κ, and frequency, ω.

$$\omega^2 = \frac{c_o^2}{h^2} + c_o^2\kappa^2 \quad \Rightarrow \quad \kappa = \pm\frac{\omega}{c_o}\sqrt{1 - \frac{c_o^2}{(\omega h)^2}} \Rightarrow \quad c_{ph} = \frac{\omega}{\kappa} = \frac{c_o}{\sqrt{1 - \frac{\frac{o}{c}}{(\omega h)^2}}} \tag{10.120}$$

It is clear from Eq. (10.120) that the solution no longer corresponds to wave motion for frequencies below a cut-off frequency, $\omega_{co} = 2\pi f_{co} = c_o/h$. The phase speed, c_{ph}, can be re-written in terms of the ratio of that cut-off frequency, ω_{co}, to the drive frequency, ω.

$$c_{ph} \equiv \frac{\omega}{\kappa} = \frac{c_o}{\sqrt{1 - \frac{\omega_{co}^2}{\omega^2}}} = \frac{c_o}{\sqrt{1 - \frac{f_{co}^2}{f^2}}} \quad \text{with} \quad \omega_{co} = 2\pi f_{co} = \frac{c_o}{h} \tag{10.121}$$

When κ becomes imaginary, the acoustic pressure in Eq. (10.117) decays exponentially, and the disturbance becomes more localized at the apex (throat) of the horn as the frequency decreases below ω_{co}. For an infinite exponential horn in air that changes its diameter by a factor of $e = 2.72$ over 1 m (i.e., $h = 1.0$ m), the cut-off frequency, $f_{co} \cong 55$ Hz.

We also neglected dissipation, so the transmitted power is independent of distance. That constant transmitted power can be calculated at the horn's apex by using Euler's Eq. (10.115) and Eq. (10.117) to calculate the gas particle velocity, $\hat{\mathbf{u}}(0)$, and the associated volume velocity, $\hat{\mathbf{U}}(0) = A(0)\hat{\mathbf{u}}(0)$.

$$\hat{\mathbf{U}}(0) = \hat{\mathbf{u}}A_o = \frac{A_o}{\rho_m c}\left[\sqrt{1 - \left(\frac{f_{co}}{f}\right)^2} - j\left(\frac{f_{co}}{f}\right)\right]\hat{\mathbf{p}}(0) \;\text{ if } f > f_{co} \tag{10.122}$$

The transmitted power, $\langle\Pi\rangle_t$, depends on the time-averaged product of pressure and volume velocity (see Sect. 1.5.4).

$$\langle\Pi\rangle_t = \frac{1}{2}\Re e\left[\hat{\mathbf{p}}(0)\hat{\mathbf{U}}^*(0)\right] = \frac{\hat{\mathbf{p}}(0)}{2}\frac{A(0)\hat{\mathbf{p}}(0)}{\rho_m c_o}\sqrt{1 - \left(\frac{f_{co}}{f}\right)^2} \text{for} f > f_{co} \tag{10.123}$$

Using Eq. (10.122), the magnitude of the volume velocity at the apex, $\left|\hat{\mathbf{U}}(0)\right|$, can be used to simplify Eq. (10.123) and compare the time-averaged power radiated down the horn to the power radiated by a simple source generating a spherically spreading wave due to a volume velocity at the surface of a spherical-pulsating source, $\hat{\mathbf{U}}(a)$, given in Eq. 12.24.

$$\left|\hat{\mathbf{U}}(0)\right| = \frac{\hat{\mathbf{p}}(0)A(0)}{\rho_m c_o}\left[\left(\sqrt{1 - \frac{f_{co}^2}{f^2}}\right)^2 + \left(\frac{f_{co}^2}{f^2}\right)^2\right]^{½} = \frac{\hat{\mathbf{p}}(0)A(0)}{\rho_m c_o} \tag{10.124}$$

$$\langle\Pi\rangle_t = \frac{1}{2}\frac{\rho_m c_o}{A(0)}\left|\hat{\mathbf{U}}(0)\right|^2\sqrt{1 - \frac{f_{co}^2}{f^2}} \tag{10.125}$$

For a spherical source radiating in an infinite three-dimensional fluid, the time-averaged power can be expressed in a similar form that excludes the frequency dependence in the square root and substitutesλ^2/π for the horn's cross-sectional area at its apex, $A(0)$.

$$\langle\Pi\rangle_t = \frac{1}{2}\frac{\rho_m c_o}{(\lambda^2/\pi)}|\mathbf{U}(a)|^2 \tag{10.126}$$

This result shows that the horn can act as a transformer to increase the power radiated by a physically compact source of volume velocity above ω_{co} since $A(0) \ll \lambda^2/\pi$. This is the reason that

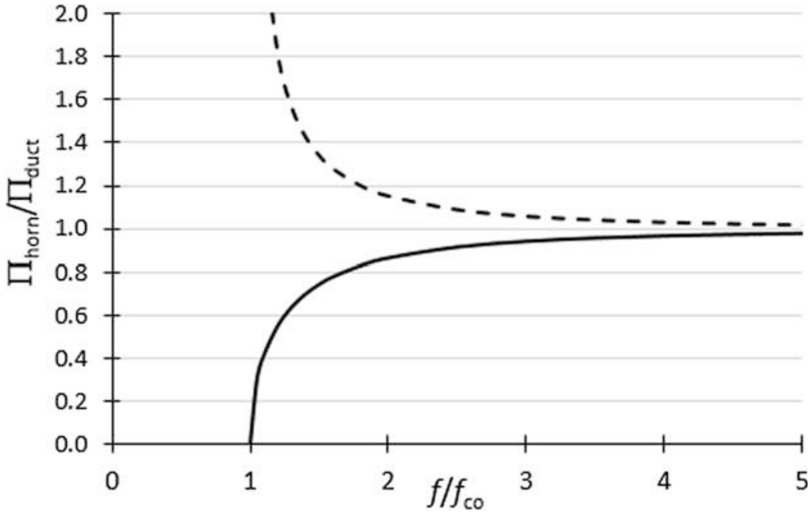

Fig. 10.20 The relative power transmission coefficient for infinitely long exponential (*solid*) and catenoidal (*dashed*) horns. Π_{horn} is compared to the power transmitted through a duct, Π_{duct}, of the same initial cross-sectional area, $A(0) = A_{pist}$, as a function of the ratio of the source's frequency to the cut-off frequency of the horn, f/f_{co}

horns are used routinely to improve the radiation efficiency of pistons with diameters that are much smaller than the wavelength of the sound they must produce. Since the propagation is reversible, it is also the reason that the horns, like those shown in Fig. 10.22 (right), were used to concentrate sound energy and deliver it to the ear of a hearing-impaired listener with increased amplitude (i.e., the "ear trumpet").

The power transmitted by a piston down a duct, $\langle \Pi_{duct} \rangle_t = (½)\rho_m c_o \left| \widehat{\mathbf{U}}(0) \right|^2$, with the same cross-sectional area as the piston's effective area, A_{pist}, can be compared to the power transmitted down an infinitely long exponential horn with the same initial area, $A_{pist} = A(0)$. As shown in Fig. 10.23, that ratio approaches unity monotonically for frequencies above cut-off (Fig. 10.20).

These results assume that a one-dimensional description of the horn used to derive the continuity Eq. (10.114) provides a sufficiently good approximation to the acoustic behavior of the medium exhibiting the wave-like behavior within the horn. Thus far, the conditions under which such an approximation might be valid have not been addressed. The surfaces of constant phase for a geometry like that depicted in Fig. 10.22 must intersect the horn's surface at a right angle. If the horn's cross-sectional area changes too rapidly, then the wave fronts will not "cling" to the horn's surface [65]. For an infinite horn, the only physical parameters that characterize its geometry are the initial area, $A(0)$, and its flare constant, h. For this quasi-one-dimensional analysis to be accurate, $r_o \cong \sqrt{A(0)} \ll h$, where r_o is the effective radius of the horn's throat at $x = 0$.

10.9.2 Salmon Horns*

As shown in Sect. 10.2, it is also possible to combine the first-order continuity and Euler equations with the equation of state to produce a wave equation for a horn in the quasi-one-dimensional limit that is a homogeneous second-order partial differential equation.

$$\frac{1}{A}\frac{\partial}{\partial x}\left(A\frac{\partial p(x,t)}{\partial x}\right) - \frac{1}{c_o^2}\frac{\partial^2 p(x,t)}{\partial t^2} = 0 \tag{10.127}$$

Our investigation of the exponential horn was motivated by the fact that $(1/A)(\partial A/\partial x) = \partial \ln(A)/\partial x$ equaled a constant for the exponential change in cross-section that was assumed in Eq. (10.116).

A more general family of solutions was suggested by Salmon [66] who required that the entire dependence of Eq. (10.127) on area be a positive constant.[18]

$$\frac{\partial^2\left(p\sqrt{A}\right)}{\partial x^2}-\left(\frac{\omega}{c_o}\right)^2\left(1-\beta^2\right)\left(p\sqrt{A}\right)=0 \text{ where } \beta^2=1-\left(\frac{\omega_{co}}{\omega}\right)^2 \tag{10.128}$$

Solutions to this time-independent Helmholtz equation are parameterized by two constants: the flare constant, h, and the constant, C, which controls the superposition of the two solutions to that second-order differential equation.

$$\begin{gathered} A(x)=A(0)\left[\cosh\left(\frac{x}{h}\right)+C\sinh\left(\frac{x}{h}\right)\right]^2 \\ \text{and } p_1(x,t)\propto \Re e\left[\frac{\widehat{\mathbf{p}}(0)}{\sqrt{A(x)}}e^{\,j(\omega t-\kappa x)}\right] \end{gathered} \tag{10.129}$$

As for any linear solution, the amplitude, $\widehat{\mathbf{p}}(0)$, is arbitrary until the initial conditions at $x=0$ are specified. For $C=1$, the exponential horn is recovered. With $C=0$, the horn's shape is catenoidal. In the limit that $h\to\infty$ and $C=(h/x_o)$, the horn's shape is conical with an apex angle, $\phi=\tan^{-1}(r_o/x_o)$, for the apex of the cone located at $x=0<x_o$ and an initial area, $A(0)=\pi r_o^2$, assuming the cone has circular cross-sections. For $0<C<\sqrt{2}$, the relative transmission coefficient, $\Pi_{\text{horn}}/\Pi_{\text{duct}}$, plotted in Fig. 10.23, has a maximum at $(f/f_{\text{co}})_{\max}$. Under that condition, with $(f/f_{\text{co}}) > (f/f_{\text{co}})_{\max}$, the relative power transmission coefficient asymptotically approaches $\Pi_{\text{horn}}/\Pi_{\text{duct}}=1$.

$$\left(\frac{\Pi_{horn}}{\Pi_{duct}}\right)_{\max}=\frac{1}{2C\sqrt{1-C^2}} \text{ for } 0<C<\sqrt{2} \text{ at } \left(\frac{f}{f_{co}}\right)_{\max}=\sqrt{\frac{1-C^2}{1-2C^2}} \tag{10.130}$$

For $C=0.5$, $(\Pi_{horn}/\Pi_{duct})_{\max}=1.15$ at $(f/f_{co})_{\max}=1.22$, providing fairly uniform transmission above the cut-off frequency.

10.9.3 Horns of Finite Length*

Our analyses of horns of infinite length (i.e., no reflected wave) have introduced several useful concepts, particularly the existence of the low-frequency cut-off, ω_{co}, but real horns are never infinitely long. Finite-length horns fall into two general categories: (*i*) The horns that terminate musical instruments depend on reflection from the "bell" to define the standing wave that determines the instrument's pitch. (*ii*) The horns used to couple sources to the surrounding space try to avoid resonances that reduce the uniformity of radiated sound as a function of frequency above cut-off.[19]

Horns of finite length will exhibit resonances at frequencies above cut-off, at least until the radiation impedance at the bell is sufficient to couple most of the energy out of the horn, thus nearly eliminating

[18] If β^2 is negative, then there is a family of sinusoidal horn shapes (e.g., a globe terminated in a cusp) that describe the shape of the bell of the flute commonly associated with Indian snake charmers or the English horn, first used in the by Rossini, in 1829, in the opera, *William Tell*. [See B. N. Nagarkar and R. D. Finch, "Sinusoidal horns," J. Acoust. Soc. Am. **50**(1) 23–31 (1971).]

[19] A nonuniform power transmission coefficient does not necessarily reduce the value of guided-wave enhancement of the coupling to an electrodynamic transducer, since human perception of low-frequency musical content is not particularly sensitive to such a nonuniform response. The best example of such a psycho-acoustic tolerance may be the success of the Bose Wave™ radio that employs a long serpentine duct that is driven by the rear of the forward-radiating speakers as shown in US Pat. No. 6,278,789 (Aug. 21, 2001).

the back-reflected wave from the bell. Although an exact calculation will be postponed until Sect. 12.8.3, a reasonable rule-of-thumb is that the resonances will be suppressed once the circumference of the bell exceeds the wavelength of the sound.

At reasonably high frequencies, horn-coupled loudspeakers can both be efficient and provide fairly uniform radiation over a significant range of frequencies. Above 1.0 kHz, $\lambda < 35$ cm, so the bell of a horn that is only 10 cm in diameter will provide acceptable performance (see Problem 17). The engineering design of such horn-coupled electrodynamic loudspeakers (commonly called compression drivers) is beyond the scope of this treatment and can involve considerations of directionality, the compliance of the space between the driver's diaphragm and the start of the horn, as well as the nonlinear distortion [67, 68] that can be produced due to the very high acoustic pressures near the throat. Several textbooks with a greater focus on audio engineering provide detailed guidance [69, 70].

Resonances in horns are particularly pronounced at low frequencies. The lowest note on a double bass or an electric bass guitar is usually $E_1 = 41.2$ Hz, based on $A_4 = 440$ Hz. The corner horn shown in Fig. 10.21 has a catenoidal shape with a flare constant, $h = 1.37$ m, selected to make $f_{co} = c_o/2\pi h = 40$ Hz. It is driven by an Axon Model 6S3 direct radiator loudspeaker. The front of that speaker radiates midrange frequencies, and the rear of the speaker drives the horn.

Also shown in Fig. 10.21 (right) is a tweeter for high frequencies with a passive cross-over network attached to the triangular top of the horn. The resonance frequencies and corresponding mode shapes were calculated using a DeltaEC model, shown in Fig. 10.22, that represent the catenoidal horn as eight CONE segments driven at constant voltage by the electrodynamic speaker with parameters listed in the VSPEAKER segment (#1). The bell of the horn is terminated with an OPNBRANCH segment (#11) that simulates radiation loading.

Talk Like an Acoustician

Wave equation	Equal-loudness contours
Dispersion relation	Fletcher-Munson curves
Bulk modulus	Sound level meter
Adiabatic compressibility	Crest factor
Specific acoustic impedance	Acoustic transfer impedance
Characteristic impedance	Principle of reciprocity
Acoustical impedance	Reciprocity calibration
Mechanical impedance	Level repulsion
Rayl	Wakeland number
Acoustic intensity	Acoustic admittance
Reference intensity	Amplitude reflection coefficient
Reference sound pressure	Amplitude transmission coefficient
Coherent sound sources	Power transmission coefficient
Linearized Euler equation	Band-stop filter
Linearized Continuity equation	Low-pass filter
Homogeneous	High-pass filter
Isotropic	Exponential horn
Conservation equation	Catenoidal horn
	Flare constant
	Cut-off frequency

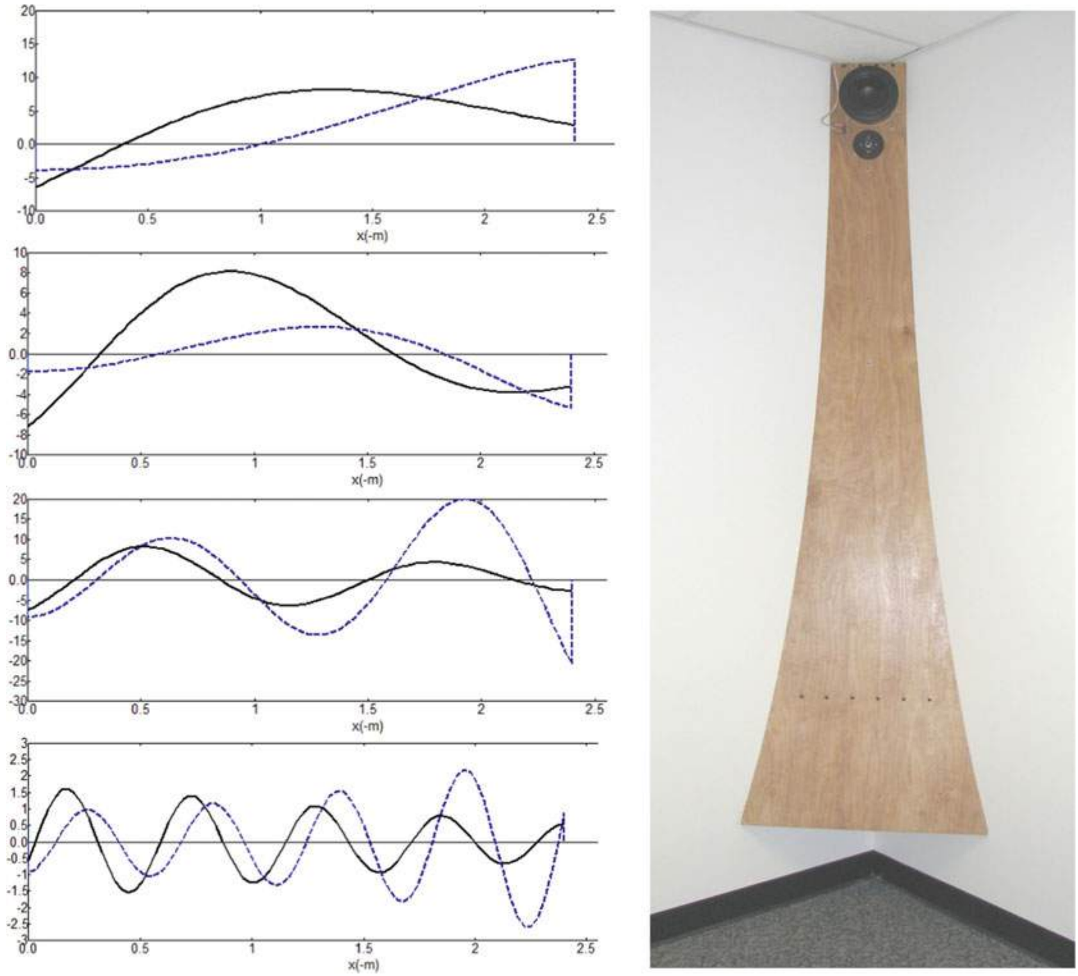

Fig. 10.21 (*Right*) Corner horn (this horn design, suggested by I. Rudnick, is particularly simple because it involves cutting a single sheet of plywood with a hand-held circular saw that has its blade set at 45°, creating a smooth cut that will produce a leak-tight seal against the walls of a room. Even though the plywood is fairly thin (3/8″ ≅ 9.5 mm), it produces a rigid boundary since it is curved initially along one axis making it very stiff against bending along an orthogonal direction. The plywood is held against the walls with a single turnbuckle anchored in the corner. The place where the turnbuckle should be attached to the plywood is found by applying force to one location that pushes the plywood smoothly against the wall. A horizontal "stringer" is then screwed and glued to the plywood to accept the hook. The stringer's position is visible in Fig. 10.21 due to the six flat-head screws that can be seen forming a line about one-sixth of the way above the bell.) created by a single sheet of plywood that is cut to produce a catenoidal change in cross-sectional area from 173 cm^2 at the top to 0.152 m^2 at the opening over a length of 8′ ≅ 2.4 m. (*Left*) Plots of the acoustic pressure (*solid black line*) that is in-phase with the volume velocity (*dashed blue line*) within the horn created when the speaker, at the throat, is driven with an electrical input of 10 V_{pk} = 7.07 V_{ac}. At $x = 0$, the volume velocity is equal to that produced by the rear of the loudspeaker. From top to bottom: $f_1 = 77$ Hz, $f_2 = 139$ Hz, $f_3 = 204$ Hz, and $f_8 = 618$ Hz

Exercises

1. **Traveling wave acoustic field variables.** Express the space and time dependence, as well as the amplitudes, for the following acoustic field variables if $p_1(x,t) = \Re e\left[\widehat{\mathbf{p}} e^{j(\omega t - kx)}\right]$.
   (a) *Acoustic density*, $\rho_1(x, t)$

```
CatenoidSpeaker(2) Student Area Catenoid
   0 BEGIN        Initial
    1 VSPEAKER    Axon 6S3
                      0.1247 a Area    m^2                 67.841 A |p|     Pa
                      5.6300 b R       ohms                145.07 B Ph(p)   deg
                  2.6000E-04 c L       H               1.1539E-02 C |U|     m^3/s
                      5.7200 d BLProd T-m                 145.07 D Ph(U)   deg
                  1.2000E-02 e M       kg                  8.2775 E Htot    W
                      1329.0 f K       N/m                 0.3914 F Edot    W
                      1.0800 g Rm      N-s/m               8.2775 G WorkIn  W
                      10.000 h |V|     V                   10.000 H Volts   V
                                                           1.6733 I Amps    A
                                                           8.3511 J Ph(V/I) deg
                                                       1.1544E-02 K |Ux|    m^3/s
ideal            Solid type                                145.07 L Ph(-Ux) deg
    2 RPN             Phase of Pressure and Volume Velocity at Throat
  This is the criterion for a coupled horn-loudspeaker resonance
Targ                  0.0000 a G or T                  -1.0976E-09 A Degrees
1B 1D -
    3 CONE            First Segment
    4 CONE            Second
    Same    3d 1.8200E-02 a AreaI   m^2                 116.66 A |p|     Pa
    Same    3e     0.6140 b PerimI  m                   83.088 B Ph(p)   deg
                   0.3000 c Length  m               1.1465E-02 C |U|     m^3/s
               2.0800E-02 d AreaF   m^2                 138.60 D Ph(U)   deg
                   0.6580 e PerimF  m                   8.2775 E Htot    W
Master-Slave Links                                     0.37868 F Edot    W
Optional Parameters
ideal            Solid type
    5 CONE            Three
    6 CONE            Four
    7 CONE            Five
    8 CONE            Six
    9 CONE            Seven
   10 CONE            Eight
    Same    9d     0.1012 a AreaI   m^2                 92.985 A |p|     Pa
    Same    9e     1.4500 b PerimI  m                   53.844 B Ph(p)   deg
    Same    3c     0.3000 c Length  m               9.2681E-03 C |U|     m^3/s
                   0.1517 d AreaF   m^2                 19.200 D Ph(U)   deg
                   1.7760 e PerimF  m                   8.2775 E Htot    W
Master-Slave Links                                      0.3545 F Edot    W
Optional Parameters
ideal            Solid type
   11 OPNBRANCH   Radiation Load
   12 RPN         Wavenumber
   13 RPN         Radiated Power
   14 RPN         Power = Press * Volume Velocity / 2
   15 HARDEND     OPNBRANCH is the only "exit"
```

Fig. 10.22 Screenshot of a DeltaEC model for the corner horn shown in Fig. 10.21 (right) that calculated the resonance frequencies and produced the mode shapes in Fig. 10.21 (left). The resonance condition was imposed by the RPN target (Seg. #2) that seeks a condition where the volume velocity and pressure are in-phase at the horn's throat

(b) *Acoustic particle velocity*, $v_1(x, t)$
(c) *Kinetic energy density*, (KE)
(d) *Potential energy density*, (PE)
(e) *Time-averaged intensity*, $\langle I \rangle_t$

2. **Standing wave acoustic field variables.** Express the space and time dependence, as well as the amplitudes, for the following acoustic field variables if $p_1(x,t) = \Re\mathrm{e}[\widehat{\mathbf{p}} \cos(kx) e^{j\omega t}]$.
   (a) *Acoustic density*, $\rho_1(x, t)$
   (b) *Acoustic particle velocity*, $v_1(x, t)$
   (c) *Kinetic energy density*, (KE)
   (d) *Potential energy density*, (PE)
   (e) *Time-averaged intensity*, $\langle I \rangle_t$
3. **Concert A$_4$.** A sound wave in dry air at $T_m = 20$ °C, with frequency, $f = 440$ Hz, has a sound pressure level of 76.0 dB, *re:* 20 μPa$_{rms}$. Determine the following characteristics of that tone.
   (a) *Time-averaged intensity*, $\langle I \rangle_t$
   (b) *Intensity level*, *re:* 1.0 x 10^{-12} W/m^2
   (c) *Peak particle speed*, v_1
   (d) *Peak-to-peak particle displacement*, $2x_1$
   (e) *Peak acoustic temperature change*, T_1
4. **Speed of shallow water gravity waves (surf).** The Euler and continuity equations for an incompressible fluid ($\rho =$ constant), with a free surface in a gravitational field, having a gravitational acceleration, g, are provided below. (For this problem, let $g = 9.8$ m/s^2.) The equilibrium depth of the fluid is h_o. Consider small-amplitude traveling surface waves $\left(\left|\widehat{\mathbf{h}}\right| \ll h_o\right)$ propagating in the +x direction: $h(x,t) = h_o + \left|\widehat{\mathbf{h}}\right| \sin(\omega t - kx)$.

$$\frac{\partial h_1(x,t)}{\partial t} + h_o \frac{\partial v_1(x,t)}{\partial x} = 0 \tag{10.131}$$

$$\frac{\partial v_1(x,t)}{\partial t} = -\frac{1}{\rho_m}\frac{\partial}{\partial x}[\rho_m g h_1(x,t)] = -g\frac{\partial h_1(x,t)}{\partial x} \tag{10.132}$$

   (a) *Which equation is which?* One of the above equations is the linearized continuity equation for this system, and the other is the linearized Euler equation. Identify which equation represents continuity and which is Euler.
   (b) *Propagation speed*. Use Eqs. (10.131) and (10.132) to derive an expression for the propagation speed (not the horizontal particle velocity v_1) of a small-amplitude surface wave. Does this agree with the results based on similitude that were calculated in Chap. 1, Problem 8d?
   (c) *Small-amplitude approximation*. Under what conditions is the vertical velocity of the surface, dh_1/dt, small compared to the horizontal particle speed, v_1? What is required so that $(dh_1/dt)/v_1 \ll 1$?
   (d) *The Boxing Day tsunami*. On 26 December 2004, at 00:58:53 UTC, there was a magnitude 9.0 earthquake off of the west coast of Northern Sumatra (3.29 N 95.94E) which launched a tsunami (tidal wave). Seven hours later, the wave reached the shores of Somalia (2.03 N 45.35E), a distance of approximately 5600 km across the Indian Ocean from the deadly quake's epicenter. Assuming that the tsunami was a "shallow water gravity wave" (which it was!), determine the average depth of the Indian Ocean along the nearly equatorial path from the epicenter to the coast of Somalia.

5. **Addition of three incoherent sound sources.** At a particular position in a shop, three machines produce individual sound pressure levels of 90, 93, and 95 dB_{SPL}, all referenced to 20 μPa_{rms}. Determine the total sound pressure level if all of the machines are running simultaneously. Assume each noise source is statistically independent of all of the others so that their powers (not pressures) are combined. Report your result in dB *re:* 20 μPa_{rms}.
6. **dB addition.** A noise is generated by 80 pure tones of different frequencies but identical power. At locations equidistant from all sources, each individual tone has a sound pressure level of 60 dB re: 20 μPa_{rms}. Determine the sound pressure level at that location if all 80 sources are radiating simultaneously.
7. **Underwater sound intensity reference level.** The sound pressure reference level currently used for sound in water is $R_{ref}\,(H_2O) = 1.0\ \mu Pa_{rms}$. What would be the corresponding sound intensity reference level in water, $I_{ref}\,(H_2O)$?
8. **Cavitation threshold.** The motion of the face of an underwater (SONAR) transducer toward the water causes a local compression, and when it moves away a half-cycle later, it creates local suction. If the suction pressure creates a tension in the fluid that exceeds the cavitation threshold, it "tears" a hole in the medium, producing bubbles.
   (a) *Hydrostatic pressure.* If the transducer is located 50 m below the surface, what is the static water pressure, p_m, remembering that the pressure on the surface is one atmosphere, $p_o = 101.3$ kPa.
   (b) *Cavitation level*. What is the intensity level, *re:* 1 μPa_{rms}, of a pressure wave that would create a peak negative pressure, $|-\widehat{\mathbf{p}}| = p_m$, and cause an instantaneous rupture in the water?
9. **Climate change.** Table 10.1 shows standard dry air having a CO_2 mole fraction of 314 ppm. As of June 2020, the mole fraction was found to have increased to 415 ppm [71]. How much does this change the sound speed in dry air?
   (a) *Approximate sound speed change*. Get an approximate result by ignoring the change in γ.
   (b) *Polytropic coefficient*. Use $\gamma_{air} = 1.4$ and $\gamma_{CO2} = 1.3$. Will the change in sound speed due to the change in γ_{mix} have the same sign as that due to the change in M_{mix}?
   (c) *Sound speed change*. Use Eq. (10.25) to calculate the change in γ, and use that result to obtain a more accurate result for the change in sound speed.
10. ***Schlagwetter-pfeife*.** The presence of methane in mines presents a significant hazard due to the possibility of underground explosions. In the late-1800s, one of the world's most famous industrial chemists, Fritz Haber,[20] invented the "methane whistle" to determine the presence of hydrogen or methane in air extracted from underground mines [72]. By 1888, these methane whistles also began to appear in the United Kingdom [73]. Air was pumped from the mine out through one whistle, and fresh air was pumped through the other. Assume the whistles were identical and in good thermal contact, so both surface air and the sub-surface air passing through the whistles were at the same temperature. Determine the concentration (mole fraction) of methane (CH_4) in the mine air if the air whistle had a frequency of 440 Hz and the pair of whistles produced 10 beats per second at 20 °C.
11. **Sonic hydrogen detector design.** Hydrogen gas is very flammable in air with the flammability ranging between mole fractions of 4% and 74%. With the possible future advent of hydrogen-powered vehicles, the National Transportation Safety Board has asked you to design an acoustic resonator that will use the change in frequency caused by a change in sound speed to alert occupants of a home if the concentration of hydrogen gas in their garage exceeds a mole fraction

[20] Fritz Haber was also one of the world's most infamous chemists, having developed the gas that was used to murder prisoners in the Nazi death camps.

of 1.5%. For the purposes of this problem, you may take the mean molecular mass of air to be $M_{air} = 29.0$ gm/mole and the mean molecular mass of hydrogen to be $M_{hydrogen} = 2.0$ gm/mole. Both gases can be treated as consisting primarily of diatomic molecules, and the temperature in the garage can be taken as 10 °C.

(a) *Frequency shift*. What is the relative change in frequency, $\delta f/f_o$, in percent, that would correspond to the addition of 1.5% of hydrogen to previously pure dry air, assuming that the resonator's frequency was f_o before the hydrogen was injected into the resonator?

(b) *Temperature effects*. How much must the temperature of the garage be increased to raise the resonator's frequency by the same amount as you calculated in part (a) if there were no hydrogen gas present in the air?

12. **Bulk modulus.** Eq. (10.20) expresses the adiabatic bulk modulus, $B_s \equiv -V(\partial p/\partial V)_s$, in terms of the square of the adiabatic sound speed, $c^2 = (\partial p/\partial \rho)_s$. Show that Eq. (10.133) is correct.

$$\frac{1}{\rho}\left(\frac{\partial p}{\partial\left({}^{1}\!/\!_{\rho}\right)}\right)_s = -\rho\left(\frac{\partial p}{\partial \rho}\right)_s \tag{10.133}$$

13. **Slow waves in a water-filled pipe.** Sound speed is determined by a medium's compressibility and its inertia. In this problem, water will provide the inertia, but if the water is contained within a pipe, the distensibility of the pipe will generally produce an increased compressibility since the pipe's walls will stretch.

(a) *Bulk modulus of water*. If the density of water is $\rho_{Water} = 1000$ kg/m^3 and the sound speed in the water is $c_{Water} = 1500$ m/s, what is the value of the bulk modulus of water?

(b) *Effective bulk modulus of a PVC pipe*. Consider a PVC pipe with a mean radius, $a = 8.0$ cm, and a wall thickness, $t = 7.0$ mm. Simple elasticity theory relates the change in the pipe radius, Δr, to the increase of pressure, Δp, within the pipe.

$$\Delta r = \frac{a^2}{tE}\Delta p \tag{10.134}$$

For PVC, the Young's modulus, $E_{PVC} = 3.40 \text{ x } 10^9$ Pa. Consider a short length of this pipe, and calculate the effective bulk modulus by calculating the change in volume, ΔV, of the pipe due to a change in the internal pressure, Δp, within the pipe.

(c) *Wave propagation speed in a water-filled PVC pipe*. If we assume that the water is incompressible (i.e., the bulk modulus of the water is infinite) in comparison to the effective bulk modulus of the PVC pipe, what is the speed of sound propagation for a pressure wave traveling in the water contained within the PVC pipe?

(d) *Effect of the water's compressibility*. In part (a) of this problem, you calculated the bulk modulus of water, and your result should have been substantially less than infinity. Will the water's compressibility increase or decrease the sound propagation speed you calculated in part (c)?

(e) *Effect of the water's compressibility*. Calculate the sound propagation speed due to the water's density and the combined bulk modulus of both the pipe and the water. [Hint: Think of the two moduli as "springs" and ask yourself if those springs add in series or parallel.]

14. **Thermophone** [74]. An array of three sheets of carbon nanotubes are stretched between two electrically conducting wires as shown in Fig. 10.23 [75]. For the purpose of this problem, we can assume that the nanotubes act as an electrical resistance and have neither heat capacity nor volume.

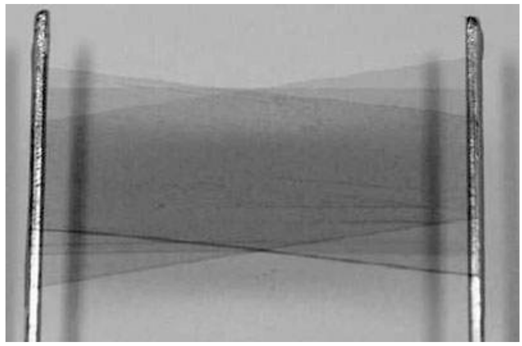

Fig. 10.23 Carbon nanotube sheets that act as an electrical resistance heating element

To test this device, it will be placed in a gas-tight cylindrical cavity with a volume of 2.5 liters = 2.5×10^{-3} m^3. Assume the mean pressure in the cavity $p_m = 101$ kPa, the mean temperature is $T_m = 300$ K, so that $c_{air} = 347$ m/s and $\gamma_{air} = 1.403$. Under those conditions, $\rho_{air} = 1.173$ kg/m^3, the specific heat of the air is $c_p = 1005$ J/kg-K, the viscosity of air is $\mu = 1.85 \times 10^{-5}$ Pa-sec, the air's thermal expansion coefficient at constant pressure is $\beta_p = (T_m)^{-1} = 3.33 \times 10^{-3}$ K^{-1}, and the air's thermal conductivity is $\kappa = 2.62 \times 10^{-2}$ W/m-K.

(a) *Thermal penetration depth*. An AC electrical current is passed through the carbon nanotube sheets that cause them to be heated at a frequency of 120 Hz. What is the thermal penetration depth, δ_κ, in air at that frequency?

(b) *Gas temperature change near the sheets*. The total surface area of the three sheets, including both the back and front surfaces of the sheets, $A_{tot} = 15$ cm^2. If the instantaneous total power, $\Pi(t)$, delivered to the sheets can be expressed as $\Pi(t) = 2.0\ \text{W}[1 - \cos(240\pi\ t)]$, and if all of that heat is deposited in a volume equal to the product of the total surface area of the sheets, A_{tot}, and the thermal penetration depth δ_κ, what is the amplitude, T_1, of the oscillating change in the temperature of the gas within that volume that is varying harmonically as $T(t) = T_m + T_1[1 - \cos(240\pi\ t)]$?

(c) *Thermally induced volume change*. During one-quarter of a cycle, the temperature of the gas changes by T_1, as calculated in part (b) of this problem. The coefficient of thermal expansion of an ideal gas at constant pressure, β_p, is provided in Eq. (10.135).

$$\beta = \frac{1}{T_m} = \frac{1}{V}\left(\frac{\partial V}{\partial T}\right)_p \tag{10.135}$$

What is the change in the volume of the gas, δV, caused by its heating during one-quarter cycle?

(d) *Thermally induced pressure change*. The wavelength of sound at 120 Hz is approximately $\lambda = c_{air}/f \cong 2.9$ m, which is much larger than any dimension of the sealed cylindrical enclosure $d \cong V^{1/3} \cong 0.14$ m. Using the change in volume, δV, calculated in part (c), and the adiabatic gas law or the acoustical impedance of a small cavity provided in Eq. (8.25), determine the corresponding change in pressure, δp, caused by the periodic heating within the 2.5 liter, air-filled cylinder.

15. **Reciprocity calibration coupler transfer impedance**. Shown in Fig. 10.24 is a schematic representation of an apparatus, taken from [45], that is used to calibrate a condenser microphone by the reciprocity method. That method requires that the acoustic transfer impedance of the cavity (shown as the "Closed Air Volume") is known.

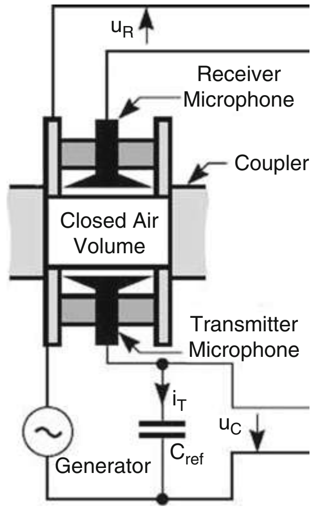

Fig. 10.24 A small cavity is created in the space between two reversible condenser microphones

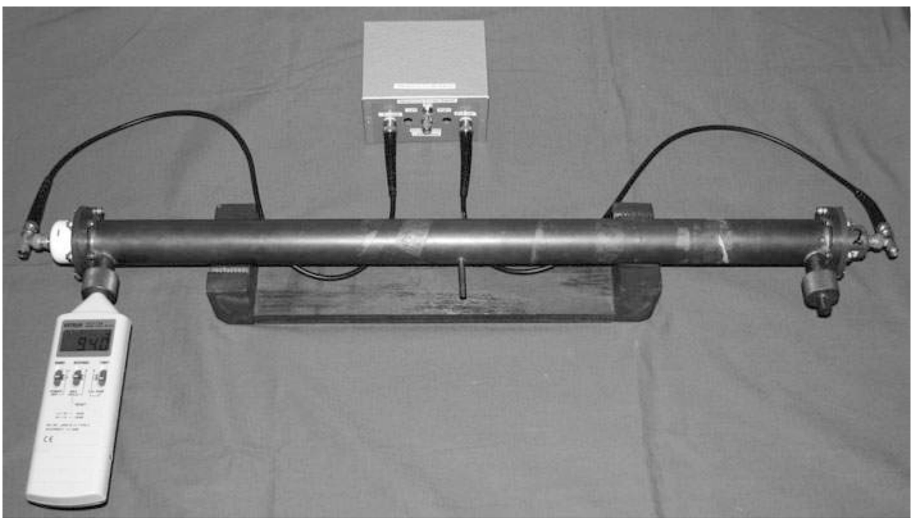

Fig. 10.25 A standing wave resonator used for reciprocity calibration is capped at each end with the small, reversible, electrodynamic transducers shown in Fig. 10.26. Two ½ inch (1.27 cm) compression fittings are located very close to the ends of the resonator. An Extech™ Model 407736, Type-2 sound level meter is placed in one fitting, and the other is plugged with a solid rod. The small tube at the center allows gases other than air to be used as the calibration medium. At the top of the photo is a custom switch box that allows the swept-sine signal produced by a dynamic signal analyzer to be routed to either reversible transducer #1 or #2 after it has been passed through a precision 1.000 ohm current-sensing resistor

Assuming that the two microphones can be treated as rigid caps and that all dimensions of the "Closed Air Volume" are much smaller than the acoustic wavelength, write an expression for the acoustic transfer impedance $\mathbf{Z_{tr}} = \widehat{\mathbf{p}}_\mathbf{R}/\widehat{\mathbf{U}}_\mathbf{T}$, where $\widehat{\mathbf{p}}_\mathbf{R}$ is the complex pressure amplitude at the "Receiver Microphone," $\widehat{\mathbf{U}}_\mathbf{T}$ is the volume velocity produced by the "Transmitter Microphone," and the volume of the "Closed Air Volume" is V.

16. **Reciprocity calibration in a plane wave resonator.** The apparatus shown in Fig. 10.25 is used to produce a reciprocity calibration of the two reversible electroacoustic transducers shown in

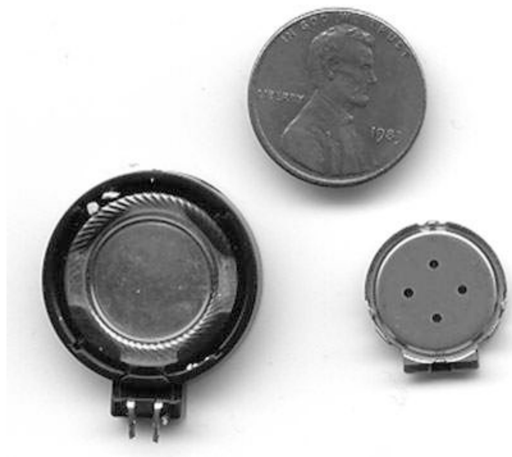

Fig. 10.26 The two small reversible electrodynamic transducers that are used for the reciprocity calibration. The US penny is shown as a size comparison. Each reversible transducer is mounted on a plate that matches the flanges at the ends of the waveguide. The free-cone resonance frequency of the larger transducer is about 2.8 kHz, and that of the smaller one is about 1.7 kHz. Each transducer is mounted on a flange that attaches to the end of the resonator shown in Fig. 10.25

Table 10.5 Summary of measured results for the reciprocity calibration of the two transducers shown in Fig. 10.26 produced using the resonator shown in Fig. 10.25

Driving transducer #1					
f_2 [Hz]	$Q_{2,1}$	i_1 [mA_{ac}]	V_2[μV_{ac}]	Level [dB_C]	$V_{m,1}$ [mV_{ac}]
485.83	71.2	3.62	292.4	111.8	81.48
Driving transducer #2					
f_2 [Hz]	$Q_{2,2}$	i_2 [mA_{ac}]	V_1[μV_{ac}]	Level [dB_C]	$V_{m,2}$ [mV_{ac}]
485.83	70.9	9.647	781.3	102.3	27.02

Fig. 10.29. The resonator tube has an inside diameter of 34.37 mm, and its length is 70.12 cm. Assume the calibration procedure took place in dry air at 20 °C and at a mean pressure, $p_m = 98$ kPa.

The data presented in Table 10.4 were produced at the resonance frequency of the second plane wave resonance, f_2, by first driving Transducer #1 with current, i_1, and measuring Transducer #2's open voltage, V_2, along with the C-weighted output of the sound level meter, $V_{m,1}$, while also measuring $Q_{2,1}$. The second data set in that table was obtained when Transducer #2 was driven. Using the dimensions of the resonator, the thermophysical properties of the air and the data in Table 10.5 make the following calculations:

(a) *Acoustic transfer impedance*. Calculate the value of the acoustic transfer impedance for the second standing wave mode of the resonator.

(b) *Transducer #1 open-circuit microphone sensitivity*. Using the appropriate measurements from Table 10.5, calculate the open-circuit sensitivity, M_1, of Transducer #1 and the sensitivity of the sound level meter by comparison to M_1.

(c) *Transducer #2 open-circuit microphone sensitivity*. Using the appropriate measurements from Table 10.5, calculate the open-circuit sensitivity, M_2, of Transducer #2 and the sensitivity of the sound level meter by comparison to M_2. What is the relative difference in the sensitivity of the sound level meter based on the two independent reciprocity calibrations?

17. **Tweeter horn.** A commercial horn with a 1″ (2.5 cm) diameter throat is 10″ (25 cm) long and opens to a bell with a diameter of 4″ (10 cm).

(a) *Flare constant*. If the horn has a cross-sectional area that grows exponentially, determine the flare constant, h.
(b) *Cut-off frequency*. If the horn were infinitely long, what would be its cut-off frequency?

References

1. M.J. Lighthill, *Waves in Fluids* (Cambridge University Press, 1978). See §2.6; ISBN 0 521 29233 6 (paperback)
2. http://www.iso.org/iso/en/ISOOnline.frontpage
3. V.A. Del Grosso, New equation for the speed of sound in natural waters (with comparisons to other equations). J. Acoust. Soc. Am. **56**(4), 1084–1091 (1974)
4. A.J. Zuckerwar, D.S. Mazel, *Sound Speed Measurements in Liquid Oxygen-Liquid Nitrogen Mixtures*, NASA Technical Paper 2464 (NASA Langley Research Center, Hampton, 1985)
5. M.R. Moldover, R.M. Gavioso, J.B. Mehl, L. Pitre, M. de Podesta, J.T. Zhang, Acoustic gas thermometry. Metrologia **51**, R1–R19 (2014)
6. M.R. Moldover et al., Measurement of the universal gas constant $\mathfrak{R}$ using a spherical acoustic resonator. J. Res. Nat. Bur. Stand. **93**, 85–144 (1988)
7. E. Polturak, S.L. Garrett, S.G. Lipson, Precision acoustic gas analyzer for binary mixtures. Rev. Sci. Inst. **57**(11), 2837–2841 (1986)
8. G.W. Swift, *Thermoacoustics: A Unifying Perspective for Some Engines and Refrigerators*, 2nd edn. (ASA Press/ Springer, 2017). See Eq. (2.74), pg. 50; ISBN 978–3–319-66932-8
9. F.W. Giacobbe, Estimation of Prandtl numbers in binary mixtures of helium and other noble gases. J. Acoust. Soc. Am. **96**(6), 3568–3680 (1994)
10. G.S.K. Wong, Speed of sound in standard air. J. Acoust. Soc. Am. **79**(5), 1359–1366 (1986)
11. M. Greenspan, Comments on 'Speed of sound in standard air'. J. Acoust. Soc. Am. **82**(1), 370–372 (1987)
12. Stanford Research Systems Model BGA244, Binary Gas Analyzer, www.thinkSRS.com
13. S. Garrett, Sonic gas analyzer for hydrogen and methane. *Proc. Acoustics 08*, Paris, 29 June–4 July, 2008, pp. 2767–2772
14. S.L. Garrett, G.W. Swift, R.E. Packard, Helium gas purity monitor for recovery systems. Physica **107B**, 601–602 (1981)
15. M.V. Golden, R.M. Keolian, S.L. Garrett, Sonic gas analyzers, in *Proc. 16th Int. Congress on Acoustics and 135th Meeting Acoust. Soc. Am.*, vol. III, (Seattle, WA, 20–26 June 1998), pp. 1705–1706
16. G.M. Sessler, J.E. West, Electret transducers: A review. J. Acoust. Soc. Am. **53**(6), 1589–1600 (1973)
17. National Semiconductor Model LM2907
18. J.N. Tjøtta, S. Tjøtta, Nonlinear equations of acoustics, in *Frontiers of Nonlinear Acoustics: Proc. 12th International Symposium on Nonlinear Acoustics*, ed. by M. F. Hamilton, D. T. Blackstock, (Elsevier Scientific Publishers, Ltd, London, 1990)
19. L.D. Landau, E.M. Lifshitz, *Fluid Mechanics*, 2nd edn. (Butterworth-Heinemann, 1987). §81; ISBN 0 7506 2767 0
20. F.M.F. Chapman, Decibels, SI units, and standards. J. Acoust. Soc. Am **108**(2), 480 (2000)
21. H. Fletcher, W.A. Munson, Loudness, its definition, measurement, and calculation. J. Acoust. Soc. Am. **5**(2), 82–108 (1933)
22. D.W. Robinson, R.S. Dadson, A re-determination of the equal-loudness relations for pure tones. Br J. Appl. Phys. **7**, 166–188 (1956)
23. ISO 226, *Acoustics – Normal Equal-Loudness Contours* (International Standards Organization, Geneva, 2003)
24. B.R. Glasberg, B.C.J. Moore, Prediction of absolute thresholds and equal loudness contours using a modified loudness model. J. Acoust. Soc. Am. **120**(2), 585–588 (2006)
25. *American National Standard for Sound Level Meters*, ANSI-ASA S1.4-1983, most recently reaffirmed by the American National Standards Institute (ANSI), 21 Mar 2006
26. S. Fidell, A review of US aircraft noise regulatory policy. Acoustics Today **11**(4), 26–34 (2015)
27. P.D. Schomer, Criteria for assessment of noise annoyance. Noise Control Eng. J. **53**(4), 132–144 (2005)
28. *American National Standard Method for the Calculation of the Speech Intelligibility Index*, ANSI-ASA S3.5-1997
29. G.W. Swift, Thermoacoustic engines. J. Acoust. Soc. Am. **84**(4), 1145–1180 (1988). See Eq. (59)
30. W.R. MacLean, Absolute measurement of sound without a primary standard. J. Acoust. Soc. Am. **12**(1), 140–146 (1940)
31. J. W. Strutt (Lord Rayleigh), Proc. London Math. Soc. **4**, 357 (1983); *Scientific Papers*, Vol. I, (Dover, 1964), pp. 140. Note: *The Scientific Papers* are available from the Acoustical Society of America in a fully-searchable version on CD-ROM

32. R.K. Cook, Absolute pressure calibrations of microphones. J. Res. Natl. Bur. Stand. **25**, 489 (1940) and J. Acoust. Soc. Am. **12**(1), 415–420 (1941)
33. G.S.K. Wong, T. F. W. Embleton (eds.), *AIP Handbook of Condenser Microphones* (Am. Inst. Phys., 1995). Chapters 8–12; ISBN 1-56396-284-5
34. R.J. Bobber, *Underwater Electroacoustic Measurements* (Naval Research Laboratory, Underwater Sound Reference Division (U.S. Govt. Printing Office), 1970). See §2.3
35. L.L. Foldy, H. Primakoff, A general theory of passive linear electroacoustic transducers and the electroacoustic reciprocity theorem. I. J. Acoust. Soc. Am. **17**(2), 109–120 (1945). Also H. Primakoff and L. L. Foldy "A general theory of passive linear electroacoustic transducers and the electroacoustic reciprocity theorem. II," J. Acoust. Soc. Am. **19**(1), 50–58 (1947)
36. R.M. Keolian, personal communication
37. R.P. Feynman, R.B. Leighton, M. Sands, *The Feynman Lectures on Physics*, vol II (Addison-Wesley, 1964). See §37–1
38. F.V. Hunt, Symmetry in the equations for electromechanical coupling. J. Acoust. Soc. Am. **22**(5), 672 (1950)
39. F.V. Hunt, *Electroacoustics: The Analysis of Transduction and Its Historical Background* (Harvard, 1954). See "Symmetry and Equivalent Circuits" and "The Burdens of Antisymmetry," pp. 105–116
40. L.E. Kinsler, A.R. Frey, A.B. Coppens, J.V. Sanders, *Fundamentals of Acoustics*, 4th edn. (Wiley, 2000). See Ch. 14.4(b), "Antireciprocal Transducers"; ISBN 0–471–84789-5
41. I. Rudnick, Unconventional reciprocity calibration of transducers. J. Acoust. Soc. Am. **63**(3), 1923–1925 (1978)
42. S.L. Garrett, S. Adams, S. Putterman, I. Rudnick, Resonant nonlinear mode conversion in He II. Phys. Rev. Lett. **41**(6), 413–416 (1978)
43. G.W. Swift, S.L. Garrett, Resonance reciprocity calibration of an ultracompliant transducer. J. Acoust. Soc. Am. **81**(5), 1619–1623 (1987)
44. R.J. Bobber, *Underwater Electroacoustic Measurements* (Naval Research Laboratory, Underwater Sound Reference Division (U.S. Govt. Printing Office), 1970)
45. G.S.K. Wong, Primary pressure calibration by reciprocity, in *AIP Handbook of Condenser Microphones*, ed. by G. S. K. Wong, T. F. W. Embleton, (1995). Am. Inst. Phys.; ISBN 1-56396-284-5
46. V. Nedzelintsky, Primary method for calibrating free-field response, in *AIP Handbook of Condenser Microphones*, ed. by G.S.K. Wong, T.F.W. Embleton, (1995). Am. Inst. Phys; ISBN 1-56396-284-5
47. I. Rudnick, M.N. Stein, Reciprocity free field calibration of microphones to 100 Kc in air. J. Acoust. Soc. Am. **20**(6), 818–825 (1948)
48. S. Barrera-Figueroa, Free-field reciprocity calibration of measurement microphones at frequencies to 150 kHz. J. Acoust. Soc. Am. **144**(4), 2572–2583 (2018)
49. E. Frederiksen, J.I. Christensen, Pressure reciprocity calibration – instrumentation, results, and uncertainty. Brüel & Kjær Tech. Rev. **1**, 5–26 (1998)
50. H.E. Bass, J. Bhattacharyya, M.A. Garcés, M. Hedlin, J.V. Olsen, R.L. Woodward, Infrasound. Acoustics Today **2**(1), 9–19 (2006)
51. T.B. Gabrielson, Reciprocity calibration for infrasound sensors. J. Acoust. Soc. Am. **141**(5), 3568 (2017)
52. L.E. Kinsler, A.R. Frey, A.B. Coppens, J.V. Sanders, *Fundamentals of Acoustics*, 4th edn. (Wiley, 2000). See Eq. (10.5.4); ISBN 0-471-84789-5
53. R.S. Wakeland, Use of electrodynamic drivers in thermoacoustic refrigerators. J. Acoust. Soc. Am. **107**(2), 827–832 (2000)
54. M.A.G. Timmer, K. de Blok, T.H. van der Meer, Review on the conversion of thermoacoustic power into electricity. J. Acoust. Soc. Am. **143**(2), 841–857 (2018)
55. Morel Acoustics USA, Inc., Brookline, MA
56. W.C. Ward, Cost-effective electrodynamic drivers with improved efficiency for thermoacoustic refrigerators. J. Acoust. Soc. Am. **100**(4), 2847 (1996)
57. M. Fitzpatrick, Electrodynamic driver for the Space Thermoacoustic Refrigerator (STAR), M.S. thesis, Physics Department, Naval Postgraduate School, Monterey, CA, 1988; DTIC report no. ADA 192337, p. 80
58. S.L. Garrett, J.A. Adeff, T.J. Hofler, Thermoacoustic refrigerator for space applications. AIAA J. Thermophys. Heat Trans. **7**(4), 595–599 (1993)
59. S.L. Garrett, High power thermoacoustic refrigerator. US Pat. No. 5,647,216 (15 July 1997)
60. J. Liu, S. Garrett, Characterization of a small moving-magnet electrodynamic linear motor for use in a thermoacoustic refrigerator. J. Acoust. Soc. Am. **118**(4), 2289–2295 (2005)
61. G.A. Yarr, J.C. Corey, Linear electrodynamic machine. US Pat. No. 5,389,844 (14 Feb. 1995)
62. C.H. Allen, I. Rudnick, A powerful high frequency siren. J. Acoust. Soc. Am. **19**(5), 857–865 (1947)
63. W.L. Nyborg, Acoustic streaming, in *Physical Acoustics*, ed. by W. P. Mason, vol. IIB, (Academic, 1964)
64. J.K. Hilliard, Historical review of horns used for audience-type sound reproduction. J. Acoust. Soc. Am. **59**(1), 1–8 (1976)

65. P.M. Morse, *Vibration and Sound*, 2nd edn. (McGraw-Hill, 1948). Reprinted by the Acoust. Soc. Am., 1995. See Fig. 58; ISBN 0-88318-876-7
66. V. Salmon, Generalized plane wave horn theory. J. Acoust. Soc. Am. **17**(3), 199–211 (1946). and "A new family of horns," J. Acoust. Soc. Am. **17**(3), 212–218 (1946)
67. I. Rudnick, On the attenuation of high amplitude waves of stable saw-tooth form propagating in horns. J. Acoust. Soc. Am. **30**(4), 339–342 (1948)
68. P. Bèquin, C.L. Morfey, Weak nonlinear propagation of sound in a finite exponential horn. J. Acoust. Soc. Am. **109** (6), 2649–2659 (2001)
69. L.L. Beranek, *Acoustics*. Acoust. Soc. Am. (1996). Chapter 9; ISBN 0-88318-494-X
70. M. Kleiner, *Electroacoustics* (Taylor & Francis, 2013). Chapter 19; ISBN 978-1-4398-3618-70
71. https://www.co2.earth/daily-co2
72. H. Witschi, Profiles in toxicology, Fritz Haber: 1868–1934. Toxicol. Sci. **55**, 1–2 (2000)
73. P.W. Mullen, *Modern Gas Analysis* (Interscience, 1955)
74. L.L. Beranek, *Acoustic Measurements* (Wiley, 1949), pp. 161–171
75. A.E. Aliev et al., Underwater sound generation using carbon nanotube projectors. Nano Letters (Am. Chem. Soc.) **10**, 2374–2380 (2010)

11 Reflection, Transmission, and Refraction

Contents

In Chap. 10, we transitioned from a lumped-element perspective to a formalism which treated fluids as continuous media that include the effects of both compressibility and inertia throughout. We described disturbances from equilibrium using a wave equation and focused attention on planewaves that could be described as propagating along one spatial dimension. In this chapter, we will examine the behavior of such one-dimensional waves propagating through media that are not homogeneous. We start with an examination of the behavior of planewaves impinging on a planar interface between two fluid media with different properties and then extend that analysis to multiple interfaces and to waves that impinge on the interface from an angle that is not perpendicular to that surface. This exploration concludes with consideration of wave propagation through a medium whose properties change slowly and continuously through space.

What does "slowly" mean in the previous sentence? To answer that question, we will break down the general problem of propagation through an inhomogeneous medium into two limiting cases. As before, such limiting cases suggest appropriate (usually simple) analytical approaches that will develop useful intuition for understanding cases that may be intermediate between the simpler limits. In this

S. L. Garrett, *Understanding Acoustics*, Graduate Texts in Physics,
https://doi.org/10.1007/978-3-030-44787-8_11

chapter, the interesting limits depend on the scale of the medium's inhomogeneity relative to the wavelength of the sound that impinges on it (from afar, since we consider only planewaves). If a wave encounters a deviate region with a size that is on the order of its own wavelength or smaller, and that region has a different density, a different compressibility, or both, then we treat the inhomogeneous region as a "scatterer." Those cases will be examined in Chap. 12 when the problem of radiation in three dimensions is analyzed and the scattering body will be driven by the impinging sound wave causing the ensonified region to behave as a radiating "source." That "scattered" sound field will be superimposed on the incident sound field.

In this chapter, we will consider the opposite limit, where the size of the boundary that separates regions with different acoustical properties is much larger than the wavelength of the sound. In fact, many cases to be examined here will assume that the extent of the boundary is infinite. In those cases, the problem is treated as one where the wave incident on such an interface will be both reflected back into the medium from which it originated and be transmitted into the second medium on the other side of the interface.

For the case where the interface is not discontinuous, what we will mean by requiring that the medium's properties (e.g., sound speed and density) "are varying slowly" will again be related to the rate at which the property changes in space relative to the wavelength of the sound. For example, if we specify the change in sound speed with position,$dc/dz \equiv g$, then g will have the units m/s per m, which is equivalent to a frequency. The wave also has a characteristic frequency, $f = c/\lambda$, that is the ratio of the sound speed to the wavelength. If $g \ll f$, then any significant change in sound speed will occur over a very large number of wavelengths.

11.1 Normal Incidence

All of us are familiar with echoes, whether produced by a handclap reflected from a large building; a loud "hello" shouted from a precipice and reflected from a bluff, as diagrammed in Fig. 11.1; or a "flutter echo" produced by some impulsive sound source reverberating between long parallel walls. In those cases, a sound wave in air impinges on a rigid solid surface. The air's particle velocity that accompanies the pressure wave (via the Euler equation) cannot penetrate the solid. To satisfy this rigid boundary condition, we can imagine a sound wave of equal amplitude, but propagating in the opposite direction, coming from within the solid toward the interface, just as was done when examining the reflection of a pulse propagating along a string in Sect. 3.2. As justified in Sect. 12.4.1, the superposition of the two waves cancels the velocity at the interface, satisfying the condition that the interface is impenetrable to the gas, while doubling the acoustic pressure amplitude on that surface.

To compare how a real wave reflects in the "rigid boundary" case (and to determine how "rigidly" the boundary behaves), let's say the magnitude of the incident planewave, $|\widehat{\mathbf{p}}_\mathbf{i}|$, approaching the boundary is 94 $\mathrm{dB_{SPL}} \Rightarrow |\widehat{\mathbf{p}}_\mathbf{i}| = \sqrt{2}$ Pa $= 1.0$ Pa_{rms}. Again, we focus on a single-frequency wave and indicate the incident wave's amplitude and phase by the complex phasor, $\widehat{\mathbf{p}}_i$. The time-averaged intensity of a 94 $\mathrm{dB_{SPL}}$ planewave in air is $\langle I_{air} \rangle_t = |\widehat{\mathbf{p}}_\mathbf{i}|^2/(2\rho c)_{air} = 10^{(94/10)} \times \ 10^{-12}\,\mathrm{W/m^2} \cong$ 2.5 $\mathrm{mW/m^2}$. (If this is not instantaneously obvious, you need to review Sect. 10.5.1.)

Let's also say the wave was reflected from a concrete wall. Since the pressure amplitude at the wall is double that of the sound wave far from the wall, and that the pressure is continuous across the interface, we can calculate the intensity of the sound that entered the wall. The density of concrete is about 2600 $\mathrm{kg/m^3}$ and the speed of compressional waves in concrete is about 3100 m/s, so $(\rho c)_{concrete} = 8.06$ MPa-s/m. Since the pressure at the wall is twice that of the wave in air, $|\widehat{\mathbf{p}}_\mathbf{t}| =$

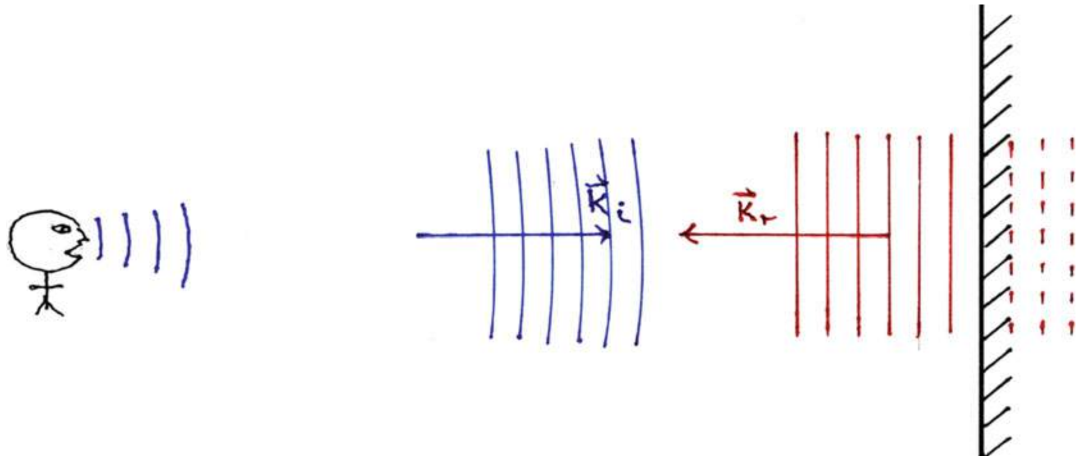

Fig. 11.1 The sound produced by this person is nearly a planewave (wave fronts shown in *blue*), characterized by the wavenumber, $\vec{k}_i$, when it is reflected by a large flat rigid surface. The duration of the sound pulse is sufficiently short that the reflected wave, characterized by $\vec{k}_r$, and the incident wave only interact near the surface. To satisfy the condition that no fluid can enter or leave the solid interface, we imagine another planewave of equal amplitude traveling back (with wave fronts shown in *red*) toward the source. Where the incident and reflected wave superimpose at the rigid surface, the pressure is doubled, but the slope of the pressure, $(dp/dx)_{x=0}$, evaluated at the interface, is zero. By Euler's equation, the total acoustic particle velocity normal to the surface vanishes, as required

$2|\widehat{\mathbf{p}}_{\mathbf{i}}| = 2\sqrt{2}$ Pa, the time-averaged intensity of the sound penetrating the concrete is $\langle I_{concrete}\rangle_t = |\widehat{\mathbf{p}}_{\mathbf{t}}|^2/(2\rho c)_{concrete} = 0.5\,\mu\text{W/m}^2$, less than 0.02% of the intensity of the sound in air.

The equations developed in this chapter can be used to show that the amplitude of a wave in air that is reflected from a concrete wall is nearly the same as the incident wave, but not quite. Our assumption that the echo had the same amplitude as the incident sound wave was just as solid as the concrete.

We can also compare the particle velocity of the sound in air with that of the compressional wave within the concrete. In dry air, a 94 dB_{SPL} sound wave would have a particle velocity amplitude of $|\widehat{\mathbf{v}}_{\mathbf{i}}| = |\widehat{\mathbf{p}}_{\mathbf{i}}|/(\rho c)_{air} = 3.3\ \text{mm/s}$. In the concrete, the pressure of the transmitted wave is twice that in air (far from the wall), but $|\widehat{\mathbf{v}}_{\mathbf{t}}| = 2|\widehat{\mathbf{p}}_{\mathbf{i}}|/(\rho c)_{concrete} = 0.35\ \mu\text{m/s}$. Again, we see that our assumption of a rigid and immobile boundary was good to about one part in ten thousand (0.01%). We can check our intensity results using Eq. (10.36), since we also know $\langle I\rangle_t = |\widehat{\mathbf{p}}_{\mathbf{t}}||\widehat{\mathbf{v}}_{\mathbf{t}}|/2$, since $\widehat{\mathbf{p}}_{\mathbf{t}}$ and $\widehat{\mathbf{v}}_{\mathbf{t}}$ are in-phase for our assumed traveling wave. In dry air at one atmosphere, $p_m = 101{,}325$ Pa, and letting $T_m = 7\ °\text{C}$, $(\rho c)_{air} = 423$ Pa-s/m. This gives $\langle I_{air}\rangle_t = 2.4\ \text{mW/m}^2$ and in the concrete $\langle I_{concrete}\rangle_t = 0.5\ \mu\text{W/m}^2$, in good agreement with the earlier calculation, as must be the case.

Using Eq. (9.38), the power dissipated per unit area due to the thermal relaxation losses at the interface can be calculated and compared to the incident intensity, since the concrete wall will behave as an isothermal boundary.[1] Since this loss mechanism is frequency dependent, let's do the calculation for $f = 1$ kHz. From the DeltaEC Thermophysical Properties of air at 300 K and 1 bar $= 10^5$ Pa,

[1] To determine if the concrete wall forces the air that it contacts to behave isothermally, we can calculate the heat capacity per unit area that is contained within a layer of the material that is one thermal penetration depth thick, $\rho\, c_P \delta_\kappa$. Using the thermophysical properties available in DeltaEC, $(\rho\, c_P\delta_\kappa)_{\text{air}} = 0.10\ \text{J/m}^2\text{-°C}$. Approximate values for concrete are $\rho = 2600\ \text{kg/m}^3$, $c_P = 880$ J/kg-°C, and $\kappa = 0.29$ W/m-°C, so at 1 kHz, $\delta_\kappa = 6.35\ \mu\text{m}$ and $(\rho\, c_P\delta_\kappa)_{\text{Concrete}} = 14.5\ \text{J/m}^2\text{-°C} \gg (\rho\, c_P\delta_\kappa)_{\text{air}} = 0.10\ \text{J/m}^2\text{-°C}$. For a more detailed discussion, see Eq. (59) for ε_s in G. W. Swift, "Thermoacoustic engines," J. Acoust. Soc. Am. **84**(4), 1145–1180 (1988).

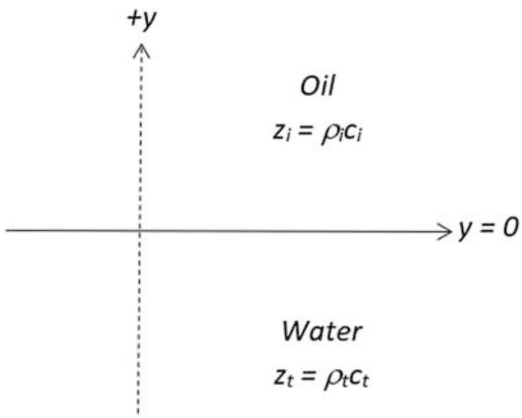

Fig. 11.2 Coordinate system for two fluids that can be thought of as oil floating on water. The dashed line is normal to the plane interface between the two fluids at $y = 0$. In this diagram, it is assumed that the sound originates from the oil which has a specific acoustic impedance of $z_i = \rho_i c_i$. A wave will be transmitted across the interface into a second medium (water) with a specific acoustic impedance $z_t = \rho_t c_t$

$\delta_\kappa = 84.6$ μm, corresponding to a thermal absorption of 0.76 μW/m^2. This is a miniscule loss (0.03%), although thermal relaxation at the interface is responsible for a slightly larger decrease in the reflected amplitude, at this frequency, than the intensity of the sound that enters the concrete. Why do we not need to calculate the viscous boundary layer dissipation?

Now that we have the behavior of a common reflection situation "under our belts," we can start our formal investigation of reflection and transmission of planewaves impinging normally on an interface between any two dissimilar media. For these calculations, keep in mind a very simple case of two immiscible liquids in a uniform gravitational field. Let's assume that we have a sea of oil floating on a sea of water, as shown in Fig. 11.2, with the "up" direction being $+y$ and $y = 0$ at the interface between the two liquids. The mass density of the oil, ρ_{oil}, is less than the density of water. To simplify the specification of variables on either side of the interface, we will designate parameters of the wave and of the medium above the interface ($y > 0$) with the subscript, i (incident), and those below the interface ($y < 0$) with the subscript, t (transmitted).

Let's imagine that a single-frequency plane sound wave originates far above the interface and is propagating in the $-y$ direction. That wave excites the interface with a pressure amplitude, $|\hat{\mathbf{p}}_\mathbf{i}|$. We can express the pressure amplitude as a function of y and t above the interface

$$p_i(y,t) = \Re e\left[\hat{\mathbf{p}}_\mathbf{i} e^{\,j(\omega t + k_i y)}\right] \quad \text{for} \quad y > 0. \tag{11.1}$$

That incident plane pressure wave also has an associated fluid particle velocity, $\hat{\mathbf{v}}_\mathbf{i}$, that is related to the pressure by the Euler equation.

$$v_i(y,t) = \Re e\left[\frac{\hat{\mathbf{p}}_\mathbf{i}}{\rho_i c_i} e^{\,j(\omega t + k_i y)}\right] = \Re e\left[\frac{\hat{\mathbf{p}}_\mathbf{i}}{z_i} e^{\,j(\omega t + k_i y)}\right] \quad \text{for} \quad y > 0 \tag{11.2}$$

In the right-hand term of Eq. (11.2), z_i is the specific acoustic impedance of the oil. Using our generic expression, Eq. (10.21), for the sound speed, c, in a fluid with an adiabatic bulk modulus, B_s, $c \equiv \sqrt{B_s/\rho}$, we see that the specific acoustic impedance is a combination of the fluid's density and compressibility,$z = \rho c = \sqrt{\rho B_s}$.

As for the echo case, there will be a wave that is reflected at the interface that will travel in a direction opposite to that of the incident wave.

$$p_r(y,t) = \Re e\left[\widehat{\mathbf{p}}_{\mathbf{r}} e^{\,j(\omega t - k_i y)}\right] \quad \text{for} \quad y > 0 \tag{11.3}$$

The presence of the incident wave will excite motion in that interface which will also generate a wave propagating into the water as well as the wave that is reflected back into the oil. To demonstrate the necessity for the simultaneous existence of the incident, reflected, and transmitted waves, we need to consider the properties of the interface between the two media.

Since we will treat these media and the waves they contain as a linear system, we can guarantee that the reflected and transmitted waves both have the same frequency as the incident wave: $\omega = \omega_i = \omega_r = \omega_t$. As we have seen for the simple harmonic oscillator, at steady state, the forced linear system can only respond at the forcing frequency. It is the incident wave that is forcing the motion of the interface. Since the frequencies of all of the waves must be the same, and the sound speeds in the two media might differ, the wavelength of the sound in the water will be different than that in the oil: $\lambda_t = c_t/f = 2\pi/k_t$.

$$p_t(y,t) = \Re e\left[\widehat{\mathbf{p}}_{\mathbf{t}} e^{\,j(\omega t + k_t y)}\right] \quad \text{for} \quad y < 0 \tag{11.4}$$

Our second requirement at the interface is that the two fluids always remain in contact. There are cases where the amplitude of the incident wave is sufficiently large to produce a vapor cavity at the interface, but we will limit our attention here to wave amplitudes that are insufficient to create such *cavitation effects* [1]. In most practical cases, the boundaries do not separate, so the normal velocities of the two fluids must match at the interface for all times.

$$v_i(0,t) + v_r(0,t) = v_t(0,t) \tag{11.5}$$

Our final requirement is dictated by the fact that the interface, $y = 0$, is only a mathematical construct—it has no mass. Since that interface is massless, Newton's Second Law of Motion would guarantee that any pressure difference across the interface would produce a non-zero force that would create infinite fluid accelerations. To guarantee that does not happen, we require that the pressure be continuous across that interface for all time.

$$p_i(0,t) + p_r(0,t) = p_t(0,t) \tag{11.6}$$

Those three conditions are sufficient to completely determine the behavior of the waves at the interface when we recognize that $v_t(y,\ t)$ is related to $p_t(y,\ t)$ by the specific acoustic impedance of the water, z_t. Taking the ratio of Eq. (11.6) to Eq. (11.5), the amplitude ratio of the reflected and transmitted waves to the amplitude of the incident wave can be calculated.

$$\frac{p_i(0,t) + p_r(0,t)}{v_i(0,t) + v_r(0,t)} = \frac{p_t(0,t)}{v_t(0,t)} = z_t \tag{11.7}$$

Recognizing that the incident and reflected waves are both in the oil, but are traveling in opposite directions, the magnitude of the specific acoustic impedance, $|z_i|$, is the same for both waves, but their signs are opposite. This leads to the further simplification of Eq. (11.7).

$$z_i \frac{p_i(0,t) + p_r(0,t)}{p_i(0,t) - p_r(0,t)} = -z_t \tag{11.8}$$

Again, because we are limiting ourselves to linear acoustics, it is only the ratios of the amplitudes that have any significance. If we double the amplitude of the incident wave, the amplitudes of the reflected and transmitted waves must also double. It is therefore reasonable to define a *pressure reflection coefficient*, $\mathbf{R} \equiv \hat{\mathbf{p}}_\mathbf{r}/\hat{\mathbf{p}}_\mathbf{i}$, as we did in Eq. (10.105). With that definition and a little algebraic manipulation, Eq. (11.8) can be re-written in a compact form to represent the magnitude of the pressure reflection coefficient, R.

$$R \equiv \frac{\hat{\mathbf{p}}_\mathbf{r}}{\hat{\mathbf{p}}_\mathbf{i}} = \frac{z_t - z_i}{z_t + z_i} = \frac{\left(z_t/z_i\right) - 1}{\left(z_t/z_i\right) + 1} \tag{11.9}$$

This result makes sense and is reminiscent of Eq. (10.105). If the two media have the same specific acoustic impedances, there is no reflection. Plugging in the specific acoustic impedances for air and concrete produces the same result as we obtained for the "echo" example that began this treatment and produced nearly perfect reflection: $R = 0.9999$.

In the case of oil over water, as shown in Fig. 11.2, then $z_i < z_t$ so R is positive and the phase of the reflected wave will be the same as the incident wave, although their amplitudes will differ, similar to the in-phase pulse reflection in Fig. 3.4. If the situation were reversed so that the incident wave originated in the water, then $z_i > z_t$ so R is negative and the phase of the reflected wave will be inverted, as shown for the pulses in Fig. 3.3.

Defining the *pressure transmission coefficient* in a similar way, $T \equiv \hat{\mathbf{p}}_\mathbf{t}/\hat{\mathbf{p}}_\mathbf{i}$, the pressure continuity boundary condition of Eq. (11.6) can now be written as $1 + R = T$.

$$T \equiv \frac{\hat{\mathbf{p}}_\mathbf{t}}{\hat{\mathbf{p}}_\mathbf{i}} = \frac{2z_t}{z_t + z_i} = \frac{2\left(z_t/z_i\right)}{\left(z_t/z_i\right) + 1} \tag{11.10}$$

The factor of two is reassuring, since we expected pressure doubling at the interface in the echo example where $z_t \gg z_i$, and we saw the same factor of two in Eq. (10.105).

For oil above water, we can use $\rho_{oil} = 950$ kg/m^3, $c_{oil} = 1540$ m/s, $z_{oil} = (\rho c)_{oil} = 1.463 \times 10^6$ Pa - s/m, and $\rho_{water} = 998$ kg/m^3, $c_{water} = 1481$ m/s, and $z_{water} = (\rho c)_{water} = 1.478 \times 10^6$ Pa-s/m. The specific acoustic impedance of these two liquids is very close, so for a planewave originating in the oil, $R = 0.005$ and $T = 1.005$. If the planewave originated in the water, $R = -0.005$ and $T = 0.995$. The fact that R is negative for sound traveling from water into oil indicates that the wave reflected back into the water from the interface is reflected with a 180° phase shift with respect to the incident wave.

If Fig. 11.2 represented air over water, as on a lake, then the impedance contrast would be similar to the echo example, if we assume dry air at one atmosphere, $p_m = 101{,}325$ Pa, and $T_m = 20$ °C, then $(\rho c)_{air} = 413$ Pa-s/m. If the wave originated in the air, the results would be similar to the echo example. If the wave originated in the water, $R = -0.9994$, so again the reflection is almost perfect, but the reflected wave is 180° out-of-phase with incident wave. The pressure transmission coefficient is $T = 0.00056$, so we call that interface, in such a situation (i.e., the wave originating in the medium of higher specific acoustic impedance), a *pressure release boundary*.

11.2 Three Media

If we had two gases in contact, then we would need a membrane to keep them from diffusing into each other. Similarly, we might be interested in the transmission of sound between two living spaces separated by a wall. There is no reason why we could not extend the same style of argument just employed with one interface between two media. We would need five waves instead of three since the

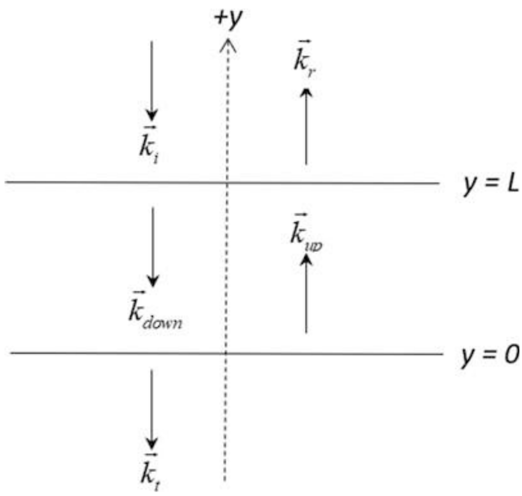

Fig. 11.3 For a planewave that propagates through three media, bounded by two parallel interfaces, two additional waves need to be included for propagation through the central region. In this diagram, two waves are "trapped" inside the central medium, between $y = 0$ and $y = L$, that has a specific acoustic impedance of $z_c = \rho_c c_c$. The wavevector of the incident planewave, $\vec{k}_i$, and the reflected wavevector, $\vec{k}_r$, are both in the upper medium with $z_i = \rho_i c_i$. The transmitted wave represented by the wavevector, $\vec{k}_t$, is in the lower medium, with specific acoustic impedance $z_t = \rho_t c_t$. All wave vectors are colinear and normal to both interfaces

central region, with specific acoustic impedance, z_c, can support both waves moving up and moving down, as shown in Fig. 11.3.

$$p_{up}(y,t) = \Re e\left[\widehat{\mathbf{p}}_{\mathbf{up}} e^{\,j(\omega t - k_c y)}\right] \quad \text{and} \quad p_{down}(y,t) = \Re e\left[\widehat{\mathbf{p}}_{\mathbf{down}} e^{\,j(\omega t + k_c y)}\right] \tag{11.11}$$

Again, linearity guarantees that these two new waves also have a frequency $\omega = \omega_{up} = \omega_{down}$, so their wavelengths and wavenumbers depend upon the speed of sound in the central medium: $\lambda_c = c_c/f = 2\pi/\left|\vec{k}_c\right|$. We would need to impose the continuity of normal particle velocity (11.5) and the continuity of pressure (11.6) on two planes, $y = 0$ and $y = L$, if the central medium has thickness, L. We are again only interested in the amplitude ratios (i.e., specification of the incident amplitude, $\widehat{\mathbf{p}}_{\mathbf{i}}$, is still arbitrary) and can calculate the complex pressure reflection coefficient, $\mathbf{R}$.

$$\mathbf{R} = \frac{\left(1 - {}^{z}\!/_{z_t}\right)\cos(k_c L) + j\left({}^{z_c}\!/_{z_t} - {}^{z_i}\!/_{z_c}\right)\sin(k_c L)}{\left(1 + {}^{z_i}\!/_{z_t}\right)\cos(k_c L) + j\left({}^{z_c}\!/_{z_t} + {}^{z_i}\!/_{z_c}\right)\sin(k_c L)} \tag{11.12}$$

The power transmission coefficient will be a scalar, as it was in Eq. (10.109), and will be related to the reflection coefficient through energy conservation, as it was in Eq. (10.110).

$$T_\Pi = \frac{4}{2 + \left({}^{z}\!/_{z_i} + {}^{z_i}\!/_{z_t}\right)\cos^2(k_c L) + \left({}^{z_c^2}\!/_{z_t z_i} + {}^{z_t z_i}\!/_{z_c^2}\right)\sin^2(k_c L)} \tag{11.13}$$

In many cases, the incident and transmitted media are the same, $z_i = z_t$, simplifying the power transmission coefficient.

$$T_\Pi = \left[1 + (1/4)\left({}^{z_c}\!/_{z_i} - {}^{z_i}\!/_{z_c}\right)^2 \sin^2(k_c L)\right]^{-1} \quad \text{if} \quad z_i = z_t \tag{11.14}$$

11.2.1 A Limp Diaphragm Separating Two Gases

If we apply Eq. (11.12) to the case of two different gases separated by a membrane with $z_c \gg z_i$ and $z_c \gg z_t$, which is so thin (i.e., $L \ll \lambda_c$) that (z_c/z_t) sin $(k_cL) \ll 1$and $\cos(k_cL) \cong 1$, then the pressure amplitude reflection coefficient is the same as (11.9), so $R \cong (z_t - z_i)/(z_t + z_i)$, making the diaphragm effectively transparent and the pressure reflection coefficient dependent only upon the relative specific acoustic impedances of the gases.

Let us consider a limp latex diaphragm, having a thickness of $0.006'' = 150$ μm, separating air from molecular hydrogen, H_2. At 1.0 kHz, with $c_{latex} \cong 1000$ m/s, $(k_cL) = \omega L/c_{latex} \cong 0.001$. Using $(\rho c)_{latex} \cong 50$ kPa-s/m, (z_c/z_t) sin $(k_cL) \cong 0.1 \ll 1$, the simplified reflection coefficient of Eq. (11.9) will provide a decent approximation.

For ideal gases, $(\rho c)_{gas} = \sqrt{\gamma p_m \rho_m}$. Since the diaphragm is assumed to be limp, the pressures of the gases on either side must be identical (otherwise the limp membrane would bulge and then burst), so$(z_t/z_i)_{gas} = \sqrt{M_t/M_i}$, where M is the molecular mass of each gas. For air and hydrogen, the ratio of specific acoustic impedances is about $\sqrt{15}$, or its reciprocal, if the planewave originates on the air side, making $R = \pm 0.59$, with the sign dependent upon whether the planewave originates on the air side (+) or the H_2 side (−).

11.2.2 An Impedance Matching Antireflective Layer

An important special case covered by Eq. (11.12) occurs when the thickness of the intermediate layer is one-quarter of a wavelength to create a perfectly transmitting condition that repeats for integer multiples of half-wavelengths being added to the original quarter wavelength, resulting in an odd-integer multiple of one-quarter of the wavelength of sound, $L = (2n - 1)\lambda_c/4$; $n = 1, 2, 3, \ldots$; hence, $(k_c\ L) = (n - ½)\pi$. In that case, $\cos(k_cL) \cong 0$ and $\sin(k_cL) = 1$. In addition, if $z_c = \sqrt{z_i z_t}$, then $\mathbf{R} = 0$ for frequencies near $f = (n - ½)c_c/2L$, and the intermediate medium is known as a *quarter-wavelength impedance matching layer*.

In high-quality optics, like camera lenses, this effect is used to make antireflective coatings that optimize the transmission of light through the lens. Since this effect is wavelength-dependent, those optical coatings look magenta when they are optimized for transmission of green light (520 nm $\lesssim \lambda_{green} \lesssim$ 570 nm), since red (620 nm $\lesssim \lambda_{red} \lesssim$ 740 nm) and blue (450 nm $\lesssim \lambda_{blue} \lesssim$ 495 nm) will have non-zero optical reflection coefficients.

Impedance matching layers are very useful for ultrasonic transducers used in medical imaging to optimize the transmission from the transducer material (typically a piezoelectric ceramic) to flesh and to maximize the return signal's excitation of the transducer during detection.

11.2.3 The "Mass Law" for Sound Transmission Through Walls

If we consider a solid wall separating two rooms, both containing air, then $z_c \gg z_i = z_t$. In that case, the power transmission coefficient of Eq. (11.14) is further simplified.

$$T_\Pi \cong \left[\frac{2z_i}{z_c \sin(k_cL)}\right]^2 \quad \text{if} \quad z_c \gg z_i = z_t \tag{11.15}$$

For reasonably small wall thicknesses, $L \ll \lambda_c = c_c/f$, $\sin(k_cL) \cong k_cL$, so the reduction of sound intensity transmission through the wall depends upon the surface mass density of the wall, $\rho_S = \rho_cL$.

$$T_{\Pi} \cong \left(\frac{2}{k_c L}\frac{z_i}{z_c}\right)^2 \cong \left[\frac{z_i}{\pi f(\rho_c L)}\right]^2 \quad \text{if} \quad k_c L \ll 1 \tag{11.16}$$

For this reason, in architectural acoustics, this result is known as the "mass law" and is particularly important for multi-occupant dwellings (e.g., apartment buildings) because the transmission of sound depends inversely on the square of both the surface mass density of the wall and of the frequency of the sound.[2] [2] This inverse-square dependence upon frequency explains why the bass from a neighbor's stereo in an adjoining apartment is more annoying than conversation.

11.2.4 Duct Constriction/Expansion Low-Pass Filters

We can exploit Eq. (11.14) for the power transmission coefficient to analyze the one-dimensional propagation through a duct that has an expansion chamber or constriction as shown in Fig. 11.4. Following the analysis in Sect. 10.8, and recognizing that such a system has the same sound speed and fluid density throughout, we can copy the five-wave procedure used in Sect. 11.2, but require the continuity of volume velocity, instead of particle velocity, to produce the analog of Eq. (11.14) where A replaces $z_i = z_t$ and A_c replaces z_c [3].

$$T_{\Pi} = \frac{1}{1 + \frac{\left[\left(A_c/A\right) - \left(A/A_c\right)\right]^2}{4}\sin^2(kL)} \tag{11.17}$$

It is worthwhile to notice that this coefficient for the power transmission is symmetric with respect to the area ratio, A_c/A, and its reciprocal, A/A_c. That means that the result does not depend upon whether the area change is produced by an expansion chamber, $A_c/A > 1$, shown in Fig. 11.4 (left), or by a constriction, $A/A_c > 1$, shown in Fig. 11.4 (right).

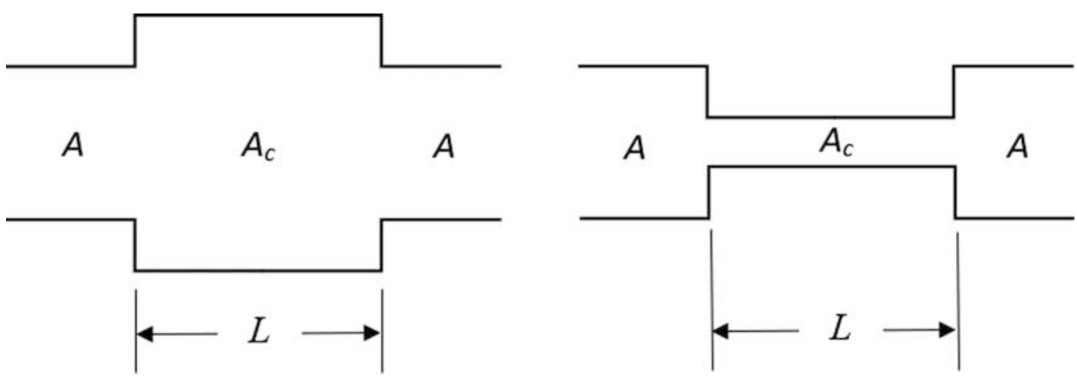

Fig. 11.4 (*Left*) A compliance with volume, $V = A_c L$, is placed in a tube of otherwise uniform cross-sectional area, A, to create a low-pass filter. (*Right*) A constriction with cross-sectional area, $A_c < A$, is placed in a tube of otherwise uniform cross-sectional area, A, to produce a low-pass filter

[2] It is important to remember that this "mass law" is a low-frequency result, as indicated in Eq. (11.16). At higher frequencies, other effects can become significant.

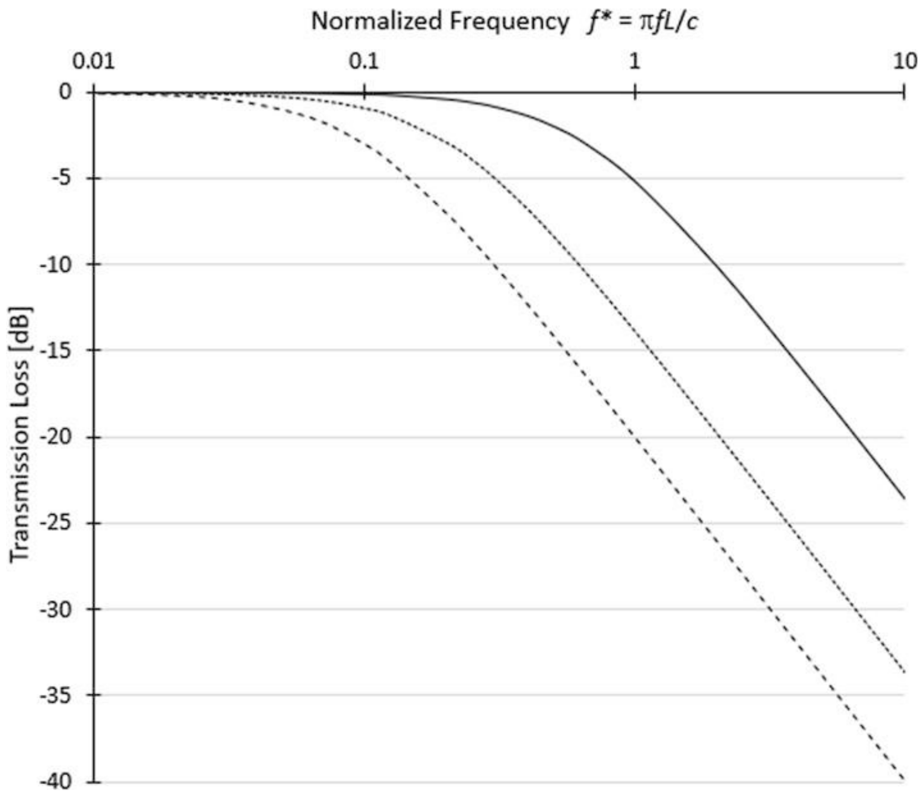

Fig. 11.5 The expansion/constriction duct transmission loss, T_Π, for small kL, in dB = $10\log_{10}T_\Pi$ for area ratios of $A_c/A = 2$ or 0.5 (*solid line*), $A_c/A = 5$ or 0.2 (*dotted line*), and $A_c/A = 10$ or 0.1 (*dashed line*) plotted against a normalized frequency, f^*, that is scaled by the length of the length of the expansion or constriction, L, and the sound speed, c: $f^* = \pi f\, L/c$, which is also $f^* = \pi L/\lambda = kL/2$

If we start by examining the limit where $L \ll \lambda$ or $kL \ll 1$, we see that either the expansion chamber or the constriction acts as a low-pass filter as shown in Fig. 11.5 for $A_c/A = 2$, $A_c/A = 5$, and $A_c/A = 10$.

$$T_\Pi = \left\{1 + \frac{\pi^2 L^2}{c^2}\left[\left(A_c/A\right) - \left(A/A_c\right)\right]^2 f^2\right\}^{-1} \quad \text{for} \quad kL \ll 1 \tag{11.18}$$

As expected from Eq. (11.18), the transmission for $kL < 1$ is reduced by 20 dB/decade, in accordance with the f^{-2} frequency dependence. It is clear from Fig. 11.5 that the frequency at which the transmission is reduced by 3 dB is dependent upon the area ratio. For $A_c/A = 2$ or 0.5, $f^*_{-3\text{dB}} = 0.665$; for $A_c/A = 5$ or 0.2, $f^*_{-3\text{dB}} = 0.208$; and for $A_c/A = 10$ or 0.1, $f^*_{-3\text{dB}} = 0.101$.

As frequency increases, the requirement that $kL < 1$ will be violated. In Fig. 11.5, that means that $f^* \leq ½$. This restriction indicates that the frequency bandwidth of the expansion/constriction strategy is rather limited as a low-pass filter. From Eq. (11.17), we see that the transmission coefficient becomes one (i.e., 0 dB, no attenuation), when $kL = \pi$ or $f^* = \pi/2$, and returns to one for all successive $kL = n\pi$ as shown in Fig. 11.6. The maximum transmission loss, $(T_\Pi)_{max}$, occurs when L is equal to an odd multiple of quarter wavelength, $(2n - 1)\lambda/4$, making $f = (2n - 1)c/4L$.

$$(T_\Pi)_{max} \cong -10\log_{10}\left[(1/4)\left(\frac{A_c}{A} + \frac{A}{A_c}\right)^2\right] \tag{11.19}$$

For $A_c/A = 5$ or 0.2, $(T_\Pi)_{max} = -8.3$ dB; and for $A_c/A = 10$ or 0.1, $(T_\Pi)_{max} = -14.1$ dB.

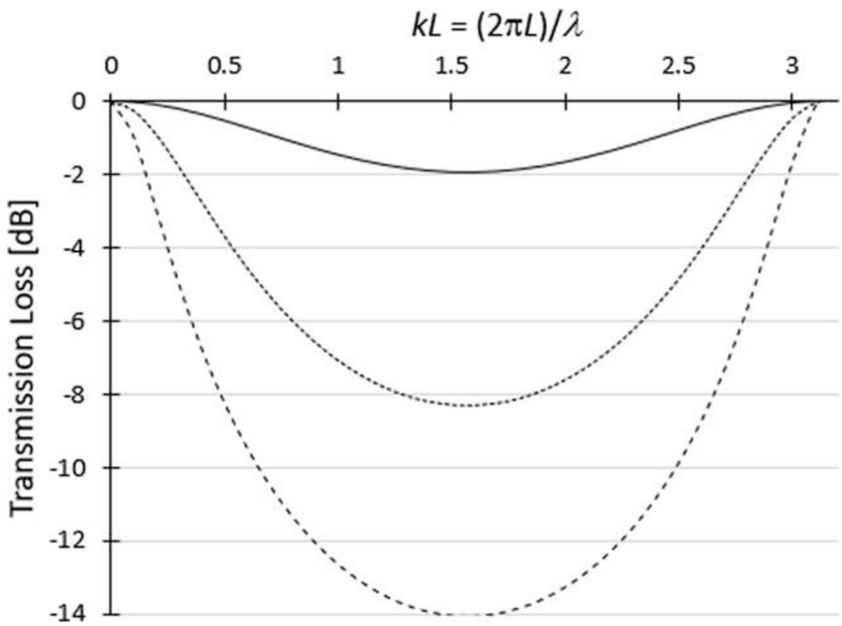

Fig. 11.6 The expansion/constriction duct transmission loss, T_{Π}, in dB $= 10\log_{10} T_{\Pi}$. Shown are area ratios of $A_c/A = 2$ or 0.5 (*solid line*), $A_c/A = 5$ or 0.2 (*dotted line*), and $A_c/A = 10$ or 0.1 (*dashed line*) plotted against a normalized frequency, $0 \leq kL = (2\pi L/\lambda) \leq \pi$. This behavior repeats for integer multiples of π with no loss for $kL = 0$ or π and maximum loss for $kL = \pi/2$

As will be shown in Sect. 13.5.4, for frequencies above $f_{1,1} = 0.578\ c/a$, where $a = \sqrt{A/\pi}$ is the radius of the circular duct, the planewave nature of propagation in the duct can no longer be guaranteed. That further limits the utility of such a strategy. Despite these limitations, elaborate combinations of expansion chambers and constrictions are used to attenuate sound in automotive exhaust mufflers using techniques that go well beyond those discussed here [4].

11.3 Snell's Law and Fermat's Principle

The previous results for planewaves normally incident on an interface between two media can be extended to planewaves that impinge on the interface from some arbitrary angle, θ_i, with respect to the normal direction that characterized the surface. The incident wavevector will now have two components, $\vec{k}_i = k_y \hat{e}_y + k_x \hat{e}_x$, where $\hat{e}_y$ and $\hat{e}_x$ are unit vectors in the +y and + x directions.

$$\begin{aligned}
p_i(x,y,t) &= \Re e\left[\hat{\mathbf{p}}_\mathbf{i} \exp j\left(\omega t + \left|\vec{k}_i\right| y\cos\theta_i - \left|\vec{k}_i\right| x \sin\theta_i\right)\right] \\
p_r(x,y,t) &= \Re e\left[\hat{\mathbf{p}}_\mathbf{r} \exp j\left(\omega t - \left|\vec{k}_i\right| y\cos\theta_r - \left|\vec{k}_i\right| x \sin\theta_r\right)\right] \\
p_t(x,y,t) &= \Re e\left[\hat{\mathbf{p}}_\mathbf{t} \exp j\left(\omega t + \left|\vec{k}_t\right| y\cos\theta_i - \left|\vec{k}_t\right| x \sin\theta_t\right)\right]
\end{aligned} \tag{11.20}$$

We can make a simple geometrical argument regarding the directions of the reflected and transmitted planewaves by adopting a perspective that was introduced by the Dutch physicist, Christiaan

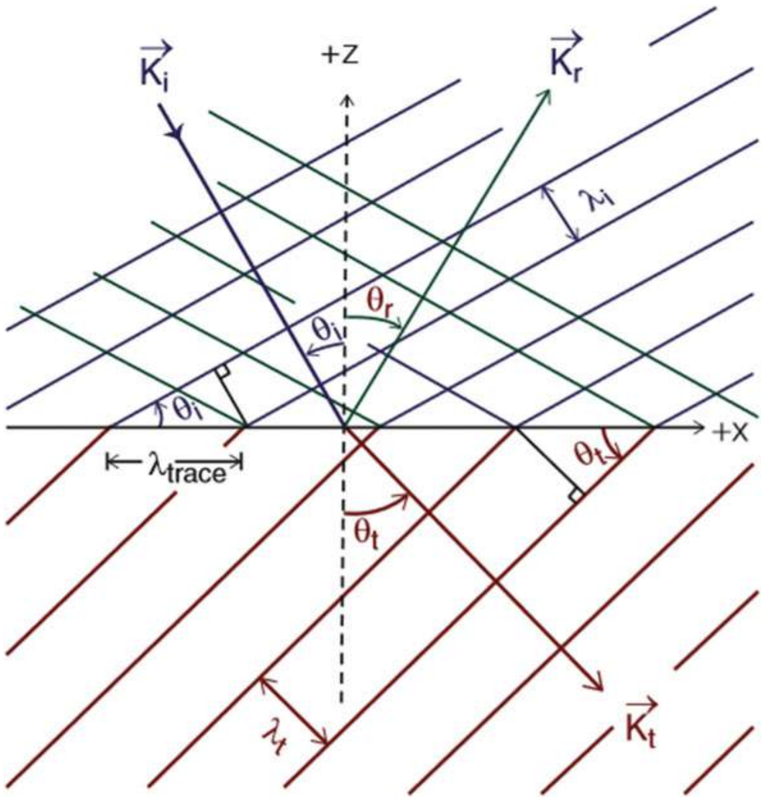

Fig. 11.7 Diagram showing an incident wave with wavevector, $\vec{k}_i$, intersecting a plane interface at an angle, θ_i, relative to the normal to the interface. Wave fronts of equal phase are shown perpendicular to the wavevector spaced by one wavelength of the incident sound, λ_i. That incident wave excites a reflected wave (*green*) and a transmitted wave (*red*). Successive maxima of pressure along the interface are separated by the "trace wavelength," λ_{trace}, that is common to all three waves. Based on the wavelengths in this figure, the sound speed in the lower medium, c_t, is greater than the sound speed in the upper medium, $c_i < c_t$. When the incident angle equals the critical angle, $\theta_i = \theta_{crit}$, then the direction of $\vec{k}_t$ is along the interface (i.e., $\theta_t = 90°$), and we have total internal reflection for all $\theta_i \geq \theta_{crit}$, so no energy is transmitted

Huygens, in 1678,[3] that makes a simple argument which matches boundary conditions at the interface. Figure 11.7 shows the incident wavevector, $\vec{k}_i$, with lines normal to $\vec{k}_i$, indicating the planes of constant pressure phase. We will imagine those lines represent the pressure maxima of the waves propagating toward the interface. Those wave fronts impinge on the interface, and we will consider each intersection of those incident wave fronts and the interface to be a source of pressure maxima for both the reflected and transmitted planewaves.

The spacing between those maxima along the interface, which we will call the *trace wavelength*, λ_{trace}, is easy to calculate from trigonometry and Garrett's First Law of Geometry[4]: $\sin\theta_i = \lambda_i/\lambda_{trace}$. For normally incident planewaves, the trace velocity $c_{trace} = f\lambda_{trace} = \infty$, since the wave fronts of equal phase intersect the interface so that the phase of the pressure on the interface is the same at all locations at every instant. Since λ_{trace} is the same for both the reflected and transmitted waves, the sound speeds

[3] C. Huygens, *Traitė de la Lumiere* (completed in 1678, published in Leyden in 1690).

[4] "Angles that look alike are alike."

in the two media will determine the angle that the reflected planewave, θ_r, and the angle transmitted planewave, θ_t, make with the direction of the normal to the interface.[5]

$$\lambda_{trace} = \frac{\lambda_i}{\sin\theta_i} = \frac{\lambda_r}{\sin\theta_r} = \frac{\lambda_t}{\sin\theta_t} \tag{11.21}$$

The sound speed, c_i, is the same for both the incident and reflected planewaves, so $\theta_r = \theta_i$; the angle of incidence equals the angle of reflection. This case is called *specular reflection*. If the interface has a surface roughness that is characterized by random assortments of "bumps" that are all much smaller in height and extent than the wavelength of sound, the reflection will be *diffuse*.

Again, in a linear system, the frequency, ω, with which the incident planewave drives the interface, must also be the frequency of the driven reflected and transmitted planewaves. Since $\lambda = c/f$, we can invert Eq. (11.21) to produce a result known as *Snell's law*.[6]

$$\frac{\sin\theta_i}{c_i} = \frac{\sin\theta_r}{c_i} = \frac{\sin\theta_t}{c_t} \tag{11.22}$$

Before moving on to calculation of the pressure reflection and transmission coefficients, it worth noticing that Snell's law could have been derived by insisting that propagation time from one location in the upper medium to some other location in the lower medium is minimized by the same condition on the angles that is expressed in Eq. (11.22). This approach utilizes *Fermat's principle* (1622)[7]: "The actual path between two points taken by a [wave] is the one that is traversed in the least time."

For the actual path to be an extremum of the total transit time, a neighboring path must take the same time; their time difference being at most second order in the deviation of the alternate path from the path of least time. Figure 11.8 provides a diagram of the path of least time (ACB) and a nearby path (AXB).

In the upper medium of Fig. 11.5, the perpendicular XE makes CE the reduction in distance traveled by the nearby path AX. The time savings by traveling via AC is therefore $t_i = \mathrm{CE}/c_i$. Similarly, in the lower medium, the perpendicular CF makes XF the additional distance traveled by the nearby path XB. The excess time in the lower medium is therefore $t_t = \mathrm{XF}/c_t$. Since $\measuredangle\mathrm{EXC} = \theta_i$ and $\measuredangle\mathrm{FCX} = \theta_t$, we can express the two transit times for the nearby path in terms of the common length XC using simple trigonometry.

$$t_i = \frac{EC}{c_i} = \frac{XC\sin\theta_i}{c_i} = t_t = \frac{XF}{c_t} = \frac{XC\sin\theta_t}{c_t} \tag{11.23}$$

Equation (11.23) also yields Snell's law after dividing through by XC.

[5] Since the trace wavelength is constant, its reciprocal, the trace wavenumber, $2\pi/\lambda_{trace}$, is also constant. In the underwater acoustic propagation community, this is commonly called "conservation of the horizontal wavenumber" [12]. Since I associate the term "conservation" with quantities that obey equations like (10.35), I prefer to consider the horizontal wavenumber to be an invariant, like the trace wavelength.

[6] Snell's law is known as Descartes' law in France. Willebrord Snellius (1580–1626) was not the first to produce that result. The law was first accurately described by the Persian scientist, Ibn Sahl, in Baghdad, where in 984, he used the law to derive lens shapes that focus light with no geometric aberrations as described in the manuscript *On Burning Mirrors and Lenses*.

[7] The principle of least time was actually first applied to reflections from a mirror much earlier, by Hero of Alexandria, around 60 CE. Since the reflected light propagates at the same speed as the incident light, this is equivalent to the path that is also the shortest geometrical distance.

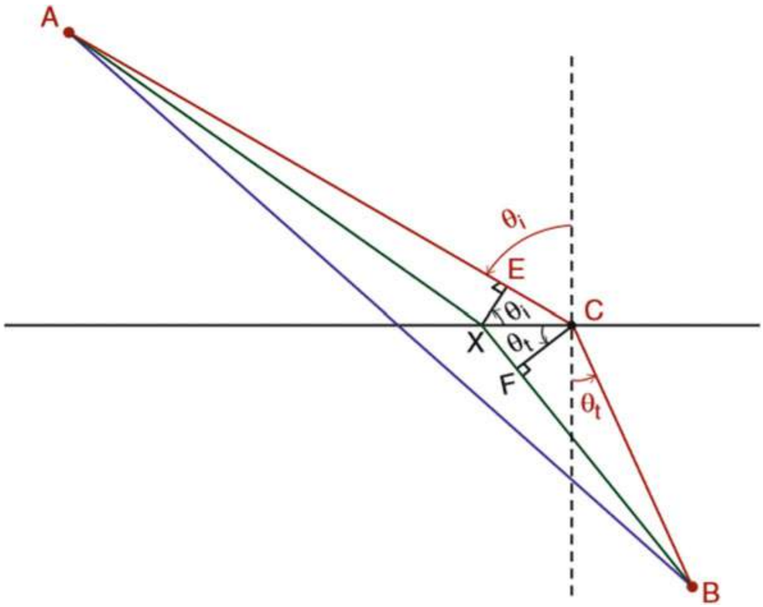

Fig. 11.8 Three paths from point A in the upper medium to point B in the lower medium. In this diagram, it is assumed that the propagation speed of the wave in the lower medium, c_t, is slower than the propagation speed in the upper medium, $c_i > c_t$. The path AB (*blue*) is the shortest distance, and the path ACB (*red*) takes the least time. The angles θ_i and θ_t can be determined by calculating the additional travel time beyond that required for ACB when going along the path through AXB (*green*) and setting that excess equal to zero [5]

11.3.1 Total Internal Reflection

In passing from a faster medium into a slower medium, $c_i > c_t$, the angle that the transmitted wavevector makes with respect to the normal at the interface, θ_t, is smaller than the incident angle, θ_i, also measured from the normal. If the incident medium has a slower sound speed than the transmission medium, $c_i < c_t$, then it is possible that the angle of transmission, θ_t, dictated by Snell's law, could become a complex number. In that case, we can define a *critical angle*, θ_{crit}, where $\theta_t = 90°$ (i.e., the transmitted wave travels along the interface but not into the second medium).

$$\sin\theta_{crit} = \frac{c_i}{c_t}; \quad \text{if} \quad c_i < c_t \tag{11.24}$$

This is a consequence of the fact that the minimum trace velocity, $c_{trace} = f\lambda_{trace}$, shown in Fig. 11.7, in the lower medium, is limited to c_t, which equals c_{trace} when $\theta_t = 90^\circ$. Using the fact that $\cos^2\theta + \sin^2\theta = 1$, the angle of transmission can be expressed in terms of the angle of incidence and the sound speed ratio.

$$\cos\theta_t = \sqrt{1 - \sin^2\theta_t} = \sqrt{1 - \left({}^{c_t}\!/_{c_i}\right)^2 \sin^2\theta_i} = -j\sqrt{\left({}^{c_t}\!/_{c_i}\right)^2 \sin^2\theta_i - 1} \tag{11.25}$$

If $c_t > c_i$, the first term under the square root becomes imaginary, which is expressed explicitly in the final term at the right of Eq. (11.25).

Substitution of Eq. (11.25) into the expression for the transmitted pressure in Eq. (11.20) produces an exponential decay of the sound with increasing distance away from the interface, for incident angles that exceed the critical angle, producing an inverse characteristic depth, $(1/\delta)$.

$$k_z = \frac{1}{\delta} = \left|\vec{k}_t\right| \sqrt{(c_t/c_i)^2 \sin^2\theta_i - 1} \tag{11.26}$$

$$p_t(x,z,t) = \Re e\left[\widehat{\mathbf{p}}_{\mathbf{t}} e^{+(y/\delta)} \mathrm{e}^{\,j\left[\omega t - \left|\vec{k}_i\right| x \sin\theta_i\right]}\right]; \quad \text{for } y \leq 0 \tag{11.27}$$

This solution is a wave that is localized just below the interface. For angles of incidence, $\theta_i < \theta_{crit}$, the transmitted wave fills the half-space of the lower medium, as shown in the lower half of Fig. 11.7. When $\theta_i = \theta_{crit}$, all of that outgoing energy collapses to the surface in a layer with exponential thickness, δ. The thickness of that layer decreases monotonically as θ_i increases beyond θ_{crit}.

If we apply the Euler equation to Eq. (11.27) to determine the velocity, v_t, normal to the surface, we find $\widehat{\mathbf{v}}_{\mathbf{t}} = j\widehat{\mathbf{p}}_{\mathbf{t}}(\omega\rho\delta)$, so the pressure and particle velocity are 90° out-of-phase. The intensity leaving the interface is zero since there is no in-phase component of pressure and velocity. That does not mean that the layer contains no energy, just that none of the energy is propagating. If there were some scattering centers (i.e., defects, voids, inclusions of material with some compressibility, and/or density contrast), the energy trapped in that layer could be reradiated (i.e., scattered; see Sect. 12.6) and escape.

The concept of *total internal reflection* was first recognized in optics. One application of total internal reflection that I find particularly inspiring occurs in the compound eyes of insects and other arthropods. With thousands of lenses, the use of an equal number of irises, like those in avian and mammalian eyes, is not particularly efficient. In the arthropod's compound eye, each lens is connected to the optic nerve by a transparent tube that contains the light by total internal reflection, due to the difference between the index of refraction (i.e., the optical equivalent of our specific acoustic impedance) between the tube and the surrounding fluid. The way that insects control the amount of light that reaches the optic nerve is by a chemical reaction in the fluid that surrounds the tube. Under bright lighting, the fluid will produce a precipitate with small particles that scatters light out of the trapped layer, thereby reducing the amount of light reaching the optic nerve. The physical structure of the compound insect eye is shown in Fig. 11.9.

Proof of this system's efficacy is the fly's ability to avoid getting swatted outdoors in broad daylight and indoors in a darkened room. (We should now pause briefly out of respect for Darwin and the power

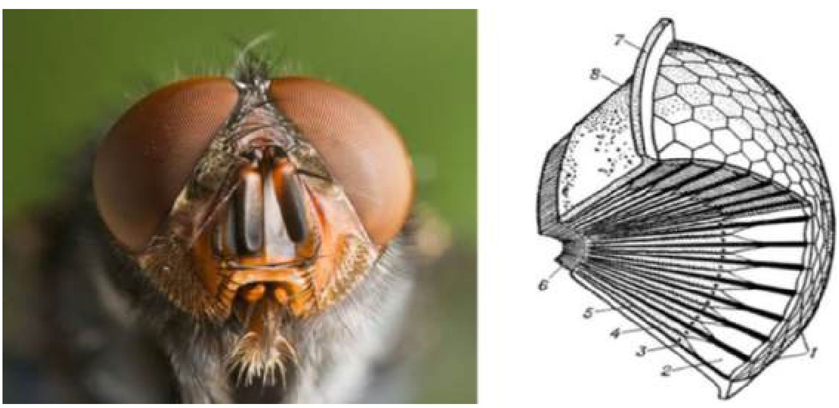

Fig. 11.9 (*Left*) The compound eyes of the blue bottle fly. (*Right*) Each of the "tubes" is optical fibers, called an *ommatidium*. They guide light from the lens to the optic nerve endings (4 and 5) using total internal reflection to regulate the transmission of the light. Ant eyes have about six *ommatidia* and dragonfly eyes have as many as 25,000. This anatomical drawing of a compound eye shows the corneal lens (1) and the crystalline cone (2) which combine to form the dioptric apparatus. At the base is the light-sensitive rhabdom (5 and 6). The space between the tubes (3) contains the pigment cells that will form a precipitate that scatters some of the optical energy out of the trapped layer at the interface if the light is too bright, effectively reducing the field of view (known in optics as the "numerical aperture" of the lens). (Photo and diagram taken from Wikipedia)

of natural selection.) I would be most interested in finding a similar system for controlling the sound amplitude that reaches the auditory nerve in any animal, although the ability to focus sound seems ubiquitous in marine mammals, as shown for the Cuvier's beaked whale in Fig. 11.18.

11.3.2 The Rayleigh Reflection Coefficient

Although we have calculated the angles of reflection and transmission for planewaves of sound impinging on a planar interface from an arbitrary direction, we have yet to calculate the amplitude reflection coefficient in terms of the specific acoustic impedances, as we did for the case of normal incidence at the interface between two media in Eq. (11.9). To produce the equivalent of Eq. (11.9) for oblique incidence (i.e., $\theta_i \neq 0°$), we need to generalize the velocity boundary condition of Eq. (11.5), since it is only the normal component of the velocity that needs to be continuous across the boundary to avoid cavitation at the interface.[8]

$$|\widehat{\mathbf{v}}_{\mathbf{i}}| \cos\theta_i + |\widehat{\mathbf{v}}_{\mathbf{r}}| \cos\theta_r = |\widehat{\mathbf{v}}_{\mathbf{t}}| \cos\theta_t \tag{11.28}$$

Pressure continuity, expressed in Eq. (11.6), is unchanged since pressure is a scalar quantity.

Forming the ratio of those boundary conditions, as we did in Eq. (11.7), leads to the desired result for the ratio of the reflected pressure to the incident pressure $R \equiv \widehat{\mathbf{p}}_{\mathbf{r}}/\widehat{\mathbf{p}}_{\mathbf{i}}$.

$$R \equiv \frac{\widehat{\mathbf{p}}_{\mathbf{r}}}{\widehat{\mathbf{p}}_{\mathbf{i}}} = \frac{\frac{z}{\cos\theta_t} - \frac{z_i}{\cos\theta_i}}{\frac{z_t}{\cos\theta_t} + \frac{z_i}{\cos\theta_i}} \tag{11.29}$$

Once again, we are confronted with an expression for the reflection coefficient that can vanish, providing perfect transmission, if the numerator of Eq. (11.29) is zero.

$$\frac{\cos\ \theta_t}{\cos\ \theta_i} = \frac{z_t}{z_i} \tag{11.30}$$

Using Snell's law to eliminate θ_t, this angle, called the *angle of intromission*, θ_{intro}, can be expressed in terms of both the impedance and sound speed or mass density ratios.

$$\sin^2(\theta_{intro}) = \frac{(z_t/z_i)^2 - 1}{(z_t/z_i)^2 - (c_t/c_i)^2} = \frac{1 - (z_i/z_t)^2}{1 - (\rho_1/\rho_2)^2} \tag{11.31}$$

Not every combination of media will have an angle of intromission that depends upon both sound speed and density ratios. For θ_{intro} to be real, both the numerator and denominator of Eq. (11.31) must have the same sign.

There are four combinations of impedance and sound speed ratios:

(i) ***No θ_{crit} and no θ_{intro}*** If both $z_t/z_i < 1$ and $c_t/c_i < 1$, there is no critical angle, so $0 < R < -1$ for all θ_i. For this case, $\theta_i > \theta_t$, so $(\cos\theta_t/\cos\theta_i) > 1$ and $z_t/z_i < 1$, so there can be no angle of intromission.

[8] If we were treating the interface between two viscous liquids or between a viscous liquid and a solid surface, then we would need to impose a "no-slip" boundary condition on the transverse components of particle velocity. This is particularly important for the fluid-solid boundary since the viscous stress on the interface can couple to shear waves into the solid and vice versa. The coupling of shear waves in the solid to viscous waves in liquids has been used to measure fluid density and viscosity.

(ii) ***Real θ_{crit} but no θ_{intro}*** If both $z_t/z_i > 1$ and $c_t/c_i > z_t/z_i$, then there will be a critical angle above which there will be total internal reflection so $R = 1$ if $\theta_i > \theta_{crit}$. Since $c_t/c_i > z_t/z_i$, the numerator of Eq. (11.31) will be positive, but the denominator will be negative, so there can be no θ_{intro}.

(iii) ***Real θ_{intro} but no θ_{crit}*** If $z_t/z_i > 1$ and $c_t/c_i < 1$, then there will be no critical angle, so $0 \leq R < 1$ for all θ_i. Since $c_t/c_i < z_t/z_i$, both the numerator and the denominator of Eq. (11.31) will be positive, so there will be an angle of intromission, $\theta_i = \theta_{intro} < 90^\circ$.

(iv) ***Real θ_{intro} and real θ_{crit}*** If $c_t/c_i > 1$ and $z_t/z_i < 1$, then there will be both a critical angle, $\theta_{crit} < 90°$, above which there will be total internal reflection so $R = 1$ if $\theta_i > \theta_{crit}$, and both the numerator and the denominator of Eq. (11.31) will be negative, so there will be an angle of intromission $\theta_i = \theta_{intro} < \theta_{crit} < 90^\circ$.

Total transmission at the angle of intromission has been observed in high-porosity marine sediments, like silty clays, which exhibit a sound speed through its bulk which is lower than that of the interstitial fluid within its pores. When high-porosity sediment is at the water/sediment interface, there can be total transmission of sound into the seafloor. Measurements of the angle of intromission in coastal regions around Italy indicate that the properties of the high-porosity sediments are surprisingly uniform over large areas [6].

11.4 Constant Sound Speed Gradients

To this point in our discussion of the refraction of sound, we have only considered plane boundaries that separate media with a discontinuity in their sound speed, density, and/or specific acoustic impedance. There are many situations of interest where the *refraction* (or bending) of a planewave of sound can create interesting and significant effects resulting from a gradual change in the acoustical properties of the medium. These effects are easily calculable in the limit that such sound speed changes are a linear function of position when those changes occur over a distance that extends over very many acoustic wavelengths.

Figure 11.10 shows two examples of sound refraction in air that supports a temperature gradient that depends upon the time of day. As expressed by the quadratic dependence of sound speed on the mean temperature of an ideal gas in Eq. (10.23), the change in sound speed, Δc, with height, z, above the ground is related to the changes in the absolute temperature, T.

$$\frac{dc}{dz} = \left(\frac{dc}{dT}\right)\left(\frac{dT}{dz}\right) = \frac{c}{2T}\left(\frac{dT}{dz}\right) \tag{11.32}$$

Similar refractive effects occur in the ocean where the speed of sound in seawater is a complicated function of temperature, salinity, and depth (pressure).

$$\begin{aligned} c = {} & 1493.0 + 3(t-10) - 0.006(t-10)^2 - 0.04(t-18)^2 \\ & + 1.2(S-35) - 0.01(t-18)(S-35) + D/61 \end{aligned} \tag{11.33}$$

In Eq. (11.33), the sound speed, c in m/s, is a function of the temperature, t, in degrees Celsius. The salinity, S, is measured in grams of salt per kilogram of water, and D is the depth below the surface measured in meters [8]. That formula is valid within ±0.2 m/s for -2 °C $\leq t \leq$ +24.5 °C, $0.030 \leq S \leq 0.042$, and $0 \leq D \leq 1000$ m.

Figure 11.11 shows the sound speed variation with depth that was measured over 9 years in the ocean 15 miles (24 km) south-east of Bermuda. Although significant sound speed variation over the 9 years is apparent within roughly 2 km of the surface, it is possible to represent the change in sound speed with depth using a *piecewise-linear approximation*.

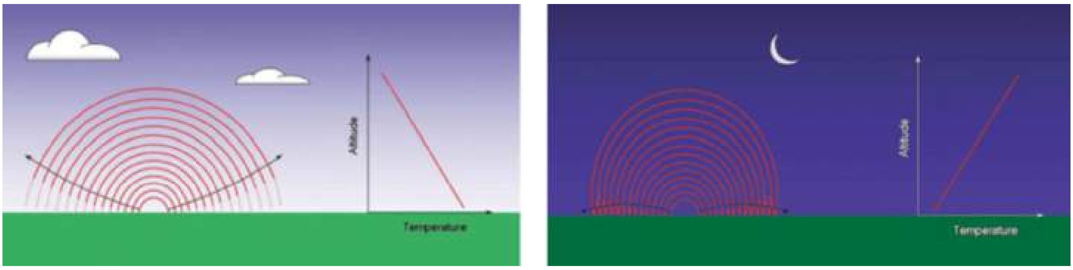

Fig. 11.10 (*Left*) During the day, the temperature of the atmosphere generally decreases with altitude above the ground causing sound waves to refract upward since the speed of sound is proportional to $\sqrt{T}$. (*Right*) The opposite conditions can occur at night when the temperature of the air in contact with the ground is colder that than the air above it (a "temperature inversion"). This causes sound to be refracted downward. If there is wind, it can also cause the sound speed to vary with height above the ground. (Figures courtesy of T. B. Gabrielson [7])

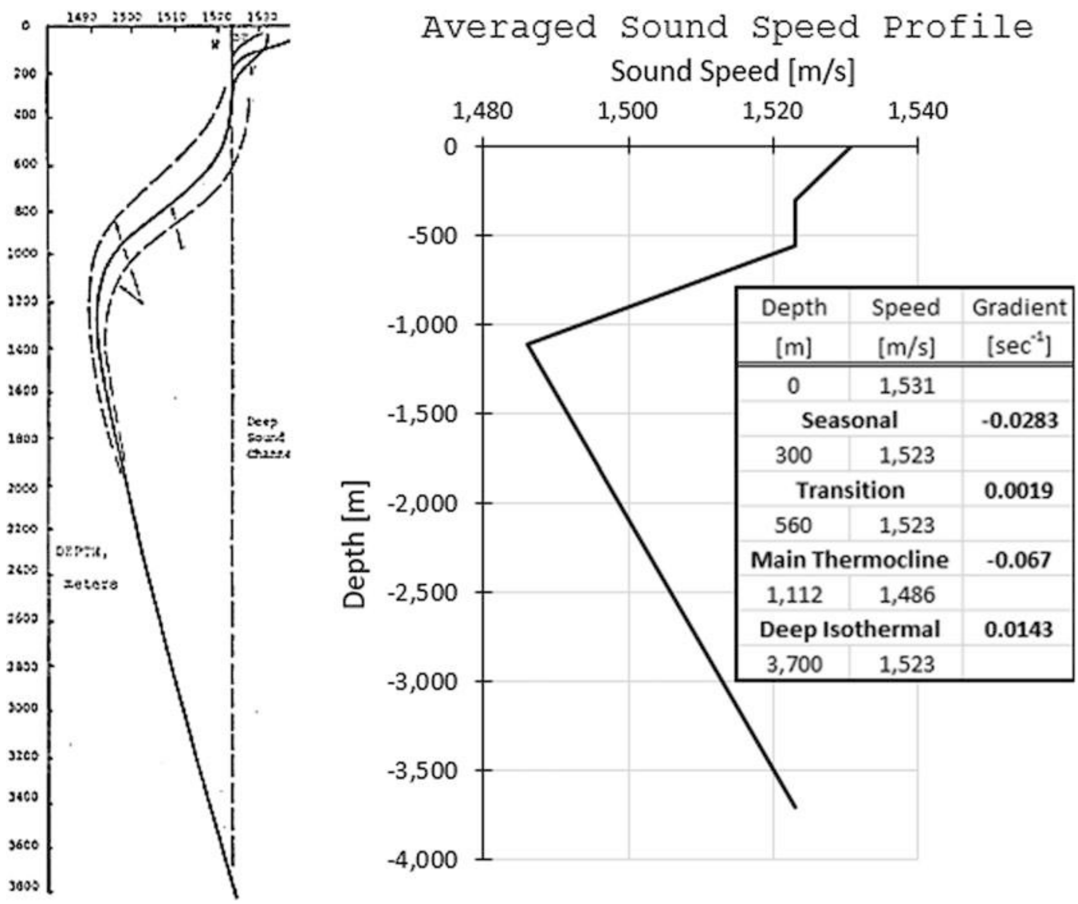

Fig. 11.11 (*Left*) These deep-ocean sound speed profiles were taken every 2 weeks over a 9-year period at a location 24 km SE of Bermuda. [9] The solid curve is the average and the dashed curves show the extremes. This typical deep-sea profile may be divided into a number of layers having different properties. At the top, the diurnal layer shows day-night variability and responds to weather changes. Below it, down to the depth of about 300 m, lays the seasonal thermocline that is above the main thermocline, which exhibits the strongest sound speed gradient. Below the thermocline, beneath 1200 m, the deep isothermal layer has a constant temperature of +4 °C. There, the sound speed's increase with depth is dominated by the increasing pressure. (*Right*) The measured sound speed profile is replaced by a piecewise-linear approximation that provides a constant sound speed gradient for each layer, as indicated by the embedded table. At a depth of approximately 3700 m, the sound speed is the same as it is at a depth of approximately 560 m. Between those two depths, sound can be trapped in the "deep sound channel" in the same way that light is trapped in an optical fiber, except the core of an optical fiber that is about 10 μm and the sound channel that is about 1 km, a height ratio of about 10^8

11.4.1 Constant Gradient's Equivalence to Solid Body Rotation

The goal in this sub-section is to develop a simple formalism that will permit calculation of the path of planewaves in a medium with a sound speed that is a linear function of height or depth. Furthermore, we would like to be able to track the trajectory of the sound (i.e., follow the direction of the wavevector) through regions of changing sound speed gradient, a process known as *ray tracing*. To do this, we must first recognize that the propagation of sound through a region of constant sound speed gradient is isomorphic to the solid body rotation of a disk, since the tangential velocity, $\vec{v}_{\tan}$, of any point on the rotating disk is proportional to its (linear) distance, $|\vec{r}|$, from the axis of rotation.

$$\vec{v}_{\tan} = \vec{r} \times \vec{\omega} \tag{11.34}$$

Since this equation refers to a rotating disk, the use of the cross-product might seem to be pedantic excess, but it is intended to remind you of your study of solid body rotational dynamics during your freshman physics course.

If we limit ourselves to linear changes in sound speed with height or depth, then the sound speed gradient is a constant: $dc/dz \equiv g$. In analogy with a rotating disk of radius, R, as diagrammed in Fig. 11.12, we can equate sound speed, c, with the tangential velocity of a point on the rim of the disk, $\vec{v}_{rim}$, and integrate our above definition; it is easy to see that g plays the same role as ω (and has the same units) in Eq. (11.34).

$$\int_0^{v_{rim}} dc = g\int_0^R dz \quad \Rightarrow \quad R = \frac{|\vec{v}_{rim}|}{g} \tag{11.35}$$

I like to think of the refraction (bending) of the sound wave's trajectory in a constant sound speed gradient by picturing the advance of the planewave fronts as represented schematically in Fig. 11.13.

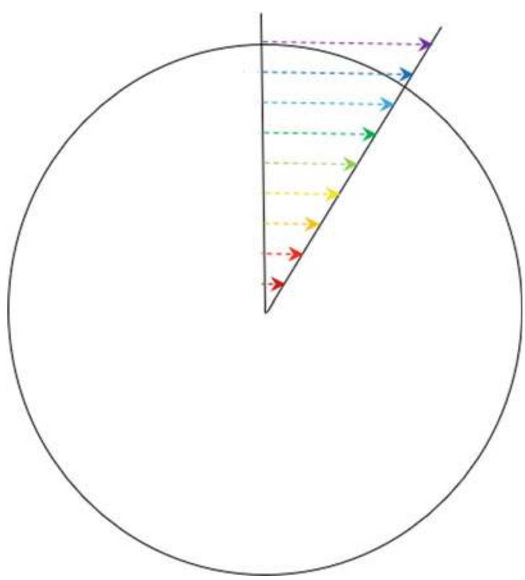

Fig. 11.12 Shown at the right is a disk that is rotating. The dashed, colored arrows indicate the tangential velocity that increases linearly with distance from the axis of rotation. Such a velocity distribution in space is identical to the assumed constant sound speed gradient that will control the refraction of sound waves

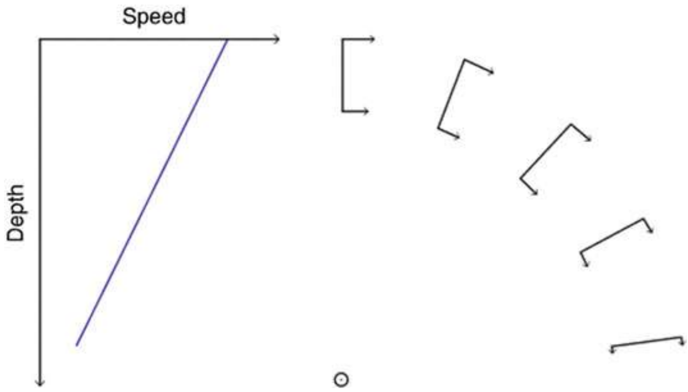

Fig. 11.13 A conceptual sketch of planewave fronts moving through a medium with the velocity gradient shown at the left. The arrows at the top of the wave fronts are always longer than the arrows at the bottom. This turns the wave front downward until the wave front is nearly horizontal. Once horizontal, both ends of the wave front will move with the same speed, and the wave will continue downward without changing direction

To introduce this "disk rotation" approach to analysis of the propagation of planewaves through a medium with constant speed gradients, let's consider the measurement of road noise during the day, when the temperature of the air is decreasing with increasing altitude, as shown in Fig. 11.10 (left).

Assume that you are asked to determine the sound pressure level created by traffic on a highway at a proposed housing location that is 150 m from the highway. By measuring the average temperature at a height of 0.5 m and at 5 m, you determine that the sound speed at 0.5 m is 342.8 m/s and at 5.0 m is 341.3 m/s. How high must your microphone be above the ground, at a distance of 150 m from the source, to ensure that you intercept sound that leaves the highway in an initially horizontal direction?

To begin, let's calculate the sound speed gradient, $\mathrm{d}c/\mathrm{d}z = g \cong \Delta c/\Delta z =$ (2.8–1.3 m/s)/4.5 m $= 0.333\ \mathrm{s}^{-1}$. Since the sound speed decreases with height, we know that the wave will be refracted upward, as shown in Fig. 11.10 (left). We'll assume that the noise is generated at the intersection of the tire and the road at $z = 0$, where $c_o = 343.0$ m/s (extrapolating down to the surface from the lowest measurement at 0.5 m above the ground).

We now need to calculate the radius, $|R|$, of this limiting ray's circular path.

$$|R| = \frac{c_o}{g} = 1029\ \text{ m} \tag{11.36}$$

A simple trigonometry identity can be used to determine the height, $h = 11.0$ m, above the ground that a microphone must be placed to receive the sound radiated by the tires. For me, drawing a sketch, like in Fig. 11.14, is always crucial.

$$\begin{aligned} \sin\theta &= \frac{150}{1029} = 0.146 \quad \Rightarrow \quad \theta = 0.146\,\text{rad} \ = 8.38^\circ \\ h &= |R| - |R|\cos\theta = |R|(1 - \cos\theta) \cong |R|\frac{\theta^2}{2} = 11.0\ \text{ m} \end{aligned} \tag{11.37}$$

The final expression above made use of the small-angle expansion of cosine in Eq. (1.6).

Although the refractive process was not understood until the twentieth century [7], reports of the existence of an acoustic "shadow zone" appeared much earlier. Below is the account of R. G. H. Kean as he watched the Battle of Gaines's Mill during the American Civil War [10]:

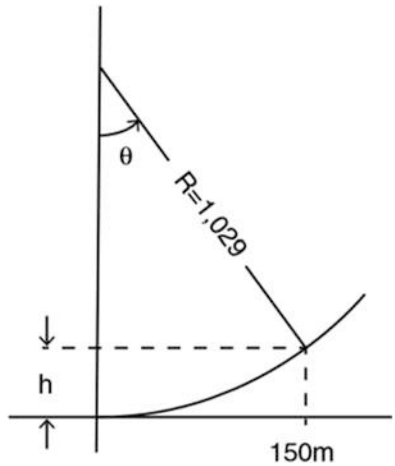

Fig. 11.14 Sketch (not to scale) of the ray path of the sound generated by the tire noise on a road surface. The observation point is 150 m from the sound source. Between the ground and the circular arc is a "shadow zone" that is created by the upward refraction of the sound produced by the sound speed gradient, $dc/dz = 0.333\ s^{-1}$, which was used to calculate the radius, $|R| = 1029$ m, applying Eq. (11.36). A microphone must be placed at least a distance, h, above the ground to intercept the tire noise. At the surface ($h = 0$), the sound speed is $c_o = 343.0$ m/s. At $h = 11.0$ m above the surface, the sound speed is 339.3 m/s

> I distinctly saw the musket-fire of both lines . . . I saw batteries of artillery on both sides come into action and fire rapidly. Yet looking for near two hours, from about 5 to 7 P.M. on a midsummer afternoon, at a battle in which at least 50,000 men were actually engaged, and doubtless at least 100 pieces of field-artillery . . . *not a single sound of the battle* was audible to General Randolph and myself . . . [However, the] cannonade of that very battle was distinctly heard at Amhurst Court-house, 100 miles west of Richmond, as I have been most credibly informed.

The process of refraction in a sound speed gradient, as illustrated in a particularly simple form in Fig. 11.14, is entirely reversible. If we were to say that we had a sound source directed 8.4° below the horizontal direction, located 11.0 m above the ground, then we could just as easily say that it would intersect the ground 150 m away, based on Fig. 11.14 and the results of Eq. (11.37).

Since much of the interest in the propagation of sound in a sound speed gradient (linear or otherwise) tends to concern sound waves that are nearly grazing the horizontal axis, the *grazing angle* is more commonly used in Snell's law than the angle measured with respect to the normal to the surface, which was our previous choice for discussion of reflection and transmission from a plane surface of discontinuity. If we now use the grazing angle, then we can rewrite Eq. (11.22) by letting θ be the angle below the horizontal and c_o be the sound speed at a location where the sound waves are propagating horizontally (i.e., $\cos 0° = 1$).

$$\frac{c}{\cos\theta} = c_o \tag{11.38}$$

Let's apply the above version of Snell's law to the example in Fig. 11.14. That ray is horizontal at $h = 0$, where $c_o = 343.0$ m/s. Assuming, as before, a constant sound speed gradient, at the "source height" of 11.0 m, $c = 339.3$ m/s. Plugging directly into Eq. (11.38), $\cos\theta = c/c_o$, so $\theta = 0.147$ radians $= 8.4°$. Of course, we could have used Eq. (11.37) to calculate the sound speed 11.0 m above the surface, since we already knew that $\theta = 8.4°$.

11.4.2 Sound Channels

We will now apply this formalism to a particularly interesting case that occurs in a sound speed profile like the one shown in Fig. 11.11, describing the deep ocean off of Bermuda, which we have approximated by a series of contiguous line segments with constant (but different) sound speed gradients. There is a sound speed minimum of $c_{min} = 1486$ m/s, at a depth of 1112 m, between the main thermocline and the deep isothermal layer. As evident from Fig. 11.13, in such a constant gradient (i.e., linear sound speed profile), the sound will "go to the slow," and therefore, we expect that some sound will become trapped around that sound speed minimum in a *sound channel*.

In this sub-section, we will trace several rays from a submerged source to develop an understanding of the channel's propagation characteristics. Assume that there is a sound source at a depth of 800 m, where the sound speed (by interpolation) is 1507 m/s. We start by calculating the upward angle from the source that will result in a horizontal ray at the top of the upper gradient, $z = 560$ m, where the sound speed is $c_{max} = 1523$ m/s. By Snell's law, as expressed in terms of the grazing angles in Eq. (11.38), $\theta_1 = \cos^{-1}(1507/1523) = 0.145$; hence, $\theta_1 = 8.31°$. The radius of the circular path of the ray, $|R_1| = c_o/g = (1523 \text{ m/s} \div 0.067 \text{ s}^{-1}) = 22.73$ km. Based on the diagram in Fig. 11.15, the sound ray intersects the top of the channel at a horizontal distance that is $r_1 = |R_1| \sin \theta_1 = 3.3$ km from the source.

From the top of the channel ($z = 560$ m), the ray will return to the channel axis along the same circular path and will intersect the axis ($z = 1112$ m) at $\theta_2 = \cos^{-1}(1486/1523)$, so $\theta_2 = 0.221$ rad $= 12.66°$. The horizontal distance, $r_2 - r_1 = |R_1| \sin \theta_2 = 5.0$ km.

The ray enters the deep isothermal layer where $|R_2| = (1486 \text{ m/s} \div 0.0143 \text{ s}^{-1}) = 103.9$ km. (The center of that circle is only a geometrical "construction point," so the fact that it is located above the stratosphere should not be a cause for our concern.) Since we have defined the bottom of the channel as the location where the sound speed in the deep isothermal layer equals the sound speed at the top of the

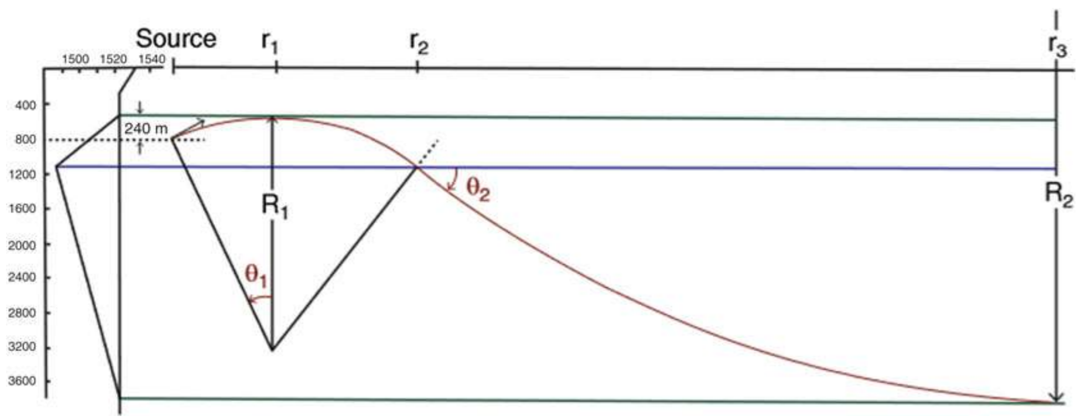

Fig. 11.15 The diagram of the sound speed vs. depth at the left is based on the piecewise-linear approximation of Fig. 11.11. There is a sound speed minimum at a depth of $z = 1112$ m that is the axis of a sound channel shown by the horizontal **blue** line. The velocity maxima are shown by the horizontal *green* lines at depths of 560 m and 3700 m, corresponding to $c_{max} = 1523$ m/s. The ray paths, ranges, depths, and especially the ray path radii, $|R_1|$ and $|R_2|$, are not drawn to scale. The limiting ray paths for a sound source located at a depth of 800 m, and horizontal distance, $r = 0$, are shown in *red*, launched at an angle of $\theta_1 = 8.31°$ above the horizontal. The turning point for the ray in the upper layer occurs at a horizontal distance from the source of r_1, while the turning point for the ray in the lower layer occurs at a horizontal distance from the source of r_3. The ray crosses the channel axis at r_2 and enters the lower layer at an angle θ_2 below the horizontal

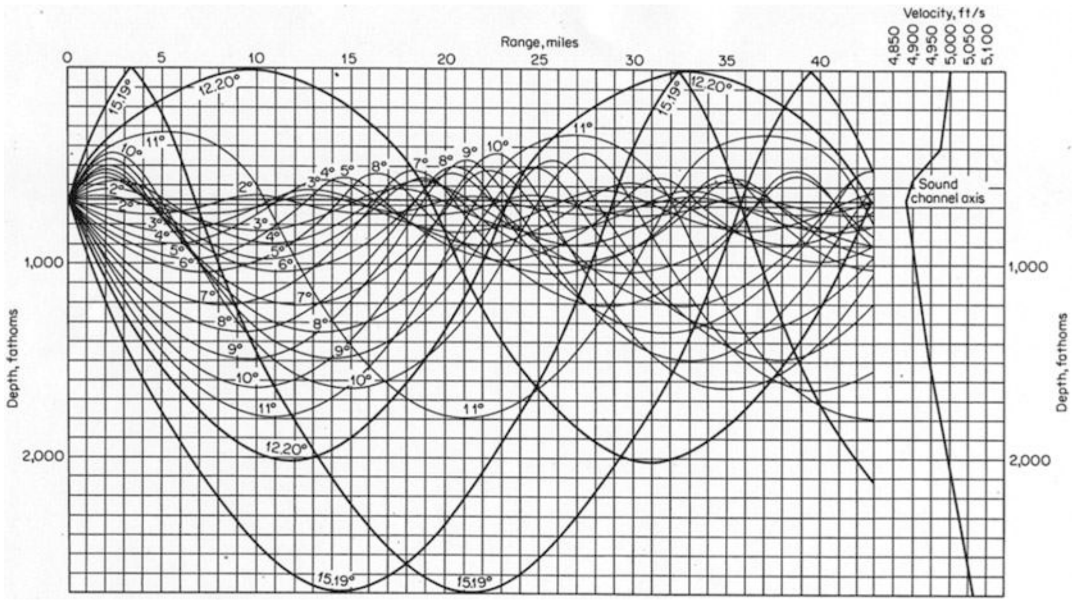

Fig. 11.16 Ray diagram for transmission paths in the deep sound channel for a source located on the channel axis. Depth is in fathoms (1 fathom = 6 feet = 1.829 m), range is in miles (1 mi = 1.609 km), and sound speed is in feet/second (1 fps = 30.48 cm/s), as a function of depth is provided at the right side of the graph. For angles $\theta > \theta_{max} = 12.2°$, waves escaping the channel are reflected from the air-water interface [11]

main thermocline, $c_{max} = 1523$ m/s, Snell's law will guarantee that it will reach that depth with a ray that is again horizontal, after traveling a horizontal distance, $r_3 - r_2 = |R_2| \sin \theta_2 = 22.8$ km. From that point at horizontal distance from the source, r_3, the path should repeat indefinitely with the cycle distance from the top of the channel back to the top of the channel being $2(r_3 - r_1) = 55.6$ km.

To calculate the angular width of the sound radiated by our source located at $z = 800$ m below the surface, which will be trapped in the channel, we need to follow a ray that leaves the source at an angle below horizontal, θ_{-1}, that will also take it to the depth ($z = 3700$ m) where the sound speed is again c_{max}. That initially downward-directed ray will also have to cross the sound channel axis at $\theta_2 = 12.66°$ if it is to become horizontal at $z = 3700$ m. Again, Snell's law guarantees that (1507 m/s $\div$ cos θ_{-1}) = (1486 m/s $\div$ cos θ_2) = 1523 m/s, so $|\theta_{-1}| = |\theta_1| = 8.31°$. That result is easy to visualize since we can imagine a "virtual source" that is located $2r_1$ away from the original source, where the ray makes an angle of $-8.31°$ with respect to the horizontal. Any ray that leaves the source within $\pm 8.31°$ will be trapped in the sound channel created by the two sound speed gradients.

Again, Snell's law makes it easy to see that an initially horizontal ray leaving our source at a depth of $z = 800$ m will go up and down in the channel from a depth of $z = 800$ m to a depth of $z = 2581$ m, where the sound speed will again be 1507 m/s and the rays will again be horizontal. Figure 11.16 diagrams ray paths from a more complicated sound channel for a source located on the channel axis [11].

The results illustrated in the previous example can be generalized by defining a maximum angle $\pm\theta_{max}$ (above or below the horizontal) that will result in the trapping of a wave launched at the channel axis, in terms of the minimum sound speed at the axis, c_{min}, and the maximum sound speed, c_{max}, at the bottom and top of the channel.

$$\cos\theta_{\max} = \frac{c_{\min}}{c_{\max}} \tag{11.39}$$

Expanding $\cos\theta_{max}$ for small angles and defining $\Delta c = c_{max} - c_{min}$, Eq. (11.39) can be approximated as $\theta_{max} \cong \sqrt{2Dc/c_{max}}$. When the source is above or below the height or depth of the channel by a distance, z_o, in a layer D thick, Snell's law, and the requirement that a trapped ray at the channel boundary is horizontal, provides the range of trapping angles, $\theta_{\pm 1} = \pm\theta_{max}\sqrt{z_o/D}$, when the source is not located on the sound channel's axis. Along the channel axis, $z_o = D$. At the extremes, $z_o = 0$, only the horizontal ray is trapped. The long-range transmission ability of the deep sound channel was used during World War II to rescue aviators that crashed at sea.[9] A downed pilot would drop a small explosive charge that was rigged to detonate near the depth of the sound channel axis. If the sound were detected with two or more hydrophones, also located at the axis depth, the reception times could be used to localize the search by triangulation. Successful rescues were made this way using hydrophones connected to shore stations that were thousands of miles from the aircraft impacts. More recently, the same ability to make localizations at sea has been used for missile-impact location [12], and measurement of the time delays has been used to measure the mean temperature of the deep ocean [13].

11.4.3 Propagation Delay*

It is interesting to calculate the difference in the propagation times for sound traveling along different paths to reach the same horizontal distance from the source. Although the path along the axis is the shortest, it is also going through the medium with the minimum sound speed. The longer (curved) paths travel through water that has a faster sound speed. Does the shorter path beat the faster path?

Let's first consider the ray that is generated on the sound channel axis and travels along a circular path to the top of the channel. The initial angle of such a ray above the horizontal is $\theta_{max} \cong \sqrt{2Dc/c_{max}}$, as already shown. The transit time, T_{upper}, for that ray can be calculated if we integrate from $\theta = 0°$ to $\theta = \theta_{max}$, where the sound speed depends upon angle, $c(\theta) = c_{max}\cos\theta$.

$$T_{upper} = \int_0^{\theta_{\max}} \frac{|R|d\theta}{c(\theta)} = \int_0^{\theta_{\max}} \frac{|R|d\theta}{c_{\max}\cos\theta} = \frac{|R|}{c_{\max}}\int_0^{\theta_{\max}} \frac{d\theta}{\cos\theta} \tag{11.40}$$

There is an analytical solution for the above definite integral, but simply writing the answer provides no useful physical insight.

$$\int_0^{\theta_{\max}} \frac{d\theta}{\cos\theta} = \int_0^{\theta_{\max}} \sec\theta \; d\theta = \ln\left[\csc\theta - \cot\theta\right]_0^{\theta_{\max}} \tag{11.41}$$

In these problems, the angles are generally small, so the series expansion of the sine and cosine functions and the binomial expansion can both be employed to simplify the integration and its interpretation.

$$\int_0^{\theta_{\max}} \frac{d\theta}{\cos\theta} \cong \int_0^{\theta_{\max}} \frac{d\theta}{\left(1 - \frac{\theta}{2}\right)} \cong \int_0^{\theta_{\max}} \left(1 + \frac{\theta^2}{2}\right) d\theta = \theta_{\max} + \frac{\theta_{\max}^3}{6} \tag{11.42}$$

The transit time for the axial ray, T_{axial}, that goes the same horizontal distance, $r = |R| \sin\ \theta_{max}$, is just $T_{axial} = r/c_{\min}$. Since $c_{min} = c_{max}\cos\theta_{max}$, the same approach can be used.

[9] In this context, the channel was known as the *SOFAR channel*, which stood for *so*und *f*ixing *a*nd *r*anging.

$$T_{axial} = \frac{|R| \sin \theta_{\max}}{c_{\max} \cos \theta_{\max}} \cong \frac{|R|}{c_{\max}} \frac{\left(\theta_{\max} - \frac{\overset{\max}{\theta}}{6}\right)}{\left(1 - \frac{\theta_{\max}^2}{2}\right)} \cong \frac{|R|}{c_{\max}} \left(\theta_{\max} - \frac{\theta_{\max}^3}{6}\right)\left(1 + \frac{\theta_{\max}^2}{2}\right) \tag{11.43}$$

We have to be vigilant at this point to be sure we are evaluating Eq. (11.43) to the same level of approximation as we had in Eq. (11.42), which is correct to third order in θ_{max}. The product of the two binomials includes a term that is linear in θ_{max} as well as two terms that are third order.

$$T_{axial} = \frac{|R|}{c_{\max}} \left(\theta_{\max} - \frac{\theta_{\max}^3}{6} + \frac{\theta_{\max}^3}{2}\right) = \frac{|R|}{c_{\max}} \left(\theta_{\max} + \frac{\theta_{\max}^3}{3}\right) \tag{11.44}$$

These calculations demonstrate that the (longer) curved path is traversed in less time than the shorter (axial) path. We can use Eq. (11.44) with Eqs. (11.40) and (11.42) to approximate the travel time difference, ΔT.

$$\Delta T = T_{axial} - T_{upper} \cong \frac{|R|}{c_{\max}} \left[\left(\theta_{\max} + \frac{\theta_{\max}^3}{3}\right) - \left(\theta_{\max} + \frac{\theta_{\max}^3}{6}\right)\right] = \frac{|R|}{c_{\max}} \frac{\theta_{\max}^3}{6} \tag{11.45}$$

11.4.4 Under Ice Propagation

Sound propagation under Arctic ice provides an interesting variation on the sound channel, since sound can be reflected specularly (i.e., $\theta_r = \theta_i$) from the ice sheet and the speed of sound under the ice increases monotonically with depth. The lack of solar heating at the surface causes the main thermocline, shown in Fig. 11.11, to be absent under Arctic ice. Typical ray paths under Arctic ice are shown in Fig. 11.17.

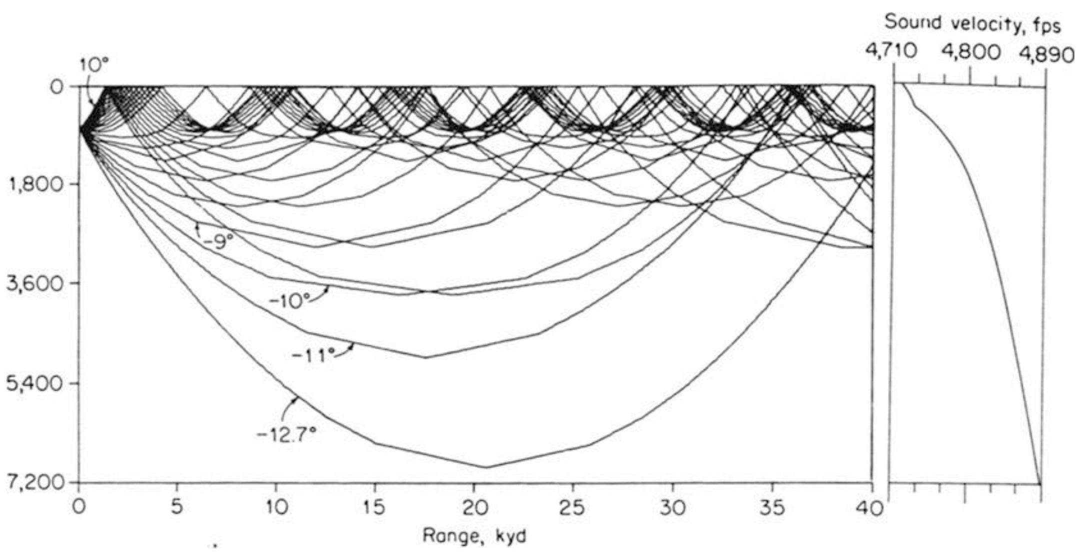

Fig. 11.17 Typical sound speed profile (*right*) and ray paths (*left*) under Arctic ice. Depth is in fathoms (1 fathom = 6 feet = 1.829 m), range is in kiloyards (1 kyd = 0.9144 km), and sound speed is in feet/second (1 fps = 30.48 cm/s) [14]

11.4.5 Sound Focusing

A final illustration of these refractive processes in constant sound speed gradients, at a much different scale than the global sound propagation in the deep sound channel, comes from the evolution of marine mammals. The Cuvier's beaked whale (*Ziphius cavirostris*) is a member of the Ziphiidae family of toothed whales. It relies on echolocation, but in an aqueous environment, the excessive hydrodynamic drag and turbulence noise that would be produced by external "ears" (i.e., pinna), like those found on land mammals, is unacceptable. In this whale, the "ear" is located internally behind the jaw (in green), as shown in Fig. 11.18.

Figure 11.19 demonstrates that this region acts like a lens. Parallel rays that enter the "channel" are focused to a single point (see Fig. 11.20). As we have done many times now, we can represent the distribution of sound speeds in the whale's mandible using a piecewise-linear approximation. In this

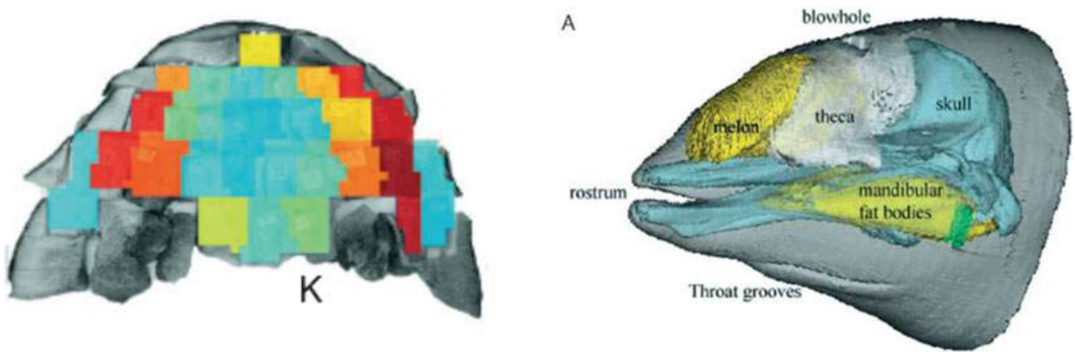

Fig. 11.18 The sound-sensing organ of the Cuvier's beaked whale is shown by the small *green* area in the drawing of the whale's head at the right. At the left is a tomographic slice through the mandibular fat body which acts as a sound channel (i.e., lens) to focus sounds from the water to the whale's sound-sensing organ. The sound speed of the mandibular fat body (in yellow at the right) shows the sound speed as a function of location (*red* corresponding to 1700 m/s and *light blue* corresponding to 1300 m/s). Diagrams from Soldervilla, et al. [15]

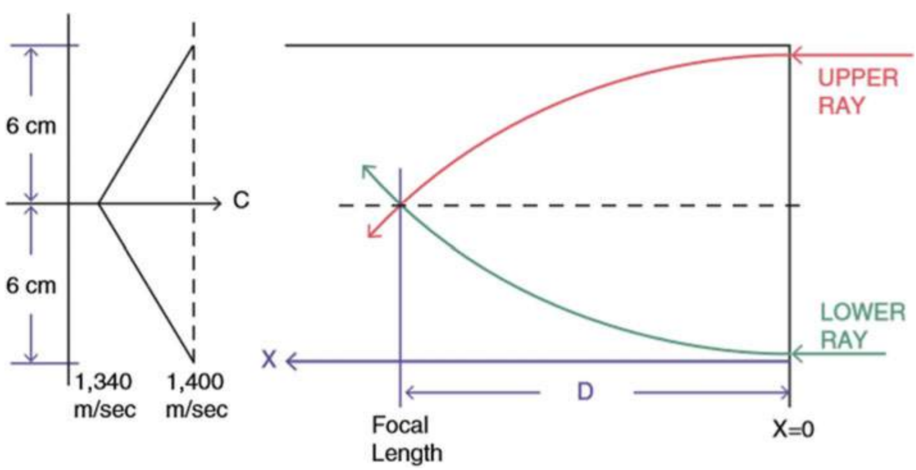

Fig. 11.19 A simplified approximation to the sound channel (i.e., lens) created by the mandibular fat body that assumes that the sound speed gradient is constant, with its minimum value (1340 m/s) along the axis, and its maximum value (1400 m/s) at the upper and lower extremes, 6.0 cm above and below the sound channel axis

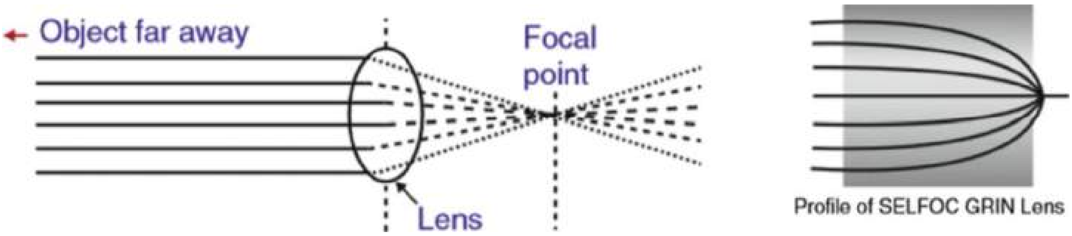

Fig. 11.20 (*Left*) Ray paths for an ordinary lens. (*Right*) Ray paths for a graded-index (GRIN) lens. In both cases, parallel rays enter the lens and are focused to a single point

case, the sound speed gradient $g = 60$ m/s ÷ 0.06 m = 1000 s^{-1}; hence, $|R| = c_o/g = 1.4$ m. Using Snell's law, $\cos\theta_{max} = 0.957$; hence, $\theta_{max} = 16.8°$. This makes the "focal length" of the whale's acoustic lens, $d_{focal} = |R| \sin\theta_{max} = 40.5$ cm, just about the extent of the mandibular fat bodies.

The strategy of using a propagation speed profile to act as a lens is very popular in fiber-optic telecommunication systems and fiber-optic sensors. As shown in Fig. 11.20, this application is intended to capture light from an LED or solid-state laser and focus that light into the core of single-mode optical fibers that typically have waveguide (core) diameters on the order of 10 microns or less. In sensor applications [16–18], it usually is used to spread the light from an optical fiber over the surface of some sensing element after which a second GRIN lens injects the modulated light back into the optical fiber.

The graded-index lens was patented by Nippon Sheet Glass in 1968 and given the trademark SELFOC®. According to the accepted evolutionary timeline [19], marine mammals had produced the acoustical equivalent of GRIN lenses for at least 32 million years before the NSG patent was issued.

Talk Like an Acoustician

Cavitation effects	Fermat's principle
Pressure reflection coefficient	Critical angle
Pressure transmission coefficient	Total internal reflection
Pressure release boundary	Angle of intromission
Impedance matching layer	Refraction
Antireflective coating	Piecewise-linear approximation
Trace wavelength	Ray tracing
Specific acoustic impedance	Grazing angle
Specular reflection	Sound channel
Diffuse reflection	SOFAR channel
Snell's law	

Exercises

1. **Air-water interface.** A 1.0 kHz planewave in water with pressure amplitude, $|\hat{\mathbf{p}}| = 100$ Pa, is normally incident on the air-water interface (i.e., the propagation direction is at a right angle to the air-water surface; hence, $\theta_i = 0°$). You may assume the speed of sound in water is 1500 m/s and the speed of sound in air is 343 m/s. The density of water can be taken as 1000 kg/m^3 and of air to be 1.19 kg/m^3.
   (a) *Transmitted amplitude*. What is the amplitude of the pressure that is transmitted into the air?
   (b) *Trace velocity*. What is the "trace velocity" of the waves along the interface?

(c) *Intensities*. What is the intensity of the incident wave in the water and the transmitted wave in air?
(d) *Transmission loss*. Express the reduction in the intensity of the wave when it crosses the interface from the water into the air in decibels.
(e) *Oblique incidence*. If the angle of incidence is increased to 45°, what is the amplitude of the pressure transmitted into the air?
(f) *Trace velocity*. What is the "trace velocity" of the waves along the interface?
(g) *Transmitted pressure*. If the planewave originates in that air and makes an angle of 45° to the normal, what is the magnitude of the acoustic pressure of the sound in the water?

2. **Matching layer.** What is the density and sound speed required for a 1.0-cm-thick layer of material that produces complete transmission of sound from water into steel if the frequency of the sound wave is 20 kHz? Let $\rho_{water} = 1000$ kg/m^3 and $c_{water} = 1500$ m/s, $\rho_{Fe} = 7700$ kg/m^3, and $c_{Fe} = 6100$ m/s.
3. **Alcohol on water.** An acoustics experiment is performed in an aquarium partially filled with water ($c = 1500$ m/s and $\rho_m = 1000$ kg/m^3). At the bottom of the aquarium, an ultrasonic transducer shoots a narrow beam of sound up to the surface of the water at an angle of 45°, and the sound beam reflects back down to the bottom of the aquarium where it hits a distance along the bottom that is 16.0 cm from the transducer. This situation is diagrammed in the upper portion of Fig. 11.21. You may assume the bottom of the aquarium is perfectly absorbing, so the beam does not bounce back up again and that the problem is entirely two dimensional.
After making the required measurement, the experimenter comes back from lunch and finds that a layer of ethyl alcohol ($c = 1150$ m/s and $\rho_m = 790$ kg/m^3) has carefully been poured on top of the water in the aquarium. (Good grief!) Now a second beam of sound comes down and hits the bottom at a distance of 22.0 cm from the ultrasonic transducer, as diagrammed in the lower portion of Fig. 11.21. How thick is the layer of alcohol on top of the water, assuming that the two liquids do not mix?
4. **Oblique incidence at a water-sediment boundary.** A sinusoidal planewave with effective pressure $p_{rms} = 100$ Pa is incident at 45° on a silt bottom with $\rho_{silt} = 2000$ kg/m^3 and $c_{silt} = 2000$ m/s.
(a) *Angle of refraction*. What angle does the planewave make with respect to the normal once it enters the silt bottom?
(b) *Transmitted pressure*. What is the effective pressure of the wave in the silt bottom?
(c) *Angle of intromission*. At what angle does the planewave have to approach the silt from the water so that there is 100% transmission into the silt and no wave reflected back into the water?

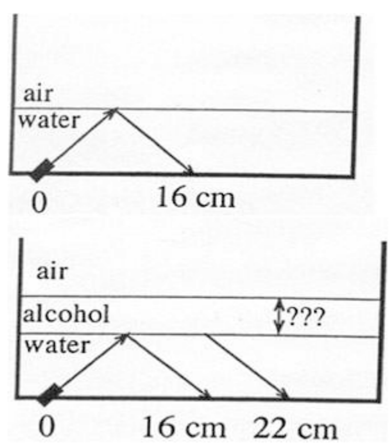

Fig. 11.21 (*Above*) The sound beam of an ultrasonic transducer bounces of the free surface of a water-filled aquarium. (*Below*) the beam is displaced after a layer of alcohol is added to the surface

5. **Critical ray and skip distance in a "mixed layer."** The sound speed at the water's surface is 1490 m/s and increases linearly to $c_o = 1491.5$ m/s with depth to the bottom of the mixed layer at $D = 100$ m. Below that depth, there is a constant negative sound speed gradient $g_2 = -0.045\ \text{s}^{-1}$. For an underwater sound source (projector) at a depth, $z_s = 60.0$ m, determine the critical (grazing) angle, θ_o, for the limiting ray that remains trapped in the mixed layer and the "skip distance," r_s, between the successive locations where the critical ray intersects the surface.
6. **Arctic refraction.** The water in the Arctic is nearly isothermal. Sound speed increases with depth because of the pressure effect. Assume the surface temperature is 0 °C, the salinity is 35 ppt, and the sound speed, in meters/second, as a function of depth, is given by the Eq. (11.46), where z is the depth below the surface expressed in meters [20].

$$c(z) = 1449 + 0.016z \tag{11.46}$$

The turning depth of the ray is 2.0 km where the sound speed is $c(2\ \text{km}) = 1481\ \text{m/s}$.

(a) *Initial grazing angle*. What is the initial angle that ray makes with the water-ice interface? Report the angle which the ray makes with the water's surface, not the angle with respect to the normal to the surface.
(b) *Return to the surface*. What is the distance along the surface at which the ray returns to the ice-water interface?

References

1. E.A. Neppiras, Acoustic cavitation. Phys. Rep. **61**(3), 159–251 (1980)
2. V.O. Knudsen, C.M. Harris, *Acoustical Design in Architecture* (Acoustical Society of America, 1978). See Rigid Partitions, pp. 208–210; ISBN 0-88318-267-X.
3. R.B. Lindsay, *Mechanical Radiation* (McGraw-Hill, 1960). See §9.6
4. T.F.W. Embleton, Mufflers, in *Noise and Vibration Control*, ed. by L. L. Beranek, (McGraw-Hill, 1971), p. 379
5. R.P. Feynman, R.B. Leighton, M. Sands, *The Feynman Lectures on Physics*, vol I (Addison-Wesley, 1965). Chapter 26–3
6. C.W. Holland, Geoacoustic inversion for fine-grained sediments. J. Acoust. Soc. Am. **111**(4), 1560–1564 (2002)
7. T.B. Gabrielson, Refraction of sound in the atmosphere. Acoustics Today **2**(2), 7–17 (2006)
8. C.C. Leroy, Simple equations for accurate and more realistic calculation of the speed of sound in sea water. J. Acoust. Soc. Am. **46**(1)(Pt. 2), 216–226 (1969)
9. L. M. Jones & W. A. VonWinkle, *Sound Velocity Profiles in an Area South of Bermuda*, Underwater Sound Laboratory Report No. 632 (1965)
10. C.D. Ross, *Civil War Acoustic Shadows* (White Mane Books, Shippensburg, 2001). "Outdoor sound propagation in the US Civil War," Appl. Acoustics **59**, 137–147 (2000)
11. M. Ewing, J.L. Worzel, Long-range sound transmission, in *Propagation of Sound in the Ocean*, vol. 3, Geo. Soc. Am. Memo. **27**, (1948)
12. H.H. Baker, Missile impact localization system. Bell Telephone Lab. Res. **39**, 195 (1961). A similar on-line discussion is available at https://insidegnss.com/on-target-offshore-scoring-of-precision-guided-munitions/
13. K.G. Sabra, B. Cornuelle, W.A. Kuperman, Sensing deep-ocean temperatures. Phys. Today **69**(2), 32–38 (2016)
14. R. J. Urick, *Sound Propagation in the Sea* (Defense Advanced Research Projects Agency Report 1979). Reprinted as *Principles of Underwater Sound* (McGraw-Hill, 1975); ISBN 0-07-066086-7
15. M.S. Soldervilla et al., Cuvier's beaked whale (*Ziphius cavirostris*) head tissue physical properties and CT imaging. J. Exp. Biol. **208**, 2319–2332 (2005)
16. S.L. Garrett, M.R. Brininstool, J.T. Newmaster, T. Hofler, Fiber optic angular orientation sensor using digital serial encoding. US Pat. No. 5,042,157 (Aug. 27, 1991)

17. A. Migliori, G.W. Swift, S.L. Garrett, Remotely readable fiber optic compass. US Pat. No. 4,577,414 (Mar. 25, 1986)
18. M.R. Brininstool, J.T. Newmaster, S.L. Garrett, Fiber-optic remote angular position sensor including a polarization track. US Pat. No. 5,073,711 (Dec. 17, 1991)
19. A. Berta, J.L. Sumich, *Marine Mammals: Evolutionary Biology* (Academic, 1999); ISBN 0-12-093225-3.
20. C.S. Clay, H. Medwin, *Acoustical Oceanography* (Wiley-Interscience, 1977), pp. 90–91; ISBN 0-471-16041-5.

Radiation and Scattering

12

Contents

S. L. Garrett, *Understanding Acoustics*, Graduate Texts in Physics,
https://doi.org/10.1007/978-3-030-44787-8_12

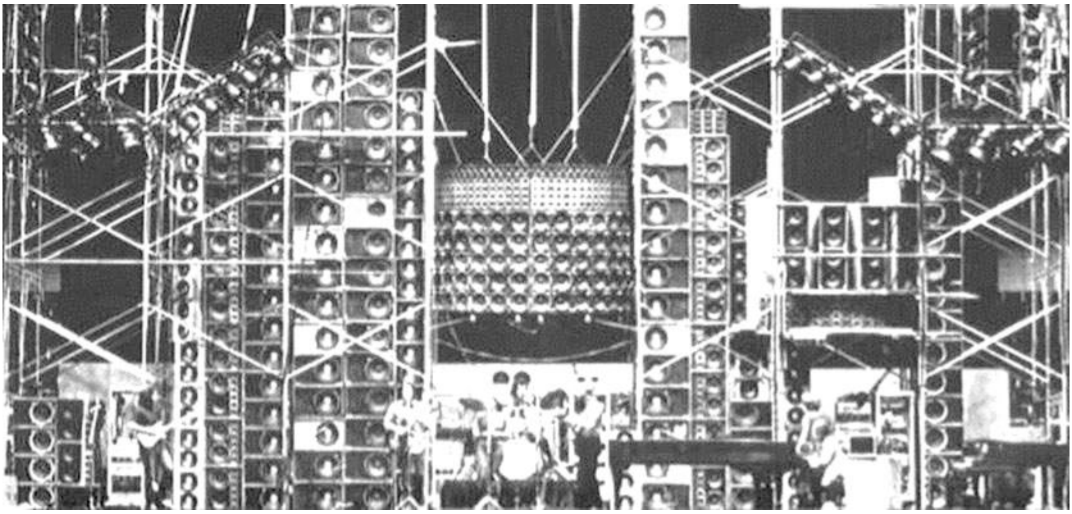

Fig. 12.1 Photograph of the sound reinforcement system used by the Grateful Dead [1]. Nearly the entire stage is occupied with discrete vertical line arrays of loudspeakers to radiate the full-frequency spectrum of their music toward the audience with minimal leakage toward the ceiling where there would be excessive reverberation that would degrade the intelligibility

At this point, we have made a rather extensive investigation into the sounds that excite Helmholtz resonators as well as the departures from equilibrium that propagate as plane waves through uniform or inhomogeneous media. We have not, as yet, dealt with how those sounds are actually produced in fluids. Our experience tells us that sound can be generated by vibrating objects (e.g., loudspeaker cones, stringed musical instruments, drums, bells), by modulated or unstable flows (e.g., jet engine exhaust, whistles, fog horns, speech), by electrical discharges in the atmosphere (i.e., thunder), or by optical absorption (e.g., modulated laser beams). In this chapter, we will develop the perspective and tools that will be used for the calculation of the radiation efficiency of various sources and combinations of sources, like the sound reinforcement system shown in Fig. 12.1.

Only sound sources that behave in accordance with linear acoustics will be examined (until Chap. 15). We will find that the entire problem of both radiation and of scattering from small discrete objects can be reduced to understanding the properties of a compact source of sound that is small compared to the wavelength of the sound it is radiating.

"Superposition is the compensation we receive for enduring the limitations of linearity." Blair Kinsman [2]

We will then combine many of these radiation units, called *monopoles*, in various ways, including the option of having different units in different locations with different relative phases. Through superposition, this will permit construction of other convenient radiators that range from transversely vibrating incompressible objects (represented by two closely spaced monopoles that are radiating 180° out-of-phase) to arrays of discrete radiators (e.g., line arrays of various sizes like those shown in Fig. 12.1). Integration over infinitesimal monopole sound sources will allow modeling of extended vibrating objects (i.e., continuous, rather than discrete) such as loudspeaker cones, lightning bolts, and laser beams.

For convenience, our initial vision of a *compact source* will be assumed to be a pulsating sphere with radius, $a \ll \lambda$. That pulsating sphere produces a sinusoidally varying volume velocity, $U_1(a,t) = \Re e\left[\widehat{\mathbf{U}}(a)e^{j\omega t}\right]$. To generate such a volume velocity, we will let the radius of that sphere,

Fig. 12.2 The loudspeaker enclosure at the right has an irregular shape and provides a total enclosed volume, V. To be treated as a "compact source," we require $V^{1/3} \ll \lambda = c/f = 2\pi c/\omega$. The loudspeaker cone, visible at the top of the enclosure, has an effective piston area, A_{pist}

r, oscillates harmonically with a single frequency, $\omega = 2\pi f$. Those radial oscillations can be represented as $r(t) = \Re e\left[a + \hat{\xi} e^{j\omega t}\right]$; hence $|U_1(a,t)| = 4\pi a^2 \omega \left|\hat{\xi}\right|$, where we have made the assumption that $a \gg \left|\hat{\xi}\right|$, so that the surface that applies force to the surrounding fluid can be treated as a spherical shell.

As will be demonstrated, an ordinary loudspeaker enclosure, like the one shown in Fig. 12.2, can be treated as a "compact source," or monopole, if its characteristic physical dimensions are small compared to the wavelength of sound produced. If the loudspeaker enclosures were approximated by a rectangular parallelepiped with volume, V, then "compactness" would require that $V^{1/3} \ll \lambda$.

The oscillatory motion of the loudspeaker cone will be the source of the oscillatory volume velocity in the surrounding fluid. If the cone's effective piston area is A_{pist}, located at $x = 0$, and its linear position as a function of time is $x_1(0,t) = \Re e[\hat{\mathbf{x}} e^{j\omega t}]$, then $\left|\hat{\mathbf{U}}(0,t)\right| = \omega |\hat{\mathbf{x}}| A_{pist} \cos(\omega t + \phi)$.

As long as the compactness criterion is satisfied, it is theoretically impossible to remotely determine the physical shape of a compact source—if the radiation from a source is that of a monopole, then it is only the source's volume velocity, $U_1(a, t)$, that is related to the sound pressure, $p_1(R,t)$, detected at distances, $R \gg a$, beyond the maximum physical extent of the source.[1]

Within the constraint of compactness, it does not matter if $\left|\hat{\mathbf{U}}(a)\right| = 4\pi a^2 \omega \left|\hat{\xi}\right|$ or $\left|\hat{\mathbf{U}}(0)\right| = A_{pist}\omega |\hat{\mathbf{x}}|$, the sound radiated into the far field will be identical. Given that realization, then for a compact source, dimensional analysis guarantees that the solution of the steady-state radiation problem reduces to calculation of the acoustic transfer impedance, $\mathbf{Z_{tr}} = \hat{\mathbf{p}}(R)/\hat{\mathbf{U}}(a)$, with units that are the same as those for the acoustic impedances we have studied in our investigation of lumped elements: $|\mathbf{Z_{tr}}| \propto \rho_m c/A$,

[1] The inability to remotely determine the shape of a sound source that is smaller than the wavelength of the sound it is radiating is known in both acoustics and in optics as the *Rayleigh resolution criterion*. See Sect. 12.8.1.

where ρ_m is the mean density of the medium, c is its sound speed, and A is a constant with the dimensions of area [m^2]. The transfer impedances for several systems were provided in Sect. 10.7.4 since they were required to make reciprocity calibrations of electroacoustic transducers.

12.1 Sound Radiation and the "Causality Sphere"

Light travels at the speed of light; sound travels at the speed of sound. Although those statements seem simplistic, if not tautological, they have calculable consequences that are significant. If a disturbance has a duration, Δt, then those speeds guarantee that the consequences of that event can initially only have influence within a distance, $d = c\Delta t$, from the source of that disturbance. The term *causality sphere* was introduced in Einstein's Theory of General Relativity as the boundary in spacetime beyond which events cannot affect an outside observer. Although most commonly associated with cosmological issues and black holes, the concept is directly relevant to every form of energy that can only move through space with a finite propagation speed.

Before attempting a direct calculation of the acoustic pressure radiated by a compact source that is pulsating in an unbounded fluid medium, it will be instructive to make a simple estimate of the acoustic transfer impedance between an oscillating source of fluid located at the origin of some coordinate system and the pressure at some remote location, a distance, R, from the origin, using only the adiabatic gas law derived in Sect. 7.1.3: $pV^\gamma =$ constant. Before making such a calculation for a source of sound radiating spherically in three dimensions, it will be reassuring to use the same procedure to reproduce a result that we have derived earlier by other means.

If we consider a close-fitting piston at the end of an infinite tube of uniform cross-section,[2] so that both the tube and the piston have a cross-sectional area, A, then that piston can launch a sound wave down the tube. If the piston produces a volume velocity, $U(0,t) = \Re e\left[\widehat{\mathbf{U}}(0)e^{j\omega t}\right]$, then the acoustic transfer impedance, $\mathbf{Z_{tr}}$, of such a tube, provided in Eq. (10.85) or in Eq. (10.106), can be used to calculate the steady-state acoustic pressure of the traveling wave produced by the piston's oscillations.

$$\widehat{\mathbf{p}} = \mathbf{Z_{tr}}\widehat{\mathbf{U}}(0) = \frac{\rho_m c}{A}\widehat{\mathbf{U}}(0) \quad \text{and} \quad p_1(x,t) = \Re e\left[\widehat{\mathbf{p}}e^{\,j(\omega t - kx)}\right] \tag{12.1}$$

This result describes a plane wave that propagates down the tube with magnitude, $|\widehat{\mathbf{p}}|$, while assuming that thermoviscous dissipation on the tube walls is negligible.

Let's now calculate this same result in another way. If we consider an interval during which the piston moves between its extreme positions, the piston will sweep out a volume in one-half of a period, $\delta V = \left|\widehat{\mathbf{U}}(0)\right|(T/2) = \left|\widehat{\mathbf{U}}(0)\right|/2f$, where $T = f^{-1} = 2\pi/\omega$ is the period of the piston's oscillations. In that time, the piston can "influence" a volume of the fluid within the tube, $V = (A\lambda/2) = (AcT/2)$, since the sound could travel a distance equal to one-half wavelength. Substitution of δV and V into the adiabatic gas law produces a corresponding δp.

[2] Making the tube infinitely long is just a computational convenience. Any tube long enough that any reflections from the end of the tube return to the region of interest long after the interval of interest would suffice. Alternatively, a tube that had an anechoic termination (e.g., absorbing wedge) or had a matching resistive termination, $R_{ac} = \rho_m c/A$, would also behave as though it were infinitely long.

$$pV^{\gamma} = const. \quad \Rightarrow \quad \frac{\delta p}{p_m} = -\gamma \frac{\delta V}{V} \quad \Rightarrow \quad \delta p = p_1 = -\gamma p_m \frac{\delta V}{V}$$
$$|\widehat{\mathbf{p}}| = \left| -\gamma p_m \frac{T}{2} \frac{\widehat{\mathbf{U}}(0)}{Ac(T/2)} \right| = \frac{\gamma p_m \left|\widehat{\mathbf{U}}(0)\right|}{Ac} = \frac{\rho_m c^2}{Ac} \left|\widehat{\mathbf{U}}(0)\right| = \frac{\rho_m c}{A} \left|\widehat{\mathbf{U}}(0)\right| \tag{12.2}$$

The result for $|\widehat{\mathbf{p}}|$ is identical to the previous result from Eq. (12.1).

The situation diagrammed in Fig. 12.3 assumes that there is a compact sphere of radius, a, at the origin of a coordinate system, $R = 0$. The radius of that sphere oscillates sinusoidally with a radial displacement magnitude, $\left|\widehat{\boldsymbol{\xi}}\right|$. The surface area of that sphere is $4\pi a^2$, so if $\left|\widehat{\boldsymbol{\xi}}\right| \ll a$, then when the sphere goes from its equilibrium value, a, to its maximum radius, $a + \left|\widehat{\boldsymbol{\xi}}\right|$, it will sweep out a volume change, $\delta V = 4\pi a^2 \left|\widehat{\boldsymbol{\xi}}\right|$. The time it takes to sweep that volume change is one-quarter of the acoustic period, $T/4 = (4f)^{-1}$.

Since the speed of sound is c, any "disturbance" created by the source during that quarter period can only influence the fluid out to a distance, $R_{\lambda/4} = c(T/4)$ from the source. Let's assume we are making a video that starts when the spherical source goes through its equilibrium radius, $r = a$, then continues

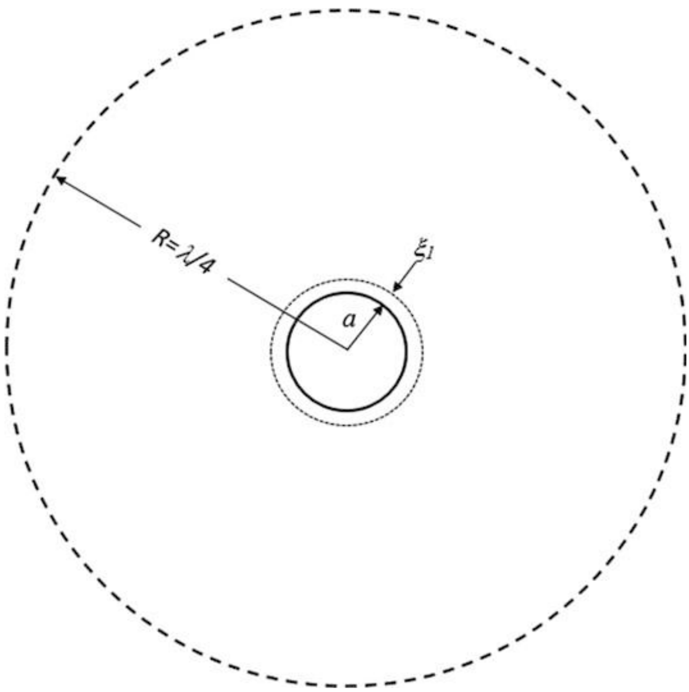

Fig. 12.3 The "Sphere of Causality." This diagram represents two concentric spheres. The inner sphere has a radius, a. That radius oscillates sinusoidally at a frequency, $f = \omega/2\pi$, with an amplitude, $\left|\widehat{\boldsymbol{\xi}}\right|$. The radius of the inner sphere goes from its equilibrium value, $r = a$, to its maximum displacement, $r = a + \left|\widehat{\boldsymbol{\xi}}\right|$, in one-quarter of an acoustic period: $T/4 = (4f)^{-1}$. During that time, the *effects* of that displacement of fluid volume, $\delta V = 4\pi a^2 \left|\widehat{\boldsymbol{\xi}}\right|$, can only propagate a distance of one-quarter wavelength from the origin, $R_{\lambda/4} = \lambda/4 = c/4f$. That distance is the radius of the causality sphere since information carried by sound can only propagate at the speed of sound, c. The volume enclosed by that "causality sphere," indicated by the dashed circle in two dimensions, is $V_{\lambda/4} = (\pi/48)\lambda^3$

expanding for one-quarter of an acoustic period, $T/4$. During that time interval, the source changes its volume by $\delta V = U_1(a)/\omega$, since the radius is changing sinusoidally with time, pushing fluid out ahead of it. Once again, as in Eq. (12.2), logarithmic differentiation of the adiabatic gas law will relate the average pressure change, $<p_1(R)>_s$, within the causality sphere of volume, $V_{\lambda/4} = (4\pi/3)R^3 = (\pi/48)\lambda^3$, to δV.

$$\frac{\langle p_1 \rangle_s}{p_m} = \gamma \frac{\delta V}{V_{\lambda/4}} \quad \Rightarrow \langle p_1 \rangle_s = \gamma p_m \frac{\left|\widehat{\mathbf{U}}(a)\right|}{\omega V_{\lambda/4}} = \rho_m c^2 \frac{\left|\widehat{\mathbf{U}}(a)\right|}{\omega V_{\lambda/4}} \tag{12.3}$$

The final version at the right of Eq. (12.3) again uses the fact that the square of the sound speed in an ideal gas is given by $c^2 = \gamma p_m/\rho_m$. We can solve for the average acoustic transfer impedance $<\mathbf{Z_{tr}}>_s = <p_1(R)/U_1(a)>_s$ between the volume velocity at the surface of the source, $U_1(a)$, and the average pressure, $<p_1(R)>_s$, at an observation point just inside the causality sphere at $R = \lambda/4$.

$$\langle \mathbf{Z_{tr}} \rangle_s = \frac{\langle p_1(R) \rangle_s}{U_1(a)} = \frac{6}{\pi^2} \frac{\rho_m c}{R\lambda} \cong 0.61 \frac{\rho_m c}{R\lambda} \tag{12.4}$$

As we will see when we solve the exact hydrodynamic equations, this approximate result is close to the exact result, which produces a numerical pre-factor for Eq. (12.4) that is 0.50 instead of 0.61.

This result is only approximate since the actual acoustic pressure within the "causality sphere" is a function of the distance from the source. We would have obtained a different result for the numerical pre-factor in Eq. (12.4) had we let the "event" last one-half period so that the source went from its minimum radius, $a - \left|\widehat{\boldsymbol{\xi}}\right|$, to its maximum radius, $a + \left|\widehat{\boldsymbol{\xi}}\right|$. That change in volume, δV, would be doubled, but the volume of the "causality sphere" would have increased by a factor of eight. Under that scenario, the numerical pre-factor in Eq. (12.4) would have decreased from 0.61 to 0.15.

This variability is due to the fact that the pressure within the causality sphere is not uniform. We expect wavelike motion, not simple hydrostatic compression, as assumed by the use of the adiabatic gas law in Eq. (12.2) to produce δp. This was not an issue in the causality calculation for the duct where p_1 was uniform throughout for a traveling wave in one dimension, since the "average" and the amplitude were identical. For the three-dimensional case, acoustic pressure amplitude is a function of distance from the source.

The purpose of such a crude calculation was to demonstrate that the earlier concepts introduced to produce an equation of state, describe sound in lumped-element networks, or for one-dimensional propagation are just as relevant to understanding the process of sound radiation. In the next section, the exact result will be derived when the wave equation is solved exactly for a spherically symmetric wave expanding in three dimensions.

12.2 Spherically Diverging Sound Waves

The exact result for the acoustic transfer impedance, $\mathbf{Z_{tr}}$, which provides the acoustic pressure at every remote location, $p_1(R)$, in terms of the volume velocity created at the source, $U_1(a)$, can be obtained if we solve the wave equation in spherical coordinates. The Euler equation, also expressed in spherical coordinates, can be used to match the radial velocity of the fluid to the radial velocity of the compact spherical source, $\widehat{\mathbf{v}}_{\mathbf{r}}(a)$, remembering that the representation of the volume velocity of the source as a pulsating sphere is only a mathematical convenience. The result will be applicable to any compact source, independent of its shape.

When the wave equation was derived in Cartesian coordinates in Sect. 10.2, the result was generalized by expressing the wave equation in vector form by introducing the Laplacian operator, $\nabla^2 = \partial^2/\partial x^2 + \partial^2/\partial y^2 + \partial^2/\partial z^2$. For the compact source in an unbounded medium, a spherical coordinate system would be appropriate (and convenient) since all directions are equivalent; we expect no variation in the sound field with either polar angle, $90° \geq \theta \geq -90°$, or azimuthal angle $0° \leq \varphi < 360°$. In spherical coordinates, the Laplacian can be written in terms of r, θ, and φ [3].

$$\nabla^2 = \frac{1}{r^2}\left[\frac{\partial}{\partial r}\left(r^2\frac{\partial}{\partial r}\right)\right] + \frac{1}{r^2 \sin\theta}\frac{\partial}{\partial\theta}\left(\sin\theta\frac{\partial}{\partial\theta}\right) + \frac{1}{r^2\sin^2\theta}\frac{\partial^2}{\partial\varphi^2} \tag{12.5}$$

Since the space surrounding our source is assumed to be isotropic, hence spherically symmetric, $p_1(R)$ does not depend upon θ or φ, so derivatives with respect to those variables must vanish. Equation (12.5) can be substituted into the linearized wave equation.

$$\nabla^2 p = \frac{1}{r^2}\left[\frac{\partial}{\partial r}\left(r^2\frac{\partial p}{\partial r}\right)\right] = \frac{1}{c^2}\frac{\partial^2 p}{\partial t^2} \tag{12.6}$$

The "product rule" for differentiation can be used to demonstrate that Eq. (12.6) is equivalent to Eq. (12.7).

$$\frac{\partial^2(rp)}{\partial r^2} = \frac{1}{c^2}\frac{\partial^2(rp)}{\partial t^2} \tag{12.7}$$

This is just a new single parameter (i.e., quasi-one-dimensional) wave equation that describes the space and time evolution of the product of radial distance from the origin and the acoustic pressure at that distance, (rp); hence the solution to Eq. (12.7) is $(pr) = \Re e\left[\widehat{\mathbf{C}} e^{\,j(\omega t \mp kr)}\right]$, where $\widehat{\mathbf{C}}$ is a constant (phasor) that may be complex to account for any required phase shift and an arbitrary designation of the time we chose to make $t = 0$. We will specify that complex (phasor) amplitude, $\widehat{\mathbf{C}}$, by matching this solution to the volume velocity of the source at its surface, $r = a$. The two solutions to Eq. (12.7) correspond to outgoing $(\omega t - kr)$ or incoming $(\omega t + kr)$ spherical waves, also referred to as divergent and convergent waves, respectively. Since we are considering radiation *from* a sound source in a homogeneous, isotropic, unbounded medium (i.e., no reflections), we will now focus only on the outgoing solution.

$$p_1(r,t) = \Re e\left[\frac{\widehat{\mathbf{C}}}{r} e^{\,j(\omega t - kr)}\right] \tag{12.8}$$

The magnitude of the acoustic pressure decreases with distance from the source. As will be demonstrated in the derivation of Eq. (12.18), the total radiated power, Π_{rad}, is independent of distance from the source's acoustic center (i.e., the origin of our spherical coordinate system) if dissipation is ignored.

To match the velocity of the fluid to the velocity of the source at its surface, $r = a$, Eq. (12.8) can be substituted into the linearized Euler equation.

$$\rho_m \frac{\partial \vec{v}}{\partial t} = -\vec{\nabla} p \tag{12.9}$$

The gradient operator, $\vec{\nabla}$, can also be expressed in spherical coordinates [3].

$$\vec{\nabla} p(r,\theta,\varphi) = \frac{\partial p(r,\theta,\varphi)}{\partial r}\hat{r} + \frac{1}{r}\frac{\partial p(r,\theta,\varphi)}{\partial \theta}\hat{\theta} + \frac{1}{r\sin\theta}\frac{\partial p(r,\theta,\varphi)}{\partial \varphi}\hat{\varphi} \tag{12.10}$$

Again, for our spherically symmetric case, $p_1(r, t)$ is independent of θ and φ, so only the first term on the right-hand side of Eq. (12.10) is required to calculate the radial component of the wave velocity, $v_r\,(r, t)$. The application of the product rule generates two terms.

$$\begin{aligned} \rho_m \frac{\partial v_r}{\partial t} &= -\frac{\partial}{\partial r}\left[\frac{\widehat{\mathbf{C}}}{r} e^{\,j(\omega t - kr)}\right] \\ &= \frac{\widehat{\mathbf{C}}}{r^2} e^{\,j(\omega t - kr)} + jk\frac{\widehat{\mathbf{C}}}{r} e^{\,j(\omega t - kr)} = \frac{\widehat{\mathbf{C}}}{r} e^{\,j(\omega t - kr)}\left[\frac{1}{r} + jk\right] \end{aligned} \tag{12.11}$$

Since we have assumed single-frequency harmonic time dependence, the time derivative in Eq. (12.11) can be replaced by $j\omega$ while recalling that $c = \omega/k$.

$$v_r(r,t) = \Re e\left[\frac{p_1(r,t)}{j\omega\rho_m}\left(\frac{1}{r} + jk\right)\right] = \Re e\left[\frac{p_1(r,t)}{\rho_m c}\left(1 + \frac{1}{jkr}\right)\right] \tag{12.12}$$

12.2.1 Compact Monopole Radiation Impedance

Equation (12.12) can be rewritten to provide the specific acoustic impedance, $\mathbf{z_{sp}} = \widehat{\mathbf{p}}/\widehat{\mathbf{v}}_\mathbf{r}$, for propagation of outgoing (diverging) spherical waves. As with plane waves, the sign of the specific acoustic impedance is reversed for incoming (convergent) spherical waves.

$$\mathbf{z_{sp}} \equiv \frac{\widehat{\mathbf{p}}}{\widehat{\mathbf{v}}_\mathbf{r}} = \frac{\rho_m c}{1 + \left(1/_{jkr}\right)} = \rho_m c\frac{(kr)^2}{1 + (kr)^2} + j\rho_m c\frac{kr}{1 + (kr)^2} = \rho_m c\cos\phi\, e^{j\phi} \tag{12.13}$$

All three versions of Eq. (12.13) are useful, although in different contexts. The rightmost version suggests a geometric interpretation based on Fig. 12.4.

For very large values of kr, the curvature of the spherical wave fronts is slight, and the wave fronts (locally) are approximately planar. For $kr = 2\pi r/\lambda \gg 1$, $\mathbf{z_{sp}} = \widehat{\mathbf{p}}/\widehat{\mathbf{v}}_\mathbf{r} \cong \rho_m c$, for the propagation of outgoing (diverging) spherical waves, as shown by the solid line in Figs. 12.5 and 12.6 that approaches that constant value as ka increases. The specific acoustic impedance becomes a real number, and the acoustic pressure, $\widehat{\mathbf{p}}$, and the radial component of the fluid's acoustic particle velocity, $\widehat{\mathbf{v}}_\mathbf{r}$, are very nearly in-phase, $\phi \cong 0°$.

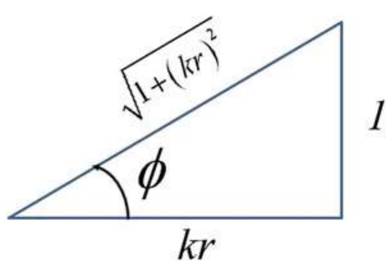

Fig. 12.4 Geometric interpretation of Eq. (12.13) representing the phase, ϕ, of the (complex) specific acoustic impedance, $\mathbf{z_{sp}}$, for an outgoing spherical wave. The phase angle, ϕ, between the acoustic pressure, $\widehat{\mathbf{p}}$, and the radial component of the acoustic particle velocity, $\widehat{\mathbf{v}}_\mathbf{r}$, is $\phi = \cot^{-1}(kr)$

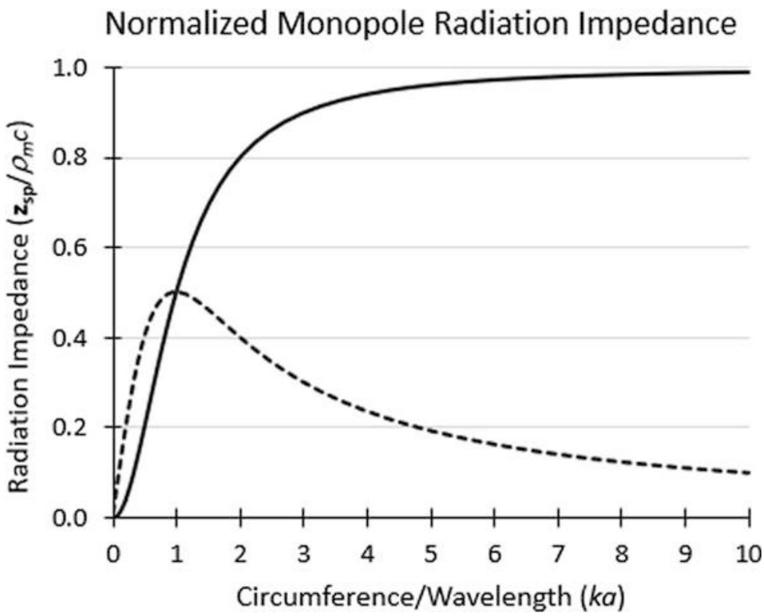

Fig. 12.5 The complex radiation impedance of a monopolar sound source, $\mathbf{z_{sp}}$, divided by the fluid medium's characteristic impedance, $\rho_m c$, from Eq. (12.13). The solid line is the real part of the radiation impedance, and the dashed line is the imaginary part. For small ka, the slope of the imaginary part is initially proportional to frequency, indicating mass-like behavior of the fluid at the monopole's surface

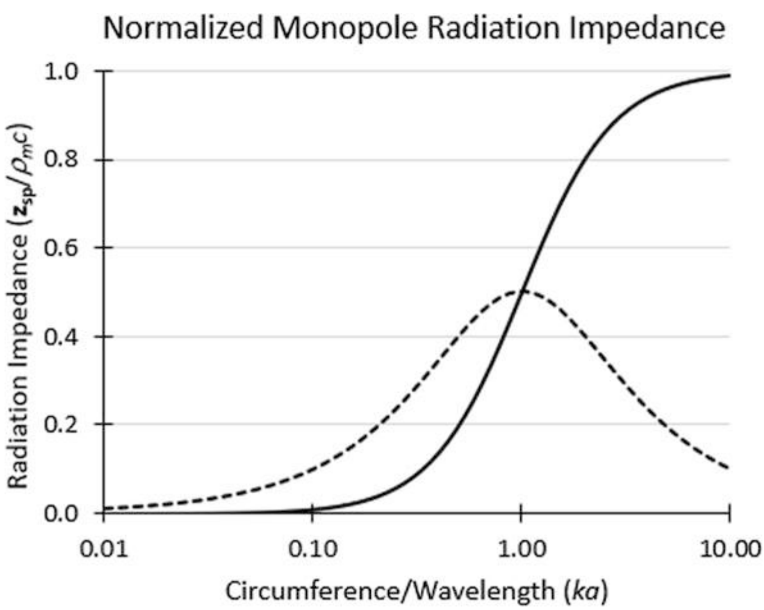

Fig. 12.6 The complex radiation impedance of a monopolar sound source, $\mathbf{z_{sp}}$, divided by the fluid medium's characteristic impedance, $\rho_m c$, from Eq. (12.13), except that the horizontal axis is now logarithmic. The solid line is the real part of the radiation impedance, and the dashed line is the imaginary part. Plotted this way, the similarity to Fig. 4.25 and Fig. 5.20, for the real and imaginary elastic modulus of a viscoelastic solid, and Fig. 14.3 or Fig. 14.4, for the sound speed and attenuation in F_2, is apparent

It is instructive to reproduce Fig. 12.5, but with a logarithmic ka axis as shown in Fig. 12.6. The similarity between the shape of the real and imaginary portions of the radiation impedance and the real and imaginary parts of the elastic modulus in Fig. 4.25 and Fig. 5.20, or the sound speed and attenuation in fluorine gas in Fig. 14.4, is not coincidental. It is a consequence of any linear response theory that is constrained by causality, as specified in the Kramers-Kronig relations of Eqs. (4.77) and (4.78), discussed in Sect. 4.4.4. Just as in those examples, the real and imaginary parts of the radiation impedance are not independent [4].

In the opposite limit, at $ka = 2\pi a/\lambda \ll 1$,[3] on the surface of the radially pulsating source, the specific acoustic impedance is almost purely imaginary, as shown by the dashed line in Figs. 12.5 and 12.6.

$$\lim_{ka \to 0} [\mathbf{z_{sp}}(a)] \cong j\rho_m cka = j\omega \rho_m a \tag{12.14}$$

Recalling our experience with the simple harmonic oscillator, Eq. (12.14) suggests that the fluid surrounding the source is behaving like an *effective mass*. The magnitude of the force, $\left|\widehat{\mathbf{F}}(a)\right|$, acting on the pulsating sphere can be obtained by integrating the pressure, $\widehat{\mathbf{p}}(a)$, over the surface of the sphere to produce the mechanical reactance, $x_{rad}(a) = \Im m[\mathbf{Z_{mech}}(a)]$, that the pulsating sphere "feels" at its surface.

$$\begin{aligned} \Im m[\mathbf{Z_{mech}}] &= \Im m\left[\frac{\widehat{\mathbf{F}}(a)}{\widehat{\mathbf{v}}_{\mathbf{r}}(a)}\right] = 4\pi a^2(\rho_m \omega a) \\ &= \omega\rho_m\left(4\pi a^3\right) = 3\omega\rho_m\left(\frac{4\pi}{3}a^3\right) \quad \text{for} \quad ka \ll 1 \end{aligned} \tag{12.15}$$

The volume of the spherical source is $V = (4\pi/3)a^3$, so the effective (inertial) *hydrodynamic mass* of the fluid surrounding the spherical source is equal to three times the mass of the fluid displaced by the source radiating sound in the small ka limit.

This is critical for the design of sound sources that operate in dense fluids (i.e., liquids rather than gases) since the source has to provide sufficient power to accelerate and decelerate the surrounding fluid as it pulsates. We generally represent this load as a *radiation reactance*, x_{rad}. As will be discussed shortly, in Sect. 12.3, for a spherical gas bubble in a liquid, this effective mass is the dominant source of inertia for simple harmonic bubble oscillations.

Although the largest component of the specific acoustic impedance at the surface of the sphere is imaginary (i.e., mass reactance), the real (i.e., resistive) component must be non-zero, because radiation of sound is the mechanism by which energy from the source is propagated into the surrounding fluid. The second version of $\mathbf{z_{sp}}$ in Eq. (12.13) is useful here since it provides the real and imaginary contributions individually.

$$\Re e\left\{\lim_{ka \to 0}[\mathbf{z_{sp}}(a)]\right\} \equiv r_{rad} \cong \rho_m c(ka)^2 \tag{12.16}$$

It is worthwhile pointing out that real impedances are commonly associated with dissipative processes that convert acoustical or vibrational energy to heat. In the case of radiation, power is removed from the source, but our calculations have been lossless (i.e., we have been using the Euler equation, not the Navier-Stokes equation). The real component of the radiation impedance is an "accounting loss" rather than an irreversible increase in entropy. For radiation, the energy propagates away; it is not absorbed, its expelled.

The total, time-averaged radiated acoustic power, $\langle \Pi_{rad} \rangle_t$, is the rate at which the source does "$p*dV$" work on the surrounding fluid for the in-phase components of the acoustic pressure, $\widehat{\mathbf{p}}(a)$, and the (radial) acoustic particle velocity, $\widehat{\mathbf{v}}_{\mathbf{r}}(a)$, at the source's surface.

---

[3] A convenient way to express the compactness criterion, $ka \ll 1$, for a compact spherical source is to say that the equatorial circumference of the source, $2\pi a$, is much less than the wavelength: $2\pi a \ll \lambda$.

$$\begin{aligned}\langle \Pi_{rad} \rangle_t &= \frac{1}{T}\int_0^T \widehat{\mathbf{F}}(a) \cdot \widehat{\mathbf{v}}_{\mathbf{r}}(a)\, \mathrm{d}t\, \mathrm{d}S = \frac{1}{T}\int_0^T |\widehat{\mathbf{p}}(a)| \left|\frac{\mathrm{d}V(a)}{\mathrm{d}t}\right| \cos\phi\, \mathrm{d}t \\ &= \frac{1}{T}\int_0^T |\widehat{\mathbf{p}}(a)| \left|\widehat{\mathbf{U}}(a)\right| \cos\phi\, \mathrm{d}t\end{aligned} \tag{12.17}$$

The component of $\widehat{\mathbf{p}}(a)$ that is in-phase with $\widehat{\mathbf{v}}_{\mathbf{r}}(a)$ can be expressed in terms of the radiation resistance, r_{rad}, which is the real part of the specific acoustic impedance, $\mathbf{z_{sp}}(a)$, on the surface of the sphere. Since $\Re e[\widehat{\mathbf{p}}(a)] = r_{rad}|\widehat{\mathbf{v}}_{\mathbf{r}}(a)|$ and $\left|\widehat{\mathbf{U}}(a)\right| = 4\pi a^2|\widehat{\mathbf{v}}_{\mathbf{r}}(a)|$, we can express Eq. (12.17) in terms of r_{rad} and $\widehat{\mathbf{v}}_{\mathbf{r}}(a)$.

Using the expression for r_{rad} in Eq. (12.16) and expressing $\widehat{\mathbf{v}}_{\mathbf{r}}(a)$ in terms of the magnitude of the source strength, $\left|\widehat{\mathbf{U}}(a)\right|$, provide a compact expression for the time-averaged power, $\langle \Pi_{rad} \rangle_t$, radiated from the source based on the real component of the specific acoustic impedance at the source's surface, $\Re e[\mathbf{z_{sp}}(a)] \equiv r_{rad}$.

$$\langle \Pi_{rad} \rangle_t = \frac{\pi}{2}\frac{\rho_m c}{\lambda^2}\left|\widehat{\mathbf{U}}(a)\right|^2 = \frac{\pi}{2}\frac{\rho_m}{c} f^2 \left|\widehat{\mathbf{U}}(a)\right|^2 \tag{12.18}$$

The right-hand version of this result demonstrates why it is more difficult to radiate low frequencies. Either the velocity of the surface needs to be increased, which frequently causes distortion, or the loudspeaker's area must be increased, assuming that $(ka)^2 \ll 1$. This is why the enclosures for reproduction of bass utilize loudspeakers of large diameter to provide adequate source strength, $\left|\widehat{\mathbf{U}}(a)\right|$, as suggested in Fig. 12.1.

12.2.2 Compact Monopole Acoustic Transfer Impedance

To determine the amplitude constant, $\widehat{\mathbf{C}}$, in Eq. (12.8), we can consider our pulsating sphere of mean radius, a, and radial velocity, $\widehat{\mathbf{v}}_{\mathbf{r}}(a) = j\omega\widehat{\boldsymbol{\xi}}$, and evaluate Eq. (12.12) at $r = a$.

$$v_r(a,t) = \Re e\left[j\omega\widehat{\boldsymbol{\xi}} e^{j\omega t}\right] = \Re e\left[\frac{\widehat{\mathbf{C}}}{a\rho_m c} e^{j(\omega t - ka)}\left(1 + \frac{1}{jka}\right)\right] \tag{12.19}$$

The compactness requirement guarantees that $ka \ll 1$, so $e^{-jka} \cong 1$ and $[1 + (1/jka)] \cong (1/jka)$. Substituting these *near-field* limits into Eq. (12.19), along with the fact that $\left|\widehat{\mathbf{U}}(a)\right| = 4\pi a^2|\widehat{\mathbf{v}}_{\mathbf{r}}(a)|$, uniquely determines the complex (phasor) pressure amplitude constant, $\widehat{\mathbf{C}}$.

$$\widehat{\mathbf{C}} = \omega\rho_m c\widehat{\boldsymbol{\xi}} ka^2 = \frac{\rho_m ck}{4\pi}\widehat{\mathbf{U}}(a) \tag{12.20}$$

Substitution of $\widehat{\mathbf{C}}$ back into Eq. (12.8) provides the exact solution for the acoustic pressure, $p_1(r,t)$, in terms of the magnitude of the source's volume velocity, $\left|\widehat{\mathbf{U}}(a)\right|$, and the wavelength of sound, $\lambda = (2\pi/k)$.

$$p_1(r,t) = \frac{\rho_m ck}{4\pi r}\left|\widehat{\mathbf{U}}(a)\right| \Re e\left[e^{j(\omega t - kr)}\right] = \frac{\rho_m c}{2r\lambda}\left|\widehat{\mathbf{U}}(a)\right| \Re e\left[e^{j(\omega t - kr)}\right] \tag{12.21}$$

The exact solution for the acoustic transfer impedance, $\mathbf{Z_{tr}}$, can be calculated from Eq. (12.21), providing the solution to this steady-state radiation problem.

$$|\mathbf{Z_{tr}}| \equiv \left|\frac{\widehat{\mathbf{p}}(R)}{\widehat{\mathbf{U}}(a)}\right| = \frac{\rho_m c}{2R\lambda} = 0.50\frac{\rho_m c}{R\lambda} \tag{12.22}$$

This result compares closely to the "causality sphere" approximation of Eq. (12.4) that was based on the adiabatic gas law but ignored the wavelike variation in pressure with position that is expressed exactly in Eq. (12.8).

The acoustic transfer impedance will now let us express the acoustic pressure, $\widehat{\mathbf{p}}(R)$, at some remote point in the far field ($kR \gg 1$), a distance, R, from the sound source's acoustic center, $R = 0$. This compact sound source of source strength, $|U_1(a)|$, radiates sound with a wavelength, $\lambda = c/f = 2\pi c/\omega$. At that location in the far field, we can assume that $\widehat{\mathbf{p}}(R)$ is in-phase with $\widehat{\mathbf{v}}_\mathbf{r}(R)$, based on Eq. (12.13), and that their ratio is given by the progressive plane wave value of the characteristic impedance $\mathbf{z_{sp}}(R) = \rho_m c$. This simplifies the calculation of the far-field time-averaged intensity of the sound, $\left\langle \vec{I}(R)\right\rangle_t$, using Eq. (10.36).

$$\begin{aligned}\left\langle \vec{I}(R)\right\rangle_t &= (½)\Re e\left[\widehat{\mathbf{p}}(R)\widehat{\mathbf{v}}_\mathbf{r}^*(R)\right] = \frac{|\widehat{\mathbf{p}}(R)|^2}{2\rho_m c}\\ &= \frac{1}{2\rho_m c}\left(\frac{\rho_m c}{2R\lambda}\left|\widehat{\mathbf{U}}(a)\right|\right)^2 = \frac{\rho_m c}{8R^2\lambda^2}\left|\widehat{\mathbf{U}}(a)\right|^2\end{aligned} \tag{12.23}$$

The time-averaged acoustic intensity is inversely proportional to the square of the distance from the sound source, but the time-averaged total radiated power, $\langle \Pi_{rad}\rangle_t$, is independent of distance, since all forms of dissipation have been neglected.

$$\langle \Pi_{rad}\rangle_t = 4\pi R^2\langle I(R)\rangle_t = \frac{\pi}{2}\frac{\rho_m c}{\lambda^2}\left|\widehat{\mathbf{U}}(a)\right|^2 \tag{12.24}$$

Of course, in the absence of any dissipation in the surrounding fluid, this is the same radiated power we calculated "locally" by using the radiation resistance "felt" by the source, $r_{rad}(a)$, on its surface (i.e., in the near field), expressed in Eq. (12.18).

12.2.3 General Multipole Expansion*

Since the monopole is such a significant concept for our understanding of radiation and scattering, it is worthwhile to review the assumptions and processes that led to the results of Eqs. (12.13), (12.15), (12.18), (12.19), (12.21), (12.22), and (12.23). Fundamentally, the three-dimensional problem of Eq. (12.5) was transformed to the quasi-one-dimensional problem of Eq. (12.6) based on a claim of spherical symmetry (i.e., isotropy) and the assertion that the shape of the pulsating source of volume velocity was irrelevant (and unknowable based on the far-field radiation pattern),[1] so that only the source strength, $\left|\widehat{\mathbf{U}}(a)\right|$, was significant for determination of the radiated sound field.

That assertion of source-shape independence was not proven, since it would be necessary to solve the full three-dimensional problem, then determine under what circumstances the higher-order multipolar contributions are negligible. The solution to the full three-dimensional problem, using the Laplacian of Eq. (12.5) in the wave equation, is a product of spherical Bessel functions, $j_n(kr)$, and the associated Legendre polynomials, $P_l^m(\cos\theta)$.

$$p(r,\theta,\vartheta;t) = \Re e\left[\sum \widehat{\mathbf{C}}_{\mathbf{n,m,l}} e^{j\omega t} j_n(kr)\sqrt{\frac{2l+1}{2\pi}\frac{(l-m)!}{(l+m)!}}P_l^m(\cos\theta)\left\{\begin{array}{c}\cos(m\varphi)\\ \sin(m\varphi)\end{array}\right\}\right] \tag{12.25}$$

The constants, $\widehat{\mathbf{C}}_{\mathbf{n,m,l}}$, are determined in the same way as we determined $\widehat{\mathbf{C}}$ in Eq. (12.8); by matching the velocity components of the wave (using Euler's equation) to the velocity distribution on the surface of the source. The complete set of functions provided in the infinite summation of Eq. (12.25) can be fit to a source of any shape where the various parts of the surface are moving in any direction and with any relative phase, although the result is still restricted to a single frequency [5]. Our solution of Eq. (12.8) corresponds to the spherically symmetric $n = 0$ spherical Bessel function, $j_0\,(kr) = \sin\,(kr)/(kr)$, which forces $m = l = 0$, so that there is no angular dependence.[4]

Our analysis, based on a compact spherical source, produced results that are applicable to sound sources that have no resemblance to a sphere, for example, a circular piston executing simple harmonic oscillations mounted in an enclosure that is a rectangular parallelepiped or the body of a dog (e.g., Fig. 12.2). The results obtained only depend upon specification of the source strength, $\left|\widehat{\mathbf{U}}(a)\right|$, and our ability to enclose the source within a spherical shell having a circumference much less than the wavelength (i.e., $ka \ll 1$) that is pulsating with a complex radial oscillation amplitude, $\widehat{\boldsymbol{\xi}}$, making the source strength magnitude, $\left|\widehat{\mathbf{U}}(a)\right| = 4\pi a^2\omega\left|\widehat{\boldsymbol{\xi}}\right|$.

After using hydrodynamic mass to calculate the resonance frequency of a bubble in the next section, we will continue to avoid dealing with the complete mathematical solution of Eq. (12.25) by using the principle of superposition to sum the acoustic fields of simple monopole sources. This will facilitate calculation of the behavior of more complex sources that lack spherical symmetry and produce a significant angular dependence of their radiated sound fields.

12.3 Bubble Resonance

Having calculated the hydrodynamic mass associated with the radial oscillations of a compact spherical source in Eq. (12.15), this concept can be applied to an interesting and important lumped-element fluidic resonator for which the hydrodynamic mass makes the entire inertial contribution. A gas bubble in a liquid will have an equilibrium radius, a, that is determined by the competition between the surface tension that will cause the bubble to collapse and the gas pressure inside the bubble that will resist the external force of the liquid pressure and of the surface tension.

The static pressure difference, $p_{in} - p_{out}$, across a curved interface is given by *Laplace's formula* that can be expressed in terms of the principle radii of curvature and the surface tension, α [6].

$$p_{in} - p_{out} = \alpha\left(\frac{1}{R_1} + \frac{1}{R_2}\right) \tag{12.26}$$

For a spherical bubble, $R_1 = R_2 = a$, where a is the radius of the bubble, so the pressure difference caused by the surface tension is $2\alpha/a$. If the gas inside the bubble is the vapor of the surrounding liquid, then there will be a minimum bubble radius, R_{min}, determined when the vapor pressure and Laplace

[4] Solutions to the full three-dimensional wave equation are available in most textbooks on advanced engineering mathematics or mathematical physics. This version was taken from E. Butkov, *Mathematical Physics* (Addison-Wesley, 1968).

pressures are equal. In the case where $a < R_{min}$, the bubble is unstable and will collapse by squeezing the vapor back into the liquid state.

For a "clean" air-water interface at 20 °C, the surface tension, $\alpha = 72.5 \times 10^{-3}$ N/m, and $P_{vap} = 2.3$ kPa, so $R_{min} = 0.063$ mm = 63 μm. As we will see, our interests are concentrated on larger bubbles, many of which may contain a non-condensable gas (e.g., air) that stabilizes the bubbles against collapse.

The gas pressure, p_{in}, within a stable bubble surrounded by water, is usually determined by the depth of the bubble below the water's surface. Since $p_{in} = p_o + \rho_m g\, z$, where p_o is atmospheric pressure, g is the acceleration due to gravity, ρ_m is the mass density of the water (not the gas!), and z is the distance below the free surface, as discussed in Sect. 8.3. If the mean radius of the bubble, a, is displaced from equilibrium by an amount, $\left|\hat{\xi}\right|$, while maintaining its spherical shape, the excess force, $\delta F\left(\hat{\xi}\right)$, that the pressure applies to the bubble's surface can be determined from the adiabatic gas law, if we assume that $a > \delta_\kappa$, so the compressions and expansions are nearly adiabatic, again using Eq. (12.2).

$$\delta p_{in} = -\gamma p_{in}\frac{\delta V}{V} = -\gamma p_{in}\frac{4\pi a^2\left|\hat{\xi}\right|}{\left({}^{4\pi}\!/_{3}\right)a^3} = -3\gamma p_{in}\frac{\left|\hat{\xi}\right|}{a} \tag{12.27}$$

Integrated over the surface area of the bubble, this excess pressure, $\delta p_{in} = |\hat{\mathbf{p}}|$, produces an excess force, $\delta F\left(\hat{\xi}\right)$, which is proportional to the amplitude of the oscillatory change in radius, $\hat{\xi}$, and motivates an expression that is equivalent to Hooke's law:

$$\delta F = \left(4\pi a^2\right)\delta p_{in} = -12\pi a\gamma p_{in}\left|\hat{\xi}\right| \quad \Rightarrow \quad \mathrm{K}_{eff} = 12\pi a\gamma p_{in} \tag{12.28}$$

The minus signs in Eqs. (12.27) and (12.28) arise because the pressure increases when $\left|\hat{\xi}\right|$ decreases. By analogy with Hooke's law, the effective stiffness constant, K_{eff}, is just the magnitude of the coefficient of such displacements, $\hat{\xi}$.

The only inertial mass of any significance is the hydrodynamic mass, m_{eff}, of the fluid that must accelerated in and out radially as the bubble's radius changes. This hydrodynamic mass can be calculated using Eq. (12.15).

$$m_{eff} = 3\rho_m V = 4\pi a^3 \rho_m \tag{12.29}$$

That effective mass can be combined with the effective gas stiffness of Eq. (12.28) to create a simple harmonic oscillator with a resonance frequency, $f_o = \omega_o/2\pi$.

$$\omega_o = \sqrt{\frac{\mathrm{K}_{eff}}{m_{eff}}} = \frac{1}{a}\sqrt{\frac{3\gamma p_{in}}{\rho_m}} \tag{12.30}$$

Here, it is important to remind ourselves that p_{in} is the gas pressure but ρ_m is the density of the surrounding water. If the restoring force due to surface tension is included, Eq. (12.30) can be modified to incorporate that additional restoring force (stiffness) [7].

$$\omega_o = \frac{1}{a\sqrt{\rho_m}}\sqrt{3\gamma p_{in} - \frac{2\alpha}{a}} \tag{12.31}$$

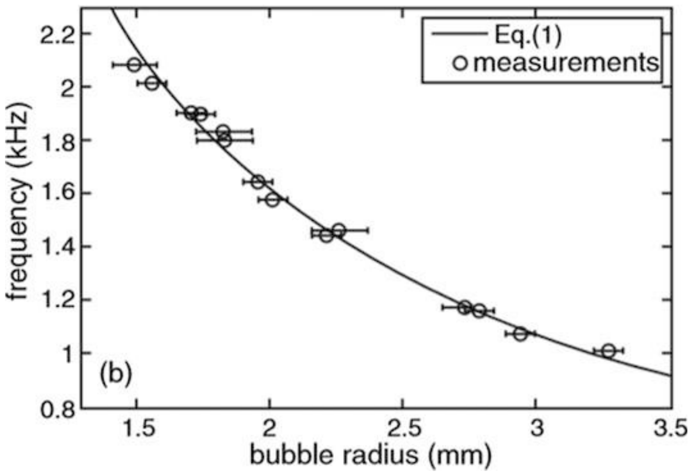

Fig. 12.7 Resonance frequencies of millimeter-sized bubbles whose resonance frequency was measured acoustically in a desktop aquarium [9]. At a frequency of 1.5 kHz, $\delta_\kappa = 68\ \mu\text{m} \ll a$, placing these measurements well within the adiabatic limit (see Fig. 12.9). The solid line represents the full theory of Commander and Prosperetti [10], which is very nearly the same as the Minnaert theory from Eq. (12.30) in this limit

Although the addition of the surface tension appears to decrease the resonance frequency in Eq. (12.31), the surface tension increases the frequency since p_{in} also would now include the Laplace pressure of Eq. (12.26). In applying either Eq. (12.30) or Eq. (12.31) to evaluate ω_o, it is important to remember that p_{in} is the pressure of the gas inside the bubble, with γ being determined by the gas, but ρ_m is the density of the surrounding fluid since it is the dominant source of inertance (i.e., kinetic energy storage).

Equations (12.30) and (12.31) were first derived by Minnaert in 1933 [7]. Although his frequency was calculated under adiabatic conditions for spherical bubbles, Strasberg has shown that even for spheroidal bubbles with a ratio of major-to-minor axes of a factor of two, the oscillation frequency differs from the Minnaert result by only 2%[5] [8]. Figure 12.7 shows some recent table-top laboratory measurements of bubble resonance frequencies vs. bubble radius which agree with Eq. (12.30) to within experimental error [9].

12.3.1 Damping of Bubble Oscillations

The damping of the bubble resonances is a consequence of losses due to radiation and due to boundary layer thermal relaxation at the air-water interface (as it was for the spherical compliance of a Helmholtz resonator calculated in Sect. 9.4.4). The reciprocal of the quality factor that characterizes each of these dissipative effects can then be summed, as in Eq. (9.40) or Eqs. (10.58) and (10.61), to determine Q_{total} in the adiabatic limit where $a \gg \delta_\kappa$.

$$\frac{1}{Q_{total}} = \frac{1}{Q_{th}} + \frac{1}{Q_{rad}} \tag{12.32}$$

Using Eq. (9.38), the time-averaged power dissipation per unit area due to thermal relaxation, $\dot{e}_{th}$, is quadratic in the amplitude of the oscillating pressure within the bubble, $|\widehat{\mathbf{p}}|^2$, and the total, time-averaged power dissipation, $\langle \Pi_{th} \rangle_t$, will be $\dot{e}_{th}$ times the surface area of the bubble.

[5] This insensitivity of resonance frequency to shape is a consequence of adiabatic invariance as demonstrated in the discussion of enclosures that cannot be modeled by separable coordinate systems, in Sect. 13.3.5.

$$\dot{e}_{th} = \frac{\gamma - 1}{4\gamma} \frac{|\widehat{\mathbf{p}}|^2}{p_m} \omega \delta_\kappa \quad \Rightarrow \quad \langle \Pi_{th} \rangle_t = 4\pi a^2 \dot{e}_{th} = \frac{\gamma - 1}{\gamma} \pi a^2 \omega \delta_\kappa \frac{|\widehat{\mathbf{p}}|^2}{p_m} \tag{12.33}$$

The total energy stored in the bubble oscillation is equal to the maximum potential energy density, $(P.E./Vol.)_{max}$, times the volume of the bubble, $(4\pi/3)a^3$. The potential energy density was calculated in Eq. (10.35).

$$\left(\frac{P.E.}{V}\right)_{max} = \frac{1}{2} \frac{|\widehat{\mathbf{p}}|^2}{\rho_m c^2} = \frac{1}{2} \frac{|\widehat{\mathbf{p}}|^2}{\gamma p_{in}} \quad \Rightarrow \quad E_{stored} = \frac{2\pi a^3}{3} \frac{|\widehat{\mathbf{p}}|^2}{\gamma p_{in}} \tag{12.34}$$

The quality factor due to thermal relaxation losses on at the spherical gas-water interface can be expressed using Eq. (B.2).

$$Q_{th} = \frac{\omega E_{stored}}{\langle \Pi_{th} \rangle_t} = \frac{2}{3(\gamma - 1)} \frac{a}{\delta_\kappa} \quad \text{for} \quad a > \delta_\kappa \tag{12.35}$$

Note that this result is identical to the result for Q_{th} calculated for thermal relaxation loss on the surface of the spherical volume with radius, R, of a Helmholtz resonator in Eq. (9.48). From Eq. (9.14), $\delta_\kappa = \sqrt{2\kappa/\rho_m c_P \omega}$, so δ_κ is proportional to $\omega^{-1/2}$. From Eq. (12.30), a is proportional to ω^{-1}, so the thermal quality factor, Q_{th}, is proportional to $\omega^{-1/2}$. In the adiabatic limit, the thermal damping, which is proportional to the reciprocal of the Q_{th}, increases with the square root of frequency, as shown in Fig. 12.8.

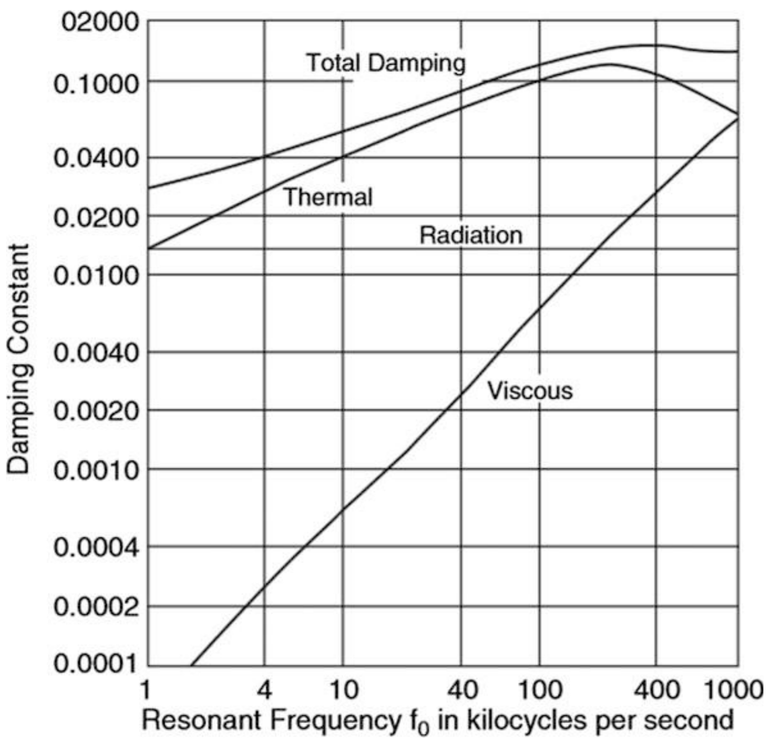

Fig. 12.8 The damping constant for an air-filled bubble in water that is shown on the vertical axis is the reciprocal of the quality factors of Eqs. (12.35) and (12.37). The observed peak in the thermal damping and in the total damping occurs where the behavior of the gas inside the bubble is transitioning between adiabatic at lower frequencies to isothermal at higher frequencies. This is shown explicitly in Fig. 12.9. The viscous damping, unimportant below 500 kHz, is due to shear stresses at the air-water interface [11].

The time-averaged power lost to acoustic radiation is given by Eqs. (12.18) and (12.24). The bubble's source strength, $\left|\widehat{\mathbf{U}}(a)\right|$, is related to the internal gas pressure oscillation amplitude, $|\widehat{\mathbf{p}}|$, by the adiabatic gas law in the form that appears in Eq. (12.2).

$$|\widehat{\mathbf{p}}| = (\gamma p_{in})\frac{\delta V}{V} = (\gamma p_{in})\frac{\left|\widehat{\mathbf{U}}(a)\right|}{\omega \ V} \quad \Rightarrow \quad \left|\widehat{\mathbf{U}}(a)\right| = \frac{\omega \ V}{\gamma p_{in}}|\widehat{\mathbf{p}}| \tag{12.36}$$

Substitution of Eq. (12.36) into the expression for quality factor used in Eq. (12.35) determines the quality factor due to the power radiated by the bubble, Q_{rad}. This reduces to another even simpler form after various substitutions.

$$Q_{rad} = \frac{\omega E_{stored}}{\Pi_{rad}} = c_{\mathrm{H_2O}}\sqrt{\frac{3\rho_{\mathrm{H_2O}}}{\gamma p_{in}}} \tag{12.37}$$

The radiation quality factor, Q_{rad}, as well as its reciprocal, corresponding to the radiative loss, is frequency independent, so by Eq. (12.30), it is also independent of the resonant bubble's radius. This behavior is illustrated in Fig. 12.8, taken from Devin [11].

The peak in the dissipation due to thermal relaxation on the air-water interface visible in Fig. 12.8 corresponds to the behavior of the gas changing over from adiabatic for larger bubbles at lower resonance frequencies to isothermal for smaller bubbles at higher frequencies. Such behavior is characteristic of a single relaxation time process like that shown in Fig. 4.25. This adiabatic-to-isothermal transition is shown explicitly in Fig. 12.9, also from Devin [11], which plots the thermal damping and the gas stiffness as a function of the ratio of the bubble's diameter, $2a$, to the thermal penetration depth, δ_κ.

To develop some appreciation for these results, consider an air-filled bubble with a diameter of 1.0 mm ($a = 5 \times 10^{-4}$ m) that is located 10 meters below the surface of the water, so that $p_{in} = 1.0$ MPa. Since $3\gamma p_{in} \cong 4.2$ MPa $\gg 2\alpha/a = 290$ Pa, Eq. (12.30) can be used to calculate the Minnaert frequency,

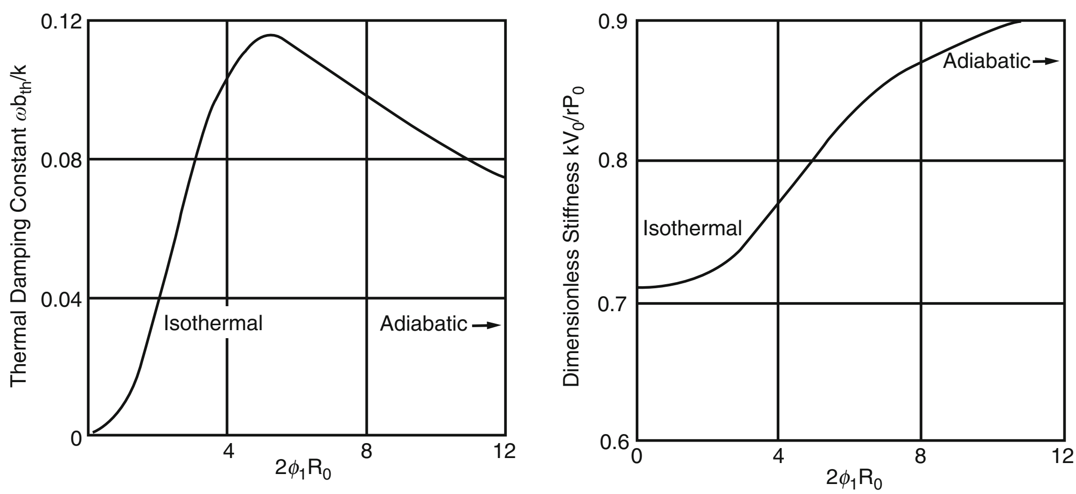

Fig. 12.9 (*Left*) The thermal damping factor is plotted as a function of the ratio of bubble diameter, $2a$, to the thermal penetration depth, δ_κ: $2\phi_1 = 2/\delta_\kappa$, or $2\phi_1 R_o = 2a/\delta_\kappa$. The damping has its peak at about $a \cong (^5/_2)\,\delta_k$. (*Right*) The transition of the stiffness of the gas within the bubble from adiabatic behavior for large bubbles to isothermal for small bubbles is also plotted in terms of $2\phi_1 R_o = 2a/\delta_\kappa$ [11]

$f_o = \omega_o/2\pi = 20.6$ kHz. At that frequency, the thermal penetration depth in air, δ_κ, is 5.9 microns. Using Eq. (12.35), $Q_{th} = 144$, and using Eq. (12.37), $Q_{rad} = 70$, making $Q_{total} = 47$.

12.4 Two In-Phase Monopoles

Armed with our understanding of the radiation from a compact source (monopole) in an unbounded homogeneous isotropic fluid medium, we can begin our investigation of more complex radiators, like the line arrays filling the stage in Fig. 12.1 and the piston source (woofer) of Fig. 12.2. We will start by consideration of just two monopole sources that are oscillating in-phase,[6] with equal amplitudes, at some frequency, $f = \omega/2\pi$, which have their acoustic centers separated by a distance, d, as shown in Fig. 12.10.

To calculate the radiated sound field of that pair of in-phase sources (sometime called a *bipole*), we will use the principle of superposition to combine the pressures produced by the two monopoles that are treated individually. There is an interesting philosophical point implicit in that approach, since the behavior of the individual monopoles was predicated on their radiation pattern being spherically symmetric. Clearly that symmetry has been broken for the case of two compact sources radiating simultaneously. The reason that we can use the superposition of spherically symmetric sources to produce a non-spherically symmetric radiation pattern is (again) the fact that we are restricting ourselves to "linear acoustics."

We are assuming that the radiation from one source does not change either the properties of the medium or the radiation behavior of the other source. There are cases where this assumption is violated, sometimes with disastrous consequences [12]. The understanding of the inter-element interactions in high-amplitude SONAR array applications became important in the late 1950s when

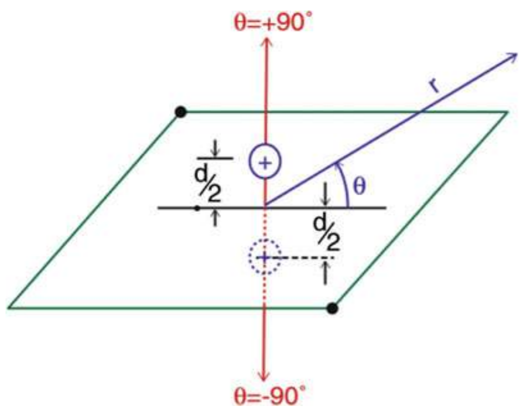

Fig. 12.10 Two compact (monopole) sound sources separated by a distance, d, that are radiating in-phase (as indicated by their "+" signs). The line through their centers (*red*) defines a unique direction. The plane (*green*) is the perpendicular bisector of the line joining the centers of the two sources. The vector, $\vec{r}$ (*blue*), is the distance from the intersection of the line and plane to an observation point that makes an angle, θ, with that symmetry plane. Due to the rotational symmetry about the line, the radiated sound field is independent of the azimuthal angle, φ

[6] It is probably worthwhile mentioning that a requirement for the existence of a constant phase relationship between two oscillators is that they must be oscillating at the same frequency. If they were oscillating at different frequencies, their relative phases would be changing linearly with time.

high-powered search SONAR arrays were developed using the then newly available lead-zirconate-titanate piezoelectric ceramic materials [13, 14].

We will restrict ourselves to the case where superposition is valid and add the pressure fields of the two monopole sources. Before calculating the pressure field by this method, we can examine a few simple cases. If the separation of the two sources is much closer than a wavelength, $d \ll \lambda$, then we have essentially doubled the source strength, and our expression for the acoustic transfer impedance of a monopole in Eq. (12.22) tells us that we have doubled the acoustic pressure and quadrupled the radiated acoustic power, based on Eq. (12.18) or Eq. (12.24).

If the separation of the two sources is exactly one-half wavelength, $d = \lambda/2$, then when the sound produced by the first source reaches the location of the second source, the two sources will be radiating 180° out-of-phase. Along the direction of the line joining the two sources, known by those who specialize in array design as the *end-fire direction* ($\theta = \pm 90°$), the radiated pressure will be zero if the strengths of the two individual monopole sources are identical. Along the equatorial plane ($\theta = 0^\circ$), shown in Fig. 12.10, the distance to either source is identical so the pressure on that plane is doubled. Those who specialize in array design call the direction defined by that plane as the *broadside direction*.

To calculate the sound field of the bipole produced at any observation point a distance, $|\vec{r}|$, from the midpoint of the line joining the sources at an angle, θ, above the equatorial plane, as shown in Figs. 12.10 and 12.11, we can simply sum the spherically symmetric radiation produced by the individual sources, given by Eq. (12.21), paying particular attention to their relative phases in the far field.

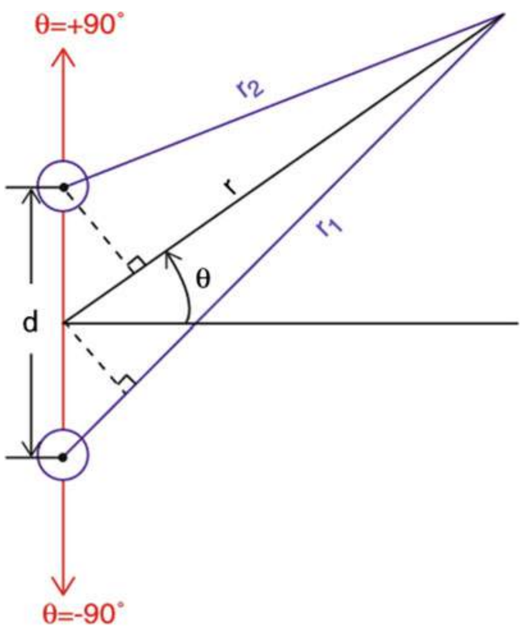

Fig. 12.11 Coordinate system for superposition of the two in-phase compact sources separated by a distance, d. The distance from the center of the two sources to the observation point is indicated by $\vec{r}$, which makes an angle, θ, with the plane that is the perpendicular bisector of the line joining the two sources. The distance from the upper source is r_2, and the distance from the lower source is r_1. The dashed perpendicular lines show the difference in path lengths between the two sources and the vector $\vec{r}$. In this diagram, the upper sources are closer than r by a distance, $\Delta r_2 \cong (d/2) \sin \theta$. The lower source is farther by a distance, $\Delta r_1 \cong (d/2) \sin \theta$

$$p\left(\left|\vec{r}\right|,\theta;t\right) = \Re e\left[\frac{\left|\widehat{\mathbf{C}}_{\mathbf{1}}\right|}{\left|\vec{r}_1\right|}e^{\,j\left(\omega t - k_1\left|\vec{r}_1\right| + \phi\right)} + \frac{\left|\widehat{\mathbf{C}}_{\mathbf{2}}\right|}{\left|\vec{r}_2\right|}e^{\,j\left(\omega t - k_2\left|\vec{r}_2\right| - \phi_2\right)}\right] \qquad (12.38)$$

For the bipole, we can let $\phi_1 = \phi_2 = 0$, since the sources are in-phase and let $k_1 = k_2 = k = \omega/c$, since the only way they can maintain a fixed phase relation is if they have the same frequency, $\omega_1 = \omega_2 = \omega$. We are assuming the source strengths are identical, having included their relative phases explicitly allowing their amplitudes to be represented by a scalar, $C = \left|\widehat{\mathbf{C}}_{\mathbf{1}}\right| = \left|\widehat{\mathbf{C}}_{\mathbf{2}}\right| = \rho_m ck\left|\widehat{\mathbf{U}}(a)\right|/4\pi$, according to Eq. (12.20).

The two distances between the observation point and the individual sources can be expressed in terms of the path length differences, Δr, that are indicated in Fig. 12.10 by the lines to the dashed perpendiculars to $\vec{r}$.

The sum expressed in Eq. (12.38) can be re-written to incorporate the bipole assumptions and the geometry of Fig. 12.10.

$$p\left(\left|\vec{r}\right|,\theta;t\right) = \Re e\left\{\left[\frac{e^{-jk\Delta r_1}}{\left(1 + {}^{\Delta r_1}\!/\!_{\left|\vec{r}\right|}\right)} + \frac{e^{+jk\Delta r_2}}{\left(1 - {}^{\Delta r_2}\!/\!_{\left|\vec{r}\right|}\right)}\right]\frac{C}{\left|\vec{r}\right|}e^{\,j\left(\omega t - k\left|\vec{r}\right|\right)}\right\} \qquad (12.39)$$

The factor at the far right of Eq. (12.39) has the form of an ordinary diverging spherical wave. The terms in square brackets require an interpretation that will become most transparent if we consider an observation point that is far from the two sources, in terms of their separation, $\left|\vec{r}\right| \gg d$. In that case, $\Delta r_1 \cong \Delta r_2 \ll \left|\vec{r}\right|$.

In the far field, $\left|\vec{r}\right| \gg d$, we can neglect the small differences created by Δr in the denominators of the terms in the square brackets of Eq. (12.39), since those involve the ratio, $\Delta r/\left|\vec{r}\right| \ll 1$. Since Δr appears within the arguments of exponentials, we will interpret their effects by expressing the path length differences applying simple trigonometry in Fig. 12.11 and Garrett's First Law of Geometry.

$$\Delta r_1 \cong \Delta r_2 \cong \frac{d}{2}\sin\theta \qquad (12.40)$$

Substitution of this far-field (i.e., $\left|\vec{r}\right| \gg d$) result into Eq. (12.39) produces a pressure distribution, $p(r,\ \theta,\ t)$, with a directional component involving the angle, θ. Given a source strength, the amplitude depends only upon the separation of the sources, d, and the wavelength of the radiated sound, $\lambda = 2\pi/k$.

$$\begin{aligned} p\left(\left|\vec{r}\right|,\theta;t\right) &\cong \Re e\left\{\left[e^{-jk\Delta r_1} + e^{+jk\Delta r_2}\right]\frac{C}{\left|\vec{r}\right|}e^{\,j\left(\omega t - k\left|\vec{r}\right|\right)}\right\} \\ &= \Re e\left\{\left[e^{-jk\frac{d}{2}\sin\theta} + e^{jk\frac{d}{2}\sin\theta}\right]\frac{C}{\left|\vec{r}\right|}e^{\,j\left(\omega t - k\left|\vec{r}\right|\right)}\right\} \end{aligned} \qquad (12.41)$$

The trigonometric identity, $\cos\theta = (1\!/\!_2)\left(e^{\,j\theta} + e^{-j\theta}\right)$, allows expression of the final result in terms of a product of the axial pressure along the equatorial plane, $\theta = 0°$, $p_{ax}\left(\left|\vec{r}\right|\right) = p\left(\left|\vec{r}\right|,\theta = 0^{\circ}\right)$, and a *directionality factor*, $H(\theta)$.

$$p\left(\left|\vec{r}\right|, \theta; t\right) = p_{ax}\left(\left|\vec{r}\right|; t\right) H(\theta) = \Re e\left\{\frac{2Ce^{\,j\left(\omega t - k\left|\vec{r}\right|\right)}}{\left|\vec{r}\right|}\right\}\left[\cos\left(\frac{kd}{2}\sin\theta\right)\right] \tag{12.42}$$

First, let's check that $p_{ax}\left(\left|\vec{r}\right|\right)H(\theta)$ in Eq. (12.42) produces the intuitive results with which this investigation was initiated.

$$H(\theta) = \cos\left(\frac{kd}{2}\sin\theta\right) \tag{12.43}$$

If $d \ll \lambda$ and $\phi = 0°$, then $kd/2 = \pi d/\lambda \ll 1$; hence $H(\theta) \cong \cos 0° = 1$ for all θ, demonstrating that the combination of two sources behaves as a single source with twice the source strength, since $p_{ax}\left(\left|\vec{r}\right|\right) = 2C/\left|\vec{r}\right|$. If $d = \lambda/2$, then $kd/2 = \pi/2$, so when $\sin\theta = \pm 1$, $H(\theta) = \cos(\pm\pi/2) = 0$; hence, we observe no sound radiated along the direction of the line joining the centers of the two monopole sources ($\theta = \pm 90°$), again, as expected.

With some confidence in Eqs. (12.42) and (12.43), we can now explore arrangements of the two sources that produce sound fields that may not be as intuitively obvious. From Eq. (12.43), it is easy to see that $H(\theta) = 1$ anytime that $(kd/2)\sin\theta_n = n\pi$, where $n = 0, 1, 2, \ldots$ There will be n directions, θ_n, where the sound radiated by the bipole will be maximum when $\sin\theta_n = 2n\pi/kd = n\lambda/d$ with $n \leq d/\lambda$. Similarly, $H(\theta) = 0$ if $(kd/2)\sin\theta = (2m + 1)\pi/2$, where $m = 0, 1, 2, \ldots$ There will be m directions, θ_m, where the sound radiated by the bipole will be zero when $\sin\theta_m = (2m + 1)\pi/kd = (2m + 1)\lambda/2d$, with $(2m + 1) \leq 2d/\lambda$.

Figure 12.12 shows the resulting beam pattern in two and three dimensions for $d/\lambda = 3/2$, or $kd = 3\pi$. There will be two nodal directions: $m = 0$, so $\sin\theta_{m=0} = 1/3$ and $\theta_{m=0} = 19.5°$, and $m = 1$, so $\sin\theta_{m=1} = 3/3$ and $\theta_{m=1} = 90°$. Note that if $m = 2$, $(2m + 1)\pi/kd = 5\pi/3\pi > 1$. There will also be

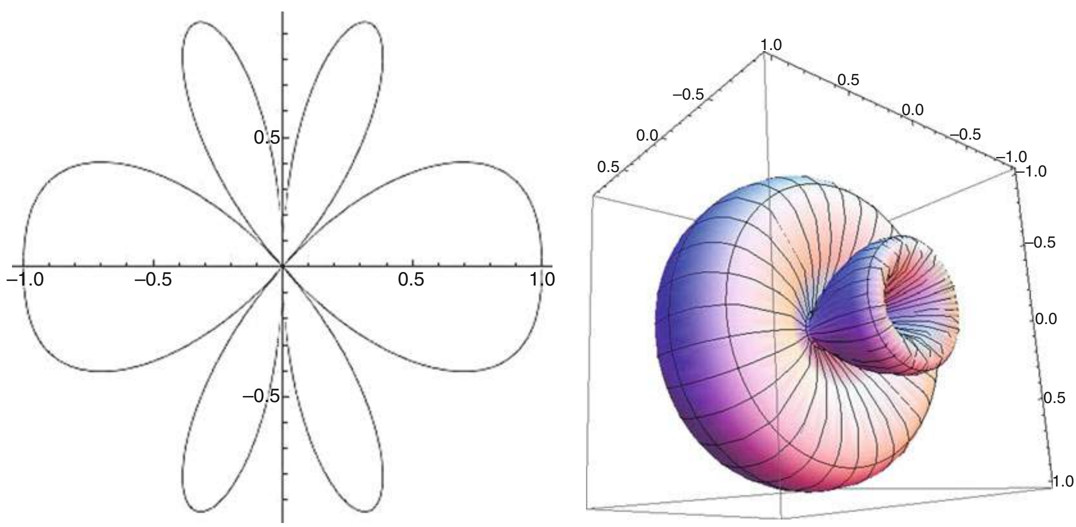

Fig. 12.12 Two representations of the directionality factor, $H(\theta)$, of the sound field radiated by a pair of in-phase compact simple sources of equal amplitude that are separated by $d = 3\lambda/2$, corresponding to $kd = 3\pi$. (*Left*) The two-dimensional representation of $H(\theta)$ provided in Eq. (12.43) that exploits the rotational symmetry about the axis joining the two sources to illustrate the essential structure of the directionality for that two-element array. (*Right*) The body of revolution formed by $H(\theta)$ is three-dimensional surface. This figure is rotated from the orientation at the left to provide a better view of the node that occurs along the polar directions. [Directionality plots courtesy of Randall Ali]

two maximal (i.e., anti-nodal) directions. With $n = 0$, sin $\theta_{n=0} = 0$, so $\theta_{n=0} = 0°$. With $n = 1$, sin $\theta_{n=1} = 2/3$, so $\theta_{n=1} = 41.8°$.

Recall that the axial symmetry guarantees that these directional nodes (i.e., zero pressure directions for sources of identical source strength) and anti-nodes (i.e., directions of maximum sound pressure) define cones in three dimensions, as shown in Fig. 12.12 (right).

12.4.1 The Method of Images

A more important feature of $H(\theta)$, as given in Eq. (12.43) for the bipole configurations shown in Figs. 12.10 and 12.11, is that along the equatorial plane ($\theta = 0°$), $H(\theta)$ always exhibits a local maximum: $dH(0)/d\theta = 0$. Based on the Euler equation, expressed in spherical coordinates in Eqs. (12.9) and (12.10),[7] the particle velocity $v_\theta(\theta = 0°)$, that is everywhere normal to the equatorial plane ($\theta = 0°$), must vanish. Since no fluid passes through that plane, the radiation field of the bipole would be unchanged if the equatorial plane was replaced by an infinite rigid boundary. This fact provides a rigorous motivation for incorporation of boundaries by the "method of images" that allows us to place "phantom" sources outside the fluid volume of interest to satisfy a boundary condition; in this case, the division of an infinite space into a semi-infinite "half-space" through the introduction of a rigid, impenetrable boundary. This result demonstrates that if a single monopole were placed a distance, $d/2$, in front of a rigid, impenetrable surface, the fact that the component of the fluid's acoustical particle velocity that is normal to that surface vanishes allows us to satisfy that boundary condition as long as we remain aware that the half-space behind the boundary is not a legitimate domain for the solution.

To initiate the discussion of the reflection of plane waves in Chap. 11, we considered the case of an echo bouncing off a large rigid surface depicted in Fig. 11.1. There, to satisfy the boundary condition, we *postulated* a counter-propagating wave to cancel the fluid particle velocity created by the incoming wave. Now we have shown explicitly that such a wave could be created by an "image source" that would also satisfy the boundary condition. In addition, the method of images has provided a solution that is not restricted to plane waves, although it contains the plane wave solution in the limit that $d/2 \gg \lambda$. The image solution also reinforces the fact that the acoustic pressure on the boundary is twice that which would have been produced by the same source radiating into an infinite (rather than semi-infinite) medium.

Figure 12.13 is a two-dimensional projection of an example where a spherical source of sound is located a distance of five wavelengths from a rigid reflector. An image source, an equal distance behind the reflector, is oscillating in-phase with the source to guarantee that the normal particle velocity at the rigid reflector will be zero. The resultant sound field within the fluid provides the classic "two-slit" interference pattern that was discovered by Thomas Young in 1803 for light waves [15]. Figure 12.13 is Young's original diagram that shows the same result as shown for a single light source in front of a rigid boundary. Young first discovered interference effects when he heard the "beats" produces by two sound sources radiating with slightly different frequencies.

Why did we not observe these interference effects when we investigated the reflection and refraction of plane waves in Chap. 11? The answer is simple: we did not look! In Chap. 11, we assumed that the plane waves consisted of pulses that were of sufficiently short duration that they interfered at the boundary but did not overlap far from the boundary, as shown in Fig. 11.1. The current

[7] Note that the definition of the polar component of the velocity v_θ, given in Eqs. (8.7) and (8.8), is $v_\theta = (j\omega\, r\rho_m)^{-1}(\partial p/\partial\theta)$ so v_θ would diverge at $r = 0$. This is not a problem because r has its minimum value at $r = a$.

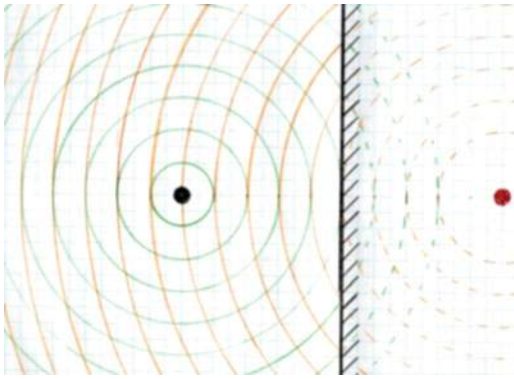

Fig. 12.13 The compact spherical source at the left (*black*) is placed a distance of five wavelengths, $d/2 = 5\lambda$, from a rigid boundary indicated by the hatched black line. The condition that the normal components of velocity at the boundary vanish is satisfied by placing an image source (*red*), oscillating in-phase with the real source (*black*), at the same distance behind the boundary. In this figure, the two sources are separated by ten wavelengths so $kd = 2\pi d/\lambda = 20\pi$. We visualize the resulting sound field with *green circles*, representing pressure maxima, separated by one wavelength, emanating from the real source and *orange circles* emanating from the image source. Behind the boundary, the circles are shown as dashed since there is no actual sound in that region. Within the fluid, any place where green and orange circles touch, the pressure will be doubled. Midway between those intersections, there will always be silence

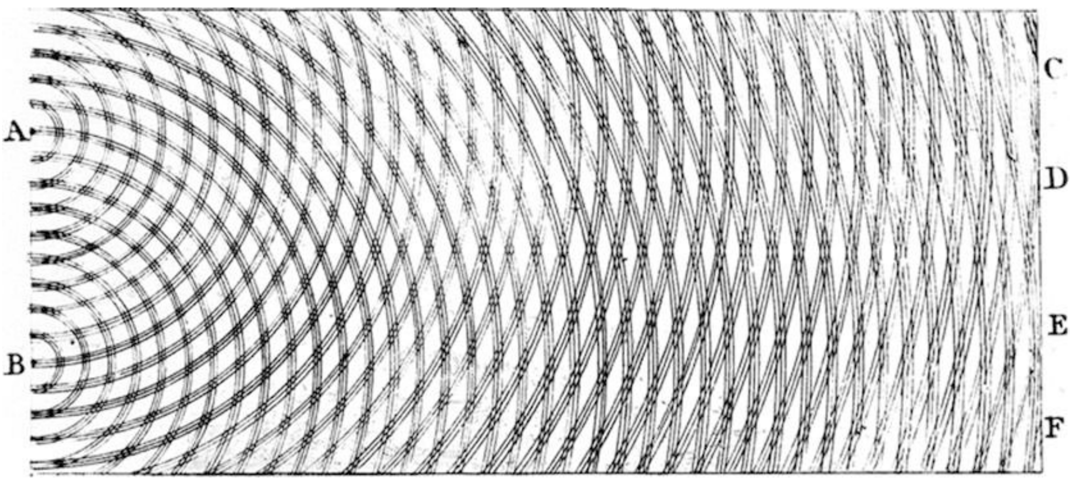

Fig. 12.14 Diagram representing the superposition of two in-phase light sources located at points A and B, separated by nine wavelengths, from the original paper by Thomas Young [15]. Amplitude doubling is apparent along the line starting at the left from the midpoint between A and B to the right of the diagram between D and E. This result is known as the "Young's double-slit experiment" and was central to the debate about the wavelike vs. the corpuscular nature of light [16].

treatment of a spherical source of sound adjacent to a rigid impenetrable boundary assumed continuous waves. If we return to Fig. 11.1, we see the incident plane wave fronts (blue) and the reflected plane wave fronts (green) produce pressure doubling where they intersect and silence half-way between.

The method of images has allowed us to solve the rather challenging problem of the sound field of a spherically radiating sound source in the proximity of a rigid boundary for an arbitrary separation between the source and the boundary. If we examine the opposite limit from that shown in Fig. 12.13 (or Fig. 12.14 for light) and consider a source that is much closer to the boundary than the wavelength of the sound it is radiating, $d/2 \ll \lambda$ or $kd \ll 1$, then we see that the source produces everywhere twice the pressure it would have if the boundary were not present. This case is commonly referred to as a *baffled source*, the "baffle" being the rigid boundary.

Since the acoustic pressure and the associated acoustic particle velocity are both doubled, the intensity of the sound is increased by a factor of four, although the radiated power is only doubled, since we can now only integrate the radiated intensity over a hemisphere. How is it possible that the same source can produce twice the acoustic pressure and radiate twice the acoustic power just by placing it very near a rigid boundary?

The answer is built into our assumptions regarding the behavior of the source. Throughout this discussion of radiation, we have assumed that the volume velocity of the source is independent of the load that it "feels" from the surrounding fluid, that is, we have assumed a "constant current" source.[8] The presence of the boundary doubled the pressure at the source (and elsewhere), so the specific acoustic impedance of the fluid at the source's surface, as expressed in Eq. (12.13), $\mathbf{z_{sp}}(a) = \widehat{\mathbf{p}}(a)/\widehat{\mathbf{v}}_\mathbf{r}(a)$, is doubled. It is possible that this increase in radiative resistance (though not hydrodynamic mass which depends upon the equilibrium fluid mass density) could reduce the volume velocity of a real source.

We can play the same trick again if we want to calculate the sound pressure radiated by a compact source of constant source strength that is located in a corner, as shown schematically in Fig. 12.15. If again we assume that $d/2 \ll \lambda$ or $kd \ll 1$, then we see that the source produces everywhere four times the pressure it would have if the boundaries were not present, again assuming the real source provides a constant volume velocity.[9] The intensity is now 16 times as large as that radiated by the same source in

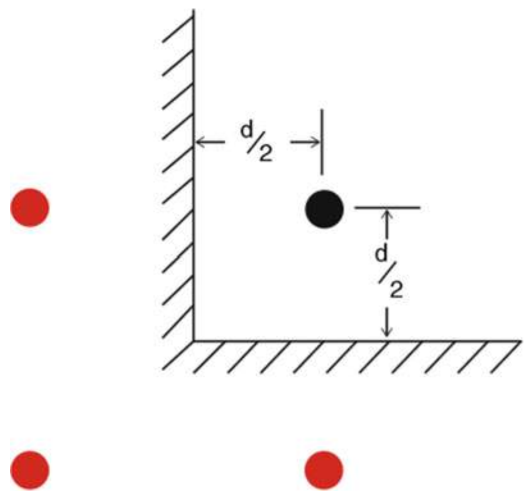

Fig. 12.15 Schematic representation of a compact spherical source located near the intersection of two rigid impenetrable plane surfaces indicated by the hatched black lines. In this case the source (*black*) creates three image sources (*red*). The upper left and bottom right image sources cannot create the zero normal acoustic particle velocity on the two orthogonal rigid surfaces without the third image source at the bottom left to provide a symmetrical quartet that ensures the orthogonal cancellation

[8] For discussion of "constant force" acoustic sources (e.g., magnetohydrodynamic transducers), see G. W. Swift and S. L. Garrett, "Resonance reciprocity calibration of an ultracompliant transducer," J. Acoust. Soc. Am. **81**(5), 1619–1623 (1987).

[9] This is the reason that the user's manual for the Bose "SoundLink Mini" recommends that those small speakers be placed near a wall or in a corner to enhance their bass response.

the absence of the two orthogonal boundary planes, but the radiated power is only 4 times as large since the intensity is now integrated only over one quadrant of a sphere.

This approach can be repeated to create a sound field for a source near the intersection of three rigid, orthogonal, impenetrable planes by reflecting the arrangement in Fig. 12.15 about the third orthogonal plane, creating a total of eight sources (i.e., seven image sources). This results in 8 times the pressure, 64 times the intensity, and 8 times the radiated power (by integration over the octet of a sphere).

Needless to say, the effects of rigid impenetrable walls are very important for sound reinforcement applications in rooms, both for enhancement of bass response when $kd < 1$[9] and for variation in the sound field amplitude with position for higher frequencies when $kd > 1$. The interference effects diagrammed in Figs. 12.13 and 12.14 produce significant variability in the acoustic intensity for different frequencies in different locations. Such variation is highly undesirable in a critical listening environment such as a recording studio (and its control booth) or a concert venue. We will revisit this problem from a different perspective (i.e., "normal modes") when we analyze the sound in three-dimensional enclosures and waveguides in Chap. 13 of this textbook.

As we could see by going from one perfectly reflecting plane to two and then to three orthogonal reflecting planes, the application of the method of images can start to become complicated. If fact, if we considered only two parallel planes with a single source located in between, an infinite number of image sources would be required, since each image source would generate another behind the opposite boundary and so on ad infinitum [17]. The method has been applied successfully to more complex problems, like sound in a wedge-shaped region [18], similar to a gently sloping beach, or curved surfaces [19], and is popular for solving boundary-value problems in other fields, such as electrostatics (i.e., image charges) near conducting or dielectric interfaces and in magnetostatics due to image current loops [20].

12.5 Two Out-Of-Phase Compact Sources (Dipoles)

We can repeat the previous analysis for two out-of-phase monopoles, separated by a distance, d, using the same analytical approaches that produced our bipole results in Eq. (12.42). This out-of-phase combination of two compact monopoles is known as a *dipole*. The results for the dipole will be useful, important, and dramatically different, since the out-of-phase superposition leads to cancellation of the radiated acoustic pressure in the limit that the separation of the two out-of-phase sources becomes very small compared to the wavelength of sound, $kd \ll 1$.

If we designate the upper source in Fig. 12.11 as having a phase $\phi_2 = 180° = \pi$ radians with $\phi_1 = 0°$, but retain our other assumptions, $k_1 = k_2 = k = \omega/c$, $\omega_1 = \omega_2 = \omega$, and let $\widehat{\mathbf{C}}_\mathbf{1} = -\widehat{\mathbf{C}}_\mathbf{2}$ and $C = \left|\widehat{\mathbf{C}}_\mathbf{1}\right| = \rho_m ck\left|\widehat{\mathbf{U}}(a)\right|/4\pi$, then we can proceed by changing the sign of one term within the square brackets in Eq. (12.39).

$$p\left(\left|\vec{r}\right|,\theta;t\right) = \Re e\left\{\left[\frac{e^{-jk\Delta r_1}}{\left(1 + {}^{\Delta r_1}\!\!/_{\left|\vec{r}\right|}\right)} - \frac{e^{+jk\Delta r_2}}{\left(1 - {}^{\Delta r_2}\!\!/_{\left|\vec{r}\right|}\right)}\right]\frac{C}{\left|\vec{r}\right|}e^{\,j\left(\omega t - k\left|\vec{r}\right|\right)}\right\} \tag{12.44}$$

Using the trigonometric relation of Eq. (12.40) to again represent the path length differences, the far-field pressure of the dipole can be expressed in analogy with the bipole result of Eq. (12.41).

$$p\left(\left|\vec{r}\right|,\theta;t\right) \cong \Re e\left\{\left[e^{-jk\frac{d}{2}\sin\theta} - e^{jk\frac{d}{2}\sin\theta}\right]\frac{C}{\left|\vec{r}\right|}e^{\,j\left(\omega t - k\left|\vec{r}\right|\right)}\right\} \tag{12.45}$$

The trigonometric identity $\sin\theta = (2j)^{-1}(e^{j\,\theta} - e^{-j\,\theta})$ allows the final result to be expressed in terms of a product of the maximum pressure along the axial direction $\theta = 90°$, $p_{ax}\left(\left|\vec{r}\right|\right) = p\left(\left|\vec{r}\right|, 90^\circ\right)$, and a directionality factor, $H_{dipole}(\theta)$.

$$\begin{aligned} p\left(\left|\vec{r}\right|,\theta\right) = p_{ax}\left(\left|\vec{r}\right|\right)H_{dipole}(\theta) &= \Re e\left\{-j\frac{2C}{\left|\vec{r}\right|}e^{-jkr}\left[\sin\left(\frac{kd}{2}\sin\theta\right)\right]\right\} \\ &= \Re e\left\{-j\frac{\rho_m ck}{2\pi\left|\vec{r}\right|}e^{-jkr}\left|\widehat{\mathbf{U}}(a)\right|\left[\sin\left(\frac{kd}{2}\sin\theta\right)\right]\right\} \\ &= \Re e\left\{-j\frac{\rho_m c}{\left|\vec{r}\right|\lambda}e^{-jkr}\left|\widehat{\mathbf{U}}(a)\right|H_{dipole}(\theta)\right\} \end{aligned} \tag{12.46}$$

Comparison of the final expression in Eq. (12.46) to the expression for the pressure produced by a monopole in Eq. (12.21) shows that $p_{ax}\left(\left|\vec{r}\right|\right)$ is twice the pressure produced by a single monopole. This is as expected. If the two anti-phase sources are separated by odd-integer multiples of the half-wavelength, $d = (2n + 1)\lambda/2$, then the pressure along the line joining their centers will be twice that of a single monopole with source strength, $\left|\widehat{\mathbf{U}}(a)\right|$. Unlike the bipole, the directionality factor, $H_{dipole}(\theta)$, suppresses acoustic pressure along the equatorial plane, $\theta = 0°$ for $kd \ll 1$. The dipolar radiation patterns are shown in Fig. 12.16 for $kd \ll 1$ and in Fig. 12.16 for $kd = 3\pi$.

If $d \ll \lambda$, then $kd/2 = \pi d/\lambda \ll 1$; hence we can use the small-angle Taylor series approximation of $\sin x \cong x$ to express $H_{dipole}(\theta) \cong (kd/2)\sin\theta$, which has a maximum value of $(kd/2)$ at $\theta = 90°$ and at $\theta = 0°$ is zero. This is what we would expect; the path lengths to both sources are always equal for any observation point on the equatorial plane, and the anti-phased sources will always sum to zero pressure along that direction. In the small kd limit, the maximum pressure is always smaller than that of a monopole of equal source strength by a factor of (kd).

$$\widehat{\mathbf{p}}_{dipole}/\widehat{\mathbf{p}}_{monopole} \propto kd \quad \text{for} \quad kd \ll 1 \tag{12.47}$$

A compact dipole source is always a less efficient radiator than a monopole of equivalent source strength (i.e., volume velocity).

It is worthwhile pointing out that the reduction in radiated pressure, symbolized by Eq. (12.46), is the reason that all loudspeakers intended for radiation of low-frequency sound are placed in some kind of enclosure so that the source strength due to the oscillations of the speaker's diaphragm that are produced by the back surface of the speaker cone does not cancel the volume velocity generated by the cone's front surface.[10]

Just as we used the bipole to produce the sound field of a source at an arbitrary distance from a rigid boundary, the dipole produces a "pressure release surface" along the entire equatorial plane. This is a convenient way to satisfy the boundary condition for a source submerged below the air-water interface. If we imagine the situation depicted in Fig. 12.13, but let the black and red simple sources be 180° out-of-phase, then the plane bisecting the line connecting the two sources will support oscillatory fluid flow perpendicular to the plane but no oscillatory pressure. The cancellation of the acoustic pressure along that plane is clearly seen in Fig. 12.12 if the green circles radiating from the black source

[10] There are schemes, such as the bass-reflex enclosure, analyzed in Sect. 8.8, that use an acoustical network, like a Helmholtz resonator or transmission line, to allow the back-side volume velocity to add to that from the front side in a way that they are more nearly in-phase over the frequencies of interest.

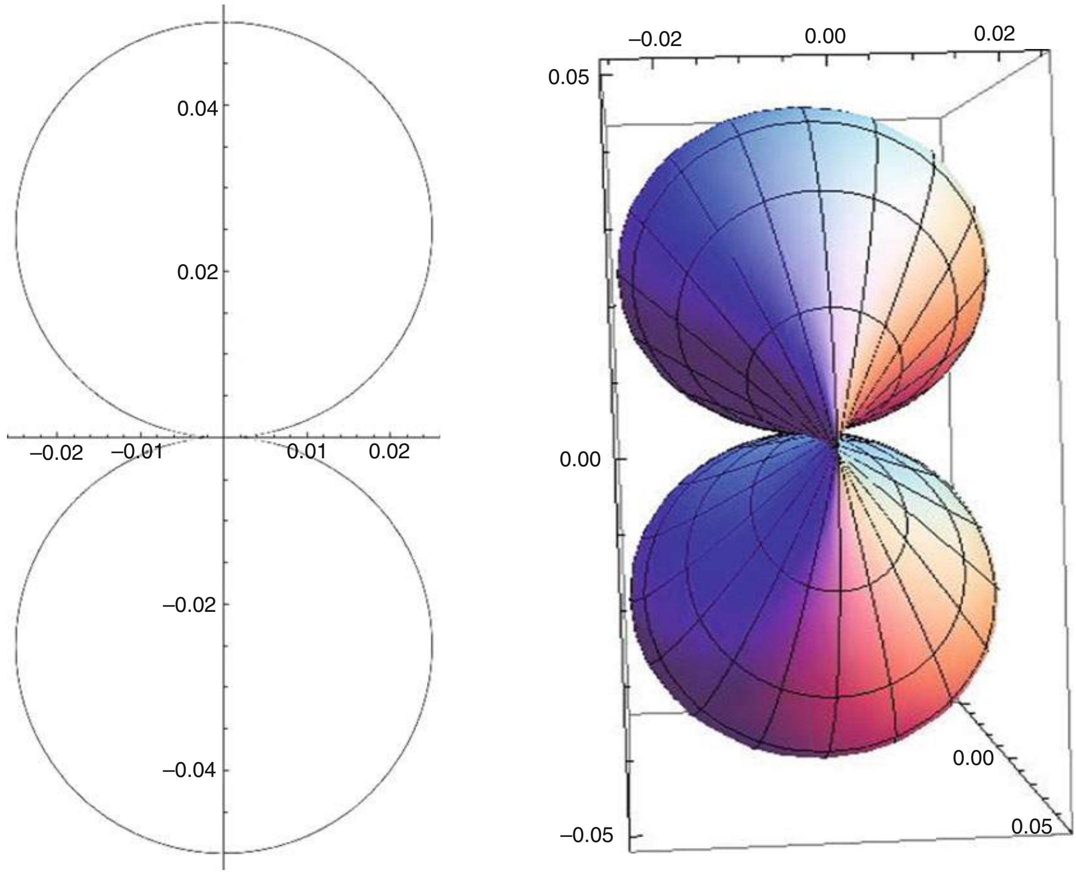

Fig. 12.16 Dipole directional pattern, $H(\theta)$, for two compact spherical sources separated by a distance, d, that is significantly less than one wavelength of sound: $kd \ll 1$. (*Left*) The radiation is bi-directional as shown by this two-dimensional plot. It is important to recognize that the directionality function in Eq. (12.46) dictates that the two lobes are out-of-phase with respect to each other. (*Right*) Body of revolution formed by $H(\theta)$ is a three-dimensional representation of the dipole's directivity, viewed along the equatorial plane, to show the null. [Directionality plots courtesy of Randall Ali]

represent pressure maxima and the orange circles radiating from the red source represent pressure minima. Where those circles intersect the pressure sums to zero.

If the separation of the two anti-phase sources is greater than a half-wavelength (i.e., $kd \geq \pi$), then the dipole will generate a directional pattern with multiple nodal surfaces (again, those surfaces are cones in three dimensions) and multiple maxima, as shown in Fig. 12.17. This is just what we saw for the bipole in that limit, shown in Fig. 12.11, which also set $kd = 3\pi$.

From Eq. (12.46), it is easy to see that $H_{dipole}(\theta) = 0$ anytime that $(kd/2) \sin \theta_m = m\pi$, where $m = 0$, 1, 2, . . . There will be m directions, θ_m, where the sound radiated by the dipole will be zero when $\sin \theta_m = 2m\pi/kd = m\lambda/d$ where $m \leq d/\lambda$. Similarly, $H_{dipole}(\theta) = 1$ if $(kd/2) \sin \theta_n = (2n + 1)\pi/2$ where $n = 0, 1, 2, \ldots$ There will be n directions, θ_n, where the sound radiated by the dipole will be maximum when $\sin \theta_n = (2n + 1)\pi/kd = (2n + 1)\lambda/2d$ where $(2n + 1) \leq 2d/\lambda$.

Figure 12.18 shows the beam pattern for $d/\lambda = 2$, or $kd = 4\pi$. There will be three nodal directions, $m = 0$, so $\sin \theta_{m=0} = 0°$ and $\sin \theta_{m=1} = 1/2$ so $\theta_{m=1} = 30°$ and $\sin \theta_{m=2} = 2/2$ and $\theta_{m=2} = 90°$. Note that if $m = 3$, $(2m + 1)\pi/kd = 7\pi/4\pi > 1$. There will be two maximal directions. With $n = 0$, $\sin \theta_{n=0} = ¼$, so $\theta_{n=0} = 14.5°$. With $n = 1$, $sin \ \ \theta_{n=1} = ¾$, so $\theta_{n=1} = 48.6°$.

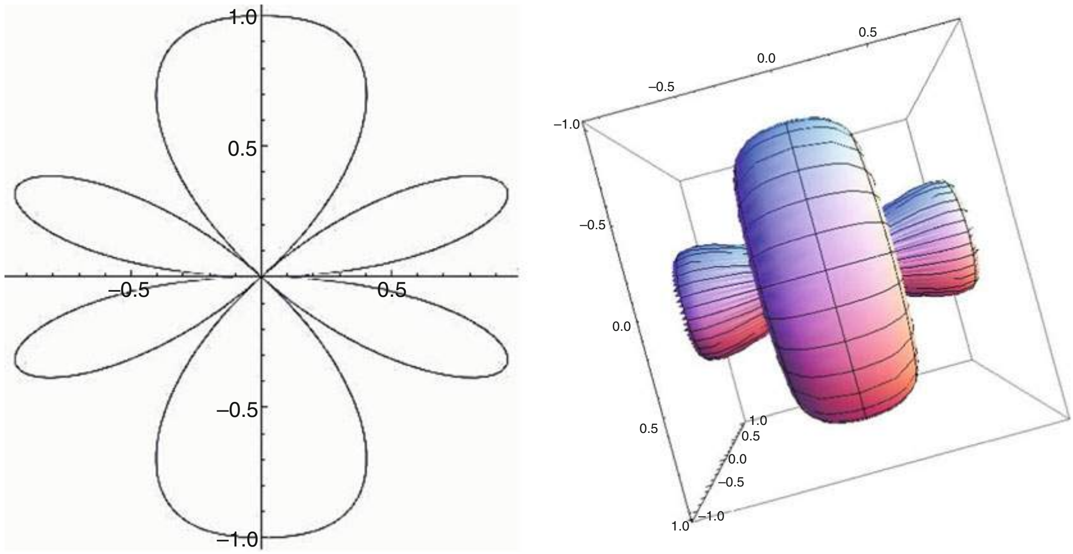

Fig. 12.17 Two representations of the directionality, $H(\theta)$, produced by the sound field radiated by a pair of compact simple sources of equal amplitude which are 180° out-of-phase (i.e., a dipole) that are separated by $3\lambda/2$, corresponding to $kd = 3\pi$. (*Left*) The two-dimensional representation of $H_{dipole}(\theta)$, provided in Eq. (12.46), that exploits the rotational symmetry about the axis joining the two sources to provide the essential structure of the directionality for that two-element array. (*Right*) The body of revolution formed by $H(\theta)$ is three-dimensional. This figure is tilted slightly from the orientation at the left to provide a better view of the anti-node that occurs along the polar directions. Comparison of this figure to Fig. 12.12 shows that they are identical, differing only in the reversal of the nodes and anti-nodes along polar and equatorial directions. [Directionality plots courtesy of Randall Ali]

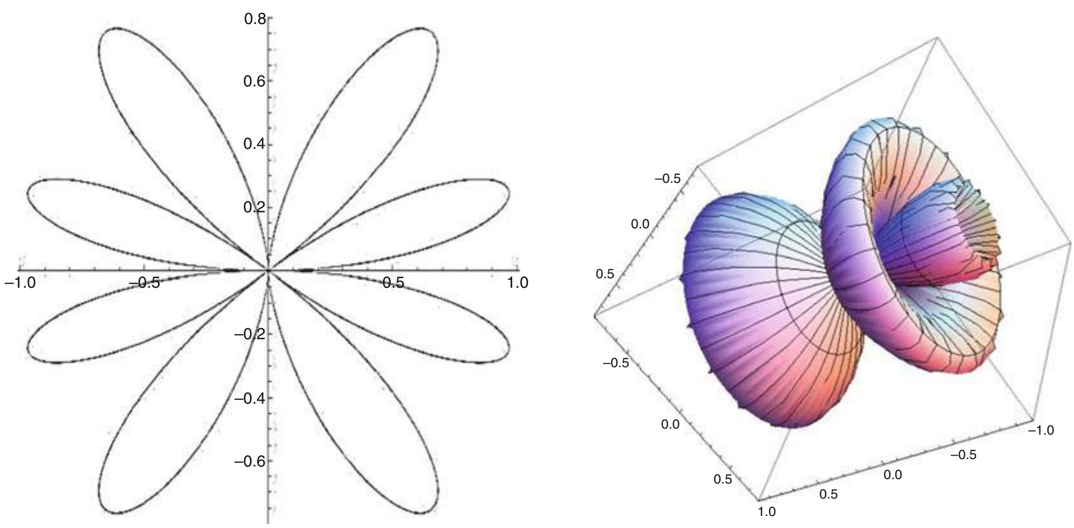

Fig. 12.18 Two representations of the directionality, $H(\theta)$, for the sound field radiated by a pair of compact simple sources of equal amplitude which are 180° out-of-phase (i.e., a dipole) that are separated by 2λ corresponding to $kd = 4\pi$. (*Left*) A two-dimensional representation that shows the nodal directions are $\theta_{null} = 0°$, 30°, and 90°. The maxima occur for $\theta_{max} = 14.5°$ and 48.6°. (*Right*) Body of revolution formed by $H(\theta)$ is a three-dimensional representation of the directionality of the sound field that is rotated to show both the nodal surface that is the equatorial plane ($\theta_{null} = 0°$) and the two conical lobes above and below the equatorial plane. [Directionality plots courtesy of Randall Ali]

12.5.1 Dipole Radiation

The compact monopole and the compact dipole play a central role in our understanding of both the radiation and the scattering of sound by objects placed in an otherwise uniform medium. In Chap. 10, the speed of sound was interpreted as being determined by the complementary (and independent) influences of the compressibility and the inertia of the medium. If an object that is much smaller than the wavelength of sound has a compressibility that differs from the surrounding medium, then the incident sound's pressure will cause that object to compress more or compress less than the surrounding medium. If we think of a bubble in a fluid, then the incident sound will cause the bubble to be compressed and expanded more than the surrounding fluid. That forced oscillatory change in the bubble's volume is equivalent to the generation of a volume velocity that will be the source of a spherically spreading sound wave producing an acoustic pressure described in Eq. (12.21) and radiating sound power to the far field as described in Eqs. (12.18) and (12.24), within an otherwise unbounded medium.

Since we still chose to limit our attention to amplitudes that are small enough that linear superposition holds, the scattered wave and the original disturbance that excited the bubble's oscillations will interfere. In case of a bubble, if the frequency of excitation produced by an incident sound wave is close to the Minnaert frequency of Eq. (12.30), the scattered pressure can even exceed the incident pressure.[11] If the scattering object is less compressible than the surrounding medium, then the less compressible object can be represented as producing a volume velocity that is out-of-phase with the incident pressure wave as a means of satisfying the boundary conditions at the surface of that less compressible object.

The characteristic of the medium that is complementary to the compressibility for determining sound speed is the medium's mass density. If a compact object has the same density as the surrounding medium, then the object will experience the same acoustic velocity as that induced in the surrounding medium by the incident sound wave. If the compact object is denser than the surrounding medium, then the object's velocity will be less than that created by the incident sound wave in the surrounding medium and will thus produce relative motion between the object and the medium. For an object that is less dense, a bubble, for example, then its induced motion will be greater than the surrounding fluid's motion, again producing relative motion between the object and the surrounding medium but with opposite sign. In both cases, the relative motion will produce dipole radiation.

This previous discussion was intended to motivate the need to produce a description of dipole radiation that is as complete and detailed as the description of monopole radiation provided in Sect. 12.2. The solution of most other problems in radiation and scattering can be expressed in terms of the superposition of compact monopoles and compact dipoles. For monopoles, the compactness criterion was expressed in terms of the equivalent radius, a, of the monopole, and the wavenumber, $k = 2\pi/\lambda$, such that $ka \ll 1$.[3] For a dipole, the compactness criterion is expressed in terms of the separation, d, as depicted in Figs. 12.10 and 12.11, of the two out-of-phase sources of volume velocity, $kd \ll 1$.

As before, our expression for the pressure radiated by a dipole, in Eq. (12.46), can be used to produce the corresponding fluid velocity using the Euler equation.

[11] A similar effect can be observed by bringing a Helmholtz resonator close to an unbaffled loudspeaker driven at a frequency close to the resonator's natural frequency. When the resonator is close to the speaker, the sound level increases.

$$p\left(\left|\vec{r}\right|,\theta\right) = \Re e\left\{-j\frac{\rho_m c}{\lambda\left|\vec{r}\right|}\left|\widehat{\mathbf{U}}(a)\right|kd\ \ \sin\theta\right\} \\ = \Re e\left\{-jk^2\frac{\rho_m c}{4\pi\left|\vec{r}\right|}\left|\vec{d}\,\widehat{\mathbf{U}}(a)\right|\cos\theta_p\right\} \quad \text{if} \ \ kd \ll 1 \tag{12.48}$$

In this expression, the magnitude of the product of the source strength and the separation of the two out-of-phase monopoles has been combined, $\left|\vec{d}\,\widehat{\mathbf{U}}(a)\right|$. That combination is known as the *dipole strength* and is sometimes given a different symbol.

I like to leave the dipole strength in the format of Eq. (12.48) to remind myself that there is now a unique direction, $\vec{d}$, associated with the dipole strength. It is also important to remember that $\left|\widehat{\mathbf{U}}(a)\right|$ is the volume velocity of one of those two monopoles, just as it was throughout the derivation that resulted in Eq. (12.46).

The appearance of the unique direction, $\vec{d}$, breaks the spherical symmetry exploited to derive the monopole radiation, although azimuthal symmetry is still preserved (i.e., rotation about the $\vec{d}$-axis has no physical significance). Since Eqs. (12.46) and (12.48) depend upon the angle, θ, measured with respect to the elevation above the plane, which is the perpendicular bisector of the $\vec{d}$, as shown in Figs. 12.10 and 12.11, the right-hand version of Eq. (12.48) introduces the polar angle, θ_p, that is measured from line joining the two out-of-phase monopoles. The amplitude of the particle velocity will also have a polar component, $\widehat{\mathbf{v}}_\theta$, as well as a radial component, $\widehat{\mathbf{v}}_\mathbf{r}$. This is dictated by the expression for the pressure gradient in spherical coordinates that was provided in Eq. (12.10).

To capture both the near- and far-field behavior, the pressure produced by the compact dipole can be expanded in a Taylor series by taking the gradient of the monopole pressure and multiplying that gradient by the separation, $\vec{d}$.

$$p_{dipole}\left(\left|\vec{r}\right|,\theta,t\right) = \Re e\left\{-k^2\frac{\rho_m c\left|\vec{d}\,\widehat{\mathbf{U}}(a)\right|}{4\pi\left|\vec{r}\right|}\cos\theta_p\left(1+\frac{j}{k\left|\vec{r}\right|}\right)e^{j\left(\omega t - k\left|\vec{r}\right|\right)}\right\} \tag{12.49}$$

In the far field, for $kr \gg 1$, Eq. (12.49) reduces to Eq. (12.48). As with the monopole, the dipole pressure field varies inversely with distance, $\left|\vec{r}\right|$, from the dipole. Use of the Euler equation and the expression for the pressure gradient in Eq. (12.10) provides expressions for the radial and polar components of the particle velocity produced by dipole radiation.

$$\widehat{\mathbf{v}}_\mathbf{r} = -k^2\frac{\left|\vec{d}\,\widehat{\mathbf{U}}(a)\right|}{4\pi\left|\vec{r}\right|}\cos\theta_p\left(1+\frac{2j}{k\left|\vec{r}\right|}-\frac{2}{\left(k\left|\vec{r}\right|\right)^2}\right)e^{j\left(\omega t - k\left|\vec{r}\right|\right)} \tag{12.50}$$

$$\widehat{\mathbf{v}}_\theta = -jk\frac{\left|\vec{d}\,\widehat{\mathbf{U}}(a)\right|}{4\pi\left|\vec{r}\right|^2}\sin\theta_p\left(1+\frac{j}{k\left|\vec{r}\right|}\right)e^{j\left(\omega t - k\left|\vec{r}\right|\right)} \tag{12.51}$$

The existence of a polar component to the velocity field should not be surprising. If we think of the dipole as one monopole expelling fluid during one-half of the acoustic cycle that is ingested by the other monopole, followed by a role reversal during the next half-cycle, there has to be a component of the fluid's velocity, at least close to the two out-of-phase monopoles, that has a polar contribution, in addition to the radial contribution. The fluid must shuttle back and forth, as illustrated by the streamlines in Fig. 12.22.

The radial component of the time-averaged radiated intensity is proportional to the in-phase product of pressure and particle velocity.

$$\langle I_r \rangle_t = \rho_m c \left(\frac{k^2 \left| \vec{d}\,\widehat{\mathbf{U}}(a) \right|}{4\pi \left| \vec{r} \right|} \right)^2 \cos^2\theta_p \quad \text{for } ka \ll 1 \tag{12.52}$$

There are no components of the intensity vector, $\vec{I}$, in either the polar or azimuthal directions: $I_{\theta_p} = I_\phi = 0$. The total radiated power, $\langle \Pi_{dipole} \rangle_t$, is just the integral of Eq. (12.52) over all directions, but $\langle I_r \rangle_t \propto r^{-2}$, so the radiated power will be independent of distance, as it was for monopoles, since dissipation is still being neglected.

$$\left\langle \Pi_{dipole} \right\rangle_t = 2\pi r^2 \int_0^\pi \langle I_r \rangle_t \sin\theta_p \; d\theta_p = \rho_m c \frac{4\pi^2}{3\lambda^4} \left| \vec{d}\,\widehat{\mathbf{U}}(a) \right|^2 = \frac{\rho_m \omega^4}{12\pi c^3} \left| \vec{d}\,\widehat{\mathbf{U}}(a) \right|^2 \tag{12.53}$$

This result has made use of the following definite integral:

$$\int_0^\pi \cos^2\theta_p \sin\theta_p \; d\theta_p = \frac{2}{3} \tag{12.54}$$

The pressure and velocity can be used to calculate the compact dipole's mechanical impedance, $\mathbf{Z_{dipole}}$, of the compact dipole, $r = a$.

$$\mathbf{Z_{dipole}}(a) = \frac{\rho_m c (\pi a^2)}{3} (ka)^4 + \frac{j\omega}{2} \left(\rho_m \frac{4\pi a^3}{3} \right) \left[1 + \frac{(ka)^2}{2} \right] \tag{12.55}$$

As with the monopole result in Eq. (12.16), the dipole's radiation resistance is the real part of Eq. (12.55). For the compact monopole, the radiation resistance is proportional to $(ka)^2$, while for the compact dipole, it is proportional to $(ka)^4$. Higher-order combinations have radiation resistances that are proportional to even higher powers of (ka). For a quadrupole, $r_{rad} \propto (ka)^6$, as addressed in Problem 10 and in Eq. (12.136).

Again, as in the case of the monopole's mechanical impedance in Eq. (12.15), the imaginary contribution is reminiscent of the mass reactance. In the dipole case, the effective mass, m_{eff}, is one-half the mass of the fluid that is displaced in the limit that $(ka) \ll 1$. When applied to two out-of-phase monopoles, this additional mass has to be accelerated and decelerated. As will be seen in Sect. 12.6, this is also the hydrodynamic mass that must be added to a rigid sphere executing oscillatory motion in a fluid, as it was in Chap. 8, Problem 3 [21].

In general, the hydrodynamic mass is proportional to the "order," m, of the monopoles that are combined to create the compact source [22].

$$\frac{m_{eff}}{\rho_m \left(\frac{4\pi a^3}{3} \right)} = \frac{3}{[(m+1) \cdot 1 \cdot 3 \cdot 5 \cdot \cdot \cdot (2m+1)]} \tag{12.56}$$

For a monopole, $m = 0$ so the ratio is 3, as calculated in Eq. (12.15). For the dipole, $m = 1$, so the ratio is ½, as calculated in Eq. (12.55). For a quadrupole, $m = 2$ so that ratio would be $^1/_{15}$.

12.5.2 Cardioid (Unidirectional) Radiation Pattern

The assumption behind our calculation of radiation from a compact spherical source was that its radiation pattern was omnidirectional. Our solution for the dipole source resulted in patterns that were bi-directional for two identical anti-phased sources that were separated by less than one-half wavelength, as shown in Fig. 12.16. In some applications, we seek a source (or receiver) that is unidirectional [23]. One way to achieve this goal is by combining a compact ($ka \ll 1$) omnidirectional (spherical) source and a compact ($kd \ll 1$) dipole.

The fact that the two lobes of the compact dipole's directional pattern are 180° out-of-phase with each other means that when a dipole is added to an omnidirectional source, their fields will add in one direction but will subtract in the opposite direction. If the far-field pressure amplitude of the omnidirectional source and the dipole are equal, then the sound field in one direction will be twice that of the omnidirectional source operating in isolation, but in the opposite direction, the omnidirectional source and the dipole will exactly cancel, and no sound will be radiated along that direction.

Such a superposition of a dipole and an omnidirectional source produces a *cardioid directionality* pattern, shown in Fig. 12.19, which appears to be heart-shaped in its two-dimensional representation. Although our definition of angle, θ, was based on elevation above the plane normal to the line connecting the source pair, as shown in Figs. 12.10 and 12.11, a more common choice is the polar angle measured from the line joining the two sources. To avoid confusion, the polar angle will be subscripted, θ_p, in this section as it was when it was introduced in the previous section.

$$H_{dipole}(\theta_p) = \cos\theta_p \quad \text{if} \quad kd \ll 1 \tag{12.57}$$

Equation (12.47) demonstrates that the ratio of the far-field radiated sound pressure from a dipole source to that from an omnidirectional compact spherical sound source is frequency dependent. Since the spacing, d, between the sources that produce the dipole is usually fixed, it is necessary to provide a frequency-dependent attenuation to the omnidirectional source if the cardioid pattern is to be maintained over a range of frequencies. This can be accomplished by high-pass filtering the signal that drives the omnidirectional source. The sum will produce a constant directional pattern as long as $kd < 1$, although the amplitude of the signal will grow linearly with frequency from low frequencies up

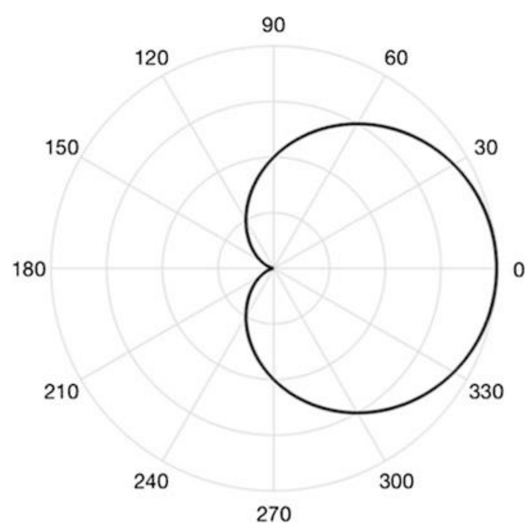

Fig. 12.19 The superposition of an omnidirectional source and a compact dipole produces the cardioid directional pattern shown in a two-dimensional representation. The pattern is called a cardioid because it resembles a heart-shaped ♥ pattern. The amplitude is twice that of the omnidirectional source for $\theta_p = 90°$ and is zero for $\theta_p = -90°$. [Directionality plot courtesy of Randall Ali]

to the frequency where $kd \cong 1$. If the amplitude of the dipole and monopole contributions are equal, their sum produces a cardioid directional function, $H_{cardioid}(\theta_p)$.

$$H_{cardioid}\left(\theta_p\right) = 1 + \cos\theta_p \tag{12.58}$$

12.5.3 Pressure Gradient Microphones

It is more common to produce a cardioid pattern for microphones than for sound sources. One obvious method would be to use two closely spaced omnidirectional microphone cartridges. The sum of their signals would provide an omnidirectional output that could be high-pass filtered (electronically), while their difference would provide the dipole signal that could be combined with the filtered "omni" signal to produce a properly frequency-weighted sum.

More clever systems can exploit acoustical networks that allow the sound pressure to access both sides of a single diaphragm. This approach was patented by Benjamin Bauer [24] and was the basis of the Shure Model 55S "Unidyne®" microphone, shown in Fig. 2.20 (right). That iconic microphone celebrated the 75th anniversary of its initial production in 2014 [25].

Bauer's approach is shown schematically in Fig. 2.19 (*left*). In that diagram, the front of the diaphragm is exposed directly to the sound pressure, $\widehat{\mathbf{p}}_{\mathbf{front}}$. The rear of the diaphragm is facing a volume (compliance) that is exposed to the same sound wave, though at a slightly different position, through a flow resistance, frequently provided by fabric, a mesh screen, or a combination of both. Figure 12.20 is a simplification of the microphone in Fig. 2.19 (left) that eliminates the transduction mechanism and shows only the diaphragm (without its suspension) and a rear-access port filled with a porous medium acting as a flow resistance, R_{flow}, providing access to the volume (compliance), V, where the internal pressure within that volume, $\widehat{\mathbf{p}}_{\mathbf{back}}$, applies a force to the rear of the diaphragm.

In Fig. 12.20, the microphone is shown in two different orientations with respect to a propagating plane wave that is assumed to be approaching from the left. Before determining the values of R_{flow} and V that would produce a cardioid directional pattern from the resulting motion of a single diaphragm, it will be useful to consider the case where $R_{flow} = 0$, so that the pressure at the port is applied directly to the rear of the diaphragm.

If $R_{flow} = 0$, then the lower orientation ($\theta_p = \pm 90°$), shown in Fig. 12.20, will have $\widehat{\mathbf{p}}_{\mathbf{front}} = \widehat{\mathbf{p}}_{\mathbf{back}} = \widehat{\mathbf{p}}_{\mathbf{rear}}$, so that there will be no net force on the diaphragm of area, A_{pist}. For the upper orientation ($\theta_p = 0°$), the sound that reaches the port must propagate an additional effective distance, $\Delta\ell$, before reaching the port.[12] The net force, $\widehat{\mathbf{F}}_{\mathbf{net}}$, caused by the pressure difference across the diaphragm, will depend upon the area of the diaphragm, A_{pist}, and the pressure gradient in the direction of propagation, $\partial p/\partial x$, produced by the plane wave as well as the orientation of the normal to the microphone's diaphragm with respect to the wave's direction of propagation, θ_p.

Since it is assumed that the presence of the microphone does not distort the sound field of the incoming plane wave, the pressure at the port, $\widehat{\mathbf{p}}_{\mathbf{rear}}$, can be expressed in terms of the pressure on the diaphragm, $\widehat{\mathbf{p}}_{\mathbf{front}}$. The pressure of a traveling plane wave can be expressed as a complex exponential, as in Eq. (10.14), to simplify calculation of the gradient.

[12] Although it is clear that the "effective distance," $\Delta\ell$, will depend upon the diameter of the enclosure, calculation of the pressure distribution and phase shift between the sound impinging on the diaphragm and the sound reaching the port is complicated, even for a spherical enclosure, requiring expansion of the sound field into a superposition of Legendre polynomials. See Ref [4], §VII.27.

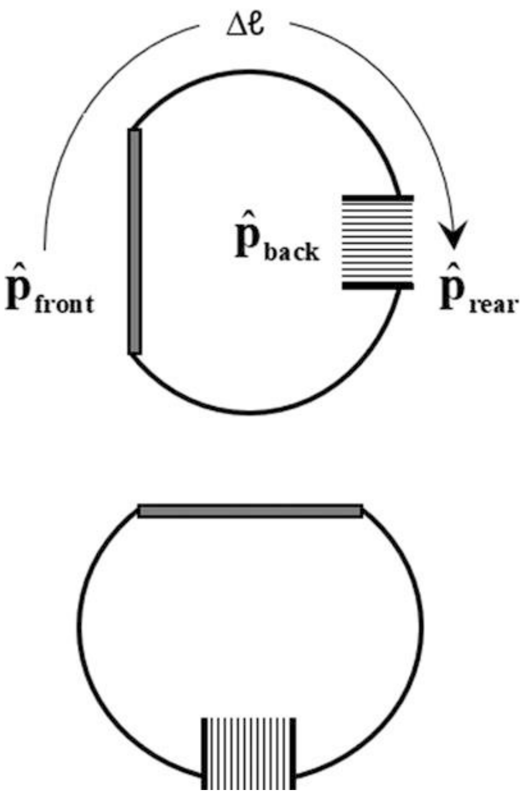

Fig. 12.20 Schematic representation of two microphone enclosures that omits any transduction mechanism, like the electrodynamic scheme shown in Fig. 2.19 (*left*). Sound pressure impinging on either the upper or lower enclosure applies a force directly on the "front" of the diaphragm (*grey rectangle*). Sound can also cause air flow through the flow resistance at the rear of the enclosure (*parallel lines*) that will create pressure within the volume (compliance) and thus apply a force to the rear of the diaphragm. Assume that a plane wave is traveling to the right and that the presence of enclosures does not perturb that wave. (*Upper*) In the orientation shown ($\theta_p = 0°$), the sound must travel an additional distance, $\Delta\ell$, before it reaches the port containing the resistance. (*Lower*) In this orientation ($\theta_p = \pm 90°$), the wave excites both the diaphragm and the resistance port at the same time (i.e., in-phase) so that $\Delta\ell = 0$

$$\widehat{\mathbf{p}}_{\mathbf{rear}} = \widehat{\mathbf{p}}_{\mathbf{front}} + \frac{\partial\left(\widehat{\mathbf{p}}_{\mathbf{front}} e^{-jkx}\right)}{\partial x}\Delta\ell = \widehat{\mathbf{p}}_{\mathbf{front}}\left[1 - jk(\Delta\ell)\cos\theta_p\right] \tag{12.59}$$

The net force across the diaphragm is proportional to the pressure difference, since R_{flow} has been temporarily set to zero and access to the rear of the diaphragm is unimpeded.

$$\widehat{\mathbf{F}}_{\mathbf{net}} = A_{pist}(\widehat{\mathbf{p}}_{\mathbf{front}} - \widehat{\mathbf{p}}_{\mathbf{rear}}) = jk\widehat{\mathbf{p}}_{\mathbf{front}} A_{pist}(\Delta\ell)\cos\theta_p \tag{12.60}$$

Since $k = \omega/c$, and $j\omega\widehat{\mathbf{v}}$ is proportional to the pressure gradient through the Euler equation, these pressure gradient microphones are also called velocity microphones.

For the case where $R_{flow} = 0$, the diaphragm in an enclosure like those shown in Fig. 12.20 will have a bi-directional sensitivity pattern like that for a compact dipole, as shown in Fig. 12.16, if the diaphragm's motion is converted to some electrical signal by an appropriate transduction mechanism.

A popular implementation of such a *pressure gradient microphone* in studio recording applications [23] is the *ribbon microphone* [26]. It that case, the "diaphragm" is a very thin corrugated metal strip placed in a magnetic field. The acoustically induced pressure difference on either side of the "ribbon" causes it to vibrate and generate an electrical voltage that is proportional to its velocity [27].

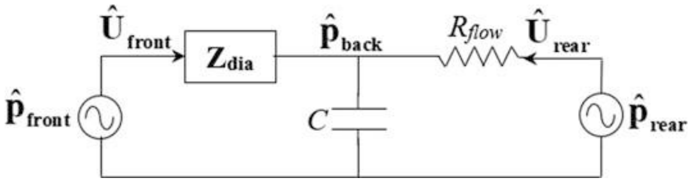

Fig. 12.21 Equivalent circuit representation of the pressure gradient microphone in Fig. 12.20. The diaphragm will respond to the pressure difference, $\Delta\hat{\mathbf{p}} = \hat{\mathbf{p}}_{\mathbf{front}} - \hat{\mathbf{p}}_{\mathbf{back}}$. The relationship between $\hat{\mathbf{p}}_{\mathbf{front}}$ and $\hat{\mathbf{p}}_{\mathbf{rear}}$ is provided in Eq. (12.59)

If $R_{flow} \neq 0$, then the combination of R_{flow} and the compliance of the microphone's enclosure volume, V, can be characterized by a time constant, τ_{RC}, that produces a low-pass filter between the acoustic pressure felt by the back of the diaphragm, $\hat{\mathbf{p}}_{\mathbf{back}}$, and the acoustic pressure at the entrance to the port, $\hat{\mathbf{p}}_{\mathbf{rear}}$, as expressed in Eq. (12.59).

$$\tau_{RC} = R_{flow}C = \frac{R_{flow}V}{\gamma p_m} \tag{12.61}$$

The net force on the diaphragm of the pressure gradient microphone, shown in Fig. 12.20, can be determined by using the equivalent circuit of Fig. 12.21. The acoustical impedance of the diaphragm, $\mathbf{Z_{dia}}$, represents the stiffness, moving mass, and mechanical damping of the microphone's diaphragm. The compliance of the volume is C, and the flow resistance of the rear port is R_{flow}.

$$\begin{aligned}\hat{\mathbf{p}}_{\mathbf{front}} &= \hat{\mathbf{U}}_{\mathbf{front}}\left(\mathbf{Z_{dia}} + \frac{1}{j\omega C}\right) - \frac{\hat{\mathbf{U}}_{\mathbf{back}}}{j\omega C}\\ \hat{\mathbf{p}}_{\mathbf{rear}} &= \frac{\hat{\mathbf{U}}_{\mathbf{front}}}{j\omega C} - \hat{\mathbf{U}}_{\mathbf{front}}R_{flow}\left(1 + \frac{1}{j\omega R_{flow}C}\right)\end{aligned} \tag{12.62}$$

The pressure difference, $\Delta\hat{\mathbf{p}}$, across the diaphragm, can be found by combining Eq. (12.59) with Eq. (12.62).

$$\frac{\Delta\hat{\mathbf{p}}}{\hat{\mathbf{p}}_{\mathbf{front}}} = \frac{\mathbf{Z_{dia}}R_{flow}\left[1 + \frac{(\Delta\ell)}{c\tau_{RC}}\cos\theta_p\right]}{\mathbf{Z_{dia}}R_{flow} - j\left[\frac{R_{flow}+\mathbf{Z_{dia}}}{\omega C}\right]} = D\left(1 + B\cos\theta_p\right) \tag{12.63}$$

Two constants have been introduced for the right-hand version of Eq. (12.63). $B = \tau_{\Delta\ell}/\tau_{RC}$ is the ratio of the front-to-back propagation delay, $\tau_{\Delta\ell} = (\Delta\ell)/c$, and the filter's time constant, τ_{RC}. D involves the physical properties of the diaphragm and its suspension, the enclosure's volume, and the flow resistance of the port.

$$B = \frac{(\Delta\ell)}{cR_{flow}C} = \frac{\tau_{\Delta\ell}}{\tau_{RC}} \quad \text{and} \quad D = \frac{\mathbf{Z_{dia}}}{\mathbf{Z_{dia}} + \left[\frac{R_{flow}+\mathbf{Z_{dia}}}{j\omega\tau_{RC}}\right]} \tag{12.64}$$

By making the propagation delay equal to the filter time constant, $B = 1$, the cardioid directionality pattern of Fig. 12.19 is produced. If $R_{flow} = \infty$, so that the port is blocked, $B = 0$ and the pattern is omnidirectional (i.e., monopolar). In the first case, where $R_{flow} = 0$, $\tau_{RC} = 0$, so $B = \infty$ and the dipole directionality of Fig. 12.16 is obtained.

12.5.4 The DIFAR Directional Sonobuoy

The ability to produce a directional sensor that was demonstrated in Sect. 12.5.1 and a commercially viable implementation that produces unidirectional (cardioid) sensitivity in air was described in Sect. 12.5.3. In underwater acoustic applications, it is often advantageous to have a hydrophone system that can determine the direction of a submerged sound source. In principle, if two such systems were deployed, then the location of the source could be determined by triangulation.

The most widely used such directional hydrophone system is the US Navy's AN/SSQ-53 DIFAR sonobuoy. During the Cold War, submarine surveillance aircraft used to eject these sonobuoys, when flying close to the ocean surface, to locate submarines. This practice was so widespread that there are sections of the ocean floor at strategically significant geographical locations (known to sailors as "choke points") that are literally covered with such sonobuoys that would be programmed to sink after a pre-determined interval after deployment, usually ranging for 30 min to 8 h. Today, such directional sonobuoys are still manufactured by a number of vendors, and smaller numbers of such sonobuoys are now used for studying marine mammals, as well as for military purposes.

The Directional Frequency Analysis and Recording (DIFAR) sonobuoy combines two orthogonal dipole sensors, usually called the N–S and the E–W dipole, with an omnidirectional hydrophone. In addition, the DIFAR system would also have an electronic magnetic compass [28] to determine the free-floating directional hydrophone's orientation and a radio-frequency transmitter that could send the hydrophone and compass information over a user-selectable choice of 96 different channels that would broadcast over a range of radio frequencies between 136.0 MHz and 173.5 MHz. Before ejection, a unique channel would be chosen for each DIFAR to allow multiple hydrophones to operate simultaneously in adjacent areas without interference.

Just as before, the N–S dipole could be summed with the omnidirectional hydrophone to produce a northward listening cardioid, or the N–S dipole could be subtracted from the omnidirectional hydrophone to produce as southward listening cardioid. A similar east-west directionality could be synthesized, all with reference to the orientation established by the internal magnetic compass. By comparing the magnitude of the received signals in each direction, the direction to the source could be determined. The use of frequency-selective signal processing could simultaneously determine the direction to different sources if their radiated sound signature had unique frequency content.

A more efficient method that uses only three dipole sensors, with axes that are separated by 120°, to obtain the desired directional information and avoid the possibility that a source could be oriented along a detection node has been described and demonstrated [29]. The function relies upon the trigonometric sum of the signals being a constant [30].

$$\sum_{k=0}^{N} \cos^2\left(\phi + \frac{2\pi k}{N}\right) = \frac{N}{2} \tag{12.65}$$

This is the generalization of the better-known trigonometric identity, $\cos^2\phi + \sin^2\phi = 1$.

12.6 Translational Oscillations of an Incompressible Sphere

As we have shown, sound sources that displace fluid by changing their volume periodically in time will behave as simple (compact) spherically symmetric radiators if $ka \ll 1$. On the other hand, two such sources in close proximity with oscillations that are 180° out-of-phase will produce a dipolar radiation field. As expressed in Eq. (12.58), the radiation efficiency of the compact dipole ($kd \ll 1$) is less than

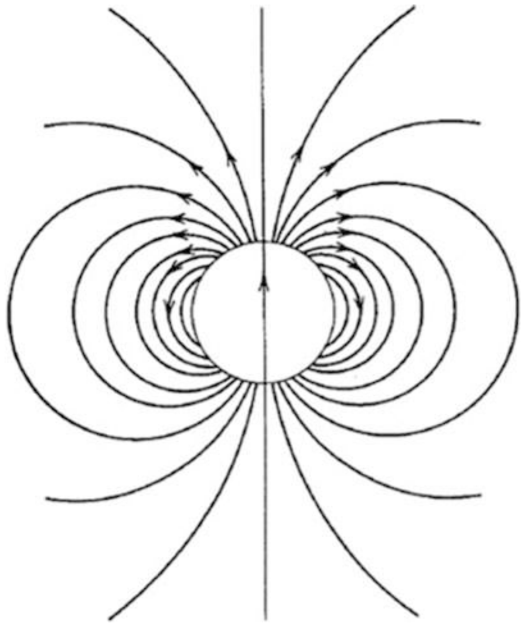

Fig. 12.22 The translational oscillatory excursions of solid objects produce fluid flow that is identical to that of two out-of-phase simple (monopole) sources, if the dimensions of the objects are small compared to the wavelength of sound at the frequency of the oscillations. The flow pattern for an incompressible sphere, shown here by the fluid's streamlines, is the same as that produced by a dipole. As the sphere moves upward, it displaces fluid that is then collected below the sphere. Since the sphere is assumed to be incompressible, the amount of fluid pushed away by the upward motion must be the same as that pulled in behind the sphere [31]

the monopole (simple source) having the same source strength. In effect, the fluid volume ejected by one of the dipole's pair of sources is ingested by the other during one-half of the cycle, and their roles reverse during the following half-cycle, so there is no net production of volume velocity. It is only the phase difference produced by the displacement of their centers which results in non-zero radiated sound pressure. This dipole behavior can therefore be produced by a rigid object of constant volume that simple oscillates (translationally) back and forth and consequently produces no net periodic change in fluid volume.

A loudspeaker that is not placed in an enclosure behaves as a rigid disk that is oscillating back and forth. The amount of fluid that is displaced in one direction by the motion of one side of disk (i.e., speaker cone) is the same as the fluid that is pulled in the opposite direction by the other side of the disk. There is no net periodic change in fluid volume. Similarly, the incompressible sphere that experiences oscillatory translational motion, as shown by the streamlines in Fig. 12.22, pushes fluid ahead while it sucks the same amount of fluid from behind.

The equivalence of the sound radiated by a rigid sphere undergoing translational oscillations to a dipole can be established again by expressing the velocity of the sphere's surface in Hankel functions and Legendre polynomials [31]. If the center of the sphere has a time-dependent velocity, $u(t) = \Re e[\widehat{\mathbf{u}}_{\mathbf{o}} e^{j\omega t}]$, and $ka \ll 1$, then its equivalent dipole strength, $\left|\vec{d}\,\widehat{\mathbf{U}}(a)\right|_{sphere}$, can be expressed by equating the time-averaged power, $\langle \Pi_{rad} \rangle_t$, calculated in Eq. (12.53), with the same result for the oscillating compact rigid sphere of volume, $V_{sphere} = 4\pi a^3/3$ [32].

$$\left|\vec{d}\,\widehat{\mathbf{U}}(a)\right|_{sphere} = \frac{3|\widehat{\mathbf{u}}_{\mathbf{o}}|}{2\sqrt{2}} V_{sphere} \cong 1.06|\widehat{\mathbf{u}}_{\mathbf{o}}| V_{sphere} \tag{12.66}$$

I like to interpret this equivalence by considering a cylinder of radius, a, having the same volume of the sphere of that radius, making the height, h, of such a cylinder equal to $4a/3$. In that picture, the volume velocity, $\left|\widehat{\mathbf{U}}(a)\right|$, generated by the disk that forms one end of the cylinder, with area, $A_{pist} = \pi a^2$, is simply $|U(a)| = A_{pist}|\widehat{\mathbf{u}}_{\mathbf{o}}|$. If the separation of the ends is set equal to $\left|\vec{d}\right| = h = 4a/3$, then the source strength of the "equivalent' cylinder is the same as that of the sphere to within 6% (0.5 dB): $\left|\vec{d}\,\widehat{\mathbf{U}}(a)\right|_{sphere} = 1.06\left|\vec{d}\,\widehat{\mathbf{U}}(a)\right|_{cylinder}$.

12.6.1 Scattering from a Compact Density Contrast

Having expressed the dipole strength of an incompressible sphere executing translational oscillations in Eq. (12.66), the scattering produced by such a compact inhomogeneity, due to its presence in a sound field, can be calculated by determining the relative motion of the fluid and the center of the sphere.[13] If we assume a plane wave, then the free-field complex pressure amplitude at the sphere's location in the absence of the rigid sphere would be $\widehat{\mathbf{p}}_{\mathbf{ff}}$. The complex amplitude of the net translational force, $\widehat{\vec{\mathbf{F}}}$, will be the integral of that pressure over the surface of the sphere in the direction determined by the gradient of the pressure where $\widehat{n} = \vec{k}/\left|\vec{k}\right|$ is the unit vector in the same direction as the plane wave's propagation and $\widehat{\mathbf{v}} = \widehat{\mathbf{p}}_{\mathbf{ff}}/\rho_m c$ is the free-field fluid particle velocity amplitude [33].

$$\begin{aligned}
\widehat{\vec{\mathbf{F}}} &= \oint_S \widehat{\mathbf{p}}_{\mathbf{ff}} d\vec{S} \cdot \widehat{n} = j\omega\rho_m V_{sphere}\widehat{\mathbf{v}}\left(3\,\frac{\sin(ka) - ka\cos(ka)}{(ka)^3}\right) \\
\widehat{\vec{\mathbf{F}}} &= j\omega\rho_m V_{sphere}\widehat{\mathbf{v}}(1-\beta) \quad \text{where } \beta \cong \frac{(ka)^2}{10} - \frac{(ka)^4}{280} + \cdots
\end{aligned} \tag{12.67}$$

For a compact source, $ka \ll 1$, so β can usually be neglected.

The complex velocity amplitude of the sphere, $\widehat{\mathbf{u}}_{\mathbf{o}}$, that appears in Eq. (12.66), is determined by the one-dimensional linearized Euler equation.

$$-\frac{\partial\left(\widehat{\mathbf{p}}_{\mathbf{ff}} e^{j\left(\omega t - k\left|\vec{r}\right|\right)}\right)}{\partial\left|\vec{r}\right|} = \rho_m \frac{\partial\left(\widehat{\mathbf{v}} e^{j\left(\omega t - k\left|\vec{r}\right|\right)}\right)}{\partial t} = j\omega\rho_m \widehat{\mathbf{u}}_{\mathbf{o}} e^{j\left(\omega t - k\left|\vec{r}\right|\right)} \tag{12.68}$$

The net force can then be approximated by the product of the free-field pressure gradient and the volume of the rigid sphere.

$$\widehat{\mathbf{F}} \cong -\left(\frac{\partial\left(\widehat{\mathbf{p}}_{\mathbf{ff}} e^{j\left(\omega t - k\left|\vec{r}\right|\right)}\right)}{\partial\left|\vec{r}\right|}\right) V_{sphere} = j\omega\rho_m \widehat{\mathbf{u}}_{\mathbf{o}} V_{sphere} e^{j\left(\omega t - k\left|\vec{r}\right|\right)} \quad \text{if } \beta = 0 \tag{12.69}$$

If there are no other external forces on the sphere's surface (possibly produced by the some elastic suspension system like that shown in Fig. 12.23) and no other contributions to fluid flow (possibly

[13] In this treatment, the fluid is assumed to be inviscid so that there are no shear forces involved in the scattering process.

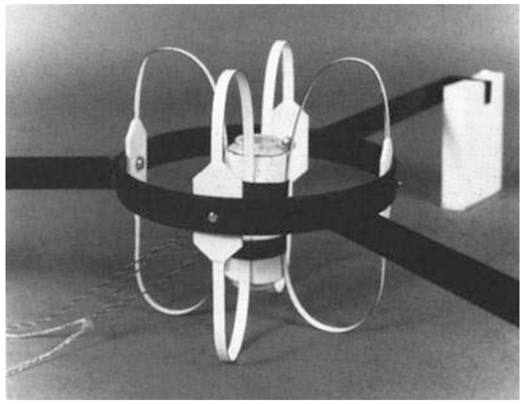

Fig. 12.23 Neutrally buoyant fluid particle velocity sensor and its suspension system. The four white plastic loops provide the elastic suspension system for the neutrally buoyant geophone (see Sect. 2.6 and Figs. 2.22 and 2.23) at the center which is 8 cm long and 3.5 cm in diameter [33]

produced by the sphere being subjected to a steady current), then it is possible to determine the ratio of the sphere's velocity amplitude, $\widehat{\mathbf{u}}_{\mathbf{o}}$, to the free-field fluid particle velocity, $\widehat{\mathbf{v}}$, in the absence of the sphere [34].

$$\left|\frac{\widehat{\mathbf{u}}_{\mathbf{o}}}{\widehat{\mathbf{v}}}\right| = \frac{3\rho_m}{\rho_m + 2\rho_s} \quad \text{where } \rho_s = \frac{m_{sphere}}{V_{sphere}} \tag{12.70}$$

This result demonstrates that the velocity of a spherical volume which has a non-zero *density contrast* with the surrounding fluid will move at a velocity that is not the same as the surrounding fluid.

This result is plausible in the limit of a neutrally buoyant sphere that has the same effective density as the surrounding fluid, $\rho_s = \rho_m$, since such an inhomogeneity must move with the fluid. Also, an immobile rigid sphere that is somehow constrained would have an infinite effective density, $\rho_s = \infty$, thus producing $|\widehat{\mathbf{u}}_{\mathbf{o}}| = 0$, based on Eq. (12.70), as implied by its assumed immobility.

The more interesting consequence of Eq. (12.70) is that an object that is less dense than the surrounding medium (e.g., a bubble) "moves ahead" of the fluid (see Problem 14). For a very low effective density object, like a gas bubble in a liquid, $\rho_s \ll \rho_m$, $\widehat{\mathbf{u}}_{\mathbf{o}} = -3\widehat{\mathbf{v}}$. In the case of scattering of sound by a bubble, this increase in translational velocity is not nearly as important as the fact that such a compressible object will radiate as a monopole when driven by $\widehat{\mathbf{p}}_{\mathbf{ff}}$. For the case of a fish with a gas-filled swim bladder, the tripling of the bladder's velocity makes it a much more sensitive detector of the acoustically induced motion of the surrounding fluid motion (see Problem 5).

Since a neutrally buoyant object with $\rho_s = \rho_m$ moves with the surrounding fluid, it is possible to make a dipole sensor by instrumenting the object with some inertial vibration sensor, like an accelerometer or a geophone (see Sect. 2.6). One advantage of such a dipole sensor over the subtraction of two monopole (omnidirectional) sensors is that there is no requirement that the two omnidirectional sensors have exactly the same sensitivity and frequency response to guarantee that resulting minimum in the directional pattern has zero sensitivity. A laboratory version of such a velocity sensor that incorporates a geophone as the motion sensor is shown in Fig. 12.23. A high-sensitivity, low-noise, two-axis fiber-optic interferometric accelerometer [35] in a neutrally buoyant case could also serve as a two-axis velocity sensor [36].

Having an expression that relates the translational velocity of a solid object driven by an externally imposed sound field to the velocity of the surrounding fluid makes it possible to use Eq. (12.49) to calculate the relative velocity amplitude, $\widehat{\mathbf{v}}_{\mathbf{rel}}$, of the rigid sphere with respect to the fluid's velocity, $\widehat{\mathbf{v}} = \widehat{\mathbf{p}}_{\mathbf{ff}}/(\rho_m c)$.

$$\widehat{\mathbf{v}}_{\mathbf{rel}} = \widehat{\mathbf{u}}_{\mathbf{o}} - \widehat{\mathbf{v}} = \frac{2(\rho_m - \rho_s)}{(\rho_m + 2\rho_s)}\widehat{\mathbf{v}} = \frac{2(\rho_m - \rho_s)}{(\rho_m + 2\rho_s)}\frac{\widehat{\mathbf{p}}_{\mathbf{ff}}}{\rho_m c} \tag{12.71}$$

For the infinitely dense sphere (i.e., fixed and rigid), $\widehat{\mathbf{v}}_{\mathbf{rel}} = -\widehat{\mathbf{v}}$; the relative velocity is the negative of the fluid's velocity. The equivalent dipole scattering strength, $\left|\vec{d}\,\widehat{\mathbf{U}}(a)\right|_{sphere}$, is given by Eq. (12.66) in terms of the relative velocities of the sphere and the fluid.

$$\left|\vec{d}\,\widehat{\mathbf{U}}(a)\right|_{sphere} = \frac{3V_{sphere}}{\sqrt{2}}\frac{(\rho_m - \rho_s)}{(\rho_m + 2\rho_s)}\frac{\widehat{\mathbf{p}}_{\mathbf{ff}}}{\rho_m c} \tag{12.72}$$

Substitution into the expression for the dipole's far-field pressure in Eq. (12.48) provides the scattered acoustic pressure, $p_{scat}\left(|\vec{r}|, \theta_d\right)$, in terms of the incident acoustic pressure, $\widehat{\mathbf{p}}_{\mathbf{ff}}$.

$$\begin{aligned} p_{scat}\left(|\vec{r}|, \theta_p\right) &= \Re e\left\{-jk^2\widehat{\mathbf{p}}_{\mathbf{ff}}e^{\,j(\omega t - k|\vec{r}|)}\frac{3V_{sphere}}{4\pi\sqrt{2}}\frac{1}{|\vec{r}|}\left(\frac{\rho_m - \rho_s}{\rho_m + 2\rho_s}\right)\cos\theta_p\right\} \\ &= \Re e\left\{\frac{-j(ka)^2}{\sqrt{2}}\widehat{\mathbf{p}}_{\mathbf{ff}}e^{\,j(\omega t - k|\vec{r}|)}\left(\frac{a}{|\vec{r}|}\right)\left(\frac{\rho_m - \rho_s}{\rho_m + 2\rho_s}\right)\cos\theta_p\right\} \end{aligned} \tag{12.73}$$

The second expression assumes that the scattering volume is spherical. Although this treatment ignores the viscous forces on the rigid sphere, it can be shown, using the results of Sect. 9.4, that such forces are usually negligible in the limit that $ka \ll 1$ [33].

The far-field intensity is proportional to the square of the acoustic pressure, as given by Eq. (10.40), so the ratio of the time-averaged scattered intensity, $\langle I_{scat}\rangle_t$, to the free-field time-averaged incident intensity, $\langle I_{ff}\rangle_t$, is proportional to $(ka)^4$.

$$\left|\frac{\langle I_{scat}\rangle_t}{\langle I_{ff}\rangle_t}\right| = \left(\frac{p\left(|\vec{r}|, \theta_p\right)}{|\widehat{\mathbf{p}}_{\mathbf{ff}}|}\right)^2 = \frac{(ka)^4}{2}\left(\frac{a}{|\vec{r}|}\right)^2\left(\frac{\rho_m - \rho_s}{\rho_m + 2\rho_s}\right)^2\cos^2\theta_p \tag{12.74}$$

The dependence of the scattered intensity has the same ω^4 frequency dependence as the scattering of light, known as *Rayleigh scattering*, which accounts for the blue color of the sky [37, 38]. In the case of light scattering from molecules, the cause is different: the electromagnetic wave induces a fluctuating dipole moment and that oscillating dipole radiates the scattered electromagnetic wave.

For the description of a scattering object's ability to produce scattered energy, it is convenient to express the ratio of the scattered power to the incident intensity in terms of a *differential scattering cross section*, $d\sigma/d\Omega$, with units of [m^2/steradian]. It is the ratio of the time-averaged power scattered into a given solid angle element, $d\Omega = \sin\theta\ d\theta\ d\varphi$, to the mean energy flux density of the incident wave (i.e., the intensity). The integral of $d\sigma/d\Omega$ over all solid angle is the *total scattering cross section*, σ. Again, using the definite integral of Eq. (12.54), the total scattering cross-section for the rigid sphere of effective density, ρ_s, can be calculated.

$$\sigma = \left(\pi a^2\right)(ka)^4\frac{28}{9}\left(\frac{\rho_m - \rho_s}{\rho_m + 2\rho_s}\right)^2 \quad \text{for } ka \ll 1 \tag{12.75}$$

In the above form, it is clear that an incompressible (i.e., rigid) spherical region with a density that is different from the surrounding medium scatters far less power than the incident plane wave intensity times the contrast region's physical cross-sectional area, πa^2. The density contrast factor is also limited to a small range: $1 \geq [(\rho_m - \rho_s)/(\rho_m + 2\rho_s)]^2 \geq 0$. If the sphere is immobilized (i.e., $\rho_s = \infty$), then $\sigma = (7/9)(\pi a^2)(ka)^4$. A similar result for a thin disk of radius, a_{disk}, is $\sigma_{disk} = (16/27)\left(\pi a_{disk}^2\right)\left(ka_{disk}\right)^4$ [39].

12.6.2 Scattering from a Compact Compressibility Contrast

The same strategy can be employed to determine the scattered pressure field due to a plane wave that impinges on a compact region that has a different compressibility than the surrounding medium. The adiabatic compressibility, K_s, of the surrounding medium is the reciprocal of its adiabatic bulk modulus, B_s, so by Eq. (10.21), $K_s = B_s^{-1} = \left(\rho_m c^2\right)^{-1}$. Again, for a compact scatterer, the shape of the scattering body is irrelevant.[5] For convenience, the compact *compressibility contrast* region will be treated as a sphere with volume, $V_{sphere} = 4\pi a^3/3$.

The radius of the sphere, a, will be modulated by the amplitude of the incident pressure wave, $\widehat{\mathbf{p}}_{\mathbf{ff}}$, that is assumed to arise due to a traveling plane wave. The volume change of that scatterer is related to the bulk modulus of the fluid in that compact region by Eq. (10.20).

$$\delta V = 3V_{sphere}\frac{\delta a}{a} = 3V_{sphere}\frac{\left|\widehat{\boldsymbol{\xi}}\right|}{a} = -V_{sphere}\frac{\left|\widehat{\mathbf{p}}_{\mathbf{ff}}\right|}{B_s} = -V_{sphere}\frac{\left|\widehat{\mathbf{p}}_{\mathbf{ff}}\right|}{\rho_s c_s^2} \tag{12.76}$$

In this case, ρ_s is the density of the fluid in the compact scattering region, and c_s^2 is the square of the sound speed of that contrasting fluid.

Just as the relative velocity of the fluid and the sphere in Eq. (12.71) was used to calculate the dipole strength in Eq. (12.72), the induced volume change, δV, in Eq. (12.76), must be compared to the change in the equilibrium volume of a region with equal volume if the medium were uniformly compressible. That difference between the volume change in the region with the compressibility contrast and the volume change that would have occurred can be used to calculate the amplitude of the equivalent scattering volume velocity, $\widehat{\mathbf{U}}_{\mathbf{scat}}(a)$.

$$\widehat{\mathbf{U}}_{\mathbf{scat}}(a) = -\omega\,\widehat{\mathbf{p}}_{\mathbf{ff}}\frac{V_{sphere}}{\rho_s c_s^2}\left(1 - \frac{\rho_s c_s^2}{\rho_m c^2}\right) \tag{12.77}$$

If the compressibility of the scattering region is the same as that of the surrounding fluid, then $\left|\widehat{\mathbf{U}}_{\mathbf{scat}}(a)\right| = 0$, as it must, so that there is no scattered wave if there is no inhomogeneity. If the scattering region is much more compressible than the surrounding fluid (e.g., a gas-filled bubble in water), then the more compressible medium dominates the induced volume velocity; hence $\left|\widehat{\mathbf{U}}_{\mathbf{scat}}(a)\right| = \omega\ \delta V$, where δV is given by Eq. (12.76).

A particularly interesting case is the incompressible sphere, where $\rho_s c_s^2 \gg \rho_m c^2$. For a steel sphere, $\rho_s {c_s}^2 \cong 290$ GPa, and for water, $\rho_m c_{H_2O}^2 \cong 2.25$ GPa. For air under standard conditions, $\rho_m c^2 = \gamma p_m \cong 142$ kPa. In that case, $\widehat{\mathbf{U}}_{\mathbf{scat}}(a)$ is determined by the compressibility of the medium (not the sphere), $\rho_m c^2$, thus producing a scattered wave that satisfies the rigid boundary condition at the sphere, $\delta V = 0$ and $\delta a = \left|\widehat{\boldsymbol{\xi}}\right| = 0$, when combined with the incident wave.

The source strength in Eq. (12.77) will produce isotropic spherical acoustic pressure waves, $p\left(\left|\vec{r}\right|\right)$, with an amplitude determined by Eq. (12.21), where the contrasting compressible region is again represented by a sphere of volume, $V_{sphere} = 4\pi a^3/3$.

$$\frac{p\left(\left|\vec{r}\right|\right)}{\left|\widehat{\mathbf{p}}_{\mathbf{ff}}\right|} = \frac{(ka)^2}{3}\left(\frac{a}{\left|\vec{r}\right|}\right)\left(\frac{\rho_m c^2}{\rho_s c_s^2} - 1\right) \tag{12.78}$$

The far-field intensity is proportional to the square of the acoustic pressure, as given by Eq. (10.40), so the ratio of the time-averaged scattered intensity, $\langle I_{scat}\rangle_t$, to the time-averaged free-field incident intensity, $\langle I_{ff}\rangle_t$, is proportional to $(ka)^4$, as it was for the rigid sphere in Eq. (12.74). Integration over all solid angle to obtain the total scattering cross-section is simplified, since this scattered sound field is isotropic.

$$\sigma = \frac{4}{9}\left(\pi a^2\right)(ka)^4\left(\frac{\rho_m c^2}{\rho_s c_s^2} - 1\right)^2 \quad \text{for } ka \ll 1 \tag{12.79}$$

Again, the total scattering cross-section, σ, will be smaller than the geometrical cross-section, πa^2, by a factor of $(ka)^4$, as it was in Eq. (12.75), except the density contrast factor, $\left[\left(\rho_m c^2/\rho_s c_s^2\right) - 1\right]^2$, can be very large. For air trapped near the water surface, $\left[\left(\rho_{H_2O} c_{H_2O}^2/\rho_{air} c_{air}^2\right) - 1\right]^2 = 2.5 \times 10^8$. Under such circumstances, the total scattering cross-section can be much larger than the physical cross section. For the case of a bubble being driven at frequencies near its Minnaert frequency, it can be even larger.

12.6.3 Scattering from a Single Bubble or a Swim Bladder

The results of the previous section are correct as long as the sound field driving the compressions and expansions of the compressibility contrast region occur at frequencies below the Minnaert frequency in Eq. (12.30). Although that frequency was calculated in Sect. 12.3, as it applied to a stable spherical gas-filled bubble in a liquid, the result is generally applicable to any compressible region regardless of the shape, as long as that region is compact [8].

Any periodic change in volume of that region requires that the surrounding fluid be accelerated. The acceleration of the surrounding fluid is conveniently represented by an effective (hydrodynamic) mass, calculated in Eq. (12.15), that is equal to three times the mass of the fluid displaced by the compressible region's volume. The competition between the compressibility of the contrast region and the inertia of the surrounding fluid will drive quasi-one-dimensional harmonic oscillations with the variation in the radius of the bubble, $\xi_1(t) = \Re e\left[\widehat{\boldsymbol{\xi}} e^{j(\omega t)}\right] = \Re e\left[\left|\widehat{\boldsymbol{\xi}}\right| e^{j(\omega t + \Theta)}\right]$, where the phase, Θ, has been included explicitly to emphasize the fact that the response of the bubble's radius to the varying pressure produced by the incident wave will not necessarily be in-phase with the acoustic pressure that is driving the bubble, as would be the case for any driven simple harmonic oscillator (see Sect. 2.5.1).

Recall that if the forcing function is applied at a frequency, ω, below the natural frequency, ω_o, which would be the Minnaert frequency of Eq. (12.30) or Eq. (12.31), then the driven system is stiffness-controlled. In the case of the bubble, this means that the bubble's radius, $a + \xi_1(t)$, will decrease when the acoustic pressure due to the incident sound wave increases. With $\omega < \omega_o$, the inertia of the surrounding fluid is not important in determining the bubble's response, and the expression for the resultant volume velocity, $\widehat{\mathbf{U}}_{\mathbf{scat}}(a)$, given in Eq. (12.77), will provide an accurate representation of the spherically symmetric scattered sound field when substituted into the monopolar transfer impedance of Eq. (12.22).

If the incident wave has a frequency that is larger than the Minnaert frequency, the bubble's behavior is mass controlled and therefore dominated by the inertia of the surrounding fluid. In this limit, there are two interesting differences. The first is that above resonance, the phase will shift by nearly 180°. This fact was exploited to extend the low-frequency performance of a bass-reflex loudspeaker enclosure in Sect. 8.8. The radius of the bubble will grow when the acoustic pressure of the incident wave is positive. Also, as the frequency increases above ω_o, the radial velocity of the bubble's surface will decrease.

If the incident sound field is oscillating at a frequency very close the bubble's natural frequency, $\omega \cong \omega_o$, then the bubble's motion will be resistance-controlled so that the amplitude of the bubble's radial velocity will be determined by its quality factor, calculated in Sect. 12.3.1.

Treating the bubble as a quasi-one-dimensional simple harmonic oscillator, the force is determined by the free-field pressure amplitude of the incident wave, $\widehat{\mathbf{p}}_{\mathbf{ff}}$, times the mean surface area of the bubble, $4\pi a^2$, assuming that $ka \ll 1$, so that $\widehat{\mathbf{p}}_{\mathbf{ff}}$ is uniform over the bubble's surface. The bubble's radial velocity, $\dot{\xi}_1(t) = \Re e\left[j\omega\widehat{\boldsymbol{\xi}}e^{j\omega t}\right]$, in response to the pressure's driving force, is given by the mechanical impedance in Eq. (2.62).

$$\left|\widehat{\mathbf{U}}_{\mathbf{scat}}(a)\right| = 4\pi a^2\dot{\xi}_1 = \left(4\pi a^2\right)^2\frac{|\widehat{\mathbf{p}}_{\mathbf{ff}}|}{|\mathbf{Z}_{\mathbf{mech}}|} = \frac{12\pi a}{\rho_m\omega_o}\frac{|\widehat{\mathbf{p}}_{\mathbf{ff}}|}{\left[\left(\frac{\omega}{\omega_o}-\frac{\omega_o}{\omega}\right)^2+\frac{1}{Q^2}\right]^{½}} \tag{12.80}$$

The acoustic transfer impedance of Eq. (12.22), $\mathbf{Z}_{\mathbf{tr}}$, relates the isotropically scattered pressure, $p(r)$, to the complex incident acoustic pressure amplitude, $\widehat{\mathbf{p}}_{\mathbf{ff}}$.

$$p\left(\left|\vec{r}\right|\right) = \mathbf{Z}_{\mathbf{tr}}\left|\widehat{\mathbf{U}}_{\mathbf{scat}}(a)\right| \quad \Rightarrow \quad \frac{p\left(\left|\vec{r}\right|\right)}{|\widehat{\mathbf{p}}_{\mathbf{ff}}|} = 3\left(\frac{a}{\left|\vec{r}\right|}\right)\left(\frac{\omega}{\omega_o}\right)\left[\left(\frac{\omega}{\omega_o}-\frac{\omega_o}{\omega}\right)^2+\frac{1}{Q^2}\right]^{-½} \tag{12.81}$$

In the limit of low frequencies, $\omega < \omega_o$, Eq. (12.81) recovers the $(ka)^2$ dependence of the radiated pressure from Eq. (12.78).

$$\lim_{\omega\to 0}\left[\frac{p\left(\left|\vec{r}\right|\right)}{|\widehat{\mathbf{p}}_{\mathbf{ff}}|}\right] = 3\left(\frac{a}{\left|\vec{r}\right|}\right)\left(\frac{\omega}{\omega_o}\right)^2 \propto (ka)^2 \tag{12.82}$$

At frequencies above the Minnaert frequency, the radiated pressure is independent of the driving frequency.

As before, the scattered pressure in Eq. (12.81) can be used to calculate the total scattering cross-section for a resonant bubble as a function of the driving frequency [40].

$$\sigma = \frac{(4\pi a^2)(\omega/\omega_o)^2}{\left[\left(\frac{\omega}{\omega_o}-\frac{\omega_o}{\omega}\right)^2+\frac{1}{Q^2}\right]} \tag{12.83}$$

Using the 1.0 mm diameter air-filled bubble at a depth of 10 m, which was the example at the end of Sect. 12.3.1, we can evaluate Eq. (12.83) at $f_o = 20.6$ kHz with $Q_{total} = 47$. With $c_{H_2O} = 1500$ m/s, $(ka) = 0.043 \ll 1$. Figure 12.24 plots the ratio of the total scattering cross-section to the bubble's geometric cross-section, $4\pi a^2$, as a function of frequency. At resonance, the bubble's scattering cross-section is $Q^2 = 2210$ times larger than its geometrical cross-section. Resonant scattering from bubbles or other gas-filled density contrast regions, like fish swim bladders, shown in Fig. 12.23, can be significant.

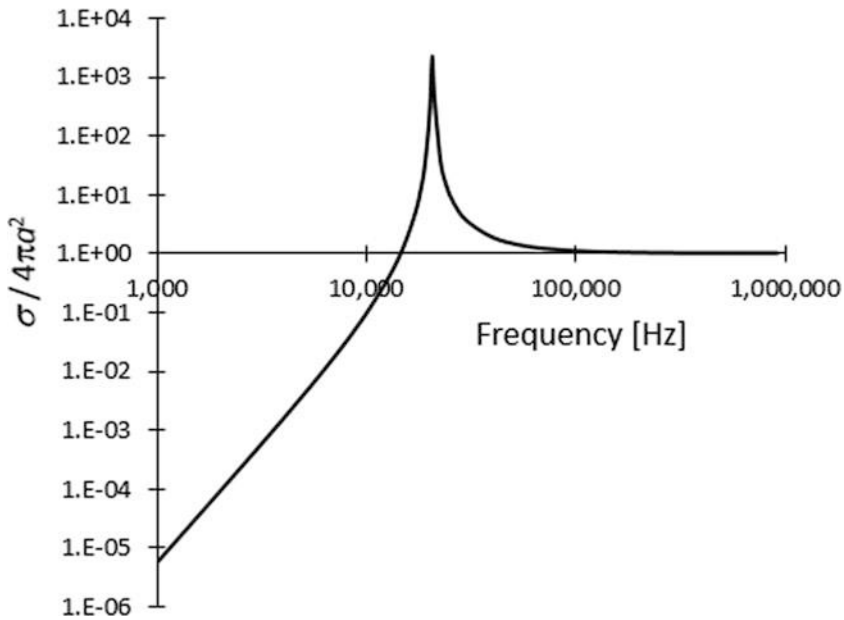

Fig. 12.24 Ratio of the scattering cross-section, σ, for a 1 millimeter diameter air-filled bubble, 10 m below the surface, to the bubble's geometric cross-sectional area, $4\pi a^2$. That bubble's Minnaert frequency is $f_o = 20.6$ kHz and its quality factor is $Q_{total} = 47$

12.6.4 Multiple Scattering in the "Effective Medium" Approximation

Multiple scattering of sound from a large number of small objects can require rather complicated computations. Like many topics addressed in this textbook, there are limiting cases that can be solved quite easily and which are both important and illustrate an approach with more general utility. If the scatterers are identical and if they are spaced in a regular lattice, then those regularly spaced identical inhomogeneities will behave as a diffraction grating, and there will be specific directions that will experience large scattered wave amplitudes at certain frequencies. The formalism that can address that case for a regular one-dimensional array of identical scattering object will be the focus of Sect. 12.7.

Another interesting and important case is that of a medium that has a dispersion of scattering particles that are positioned randomly and have a variety of different sizes. Such a medium might be a "bubble cloud" if the scatters were gas bubbles of different sizes in a fluid medium or a fog consisting of liquid droplets dispersed within a gaseous medium. For both the bubble cloud and the fog, if the $(k\overline{a}) \ll 1$, for the effective average scatterer radius, $\overline{a}$, and if there is a high number density of compact scattering regions, then an approach known as the *mean field approximation* can create a useful representation of multiple scattering.

In the long wavelength limit at frequencies much lower than the lowest bubble resonance frequency of the largest bubble, a bubble cloud will have an effective density that is close to that of the liquid, but its compressibility will be dramatically larger than the liquid, even if the gaseous fraction is small. This can result in a sound speed within the bubble cloud that is slower than the speed of sound in either the surrounding liquid or the gas that fills the bubbles. In a fog, the sound speed will be close to that of the speed in the pure gas since the presence of fluid droplets produces only a small increase in both the mean bulk modulus and the mean density.

Such a mean field approximation can be developed by considering the volume fraction of each component.[14] For a bubble cloud, the minority species is the gas phase that occupies a volume fraction, x. The liquid phase occupies the remaining volume, $(1 - x)$. The effective density of the mixture can be approximated by the mass density weighted fraction of the individual components' mass densities.

$$\rho_{mean} = x\rho_{gas} + (1 - x)\rho_{liquid} \tag{12.84}$$

The mean field bulk modulus, B_{mean}, can be calculated by remembering that the stiffness of two springs that are placed in series is the parallel combination of their individual stiffnesses (see Sect. 2.2.1).

$$B_{mean} = \left[\left(\frac{x}{B_{gas}}\right) + \frac{(1 - x)}{B_{liquid}}\right]^{-1} \tag{12.85}$$

Using the definition of the sound speed in Eq. (10.21), Eqs. (12.84) and (12.85) can be combined to produce an effective sound speed, c_{eff}, for the mixture.

$$\frac{1}{c_{eff}^2} = \frac{\rho_{mean}}{B_{mean}} = \left[x\rho_{gas} + (1 - x)\rho_{liquid}\right]\left[\left(\frac{x}{B_{gas}}\right) + \frac{(1 - x)}{B_{liquid}}\right] \tag{12.86}$$

Figure 12.25 is a plot of that effective sound speed for a bubble cloud with air at atmospheric pressure ($\rho_{gas} = 1.21$ kg/m^3, $B_{gas} = 142$ kPa) and water ($\rho_{liquid} = 1000$ kg/m^3, $B_{liquid} = 2.25$ GPa). As required, the effective sound speed is equal to the speed of sound in pure water, $c_{H_2O} = 1500$ m/s, if there are no bubbles ($x = 0$), and the speed of sound in air, $c_{Air} = 344$ m/s, when there is no water ($x = 1$). There is also a substantial range of gas volume fractions (sometime called *void fractions*)

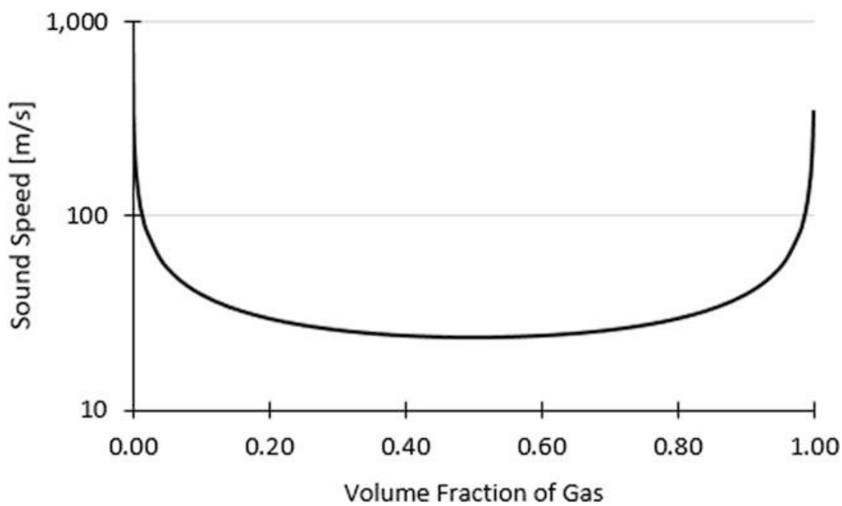

Fig. 12.25 Effective sound speed in a bubble cloud as a function of gas volume fraction if the dispersion of bubbles with various radii contains air near atmospheric pressure and the surrounding liquid is water. It is assumed that all the bubbles are small enough that $(k\bar{a}) \ll 1$, and the frequencies of interest are all well below the lowest bubble resonance frequency. At zero void fraction, the speed is just that in pure water

[14] In this simplified treatment, it is assumed that the gas in the bubbles is not condensable so that the evaporation and condensation of the liquid's vapor can be ignored. A more complete theory that incorporates evaporation and condensation for both bubbles and for fogs is given in Ref. [3], §64, Problems 1 (bubbles) and 2 (fog).

where the sound speed is much less than the sound speed in air. For $0.01 < x < 0.99$, $c_{eff} < 100$ m/s and for $0.06 < x < 0.94$, $c_{eff} < 50$ m/s, with a broad minimum effective sound speed of 24 m/s around $x = 0.50$ [41][15]

The very low value of c_{eff} for a bubbly liquid can be observed if cocoa powder is placed in a mug that is then filled with hot water. The air trapped in the powder will form bubbles that will rise and coalesce over the span of less than a minute. If the mug is tapped with a spoon, the frequency of the sound will change with time, rising in pitch as the bubbles move to the surface. In some cases, the frequency change can be more than three octaves. This rise in pitch is commonly known as "the hot chocolate effect" [42].

The same effect can also be observed when a glass is filled with hot tap water, particularly if the tap is partially throttled. The water will be cloudy due to the formation of small bubbles that will coalesce and rise causing the pitch of the quarter wavelength standing wave resonance (assuming the bottom is rigid and the top is a pressure-released surface) that is excited in the bubbly liquid to increase in frequency.

The sound speed reduction due to the introduction of bubbles in a solvent has developed into a technique for the analysis of transient dissolution processes for chemical compounds that is known as Broadband Acoustic Resonance Dissolution Spectroscopy (BARDS) [43]. Various extensions of this approach have been developed to study other effects like wettability of pharmaceutical powers [44].

The effect on sound speed is not nearly as dramatic for a fog of small liquid droplets suspended in a gaseous medium. For small droplet concentrations, the stiffness of the gas is increased slightly because the relatively incompressible liquid droplets exclude some of the more compressible gas volume. That effect is overwhelmed by the increase in the medium's effective mass density, although at typical droplet volume fractions, the reduction in the effective sound speed is small.

12.7 N-Element Discrete Line Array

The same procedure we applied to the superposition of two compact sources of equal source strength and frequency in Sect. 12.4 can be applied to any number, N, of such sources that are separated by a uniform distance, d, between adjacent sources along a line. Figure 12.26 provides a coordinate system where we measure the angle, θ, above the plane normal to the line joining the sources, with $|\vec{r}|$ as distance from the central source to the observation point. As before, there will be no azimuthal dependence to sound field due to the rotational symmetry about the axis joining the sources.

As before, we can sum the contribution of each simple source at the observation point a distance, r_n, from the nth element, where $n = 0, 1, 2, \ldots (N - 1)$.

$$p(r,t) = \Re e\left[\sum_{n=0}^{N-1} \frac{\widehat{\mathbf{C}}_{\mathbf{n}}}{r_n} e^{\,j(\omega t - kr_n + \phi_n)}\right] \tag{12.87}$$

Each straight-line path from each source to the observation point has a different length. In the far-field approximation ($kr \gg 1$), these path length differences, Δr_n, have little effect on the relative pressure amplitude radiated to the observation point but can produce a significant difference in the summation through their associated phase differences. Using the geometry of Fig. 12.26, the dashed blue line is drawn perpendicular to each propagation path providing the difference in the propagation distance that

[15] This result is known as "Wood's equation." In the first edition of A. B. Wood, *A Textbook of Sound* (MacMillan, New York, 1930), Wood quotes Mallock's result from [40], but in the second edition, there is no mention of Mallock.

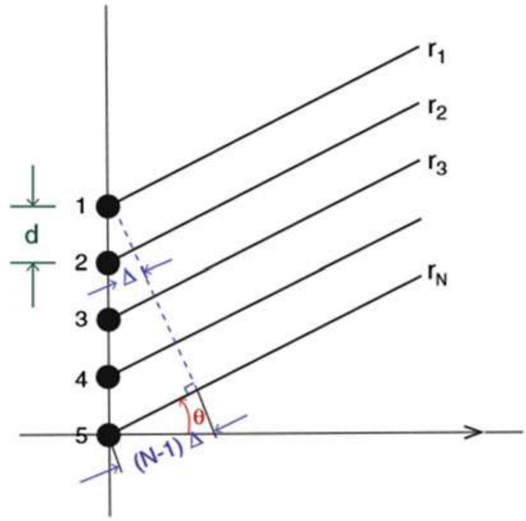

Fig. 12.26 Coordinate system for the superposition of $N = 5$ compact sources that are separated from each other by a uniform distance, d. The resultant sound field will be symmetric about the line joining the sources so that there will be no azimuthal variation. The dashed black lines illustrate the path length differences between the observation point a distance, r_1, from the top source and the individual paths

is proportional to the n-index of each source and to the inter-element separation, d, between adjacent sources.

$$\Delta r_n = nd \sin\theta \equiv n\Delta \tag{12.88}$$

Considering sources of equal amplitude, $\widehat{\mathbf{C}}_\mathbf{n} = C$, that are all oscillating in-phase, $\phi_n = \phi = 0°$, then both C_n and $r_n \cong r$ can be brought out in front of the summation of Eq. (12.87).

$$p\left(\left|\vec{r}\right|, \theta, t\right) = \frac{C}{\left|\vec{r}\right|} \Re e\left[e^{j\left(\omega t - k\left|\vec{r}\right|\right)} \sum_{n=0}^{N-1} e^{-j(nk\Delta)}\right] \tag{12.89}$$

The summation has been transformed to a geometric series that can be evaluated by standard techniques [45].

$$\sum_{k=1}^{n} aq^{k-1} = \frac{a(1-q^n)}{1-q}; \quad q \neq 1 \tag{12.90}$$

Application of Eq. (12.90) to Eq. (12.89) results in the geometric series where $q \equiv e^{-jk\Delta}$.

$$\sum_{n=0}^{N-1} q^n = \frac{1 - e^{-jkN\Delta}}{1 - e^{-jk\Delta}} = \left[\frac{\sin(kN\Delta/2)}{\sin(k\Delta/2)}\right] \tag{12.91}$$

We are left with the desired directionality, $H(\theta)$, with an axial pressure that is N times the amplitude of each individual source [46].

$$H(\theta) = \left|\frac{\sin\left(N\frac{kd}{2}\sin\theta\right)}{N\sin\left(\frac{kd}{2}\sin\theta\right)}\right| \tag{12.92}$$

To appreciate the discrete line array's directionality, $H(\theta)$, it is useful to plot both the numerator and denominator of Eq. (12.92) separately. Figure 12.27 provides such a graph, as well as the absolute value of the ratio, for the case where $kd = 8$ (so $d = 8\lambda/2\pi = 1.273\lambda$) and $N = 5$, with all sources radiating in phase ($\phi_n = 0°$).

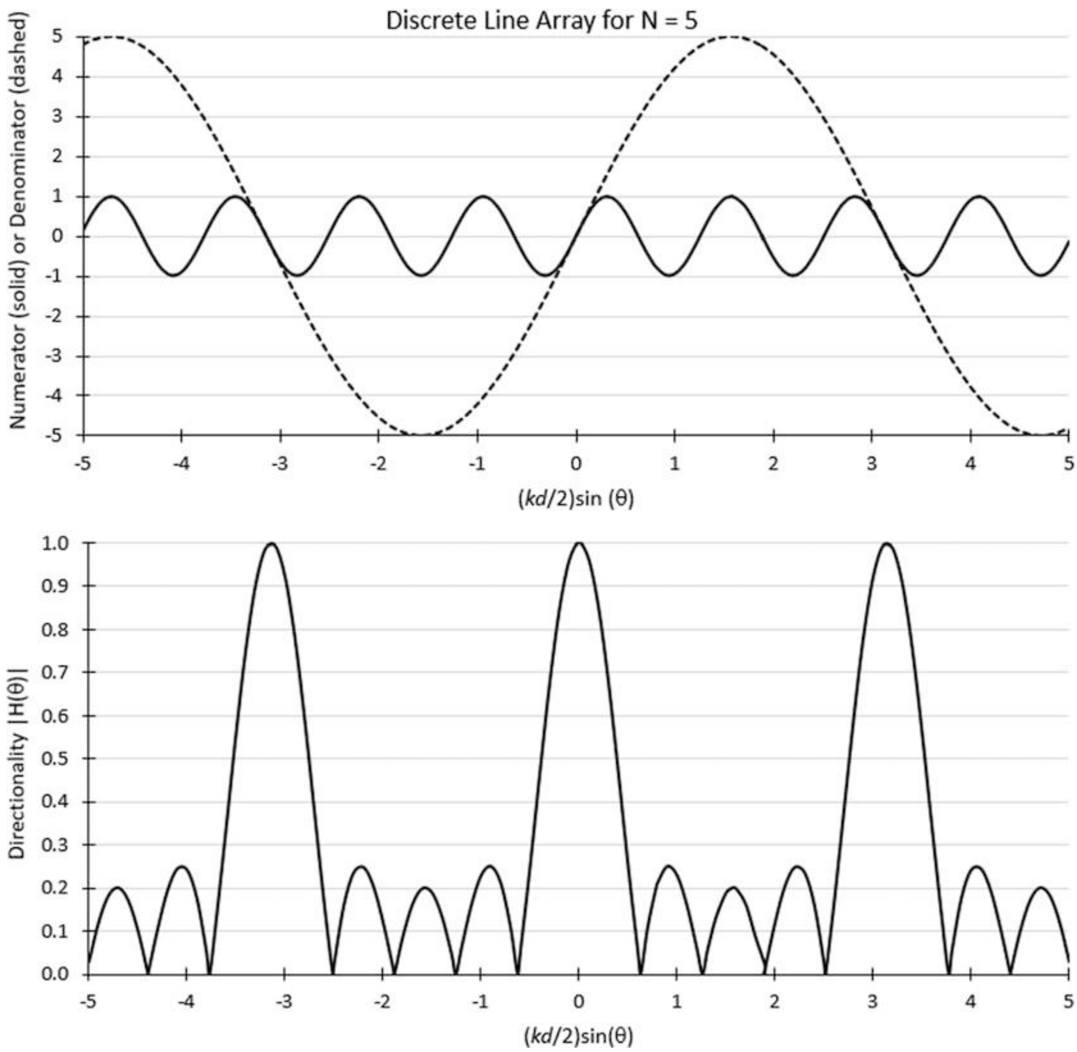

Fig. 12.27 (*Above*) Plot of the numerator and denominator of Eq. (12.92) for $kd = 8$ (so $d = 8\lambda/2\pi = 1.273\lambda$) and $N = 5$ vs. $(kd/2) \sin \theta$. (*Below*) Absolute value of the numerator divided by the denominator. A polar plot is provided in Fig. 12.28

At the origin ($\sin \theta = 0$), the value of the ratio is unity, as can be shown if you expand both sine functions in a power series and keep only the leading (first-order) terms. The directionality has local maxima when there is a path length difference of one wavelength between adjacent sources. For that case, the denominator vanishes at $(kd/2) \sin \theta = n\pi$; $n = 0, 1, 2, \ldots$ Since N is an integer, the numerator also goes to zero.

When the total length of the array, $L = (N - 1)\, d$, is much less than a wavelength, the array behaves like an omnidirectional simple source with a source strength that is N-times greater than the individual (identical) elements. As the separation increases, the radiated pressure in the polar direction ($\theta = 90°$) decreases until $d = \lambda/2$, which produces a minimum at $\theta = 90°$ if N is an even number, while the angular width of the major lobe becomes narrower with increasing N.

The directional pattern of Eq. (12.92) has nulls in directions determined by$(Nkd/2) \sin \theta = m\pi$, where $m = 0, 1, 2, \ldots, Nd/\lambda$. For the central beam ($\theta = 0°$), the nulls occur at $\sin \theta = \pm\lambda/Nd$. For large values of N, the full width[16] of the central maximum is $2\theta = 2\lambda/Nd \cong 2\lambda/L$. The beam pattern becomes more "focused" as the length of the array increases. This fact is responsible for the tall line arrays that are visible on stage in Fig. 12.1.

12.7.1 Beam Steering and Shading

A discrete line array can produce a narrow beam. Since the previous analysis sets the relative phases of all of the monopole sources to zero, the main lobe was always aligned with the plane that is the perpendicular bisector of the line, as seen in Fig. 12.28. There are applications where the main-lobe directionality of a line array of sources or sensors would be more useful if the main lobe could be steered toward other orientations. This can be accomplished introducing progressive times delays, τ_n, to each element in the line array such that $\tau_n = (n-1)\tau_1$, for $n = 2, 3, 4, \ldots$ Those delays would produce phase shifts, $\phi_n = (n-1)\phi_1 = (n-1)\omega\tau_1$, that can be included in the exponential factor for each term in the summation of Eq. (12.87). Such delays would be equivalent to increasing or decreasing the path length differences, Δr_n, that were calculated in Eq. (12.88).

Referring to Fig. 12.26, if the signal sent to the $n = 2$ element was delayed by the travel time from $n = 2$ to $n = 1$, $\tau_2 = d/c$, then the signal from $n = 2$ would be in-phase with the signal from $n = 1$ when it arrived at element 1 and those two signals would add constructively in the direction along their common axis. Similarly, if the $n = 3$ element was delayed by twice that amount, $\tau_3 = 2\tau_2$, the signal from $n = 3$ would add in-phase to both the delayed $n = 2$ signal and the $n = 1$ signal, and their superposition would make the amplitude of the signal be three times as large in the direction along their common axis. Such an arrangement is called an *end-fire array* since the strongest signal radiates from the end of the array along the direction of array's axis.

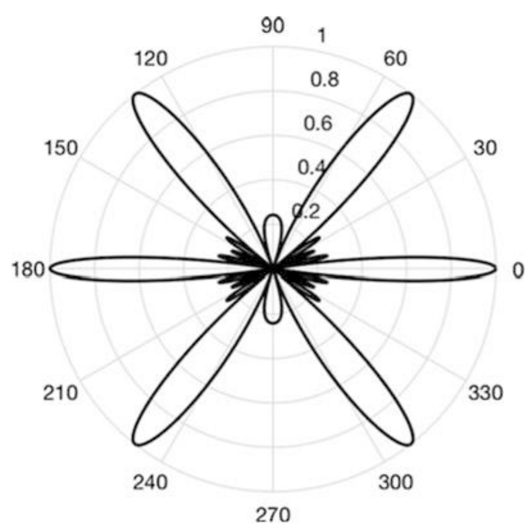

Fig. 12.28 Two-dimensional polar plot of the directionality of a five-element ($N = 5$) discrete array of in-phase ($\phi_n = \phi = 0°$) simple sources that are separated by $d = 8/k$ (so $d = 8\lambda/2\pi = 1.273\ \lambda$). It is important to remember that the three-dimensional radiation pattern has azimuthal symmetry so that the actual radiation pattern is obtained if this two-dimensional plot is rotated about the polar (90° – 270°) axis

[16] Definitions of "beam width" vary. Above we have defined the width as the angular separation of adjacent nulls. Other common designations of broadside beam width are angular separation of the beam pattern that are −3 dB, −6 dB, −10 dB or − 20 dB from the maximum at $\theta = 0°$.

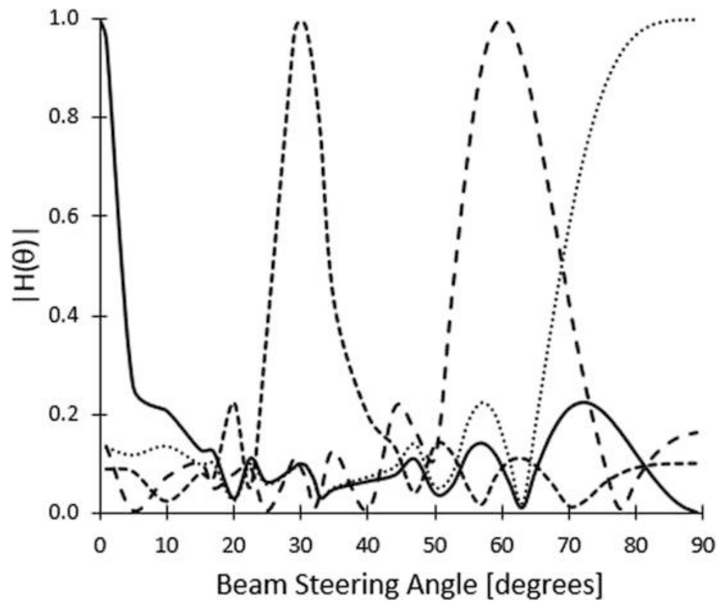

Fig. 12.29 Directionality of an $N = 10$ element line array that is 8.1 wavelengths long. The *solid line* represents broadside directivity ($\theta_\tau = 0°$) and produces a -3 dB full width, $\Delta\theta_{-3\mathrm{dB}} = 2.8°$. The *dotted line* represents end-fire directivity ($\theta_\tau = 90°$) and produces a -3 dB full width, $\Delta\theta_{-3\mathrm{dB}} = 36.2°$. Also shown are two intermediate cases with $\theta_\tau = 30°$ (*shorter dashed line*) having $\Delta\theta_{-3\mathrm{dB}} = 6.6°$ and $\theta_\tau = 60°$ (*longer dashed line*) having $\Delta\theta_{-3\mathrm{dB}} = 11.5°$

In general, the direction of the main lobe, θ_τ, will be determined by the delay time, τ_1, between each radiating element (monopole).

$$\sin\theta_\tau = c\tau_1/d \tag{12.93}$$

If there is no time delay, $\tau_1 = 0$, then the axis of the main lobe is on the plane that is the perpendicular bisector of the line joining the N-elements of the array and $\theta_\tau = 0°$. If $\tau_1 = \pm d/c$, as in the initial discussion, then $\theta_\tau = \pm 90°$, producing the end-fire condition. Introduction of the non-zero phase delays, ϕ_n, in Eq. (12.87), produces the expected modification to the zero delay directionality result in Eq. (12.92).

$$H(\theta) = \left| \frac{\sin\left[N\frac{kd}{2}(\sin\theta - \sin\theta_\tau)\right]}{N\sin\left[\frac{kd}{2}(\sin\theta - \sin\theta_\tau)\right]} \right| \tag{12.94}$$

As shown in Fig. 12.29, an undesirable consequence of the beam steering is the broadening of the main lobe as the steering angle increases from broadside ($\theta_\tau = 0°$) to end-fire ($\theta_\tau = 90°$).

The use of modern digital electronics makes the insertion of the individual element time delays both simple and accurate. Long ago, in the era of vacuum tube analog electronics, a low-frequency end-fire array was constructed to produce a directional sound reinforcement system for the Hollywood Bowl in Los Angeles, CA. The Bowl is an outdoor venue with a band shell over the stage area. Since low-frequency sound travels great distances (see Chap. 14), there were complaints from homeowners in the surrounding neighborhood of Griffith Park who were bothered by those sounds.

To produce a directional low-frequency array that would concentrate the reinforcement in the direction of the audience and limit the spreading to the surrounding communities, an analog delay system was constructed that consisted of one loudspeaker at one end of a long tube. The other end of the tube was terminated by an anechoic wedge absorber to eliminate reflections. All along the length of that tube, microphones were inserted, and their delayed signals were amplified to drive individual bass enclosures at the microphone locations. The propagation delay of the sound in the tube was exactly that required to satisfy the end-fire condition, $\theta_\tau = 90°$.

As a final comment regarding the practical implementation of line arrays, it is worthwhile to remember that the directionality of a line array is scaled by the ratio of the array's overall length, L, to the wavelength of the radiated sound, λ. For sound reinforcement systems that are used to enhance musical performances, the range of wavelengths is very large. For that reason, in Fig. 12.1, it is easy to see that the longest arrays are for projection of bass, and the shortest arrays were for treble, with intermediate-length arrays dedicated to the mid-frequencies. Such large sound reinforcement systems are not economically justified for smaller venues.

One common approach to keep the directivity of a line array fairly constant over a significant frequency range is to provide passive cross-over circuits that apply the lowest frequency material to all the speakers in the line array but to provide progressive attenuation to the outer elements for higher frequencies in an attempt to keep the effective length of the array more constant with respect to the wavelength of the radiated sound.

The adjustment of the individual amplitude coefficients, C_n, that appear in Eq. (12.87) in a discrete line array, produces a *shaded array*. Various shading strategies are also adopted to suppress side lobes, although they always reduce the directionality of the main lobe since they make the effective overall length of the array less than its physical length. Of course, that was the objective of the shading scheme to increase the frequency range of a single array while trying to maintain a more constant directivity. For large numbers of individual elements in an array, combination of delays and shading allow adaptive steering of both beams and nulls. This can be very useful when trying to find quiet targets in environments cluttered by discrete noise sources.

12.7.2 Continuous Line Array

There are line sources that can be considered a continuous distribution of source strength. One example is the ionization path of lightning, and another is the tire noise that is radiated continuously from the surface of a highway. Instead of considering the superposition of discrete sources, as we did in the previous section, in this section we will assume that there is a continuous distribution of volume velocity along a straight line of total length, L, as diagrammed in Fig. 12.30, where we have assumed that the source is aligned with the z axis and is centered at the x-y plane.

If each differential element of volume velocity, $\mathrm{d}\left|\widehat{\mathbf{U}}(a)\right| = 2\pi a|\widehat{\mathbf{v}}_{\mathbf{r}}(a)|\,\mathrm{d}z$, where $\widehat{\mathbf{v}}_{\mathbf{r}}(a)$ is the radial velocity of the cylindrical line source at its surface, is treated as a differential source of acoustic pressure, $\mathrm{d}p_1\left(\left|\vec{R}\right|\right)$, then the total pressure is given by the integral from $-L/2$ to $+L/2$ over all the differential source strength elements. That integral can be evaluated by using the expression for the pressure radiated by a simple source in Eq. (12.21).

$$
\begin{aligned}
p_1\left(\left|\vec{R}\right|,\theta,t\right) &= \Re e\left[\int_{-L/2}^{L/2}\mathrm{d}p_1 = \frac{j\rho_m cck}{4\pi}\int_{-L/2}^{L/2}\frac{e^{j\left(\omega t-k\left|\vec{R}\right|\right)}}{\left|\vec{R}\right|}\;\mathrm{d}\widehat{\mathbf{U}}(a)\right] \\
&= \Re e\left[\frac{j\rho_m cka\widehat{\mathbf{v}}_{\mathbf{r}}(a)}{2}\int_{-L/2}^{L/2}\frac{e^{j\left(\omega t-k\left|\vec{R}\right|\right)}}{\left|\vec{R}\right|}\mathrm{d}z\right]
\end{aligned}
\tag{12.95}
$$

In the far-field limit, $\left|\vec{r}\right| \gg L$, the numerator of the term within the integral of Eq. (12.95) can be approximated by $\left|\vec{R}\right| \cong \left|\vec{r}\right|\sin\theta$.

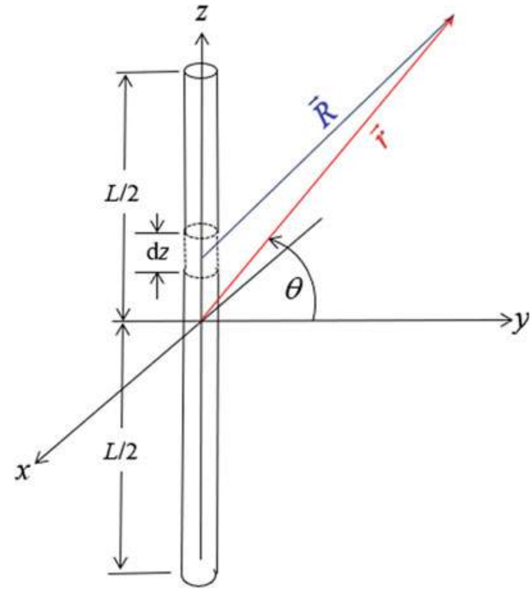

Fig. 12.30 A schematic representation of a continuous line source of length, L, is assumed to produce a volume velocity amplitude of $\left|\widehat{\mathbf{U}}(a)\right|$ by a harmonic change in its radius, a, that is uniform along its full length. Each differential element of volume velocity along the length of the cylindrical line source of length, dz, produces a differential source strength, $\mathrm{d}\left|\widehat{\mathbf{U}}(a)\right| = 2\pi a|\widehat{\mathbf{v}}_{\mathbf{r}}(a)|\,\mathrm{d}z$, where $\widehat{\mathbf{v}}_{\mathbf{r}}(a)$ is the amplitude of the radial velocity of the cylindrical line source at its surface

$$p_1\left(\left|\vec{r}\right|,\theta,t\right) \cong \Re e\left[j\frac{\rho_m cka\widehat{\mathbf{v}}_{\mathbf{r}}(\mathrm{a})}{2}\frac{e^{j\left(\omega t-k\left|\vec{r}\right|\right)}}{\left|\vec{r}\right|}\int_{-L/2}^{L/2} e^{jkz\sin\theta}\,\mathrm{d}z\right] \tag{12.96}$$

The integral can be evaluated since its argument is an exponential.

$$\int_{-L/2}^{L/2} e^{jkz\sin\theta}\mathrm{d}z = \frac{e^{jkz\sin\theta}}{jk\sin\theta}\bigg|_{-L/2}^{L/2} = \frac{e^{j\frac{kL}{2}\sin\theta} - e^{-j\frac{kL}{2}\sin\theta}}{jk\sin\theta} = \frac{2\sin\left(\frac{kL}{2}\sin\theta\right)}{k\sin\theta} \tag{12.97}$$

Expression of this result can be simplified by use of the "sinc" function: sinc(x) ≡ (sin x)/x, which is plotted in Fig. 12.31.[17]

$$H(\theta) = \left|\mathrm{sinc}\left(\frac{kL}{2}\sin\theta\right)\right| \tag{12.98}$$

The far-field acoustic pressure along the equatorial plane is related to the total source strength, $\left|\widehat{\mathbf{U}}(a)\right| = 2\pi a|\widehat{\mathbf{v}}_{\mathbf{r}}|L$.

$$p_{ax}\left(\left|\vec{r}\right|\right) = \frac{\rho_m c|\widehat{\mathbf{v}}_{\mathbf{r}}|kLa}{2\left|\vec{r}\right|} = \frac{\rho_m c}{2\left|\vec{r}\right|\lambda}\left|\widehat{\mathbf{U}}(a)\right| \tag{12.99}$$

Once again, we see that the amplitude of the axial pressure field, p_{ax}, is given by our earlier expression for the monopolar acoustic transfer impedance, $\mathbf{Z_{tr}}$, of Eq. (12.22).

[17] The sinc function is also known as a zeroth-order spherical Bessel function of the first kind: $j_o(z) = (\sin z)/z$. For example, see M. Abramowitz and I. A. Stegun, *Handbook of Mathematical Functions with Formulas, Graphs, and Mathematical Tables,* National Bureau of Standards, Applied Mathematics Series #55, pg. 438.

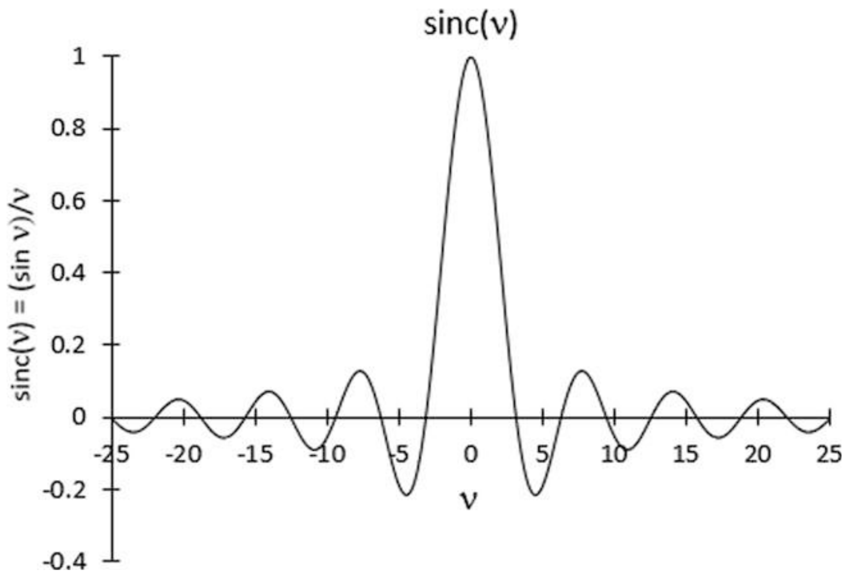

Fig. 12.31 Plot of $\mathrm{sinc}(\nu) = \sin(\nu)/\nu$ over the interval $-25 \leq \nu \leq +25$. For application to a continuous line source of length L, where $\nu = (kL/2)\sin\theta$

12.8 Baffled Piston

The most ubiquitous man-made electroacoustic source of sound is the baffled piston.[18] As will be demonstrated in this section, the radiation from a circular piston of radius, a, has a frequency dependence which will produce a uniform sound power that is fairly constant over a broad range of frequencies if the source of volume velocity (e.g., created by an electrodynamic loudspeaker) is operating in its mass-controlled region. The radiated sound is also reasonably omnidirectional if the circumference of the piston is less than the radiated wavelength (i.e., $2\pi a \lesssim \lambda$ or $ka \lesssim 1$).

As with the analysis of the continuous line array in Sect. 12.7, each differential surface element of a baffled piston can be treated as a differential pressure source to be summed by integration over the surface of the piston to produce the total radiation field produced by that piston. As demonstrated in the case of a simple source in the proximity of a rigid boundary, the differential source element on the surface of the baffled piston produces twice the far-field pressure of an equivalent source radiating omnidirectionally in an unbounded medium. If it is assumed that the amplitude and phase of the normal surface velocity of the piston, $|\widehat{v}_\perp| \equiv v_\perp$, is uniform over the entire piston,[19] then the differential element of volume velocity that corresponds to a differential element of the piston's area, dS, can be written as $\mathrm{d}\left|\widehat{\mathbf{U}}\right| = v_\perp \mathrm{d}S$.

[18] The moving-coil electrodynamic loudspeaker was invented by two Danish engineers, Peter Laurits Jensen and Edwin S. Pridham, in 1915.

[19] Since no piston is infinitely rigid, there will be some frequency above which the piston will no longer have a uniform perpendicular velocity, $v_\perp$, over the entire surface of the piston. Loudspeaker designers refer to this behavior as "cone breakup." In some clever designs that have the loudspeaker's "dust cap" bonded directly to the voice coil former (i.e., the hollow cylinder around which the coil is wound), the breakup of the cone at radii greater than the dust cap's radius is used to make the oscillation of the dust cap the primary sound source, since the cone breakup results in waves propagating along the cone which produces no net (integrated) volume velocity. For radiation from flexing disks, see M. Greenspan, "Piston radiator: Some extensions to the theory," J. Acoust. Soc. Am. **65**(3), 608–621 (1979).

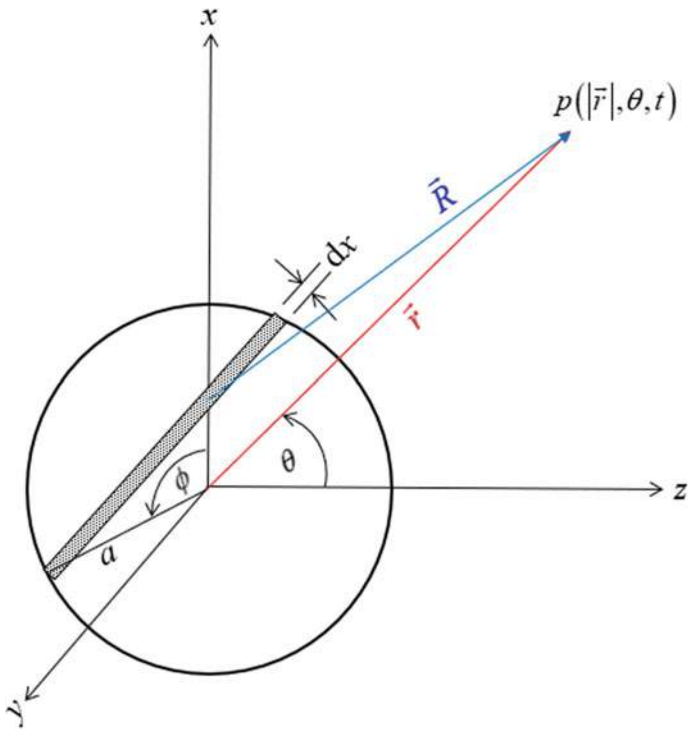

Fig. 12.32 Geometry used for calculation of the far-field pressure, $p\left(|\vec{r}|, \theta, t\right)$, produced by the vibration of a rigid piston of radius, a, that is oscillating with a velocity, $|\widehat{\mathbf{v}}_{\perp}|$, in an infinite baffle represented by the x-y plane

As shown in Fig. 12.32, the differential element of piston area is chosen to be a strip of height, dx, and width, $2a$ sin (ϕ), so d$S = 2a$ sin (ϕ) dx. The pressure radiated to the far field ($kr \gg 1$) by that differential strip is related to the differential volume velocity, $\mathrm{d}\left|\widehat{\mathbf{U}}(\phi)\right|$, that strip imparts to the adjacent fluid medium.

$$p\left(\left|\vec{R}\right|, \theta, t\right) = \Re e\left[j\frac{\rho_m ckv_{\perp}}{2\pi}\int_S \frac{e^{j\left(\omega t - k\left|\vec{R}\right|\right)}}{\left|\vec{R}\right|}\mathrm{d}S\right] \tag{12.100}$$

To evaluate this integral, an expression for the vector, $\vec{R}$, that connects a point on the surface of the piston to an observation point, $p\left(|\vec{r}|, \theta, t\right)$, in the far field is required.

$$\vec{R} = \left(|\vec{r}|\sin\theta - x\right)\widehat{e}_x + |\vec{r}|\cos\theta\ \widehat{e}_y = \left(|\vec{r}|\sin\theta - a\cos\phi\right)\widehat{e}_x + |\vec{r}|\cos\theta\ \widehat{e}_y \tag{12.101}$$

$\widehat{e}_x$ is the unit vector in the x direction and $\widehat{e}_y$ is the unit vector in the y direction. The magnitude of $\left|\vec{R}\right|$ in the far field can be expressed as the Pythagorean sum.

$$\begin{aligned}\left|\vec{R}\right| &= |\vec{r}|\sqrt{\left(\sin\theta - \frac{a}{|\vec{r}|}\cos\phi\right)^2 + \cos^2\theta} \\ &= |\vec{r}|\sqrt{1 - \frac{2a}{|\vec{r}|}\sin\theta\cos\phi - \left(\frac{a}{|\vec{r}|}\right)^2\cos^2\phi}\end{aligned} \tag{12.102}$$

In the far field, that distance can be approximated by the binomial expansion which is valid for $a/r \ll 1$.

$$\left|\vec{R}\right| \cong \left|\vec{r}\right|\left[1-\left(\frac{a}{\left|\vec{r}\right|}\right)\sin\theta\cos\phi\right] = \left|\vec{r}\right| - a\sin\theta\cos\phi \tag{12.103}$$

As usual, in the far field, we will ignore the effects of the variation in $\left|\vec{r}\right|$ for the amplitude of the spherical spreading but include it for the superposition of phases. Combining Eq. (12.103) with the expression for the differential element of area, $\mathrm{d}S = 2a \sin(\phi)\,\mathrm{d}x$, Eq. (12.100) can be re-written as an integral over dx.

$$p\left(\left|\vec{r}\right|,\theta,t\right) = \Re e\left[j\frac{\rho_m ckav_\perp}{\pi}\frac{e^{j(\omega t - k|\vec{r}|)}}{\left|\vec{r}\right|}\int_{-a}^{a} e^{jka\ \sin\theta\cos\phi}\sin\phi\,\mathrm{d}\phi\right] \tag{12.104}$$

The integral can be re-cast into a "standard form" by substituting the integration variable, $\mathrm{d}x = a\sin(\phi)\,\mathrm{d}\phi$, and changing the corresponding limits of integration.

$$p\left(\left|\vec{r}\right|,\theta,t\right) = \Re e\left[j\frac{\rho_m cka^2v_\perp}{\pi}\frac{e^{j(\omega t - k|\vec{r}|)}}{\left|\vec{r}\right|}\int_{0}^{\pi} e^{jka\ \sin\theta\cos\phi}\sin^2\phi\,\mathrm{d}\phi\right] \tag{12.105}$$

The complex exponential in the argument of the integral can be expressed as the sum of trigonometric functions: $e^{jx} = \cos(x) + j\sin(x)$. That integration over the imaginary component vanishes by symmetry leaving an integral definition of the J_1 Bessel function of the first kind [47]. The first three of these Bessel and Neumann functions were plotted in Figs. 6.8 and 6.9.

$$J_\nu(z) = \frac{(z/2)^\nu}{\pi^{1/2}\Gamma(\nu+½)}\int_0^\pi \cos(z\cos\phi)\sin^{2\nu}\phi\,\mathrm{d}\phi \tag{12.106}$$

The Gamma function, $\Gamma(\nu + ½)$, is a generalization of the factorial for non-integers, $z! = \Gamma(z+1)$. It can be evaluated by use of Euler's integral.

$$\Gamma(z) = \int_0^\infty t^{z-1}e^{-t}\,\mathrm{d}t \tag{12.107}$$

For $\nu = 1$ and $z = 1.5$, $2\,\Gamma(1.5) = \sqrt{\pi}$. Equations (12.106) and (12.107) produce an integral expression for $J_1(z)$.

$$J_1(z) = \frac{z}{\pi}\int_0^\pi \cos(z\cos\phi)\sin^2\phi\,\mathrm{d}\phi \tag{12.108}$$

Comparing Eq. (12.108) with Eq. (12.105), the magnitude of the far-field pressure of a baffled oscillating rigid piston can be expressed as the product of an axial pressure, $p_{ax}\left(\left|\vec{r}\right|\right)$, and the directionality, $H(\theta)$, in terms of the piston's volume velocity, $\left|\widehat{\mathbf{U}}\right| = A_{pist}v_\perp$.

$$\begin{aligned} p\left(\left|\vec{r}\right|,\theta\right) &= p_{ax}\left(\left|\vec{r}\right|\right)H(\theta) = \frac{\rho_m cka^2v_\perp}{2\left|\vec{r}\right|}\left[\frac{2J_1(ka\sin\theta)}{ka\sin\theta}\right] \\ &= \frac{\rho_m c}{\left|\vec{r}\right|\lambda}\left|\widehat{\mathbf{U}}\right|\left|\frac{2J_1(\nu)}{\nu}\right| \quad \text{for}\ \ \nu = (ka)\sin\theta \end{aligned} \tag{12.109}$$

The final expression demonstrates again that the monopole's acoustic transfer impedance, $\mathbf{Z_{tr}}$, provides the magnitude of the axial (maximum) far-field pressure in terms of the volume velocity of the

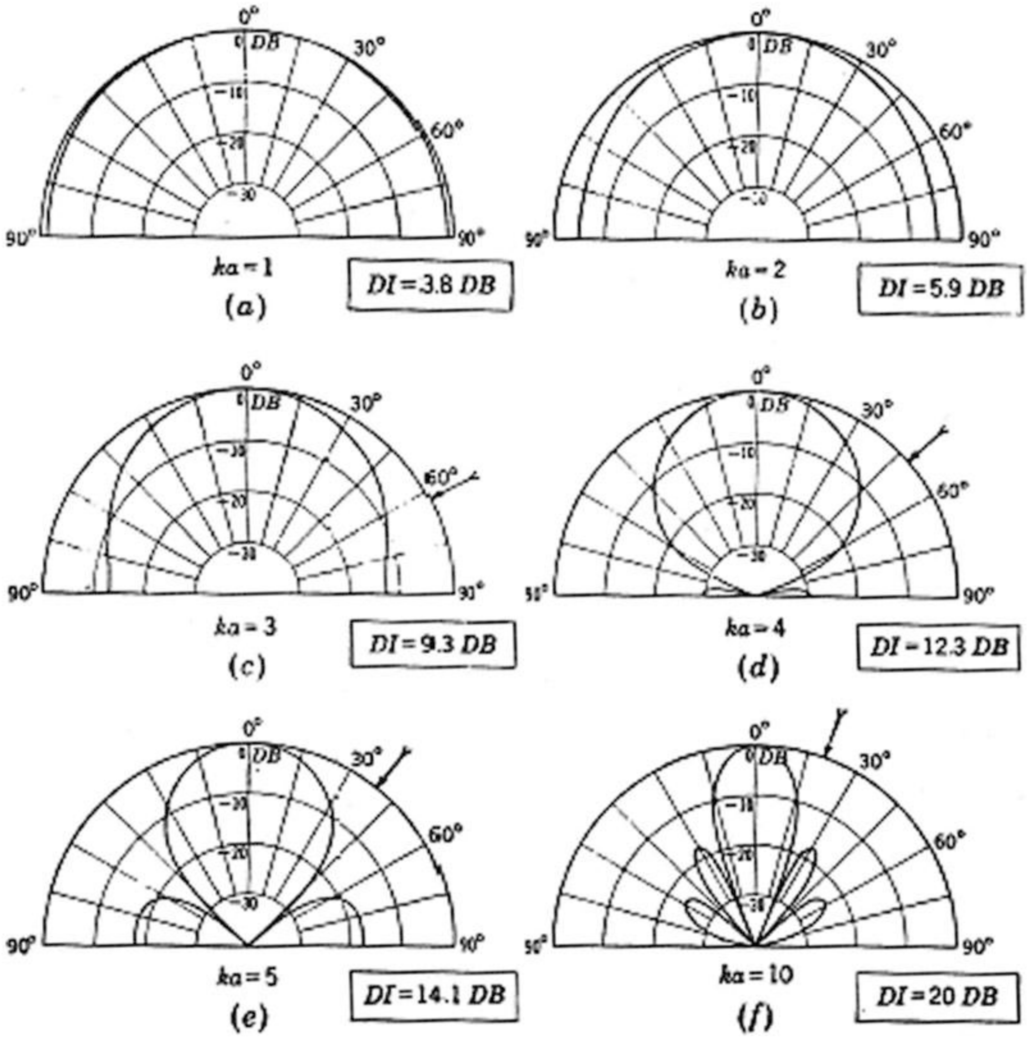

Fig. 12.33 Beam patterns for a baffled, rigid, circular piston as a function of $ka = 2\pi a/\lambda$ from $ka = 1$ (nearly omnidirectional) to $ka = 10$. The relative strength of the first side lobe, 31° from the polar axis, for $ka = 10$, is −17.6 dB. The angle that the first nodal cone makes with the polar axis for $ka = 10$ is $\theta_1 = 22.5°$. The directivity, D, is the reciprocal of $H^2(\theta)$ integrated over all solid angles (see Sect. 12.8.2). The directivity index, (DI), is 10 $\log_{10}(D)$. The arrows in (c) through (f) show one direction of DI = 0 [49]

source, although the expression is twice that of Eq. (12.22) since the source is baffled and therefore radiates into a *semi-infinite half-space*. Several directional patterns, $|H(\theta)| = 2\ J_1(v)/v$, for various values of $1 \leq (ka) \leq 10$, where $v = ka \sin\theta$, are plotted in Fig. 12.33.

The relative amplitudes of the lobes are determined by the values of the maxima of $|H(\theta)| = 2\ J_1(v)/v$. Fortunately, the derivative of $J_1(v)/v$ is related to $J_2(v)$ [48].

$$\left(\frac{1}{z}\frac{\mathrm{d}}{\mathrm{d}z}\right)^k \{z^{-\nu}J_\nu(z)\} = (-1)^k z^{-\nu-k} J_{\nu+k}(z);\quad k = 0, 1, 2\ldots$$
$$\Rightarrow\quad \frac{\mathrm{d}}{\mathrm{d}z}\left(\frac{J_1(z)}{z}\right) = -\frac{J_2(z)}{z} \tag{12.110}$$

The first *minor lobe* (i.e., $\theta \neq 0°$) will occur for values of J_2 $(j_{2,n}) = 0$. This extremum occurs at $j_{2,1} = 5.13562$, where $2J_1$ $(j_{2,1})/j_{2,1} \cong 0.132$. That first minor lobe will occur in the direction where $ka \sin\theta = j_{2,1} = 5.13562$. Since the Taylor series expansion of $J_1(z)$ about the origin is $J_1(z) = z/2 + z^3/16 - \ldots$, the value of $2J_1(0)/0 = z/z = 1$. Therefore, the ratio of the amplitude of the main lobe to the amplitude of the first minor lobe is 20 $\log_{10}$ (0.132) $= -17.6$ dB.

For a baffled rigid piston operating at a frequency such that $ka = 10$ as shown in Fig. 12.33(f), the first side lobe will be directed along $\theta_{n=1} = \sin^{-1}$ $(5.136/ka) = 31°$, and the first null will occur at $\theta_{m=1} = \sin^{-1}$ $(3.83/ka) = 22.5°$. The second null visible in Fig. 12.33(f) for the case of $ka = 10$ occurs at $\theta_{m=2} = \sin^{-1}$ $(7.016/ka) = 44.6°$. Since $j_{1,3} = 10.17347$, the apparent null at 90° in Fig. 12.32(f) for the $ka = 10$ example is not exactly zero. The second side lobe for $ka = 10$ occurs at $j_{2,2} = 8.417$ so $\theta_{n=2} = \sin^{-1}$ $(8.417/ka) = 57.3°$.

12.8.1 Rayleigh Resolution Criterion

To reiterate the results of the previous section, the peaks and nulls of the directionality can be determined in the same way as was done for the discrete line array and continuous line source, except that the values of the arguments, $j_{1,m}$, of the $J_1(j_{1,m})$ Bessel function corresponding to the nulls and extrema are not simply integer multiples of π or π/2. The nulls occur for directions, θ_{m}, where $ka \sin \theta_{\mathrm{m}} = j_{1,m}$. Values of $j_{1,m}$ are available in mathematical tables [50], and some for small values of n and m are provided in Appendix C. The first null occurs for $j_{1,1} = 3.83171$. Subsequent zero crossings occur at $j_{1,2} = 7.01559$, $j_{1,3} = 10.17347$, $j_{1,4} = 13.32369$, etc.

$$\sin\theta_1 = \frac{3.83}{ka} = \frac{3.83}{2\pi}\left(\frac{\lambda}{a}\right) = 0.61\left(\frac{\lambda}{a}\right) = 1.22\left(\frac{\lambda}{D}\right) \qquad (12.111)$$

The result at the far-right expression in Eq. (12.111) is known in optics as the *Rayleigh resolution criterion*. It is used as the minimum observable diffraction-limited angular separation between two objects viewed through an aperture of diameter $D = 2a$.[20] We can consider two sound sources located in the far field that are separated by some angle, θ, with one source located at $+\theta/2$ and the other at $-\theta/2$. If the "piston" is the baffled diaphragm of a microphone, then the argument of the $|H(\theta)|$ is determined by $v = ka \sin\theta$, when substituted into Eq. (12.109). The ability to resolve two sources of equal amplitudes that are separated by some angle, θ, is illustrated in Fig. 12.34.

12.8.2 Directionality and Directivity

It is possible to quantify the directivity of an extended source by comparing the axial pressure at some distance, r, in the far field, with a simple source that radiates the same time-averaged power omnidirectionally. That ratio is called the directivity, D.

[20] In Rayleigh's own words, "This rule is convenient on account of its simplicity and it is sufficiently accurate in view of the necessary uncertainty as to what exactly is meant by resolution." J. W. Strutt (Lord Rayleigh), "Investigations in optics, with special reference to the spectroscope," Phil. Mag. **8**(49), 261–274 (1879). See §1. Resolving, or Separating, Power of Optical Instruments; also *Collected Works* (Dover, New York, 1963), Vol. I, pp. 415–418.

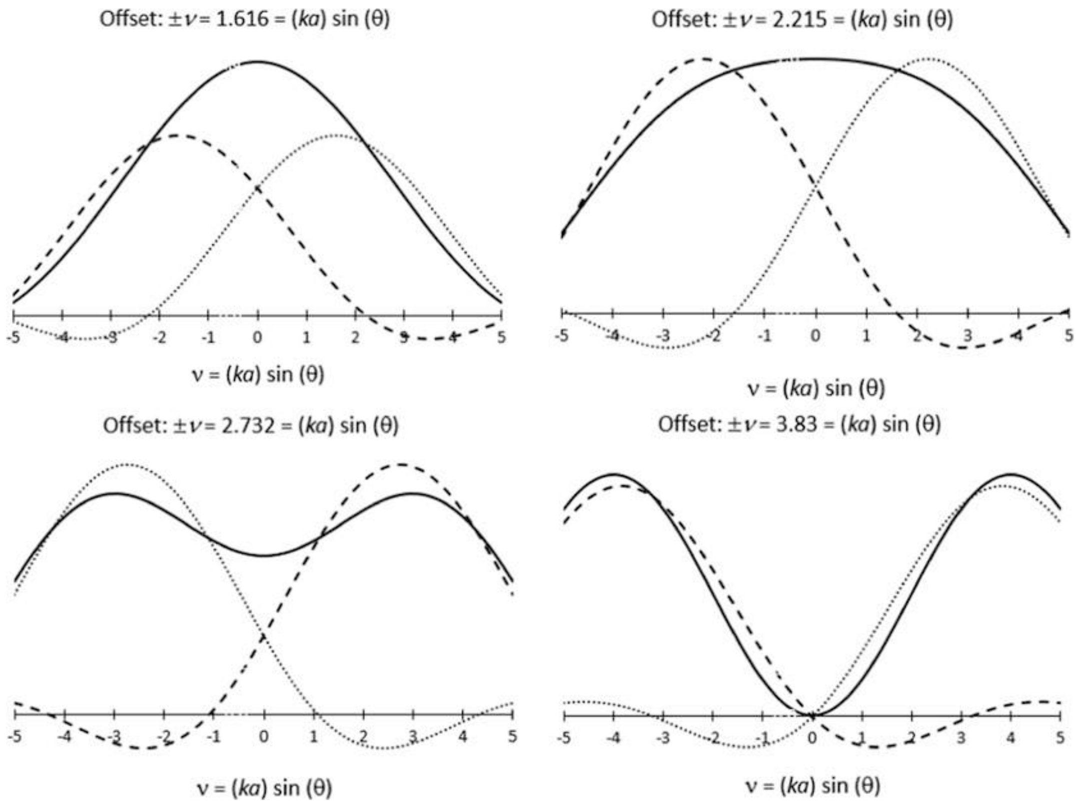

Fig. 12.34 Illustration of the "Rayleigh resolution criterion" showing the image of two sources that have different angular separation. The dotted and dashed lines represent the received amplitude of individual signals located at $\pm\theta = sin^{-1}(\nu/ka)$ as function of $\nu = (ka)\sin\theta$. The solid line is the sum of their signals. (*Above*) These two peaks are not resolved. For $\nu = 1.616$, the two peaks cross at their -3 dB points, and for $\nu = 2.215$, the two peaks cross at their -6 dB points. Those appear as a single object although the apparent angular width has been increased over the width of the individual sources. (*Below*) These two peaks are resolved. For $\nu = 2.732$, the two peaks cross at their -10 dB points, and for $\nu = 3.83$, the two peaks cross where both have zero amplitude

$$D = \frac{\langle I_{ax}(r)\rangle_t}{\langle I_{omni}(r)\rangle_t} = \frac{|\widehat{\mathbf{p}}_{\mathbf{ax}}(r)|^2}{|\widehat{\mathbf{p}}_{\mathbf{omni}}(r)|^2} \tag{12.112}$$

The total power radiated by the directional source requires the integration of the $H^2(\theta)$ over all *solid angle*, dΩ.

$$\mathrm{d}\Omega \equiv \frac{\mathrm{d}S}{r^2} \tag{12.113}$$

This is similar to the two-dimensional definition of angle as the arc length divided by the radius which, though dimensionless, is given the unit "radian." Solid angle is also dimensionless and its unit is the *steradian*. If Eq. (12.113) is integrated over the entire surface of a sphere of any radius, the solid angle has its maximum value of 4π steradians.

The total time-averaged power, $\langle\Pi\rangle_t$, radiated by a sound source can be obtained by integrating the square of the far-field pressure over all solid angle.

$$\langle \Pi \rangle_t = \frac{1}{2\rho_m c} \int_{4\pi} p_1^2(r,\theta,\phi)\, r^2 \mathrm{d}\Omega = \frac{r^2 |\mathbf{p_{ax}}(r)|^2}{2\rho_m c} \int_{4\pi} H^2(\theta,\phi) \mathrm{d}\Omega \tag{12.114}$$

For a compact omnidirectional source, $H_{omni}(\theta) = 1$, so that the total time-averaged radiated power, $\langle \Pi_{omni} \rangle_t = 4\pi r^2 |\widehat{\mathbf{p}}_{\mathbf{omni}}|^2 / 2\rho_m c$. The ratio of the on-axis time-averaged intensity, $\langle I_{ax}(r) \rangle_t$, as expressed in Eq. (12.112), to the on-axis time-averaged intensity of an monopole with equivalent source strength, $\langle I_{omni}(r) \rangle_t$, produces an expression that relates the square of the directionality, $H^2(\theta)$, to the *directivity*, D.

$$D = \frac{|\widehat{\mathbf{p}}_{\mathbf{ax}}(r)|^2}{|\widehat{\mathbf{p}}_{\mathbf{omni}}(r)|^2} = \frac{4\pi}{\int_{4\pi} H^2(\theta,\phi) \mathrm{d}\Omega} \tag{12.115}$$

This integral can be evaluated for a continuous line source of directionality, $|H(\theta)|$, given by Eq. (12.98), if the integration variable is changed from $\mathrm{d}\Omega$ to $\mathrm{d}v = (½)kL \cos(\theta)\mathrm{d}\theta$.

$$D_{line} = \frac{(kL/2)}{\int_0^{kL/2} \left(\frac{\sin v}{v}\right)^2 \mathrm{d}v} \tag{12.116}$$

If the line array is very long (i.e., $kL \gg 1$), then the limit of integration can be taken to infinity since v^2 in the denominator of the integral will limit the result since $|\sin v| \leq 1$. The definite integral is available in standard integral tables [51].

$$\int_0^\infty \frac{\sin^2 ax}{x^2} \mathrm{d}x = \frac{a\pi}{2} \tag{12.117}$$

For long line arrays, substitution of Eq. (12.117) into Eq. (12.116) produces an approximate directionality for a long line array.

$$\lim_{kL \to \infty} D_{line} = \frac{kL}{\pi} = \frac{2L}{\lambda} \tag{12.118}$$

For a rigid circular piston in a baffle, substitution of $|H(\theta)|$ from Eq. (12.109) into Eq. (12.115) produces an integral that is similar to Eq. (12.116).

$$D_{piston} = \frac{4\pi}{\int_0^{\pi/2} \left[\frac{2J_1(ka\sin\theta)}{ka\sin\theta}\right]^2 2\pi \sin\theta \;\mathrm{d}\theta} = \frac{(ka)^2}{1 - \frac{J_1(2ka)}{ka}} \tag{12.119}$$

The low-frequency directionality of the baffled piston can be obtained from the series expansion of $J_1(x) = (x/2) + (x^3/16) + \ldots$

$$\lim_{ka \to 0} \left[D_{piston}\right] = 2 \tag{12.120}$$

This result for a baffled piston in the low-frequency limit is reasonable because we have assumed that the baffle restricts radiation only into a semi-infinite half-space. Because of the oscillatory behavior of $J_1(2ka)$ and the fact that $|J_1(x)| < 0.582$, the high-frequency limit of the piston's directionality can be calculated directly from Eq. (12.119).

$$\lim_{ka \to \infty} \left[D_{piston}\right] = (ka)^2 \tag{12.121}$$

For many applications, it is useful to express the directivity as a *directivity index*, DI, that is often also referred to as the *array gain*.

$$DI = 10 \log_{10} D \tag{12.122}$$

The polar plots of piston directionality in Fig. 12.33 also include the directivity index reported in decibels.

12.8.3 Radiation Impedance of a Baffled Circular Piston

At the surface of the baffled rigid piston, the fluid exerts a force that has components that are both in-phase with the piston's velocity (manifested as a mechanical radiation resistance) and that are in-phase with the piston's acceleration (manifested as hydrodynamic mass loading). It was fairly easy to derive the hydrodynamic mass for a compact spherical source resulting in Eq. (12.15) and the radiation resistance in Eq. (12.16), and somewhat more difficult to do the same for a dipole to obtain the results in Eq. (12.55). The equivalent calculations for a baffled rigid piston are more complicated, since Bessel functions are required, [52], but result in an expression for the resistive component that is proportional to a function, $R_1(2ka)$, and for the reactive component that is proportional to another function, $X_1(2ka)$. The mechanical impedance, $\mathbf{Z_{mech}}$, is evaluated at the surface of the oscillating piston.

$$\mathbf{Z_{mech}} \equiv \frac{\widehat{\mathbf{F}}}{\widehat{\mathbf{v}}_\perp} = \rho_m c \pi a^2 [R_1 + jX_1] \tag{12.123}$$

The resistive coefficient of the mechanical reactance, R_1, is related to the J_1 Bessel function.

$$\begin{aligned} R_1(2ka) &= 1 - \frac{2J_1(2ka)}{2ka} \quad \text{for all values of } (2ka) \\ &\cong \frac{(2ka)^2}{2\cdot 4} - \frac{(2ka)^4}{2\cdot 4^2 \cdot 6} + \frac{(2ka)^6}{2\cdot 4^2\cdot 6^2\cdot 8}\cdots \quad \text{for } (2ka) < 2 \end{aligned} \tag{12.124}$$

For small values of $2ka$, R_1 $(2ka \ll 1) = (ka)^2/2$. At high frequencies, R_1 $(ka \gg 1)$ approaches one, as shown by the solid line in Fig. 12.34, so the piston radiates plane waves, as expected.

The quadratic dependence of the radiation resistance on frequency, $R_1 \propto \omega^2$, for small values of $2ka$, is responsible for the large frequency bandwidth of direct-radiating loudspeakers. Electrodynamic speakers are typically operated at frequencies above their natural (free-cone) resonance frequency and are therefore operated in their mass-controlled regime. As such, their acceleration is constant, but the velocity of their speaker cone, $v_\perp$, is decreasing linearly with frequency: $|\widehat{\mathbf{v}}_\perp| \propto \omega^{-1}$. Since the time-averaged radiated power is proportional to the square of that velocity, $\langle \Pi_{rad} \rangle = (½)(\rho_m c\pi a^2)R_1|\widehat{\mathbf{v}}_\perp|^2$, $\langle \Pi_{rad} \rangle_t$ it is frequency independent, as long as the piston remains rigid at those frequencies and $2ka \le 1$.

The reactive function can be expressed as an integral that is related to the first-order Struve function, $H_1(2ka)$ [53].

$$\begin{aligned} X_1(2ka) &= \frac{2H_1(2ka)}{(2ka)} = \frac{4}{\pi}\int_0^{\pi/2} \sin(2ka\cos\alpha)\sin^2\alpha \; d\alpha \\ &\cong \frac{2}{\pi} - J_0(2ka) + \left(\frac{16}{\pi} - 5\right)\frac{\sin(2ka)}{2ka} + \left(12 - \frac{36}{\pi}\right)\frac{1 - \cos(2ka)}{(2ka)^2} \\ &\cong \frac{4}{\pi}\left[\frac{2ka}{3} - \frac{(2ka)^3}{3^2\cdot 5} + \frac{(2ka)^5}{3^2\cdot 5^2\cdot 7} - \cdots\right] \quad \text{for } (2ka) < 2 \end{aligned} \tag{12.125}$$

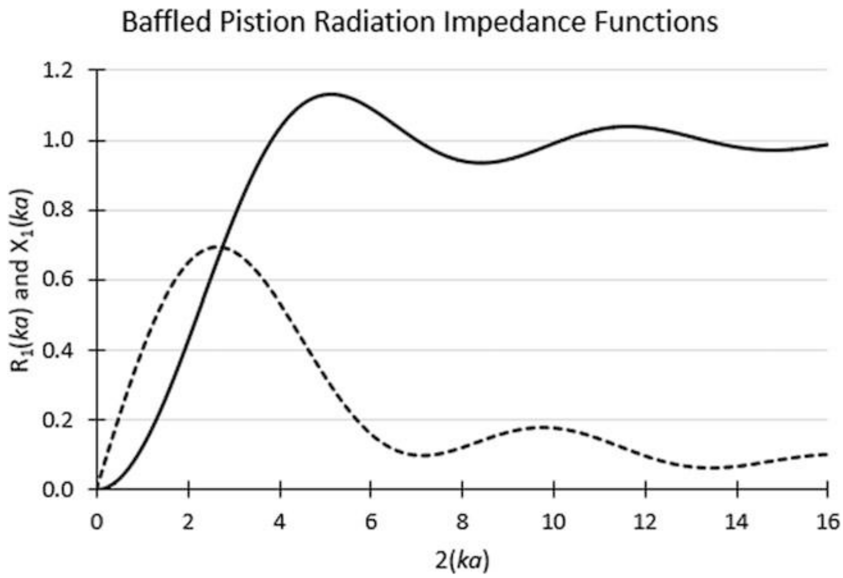

Fig. 12.35 Functional dependence of the real (resistive) mechanical reactance, $R_1(2ka)$, as a *solid line*, and imaginary (reactive), $X_1(2ka)$, as a *dotted line*, plotted as a function of $2(ka)$, for a rigid, baffled piston. For small values of $2(ka)$, the initial slope of $R_1(2ka)$ is proportional to $(2ka)^2$, and the initial slope of $X_1(2ka)$ is proportional to $2(ka)$

The middle version is valid to within about ±½% for all values of (2 ka) [54]. The frequency variation of both components of the baffled piston's radiation impedance functions, R_1 and X_1, is plotted in Fig. 12.35.

For small values of 2 ka, $X_1(2ka \ll 1) = 8(ka)/3\pi$. As before, we expect the reactive part of the mechanical radiation impedance, $\rho_m c\pi a^2 X_1$, to represent the baffled piston's (near-field) hydrodynamic mass loading. From Eqs. (12.123) and (12.125), the force corresponding to this mass reactance can be written in terms of the fluid density times a cylindrical volume of fluid that has the same area as the piston, πa^2, and a height, $\ell_{Baffled} = (8a/3\pi) \cong 0.85\ a$, if we let $\omega = ck$. As shown below, for the baffled piston, $m_{eff} = \rho_m(8/3)a^3$ when $(2ka) < 1$.

$$\begin{aligned}\lim_{2ka\to 0}[\mathbf{F}_{\mathbf{Reactive}}] &= j\Im\mathrm{m}[\mathbf{Z}_{\mathbf{mech}}v_\perp] = j\rho_m c\pi a^2 \frac{8}{3\pi}(ka)\\ &= j\omega\left(\rho_m \pi a^2 \cdot \frac{8a}{3\pi}\right) = j\omega m_{eff} = j\omega\rho_m\left(\frac{8}{3}a^3\right)\end{aligned} \tag{12.126}$$

That hydrodynamic mass was added to the head mass of the Tonpilz transducer in Sect. 4.3.1. We postulated an effective mass correction (without proof!), in Sect. 8.5.2, when we added an empirical "effective length" correction, $L_{eff} = L + 1.24a$ from Eq. (8.53), to the physical length, L, of the neck of our 500 mL Helmholtz resonators.

According to the results of Eq. (12.126), 0.85a of the empirical correction, 1.24a, was due to the effective mass of the fluid that leaves the neck and enters the compliance (volume) if that junction can be modeled as a "baffled piston." That leaves 0.39a that would be the effective mass for the fluid in the other end of the neck.

That total correction was about 15% smaller in Sect. 8.6.11 where we used DeltaEC to produce the necessary neck length correction because DeltaEC included the frequency reduction due to thermoviscous effects in the neck and the compliance: $L_{eff} = L + 1.08\ a$.

It is a good idea to compare the results for the radiation impedance of the baffled piston plotted in Fig. 12.35 with those of the simple spherical source (monopole) that were plotted in Figs. 12.5 and 12.6. Both exhibit an initially quadratic increase in the real part and an initially linear increase in the imaginary part. Both have the imaginary part decreasing toward zero, and both have the real part approaching one for large ka.

Because the spherical source can only produce radial fluid velocities, there is no “waviness” in either R_1 of X_1 at higher values of ka in Figs. 12.5 and 12.6. For the baffled piston, at larger values of ka, pressure created by the motion of one portion of the piston can interfere with other parts, thus producing the oscillations of R_1 of X_1 seen in Fig. 12.35.

12.8.4 Radiation Impedance of a Baffled Rectangular Piston*

A similar derivation for the radiation impedance of a rigid baffled rectangular piston can be made by integrating the differential element of volume velocity that corresponds to a differential element of the piston’s area, dS, written as $\mathrm{d}\left|\widehat{\mathbf{U}}\right| = v_\perp \mathrm{d}S$, using the geometry of Fig. 12.32, but for a region of width, w, and height, h. If w and h are not too different, the radiation resistance and reactance can be written for such a rectangular piston [55].

$$R_1 + jX_1 = \begin{cases} \dfrac{k^2}{16}\left(w^2 + h^2\right) + j\dfrac{8k}{9\pi}\dfrac{w^2 + wh + h^2}{w + h} & \text{for } kw \ll 1 \text{ and } kh \ll 1 \\ 1 + j\dfrac{8}{\pi k(w + h)} & \text{for } kw \gg 1 \text{ and } kh \gg 1 \end{cases} \tag{12.127}$$

As with the baffled circular piston, for large kw and kh, the radiation resistance is just that for plane waves, as it was in Eq. (12.124) for the circular piston. Also, if we consider a square piston with $w = h$, then in the small kh limit, in analogy with Eq. (12.123), $m_{eff} = \rho_m(4h/3\pi)A_{pist}$ for the square piston which is almost equal to $m_{eff} = \rho_m(8a/3\pi)A_{pist}$ for the circular piston since equal values of A_{pist} would make $h = a\sqrt{\pi} \cong 1.77a$ for the square piston.

12.8.5 On-Axis Near-Field Pressure from a Circular Baffled Piston*

This exploration of radiation from a baffled, rigid piston will conclude with an examination of the boundary between the near and far fields. Based on the earlier investigations of extended sources with dimensions that are larger than the wavelength of sound, we expect interference effects. These are also observed with piston sources when the frequency of sound corresponds to $ka > 2\pi$.

We can estimate the distance along the axis of the piston where the transition is observed from near-field (interference) to the far-field (spherical spreading) behavior. In the far field, a smooth monotonic decrease in the acoustic pressure amplitude is expected that varies inversely with distance from the surface of the piston according to $p_{ax}(r)$ in Eq. (12.109).

Figure 12.36 provides a diagram of a piston with the arc of a circle centered at a point a distance, R, from the surface of the piston. If we have chosen R such that the distance from the edge of the piston to the point at R is $R + \lambda$, then we can think of the piston as being separated into a central disk where the path length differences, Δ, are less than or equal to $\lambda/2$ and an outer ring with $\lambda/2 \leq \Delta \leq \lambda$. The radius of the inner disk can be set to $b = a/\sqrt{2}$. If the surface areas of the ring, $A_{ring} = \pi(a^2 - b^2)$, and the disk, $A_{disk} = \pi b^2$, are roughly equal (they are exactly equal if $b = a/\sqrt{2}$), then the pressure generated at R due

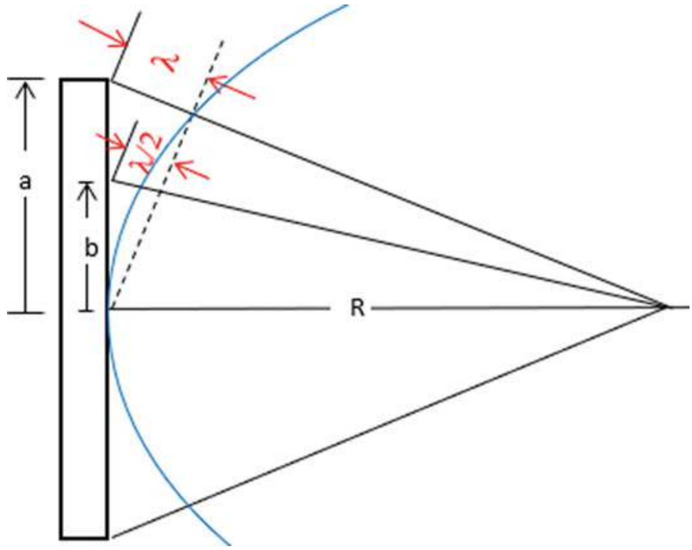

Fig. 12.36 A simple geometric construction that can be used to estimate the distance from the surface of a piston where we expect the last destructive interference to occur on the axis of the piston. The rigid, baffled piston has a radius, *a*, that is significant when compared to the wavelengths of sound radiated by the piston. The inner radius, *b*, is chosen so that the areas of the inner disk and outer ring are equal. The radius of the orange arc is *R*

to the volume velocity created by the inner disk will cancel the pressure generated at *R* due to the volume velocity created by the outer ring.

From the geometry of Fig. 12.36, the value of *R* beyond which there can be no further interference, R_{min}, can be calculated using the right triangle of height *a*, base *R*, and hypotenuse, $R + \lambda$.

$$(R+\lambda)^2 = R^2 + a^2 \tag{12.128}$$

Expansion of the binomial and cancellation of R^2, common to both sides, produces the required value of R_{min}.

$$\frac{2R_{min}}{\lambda} = \frac{a^2}{\lambda^2} - 1 \quad \Rightarrow \quad R_{min} = \frac{a^2}{2\lambda} - \frac{\lambda}{2} \tag{12.129}$$

Destructive interference along the axis can only occur for pistons with $ka = 2\pi a/\lambda > 2\pi$. The distance, R_{min}, which determines the farthest axial null is $r_1 \cong a^2/2\lambda = a(ka)/4\pi$. Examination of Fig. 12.36 shows that this approximation becomes more accurate as *ka* increases in accordance with Eq. (12.129).

As we move away from the piston, past *R*, we initially expect the axial pressure amplitude to increase then eventually decrease due to the $1/r$ behavior of $p_{ax}(r)$ in the far field, as described in Eq. (12.109). A more detailed calculation gives the location, r_1, of the peak in the axial response beyond *R* [56].

$$r_1 = \frac{a^2}{\lambda} - \frac{\lambda}{4} \quad \Rightarrow \quad \frac{r_1}{a} = \frac{(ka)}{2\pi} - \frac{\pi}{2(ka)} \tag{12.130}$$

Figure 12.37 provides plots of the axial pressure, $p_{ax}(r)$, for three values of $2\pi \le ka \le 8\pi$, and the caption provides the corresponding values for r_1. Depending upon the accuracy required for prediction of the far-field behavior, it is generally a good policy to make the start of the far field twice r_1, although some choose to define r_1 as the start of the far field. Figure 12.37 provides the same representation for

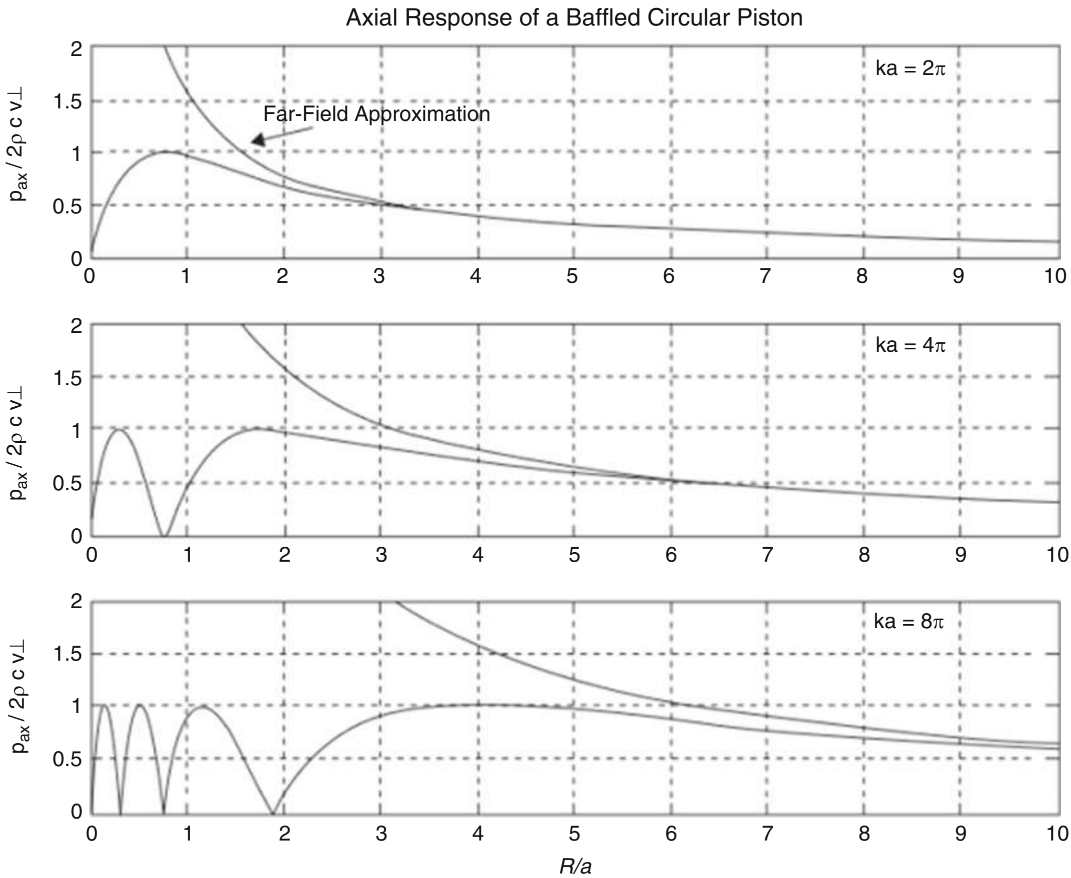

Fig. 12.37 On-axis pressure for three rigid, baffled pistons with $2\pi \leq ka \leq 8\pi$. As the radius of the piston, a, becomes larger than the wavelength of sound. $\lambda = 2\pi/k$, there are more opportunities for constructive and destructive interference from various parts of the piston to modulate the sound pressure amplitude along the axis at distances smaller than $R \cong a^2/\lambda$. According to Eq. (12.129), for $ka = 2\pi$, $r_1 = 3a/4$, for $ka = 4\pi$, $r_1 = 7a/4$, and for $ka = 8\pi$, $r_1 = 15a/4$. The smooth line shows the far-field pressure that varies inversely with distance, r, from the piston. [Graphs courtesy of A. A. Atchley]

the variation in axial pressure in the near field but uses a logarithmic representation of the x axis so that the rapid oscillations of the axial pressure near the piston for large ka can be resolved. In both figures, the number of maxima in the near field axial interference pattern is roughly equal to the number of wavelengths required to span one piston radius.

A good approximation of the peak pressure amplitude from the surface of the piston out to the far field which removes the interference effects is provided below and is shown in Fig. 12.38 as the dotted line labeled "MM" [57].

$$|p_{ax}(r)| = \frac{p_{ax}(0)}{\sqrt{1 + (r/a)^2}} \tag{12.131}$$

The dotted line labeled "M" in Fig. 12.37 is represented by a similar expression [58].

$$|p_{ax}(r)| = \frac{2p_{ax}(0)}{\sqrt{1 + (2r/a)^2}} \tag{12.132}$$

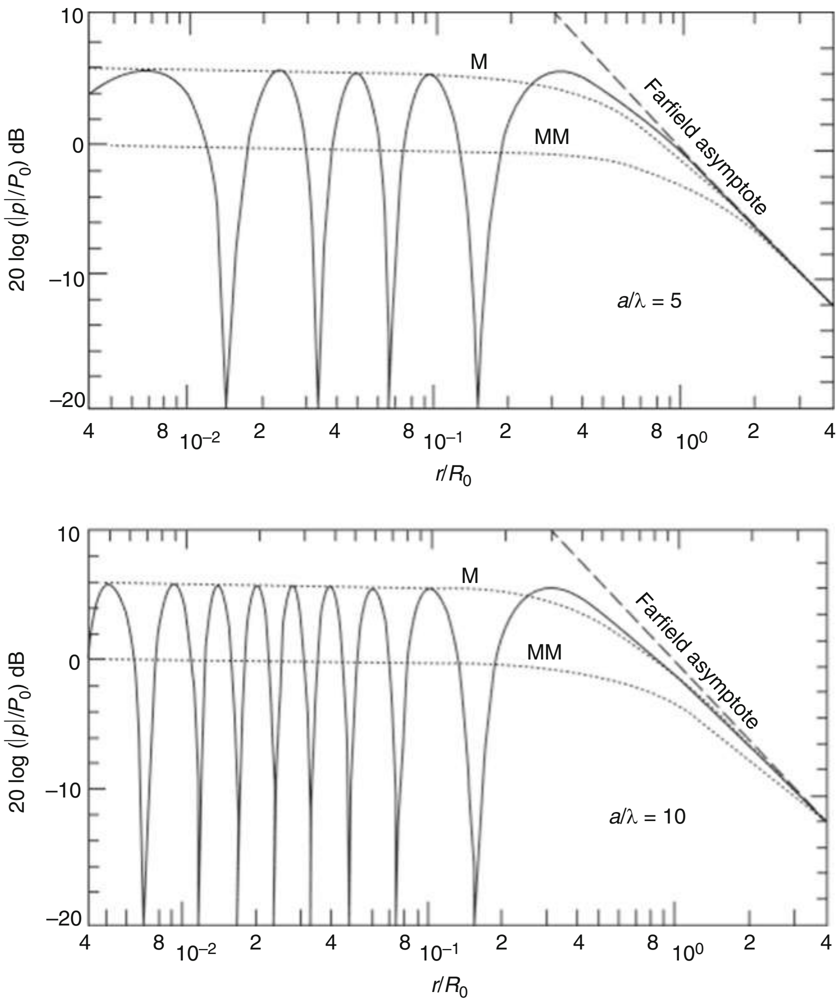

Fig. 12.38 Plot of the log of the amplitude of the on-axis pressure from a rigid, baffled piston vs. the log of the distance from the surface of the piston scaled by the radius of the piston, $R_o = a$. In this figure, the distance is plotted on a logarithmic axis to make the spacing of the interference pattern appears roughly constant. In this log-log representation, the far-field asymptote is the straight (dashed) line with slope -1. The upper plot is for $ka = 10\pi$ ($a/\lambda = 5$), and the lower plot is for $ka = 20\pi$ ($a/\lambda = 10$). The dotted lines, "M" and "MM," are useful for approximation of the near-field pressure amplitudes [59]

These approximations have been useful in the design of nonlinear underwater sound sources (see Sect. 15.3.3), where a significant amount of nonlinear mixing takes place in the near field.

12.9 Radiation Impedance of an Unbaffled Piston

The "effective mass" added to the surface of a circular baffled piston due to the fluid loading was calculated exactly in Sect. 12.8.3 and produced a hydrodynamic load that was equivalent to the mass of fluid contained in a cylindrical volume that had the same area as the piston, πa^2, and a height of $\ell_{Baffle} = (8a/3\pi) \cong 0.85\ a$, if $ka \ll 1$. That correction was not enough to account for the experimental result in Sect. 8.5.2 that required $\ell_{Flask} = 1.24\ a$, as expected, because there was additional kinetic energy due to the entrained flow at both ends of the Helmholtz resonator's neck. The end of the neck that enters the compliance should have a flow field that is similar to that of the baffled piston but the other end is unbaffled; the entrained gas that oscillates at that open end can have a component that moves "backward" without the constraint imposed by the baffle.

It turns out that the exact solution for the radiation impedance of an unbaffled circular piston is considerably more difficult than the solution for the baffled piston, and an exact result for radiation from the end of a tube of infinite length with thin, rigid walls was not obtained until 1948 [60].[21]

$$\lim_{ka\to 0}\left[\frac{h}{a}\right] = \frac{1}{\pi}\int_0^{\infty}\frac{1}{x^2}\ln\frac{1}{2I_1(x)K_1(x)}\,dx = 0.6133$$
$$\Rightarrow\quad \ell_{L\&S} = 0.6133a \quad \text{if}\ \ ka \ll 1 \tag{12.133}$$

$I_1(x)$ and $K_1(x)$ are the modified Bessel functions (of complex argument) that were plotted in Fig. 6.20. The variation in ℓ/a as a function of (ka) for the unbaffled piston is plotted in Fig. 12.40. Until then, the unbaffled end correction was based on experimental measurements on closed-open pipes, as illustrated schematically in Fig. 12.39. Rayleigh found $\ell/a \cong 0.6$ using organ pipes with and without a flange [61].[22]

Rather than attempt an exact derivation of the result in Eq. (12.133) for the unbaffled piston, it will be easier to argue that the radiation from the unbaffled piston, at small values of ka, should be similar to the radiation from the spherical source (i.e., a compact monopole), analyzed in Sect. 12.2.1, since the body of the closed-open resonator in Fig. 12.39 does not exclude much volume from the infinite space surrounding the piston.

Since it is the volume velocity produced by the unbaffled piston that determines the sound radiation, we can ask what should be the radius, b, of the "equivalent" spherical source to provide the same radiating area as the piston of radius, a: $A_{pist} = \pi a^2 = A_{sphere} = 4\pi b^2$. This equivalence requires that $b = a/2$ resulting in an equivalent hydrodynamic mass, m_{eff}, for the monopole equivalent.

$$m_{eff} = 3\rho_m V_{sphere} = 3\rho_m(4\pi/3)(a/2)^3 = (½)a\left(\pi a^2\right) = (a/2)A_{pist} \tag{12.134}$$

By that argument, for an unbaffled piston, the effective length correction is $\ell_{Unbaffled} \cong 0.5a$. That result is 18% less than the exact result in Eq. (12.133), and both results are less than $\ell_{Baffled} = 0.85a$ for the baffled circular piston.

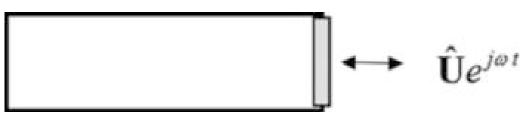

Fig. 12.39 Schematic representation of a closed-open pipe. Motion of the fluid oscillating at the open is represented by the piston shown as the dotted rectangle that produces a sinusoidal volume velocity, $\hat{\mathbf{U}}e^{j\omega t}$

[21] The solution was sufficiently difficult that one of the authors was the theoretical physicist, Julian Schwinger (1918–1994), who shared the 1965 Nobel Prize in Physics for quantum electrodynamics with Sin-Itiro Tomonaga and Richard Feynman. The other, Harold Lavine, continued his career as a mathematics professor at Stanford University, specializing in integral equations.

[22] Rayleigh also reports a "careful experimental determination" made by Blaikley [Phil. Mag. **7**, 339, (1879)] that used a brass tube of 5.3 cm diameter that had one end submerged in water to produce the adjustable distance for the closed end and five tuning forks for frequencies between 254 Hz and 707 Hz. The length of the tube above the water was adjusted to be co-resonant with the forks and resulted in an experimental effective length at the open end of $\ell = (0.576 \pm 0.014)\ a$.

Fig. 12.40 Plot of the end correction for radiation from an unbaffled pipe in terms of the pipe's radius: ℓ/a for $0 \geq ka < 4$ from Levine and Schwinger [60]

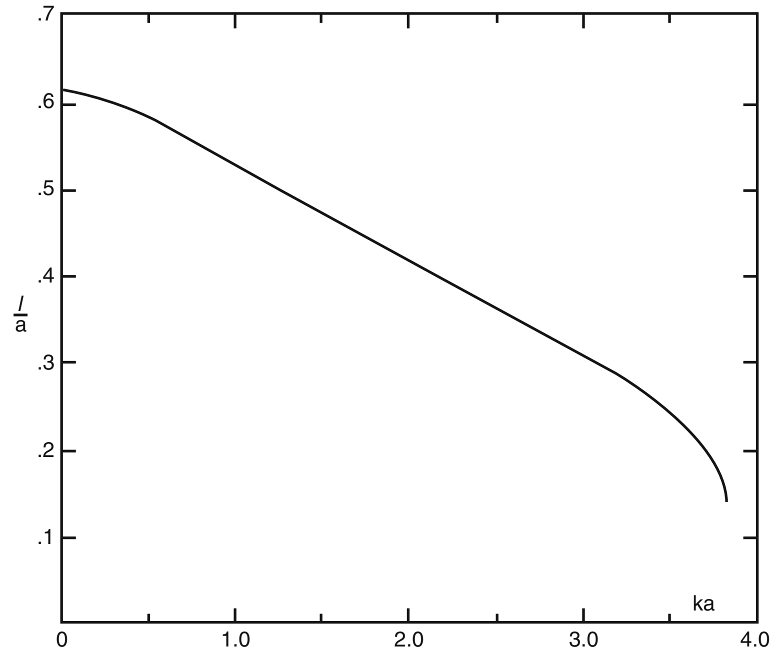

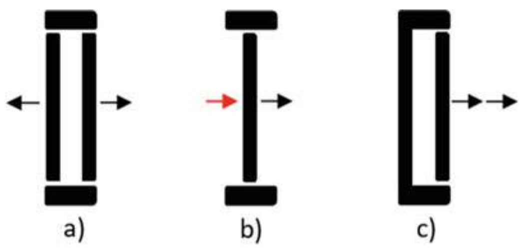

Fig. 12.41 The flow field from an unbaffled piston is constructed from the superposition of two anti-phase baffled pistons in (**a**) plus the field of a rigid disk oscillating along its axis in (**b**) to produce the required flow in (**c**), since disk's oscillations cancel the rearward piston and doubles the forward piston's flow. (Figure courtesy of D. A. Brown)

Before leaving this topic, it is worthwhile mentioning the calculation of the unflanged end correction made by Lev Gutin a decade before the publication of the Levine and Schwinger result. Gutin used the superposition two oppositely phased baffled pistons plus the translational oscillations of a rigid disk to produce the flow field of an unbaffled piston as shown schematically in Fig. 12.41 [62].

Gutin's calculation resulted in an effective length correction in the small *ka* limit of $\ell_{Gutin} = 0.636\ a$. This is only 3.7% larger than today's accepted value of $\ell_{L\ \&\ S} = 0.6133\ a$.

Bringing this back to the measured effective length for the 500 ml boiling flask used to study the frequency of a Helmholtz resonator in Sect. 8.5.2, we see that simply adding a baffled correction to one end of the resonator's neck and an unbaffled correction to the other end produces a "theoretical" correction of $\ell = [(8/3\pi) + 0.6133]a \cong 1.462a$. That is greater than the measured value of $\ell = 1.24a$, even in the absence of the resonance frequency reduction due to the inclusion of thermoviscous losses in the DeltaEC model of Fig. 8.27, which resulted in a correction of only $\ell_{DeltaEC} = 1.07\ a$. Those frequency measurements in Fig. 8.17 were clearly within the small *ka* limit: $ka \cong 0.05 \ll 1$.

In conclusion, it is fair to say that the kinetic energy of the gas oscillations at the end of a duct that is either baffled or unbaffled requires the addition of some hydrodynamic mass to account for the flow at the exits of such ducts. It is also fair to say that the effective length correction required to incorporate the entrained flow is sensitive to the actual circumstances that influence those entrained flows. James Mehl studied the duct end correction using a boundary-integral equation and examined the effects of the rounding of duct edges and the effects of finite chamber size and provides an extensive list of references to articles that have studied such *end corrections* [63].

12.10 Linear Superposition

Chapter 12 is the longest chapter in this textbook. Although its title is "Radiation and Scattering," it could easily have been entitled "Multiple Applications of Linear Superposition." It started by examining the sound radiated by a "compact" source of oscillatory volume velocity in an approximate model that demonstrated that the periodic insertion and removal of fluid could only affect the acoustic pressure variations within a "causality sphere" whose volume was limited by the speed of sound. Going beyond that perspective, it was possible to obtain an exact solution for the spherically symmetric waves produced such a sound source by solving the wave equation in an infinite, homogeneous, and isotropic three-dimensional fluid medium and assuming that the volume velocity was produced by a sphere whose radius underwent a harmonic variation as a function of time.

The solution for a compact monopole source also permitted the calculation of the complex radiation impedance at the source's surface. We used the imaginary component of that radiation impedance to demonstrate that it was necessary for the source to overcome the inertia of the surrounding fluid. Quantifying that fluid inertia facilitated the calculation of the simple harmonic oscillations of a gas bubble in a liquid. The real component of that radiation impedance was used to calculate the time-averaged acoustical power that such a simple monopole source would radiate.

Armed with the behavior of a compact monopole, we used linear superposition to examine the behavior of various collections of such monopoles, both discrete (e.g., to examine sources near reflecting surfaces and linear arrays) and continuous (e.g., to integrate the effects of infinitesimal sources over the surface area of a pulsating tube or the surface of an oscillating piston).

The most significant superposition was that of two sources that were separated by a small fraction of a wavelength, $kd \ll 1$, and were 180° out-of-phase, thus producing a "compact dipole." That significance was due to the fact that the flow produced by such a dipole was equivalent to the flow produced when a rigid sphere (or other solid object) makes translational oscillatory excursions through an otherwise stagnant fluid.

The compact monopole and the compact dipole provided a basis for the calculation of sound that is scattered by inhomogeneities in a fluid that are small compared to the wavelengths of the sound scattered by such inhomogeneities. Sound waves in fluids are a consequence of the competition between the fluid's compressibility and mass density. Monopoles let us calculate the sound scattered from compressibility contrasts, and dipoles did the same for scattering from density contrasts.

As was the case so many times in this textbook, very simple systems examined in limits that permitted calculation of their acoustical behavior have provided models that can guide our intuition and create a vocabulary for the understanding of a much greater range of systems. A stage with hundreds of loudspeakers in dozens of clusters, as shown in Fig. 12.1, can make perfect sense from the right perspective.

Talk Like an Acoustician

Causality sphere	
Monopole	Directivity index
Compact source	Dipole
Compactness criterion	Dipole strength
Rayleigh resolution criterion	Pressure gradient microphone
Acoustic transfer impedance	Ribbon microphone
Specific acoustic impedance	Cardioid directionality
Characteristic impedance	Semi-infinite half-space
Radiation reactance	Minor lobe
Radiation resistance	Solid angle
Effective mass	Steradian
Hydrodynamic mass	Density contrast
End correction	Compressibility contrast
Laplace's formula	Differential scattering cross section
Source strength	Total scattering cross section
Far field	Rayleigh scattering
Near field	Mean field approximation
Bipole	Void fraction
End-fire direction	Array gain
Broadside direction	Beam steering
Directionality factor	End-fire array
Baffled source	Shaded array
Directivity	End corrections

Exercises

1. **Big sphere at high frequency**. A pulsating sphere operates at a frequency such that $ka \gg 1$ with a radius, $r(t) = \Re e\left[\hat{\boldsymbol{\xi}} e^{j\omega t}\right]$, so the amplitude of the radial velocity at the surface of the sphere is $|\hat{\mathbf{v}}_r| = \omega\left|\hat{\boldsymbol{\xi}}\right|$ and $\left|\hat{\boldsymbol{\xi}}\right| \ll a$. Calculate ($a$) the radiated pressure amplitude, (b) particle velocity amplitude, and (c) the time-averaged intensity as a function of the distance from the center of the sphere, along with (d) the total time-averaged radiated power.
2. **Spherical (monopole) source in air**. A compact source in air radiates 10 mW of time-averaged acoustical power at 400 Hz in air at 20 °C with $p_m = 100$ kPa. At a distance of 0.5 m from the center of the source, calculate (a) the radiated time-averaged intensity, (b) the amplitude of the acoustic pressure, (c) the amplitude of the particle speed and its phase relative to the acoustic pressure, and (d) the peak-to-peak particle displacement of the air.
3. **Radiation from a point source**. A spherical point source is radiating sinusoidally in air; the resultant radiation propagates through free space. The acoustic power of this source is 1000 W at 1000 Hz.
   (a) *Amplitude*. Calculate the time-averaged intensity, the sound pressure amplitude, and the acoustic particle velocity at 1.0 and 10.0 meters from the center of the source.
   (b) *Phase*. Calculate the phase angle (in degrees) between the sound pressure and particle velocity at distances of 0.5, 1.0, and 10.0 meters from the source.
4. **Spherical spreading**. You are assigned to check the quality of a new anechoic room that has been built by your employer. You decide to test the room by making a measurement of the pressure detected by a microphone as a function of the separation between the microphone and the sound

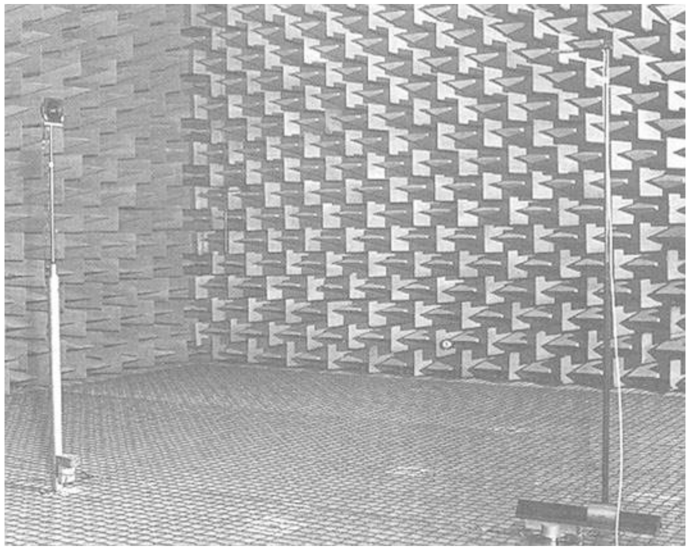

Fig. 12.42 Sound source (loudspeaker) and microphone located in an anechoic chamber

source that is an ordinary loudspeaker in a room as shown in Fig. 12.42. You do not have a priori knowledge of the distances between the *acoustic centers* of the microphone and speaker and the points on those two transducers between which you are measuring their physical separation, d.
To compensate for this uncertainty, you define the effective acoustic separation, $d_{ac} = d + a$, to be the measured physical separation, d, plus some (possibly frequency-dependent) length, a, that may be positive or negative.
If the room is truly anechoic, then the decrease in microphone output voltage, $V(d)$, as a function of source-receiver physical separation, $d + a$, should exhibit spherical spreading, indicated by Eq. (12.135), where B is a constant and a is an adjustable parameter that accounts for the fact that the measured distance and the distance between the acoustic centers of the source and receiver might be different from their physical separation, d.

$$V(d) = \frac{B}{d+a} \tag{12.135}$$

Transform this equation so that the data can be plotted in a way that represents the spherical spreading as a straight line vs. the measured (physical) separation, d, between the source and microphone, to produce a value of a that can be determined from the slope of the line, its intercept, or both the slope and the intercept. Write an expression for a in terms of the slope and/or intercept of your transformed equation.

5. **Swim bladder resonance**. Many fish species use an air-filled sac, known as a "swim bladder," to control their buoyancy. Fish also use "constrictor muscles," shown schematically in Fig. 12.43, to excite motion of that organ to generate sound, usually consisting of a train of repetitive pulses that are typically in the frequency range of 100 Hz to 1.0 kHz, and also to receive sounds, since Eq. (12.77) demonstrates that the air-filled bladder will compress much more than the surrounding water in response to an impinging sound wave [64].
If such a fish is swimming at a depth of 5 m below the water's surface, what would have to be the volume of the swim bladder, V_{swim}, so that it would be resonant at 500 Hz? To simplify the calculation, it is reasonable to assume that the mass density of fish flesh is roughly equivalent to that

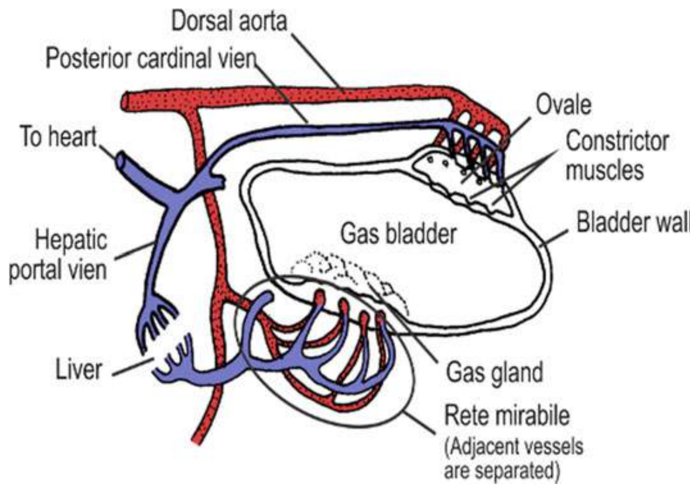

Fig. 12.43 Swim bladder anatomy

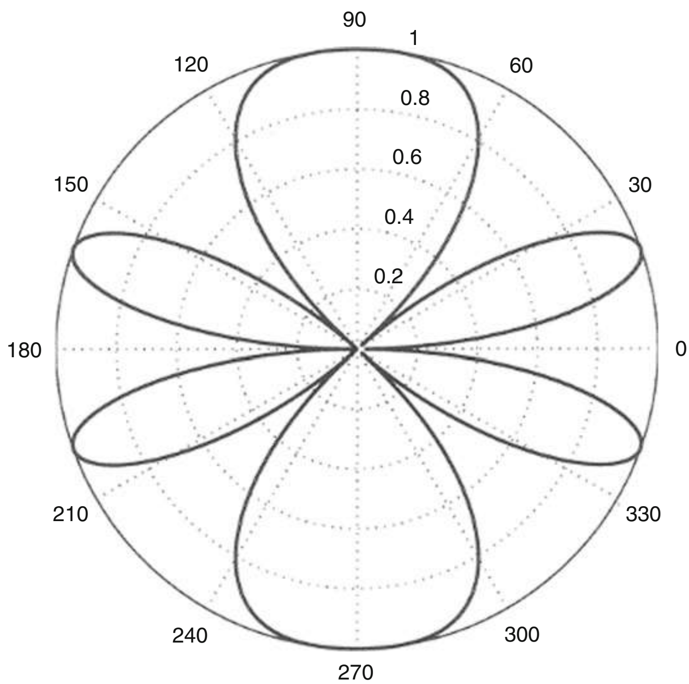

Fig. 12.44 Directional pattern for two sound sources of equal amplitude separated by a distance, *d*, between their centers

of the surrounding water, so the hydrodynamic mass loading would be approximately the same as assumed for a bubble in Eq. (12.29). Although the swim bladder is not spherical, its equivalent radius, $a_{eff} = (3V_{swim}/4\pi)^{1/3}$, still makes $(ka_{eff}) \ll 1$, so its approximately prolate spheroidal shape will not create a substantial difference between the resonance frequency of the bladder and an equivalent spherical volume [8].

6. **Train in the tunnel**. A train traveling at 60 mph enters a long tunnel with the same cross-sectional area and frontal shape as the train. Assume both gas leakage around the train and friction between the train and tunnel walls are negligible. Estimate the amplitude of the pressure wave created in the tunnel. [*Hint*: One approach might be to think about the speed of the wave front and the speed of the train (piston), then apply that trusty adiabatic gas law.]

7. **Far-field radiation pattern**. The far-field radiation pattern, shown in Fig. 12.44, was created by two simple (compact) sound sources of equal source strength separated by a distance, d. The two sources are aligned along the vertical axis (the 90° – 270° axis) of the figure and radiate with equal amplitude.
   (a) *Bipole or Dipole*. What is the phase difference between the two sources in degrees?
   (b) *Separation.* What is the value of kd for this pair of sources?
8. **Four-element line array**. The far-field radiation pattern shown in Fig. 12.45 was created by four simple (compact) sound sources that are oscillating in-phase and are separated by a distance, d, along a straight line. The total length of the array is $L = 3d$. What is the value of d, expressed in terms of the wavelength of sound that is being radiated?
9. **Continuous line source**. One quadrant of the far-field directional radiation pattern produced by a uniform line source is shown in Fig. 12.46. The uniform line array is oriented along the 90°– 270° axis. Nodal cones are shown making angles with the vertical axis (i.e., $\theta_p = 0°$) of approximately 15°, 32°, and 52°.

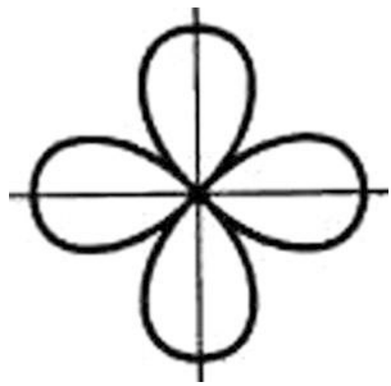

Fig. 12.45 Directional pattern for a four-element line array

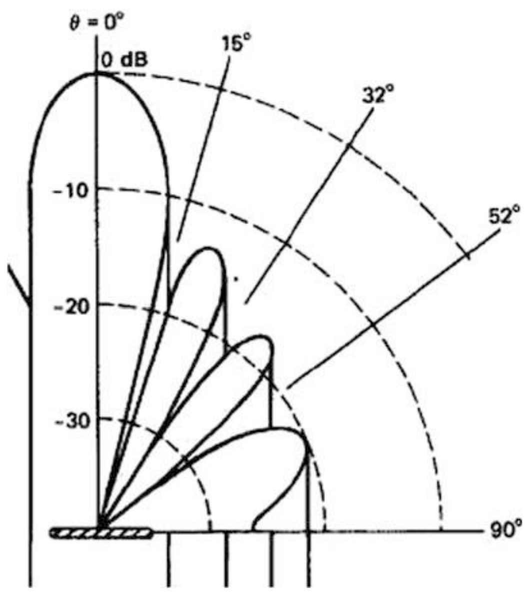

Fig. 12.46 Directional pattern of a continuous line array

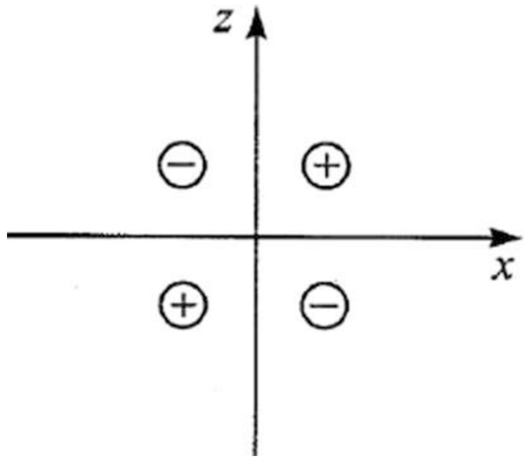

Fig. 12.47 Quadratic quadrapole

Determine the dimensionless length of the line array, $2\pi L/\lambda = kL$, where L is the physical length of the array and λ is the wavelength of the sound radiated by the uniform line source.

10. **Quadratic quadrupole radiation impedance.**[23] A quadratic quadrupole is a compact collection of four simple sources. As shown in Fig. 12.47, one pair are in-phase ($\phi = 0°$) as indicated by the $\oplus$ symbol, and the other pair have $\phi = 180°$ out-of-phase with the first pair as indicated by the $\ominus$ symbol. The radius of each simple source is a. The radiation impedance for such a quadrupole is given in Eq. (12.136) for $ka < 1$.

$$\mathbf{Z}_{\mathbf{quad}} = \rho_m c \frac{4\pi a^2 (ka)^6}{1215} - j\omega \rho_m \frac{4\pi a^3}{45} \left[1 + \frac{(ka)^2}{9} + \frac{4(ka)^4}{81} + \cdots \right] \tag{12.136}$$

(a) *Impedances*. There are three types of impedances that are commonly used in acoustics. Is the impedance in Eq. (12.136) a characteristic, mechanical, or acoustical impedance?

(b) *Effective radiation mass*. In the limit of sources whose circumference is significantly smaller than one wavelength (i.e., $2\pi a \ll \lambda$), express the "effective mass" of that collection of four oscillating simple sources in terms of mass of the fluid displaced by one spherical source with radius, a.

11. **Long line array**. A line array of simple sources is designed so that $kL = 50$.
   (a) *Major lobes.* How many maxima does it produce for $0° \le \theta \le 90°$?
   (b) *Nodal lines.* How many nodal lines (in the two-dimensional representation) are there within the same angular interval?
   (c) *Beam width.* Find the full angular beam width, $\Delta\theta$, of the lobe centered at $\theta = 0°$ if the full beam width is defined as the angle between the nodal directions that limit the central lobe.
   (d) *Other beam width definitions*. What is the angular width of the beam if that beam width corresponds to a ratio of the main lobe amplitude to the down 3 dB, 6 dB, 10 dB, and 20 dB full angular widths: $\Delta\theta_{-3\text{dB}}$, $\Delta\theta_{-6\text{dB}}$, $\Delta\theta_{-10\text{dB}}$, and $\Delta\theta_{-20\text{dB}}$.

---

[23] There are also "linear quadrupoles" that consist of a double-strength source at the center and two sources with phase opposite to the central source, all arranged in a straight line:

$\ominus \qquad \oplus\oplus \qquad \ominus.$

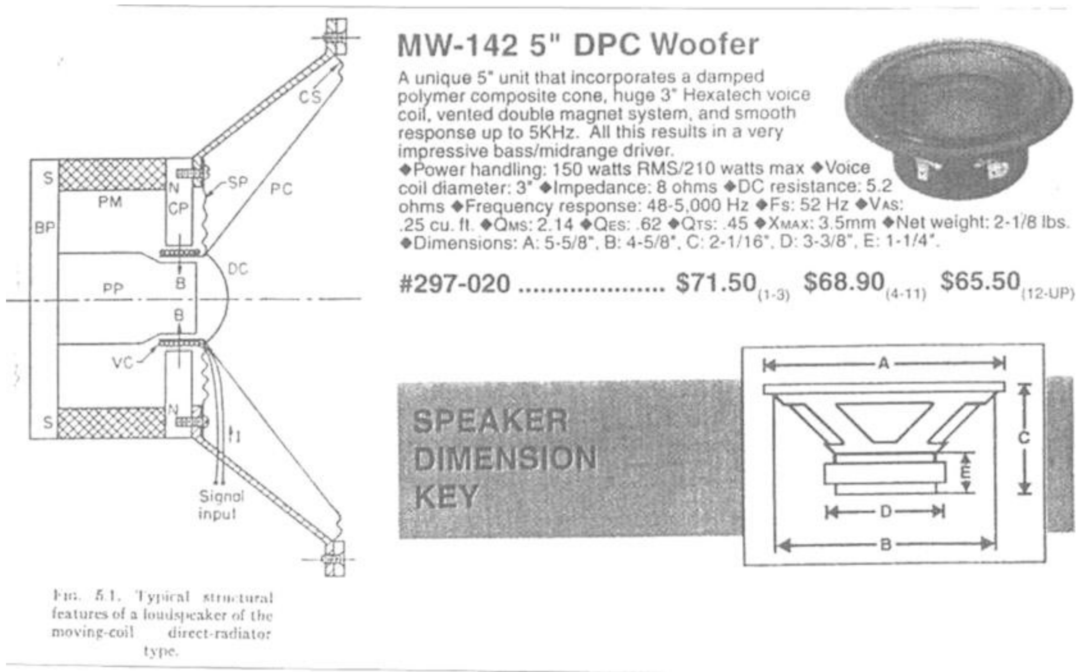

Fig. 12.48 (*Left*) Cross-section of a conventional moving-coil direct radiator type loudspeaker showing the suspension (CS), the spider (SP), speaker cone (PC), dust cap (DC), and voice coil (VC). The radial magnetic field (B) is produced by the permanent magnetic material (PM) with north (N) and south (S) magnetic polarity, the central pole piece (PP), the backplate (BP), and the front pole piece (CP). Figure from Hunt [65]. (*Right*) Catalog listing a 5" Morel model MW-142 loudspeaker

(e) *Lobe amplitude ratio*. What is the ratio of the amplitude of the peak of the first side lobe to the peak of the central lobe? Report that ratio in dB.

12. **Piston angular null**. A baffled circular piston of radius, a, radiates sound at frequency, ω. What is the smallest angle, θ_1, with respect to the piston's axis, at which the radiated sound pressure is zero. Express your answer in terms of the wavenumber, $k = \omega/c$, and the radius of the piston.
13. **"Flat" frequency range for an electrodynamic loudspeaker**. The speaker shown in Fig. 12.48 (rsight) has a moving mass $m_o = 11.8$ g, a suspension stiffness, $K = 1440$ N/m, a mechanical resistance, $R_m = 1.9$ kg/s, and a force factor, $(B\ell) = 7.1$ N/A. The effective diameter of the piston is $2a = 11.0$ cm. Assume it is mounted in an infinite baffle like that shown in Fig. 8.37.

(a) *Free-cone resonance.* Calculate the free-cone resonance frequency, f_o, of this speaker.

(b) *Forced motion.* Assume the speaker is mounted in an infinite baffle and it is driven by a sinusoidal current, $I(t) = 1.41 \cos(\omega t)$ amperes. The force on the piston produced by this current flowing through the speaker's voice coil is $F(t) = (B\ell)I(t)$. Plot the magnitude and phase (with respect to the driving current) of the volume velocity, $\widehat{\mathbf{U}}(f)$, created by the piston from 10 Hz to 3500 Hz. Use logarithmic axes for both frequency and volume velocity but plot phase angle on a linear scale, preferably on the same graph. You may neglect any fluid loading of the piston (e.g., effective hydrodynamic mass) in all parts of these calculations.

(c) *Effective air mass.* What is the hydrodynamic mass of the air that is being accelerated by the front face of the piston for $ka < 1$ if $p_m = 100$ kPa and $c = 20\ °C$.[24] Compare this result to the speaker's moving mass, m_o.

(d) *Radiated power.* The (mechanical) radiation resistance, $\rho_m c\pi a^2 R_1(2ka)$, can be used to convert the volume velocity calculated in part (*b*) to the time-averaged radiated power, $\langle \Pi_{rad} \rangle_t = (½)\Re e[\mathbf{Z_{mech}}]\left|\widehat{\mathbf{U}}/A_{pist}\right|^2$. Plot the radiated power in dB *re:* 1 watt vs. the log of frequency from 10 Hz to 3500 Hz.

(e) *"Flat" region of the speaker's far-field radiation.* Over what range of frequencies is the speaker's time-averaged radiated power constant to within ±2 dB? Provide the limiting frequencies, f_{min} and f_{max}, as well as the ±2 dB frequency bandwidth, $\Delta f_{\pm 2\text{dB}} = f_{max} - f_{min}$.

14. **Party balloon**. A young child is in the back seat of an automobile that is initially at rest will all of the windows closed. In the hand of the child's outstretched arm is a string that is attached to a helium-filled balloon. If the car accelerates forward, does the balloon get closer to the child or to the driver? Is your answer consistent with Eq. (12.71) and with the Equivalence Principle of Einstein's Theory of General Relativity?

15. **Thermoacoustic sound source suspension and dipole radiation**. The device shown in Fig. 12.49 represents the DeltaEC model (segments numbered 1 through 11) of a nuclear-powered thermoacoustic engine (resonator) [66]. It is only free to move in the vertical direction as it is suspended between two identical springs, each with stiffness, K. The resonator is a rigid body with a total mass of 0.35 kg. Heat produced by nuclear fission of enriched ^{235}U maintains a standing acoustic wave within the resonator that causes the gas mixture (80% helium, 20% argon), at a mean pressure of $p_m = 2.0$ MPa, to oscillate back and forth within the resonator. The gas resonance occurs at the fundamental, half-wavelength, frequency, $f_1 = 1588$ Hz.

(a) *Resonator length.* If the mean temperature of the gas mixture in the resonator is 30 °C, what is the length of the resonator?

(b) *Force*. The oscillatory motion of the gas causes a reaction force on the ends of the resonator. (Think of the gas in the resonator bouncing back and forth between the resonator end caps of segments #1 and #11.) If the moving gas has an effective mass, $m = 6 \times 10^{-4}$ kg, according to the DeltaEC model, the effective (peak) velocity of that effective mass is 16 m/s. What is the magnitude of the peak force that the oscillatory gas applies to the resonator?

(c) *Static deflection*. If the total mass of the resonator is 0.35 kg, what is the stiffness of one of the two identical springs, K, so that the resonator's weight in a gravitational field of acceleration, $g = 9.8$ m/s^2, causes the resonator to drop by only 1.0 mm?

(d) *Suspension resonance frequency*. Using the stiffness calculated above in part (c), what is the natural frequency of the mass-spring system (ignoring the gas motion), remembering that both springs contribute to the restoring force?

(e) *Resonator displacement.* Using the force calculated in part (a), what is the resonator's peak-to-peak oscillatory displacement?

(f) *Radiated dipole power.* Using the displacement calculated in part (*e*) and the resonator's length calculated in part (a), what is the acoustic power radiated by the oscillatory

[24] With the loudspeaker mounted in an infinite baffle, there would also be an equal hydrodynamic mass due to the sound radiated into the space on the other side of the baffle. With the same speaker mounted in a sealed box, the rear of the cone would feel the stiffness of the gas within the box. For this problem, we will ignore that rear radiation.

Fig. 12.49 Schematic representation of an elastically suspended thermoacoustic resonator

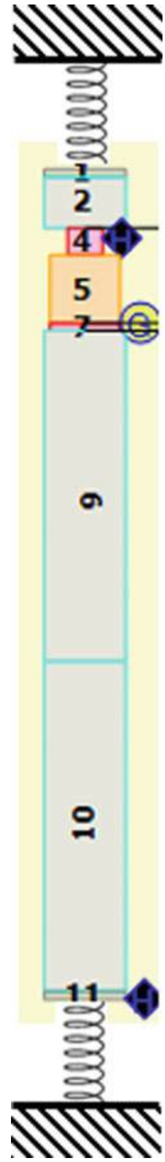

displacement of the cylindrical resonator if each of the resonator's end caps has an area, $A_{end} = 2.8\ \text{cm}^2$, and the surrounding fluid is water?

References

1. R. Weir, J. Garcia, D. Healy, R. Wickersham, Large room acoustics versus music. J. Acoust. Soc. Am. **58**, S1 (1975)
2. B. Kinsman, *Wind Waves: Their Generation and Propagation on the Ocean Surface* (Prentice-Hall, Englewood Cliffs, 1965)
3. L.D. Landau, E.M. Lifshitz, *Fluid Mechanics*, 2nd edn. (Butterworth-Heinemann, Boston, 1987). See §15; ISBN:0-7506-2767-0. ISBN:0-7506-2767-0

4. V. Mangulis, Relation between the radiation impedance, pressure in the far field, and baffle impedance. J. Acoust. Soc. Am. **36**, 212–213 (1964)
5. P.M. Morse, *Vibration and Sound*, 2nd edn. (McGraw-Hill, New York, 1948). See §27. Reprinted by the Acoust. Soc. Am., 1995; ISBN:0-88318-876-7
6. L.D. Landau, E.M. Lifshitz, *Fluid Mechanics*, 2nd edn. (Butterworth-Heinemann, Boston, 1987). §61; ISBN:0-7506-2767-0
7. M. Minnaert, Musical air bubbles and the sounds of running water. Philos. Mag. **16**, 235–248 (1933)
8. M. Strasberg, The pulsation frequency of nonspherical gas bubbles in liquids. J. Acoust. Soc. Am. **25**(3), 536–537 (1953)
9. T.F. Argo IV, P.S. Wilson, V. Palan, Measurement of the resonance frequency of single bubbles using a laser Doppler vibrometer. J. Acoust. Soc. Am. **123**(6), EL212–EL125 (2008)
10. K.W. Commander, A. Prosperetti, Linear pressure waves in bubbly liquids: comparison between theory and experiments. J. Acoust. Soc. Am. **85**(2), 732–746 (1989)
11. C. Devin Jr., Survey of thermal, radiation, and viscous damping of pulsating air bubbles in water. J. Acoust. Soc. Am. **31**(12), 1654–1667 (1959)
12. O.B. Wilson, *An Introduction to the Theory and Design of Sonar Transducers* (Peninsula, Los Altos, 1989). ISBN:978-0932146229
13. R.L. Prichard, Mutual acoustic impedance between radiators in an infinite rigid plane. J. Acoust. Soc. Am. **32**(6), 730–737 (1960)
14. S. Hanish, *A Treatise on Acoustic Radiation, Vol. IV – Mutual Radiation Impedance and Other Special Topics* (Naval Research Lab, Washington, DC, 1987)
15. T. Young, The Bakerian Lecture [1803]: experiments and calculations relative to physical optics. Phil. Trans. R. Soc. London **94**, 1–16 (1804)
16. A. Howie, J.E. Ffowcs-Williams, Preface. Phil. Trans. R. Soc. London **A360**, 805–806 (2002)
17. J. Cui, M.F. Hamilton, P.S. Wilson, E.A. Zabolotskaya, Bubble pulsations between parallel plates. J. Acoust. Soc. Am. **119**(4), 2067–2072 (2006)
18. A.D. Pierce, *Acoustics: An Introduction to Its Physical Principles and Applications* (McGraw-Hill, New York, 1981), pp. 482–486; ISBN:0-07-049961-6. Also reprinted by the Acoustical Society of America, 3rd ed. 2019; ISBN 978-3-030-11214-1
19. W.R. Smythe, *Static and Dynamic Electricity* (McGraw-Hill, London, 1939). §5.08
20. J.D. Jackson, *Classical Electrodynamics* (Wiley, New York, 1962). See Prob. 5.8
21. L.D. Landau, E.M. Lifshitz, *Fluid Mechanics*, 2nd edn. (Butterworth-Heinemann, Boston, 1987). §11; ISBN:0-7506-2767-0
22. P.M. Morse, K.U. Ingard, *Theoretical Acoustics* (McGraw-Hill, New York, 1968). §7.1
23. A.U. Case, The vocal microphone: technology and practice. Phys. Today **69**(3), 74–75 (2016)
24. B. Baumzweiger, Microphone apparatus, US Patent No. 2,184,247, 19 Dec 1939
25. M.S. Pettersen, 75$^{\text{th}}$ anniversary of the Shure Unidyne® microphone. J. Acoust. Soc. Am. **136**(4), 2129 (2014)
26. W.L. Dooley, Ribbon microphones. J. Acoust. Soc. Am. **136**(4), 2130 (2014)
27. L.L. Beranek, *Acoustics* (Acoustical Society of America, New York, 1996). See Part XVI, §6.7; ISBN:0-88318-494-X
28. T.B. Gabrielson, *Theory of operation for the DIFAR flux-gate compass*. Naval Air Development Center Technical Memorandum 3031-86-02, April 1986
29. D.A. Brown, Bearing measurements using a compact wideband sensor by forming three dipoles. J. Acoust. Soc. Am. **134**(5), 4052 (2013). Also see D.A. Brown, B. Aronov, C.L. Bachand, Acoustic transducers for underwater navigation and communication. U.S. Patent No. 8,638,640, 28 Jan 2014. Fig. 10A
30. R.M. Keolian, S.L. Garrett, C.B. Cameron, Demodulators for optical fiber interferometers with [3 X 3] outputs. U.S. Patent No. 5,313,266, 17 May 1994. See Fig. 17
31. S. Tempkin, *Elements of Acoustics* (Wiley, New York, 1981). See §5.5; ISBN:0-471-05990-0
32. L.D. Landau, E.M. Lifshitz, *Fluid Mechanics*, 2nd edn. (Butterworth-Heinemann, Boston, 1987). §74, see Problem 1; ISBN:0-7506-2767-0
33. T.B. Gabrielson, D.L. Gardner, S.L. Garrett, A simple neutrally-buoyant sensor for direct measurement of particle velocity and intensity in water. J. Acoust. Soc. Am. **97**(4), 2227–2237 (1995)
34. L.D. Landau, E.M. Lifshitz, *Fluid Mechanics*, 2nd edn. (Butterworth-Heinemann, Boston, 1987). For an alternative derivation see §11, Problem 1; ISBN:0-7506-2767-0
35. S.L. Garrett, D.L. Gardner, Multiple axis fiber optic interferometric seismic sensor. U.S. Patent No. 4,893,930, 16 Jan 1990
36. D.L. Gardner, S.L. Garrett, A fiber optic interferometric seismic sensor with hydrophone applications. U.S. Navy J. Underw. Acoust. JUA(USN) **38**(1), 1–21 (1988)
37. J.W. Strutt (Lord Rayleigh), On the light from the sky, its polarization and colour. Philos. Mag. **XLI**, 107–120 and 274–279 (1871); *Scientific Papers*, Vol. I (Dover, 1964) §8

38. J.W. Strutt (Lord Rayleigh), On the scattering of light from small particles. Philos. Mag. **XLI**, 447–454 (1871); *Scientific Papers*, Vol. I (Dover, 1964) §9
39. H. Lamb, *The Dynamical Theory of Sound*, 2nd edn. (Arnold, London, 1925). §79. Reprinted by Dover, 1960
40. T.G. Leighton, *The Acoustic Bubble* (Cambridge University Press, Cambridge, 1994). ISBN:0-12441-920-8. See §4.1.2
41. A. Mallock, The damping of sound in frothy liquids. Proc. R. Soc. A **84**(572), 391–395 (1910)
42. F.S. Crawford, The hot chocolate effect. Am. J. Phys. **50**(5), 398–404 (1982)
43. D. Fitzpatrick, J. Kruse, B. Vos, O. Foley, D. Gleeson, E. O'Gorman, R. O'Keefe, Principles and Application of Broadband Acoustic Resonance Dissolution Spectroscopy (BARDS): a sound approach for the analysis of compounds. Anal. Chem. **84**, 2202–2210 (2012)
44. R.V.G. Peddapatla, M. Rizwan Ahmed, C.A. Blackshields, M.J. Sousa-Gallagher, S. McSweeney, J. Kruse, A.M. Crean, D. Fitzpatrick, Broadband Acoustic Resonance Dissolution Spectroscopy (BARDS): a novel approach to investigate the wettability of pharmaceutical power blends. Mol. Pharm. **15**, 31–39 (2018)
45. I.S. Gradshteyn, I.M. Ryzhik, *Tables of Integrals, Series, and Products*, 4th edn. (Academic, London, 1980). See Eq. (0.112); ISBN:0-12-294760-6
46. K.U. Ingard, *Fundamentals of Waves and Oscillations* (Cambridge University Press, Cambridge, 1988). ISBN:0-521-33957-X
47. M. Abramowitz, I.A. Stegun, *Handbook of Mathematical Functions with Formulas, Graphs, and Mathematical Tables*, National Bureau of Standards, Applied Mathematics Series #55. p. 360, Eq. 9.1.20
48. M. Abramowitz, I.A. Stegun, *Handbook of Mathematical Functions with Formulas, Graphs, and Mathematical Tables*, National Bureau of Standards, Applied Mathematics Series #55. p. 360, Eq. 9.1.30
49. L.L. Beranek, *Acoustics* (Acoustical Society of America, New York, 1996). See Part X, §4.3; ISBN:0-88318-494-X
50. M. Abramowitz, I.A. Stegun, *Handbook of Mathematical Functions with Formulas, Graphs, and Mathematical Tables*, National Bureau of Standards, Applied Mathematics Series #55. p. 409, Table 9.5: Zeros and Associated values of Bessel Functions and Their Derivatives
51. I.S. Gradshteyn, I.M. Ryzhik, *Tables of Integrals, Series, and Products*, 4th edn. (Academic, London, 1980). p. 446, Eq. 3.821(9); ISBN:0-12-294760-6
52. P.M. Morse, K.U. Ingard, *Theoretical Acoustics* (McGraw-Hill, New York, 1968), pp. 383–387
53. M. Abramowitz, I.A. Stegun, *Handbook of Mathematical Functions with Formulas, Graphs, and Mathematical Tables*, National Bureau of Standards, Applied Mathematics Series #55. Chapter 12: Struve Functions and Related Functions, p. 496ff
54. R.M. Aarts, A.J.E.M. Janssen, Efficient approximation of the Struve function in the calculation of sound radiation quantities. J. Acoust. Soc. Am. **140**(6), 4154–4160 (2016)
55. P.M. Morse, U.K. Ingard, *Theoretical Acoustics* (McGraw-Hill, New York, 1968). See Eq. (7.4.45)
56. M. Greenspan, Piston radiator: some extensions of the theory. J. Acoust. Soc. Am. **65**(3), 608–621 (1979)
57. R.H. Mellen, M.B. Moffett, A model for parametric sonar radiator design. U. S. Navy J. Underw. Acoust. **22**, 105–116 (1972)
58. H.M. Merklinger, *High intensity effects in the non-linear acoustic parametric end-fire array*. Ph.D. thesis, University of Birmingham, 1971
59. D.T. Blackstock, *Fundamentals of Physical Acoustics* (Wiley, New York, 2000). Chapter 13, §C; ISBN:0-471-31979-1
60. H. Levine, J. Schwinger, On the radiation of sound from an unflanged circular pipe. Phys. Rev. **73**(4), 383–406 (1948)
61. J.W. Strutt (Lord Rayleigh), *Theory of Sound*, vol II, 2nd edn. (Macmillan, London, 1896). (Dover, 1945). §314 and App. A
62. L. Gutin, Uber das Schallfeld der Kolbenstrahlern. Tech. Phys. USSR **4**, 404 (1937). Note that this is a German translation of an article that originally appeared in Russian
63. J.B. Mehl, Greenspan acoustic viscometer: numerical calculation of fields and duct-end effects. J. Acoust. Soc. Am. **106**(1), 73–82 (1999)
64. N.A.M. Schellart, A.N. Popper, Functional aspects of the evolution of the auditory system in Actinopterygian fish, in *The Evolutionary Biology of Hearing*, ed. by D. B. Webster, R. R. Fay, A. N. Popper, (Springer, New York, 1992), pp. 295–322
65. F.V. Hunt, *Electroacoustics* (Harvard University Press, Cambridge, MA, 1954). See Fig. 5.1
66. S.L. Garrett, J.A. Smith, R.W.M. Smith, B.J. Heidrich, M.D. Heibel, Fission powered in-core thermoacoustic sensor. Appl. Phys. Lett. **108**, 144102 (2016). Using the sound of nuclear energy. Nucl. Technol. **195**(3), 353–362 (2016)

Three-Dimensional Enclosures 13

Contents

In this chapter, solutions to the wave equation that satisfies the boundary conditions within three-dimensional enclosures of different shapes are derived. This treatment is very similar to the two-dimensional solutions for waves on a membrane of Chap. 6. Many of the concepts introduced in Sect. 6.1 for rectangular membranes and Sect. 6.2 for circular membranes are repeated here with only slight modifications. These concepts include separation of variables, normal modes, modal degeneracy, and density of modes, as well as adiabatic invariance and the splitting of degenerate modes by perturbations. Throughout this chapter, familiarity with the results of Chap. 6 will be

S. L. Garrett, *Understanding Acoustics*, Graduate Texts in Physics,
https://doi.org/10.1007/978-3-030-44787-8_13

assumed. The similarities between the standing-wave solutions within enclosures of different shapes are stressed. At high enough frequencies, where the individual modes overlap significantly, statistical energy analysis will be introduced to describe the diffuse (reverberant) sound field.

The formalism developed for three-dimensional enclosures also provides the description for sound propagation in waveguides, since a waveguide can be treated as a three-dimensional enclosure where one of the dimensions is extended to infinity.

13.1 Separation of Variables in Cartesian Coordinates

The linearized wave equation for the acoustic pressure, p, can be written in a vector form that is independent of any particular coordinate system.

$$\nabla^2 p_1\left(\vec{x}, t\right) = \frac{1}{c^2}\frac{\partial^2 p_1\left(\vec{x}, t\right)}{\partial t^2} \tag{13.1}$$

The expression of the Laplacian operator, ∇^2, in terms of partial derivatives, depends upon the choice of coordinate system. The simplest coordinate system is Cartesian. We will continue to assume that pressure is time-harmonic, $p_1(x, y, z, t) = \Re e[\widehat{\mathbf{p}}(x, y, z)e^{j\omega t}]$. Since $k = \omega / c$, Eq. (13.1) can be written in the time-independent form known as the Helmholtz equation.

$$\nabla^2 p_1 = \frac{\partial^2 p_1}{\partial x^2} + \frac{\partial^2 p_1}{\partial y^2} + \frac{\partial^2 p_1}{\partial z^2} = -k^2 p_1 \tag{13.2}$$

The Helmholtz equation is a partial differential equation. In Cartesian coordinates, it can be separated into three ordinary differential equations by assuming that variation of the pressure in each spatial coordinate is independent of the other coordinates[1] [1].

$$p_1(x, y, z, t) \equiv \Re e\left[X(x)Y(y)Z(z)e^{j\omega t}\right] \tag{13.3}$$

Substitution of Eq. (13.3) into Eq. (13.2) produces an equation where the partial derivatives become ordinary derivatives. Since each function now depends only upon a single coordinate, it is no longer necessary to use partial derivatives.

$$YZ\frac{d^2X}{dx^2} + XZ\frac{d^2Y}{dy^2} + XY\frac{d^2Z}{dz^2} + k^2XYZ = 0 \tag{13.4}$$

Dividing through by XYZ makes each term independent of the others.

$$\frac{1}{X}\frac{d^2X}{dx^2} + \frac{1}{Y}\frac{d^2Y}{dy^2} + \frac{1}{Z}\frac{d^2Z}{dz^2} + k^2 = 0 \tag{13.5}$$

Since each term in the separated Helmholtz equation (13.5) depends upon a different coordinate, and their sum is equal to a constant, $-k^2$, each term must be separately equal to a constant. This is the same as the "separation condition" imposed in the two-dimensional case in Eq. (6.8).

[1] The three-dimensional Helmholtz equation can be separated in 11 coordinate systems. With the exception of confocal paraboloidal coordinates, all are particular cases of the confocal ellipsoidal system: Cartesian, confocal ellipsoidal, confocal paraboloidal, conical, cylindrical, elliptic cylindrical, oblate spheroidal, paraboloidal, parabolic cylindrical, prolate spheroidal, and spherical coordinates. http://mathworld.wolfram.com/HelmholtzDifferentialEquation.html

$$k^2 = \frac{\omega^2}{c^2} = k_x^2 + k_y^2 + k_z^2 \tag{13.6}$$

Each term then generates a simple harmonic oscillator equation.

$$\frac{d^2X}{dx^2} + k_x^2 X = 0 \tag{13.7}$$

By this time, we are quite familiar with the solutions to the above ordinary, second-order, homogeneous differential equation. Instead of both sine and cosine functions, in the following, only cosine functions will be chosen (for reasons that will become apparent once rigid boundary conditions are imposed), and three phase factors will be included to retain the generality of the solution.

$$p_1(x, y, z, t) = \Re\mathrm{e}\left[\widehat{\mathbf{p}} \cos\left(k_x x + \phi_x\right) \cos\left(k_y y + \phi_y\right) \cos\left(k_z z + \phi_z\right) e^{j\omega t}\right] \tag{13.8}$$

To emphasize that this is could be a traveling plane wave (before imposition of boundary conditions), the solution can be written as a product of complex exponentials.

$$p_1(x, y, z, t) = \Re\mathrm{e}\left[|\widehat{\mathbf{p}}| e^{\,j(\omega t + \phi)} e^{\,j\left(\mp k_x x + k_y y + k_z z\right)}\right] \tag{13.9}$$

13.1.1 Rigid-Walled Rectangular Room

If we consider a fluid confined in a rectangular room with rigid impenetrable walls, then we can impose the six boundary conditions on the normal component of the fluid velocity at each of the six planes that define the interior of the room. From the Euler equation, we see that this condition is equivalent to requiring that the slope of the pressure normal to the boundary vanishes.

$$\frac{\partial u_x(0)}{\partial t} = 0 = -\frac{1}{\rho_m}\left(\frac{\partial p_1}{\partial x}\right)_{x=0} \quad \Rightarrow \quad \left(\frac{\partial p_1}{\partial x}\right)_{x=0} = 0 \tag{13.10}$$

At the planes which pass through the origin of coordinates, we can eliminate all of the phases in Eq. (13.8), ϕ_i, since the cosine terms all have zero slope at $x = y = z = 0$. If we introduce the lengths of the enclosure's edges as L_x, L_y, and L_z, then the solutions (*eigenvalues*) are quantized in a way that satisfies the remaining three (zero slope) boundary conditions of Eq. (13.10) at $x = L_x$, $y = L_y$, and $z = L_z$.

$$k_x = \frac{n_x \pi}{L_x}; \quad k_y = \frac{n_y \pi}{L_y}; \quad k_z = \frac{n_z \pi}{L_z}; \quad n = 0, 1, 2, \ldots \tag{13.11}$$

The modal frequencies, f_{ijk}, are then designated by three integers: $i = n_x$, $j = n_y$, and $k = n_z$.

$$f_{ijk} = \frac{\omega_{ijk}}{2\pi} = \frac{c}{2}\sqrt{\left(\frac{n_x}{L_x}\right)^2 + \left(\frac{n_y}{L_y}\right)^2 + \left(\frac{n_z}{L_z}\right)^2} \tag{13.12}$$

Each mode can then be written as the product expressed in Eq. (13.3) and repeated in Eq. (13.13), where the complex (phasor) amplitude of each mode, $\widehat{\mathbf{A}}_{\mathbf{ijk}}$, is dependent upon the source impedance (i.e., a volume velocity source or a pressure source or something in between), its amplitude, and the location of the source within the standing wave field.

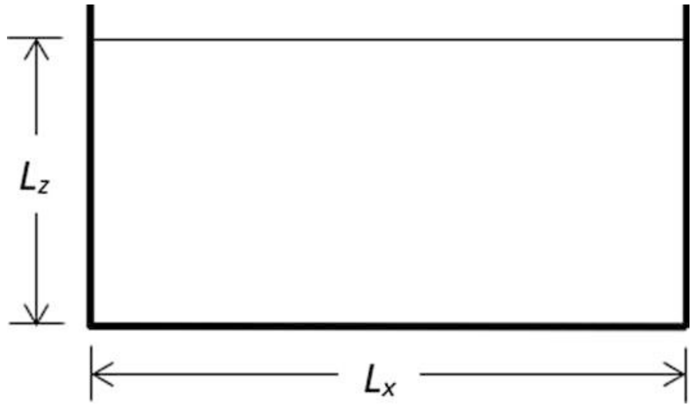

Fig. 13.1 Representation of a rigid-walled enclosure containing a liquid with a pressure-released free surface at the plane, $z = L_z$

$$p_{ijk}(x, y, z, t) = \Re e\left[\widehat{\mathbf{A}}_{\mathbf{ijk}} \cos(k_x x)\cos\left(k_y y\right)\cos(k_z z)e^{j\omega_{ijk}t}\right] \tag{13.13}$$

Of course, there are other possible boundary conditions. The other extreme is a perfectly pressure-released boundary condition. One such example might be approximated by a fish tank or swimming pool shown schematically in Fig. 13.1, where the thickness of the boundaries is intended to emphasize the rigidity of the five planes that contain the liquid. (Note that it is very difficult to produce a container that behaves as a rigid boundary since water is very nearly incompressible.)

At the free surface of the water (i.e., the water-air interface), the normal component of the fluid velocity, u_z, is unrestricted, and the acoustic pressure amplitude, $p_1(L_z)$, is zero (but not the slope!). On the x-y plane at $z = 0$, we have the original "rigid" boundary condition, so the form of the solution is the same as in the rigid enclosure case Eq. (13.13), but at $z = L_z$, $p_1(x, y, z = 0, t)$ must vanish for all times. If we impose the pressure-released boundary condition at $z = L_z$ (the air-water interface), then the quantization condition on k_z changes to that for a closed-open pipe (see Sect. 10.6.2).

$$k_x = \frac{n_x \pi}{L_x}; \quad k_y = \frac{n_y \pi}{L_y}; \quad k_z = \frac{(2n_z - 1)\pi}{2L_z}; \quad \begin{cases} n_x, n_y = 0, 1, 2, \ldots \\ n_z = 1, 2, 3, \ldots \end{cases} \tag{13.14}$$

The $n_z = 0$ solution does not exist since constant pressure in the z direction is not an option that satisfies the boundary conditions at $z = L_z$ and $z = 0$ simultaneously.

13.1.2 Mode Characterization

For the rigid-walled rectangular enclosure, the modes can be classified into three categories:

- Axial: only one mode number is non-zero.
- Tangential: only one mode number is zero.
- Oblique: no mode number is zero.

Each mode is unique and has a complex amplitude, $\widehat{\mathbf{A}}_{\mathbf{ijk}}$, which is a function of how and where it is excited, although the frequencies of the individual modes may not be unique. Depending upon the excitation, some values of $\left|\widehat{\mathbf{A}}_{\mathbf{ijk}}\right|$ may be zero. As discussed in Sect. 6.1.2, when two or more different modes share the same frequency, they are called *degenerate modes*.

Table 13.1 Modes of a cubical room with $L_x = L_y = L_z$ and a rectangular room where $L_y = L_x\sqrt{2}$ and $L_z = L_x/\sqrt{2}$

Cubical room				Rectangular room			
$2L_xf_{ijk}/c$	n_x	n_y	n_z	$2L_xf_{ijk}/c$	n_x	n_y	n_z
1.000	1	0	0	0.707	0	1	0
	0	1	0	1.000	1	0	0
	0	0	1	1.225	1	1	0
1.414	1	1	0	1.414	0	0	1
	1	0	1		0	2	0
	0	1	1	1581	0	1	1
1.732	1	1	1	1.732	1	0	1
2.000	2	0	0		1	2	0
	0	2	0	1.871	1	1	1
	0	0	2	2.000	2	0	0
2.236	2	1	0		0	2	1
	1	2	0	2.121	2	1	0
	2	0	1		0	3	0
	1	0	2	2.236	1	2	1
	0	2	1	2.345	1	3	0
	0	1	2	2.449	2	0	1
2.449	2	1	1		2	2	0
	1	2	1	2.550	2	1	1
	1	1	2		0	3	1
2.828	2	2	0	2.739	1	3	1
	2	0	2	2.828	0	0	2
	0	2	2		0	4	0
3.000	3	0	0	2.915	0	1	2
	0	3	0		2	3	0
	0	0	3	3.000	1	0	2
	2	2	1		3	0	0
	2	1	2		1	4	0
	1	2	2				

If the enclosure is cubical (i.e., $L_x = L_y = L_z$), then there will be many degenerate modes. Even if the dimensions of the room are not identical, there can be "accidental degeneracies." The normalized modal frequencies, $(2L_xf_{ijk})/c$, for a cubical room with $L_x = L_y = L_z$ and for a rectangular room with $L_y = L_x\sqrt{2}$, and $L_z = L_x/\sqrt{2}$, are given in Table 13.1 [2]. For the cubical room, there are 28 distinct modes but only 8 unique normalized frequencies less than or equal to $2L_xf_{3,\,0,\,0}/c = 3.00$. For the rectangular room, there are 27 distinct modes but 17 unique normalized frequencies less than or equal to $2L_xf_{3,\,0,\,0}/c = 3.00$.

The volumes of both rooms are the same as are the total number of modes, to within a single mode. The number of degenerate modes is larger for the cubical room, but the rectangular room also has several degenerate modes, even though the ratios of the boundary lengths are irrational numbers.

13.1.3 Mode Excitation

As with any linear model, the amplitude coefficients of the individual modes described by Eq. (13.13), $\widehat{\mathbf{A}}_{\mathbf{ijk}}$, are undetermined until the method of excitation is specified. If we assume that a mode will be excited by a volume velocity source, like a loudspeaker, and that the volume velocity produced by the source is independent of the acoustic load (i.e., a "constant current" source), then the amplitude of a given mode will depend upon the local value of the fluid's impedance. In any corner of a rectangular room, the pressure is a maximum for all modes, and the fluid's particle velocity must vanish. This makes the impedance (theoretically) infinite at those eight locations so a constant volume velocity source would produce infinite acoustic pressure amplitudes. In reality, the magnitude of the impedance will depend upon the damping of the mode, as reflected in the quality factor of the mode, Q_{ijk}. We have done this calculation to relate $|\mathbf{Z}_{\mathbf{ac}}|$ to Q_n for a one-dimensional resonator in Eq. (10.64).

When the loudspeaker is located in the corner of a rigid-walled room, all of the modes can be excited. Of course, which specific mode might be excited will depend upon the frequencies produced by the loudspeaker. If the same speaker were moved from the corner to an edge where two walls intersect and was half-way between the other two walls, then only one-half as many modes could be excited. For example, if the speaker were placed at $x = L_x/2$ with $y = 0$ and $z = 0$, then $\left|\widehat{\mathbf{A}}_{\mathbf{ijk}}\right|$ could only be non-zero if i were an odd integer, so $p_{ijk}\ (L_x/2, 0\ 0) \neq 0$. If i is an even number, then the speaker is located at an acoustic pressure node, and the impedance would be zero.

If the speaker is then moved away from the edge to the center of one wall, another half of the modes could not be excited in that position; only one-quarter of the modes could be excited. Now if the speaker were lifted off of that wall and placed in the exact center of the room, another half of the modes would be excluded and only one-eighth of the modes could be excited.

Equation (13.13) describes the pressure field in a rectangular, rigid-walled enclosure. If a volume velocity source is located at a pressure node for any mode, that mode cannot be excited and $\left|\widehat{\mathbf{A}}_{\mathbf{ijk}}\right|$ for that mode would be zero.

13.1.4 Density of Modes

In a one-dimensional resonator (e.g., a rigid tube with rigid ends), the normal modes were equally spaced in frequency, and only one integer index, n (the mode number), was required to specify each modal frequency.

$$f_n = n\frac{c}{2L} \quad \Rightarrow \quad n = \frac{2f_nL}{c} \tag{13.15}$$

The *density of modes* is the number of modes within a frequency band that is Δf wide. For the one-dimensional case, dn/df is a constant,

$$\frac{dn}{df} = \frac{2L}{c} \quad \Rightarrow \quad \Delta n = \frac{2L}{c}\Delta f \tag{13.16}$$

We can visualize the results of Eqs. (13.15) and (13.16) by looking at the modes as points on the one-dimensional k_x-axis shown in Fig. 13.2.

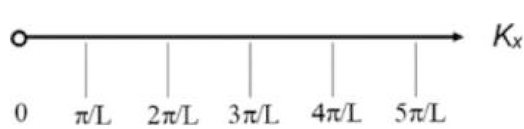

Fig. 13.2 A graphical representation of the modes in a one-dimensional closed-closed resonator. Each mode is represented as a discrete point on the (wavenumber) k_x-axis. Since the spacing between adjacent modes is uniform, the density of modes is also a constant

Constant spacing in one-dimensional k-space corresponds to a linearly increasing number of modes with increasing frequency (bandwidth) and a constant density of modes.

In higher-dimensional spaces, the density of modes is a function of frequency. For a two-dimensional system, like the rectangular membranes in Sect. 6.1 and the circular membrane in Sect. 6.2, the number of modes with frequencies below some maximum frequency, f_{max}, increased with the square of that frequency. In that two-dimensional case, the number of modes was approximated by the k-space reciprocal area, $\forall$, contained within the quadrant of a circle that had a radius, $\left|\vec{k}\right| = 2\pi f_{max}/c$. This geometrical construction for a two-dimensional system is illustrated in Fig. 6.5.

In three-dimensional enclosures, the density of modes is also a function of frequency. The number of modes, N, with frequency less than f_{max}, is equal to the number of points representing individual modes contained within the volume of an octet of a k-space sphere (i.e., only positive values of k) in *wavenumber space* or *k-space* with a radius $k_{max} = \omega_{max}/c = 2\pi f_{max}/c$. The volume of a "unit cell" in k-space is $\pi^3/(L_x L_y L_z)$. In analogy with Eq. (6.15), the number of modes can be approximated by the volume of the octet of the sphere divided by the volume of the unit cell.

$$N = \frac{\text{Octet Volume}}{\text{Unit Cell}} \cong \frac{(\pi/6)k_{max}^3}{\pi^3/\left(L_x L_y L_z\right)} = \frac{4\pi f_{max}^3 V}{3c^3} \tag{13.17}$$

To obtain the density of modes, we differentiate Eq. (13.17) as we did in two dimensions in Eq. (6.19).

$$\frac{dN}{df} \cong \frac{4\pi f^2 V}{c^3} \tag{13.18}$$

A more accurate result can be obtained if we include points in k-space representing the axial modes (on the 12 edges of total length, L) and points in k-space representing tangential modes (on the six planes of total area A).

$$\frac{dN}{df} \cong \frac{4\pi f^2 V}{c^3} + \frac{\pi f A}{2c^2} + \frac{L}{8c} \tag{13.19}$$

This result should be compared with the similar two-dimensional result for a rectangular membrane in Eq. (6.19) or the circular membrane in Eq. (6.34).

To determine when our analysis should transition between the discrete modal picture we have just developed and the statistical approach we are about to introduce, we need to understand the concept of *reverberation time*.

13.2 Statistical Energy Analysis

We would like to know when it is reasonable to calculate the sound level in an enclosure using a modal model and when it would be more fruitful to ignore the enclosure's modal structure and apply statistical energy analysis to determine sound levels by writing an energy balance equation to calculate the rate of change of the sound level in an enclosure.

Time-averaged acoustic power, $\langle\Pi\rangle_t$, enters the enclosure from a source (e.g., a loudspeaker or an orchestra) and power "leaves" by passing through the boundary (through a window?), converting to heat due to thermoviscous absorptive processes at the boundaries (see Eq. (9.38)) or at the surface of

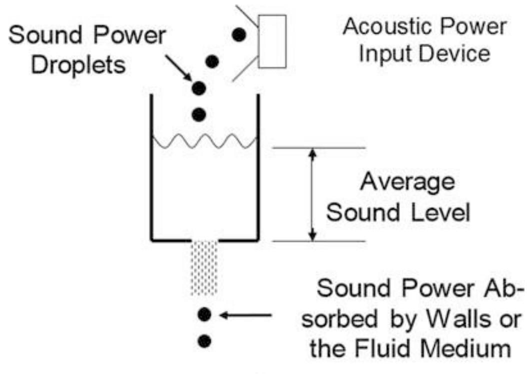

Fig. 13.3 The steady-state sound level in an enclosure is analogous to filling a leaky bucket. Sound energy (droplets) enters the bucket representing the sound source. Fluid leaves the bucket through a leak representing absorption by the walls and the contents of the enclosure. The leakage rate is proportional to the depth of the fluid. When the amount that enters and the amount that leaves are equal, the liquid level, analogous to the sound level, achieves steady state

objects in the room (e.g., upholstered seats, people's clothing) or due to attenuation within the fluid itself (see Sects. 14.3 and 14.5.1). Figure 13.3 illustrates a "bucket" analogy that, though crude, accurately represents the energy balance approach.

The energy balance approach to calculation of the sound pressure in a diffuse sound field within an enclosure is analogous to a bucket that is filled with "sound droplets" by some source represented schematically in Fig. 13.3 by a loudspeaker. Droplets (energy) leak out of the bucket through a hole that provides some flow resistance. Steady state is achieved when the level of the fluid in the bucket (analogous to the average sound level) is sufficient to force fluid through the resistance at the same rate at which fluid is entering the bucket. If the resistance of the leak is large (representing very little absorption, thus making it difficult for the sound to leave), then the steady-state level will be high, and it will take more time to reach that level since the power of the sound source is constant (analogous to the number of droplets per second). If the resistance is small, then it is easy for the sound to leave the enclosure (by being absorbed and turned into heat and/or escaping through a door or window). The level then will reach its steady-state value that is lower and the time to reach steady state is shorter.

Instead of treating modes individually, the problem can be approached from another direction. Let's assume that the density of modes is so high, and individual modes are so closely spaced, both in frequency and in wave-vector direction, and that the acoustic energy in the room distributes itself uniformly among the available modes (as we did by invoking the Equipartition Theorem for the distribution of thermal energy when calculating heat capacities of ideal gases in Sect. 7.1.1). We have previously derived a conservation equation (10.35), for both the kinetic and potential energy density of sound waves.

$$\frac{\partial}{\partial t}\left[\frac{1}{2}\rho_m v_1^2 + \frac{1}{2}\frac{p_1^2}{\rho_m c^2}\right] + \nabla \bullet \left(p_1 \vec{v}_1\right) = 0 \tag{13.20}$$

Since the total energy density is the sum of the instantaneous kinetic and potential energy densities, and the time-averaged value of both energy densities are equal (by the virial theorem in Sect. 2.3.1), we can choose to express the total as the maximum value of either. For this analysis, we chose the potential energy density, ε, since we are normally interested in sound pressure.

$$\varepsilon = \frac{PE}{V} = \frac{p_r^2}{\rho_m c^2} \tag{13.21}$$

The square of the acoustic pressure, ${p_r}^2$, is the mean square pressure based on the incoherent sum of all of the pressures of all of the modes averaged over all angles. As a more operational definition, the square root, $\sqrt{p_r^2} \equiv p_{rms}$, provides the root-mean-squared pressure that would be measured by an omnidirectional microphone. If the sound field within the enclosure is truly a *diffuse sound field*, we can make the further claim that ${p_r}^2$ is independent of location within the enclosure and incident from all angles.

Sound energy leaves the enclosure by converting to heat through absorption within the medium or by thermal or viscous interactions with the boundaries. For development of this model, it is customary to ignore the attenuation within the medium and define an absorption coefficient that designates the fraction of energy that is not reflected at the wall. The "bulk" losses for frequencies below about 5 kHz and enclosures with volumes less than 10^6 ft^3 (30,000 m^3) will usually be insignificant compared to the surface absorption, besides, it is easy to put the bulk losses back into the equation later, as in Eq. (13.30).

Assuming that the sound that impinges on a wall does so with equal probability from all angles, the time-averaged intensity (power impinging per unit area) of the sound can be calculated by examination of an infinitesimal volume, dV, containing the energy, ε (dV), coming toward from a wall from all directions at the speed of sound, c. The energy will reach a "patch" of the wall having an area, dS, and be partially reflected and partially absorbed during an infinitesimal time, dt, as shown in Fig. 13.4.

The area of the "patch" will depend upon the viewing angle. Energy arriving from a direction normal to the patch will see an area of dS, but sound that is nearly perpendicular to the patch will see nearly zero area. That is, the effective area of the patch, $dS_{eff} = dS \cos\theta$, where θ is the angle with respect to the normal to the patch. Also, an incoming ray arriving at the patch from an angle, θ , must be within a distance, $c\,dt \sin\theta$, to arrive in a time, dt. Combining these two orientational effects with the fact that *half of the energy is traveling away from the patch*, we can calculate the energy that impinges on our patch during a time, dt, by integrating over the arrival angle, θ.

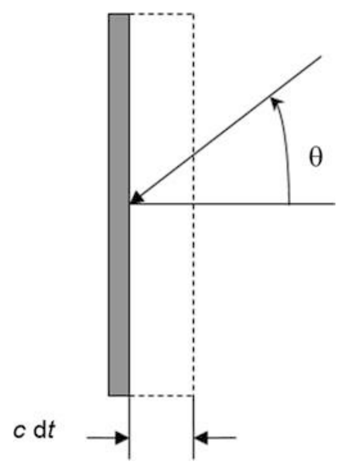

Fig. 13.4 The geometry used to calculate the time-averaged incident energy flux (intensity) impinging on a differential element of area, dS, at the enclosure boundary (wall), from a diffuse sound field

$$\frac{dE}{dS} = \frac{\varepsilon(cdt)}{2} \int_0^{\pi/2} \sin\theta \cos\theta \, d\theta = \frac{\varepsilon c}{4} dt \tag{13.22}$$

This result is exactly the same as was derived in the kinetic theory calculations in Sect. 9.5.2.

How much sound gets absorbed by the walls? The amount of absorbed energy will vary depending upon the nature of the surface (e.g., rigid concrete or porous carpet). In keeping with our statistical treatment, if there are n different surface treatments, each with area, A_i, and absorption coefficient, α_i, the average absorption coefficient (or effective absorptive area) for the entire enclosure, $<A>$, is the properly weighted sum over all of the enclosure's surfaces.

$$\langle A \rangle = \sum_{i=1}^{n} \alpha_i A_i \tag{13.23}$$

These surfaces are not limited to the walls, but could include seats and their occupants, over-garments, wall treatments (e.g., drapes), etc.

We are now in a position to write the *energy balance equation*.

$$\frac{d(\varepsilon V)}{dt} + \langle A \rangle \frac{c\varepsilon}{4} = \langle \Pi \rangle_t \tag{13.24}$$

The solution to such a first-order differential equation is well known.

$$\varepsilon(t) = \frac{p_{eff}^2}{\rho_m c^2} = \frac{4\langle \Pi \rangle_t}{c\langle A \rangle}\left(1 - e^{-t/\tau_E}\right) \tag{13.25}$$

The exponential time, $\tau_E = 4\ V/c < A>$, represents the time required for the *energy* in the diffuse field to reach $63.2\% = 1 - e^{-1}$ of its steady-state value after the source is turned on or to decay from its steady-state value, $\varepsilon\ (t = \infty)$, given in Eq. (13.27), by 63.2% after the source is turned off. It is useful to remember that we have usually designated the exponential equilibration time, τ, to represent the change in *amplitude* not *energy*. Since the energy is a quadratic function of the amplitude, $\tau = 2\tau_E$.

If the absorption is small, then it takes a long time for the sound pressure to reach the steady-state value corresponding to the steady-state energy density, $\varepsilon(t = \infty)$.

$$\varepsilon(t = \infty) = \frac{4\langle \Pi \rangle_t}{c\langle A \rangle} = \frac{p_r^2(t = \infty)}{\rho_m c^2} \tag{13.26}$$

Similarly, if the average absorptive area, $<A>$, is small, the enclosure will take more time to respond to changes in source sound level.

13.2.1 The Sabine Equation

Wallace Clement Sabine (1868–1919) was a young physics professor at Harvard University when he was asked, in 1885, by Charles Eliot, then president of the university, if he could do something about the poor speech intelligibility in the lecture hall at the Fogg Art Museum on campus [3]. To determine the origin of the problem, Sabine measured the time it took for sound to decay in various rooms on campus, using only a "clapboard" to create an impulse, his hearing, and a stopwatch. On 30 October

1898, he discovered a correlation between that decay time and the volume of the rooms and their average absorptive area. The resulting relation is known as the Sabine equation.[2]

$$T_{60} = \tau_E Ln\left[10^6\right] = 13.82\tau_E = 13.82\frac{4V}{c\langle A\rangle} = 0.16\frac{V}{\langle A\rangle} \tag{13.27}$$

The numerical value in the rightmost term of Eq. (13.27) applies only to sound in air if both volume, *V*, and average absorptive area, <*A*>, are measured in metric units. If the dimensions of the room are measured in English units (feet), then the numerical factor in Eq. (13.27) becomes 0.047.

The reverberation time, T_{60}, was chosen because it was approximately the time required for the decaying sound Sabine was timing to become inaudible after the initial impulse. Today, T_{60} corresponds to the time it takes for sound to decay by 60 dB (for the time-averaged acoustic intensity[3] to decay by a factor of one million). In terms of the exponential energy decay time, τ_E, $T_{60} = ln\ [10^6]\ \tau_E = 13.83\tau_E$. Today's high-quality electroacoustics and digital recording and post-processing makes it possible in many circumstances to obtain very precise determinations of the reverberation time, as shown in Fig. 13.5.

Sabine's success improving the acoustics at the Fogg Auditorium led him to a commission for the design of Boston's Symphony Hall, shown in Fig. 13.6, with a maximum seating of 2625, which opened 15 October 1900. To this day, it is still considered one of the world's best concert halls [4]. Its successful opening ushered in a new era for the use of scientific methods in the design of musical performance spaces.

The technology for determining the frequency-dependent, angle-averaged sound absorption of surfaces based on measurements of their fundamental physical properties (e.g., average hydraulic pore radius, porosity, and tortuosity) is not widely understood within the architectural community, and the instrumentation for measurement of the fundamental properties (complex flow resistance and

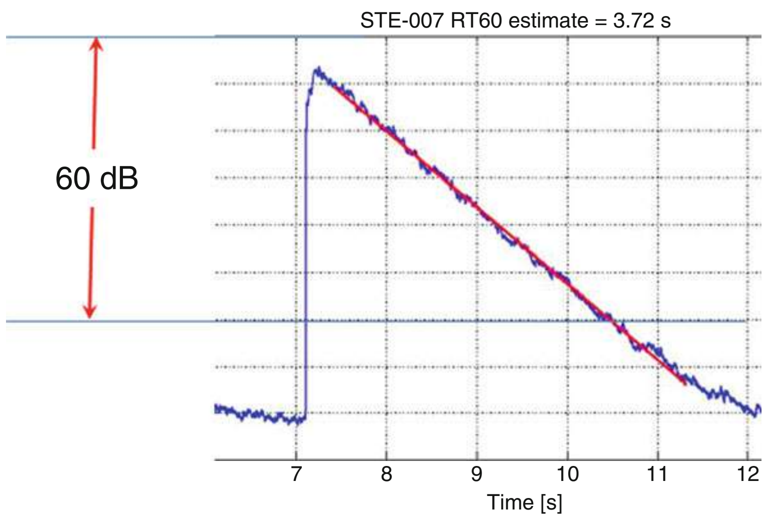

Fig. 13.5 Reverberation decay record for a very noisy (reverberant) dining hall at the YMCA Camp Fitch on the shore of Lake Erie, in Pennsylvania. The vertical axis displays the received dB level. The straight line (*red*) fit to the data is equivalent to a $T_{60} = 3.72$ s. (Data courtesy of Matthew E. Poese)

[2] Tradition has it that when Sabine realized the inverse relationship between reverberation time and average absorptive area, he ran downstairs from his study, shouting to his mother, "Mother, it's a hyperbola!"

[3] The interval selected for the time averaging of the sound pressure level measurement, τ_{ave}, needs to be long enough to integrate over the desired range of frequencies, $\Delta\omega \cong \tau_{ave}^{-1}$, yet short enough that it will not dominate the reverberant decay: $\tau_{ave} < \tau_E$.

Fig. 13.6 View of Boston Symphony Hall from the back of the upper balcony facing the stage [4]. In addition to the uniformity of the reverberation times shown in Table 13.2, the rectangular hall has many "sound scatterers" of different shapes and sizes (statues, alcoves, proscenium arch, and balcony facings, along with other assorted "protuberances") to scatter sound of different wavelengths and thus encourage a uniform angular distribution among the reflections [5]

complex compressibility) are not widely available [6]. For that reason, the standard method for measurement of absorption coefficients uses the measurement of change in reverberation time of an enclosure with and without the absorptive sample present [7, 8].

$$a_s = a_o + 0.16\frac{V}{S_s}\left(\frac{1}{T_s} - \frac{1}{T_o}\right) \tag{13.28}$$

The average absorptivity of the empty test enclosure is a_o. The reverberation time of the empty enclosure, $T_{60} = T_o$. The reverberation time within the same enclosure with an area, S_s, of absorbing material is reduced to T_s.

To incorporate absorption within the medium, the Sabine equation (13.27) can be augmented with an energy attenuation coefficient, m.

$$T_{60} = \frac{0.16\ V}{\langle A\rangle + 4mV} \tag{13.29}$$

The expression in Eq. (13.29) is usually deemed adequate for architectural applications. A useful correlation for the attenuation coefficient in air (in units of inverse meters), for frequencies between 1500 Hz $\leq f \leq$ 10,000 Hz, and relative humidity, $20 \leq RH(\%) \leq 70$, is given in Eq. (13.31).

$$m = 5.5 \times 10^{-4}(50/RH\%)(\,f/1000)^{1.7} \tag{13.30}$$

The validity of this correlation is established in Chap. 14, Problem 1, using values taken from the American National Standards Institute [9].

13.2.2 Critical Distance and the Schroeder Frequency

The pressure radiated by a simple source (i.e., a compact monopole) can also be expressed in terms of its time-averaged radiated power, $\langle \Pi_{rad} \rangle_t$, using the expression for time-averaged intensity in Eq. (12.24) and the fact that the monopole field is spherically symmetric.

$$\langle \Pi_{rad} \rangle_t = 4\pi R^2 \left| \left\langle \vec{I} \right\rangle_t \right| = 4\pi R^2 \frac{p_1^2(R)}{2\rho_m c} \quad \Rightarrow \quad \frac{p_1^2(R)}{2} = p_{rms}^2 = \frac{\rho_m c}{4\pi R^2} \langle \Pi_{rad} \rangle_t \tag{13.31}$$

That radiated pressure can be equated to the steady-state pressure in the diffuse sound field, $p_r^2(t = \infty)$, that was calculated in Eq. (13.26), to determine the *critical distance*, r_d, where the direct and diffuse sound field energies would be equal.

$$p_r^2(t = \infty) = \rho_m c \frac{4\langle \Pi_{rad} \rangle_t}{\langle A \rangle} = \frac{\rho_m c}{4\pi r_d^2} \langle \Pi_{rad} \rangle_t \quad \Rightarrow \quad r_d = \frac{1}{4}\sqrt{\frac{\langle A \rangle}{\pi}} \tag{13.32}$$

At distances from a source greater than r_d, the diffuse field will dominate. At distances less than r_d from the source, the direct radiation will dominate. This is particularly important when considering sound absorption in a factory situation. Adding absorption to the walls will not help reduce the noise a worker will have to tolerate if (s)he is closer to the source (e.g., a punch press, band saw, grinder) than r_d.

We have now analyzed the modes of a rectangular enclosure that is suited to the low-frequency behavior of sound in the enclosure. We have also analyzed the behavior at high frequencies, when the modes have sufficient overlap that the sound field can be treated as being both isotropic and homogeneous (i.e., diffuse). It is therefore imperative to identify a cross-over frequency between those two regimes.

Ever since the discussion of the simple harmonic oscillator in Sect. 2.5.2, the "width" of a resonance (mode) has been related to the bandwidth, Δf_{-3dB}, over which the power in the resonance is within 3 dB of its peak value, or, equivalently, that the pressure amplitude is within $\sqrt{2}$ of the amplitude at resonance, as indicated in Eq. (2.68). Using our multiple definitions for the quality factor, Q, in Appendix B, our appreciation of the fact that the energy decay rate, τ_E, is one-half the exponential amplitude decay rate, τ, and the fact that $T_{60} = 13.82\tau_E$ in Eq. (13.27), it is possible to express the -3 dB bandwidth, Δf_{-3dB}, in terms of T_{60}.

$$Q = \frac{f}{\Delta f_{-3dB}} = \frac{1}{2}\omega\tau = \pi f \tau = 2\pi f \tau_E \quad \Rightarrow \quad \Delta f_{-3dB} = \frac{13.82}{2\pi T_{60}} \cong \frac{2.2}{T_{60}} \tag{13.33}$$

Manfred Schroeder suggested that the cross-over frequency between modal behavior and the diffuse sound field approach should correspond with the frequency where there are three modes within a frequency bandwidth of Δf_{-3dB}.[4] Using the leading term in our approximation for the density of modes

[4] The choice of three "available" modes within the -3 dB bandwidth is, of course, rather arbitrary. P. M. Morse in his textbook, *Vibration and Sound* (McGraw-Hill, 1948), provides (in Eq. 34.8) a more detailed criterion that also incorporates the spread in the frequency range radiated by the source.

$$f_{min} = \left\{ \frac{c^3}{4\pi V + [\Delta f + (4/T_{60})]} \right\}^{1/2}$$

Based on the acceptance by the architectural acoustics community of the Schroeder frequency, apparently Eq. (13.34) is adequate for most applications.

Table 13.2 Average measured reverberation times, T_{60}, in six consecutive one-octave bands of frequencies for the unoccupied (empty) and occupied (full) concert hall [4].

Band center (Hz)	125	250	500	1000	2000	4000
T_{60}-empty (seconds)	2.13	2.29	2.40	2.63	2.66	2.38
T_{60}-full (seconds)	1.95	1.85	1.85	1.85	1.65	1.30

One of the reasons the hall, shown in Fig. 13.6, is so highly rated is that the reverberation times are amazingly uniform across a broad range of frequencies

in Eq. (13.18), Schroeder's "three mode overlap" criterion can be determined in terms of the enclosure volume, V, and the reverberation time, T_{60}.

$$\frac{dN}{df}\Delta f = 3 = \frac{2.2}{T_{60}}\frac{4\pi V}{c^3}f_S^2 \tag{13.34}$$

Solving for frequency, we obtain the cross-over frequency, known as the *Schroeder frequency*, f_S, where the third expression in Eq. (13.36) assumes a sound speed $c = 343$ m/s [10].

$$f_S = \left(\frac{c^3}{4\ln 10}\right)^{1/2}\left(\frac{T_{60}}{V}\right)^{1/2} = c\left(\frac{6}{\langle A\rangle}\right)^{1/2} \cong 2000\left(\frac{T_{60}}{V}\right)^{1/2} \tag{13.35}$$

For a room about the size of a typical classroom (10 m × 8 m × 4 m = 320 m^3), with $T_{60} \cong 0.4$ s, the Schroeder frequency is $f_S \cong 70$ Hz. The lowest-frequency normal mode in such a classroom would be $f_{1,0,0} = c/2L_x = 17$ Hz, so there are about 2 octaves of mode-dominated behavior below 70 Hz.

As shown in Table 13.2, for Boston Symphony Hall ($V = 26{,}900$ m^3), $T_{60} = 1.85$ s at 500 Hz when the hall is fully occupied. This corresponds to $f_S \cong 17$ Hz, so a diffuse sound field model can be used throughout the range of human hearing. Of course, in rooms with smaller volumes (<100 m^3), the response will exhibit substantial location dependence (i.e., the behavior will be modal) for frequencies below 200 Hz [11].

It is worth noting that the Schroeder frequency and the critical distance are just two aspects of the same phenomena that measure the dominance of the diffuse field relative to the sound that is radiated directly by a source. Converting f_S to a length by dividing c by λ_S, their equivalence becomes clear.

$$\frac{c}{f_S} = \lambda_S \cong 3r_d \tag{13.36}$$

The primary purpose for our investigation into the properties of sound waves confined within a rectangular enclosure was to illustrate the differences between three-dimensional resonators and one-dimensional resonators. The following is a compilation of those differences:

- **Three indices** are required to specify a mode uniquely and the order of those indices is significant. For example, if an enclosure is not cubical, $f_{1,0,2} \neq f_{2,0,1}$.
- The relationship among resonances is **anharmonic**, even for "ideal" boundary conditions. The ratio of the frequencies of the overtones to that of the fundamental is not given by integer multiples, as it for the modes of a one-dimensional resonator (or a guitar string).
- Different modes may be **degenerate**, having the same natural frequency but different mode shapes.
- Like other standing-wave systems, **excitation** of an individual mode by a source will depend upon the location of the source in relation to the modal shape. It will also depend upon the source's impedance (i.e., whether the source produces a volume velocity that is independent of the room impedance, or a pressure that is independent of the room impedance, or something in between those limits).

- The number of modes within a given range of frequencies, Δf, (or the **density of modes**) is not a constant, as it was for the one-dimensional resonator. The number of modes below a certain frequency is cubic in that frequency and the density of modes is a quadratic function of the frequency in three dimensions.
- When the modal density is large enough that the frequency spacing between successive modes is smaller than the -3 dB bandwidth of the individual modes (i.e., $f > f_S$), it is possible to describe the sound field within the enclosure as "diffuse." In that limit, it is useful to apply statistical energy analysis by assuming that the power is distributed uniformly among all available modes (as we did for the energy of individual particles in an ideal gas using the Equipartition Theorem). That analytical approach can be used to predict both the steady-state, root-mean-square pressure of the sound field in terms of the time-averaged acoustic power input to the room, $\langle \Pi \rangle_t$, and also predict the characteristic exponential time, τ_E, required for the room to achieve its steady-state pressure.
- In architectural applications, when τ_E is used to describe exponential the decay time of the sound field after the sound source is abruptly terminated, it is commonly re-defined as a "**reverberation time**," $T_{60} = \tau_E \ln(10^6) = 13.82\ \tau_E$, that corresponds to the time which is required for the acoustic energy to decay by a factor of one million.

13.3 Modes of a Cylindrical Enclosure

As we are about to discover, the techniques and results that were applied to the resonances of a rectangular enclosure will serve us well again as we investigate the resonances within enclosures of other shapes. Our first venture beyond the Cartesian world-view will be the analysis of a rigid-walled cylindrical resonator like the one shown in Fig. 13.7. In physical and engineering acoustics, the cylindrical resonator is more common than the rectangular enclosure that is nearly ubiquitous for loudspeaker enclosures[5] and in architectural analyses.

There are several reasons that cylindrical shapes are so common. For systems that are required to contain substantial internal pressures (or to protect inhabitants from external pressures, such as in submarines), the cylinder is a much more efficient shape to exploit the strength of the container's materials. (When was the last time you saw a rectangular bottle used for storage of compressed gases or propane for bar-b-ques?) It is also useful because if the oscillatory motion of the fluid within the resonator is purely radial, there will be no viscous "scrubbing losses" on the cylindrical surface.

13.3.1 Pressure Field Within a Rigid Cylinder and Normal Modes

As in Sect. 6.2.1, the solution to the Helmholtz equation (13.2) in cylindrical coordinates is more complicated than the solution in Cartesian coordinates because the azimuthal and radial motions of the oscillating fluid are not independent. As before, the rationale for our acceptance of this complication is that it will be much simpler to impose the boundary conditions at $r = a$ in cylindrical coordinates. If the

[5] A notable exception are the cylindrical speaker enclosures made in ACS 097S, a First Year Seminar at Penn State. Those enclosures use PVC plumbing to provide the "pressure barrier" between the volume velocity produced by the front and rear of the loudspeaker cone described in S. L. Garrett and J. F. Heake, "Hey kid! Wanna build a loudspeaker? The first one's free," Audio Engineering Society Convention Paper #5882, 10–13 October 2003 or S. L. Garrett, "Two-Way Loudspeaker Enclosure Assembly and Testing as a Freshman Seminar", *Proc. 17th Int. Cong. Sound & Vibration* (Curran Assoc., 2011); ISBN 97816617822551.

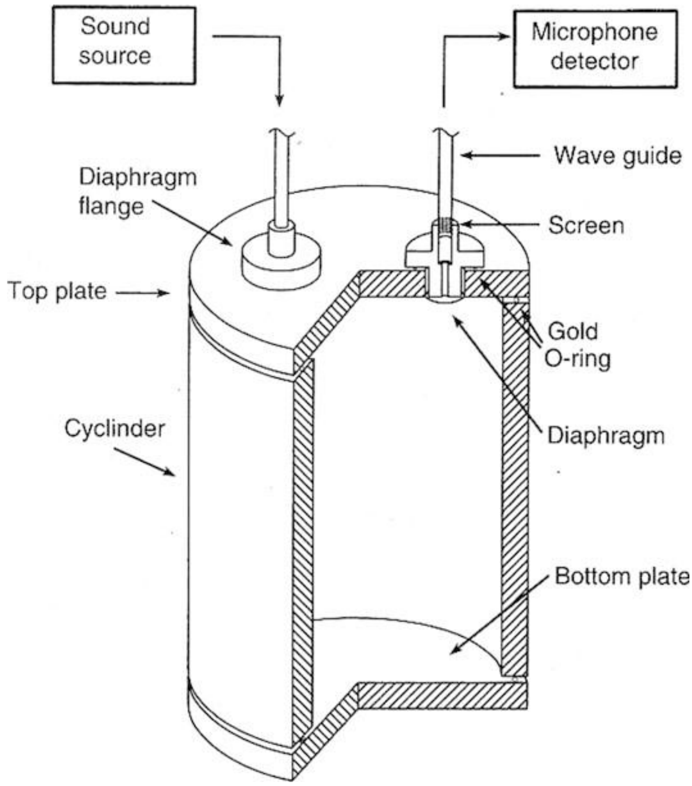

Fig. 13.7 Cylindrical resonator made of stainless steel used at the National Bureau of Standards to measure the speed of sound at very low or very high temperatures. This versatility is facilitated by using waveguides terminated by metallic diaphragms to allow the sound source and microphone to be far from the resonator [12]

Cartesian solution were retained, the rigidity of the cylindrical surface would be imposed by requiring that the radial component of the velocity vanish and writing $u_r(x^2 + y^2 = a^2) = 0$. Specification of the radial component of velocity (or the gradient of the pressure relative to the normal to the cylindrical surface) would be even more challenging.

Faced with this difficulty, we abandon the Cartesian description and accept the fact that we will have to introduce functions that are not superpositions of either simple trigonometric or simple exponential functions as the price we have to pay for simplification in specification of the boundary conditions. As before, we assume single-frequency harmonic time variation and start with the linearized, time-independent Helmholtz equation, but this time we express the Laplacian operator, ∇^2, in cylindrical coordinates.

$$\nabla^2 p_1 = \frac{\partial^2 p_1}{\partial r^2} + \frac{1}{r}\frac{\partial p_1}{\partial r} + \frac{1}{r^2}\frac{\partial^2 p_1}{\partial \theta^2} + \frac{\partial^2 p_1}{\partial z^2} = -k^2 p_1 \tag{13.37}$$

The acoustic pressure, $p_1(r, \theta, z)$, is then expressed using separation of variables,[1] as a product of functions, each of which depending only upon a single coordinate.

$$p_1(r, \theta, z, t) = \Re e\left[R(r)\Theta(\theta)Z(z)e^{j\omega t}\right] \tag{13.38}$$

Substitution of Eq. (13.38) into the Helmholtz equation (13.37) produces the equivalent of Eq. (13.4).

$$\Theta Z\frac{d^2R}{dr^2} + \frac{\Theta Z}{r}\frac{dR}{dr} + \frac{RZ}{r^2}\frac{d^2\Theta}{d\theta^2} + R\Theta\frac{d^2Z}{dz^2} + k^2 R\Theta Z = 0 \tag{13.39}$$

In this case, multiplying through by $r^2/R\Theta Z$ generates three independent, second-order, ordinary differential operators.

$$\frac{r^2}{R}\frac{d^2R}{dr^2}+\frac{r}{R}\frac{dR}{dr}+\frac{1}{\Theta}\frac{d^2\Theta}{d\theta^2}+\frac{r^2}{Z}\frac{d^2Z}{dz^2}+k^2r^2=0 \tag{13.40}$$

As before, the only way Eq. (13.40) can be satisfied by three independent functions is for each independent function of only one of the coordinates to be equal to a constant and that those constants sum to $-k^2$. The solution for $Z(z)$ is identical with the one-dimensional resonator problem.

$$\frac{d^2Z}{dz^2}+k_z^2Z=0 \tag{13.41}$$

If the ends of the cylinder are rigid, so that $u_z\,(0)=u_z\,(L_z)=0$, then the values of k_z are quantized exactly as they were in the analysis of the closed-closed one-dimensional resonator in Eq. (10.45).

$$k_z=\frac{n_z\pi}{L_z};\quad n_z=0,1,2,\,\ldots \tag{13.42}$$

Here, the fact that $n_z=0$ is an acceptable solution admits modes within the cylindrical enclosure that might have variations of p_1 with radius, r, and/or with azimuthal angle, θ, but which do not vary with axial height, z.

With the exception of the axial modes that have only z dependence, for a cylindrical enclosure, it is not possible to separate the modes into a form where the fluid motion has purely azimuthal motion that is independent of the radial coordinate, r. For "sloshing modes" that have $u_\theta\neq 0$, the magnitude of u_θ is not independent of radius, r. The magnitude of the fluid velocity along the azimuthal direction, θ, is greatest at the largest values of r, near the outer boundary, $r=a$, and must vanish near the origin, $r=0$. This coordinate coupling can be appreciated from the form of the azimuthal component of the linearized Euler equation when expressed in cylindrical coordinates [13].

$$\frac{\partial u_\theta}{\partial t}=-\frac{1}{\rho_m r}\frac{\partial p_1}{\partial\theta} \tag{13.43}$$

This interdependence of the radial and azimuthal functions will become apparent when addressing the solution for the angular azimuthal function, $\Theta(\theta\,)$.

$$\frac{d^2\Theta}{d\theta^2}+m^2\Theta=0 \tag{13.44}$$

Again, the solutions to this equation are simple and (by this time) well known. What is less familiar may be the quantization of m by imposition of *periodic boundary conditions* that satisfy the requirement that the solution for the pressure be single-valued. The solutions for $\Theta(\theta\,)$ can be expressed as complex exponentials or sine and cosine functions or, as before in Eq. (13.8), as cosine functions that include a potentially mode-dependent phase factor, $\varphi_{m,\,n}$.

$$\Theta(\theta)=\cos\left(m\theta+\varphi_{m,n}\right) \tag{13.45}$$

At this moment, it will not be obvious why a double index was assigned to the phase factor, but it will be fully justified shortly.

Since cylindrical coordinates have been chosen to specify each unique position within the resonator, the physically realizable values of the azimuthal coordinate are limited to $0\leq\theta<2\pi$. If the value of θ exceeds 2π, we have gone around the resonator more than once and therefore $\Theta(\theta\,)=\Theta(\theta\,+2n\pi)$

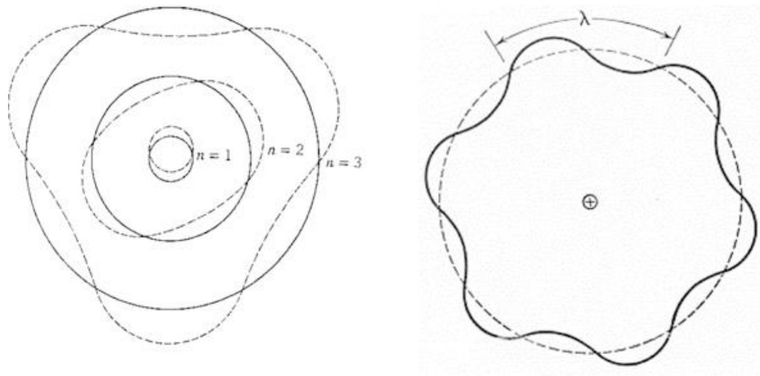

Fig. 13.8 The imposition of a periodic boundary condition on the azimuthal modes of a cylindrical enclosure is similar to the Bohr-Sommerfeld quantization condition for electron "orbits" around a hydrogen nucleus using figures taken from two elementary textbooks on "modern physics." At the *left*, one, two, and three wavelength disturbances (*dashed lines*) along the circumferences (*solid lines*) are shown corresponding to the $m = 1$, $m = 2$ and $m = 3$ modes [14]. At the *right* is drawn the $m = 6$ mode where the equilibrium pressure is shown as the dashed line and six wavelengths, $\boldsymbol{\lambda}$, are shown as a *solid line* [15]

where $n = 0, 1, 2, \ldots$ It is easy to see from Fig. 13.8 that the only way for this "periodic boundary condition" to be satisfied is if m is also an integer: $m = 0, 1, 2, \ldots$.

A more physical way to understand the integer quantization of the acoustic pressure for azimuthal variations is to see that in a cylindrical geometry the boundary condition on the solution requires that both the pressure and the slope of the pressure be continuous with angle where the ends of the wave join. That condition cannot be satisfied if only a half-wavelength fits within the circumference, $2\pi a$. As can be seen in Fig. 13.8, the continuity of pressure and the slope of pressure requires that integer numbers of wavelength fit within a circumference

With the solutions for $\Theta(\theta)$ in hand, we are now able to address the differential equation that determines the radial function, $R(r)$.

$$r^2 \frac{d^2R}{dr^2} + r\frac{dR}{dr} + \left(k^2r^2 - m^2\right)R = 0 \tag{13.46}$$

Before finding the solutions for $R(r)$, the form of Eq. (13.46) is worthy of comment. Since we have determined that m is an integer, Eq. (13.46) really represents an infinite number of second-order, homogeneous, ordinary differential equations—one equation for each integer value of m. Also, this is clearly not a simple harmonic oscillator equation, even if $m = 0$.

As demonstrated previously in Sect. 6.2.1, Eq. (13.46) for $R(r)$ is Bessel's equation. Since it is a second-order differential equation, it will have two linearly independent solutions for each integer value of m, but none of those functions will be sines or cosines. They are integer-order Bessel functions of the first and second kinds, sometimes referred to as Bessel functions, $J_m(kr)$, and Neumann functions, $Y_m(kr)$. The first three of each of the functions were plotted in Figs. 6.8 and 6.9. The subscript indicates the integer value of m that appears in Bessel's equation (13.46).

The next step in this procedure is the imposition of radial boundary conditions that will quantize the values of k_r. For a rigid cylinder, we have only the condition that the boundary be impenetrable to the fluid, so $u_r(a) = 0$. This requirement can be implemented by way of the linearized Euler equation [16].

$$\nabla_r R(a) = \frac{dR(a)}{dr} = \frac{d[J_m(ka)]}{dr} = -\rho_m \frac{\partial u_r(a)}{\partial t} = 0 \tag{13.47}$$

What about the Neumann solutions? Those solutions cannot satisfy the boundary condition at $r = 0$ if we require that our solutions, $R(r)$, remain finite at $r = a$ because $Y_m(0) = -\infty$ for all values of m (see Fig. 6.9). If we were solving for the radial modes of an annulus, with outer radius, a, and inner radius, $b \neq 0$ (see Sect. 13.3.3), then the Neumann solutions, $Y_m(kr)$, would have to be added to the Bessel solutions to satisfy the inner and the outer boundary conditions simultaneously.

$$\begin{aligned}\nabla_r R(b) &= \frac{dR(b)}{dr} = \frac{d[AY_m(kb) + BJ_m(kb)]}{dr} = -\rho_m \frac{\partial u_r(b)}{\partial t} = 0\\ \nabla_r R(a) &= \frac{dR(a)}{dr} = \frac{d[AY_m(ka) + BJ_m(ka)]}{dr} = -\rho_m \frac{\partial u_r(a)}{\partial t} = 0\end{aligned} \tag{13.48}$$

Since there are multiple solutions for $R(r)$ that are coupled to the solutions for $\Theta(\theta)$, the quantization of k_θ and k_r are coupled. For each value of $m = 0, 1, 2, \ldots$, there is a different function that describes the radial pressure amplitude variation. For each value of those m functions, there are n different values of kr where the slope of $J_m(ka)$ vanishes, corresponding to $d[J_m(ka)]/dr \equiv J'_m(ka) = 0$ in Eq. (13.47).

Although this boundary condition is analogous to the requirement that the slopes of the sine or cosine functions vanish for the $Z(z)$ solutions, the extrema of the Bessel functions are not simply related to integer multiples of π. Fortunately, the arguments, $\alpha_{mn} = k_{mn}a$, corresponding to the extrema of Bessel and Neumann functions, are tabulated in many books on "special functions." Some values taken from Abramowitz and Stegun [17] are provided in Table 13.3 as well as in Appendix C.

Table 13.3 Values of the arguments, $j'_{m,s} = \alpha_{mn}$, of integer-order Bessel functions ($0 \leq m \leq 2$) which make the slope of the function vanish

Bessel functions of integer order						
Zeros and associated values of Bessel functions and their derivatives						
x	$j'_{0,x}$	$J_0(j'_{0,x})$	$j'_{1,x}$	$J_1(j'_{1,x})$	$j'_{2,x}$	$J_2(j'_{2,x})$
1	0.00000 00000	+1.00000 00000	1.84118	+0.58187	3.05424	+0.48650
2	3.83170 59702	−0.40275 93957	5.33144	−0.34613	6.70613	−0.31353
3	7.01558 66698	+0.30011 57525	8.53632	+0.27330	9.96947	+0.25474
4	10.17346 81351	−0.24970 48771	11.70600	−0.23330	13.17037	−0.22088
5	13.32369 19363	+0.21835 94072	14.86359	+0.20701	16.34752	+0.19794
6	16.47063 00509	−0.19646 53,715	18.01553	−0.18802	19.51291	−0.18101
7	19.61585 85105	+0.18006 33753	21.16437	+0.17346	22.67158	+0.16784
8	22.76008 43806	−0.16718 46005	24.31133	−0.16184	25.82604	−0.15720
9	25.90367 20876	+0.15672 49863	27.45705	+0.15228	28.97767	+0.14836
10	29.04682 85349	−0.14801 11100	30.60192	−0.14424	32.12733	−0.14088
11	32.18967 99110	+0.14060 57982	33.74618	+0.13736	35.27554	+0.13443
12	35.33230 75501	−0.13421 12403	36.88999	−0.13137	38.42265	−0.12879
13	38.47476 62348	+0.12861 66221	40.03344	+0.12611	41.56893	+0.12381
14	41.61709 42128	−0.12366 79608	43.17663	−0.12143	44.71455	−0.11937
13	44.75931 89977	+0.11924 98120	46.31960	+0.11724	47.85964	+0.11537
16	47.90146 08872	−0.11527 36941	49.46239	−0.11345	51.00430	−0.11176
17	51.04353 51836	+0.11167 04969	52.60504	+0.11001	54.14860	+0.10846
18	54.18555 36411	−0.10838 53489	55.74757	−0.10687	57.29260	−0.10544
19	57.32752 54379	+0.10537 40554	58.89000	+0.10397	60.43635	+0.10266
20	60.46945 78453	−0.10260 05671	62.03235	−0.10131	63.57989	−0.10008

Also tabulated are the values of the Bessel function at the associate extrema, $J_m(j'_{m,s})$ [17]

$$k_{mn} = \frac{\alpha_{mn}}{a} \quad \text{where} \quad \frac{d[J_m(\alpha_{mn})]}{dx} = 0 \tag{13.49}$$

The form of k_{mn} in Eq. (13.49) was chosen to emphasize the similarity to the quantization condition for the axial solutions in Eq. (13.42), $k_z = n_z\pi / L_z$, derived initially. In this case, the numerical factor, α_{nm}, takes the place of $n_z\pi$, and the characteristic resonator dimension in this case is the radius, a, instead of the height of the cylinder, L_z.

The frequencies of the modes within a rigid-walled cylindrical waveguide can now be written in terms of the Pythagorean sum of k_{mn} and k_z, where the integer index, $l = n_z$.

$$f_{lmn} = \frac{c}{2}\sqrt{\left(\frac{n_z}{L_z}\right)^2 + \left(\frac{\alpha_{mn}}{\pi a}\right)^2} \tag{13.50}$$

The complete expression for the acoustic pressure, $p_1(r, \theta, z, t)$, for each normal-mode standing wave within the rigid-walled cylindrical enclosure is the product of the separate functions.

$$p_1(r,\theta,z,t) = \Re\mathrm{e}\left[\widehat{\mathbf{A}}_{\mathbf{l\,m\,n}} \cos(k_{zl}z) J_m(k_{m\,n}r) \cos(m\theta + \varphi_{lm\,n}) e^{j\omega_{lm\,n}t}\right] \tag{13.51}$$

As before, each complex (phasor) modal amplitude, $\widehat{\mathbf{A}}_{\mathbf{lmn}}$, depends upon the excitation coupling. The phase factor, φ_{mn}, is included to allow for the *twofold degeneracy* produced by the fact that the nodal diameters for modes with $m \geq 1$ can have an arbitrary angular orientation with respect to the chosen coordinate axes in the absence of any features that might break the azimuthal symmetry (e.g., see Fig. 13.15).

One obvious feature that would break azimuthal symmetry would be the inclusion of a speaker (e.g., a volume velocity source) at some specific angular location, θ_{drive}, other than on the axis of the cylinder ($r = 0$). In that case, φ_{mn} would be chosen to lock the nodal diameters for modes with $m \geq 1$ to the transducer's location.

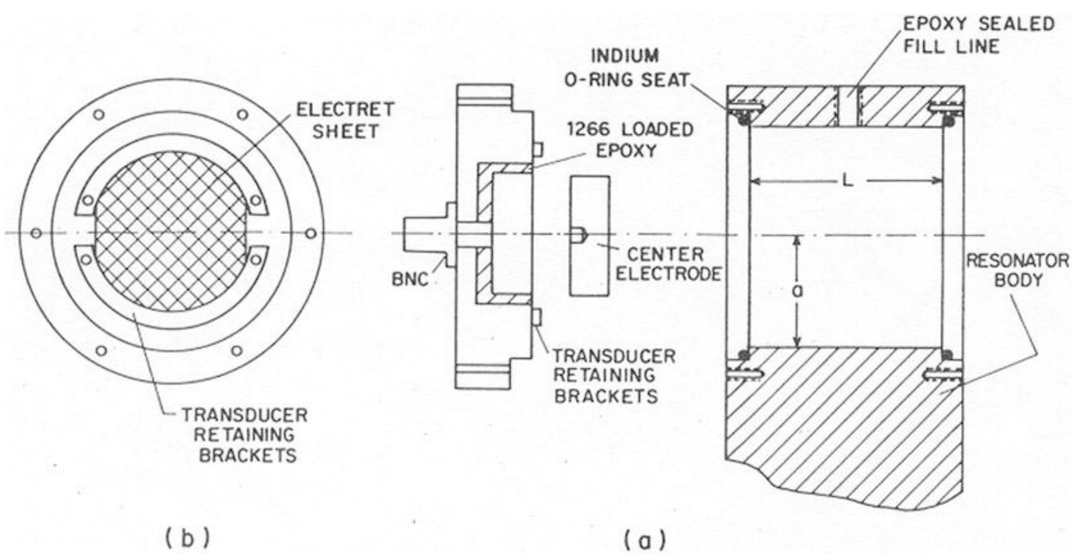

Fig. 13.9 Cylindrical resonator of equal length and diameter, $L = 2a = 5.00$ cm. The circular end caps are reversible electret condenser transducers (see Sect. 6.3.3) that have a slightly smaller diameter than the resonator cavity [18]

Table 13.4 Summary of Bessel mode frequencies and location of nodal circles for the lowest-frequency $m = 1$, 2, and 3 modes, assuming $l = 0$.

n_z	m	n	α_{mn}	f_{lmn} (Hz)	Nodal circles		
					Node (r/a)	Node (r/a)	Node (r/a)
0	0	1	3.831706	24,393	0.6276		
0	0	2	7.015587	44,663	0.3428	0.7868	
0	0	3	10.17347	64,766	0.2364	0.5426	0.8506
0	1	1	1.84118	11,721	0		
0	1	2	5.33144	33,941	0	0.7187	
0	1	3	8.53632	54,344	0	0.4489	0.8219
0	2	1	3.05424	19,444	0		
0	2	2	6.70613	42,693	0	0.7658	
0	2	3	9.96947	63,468	0	0.5151	0.8443

The corresponding values of α_{mn} appear in Table 13.3

The frequencies are based on a rigid-walled cylindrical resonator of radius, $a = 2.50$ cm, and a sound speed near that of helium gas at 16 °C: $c = 1000$ m/s. The radial and azimuthal mode shapes are sketched in Fig. 13.10. The ratios of the radius of the nodal circles to the radius of the cylinder, r/a, were determined by the values of the zero crossings of the corresponding Bessel functions.

The rigid-walled cylindrical resonator in Fig. 13.9 will be used to illustrate the application of the solution for the normal mode frequencies in Eq. (13.50). That resonator was designed to measure the isotopic ratio of ^{3}He to ^{4}He by measuring the speed of sound in such a gas mixture [18]. The frequencies of the axial (height) modes are as easy to calculate as they were for the closed-closed case of the one-dimensional resonator.

Since the resonator was used to measure sound speed in a helium isotopic mixture, the frequencies in Table 13.4 and Eqs. (13.53) and (13.54) assume a sound speed, $c = 1000$ m/s, corresponding to the sound speed in pure ^{4}He at about 289 K (16 °C).

$$f_{l,0,0} = l\left(\frac{c}{2L_z}\right) = l \bullet 10{,}000 \text{ Hz}; \quad l = 0, 1, 2, \ldots \tag{13.52}$$

The Bessel mode frequencies (i.e., $l = 0$) are just as easy to calculate except that we will not be able to use consecutive integers to relate the radius to the resonance frequency.

$$f_{0,m,n} = \alpha_{mn}\left(\frac{c}{2\pi a}\right) = \alpha_{mn} \cdot \; 6{,}366.2 \text{ Hz} \tag{13.53}$$

The first three resonances of the three lowest-frequency Bessel modes for this example are summarized in Table 13.4. That table also includes the ratios of the radii of the nodal circles to the radius of the cylinder, r/a, as determined by the values of the zero crossings of the corresponding Bessel functions. Two-dimensional representations of the mode shapes are provided in Fig. 13.10.

Figure 13.10 shows the nodal locations and the relative phases of the different parts of the resonator for those modes. It does not reveal anything about the relative amplitudes as a function of mode number. The tendency for the acoustic pressure to be localized nearer to $r = a$ as the non-axial mode number increases is best illustrated in Fig. 13.11.

13.3.2 Modal Density Within a Rigid Cylinder

The order of the modes in Table 13.4 was determined by the mode number sequence. Inspection of Table 13.4 shows that this does not place the modes in ascending order with respect to frequency.

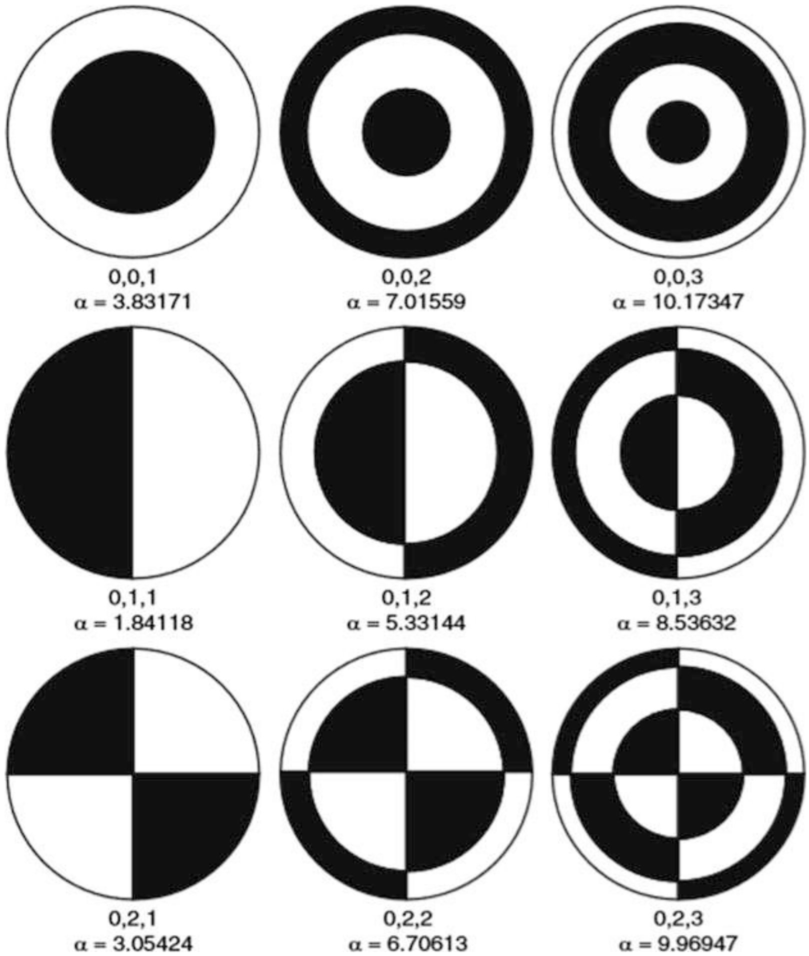

Fig. 13.10 Nodal circles and nodal diameters are drawn to scale for the first three $m = 0$, 1, and 2 modes of a cylindrical resonator. *Black* regions are 180° out-of-phase with *white* regions. Under each (triplet) mode number designation is the value of $\boldsymbol{\alpha} = ka$ for that mode

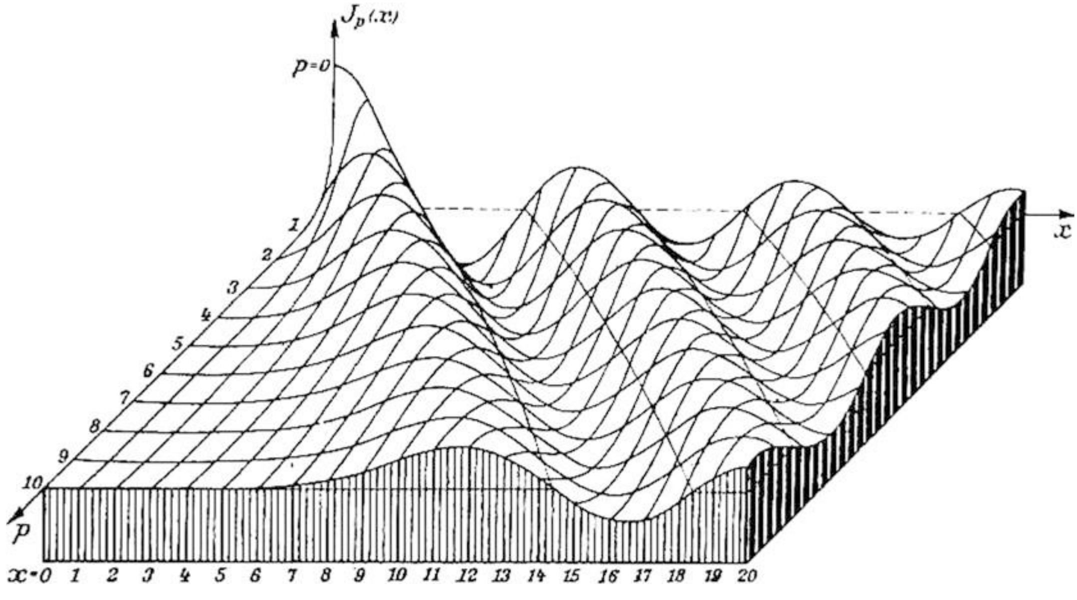

Fig. 13.11 Plots of Bessel functions of the first kind, $J_m(x)$, as a function both of the argument, x, and of the function index, $p = m$. As p increases, more of the amplitude is localized near the perimeter of the cylinder [19]

Table 13.5 Lowest-frequency modes, rounded to integer frequencies, of the helium-filled resonator shown in Fig. 13.9

Order	l	m	n	f_{lmn} (Hz)	Order	l	m	n	f_{lmn} (HZ)
1	1	0	0	10,000	22	2	4	1	39,319
2	0	1	1	11,721	23	2	1	2	39,395
3	1	1	1	15,407	24	4	0	0	40,000
4	0	2	1	19,444	25	3	3	1	40,191
5	2	0	0	20,000	26	4	1	1	41,682
6	1	2	1	21,865	27	1	5	1	42,049
7	2	1	1	23,182	28	0	2	2	42,693
8	0	0	1	24,393	29	1	2	1	43,848
9	1	0	1	26,364	30	4	2	1	44,475
10	0	3	1	26,746	31	0	0	2	44,663
11	2	2	1	27,894	32	3	4	1	45,233
12	1	3	1	28,554	33	3	1	2	45,299
13	3	0	0	30,000	34	2	5	1	45,477
14	2	0	1	31,544	35	1	0	2	45,768
15	3	1	1	32,209	36	4	0	1	46,851
16	2	3	1	33,397	37	2	2	2	47,145
17	0	1	2	33,941	38	4	3	1	48,118
18	1	4	1	35,299	39	1	6	1	48,790
19	1	1	2	35,383	40	2	0	2	48,936
20	3	2	1	35,750	41	5	0	0	50,000
21	3	0	1	38,666	42	3	5	1	50,677

The modes are listed in ascending order of their frequencies up to frequencies less than or equal to 50 kHz. The number of modes with frequencies less than the first five axial mode frequencies is plotted in Fig. 13.12. This table is based on Eq. (13.54) and assumes that $c = 1000$ m/s

Using the previous expression for modal frequency in Eq. (13.50), and modifying it for this specific example in Fig. 13.9, the frequencies of the individual modes can be calculated and placed in order of ascending frequency, as shown in Table 13.5.

$$f_{lmn} = \frac{c}{2}\sqrt{\left(\frac{n_z}{L_z}\right)^2 + \left(\frac{\alpha_{mn}}{\pi a}\right)^2} = 500\text{Hz}\sqrt{\left(\frac{l}{0.05}\right)^2 + \left(\frac{\alpha_{mn}}{0.025\pi}\right)^2} \tag{13.54}$$

As was done for the rectangular enclosure in Eqs. (13.17) and (13.19), we can write an expression to predict the number of modes below a maximum frequency, $f_{\max}$.

$$N \cong \frac{4\pi f_{\max}^3 V}{3c^3} + \frac{\pi f_{\max}^2 A}{4c^2} + \frac{f_{\max} L}{8c} \tag{13.55}$$

For a cylindrical enclosure, $V = \pi a^2 L_z$ and $A = 2\pi a^2 + 2\pi a L_z$, as expected, but the total effective "edge length," $L = 4\pi a + 4L_z$, has a form that could not have been easily anticipated [20]. For our example, the polynomial approximation in Eq. (13.55) is plotted in Fig. 13.12, along with the cumulative mode count for the modes having frequencies less than 1 Hz above the frequency of the pure axial modes up to a maximum frequency, $f_{\max} = f_{5,0,0} + 1 = 50{,}001$ Hz.

From the excellent agreement illustrated in Fig. 13.12 between the modal frequencies in Table 13.5 and the k-space volume polynomial approximation of Eq. (13.55), it is clear that the approximation is quite good for a resonator of modest aspect ratio (i.e., $L_z \cong 2a$), even when the mode indices are fairly low.

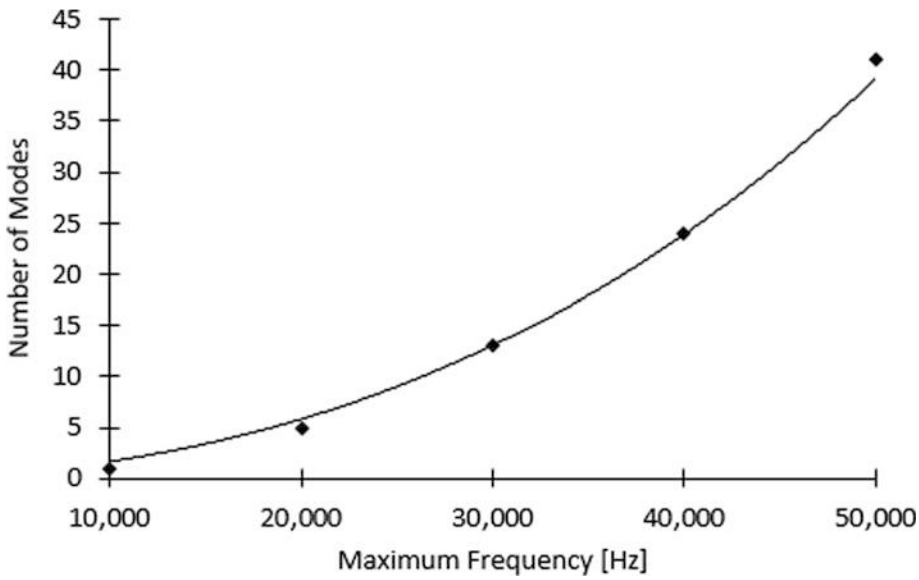

Fig. 13.12 Plot of the number of modes with frequencies less than the value on the x axis for the sample resonator shown in Fig. 13.9. The *diamonds* represent the number of modes listed in Table 13.5. The line is the polynomial approximation in Eq. (13.55)

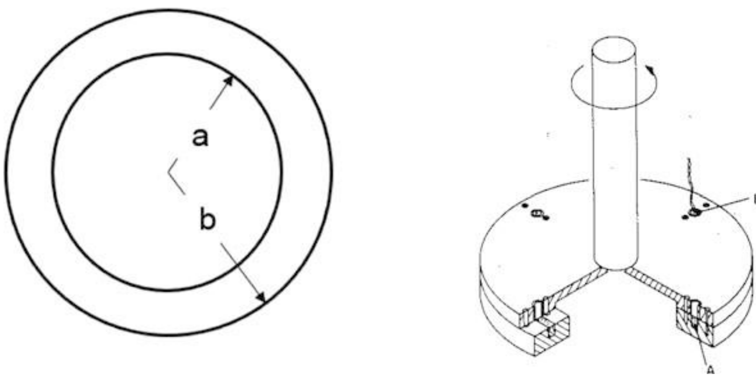

Fig. 13.13 (*Left*) Plan view of an annular (toroidal) resonator with inner radius, a, and outer radius, $b \equiv (1 + \boldsymbol{\delta}\,)\,a$. The resonator's radial cross-section is rectangular. The height of the resonator is L_z, as before, and its width is $b - a$. (*Right*) Cut-away view of a toroidal resonator mounted on a shaft for rotation [21]. The dotted material, labeled "A" in the toroid, represents the annular duct of rectangular cross-section that contains the fluid. A transducer on the "roof" of the resonator is indicated as "B" with lead wires attached

13.3.3 Modes of a Rigid-Walled Toroidal Enclosure*

We ignored the Neumann solutions for the cylindrical enclosure because they became infinite at $r = 0$. For a toroidal resonator, like the one shown in Fig. 13.13 (Right), we need the Neumann solutions to simultaneously match the inner and outer radial boundary conditions. Since there is no fluid on the axis of the torus, $r = 0$, the fact that $N_m(0)$ diverges does not present any difficulty.

The general solution for the pressure can be expressed in polar coordinates as before with the azimuthal component expressed as a trigonometric function.

$$p_1(r,\theta) = [AJ_m(k_{mn}r) + BN_m(k_{mn}r)]\cos\left(m\theta + \varphi_{m,n}\right) \tag{13.56}$$

From the Euler equation [16], the impenetrability of the walls requires that the radial pressure gradient must vanish. This boundary condition leads to pair of equations.

$$\begin{aligned} \left(\frac{\partial p}{\partial r}\right)_{r=a} &= 0 \quad \Rightarrow \quad [AJ'_m(k_{mn}a) + BN'_m(k_{mn}a)] = 0 \\ \left(\frac{\partial p}{\partial r}\right)_{r=b} &= 0 \quad \Rightarrow \quad [AJ'_m(k_{mn}b) + BN'_m(k_{mn}b)] = 0 \end{aligned} \tag{13.57}$$

In Eq. (13.57), the prime symbol indicates differentiation of the functions with respect to the radius. Setting the determinate of the coefficients to zero leads to a transcendental equation that can be solved for the natural frequencies.

$$J'_m(k_{mn}a)\cdot N'_m(k_{mn}b) - J'_m(k_{mn}b)\cdot N'_m(k_{mn}a) = 0 \tag{13.58}$$

Needless to say, the general solution is messy [22].

If we restrict our attention to the case where the difference between the outer and inner radii, $(b - a)$, is small compared to their average, $(b + a)/2$, then there will be many azimuthal modes ($m > 0$) with frequencies that are lower than the first radial or height modes. Assuming also that $L_z \ll a$, the first height mode will occur at approximately $f_{1,0,0} = c/2L_z$, and the first radial mode will occur at approximately $f_{0,0,1} = c/2(b-a)$.

The lowest-frequency azimuthal mode, $f_{0,1,0}$, will correspond to one complete wavelength fitting within the effective circumference of the toroid as already shown schematically in Fig. 13.8. The fact that the first mode corresponds to one full wavelength arises again from the requirement that the azimuthal boundary condition is periodic and the function describing the amplitude of the acoustic pressure, $p_1(r, \theta, z, t)$, is single-valued. The ends of the wave must match in both pressure amplitude and slope. (No "kinky" solutions are acceptable, although not on moral grounds.)

Subsequent azimuthal modes will be integer multiples of the fundamental azimuthal mode as long as $f_{0,m,0}$ is less than $f_{0,0,1}$ or $f_{1,0,0}$.

$$f_{0,m,0} = m\left(\frac{c}{2\pi a_{eff}}\right) \tag{13.59}$$

The obvious choices for a_{eff} would be some arithmetic or geometric average of the inner and outer radii. To first order in $\delta \equiv (b-a)/a$, the average $(a + b)/2$, the geometric mean, $(ab)^{1/2}$, and the Pythagorean average, $\sqrt{\left(a^2 + b^2\right)/2}$, all give $a_{eff} \cong b(1-\delta/2)$. Maynard has calculated the result that is correct to second order in δ [23].

$$a_{eff} = a\sqrt{1 + \delta + \left(\delta^2/6\right)} \tag{13.60}$$

The measured frequency response of a toroidal resonator is shown in the photograph of a spectrum analyzer's screen in Fig. 13.14. For this example, there are 24 equally spaced azimuthal modes with frequencies provided by Eq. (13.59). Those modes are excited and detected by capacitive electret transducers located on the "roof" of the resonator as shown in Fig. 13.13 (Right). Their amplitude initially grows with increasing frequency as the half-wavelength of the modes approach the diameter of the transducers. The amplitude decreases as the wavelength continues to decrease for successively higher-frequency azimuthal modes, since some portions of the transducer's diaphragm are being driven out-of-phase with other portions.

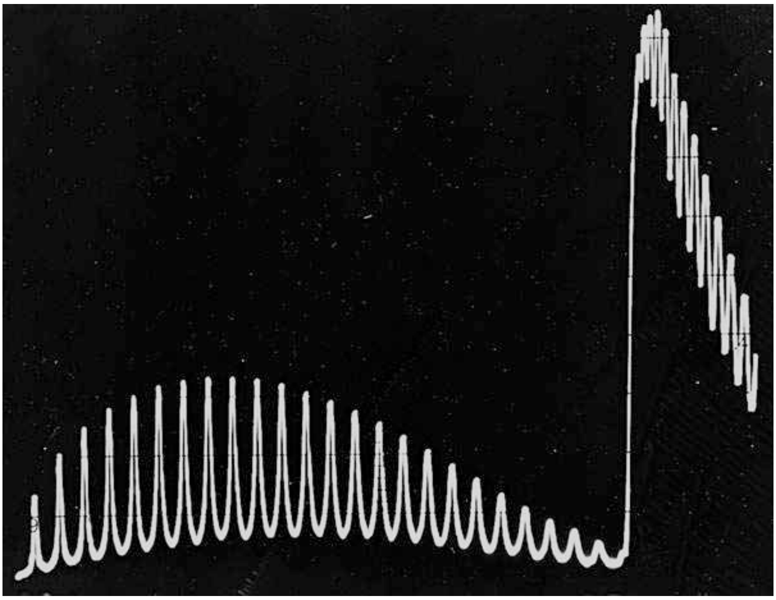

Fig. 13.14 Amplitude vs. frequency as measured by a Hewlett-Packard Model 3580A Spectrum Analyzer for a toroidal resonator that has $|a - b| \ll (a + b)/2$. The modes are excited and detected by transducers mounted on the "roof" of a resonator similar to the resonator depicted in Fig. 13.13 (Right). Above the 24th azimuthal mode, the amplitude of the signal jumps as the first height mode is excited. The amplitude jump is due to the fact that the transducers on the roof couple preferentially to height modes

Above the 24th azimuthal mode, the amplitude of the signal jumps as the first height mode at frequency, $f_{1,\ 0,\ 0} = (c/2L_z)$, is excited. The first height mode is followed by a succession of mixed modes with frequencies, $f_{1,m,0}$. Eleven such mixed modes are visible in Fig. 13.14 ($f_{1,1,0}$ through $f_{1,11,0}$) before the frequency limit of the spectrum analyzer display at 50 kHz is exceeded.

13.3.4 Modal Degeneracy and Mode Splitting

As demonstrated in the analysis of a rectangular room, the degeneracy of modes is related to the symmetry of the enclosure. In Table 13.1, the cubical room had a larger fraction of degenerate modes than the rectangular room. In a cylindrical enclosure, the rotational symmetry makes each azimuthal ($m \geq 1$) mode twofold degenerate. Since we can consider standing waves to be the superposition of traveling waves (see Sect. 3.3.1), the degeneracy of azimuthal modes in a cylindrical enclosure can be viewed from the standing wave perspective or from the traveling wave perspective. For example, when viewed as a standing wave, the nodal diameter of the $m = 1$ mode can be vertical or horizontal (as shown in Fig. 13.15) or have any angular orientation with respect to the coordinate axes (as a superposition of the horizontal and vertical components). This is an example of its twofold degeneracy.

That degeneracy can be "split" if there is some additional feature within the resonator that breaks the azimuthal symmetry. For example, if an incompressible obstacle were placed in the resonator along the circular boundary, as shown in Fig. 13.15, then the mode with the (pressure) nodal diameter passing through the obstacle will have a lower frequency than the mode with the orthogonal nodal diameter.

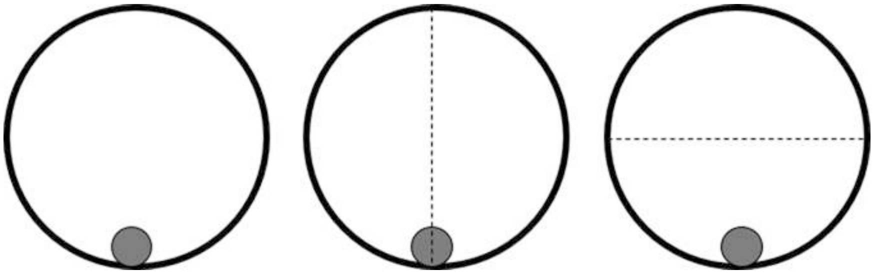

Fig. 13.15 (*Left*) A cylindrical resonator is drawn with a rigid, incompressible object, shown as a gray circle, located adjacent to the cylindrical boundary. If the 0,1,1 mode is excited, then the resonance frequency of the mode will depend upon the orientation of the nodal diameter (shown as a *dashed line*) with respect to that obstacle. (*Center*) Since the acoustic pressure along the node is zero, the frequency of the mode that has a nodal line that intersects the obstacle will be lower than the degenerate mode (in the absence of the obstacle). (*Right*) The mode that has the nodal line that is farthest away from the incompressible obstacle will have a frequency that is higher than the degenerate modes

In the case where the obstacle is located on the (pressure) nodal line, there are no acoustic pressure oscillations, and the fact that the obstacle is incompressible does not change the potential energy of the mode. On the other hand, the nodal line is the location where the azimuthal component of the pressure gradient, $\nabla_\theta p_1$, is greatest and therefore where the azimuthal component of the velocity, u_θ, is greatest. Since the obstacle is rigid, the fluid must accelerate to pass around the obstacle so the square of the local fluid velocity is positive-definite and must increase, therefore increasing the kinetic energy of the fluid. By Rayleigh's method (see Sect. 3.3.2), this increase in kinetic energy will reduce the resonance frequency for that mode since the potential energy is unchanged.

An alternative understanding that leads to the same result (a reduction in modal resonance frequency) is to assume that the perimeter (hence, the azimuthal acoustic path-length) of the cylinder has increased due to the obstacle. Since the frequency of the azimuthal mode depends upon the circumference (which is more obvious if we consider the azimuthal solutions corresponding to integer wavelengths fitting into an effective circumference, $2\pi a_{eff}$, for a toroidal enclosure), again, the modal frequency is reduced.

When the nodal line is farthest from the obstacle, the acoustic pressure oscillations, p_1, are the largest at the location of the obstacle. Since the fluid has become less compressible in that region, the potential energy must increase, as must the resonance frequency. Alternatively, we can imagine that the obstacle could morph into a wedge of the same volume as that of the obstacle. This would reduce the effective circumference and also result in an increase in the resonance frequency of the mode above the degenerate frequency value in the absence of the obstacle.

Just as the modal degeneracy can be lifted by consideration of a standing wave interpretation, it is also possible to split the degeneracy from the traveling wave viewpoint. Since the standing wave can be constructed from two counter-propagating traveling waves, we can split the degeneracy in the azimuthal modes by allowing the fluid within the cylindrical or toroidal enclosure to be rotating in either the clockwise or counter-clockwise directions.

If the fluid is rotating in the clockwise direction, then the speed of sound for the clockwise propagating wave will be increased, and the speed of the counter-clockwise wave will be decreased. Again, picturing the azimuthal modes as consisting of integer numbers of wavelengths fitting within an effective circumference, $2\pi a_{eff}$, the clockwise mode will have a higher frequency than the unperturbed mode, and the counter-clockwise mode will have a lower frequency. Experimental results for the "Doppler" splitting of an azimuthal mode due to fluid rotation are shown in Figs. 13.16 and Fig. 13.25 [21].

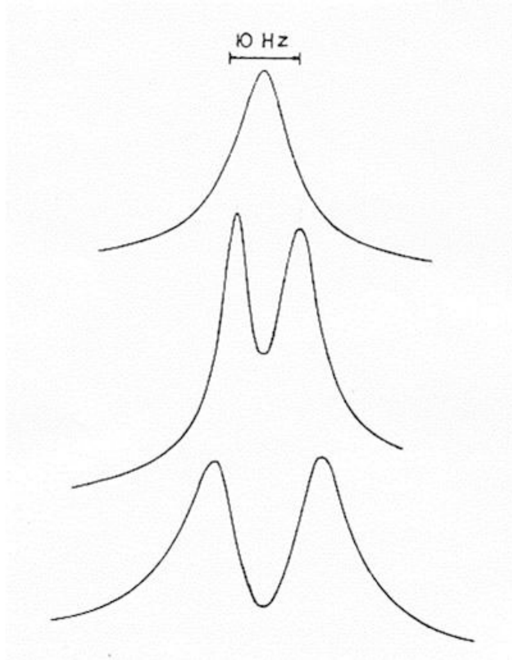

Fig. 13.16 The amplitude of a degenerate azimuthal resonance of a cylindrical resonator (*top*) is shown plotted vs. frequency. As the fluid begins to rotate, the mode "splits" into two distinct resonances whose frequency difference increases with increasing rotational velocity. Since the frequency difference between the two amplitude peaks can be measured with great accuracy [24], it is possible to use the splitting of the resonance to accurately determine the fluid's rotational velocity

13.3.5 Modes in Non-separable Coordinate Geometries

Not all enclosures will have shapes that conform to the 11 coordinate systems in which the Helmholtz equation is separable [1]. Although there is a proliferating variety numerical software package that can solve the Helmholtz equation in arbitrary geometries by finite-element or boundary-element methods, such programs do not (yet) provide any useful classification system for the resulting normal mode shapes and frequencies. Also, if the solution is important, it is essential that an alternative analytical approximation technique be available to check the accuracy of the numerical answers,[6] especially if the modal analysis is being made as part of the design process and a physical model of the system does not yet exist to allow the numerical results can be tested experimentally.

The principle of *adiabatic invariance* was introduced first in Sect. 2.3.4, where it was applied to a simple harmonic oscillator, then again for two-dimensional systems in Sect. 6.2.3, to address the problem of non-separable geometries that described the boundaries of membranes. Adiabatic invariance was then employed to approximate the frequencies and mode shapes of wedge-shaped membranes in Sect. 6.2.4. The same approach will now be applied to a non-separable three-dimensional enclosure. In this case, the enclosure is the cargo bay of the Space Shuttle, shown in plan view and in cross-section in Fig. 13.17.

The cross-section of the Space Shuttle cargo bay is similar to a rigid-rigid cylinder, like those shown in Figs. 13.1 and 13.9, except that the cross-section is not circular but is a hemi-ellipse that is joined to a truncated portion of an irregular octagon. As with the application of adiabatic invariance to the two-dimensional membranes, we will exploit the fact that the ratio of the energy of a mode, E_{lmn}, to its normal mode frequency, f_{lmn}, remains constant if the constraints on the system (i.e., the boundary

[6] "A computer can provide the wrong answer with seven-digit accuracy thousands of times each second."

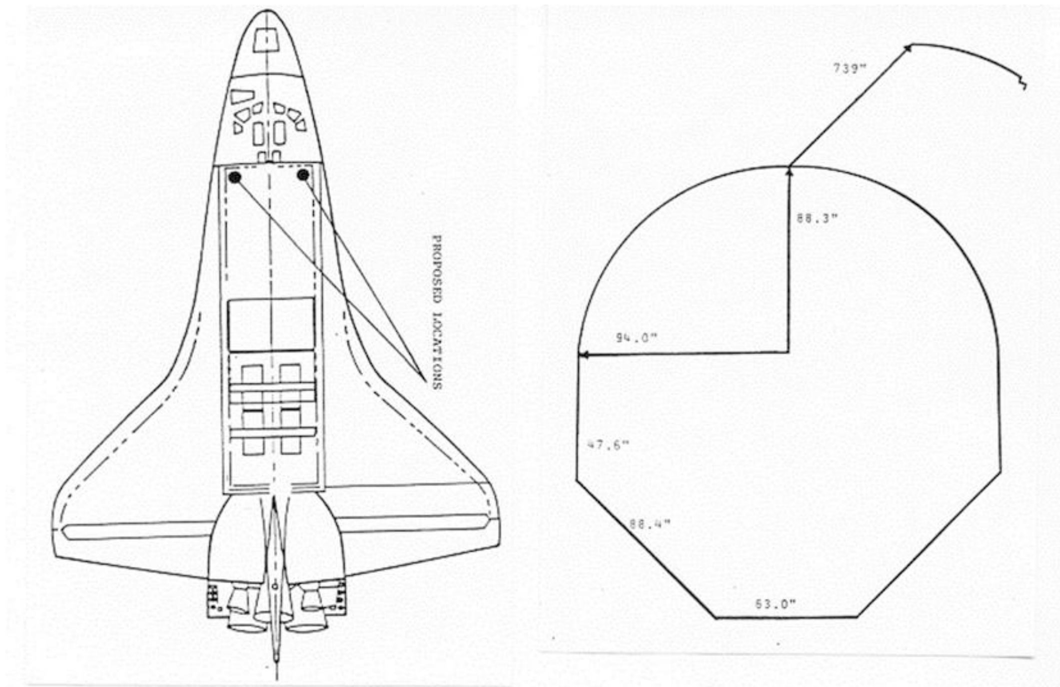

Fig. 13.17 (*Left*) Plan view of the Space Shuttle and (*Right*) cross-section of the Shuttle's cargo bay. The cargo bay's cross-section is a hemi-ellipse, which provides the cargo bay's doors, above a truncated portion of an irregular octagon. The hemi-ellipse has a semi-major axis of 94″ = 2.39 m and a semi-minor axis of 88.3″ = 2.24 m. The bottom of the octagonal section is 53″ = 1.35 m, with the slanted side lengths of 88.4″ = 2.25 m and vertical side lengths of 47.6″ = 1.21 m

conditions) are deformed slowly when compared to the period of oscillation. Said differently, the "adiabatic" portion of the principle requires that the deformation of the boundaries occurs over a time that is many times greater than the period of oscillation, $T_{lmn} = f_{lmn}^{-1}$ [25].

$$\left(\frac{E_{lmn}}{f_{lmn}}\right)_{\text{Adiabatic}} = (\text{constant})_{lmn} \tag{13.61}$$

As will be demonstrated in Sect. 15.4.4, the sound within an enclosure exerts a non-zero, time-averaged radiation pressure on the boundaries that is proportional to the square of the sound amplitude, expressed as either acoustic pressure or acoustic velocity. The energy of the system will be changed if the boundaries move in a way that increases or decreases the energy of the mode by doing "$p\mathrm{d}V$ work" against that radiation pressure. If that magnitude of the radiation pressure is fairly uniform at the boundaries, and if the deformation results in no net change in the enclosure's volume, Eq. (13.61) requires that the modal frequency will remain constant.

If the length of the cargo bay remains constant, then the frequencies of the acoustic modes of the cargo bay, f_{lmn}, will be the same as those of a cylindrical resonator of length, L_z, and radius, a, if the cargo bay's cross-sectional area is set equal to πa^2. This approach was tested experimentally using a scale model of the cargo bay, made from a transparent plastic, shown in Fig. 13.18.

The normal mode frequencies corresponding to each mode were determined by exciting the cavity at a corner using a compression driver that was connected to a flexible tube, visible at the bottom right in Fig. 13.18. Those measured frequencies are provided in Table 13.6. A small probe microphone that

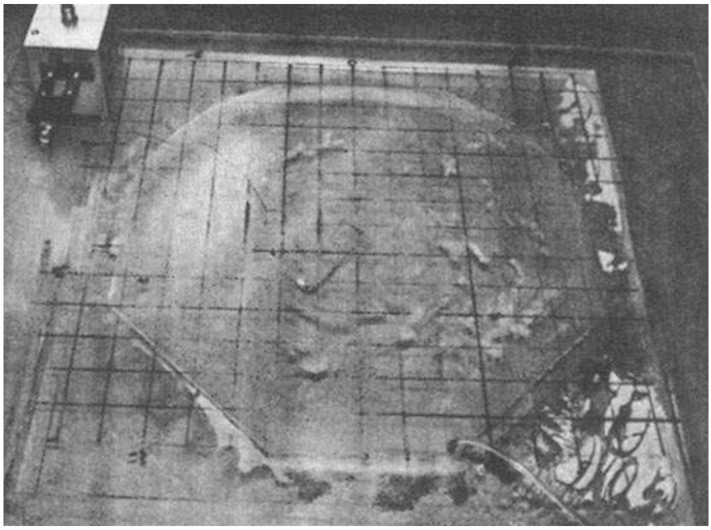

Fig. 13.18 Photograph of a two-dimensional transparent plastic model of the Space Shuttle's cargo bay, shown Fig. 13.17. The grid lines drawn on the top of the model helped locate the microphone used to plot the equal acoustic pressure contours presented in Fig. 13.19

Table 13.6 The measured frequencies of the normal modes of the space shuttle cargo bay model are identified with the corresponding mode numbers for a cylindrical enclosure

Mode	Freq. (Hz)	Ratio $f_{0,m,n}/f_{0,1,1}$	Cylinder $f_{0,m,n}/f_{0,1,1}$	Δ%
0,1,1	41.1	1.000	1.000	0
0,2,1	67.4	1.635	1.658	−1.4
0,0,1	85.3	2.076	2.082	−0.3
0,3,1	94.0	2.287	2.283	+0.2
0,4,1	114.5	2.782	2.891	−3.8

The percentage difference between the measured frequency ratios and the frequency ratios for a cylindrical enclosure, Δ%, has an average of −1.3% ± 1.8%

penetrated the base of the model was then used to trace the pressure nodes by sliding the enclosure along the base. The lines where the acoustic pressure had half the maximum value (measured at the perimeter) were also traced. Both the nodal lines (solid) and half-amplitude lines (dashed) are shown for the four lowest-frequency purely "azimuthal modes" in Fig. 13.19.

It is worth examining the nodal lines in Fig. 13.19 and comparing those nodal lines to the nodal diameters for the corresponding azimuthal modes of cylindrical enclosures that are shown in Fig. 13.10. Because the height of the model cavity, L_z, is very short, $L_z \ll a$, the lowest-frequency "height mode" occurs at a frequency well above any of the purely azimuthal modes in Fig. 13.19: $f_{1,0,0} = c/2L_z \gg f_{0,m,0}$. The similarity between the cylindrical nodal diameters and model's nodal lines provides confirmation that the mode number identification used for the modes of the cargo bay, based on a cylindrical mode classification system, is justified and also provides a convenient nomenclature that can be used to identify the individual modes.

The accuracy of normal mode frequency predictions are established in Table 13.6 by forming the ratio of the measured mode frequencies, $f_{0,m,n}$, to the lowest-frequency measured mode, $f_{0,1,0}$. That ratio is comparted to the same ratio for the cylindrical enclosure's modes that are determined by Eq. (13.50).

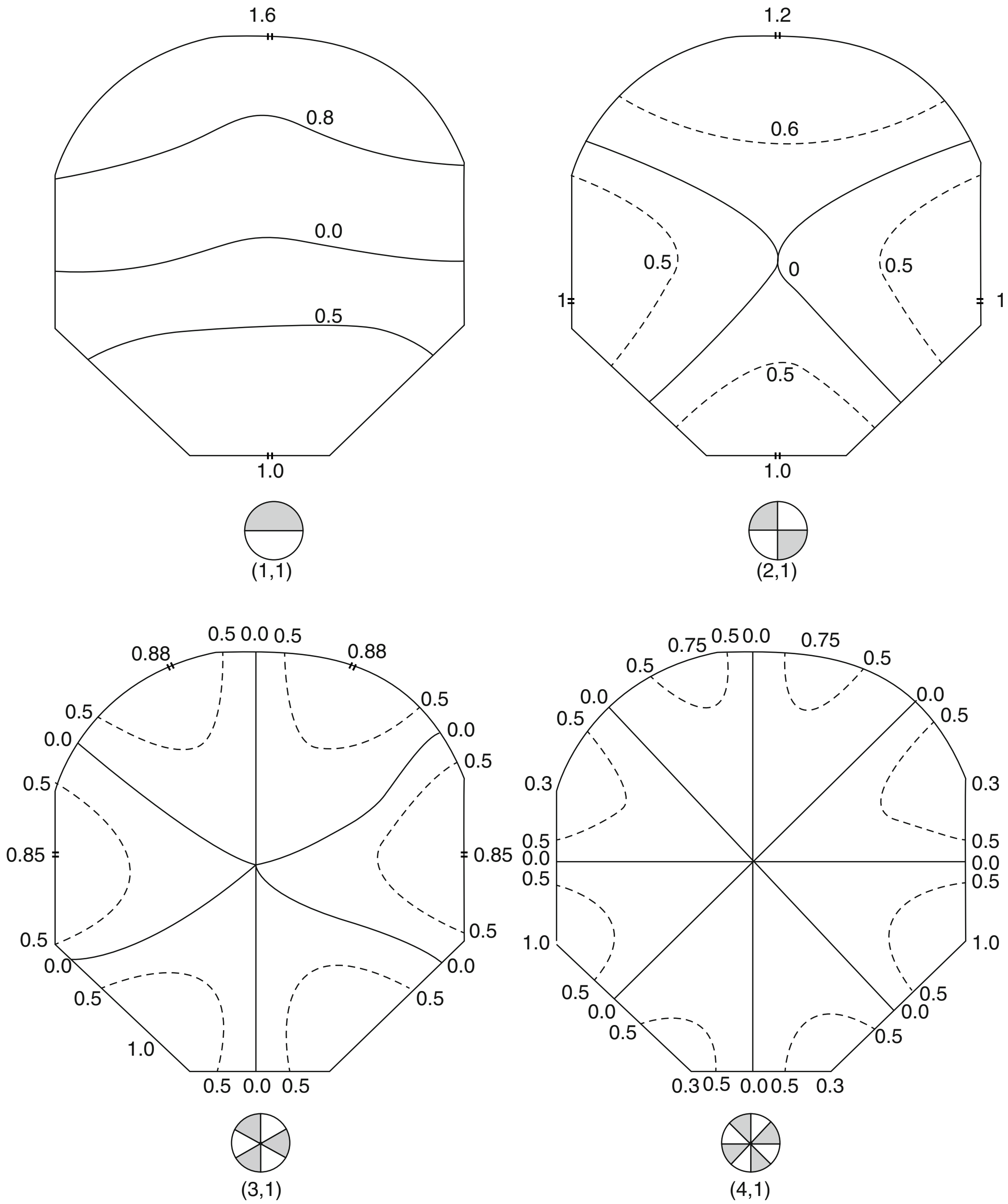

Fig. 13.19 Measured acoustic pressure contours for the lowest-frequency azimuthal modes $(0,m,0)$ using the plastic quasi-two-dimensional mock-up in Fig. 13.18 of the Space Shuttle's cargo bay. The lines shown in the contour maps are pressure nodal lines or half-amplitude lines. Below each contour map is the corresponding pressure distribution for a rigid-walled cylindrical resonator similar to those provided in Fig. 13.10

13.4 Radial Modes of Spherical Resonators

Spherical enclosures have played an important role in high-precision acoustical measurements because they can achieve high quality factors since there is no fluid shearing at the boundary for the radial modes of a spherical resonator; therefore, there are no viscous losses associated with those modes. In

Chap. 12, only the outgoing solution for three-dimensional spherical spreading in Eq. (12.8) was investigated because that chapter's focus was on radiation and scattering in an unbounded medium. In a spherical resonator, there is a boundary that reflects the outgoing spherical wave and produces a converging spherically symmetric wave that produces radial standing-wave modes when superimposed on the outgoing wave, just as the addition of a right- and left-going plane waves created standing waves in Eqs. (3.18) and (3.19).

The proper superposition of the diverging and converging spherical waves must eliminate the infinite pressure that occurs at the origin, $r = 0$. This divergence did not create any difficulty for the radiation calculations in Chap. 12 because it was assumed that the radius, a, of the volume velocity source was non-zero. To eliminate that unphysical infinity, the superposition of the outgoing and converging spherical waves will be formed from their difference.

$$\begin{aligned} p_1(r,t) &= \Re e\left[\frac{\widehat{\mathbf{C}}}{r} e^{\,j(\omega t-kr)} - \frac{\widehat{\mathbf{C}}}{r} e^{\,j(\omega t+kr)}\right] = \Re e\left[\frac{-\widehat{\mathbf{C}}e^{j\omega t}}{r}\left(e^{jkr} - e^{-jkr}\right)\right] \\ &= \Re e\left[\frac{2j\widehat{\mathbf{C}}e^{j\omega t}}{r}\sin(kr)\right] = \frac{C'}{r}\sin(kr)\cos(\omega t+\varphi) \end{aligned} \tag{13.62}$$

At the origin, for $r = 0$, Eq. (13.62) produces $p_1(0, t) = kC' \cos(\omega t + \varphi)$ when the small (kr) expansion of $\sin(kr)$ is used to evaluate the radial acoustic pressure at $r = 0$. In the final expression, all of the constants have been coalesced into a scalar amplitude, C', to emphasize the similarity with other standing-wave solutions like Eq. (10.44).

13.4.1 Pressure-Released Spherical Resonator

If the spherical boundary is pressure-released and located at a radial distance, a, from the center of the sphere, then the radial modes are harmonic.

$$p_1(a) = 0 = \frac{C'}{a}\sin\left(k_{0,0,n}^{\text{release}}a\right) \quad \Rightarrow \quad k_{0,0,n}^{\text{release}} = \frac{n\pi}{a};\ \ n = 1,\ 2,\ 3,\ \ldots \tag{13.63}$$

This is easy to implement for a water-filled thin-walled glass sphere. Since water is nearly incompressible, the thin glass wall of the spherical vessel moves with the water. If additional precision is required, the effective radius of such a spherical resonator can be increased by an amount determined by the mass density of the thin glass in exactly the same way the thin gold layer created a density-weighted increase in the effective length of a resonant bar for the analysis of the quartz micro-balance in Sect. 5.1.2.

Wilson and Leonard used a commercial round-bottom Pyrex™ boiling flask as a pressure-released spherical resonator to contain the water so that very small sound absorption could be measured in a laboratory over the range of frequencies between 50 kHz and 500 kHz [26]. The sphere was suspended from a support using three 250-μm-diameter steel wires so that any loss due to sound transmission through the supports was minimized. The sphere was placed in a vacuum chamber with the air pressure reduced to less than 1.0 mmHg (133 Pa) to minimize radiation losses. In addition to the absence of any viscous dissipation, the thermal relaxation losses at the boundary were also negligible because the thermal expansion coefficient of water is so close to zero at room temperatures[7] and the boundary was

[7] The expansion coefficient vanishes at 4 °C where the density of water is a maximum. If ice were not less dense than water, you would not be reading this footnote, since when water froze in the winter, it would sink to the bottom of the lake and more ice would form at the surface and sink. The fact that ice floats insulates the water below. Since all animals evolved from a watery origin, it is possible that there might be no animal life as we know it on this planet if ice were denser than water.

pressure-released. A similar pressure-released spherical resonator would correspond to a gas-filled spherical balloon in a vacuum, like the Echo satellites, which were placed in low Earth orbit near the beginning of the US space program in August 1960 (see Problem 11 and Fig. 13.34) [27]. Such a pressure-released boundary condition for a spherical resonator has also been shown to be an accurate representation of the modes of the liquid (aqueous humor) in the mammalian eyeball [28].

13.4.2 Rigid-Walled Spherical Resonator

If the boundary of the spherical resonator is rigid and impenetrable, then the Euler equation can be used to relate the standing-wave pressure, $p_1(r)$, in Eq. (13.62), to the radial velocity of the fluid at the boundary, $u_r(a)$.

$$\nabla_r p_1(a) \propto \frac{dp_1(a)}{dr} = C' \left[\frac{k_{0,0,n}^{\text{rigid}} \cos(kr)}{r} - \frac{\sin\left(k_{0,0,n}^{\text{rigid}} r\right)}{r^2} \right]_{r=a} \propto -\rho_m \frac{\partial u_r(a)}{\partial t} = 0$$
$$\frac{\left(k_{0,0,n}^{\text{rigid}} a\right) \cos\left(k_{0,0,n}^{\text{rigid}} r\right)}{a} = \frac{\sin\left(k_{0,0,n}^{\text{rigid}} a\right)}{a^2} \quad \Rightarrow \quad \tan\left(k_{0,0,n}^{\text{rigid}} a\right) = \left(k_{0,0,n}^{\text{rigid}} a\right) \tag{13.64}$$

The values of $k_{0,0,n}^{\text{rigid}}$ are thus quantified by a simple transcendental equation whose solutions will be familiar from earlier investigations of a mass-loaded string in Sect. 3.6. The values of (ka) that satisfy Eq. (13.64) are provided in Table 13.7.

The frequencies of radial modes of a gas-filled spherical resonator were used by scientists at the US National Bureau of Standards, in Gaithersburg, MD, to produce the most accurate value of Boltzmann's constant, k_B, and the universal gas constant, $\Re$ [29]. The Bureau's acoustical determination of these fundamental constants constituted a reduction in their uncertainty by a factor of 5 over previous determinations and subsequently was made less than 1 ppm by using microwave resonance frequencies and the speed of light (known to 1 ppb) to determine the sphere's volume[8] [30]. A cross-sectional diagram of the resonator and its surrounding pressure vessel is provided in Fig. 13.20.

For large values of n, $\left(k_{0,0,n}^{\text{rigid}} a\right) \cong (n + ½)\pi$

Table 13.7 Solutions for the radial mode frequencies, $f_{0,0,n}^{\text{rigid}} = \left(k_{0,0,n}^{\text{rigid}} a\right) c/(2\pi a)$, for a rigid, impenetrable spherical resonator based on Eq. (13.64)

Radial mode	$(k_{0,0,n}a)$	$(k_{0,\,0,\,n}a)/\pi$
1	4.49341	1.430
2	7.72525	2.459
3	10.90412	3.471
4	14.06619	4.477
5	17.22076	5.482
6	20.37130	6.484
7	23.51945	7.486

[8] Boltzmann's constant, k_B, and the universal gas constant, $\Re$, are the second least precisely known physical constants after Newton's Universal Gravitational Constant, G. As of 20 May 2019, the value of k_B and $\Re$ are taken as being exact (see Appendix A).

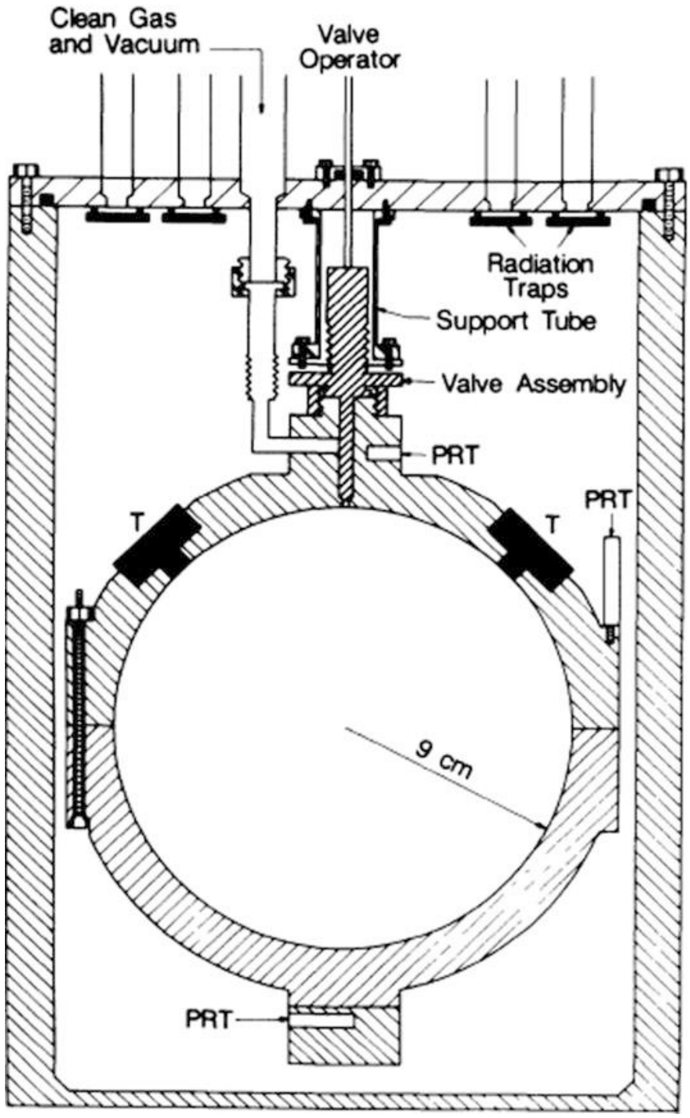

Fig. 13.20 Cross-sectional diagram of the spherical resonator and pressure vessel that were used by the US National Bureau of Standards (now known as the National Institute for Standards and Technology) to determine the universal gas constant, ℜ [29]. The transducer assemblies are indicated as "T," and the locations of the platinum resistance thermometers are indicated by "PRT." The pressure vessel was immersed in a stirred liquid bath (not shown) which maintained the temperature of the apparatus and the gas within the sphere at a constant temperature

13.5 Waveguides

The conceptual and mathematical apparatus that has just been developed to understand the sound field in three-dimensional rectangular or cylindrical enclosures can easily be extended to describe sound propagation in a waveguide. Waveguides can be man-made or can occur naturally.[9] They are important because sound waves that are contained within a waveguide do not suffer the $1/r$ decrease in sound

[9] The National Weather Service in Tallahassee, FL, felt obligated to issue a weather statement on 9 March 2011 in response to "strange sounds being reported in their area explaining that the unusual sound that was observed was 'caused by thunder from a distant lightning strokes . . . bouncing off a very stable layer above the ground. This is called ducting . . . and can allow sound to travel unusually long distances.'"

pressure amplitude that accompanies three-dimensional spherical spreading. Such waveguides have utility in the transmission of sound from the source to a receiver. One early waveguide is the stethoscope invented in 1816 by the Parisian physician, René Laennec [31]. Waveguides (called speaking tubes) were also used on sailing ships, at least as early as the 1780, to communicate orders from the ship's captain to sailors, and they were still in use on naval warships during World War II.

13.5.1 Rectangular Waveguide

Consider the waveguide of rectangular cross-section shown in Fig. 13.21. Application of the wavenumber quantization conditions for a rectangular enclosure in Eq. (13.11) will apply, but now $L_z = \infty$.

As a consequence, k_z is no longer restricted to only discrete values, but becomes a continuous variable. The separation condition of Eq. (13.6) will now determine k_z as a function of the frequency, ω, at which the waveguide is being excited.

$$k_z^2 = \left(\frac{\omega}{c}\right) - k_x^2 - k_y^2 \text{ where } k_x = \frac{\ell\pi}{L_x} \text{ and } k_y = \frac{m\pi}{L_y}; \quad \ell, m = 0, 1, 2, 3, \ldots \tag{13.65}$$

The corresponding sound field can be written as in Eq. (13.13) except that the option for boundary conditions that are not all rigid and impenetrable will be retained by the choice of either sine or cosine functional dependence (or their superposition) in the x and y directions, as indicated by the curly brackets.

$$p_{\ell m}(x, y, z; t) = \Re e\left[\widehat{\mathbf{A}}_{\mathbf{lm}} \left\{ \begin{array}{c} \sin(k_x x) \\ \cos(k_x x) \end{array} \right\} \left\{ \begin{array}{c} \sin(k_y y) \\ \cos(k_y y) \end{array} \right\} e^{j(\omega t - k_z z)}\right] \tag{13.66}$$

Notice that the complex amplitude pre-factor (phasor), $\widehat{\mathbf{A}}_{\mathbf{lm}}$, has only two indices since the z wavenumber, k_z, is not quantized.

The quantized wavenumbers that satisfy the transverse boundary conditions for a waveguide of rectangular cross-section can be combined into a single wavenumber with two subscripted indices, where k_x and k_y are specified in Eq. (13.65), for a rigid-walled rectangular waveguide.

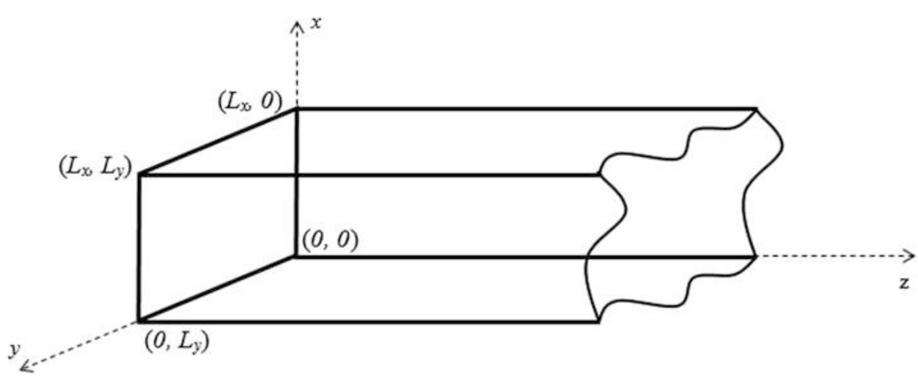

Fig. 13.21 Waveguide of rectangular cross-section that extends to infinity in the z direction

$$k_{\ell m}^2 \equiv k_x^2 + k_y^2 \quad \Rightarrow \quad k_z = \pm\sqrt{\left(\frac{\omega}{c}\right)^2 - k_{\ell m}^2} = \pm\left(\frac{\omega}{c}\right)\sqrt{1 - \left(\frac{\omega_{\ell m}}{\omega}\right)^2} \tag{13.67}$$

This wavenumber consolidation makes it possible to generalize the following results to rigid-walled waveguides of circular cross-section later in Sect. 13.5.4, by letting $k_{\ell m} = \alpha_{mn}/a$, where α_{mn} is quantized by Eq. (13.49).

The consequences for k_z that arise from Eq. (13.67) are significant. For the plane wave mode, when the wave fronts within the guide are normal to the z direction and there is no variation in the pressure or particle velocity in the transverse plane (i.e., $k_x = k_y = 0$), then $\Im m[k_z] = 0$, and $k_z = \omega/c$.[10] On the other hand, if $k_{\ell m} > \omega/c$, then the real part of the wavenumber will vanish, $\Re e[k_z] = 0$. Substitution of a purely imaginary value of k_z into the pressure field within the waveguide, as specified in Eq. (13.66), creates a pressure field that decays exponentially with distance beyond the source of such a disturbance within the waveguide. The characteristic exponential decay distance, $\delta = \Im m\left[k_z^{-1}\right]$, for frequencies well below cut-off for a particular higher-order mode, $\omega \ll \omega_{\ell m}$, will be determined by the height or width or combination of the height and width of the waveguide, depending upon the mode.

$$\lim_{\omega \to 0}[\delta] = \frac{j}{k_{\ell m}} = j\frac{L_x}{\ell\pi} \;\text{ or }\; j\frac{L_y}{m\pi} \;\text{ or }\; j\sqrt{\left(\frac{L_x}{\ell\pi}\right)^2 + \left(\frac{L_y}{m\pi}\right)^2} \;\text{ if }\; \omega < \omega_{\ell m} \tag{13.68}$$

The frequency at which a non-plane wave mode with $k_x \neq 0$ or $k_y \neq 0$ or both k_x and k_y being non-zero is known as the *cut-off frequency*, $\omega_{co} = 2\pi f_{co}$, for that mode. Such exponentially decaying behavior was demonstrated for sound propagation in exponential horns in Sect. 10.9.1 for frequencies below the cut-off determined by the horn's flare constant. Each waveguide mode will have its unique cut-off frequencies determined by $k_{\ell m}$: $2\pi f_{co} = \omega_{co} = ck_{\ell m}$.

13.5.2 Phase Speed and Group Speed

The phase speed for propagation down the waveguide is $c_{ph} = \omega/k_z$. Below cut-off for any of the higher-order modes of the waveguide, $\omega < \omega_{co} = c\,k_{\ell m}$, only plane waves will propagate down the guide. In that case, $k_z = \omega/c$, so $c_{ph} = c$, as was the case for plane waves propagating in an unbounded medium with a constant thermodynamic sound speed, c. At frequencies that are high enough that one or more non-plane modes can be excited, $\omega > \omega_{\ell m}$, the phase speed becomes a function of frequency.

$$c_{ph} = \frac{\omega}{k_z} = \frac{c}{\sqrt{1 - \left(\frac{\omega_{co}}{\omega}\right)^2}} \tag{13.69}$$

This phase speed is plotted in Fig. 13.22 for the plane wave (0,0) mode and the next two highest-frequency non-plane modes, (1,0) and (2,0), where it has been assumed that $L_x \gg L_y$ so $\omega_{2,0} < \omega_{0,1}$.

It is useful to make a geometrical interpretation of the variation of the phase speed in a waveguide with the frequency of the sound, ω, that is propagating within. Just as the boundary conditions were satisfied in a rigidly terminated resonator by the superposition of two counter-propagating traveling waves, it is possible to extend that same model to a waveguide if we let the two traveling plane waves propagate in different directions.

[10] There will necessarily be some variation in the plane wave's velocity in the z direction within the very thin thermoviscous boundary layer specified in Eqs. (9.14) and (9.33). The attenuation and dispersion created by these boundary layer effects will be calculated in Sect. 13.5.5.

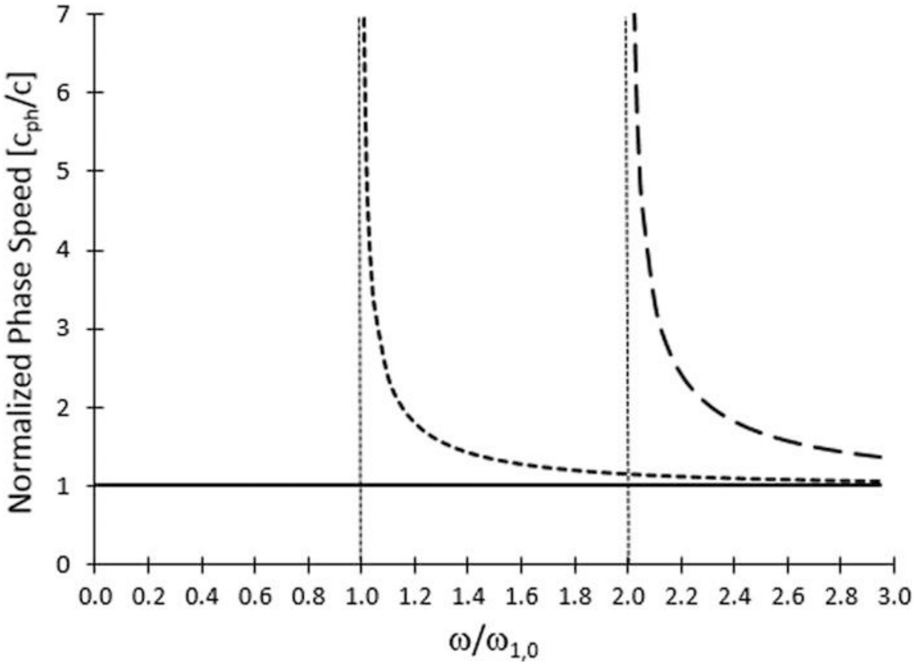

Fig. 13.22 Phase speed, c_{ph}, relative to the thermodynamic sound speed, $c = \sqrt{(\partial p/\partial \rho)_s}$, as a function of frequency, ω, relative to the cut-off frequency, $\omega_{1,0}$, of the first non-planar mode. The phase speed of the plane wave mode (0,0) is the *solid line*. The *short-dashed line* is the relative phase speed of the (0,1) mode, and the *long-dashed line* is the relative phase speed of the (2,0) mode. In this figure, it is assumed that $L_x \gg L_y$ so $\omega_{2,0} < \omega_{0,1}$

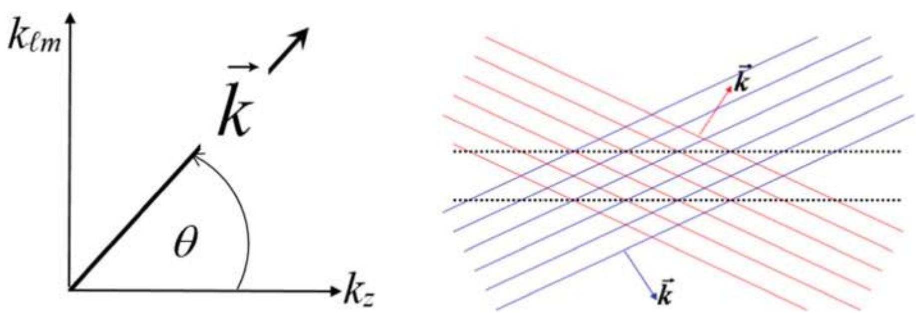

Fig. 13.23 (*Left*) The wavevector (*bold arrow*), $\vec{k}$, that characterizes the direction of the plane wave is projected on to the z axis to produce k_z and on to the y axis to produce the cut-off wavenumber, $k_{\ell m}$. In accordance with the separation equation (13.65), the Pythagorean sum of k_x and $k_{\ell m}$ is length of $\left|\vec{k}\right|$. (*Right*) The top and bottom boundaries of the waveguide are shown as horizontal dotted lines. The wave fronts of the two traveling plane waves always overlap at both boundaries indicating that those rigid surfaces correspond to the locations of the acoustic pressure amplitude maxima

In Fig. 13.23 (Right), there are two plane waves indicated by equally spaced wave fronts and two wavevectors, $\vec{k}$, that are perpendicular to their respective wave fronts. For one set of wave fronts, the angle that $\vec{k}$ makes with the z axis is θ. For the other set of wave fronts, the angle that $\vec{k}$ makes with the z axis is $-\theta$. Using the diagram in Fig. 13.23 (Left) that projects $\vec{k}$ onto k_z and $k_{\ell m}$, the angle, θ, that $\vec{k}$

makes with the z axis can easily be written, and the phase speed, c_{ph}, can be expressed in terms of that angle, as well.

$$\cos\theta = \frac{k_z}{\left|\vec{k}\right|} \quad \Rightarrow \quad c_{ph} = \frac{\omega}{k_z} = \frac{\omega}{\left|\vec{k}\right|\cos\theta} = \frac{c}{\cos\theta} \tag{13.70}$$

The top and bottom of the waveguide are represented by the horizontal dotted lines in Fig. 13.23 (Right). Inspection of that figure reveals that both sets of wave fronts, moving in different directions determined by their respective wavevectors, $\vec{k}$, always intersect at the waveguide boundaries, making that intersection a pressure maximum, as it must be if the boundary is rigid and impenetrable.

With this geometric interpretation in mind, the following picture emerges for the relationship between phase speed; the wave's frequency, ω; and the cut-off frequency, $\omega_{\ell m}$. For a plane wave mode with frequency, $\omega < \omega_{\ell m}$, that wavevector, $\vec{k}$, is aligned with the z axis and $\theta = 0°$, so $c_{ph} = c$. If a higher-order waveguide mode is excited, so $\omega > \omega_{\ell m}$, then at cut-off, the wavevector, $\vec{k}$, is parallel to $k_{\ell m}$ and $k_z = 0$. In that case, there is a simple standing wave created by the superposition of the two plane waves traveling in opposite directions and $\theta = 90°$. The wave fronts are parallel to the waveguide boundaries, so the phase is identical at all times everywhere along the waveguide, assuming the sound field within the waveguide has reached steady state. For the phase to (instantaneously) be the same over any non-zero distance, the phase speed must be infinite. This infinite phase speed at the cut-off frequency is apparent from Fig. 13.22, since the curves representing the phase speed of the non-plane wave modes are asymptotic to the vertical lines that extend from each mode's cut-off frequency.

At cut-off, the two traveling waves are moving up and down (i.e., $\theta = 90°$) in Fig. 13.23 (Right); they are making no progress whatsoever in the z direction. If the sound energy is to travel down the waveguide in the z direction, $\theta < 90°$. For example, if $\tan\theta = 10$ (so $\theta = 84.3°$), then the plane waves move forward along the z axis by one-tenth as far as the wave fronts have moved going up and down between the waveguide's rigid boundaries during the same time interval. The speed at which the sound energy moves forward along the $+z$ axis, down the waveguide, is the group speed, c_{gr}. Figure 13.23 (Left) can be used to express the group speed in terms of the angle, θ, that the wavevector, $\vec{k}$, makes with the z axis.

$$c_{gr} = c\cos\theta = c\sqrt{1 - \left(\frac{\omega_{\ell m}}{\omega}\right)^2} \quad \Rightarrow \quad c_{gr}c_{ph} = c^2 \tag{13.71}$$

13.5.3 Driven Waveguide

As with any linear system, the complex (phasor) amplitude coefficient, $\widehat{\mathbf{A}}_{\mathbf{lm}}$, of the sound field within the waveguide, as expressed in Eq. (13.66), depends upon the amplitude of the excitation and the geometrical distribution of the sources that create the excitation. A two-dimensional Fourier decomposition can be used to calculate the values of $\widehat{\mathbf{A}}_{\mathbf{lm}}$, just as the harmonic content of a plucked string was calculated in terms of the string's normal modes in Sect. 3.5. Rather than make such a calculation, it will be instructive to exam the excitation of a waveguide by two rectangular pistons placed in the end of a waveguide of square cross-section, illustrated in Fig. 13.24.

For a rigid-walled rectangular waveguide, like those shown in Figs. 13.21 and 13.24, the excitation of a mode will depend upon the projection of the piston's volume velocity complex amplitude distribution, $\widehat{\mathbf{U}}(x, y)$, upon the basis functions defined by the wavenumbers in Eq. (13.65) that satisfy

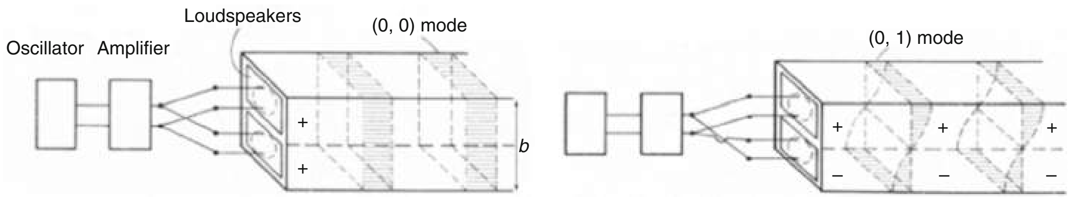

Fig. 13.24 (*Left*) A waveguide of square cross-section is driven by two identical rectangular pistons located that the end of the waveguide, $z = 0$. If both pistons are driven in-phase, then only the plane wave mode (0,0) can be excited. (*Right*) If the two rectangular pistons are driven 180° out-of-phase, so the net volume velocity is zero, then no plane wave is generated. If the drive frequency, $\boldsymbol{\omega}$, is greater than the cut-off frequency, $\boldsymbol{\omega}_{0,1}$, $= \boldsymbol{\pi}c/b$, then the (0,1) mode will be excited [32]

the boundary conditions. Since those cosine functions are all orthogonal (for the rigid waveguide, but not necessarily for the functions that satisfy more general boundary conditions), a piston with a uniform distribution of volume velocity, $\left|\widehat{\mathbf{U}}(x, y)\right| =$ constant, can only excite the plane wave (0,0) mode at any frequency. That sound will propagate down the waveguide in the +z direction with $c_{ph} = c_{gr} = c$. This plane wave excitation is illustrated in Fig. 13.24 (Left).

If the piston's volume velocity distribution has a non-zero projection onto the basis functions that satisfy the waveguide's boundary conditions in the x and y directions, then those modes will be excited, as long as the excitation frequency, ω, equals or exceeds that mode's cut-off frequency, $\omega \geq \omega_{\ell m}$.

In Fig. 13.24 (Right), the upper piston moves forward while the lower piston moves backward. The net volume velocity is zero so there will be no coupling to the plane wave mode. If the frequency of vibration of those two transducer segments, ω, is less than the cut-off frequency for the (0,1) mode, $\omega < \omega_{0,\ 1} = \pi c/b$, where $b = L_y$, then the fluid being pushed forward and pulled back by the two transducer segments will just "slosh" between those segments, and all of the fluid's motion will be confined to a distance of about $z \leq L_z = b$, as would be expected for an exponentially decaying mode that decays with a distance, δ, given by Eq. (13.68).

If the drive frequency of the two out-of-phase transducers in Fig. 13.24 (Right) is higher than the cut-off frequency for the (0,1) mode, $\omega > \omega_{0,\ 1} = \pi c/b$, then the transducers will excite the (0,1) mode that will propagate down the waveguide in the +z direction with the phase and group speeds determined by Eqs. (13.69) and (13.71).

13.5.4 Cylindrical Waveguide

With the exception of rectangular ducts used for space heating and air conditioning inside buildings, most acoustical waveguides have a circular cross-section. From the acoustical perspective, waveguides of circular cross-section are preferred because cylindrical tubes deform much less than rectangular tubes of equal wall thickness when subjected to a static or dynamic (acoustic) pressure difference between the fluid inside and the medium surrounding the waveguide. They also have the minimum perimeter for any cross-sectional area, so boundary layer thermoviscous dissipation is minimized (see Sect. 13.5.5). Because we chose to specify the transverse composite wavenumber for the rectangular waveguide as $k_{\ell m}$, all of the results for cut-off frequency, ω_{mn}; phase speed, c_{ph}; and group speed, c_{gr}, will be identical to the rectangular case if $k_{\ell m} = \alpha_{mn}/a$ for the cylindrical waveguide, where α_{mn} is quantized by Eq. (13.49).

$$f_{co} = \frac{\omega_{co}}{2\pi} = \frac{\omega_{mn}}{2\pi} = c\frac{k_{mn}}{2\pi} = c\frac{\alpha_{mn}}{2\pi a}$$
$$c_{ph} = \frac{\omega}{k_z} = \frac{c}{\sqrt{1 - \left(\frac{\omega_{co}}{\omega}\right)^2}} \quad \text{and} \quad c_{gr} = \frac{c^2}{c_{ph}} \tag{13.72}$$

Of course, in Eq. (13.72), m is the azimuthal mode number and the order of the Bessel function associated with that mode, and n indicates the number of nodal circles, as diagrammed in Fig. 13.10.

The excitation of a specific mode will depend upon the projection of the transducer's volume velocity distribution on the transverse basis functions, $J_m(k_{mn}r)$ and $\cos(m\theta + \varphi_{mn})$, described in Eq. (13.51). For a rigid-walled cylindrical waveguide with radius, a, Eq. (13.72) and Table 13.3 place the cut-off frequency of the lowest-frequency non-plane wave mode at $f_{1,1} = \alpha_{1,1}(c/2\pi a) \cong 1.8412(c/2\pi a) = 0.293\ c/a$. The transverse pressure distribution of the (1,1) mode is shown in Fig. 13.10.

If the transducer produces a uniform volume velocity and is centered on the waveguide's axis, then the symmetry of such an excitation will not couple to the (1,1) mode because the (1,1) mode, as well as any other azimuthal mode, $m \geq 1$, presents a pressure that is equally positive and negative about any diameter. In that case, the lowest-frequency purely radial mode would be the lowest-frequency non-plane wave mode that could be excited at frequency, $f_{0,1} > \alpha_{0,1}(c/2\pi a) \cong 3.8317(c/2\pi a) \cong 0.61\ (c/a)$. That mode also has regions where the pressure at the perimeter is out-of-phase with the pressure at the center. Table 13.4 indicates that the pressure at $r \geq 0.6276a$ will be out-of-phase with the pressure in the central region.

To calculate the net pressure, the radial pressure variation given by the Bessel function, $J_o(k_{0,1}r)$, must be integrated over the waveguide's circular cross-section, as was done previously for circular membranes in Sect. 6.2.5, to obtain the effective piston area, A_{eff}.

$$A_{eff} = \iint_S J_o(k_{0,1}r)\,dS = \int_0^a J_o(k_{0,1}r)\,2\pi r\,dr \tag{13.73}$$

Using the identity in Eq. (C.27), the integral in Eq. (13.73) can be evaluated.

$$A_{eff} = \frac{1}{k_{0,1}^2}\int_0^{k_{0,1}a} J_0(x)\,2\pi x\,dx = 2\pi\frac{k_{0,1}a}{k_{0,1}^2}J_1(k_{0,1}a) = 2\pi a^2\frac{J_1(\alpha_{0,1})}{\alpha_{0,1}} = 0 \tag{13.74}$$

A uniform piston with the same cross-sectional area as the waveguide will not excite the first radial mode. If the goal was to preferentially excite the first radial mode, the piston's volume velocity would be non-zero for $r < 0.6276a$ and zero for $0.6276a < r \leq a$. Ideally, an annulus that would extend to the perimeter, $r = a$, and have an inner radius, $b = 0.6276a$, that produces a volume velocity that was equal and 180° out-of-phase with the central disk would provide optimal coupling to the (0,1) mode. On the other hand, a full area transducer, like that shown in Fig. 13.13, would excite the longitudinal modes strongly while suppressing both the azimuthal modes and the first radial mode.

13.5.5 Attenuation from Thermoviscous Boundary Losses

The calculation of the attenuation of a plane wave propagating down a waveguide is straightforward using the expression for *thermoviscous losses* provided in Eq. (9.38). That equation can be re-written by using the Euler relation for plane waves from Eq. (10.26), $\hat{\mathbf{v}} = \hat{\mathbf{p}}/(\rho_m c)$, and assuming that the fluid within the waveguide is an ideal gas, $\gamma p_m = \rho_m c^2$. For simplicity, a cylindrical resonator is assumed, so the perimeter of the waveguide is $2\pi a$ and its cross-sectional area is πa^2. For a rectangular waveguide, the corresponding geometrical factors would be $2(L_x + L_y)$ and $L_x L_y$.

$$2\pi a \dot{e}_{tv} = \frac{\dot{E}}{L} = \frac{\langle \Pi \rangle_t}{L} = -\left(\delta_\nu + \frac{\gamma - 1}{\gamma}\delta_\kappa\right)\frac{2\pi a\omega|\widehat{\mathbf{p}}|^2}{4\gamma p_m} \tag{13.75}$$

That time-averaged power dissipation per unit length, $\langle \Pi \rangle_t/L$, on the surface of the waveguide, can be compared to the acoustic energy stored per unit length by expressing the total energy density as the maximum potential energy density, provided in Eq. (10.35), multiplied by the waveguide's cross-sectional area (i.e., volume per unit length, L).

$$\frac{E_{stored}}{L} = \pi a^2 (PE)_{\max} = \frac{\pi a^2 |\widehat{\mathbf{p}}|^2}{2\rho_m c^2} = \frac{\pi a^2 |\widehat{\mathbf{p}}|^2}{2\gamma p_m} \tag{13.76}$$

The ratio of Eqs. (13.75) and (13.76) is a constant for any frequency, ω, as long as the waveguide is excited in only its plane wave mode.

$$\frac{\dot{E}}{E} = -\frac{\left(\delta_\nu + \frac{\gamma-1}{\gamma}\delta_\kappa\right)}{a}\omega \equiv \frac{-1}{\tau_{tv}} \tag{13.77}$$

This form is rather satisfying. The pre-factor is simply the ratio of a "blended" boundary layer thickness, taking both the viscous and thermal dissipation into account, to the radius of the circular waveguide. Of course, since the waveguide is a linear system, the acoustic amplitude, $|\widehat{\mathbf{p}}|$, has cancelled out of that ratio. Since both δ_ν and δ_κ are proportional to $\omega^{-1/2}$, $\dot{E}/E \propto \sqrt{\omega}$.

When the rate of change of any variable is proportional to its value, then the variable will either decay or grow exponentially. Since this ratio is negative in Eq. (13.77), the sound amplitude will decay exponentially as the sound propagates down the waveguide. The corresponding thermoviscous exponential decay time, τ_{tv}, is just the reciprocal of $\dot{E}/E$. The distance of travel and the travel time are simply related by the sound speed, c, so the spatial attenuation coefficient, $\alpha_{tv} = (c\tau_{tv})^{-1}$.

$$\alpha_{tv} = \frac{1}{c\tau_{tv}} = -\frac{\left(\delta_\nu + \frac{\gamma-1}{\gamma}\delta_\kappa\right)}{a}\frac{\omega}{c} \propto \sqrt{\omega} \tag{13.78}$$

The resulting attenuation of the plane wave as a function of distance can be expressed in terms of the product of the plane wave solution of Eq. (13.66) and a decaying exponential factor.

$$p_{0,0,k}(x, y, z, t) = \Re\mathrm{e}\left[\widehat{\mathbf{A}}_{\mathbf{0,0}} e^{-\alpha_{tv} z} e^{\,j(\omega t - k_z z)}\right] \tag{13.79}$$

The thermoviscous boundary layer attenuation for higher-order waveguide modes can be related to the plane wave attenuation by invoking the geometrical perspective developed with the aid of Fig. 13.23. That perspective treats the higher-order waveguide modes as a combination of two traveling waves with wavevectors which make an angle, $\pm\theta$, with the z axis of the waveguide. From that perspective, the higher-order modes travel a distance that is $(\cos\theta)^{-1}$ longer than the plane wave mode. That perspective produced a simple expression for group speed and can also determine the attenuation constant for non-plane wave modes, $\alpha = \alpha_{tv}/\cos\theta$.

The effect of the thermoviscous boundary layers also introduces some dispersion. Within the thermal boundary layer, δ_κ, the compressibility of the gas transitions from its adiabatic value far from the walls to an isothermal compressibility at the wall. Also, within the viscous boundary layer thickness, the effective density of the gas is increasing toward infinity since the no-slip boundary condition at the wall makes the gas immobile. This small increase in compressibility and simultaneous increase in the effective density both conspire to reduce the sound speed. Since both boundary layer thicknesses are usually small compared to the waveguide's radius, the resulting dispersion is generally negligible in waveguides of large cross-section.

Talk Like an Acoustician

Eigenvalues	Energy balance equation
Axial mode	Critical distance
Tangential mode	Schroeder frequency
Oblique mode	Periodic boundary conditions
Degenerate modes	Twofold degeneracy
Density of modes	Adiabatic invariance
Wavenumber space	Cut-off frequency
k-space	Thermoviscous losses
Diffuse sound field	

Exercises

For these problems, unless otherwise specified, assume the sound speed in air is 345 m/s, in water is 1500 m/s, and in liquid is ^{4}He at 1.20 K and saturated vapor pressure is 237.4 m/s.

1. **The Golden Temple.** A rectangular room is $L_y = 20$ m wide, $L_x = 32.36$ m deep, and $L_z = 12.36$ m high. Those dimensions are in the "golden ratio."
   (a) *Modes*. Calculate the frequencies of the 27 lowest-frequency modes of the room. Tabulate the modes in ascending order of frequency (lowest to highest), indicating the mode numbers corresponding to each frequency.
   (b) *Modal excitation and detection*. Assume the modes are excited by a volume velocity source located in a corner of the room. Indicate which of the 27 lowest-frequency modes listed above would be detected by a microphone placed exactly in the center of the room (i.e., $x = L_x/2$, $y = L_y/2$, and $z = L_z/2$).

Unless otherwise indicated, you may assume that the walls of the temple are made of wood-paneling (1/2″ thick backed by a 3″ deep air space). On each of the two long walls, are five pairs of glass windows (windowpanes, one above the other) that are 3.0 m wide and 4.85 m tall (a total of 20 windows). The window pairs on each wall are separated by five 2.0-m-wide fiberglass panels (total of 10 panels) that are 2″ thick and mounted off of the wall by a 1″ airspace that reaches from the floor to the ceiling to help reduce reverberation time. The ceiling is covered entirely with acoustical plaster. The floor has thick carpet laid directly over a concrete base. There are 192 upholstered (cloth covered) seats.

Table 13.8 can be used to determine the sound absorption coefficients of the temple's surfaces and its contents for this problem, but the reader is cautioned to use a more comprehensive and authoritative sources for design of actual venues. The most comprehensive compilation of such data for use in reverberation time calculations that I have found is provided by Cyril Harris in *Noise Control in Buildings: A Practical Guide for Architects and Engineers* [33].

Table 13.8 Representative average Sabine absorptivity for various surfaces

Octave-band center frequency (Hz) →	125	250	500	1000	2000
Material	Absorptivity				
½″ wood paneled walls w/3″ air space	0.30	0.25	0.20	0.17	0.15
Windowpane glass	0.35	0.25	0.18	0.12	0.07
2″ thick fiberglass w/1″ air space	0.35	0.65	0.80	0.90	0.85
Acoustical plaster	0.07	0.17	0.40	0.55	0.65
Thick carpel	0.02	0.06	0.14	0.35	0.60
Upholstered (cloth covered) seats/seat	0.20	0.35	0.55	0.65	0.60

(c) *Schroeder frequency*. Calculate the room's Schroeder frequency, f_S, based on the average absorption, $<A>$, at 125 Hz. Using the approximate analytical expression for number of modes of the room, estimate the number of modes in the room with frequencies less than f_S.

(d) *Reverberation time*. Calculate reverberation times at 125 Hz, 500 Hz, and 2 kHz using the Sabine Equation.

(e) *The Eyring and Norris reverberation time*. An alternative to the Sabine equation was proposed by Carl Eyring, at Bell Labs, which is more accurate for more absorptive ("dead") rooms and reduces to the Sabine's result in "live" rooms where the total surface area of the room is S and $<A>/S \ll 1$ [34].

$$T_{60} = \frac{0.161 \;\; V}{-S \ln\left[1 - (\langle A \rangle / S)\right]} \tag{13.80}$$

The use of the numerical pre-factor assumes that S, $<A>$, and V are all expressed in metric units. Recalculate the reverberation times from part (d) using the Eyring-Norris expression.

(f) *Critical distance*. Calculate the distance, r_d, that a listener must be from a person speaking (assume 500 Hz), without electronic sound reinforcement, at the front of the room, so that the listener receives equal amounts of direct and diffuse sound pressure.

(g) *Steady-state diffuse sound pressure level.* If a solo violinist produces a B_4 note (at approximately 494 Hz) that radiates 2.0 mW of acoustic power into the room, what is the approximate sound pressure level (in dB *re:* 20 μPa_{rms}) observed in the diffuse sound field?

(h) *Bulk absorption.* Using the approximate expression for bulk absorption in Eq. (13.30), calculate the importance of $4\, mV/<A>$ relative to surface absorption at 125 Hz, 500 Hz, and 2 kHz, if the relative humidity is 50%.

2. **Hot tub modes**. Calculate the ten lowest-frequency modes of a rigid-walled circular swimming pool that is 5.0 m in diameter and is filled with water to a depth of 2.0 m. The surface above the water is pressure-released by the water-air interface.

3. **Toroidal resonator**. Shown in Fig. 13.25 is the spectrum (amplitude vs. frequency) of a rigid-walled toroidal resonator with inner, a, and outer, b, radii such that $|a - b| \ll (a + b)/2$ and $|a - b| < L_z$. The modes of the resonator are excited and detected using a speaker and microphone mounted on the "roof" of the toroid. There are 25 azimuthal modes with frequencies less than the first height mode.

   (a) *Effective radius.* If $L_z = 1.00$ cm, what is the mean radius, a_{eff}, of the toroid if the fluid in the toroid is liquid helium with a sound speed (non-rotating) of $c_1 = 237.4$ m/sec and the split degenerate modes in Fig. 13.25 correspond to $m = 24$?

   (b) *Doppler mode splitting*. Shown in Fig. 13.25 is a degenerate pair of azimuthal modes that have been split into two distinct modes by uniform rotation of the fluid within the toroid with an

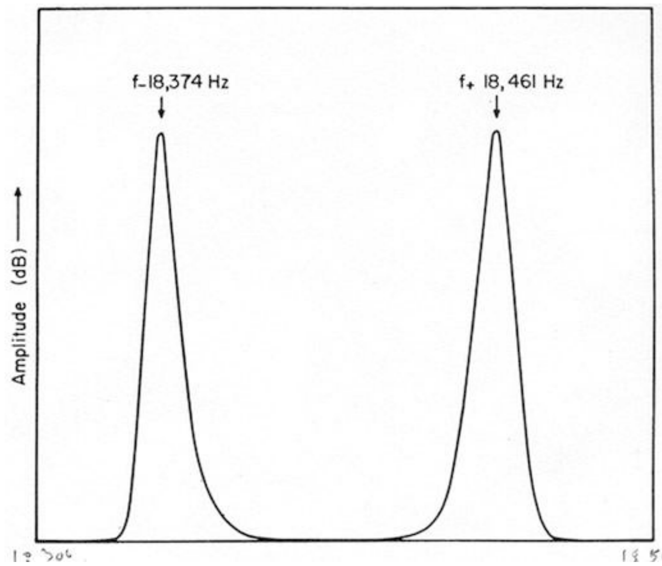

Fig. 13.25 Degenerate modes of a toroidal resonator that are split due to steady flow in the torus

Frequency (Hz)	Detectable by M_{middle}?	Detectable by M_{center}?
430	NO	YES
860		
1290		
1720		
2010		
2056		
2150		

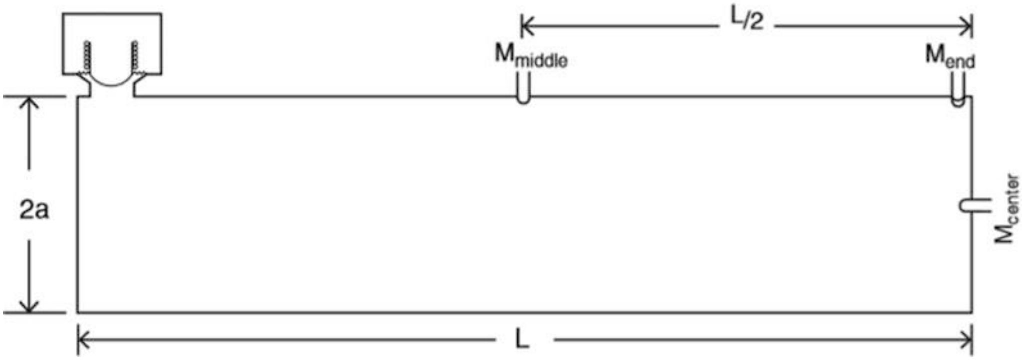

Fig. 13.26 Cross-sectional diagram of a cylindrical resonator that is L long and has a diameter, $D = 2a$. It is driven by an electrodynamic loudspeaker at the left end of the tube and three microphones are located as shown

azimuthal velocity, v_θ, in the clockwise direction. Based on the frequencies of the split modes, $f_+ = 18{,}461$ Hz and $f_- = 18{,}374$ Hz, what is the fluid's speed of rotation?

4. **Cylindrical resonator.** A rigid-walled cylindrical resonator with diameter, $D = 2a$, and length, L, is shown in Fig. 13.26 in cross-section. It is driven by the small electrodynamic loudspeaker

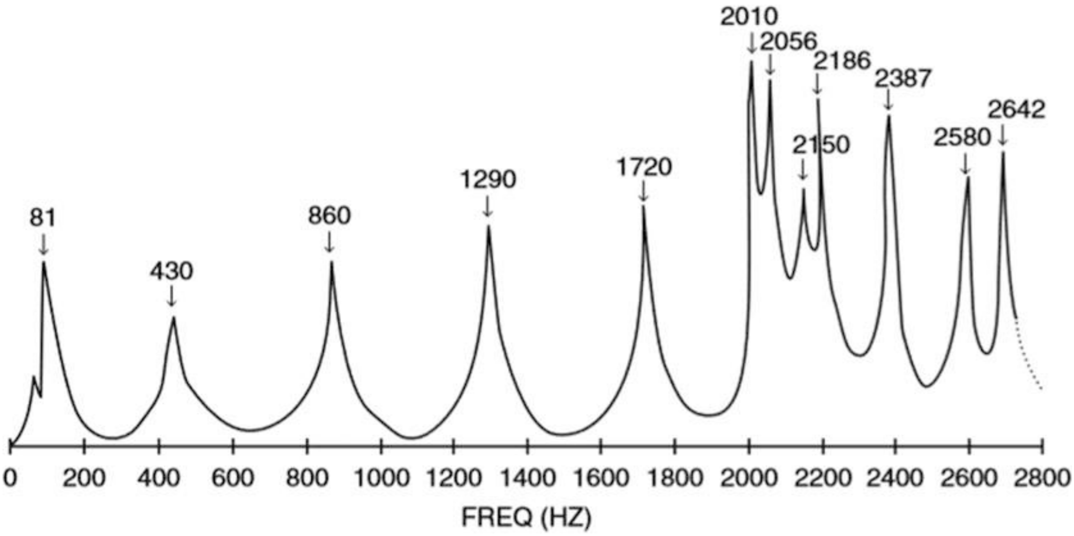

Fig. 13.27 Sketch of the frequency response of the cylindrical resonator shown in Fig. 13.26. The frequency of each resonance is indicated by the arrow, ↓, and is labeled by its frequency in hertz. The signal being displayed was acquired by M_{end}, located at the intersection of the tube and the end cap opposite the loudspeaker

adjacent to one end at the intersection of one end cap and the cylindrical wall. The resonator contains three microphones: M_{end} is located on the cylindrical wall at the rigid end opposite the speaker, M_{middle} is also on the cylindrical wall but at the middle of the resonator, and M_{center} is at the center of the rigid end cap on the end of the resonator that is opposite the speaker.

Sketched in Fig. 13.27 is the resonance spectrum produced by driving by the loudspeaker and detecting the sound pressure using M_{end}. The frequency of each peak in the spectrum is labeled.

(a) *Sound speed.* If $L = 40$ cm, what is the speed of sound of the gas contained within the resonator?
(b) *Resonator radius.* What is the radius, a (in centimeters), of the resonator?
(c) *Resonance detectability.* Complete the table below by indicating which of the resonance peaks would be observable at the middle microphone M_{middle} and at the microphone at the center of the rigid end M_{center} by placing a YES in the space if the microphone detects the mode and a NO in the space if that microphone does not detect the mode.

5. **Pressure-released rectangular waveguide.** The data for phase speed, c_{ph} vs. frequency, provided in Table 13.9, was obtained for a rectangular, water-filled waveguide, with an anechoic termination, that has a free surface (the air-water interface) and boundaries lined with highly compressible closed-cell foam making all of the boundaries pressure-released. The acoustic pressure in the waveguide was determined by inserting a small hydrophone below the free surface. The hydrophone's location was determined (± 0.5 mm) from a scale attached to the top of the waveguide over distance up to 3 m from the source. The phase speed was determined with an oscilloscope in the x-y (Lissajous) mode, and the distance was recorded to determine the wavelength in the z direction by measuring the distance between successive changes in phase of 360° at precisely known frequencies. Photographs of the waveguide and the anechoic termination are provided in Fig. 13.28.

   The phase speed can be expressed in terms of two parameters, the thermodynamic speed of sound in the medium, c_o, and the cut-off frequency, f_{co}. Transform Eqs. (1.117) or (13.69) so the data in Table 13.9 can be plotted as a straight line and use a best-fit straight line to extract the values for c_o and f_{co} and their estimated statistical uncertainties.

Table 13.9 Phase speed in a pressure-released waveguide

Frequency (Hz)	C_{phase} (m/s)
16,000	1952
15,000	2064
14,000	2218
13,500	2330
12,500	2700
12,000	2986
11,500	3496
11,250	3890
11,000	4536
10,750	5870

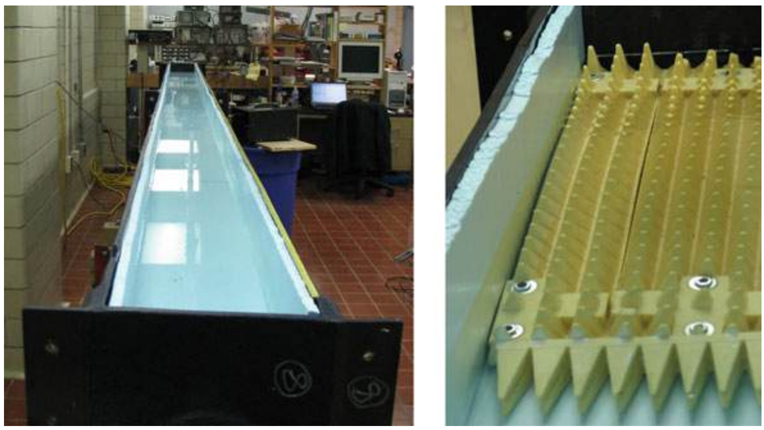

Fig. 13.28 Waveguide and anechoic termination. (*Left*) The waveguide is filled with water to a depth of about 17 cm. The three walls of the waveguide are lined with Styrofoam™ to provide a pressure-released surfaces. Note the millimeter scale attached to the top-right edge of the guide. (*Right*) The anechoic termination, not visible at the left, is shown. It is designed to provide a gently sloping beach of sound absorptive rubber "pyramids"

Fig. 13.29 Cylindrical waveguide with a source that is indicated by the *solid black circle* is located at an intersection of a rigid end cap and the cylindrical waveguide wall

6. **Cylindrical waveguide**. An air-filled (c = 345 m/sec) semi-infinite rigid tube of circular cross-section (radius, $a = 2$ cm) is driven at the closed end by a compact source located inside the (closed) end-plane at an intersection of the plane and the tube ($z = 0$), shown schematically in Fig. 13.29 as the black circle.
   (a) *Number of modes*. If the source is driven sinusoidally at a frequency, $f = 12.0$ kHz, how many propagating modes will be excited and what will be their phase speeds?

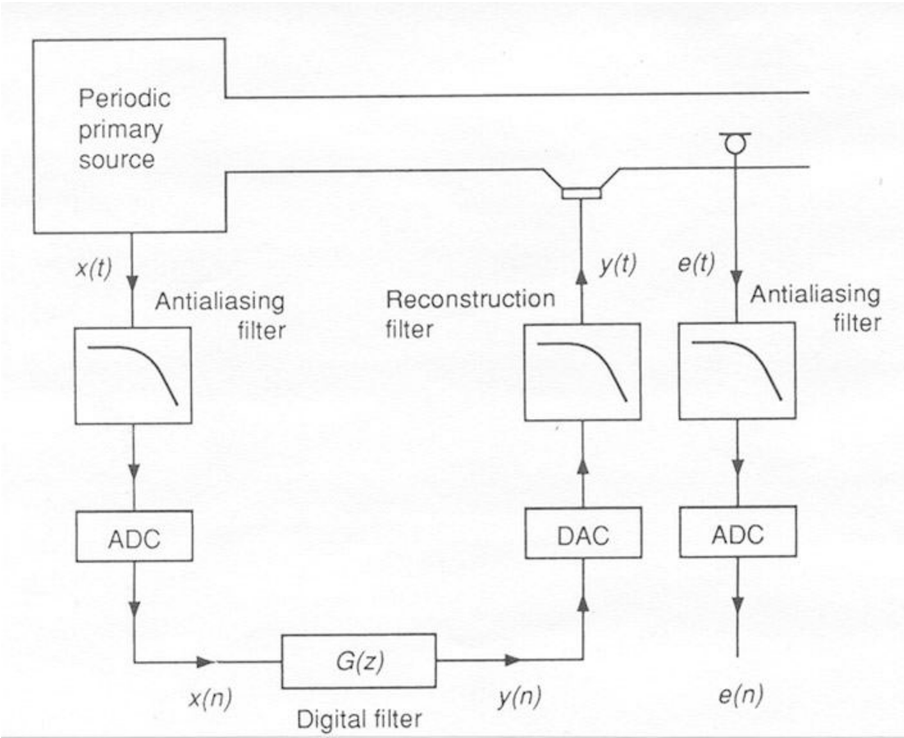

Fig. 13.30 Block diagram of an active noise cancellation system. The duct which contains the loudspeaker and the microphone has a square cross-section that is 1.0 ft × 1.0 ft

(b) *Excitation of modes.* If the source is moved to the center of the end cap, which of the above modes will no longer be excited?

7. **Group speed**. A 20-m-long piece of 6″ (nominal) Schedule 40 PVC pipe (inner radius, $a = 5.11$ cm) [35] contains air ($c = 345$ m/s) at atmospheric pressure and is closed at both ends by rigid terminations. A 20.0-millisecond-long tone burst containing 100 cycles of a 5 kHz tone is launched from one of the rigid ends at the intersection of the end and the pipe wall. (See the diagram for Problem 6 in Fig. 13.29.) The pulse propagates to the other end where it is reflected and arrives back at the first end. What is maximum difference in arrival times of the pulse that has been "dispersed" by the fact that the group speed is different for acoustic energy that travels in the different modes? [Hint: The first arrival will be the leading edge of the pulse that made the round trip at the thermodynamic sound speed c_o: $t_{first} = (40\text{ m})/(345\text{ m/s}) = 116$ ms.]
8. **Active noise cancellation in an air conditioning duct**. Shown in Fig. 13.30 is the block diagram for an active noise control system that injects sound with a loudspeaker that is intended to cancel the sound produced by the "periodic primary source," for example, a fan that is part of the ventilation system [36]. If the rigid-walled duct has a square cross-section with inside dimension of 1.0 ft. × 1.0 ft., what is the highest-frequency component of the noise that can be cancelled if the control algorithm can only process plane wave fronts traveling at the thermodynamic sound speed in air ($c = 345$ m/s)?
9. **Paddle-driven rectangular waveguide**. Shown below is the top view of a rigid-walled waveguide that is being driven by a rigid paddle that oscillates sinusoidally at radian frequency, $\omega = 1400$ rad/s, about a fixed axis with an amplitude, $\theta_o = 0.20$ radians, so that $\theta(t) = 0.20 \sin(\omega t)$.

The width of the waveguide, $W = 40$ cm, and the height of the waveguide is much less that its width, $H \ll W$. The waveguide extends to infinity in the z direction and is filled with sulfur hexafluoride gas (SF_6) which has a sound speed $c = 151$ m/s at room temperature (Fig. 13.31).

(a) *Phase Speed*. What is the phase speed, $c_{ph,}$ of the only mode which the paddle is capable of exciting that can propagate down the waveguide in the z direction?

(b) *Group Speed*. If the paddle creates a pulse with 17 cycles at the same frequency, $\omega = 1400$ rad/s, by increasing the amplitude of its motion from 0 radians to 0.2 radians and back to 0 radians with the sine-squared amplitude envelope shown in Fig. 13.32, how long does it take for the center of the envelope to travel 100 meters down the waveguide?

10. **Modes in a non-separable nuclear reactor coolant pool**. Shown in Fig. 13.33 is the plan view of a nuclear research reactor cooling pool [37]. It is filed with light (ordinary) water to a depth of 24 ft. = 7.32 m. Other dimensions are included in the caption of Fig. 13.33.
    (a) *Transformed dimensions.* What is the equivalent length of the pool, if it is transformed into a uniform rectangular shape that is 4.27 m wide and the depth remains 7.32 m?
    (b) *Lowest-frequency modes.* Assuming that the surface of the pool is pressure-released and all the other five boundaries are rigid and impenetrable, determine the 20 lowest-frequency modes and their corresponding mode numbers. Present your results in tabular form.
    (c) *Schroeder frequency and critical distance.* The reverberation time measured at 1.6 kHz was $T_{60} = 0.17$ s. What are the values of the Schroeder frequency, f_S, and the critical distance, r_d?
    (d) *Number of modes below f_S.* Determine the approximate number of modes at frequencies below f_S.

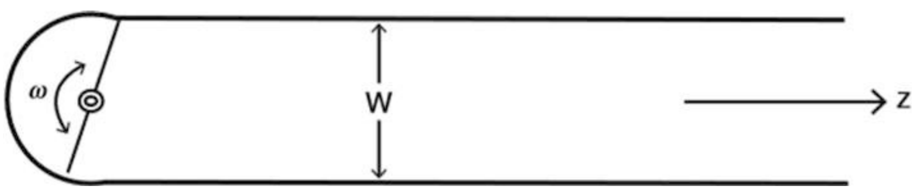

Fig. 13.31 This waveguide is excited by the rotational oscillations of the paddle vibrating at angular frequency, ω

Fig. 13.32 Pulse train generated by the oscillating paddle in Fig. 13.31

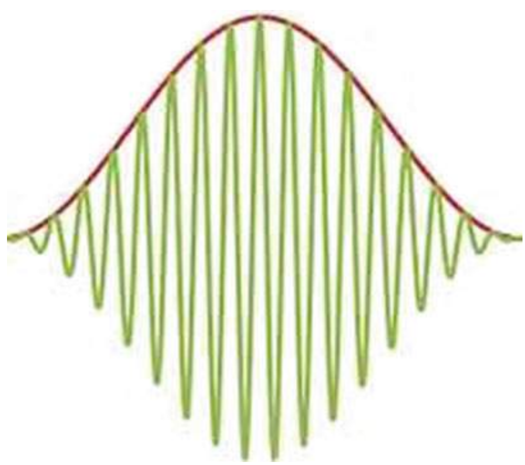

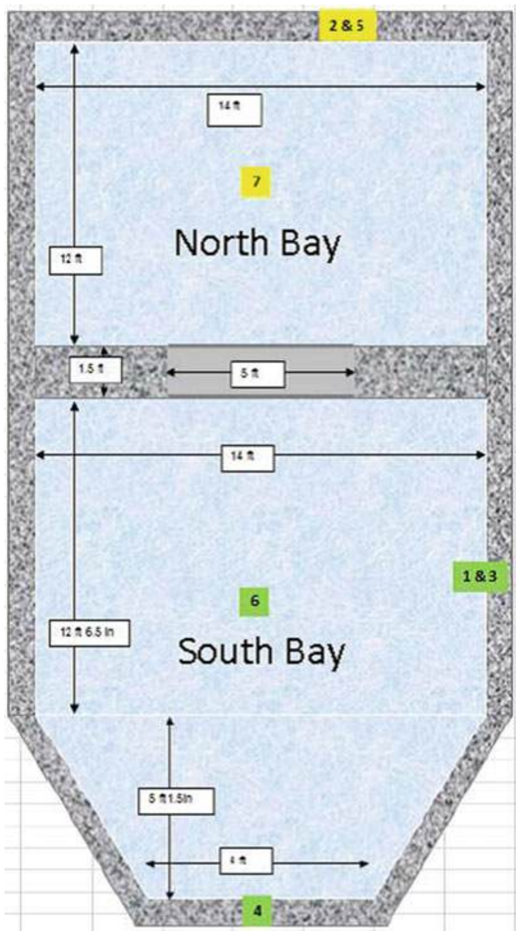

Fig. 13.33 Plan view of the two coupled pools in the Breazeale Nuclear Reactor. The depth of the water in both bays is 7.32 m (24′). The "floor" of the South Bay is an irregular hemi-hexagon. The reactor's core is usually located at about the center of that hexagonal portion. For modal calculations, assume that the pool is acoustically equivalent to a rectangular pool with the same planar area. The narrowest portion of the South Bay is 1.22 m wide, and the 14-ft.-wide rectangular portion extends 3.82 m behind the dividing wall. That wall is 46 cm thick and has a 1.52-m-wide gap. Under that adiabatic transformation, the "equivalent" reactor pool should be 4.27 m (14′) wide. Your transformation should preserve the volume of the water contained in both bays. The hemi-hexagonal South Bay has a volume, $V_{reactor} = 151\ \mathrm{m}^3 \cong$ 40,000 gallons. The North Bay has a volume, $V_{storage} = 114\ \mathrm{m}^3 \cong$ 30,000 gallons. Your modal analysis will designate the vertical direction as the z axis, the width as the x axis (horizontal in this figure), and the length as the y axis (vertical in this figure)

(e) *Density of modes.* What is the density of modes having frequencies below f_S?

11. **Echo satellite**. A gas-filled balloon was launched into low Earth orbit on 12 Aug 1960 to act as a reflector of radio waves used for communications. The balloon, shown symbolically on the postage stamp in Fig. 13.34, had a diameter of 30.5 m, and the balloon's material was 12.7-micron-thick metalized PET (Mylar™) film [27]. The Echo I satellite re-entered the Earth's atmosphere and burnt up on 24 May 1968.

(a) *Radial modes.* The fundamental frequency of radial mode of the gas inside the balloon was $f_{0,0,1}^{\text{release}} = 3.6$ Hz. What were the frequencies of the next three higher-frequency radial modes?

(b) *Gas sound speed.* What was the speed of sound of the gas contained within the balloon?

Fig. 13.34 US postage stamp commemorating the Echo Program

+	-	+
-	+	-
+	-	+

Fig. 13.35 Nine-segment transducer that excites a waveguide with the same cross-sectional area

12. **Modes of a rigid-walled spherical resonator**. Determine the three lowest-frequency radial resonance frequencies for the spherical resonator used by the US National Bureau of Standards, shown in Fig. 13.20, to determine the universal gas constant, $\Re \equiv 8.314462$ J mol^{-1} K^{-1}, if the sphere was filled with argon at $T = 273.16$ K and standard atmospheric pressure, $p_m = 101{,}325$ Pa. The radius of the sphere is $a = 9.000$ cm.
13. **Effective radius of the Space Shuttle cargo bay model in** Fig. 13.18. Assuming the plastic model of the cargo bay contains air, what is the value of the cargo bay model's effective radius, a, and its uncertainty, based on the frequencies provided in Table 13.6?
14. **Waveguide mode excitation**. An air-filled waveguide is excited at $z = 0$ with a transducer that is diagrammed in Fig. 13.35. The waveguide and transducer both have $L_x = 15$ cm and $L_y = 12$ cm. The phasing of the nine independent transducer segments is indicated by the + and – signs.
    (a) *Plane wave mode*. Will the plane wave mode of the waveguide be excited if the amplitude of all sections are the same?
    (b) *Lowest-frequency non-plane wave modes.* What are the mode numbers and cut-off frequencies of the three lowest-frequency non-plane wave modes that will be excited by this transducer?
    (c) *Impulse excitation.* If all of the transducer's segments are excited by a single pulse of very short duration, and the indicated phasing is maintained (e.g., the central segment moves forward and the ones above and below it move backward), which mode will be detected first by a microphone placed a great distance, $z \gg L_x$ and $z \gg L_y$, from the transducer?

References

1. L.P. Eisenhart, Separable systems in Euclidean 3-space. Phys. Rev. **45**(6), 427–428 (1934)

2. P.M. Morse, *Vibration and Sound*, 2nd edn (McGraw-Hill, New York, 1948), p. 396. Reprinted (ASA, 1981). ISBN 0-88318-876-7
3. B.F.G. Katz, E.A. Wetherill, The fall and rise of the Fogg art Museum lecture hall: A forensic study. Acoust. Today **3** (3), 10–16 (2007)
4. L. L. Beranek, *Concert and Opera Halls: How they Sound* (Acoustical Society of America, New York, 1996); ISBN 1-56396-530-5
5. L.L. Beranek, Concert hall acoustics: Recent findings. J. Acoust. Soc. Am. **139**(4), 1548–1556 (2016)
6. J. Liu, S. Garrett, Relationship between Nusselt number and the thermoviscous (Rott) functions. J. Acoust. Soc. Am. **119**(3), 1457–1462 (2006). See for discussion of complex compressibility
7. *Sound Absorption and Sound Absorption Coefficients by the Reverberation Room Method*, ASTM C423 (American Society for Testing and Materials, Philadelphia, PA 19103)
8. *Measurement of Sound Absorption in a Reverberation Room*, ISO 354 (International Organization for Standardization, CH-1211 Geneva 20, Switzerland)
9. R.J. Peppin, A. Scharine, *Methods for Calculation of the Absorption of Sound in the Atmosphere* (American National Standard, ANSI/ASA S1.26-2014). See §5.2.1
10. M.R. Schroeder, The 'Schroeder frequency' revisited. J. Acoust. Soc. Am. **99**(5), 3240–3241 (1996)
11. M. Kleiner, J. Tichy, *Acoustics of Small Rooms* (Taylor & Francis, Boca Raton, 2014); ISBN 978-0-203-86924-6 (eBook-PDF)
12. K.A. Gillis, M.R. Moldover, A.R.H. Goodwin, Accurate acoustic measurements in gases under difficult conditions. Rev. Sci. Inst. **62**, 2213–2217 (1991)
13. L.D. Landau, E.M. Lifshitz, *Fluid Mechanics*, 2nd edn. (Butterworth-Heinemann, Oxford, 1987). ISBN 0 7506 2767 0. §15
14. R. Eisberg, R. Resnick, *Quantum Physics of Atoms, Molecules, Solids, Nuclei, and Particles* (Wiley, New York, 1974); ISBN 0-471-23464-8
15. R.T. Weidner, R.L. Sells, *Elementary Modern Physics* (Allyn and Bacon, Boston, 1960)
16. L.D. Landau, E.M. Lifshitz, *Fluid Mechanics*, 2nd edn (Butterworth-Heinemann, Oxford, 1987). See Eq (15.18); ISBN 0 7506 2767 0
17. M. Abramowitz, I. Stegun, *Handbook of Mathematical Functions with Formulas, Graphs, and Mathematical Tables* (National Bureau of Standards, Applied Mathematics Series #55, 1964)
18. E. Polturak, S.L. Garrett, S.G. Lipson, Precision acoustic gas analyzer for binary gas mixtures. Rev. Sci. Inst. **57**(11), 2837–2841 (1986)
19. E. Jahnke, F. Emde, *Tables of Functions with Formulae and Curves*, 4th edn (Dover, New York, 1945)
20. P.M. Morse, *Vibration and Sound*, 2nd edn (McGraw-Hill, 1948). Reprinted by the Acoust. Soc. Am., 1995. See §32; ISBN 0-88318-876-7
21. I. Rudnick, Physical Acoustics at UCLA in the Study of Superfluid Helium, in Proc. E. Fermi Summer School, Varenna, Italy, 1974
22. P.M. Morse, K.U. Ingard, *Theoretical Acoustics* (McGraw-Hill, 1968), Problem 19, pp. 603–604
23. J.D. Maynard, *Topics in Acoustics*, Class Notes (The Pennsylvania State University (2006)
24. D.C. Swanson, Precision spectral peak frequency measurement using a window leakage ratio function. Mech. Systems and Sig. Process **54–55**, 1–15 (2015)
25. M. Greenspan, Simple derivation of the Boltzmann-Ehrenfest adiabatic principle. J. Acoust. Soc. Am. **27**(1), 34–35 (1955)
26. O.B. Wilson, R.W. Leonard, Measurements of sound absorption in aqueous salt solutions using a resonance method. J. Acoust. Soc. Am. **26**(2), 223–226 (1954)
27. H.M. Jones, I.I. Shapiro, P.E. Zadunaisky, Solar radiation effects, gas leakage rates, and air densities inferred from the orbit of Echo I, in *Proceedings 2nd International Space Science Symposium*, ed. by H.C. Van De Hulst, C. De Jager, A.F. Moore, Florence, April 10–14, 1961 (North Holland, 1961)
28. P.-J. Shih, Y.-R. Guo, Resonance frequency of fluid-filled and prestressed spherical shell – A model of the human eyeball. J. Acoust. Soc. Am. **139**(4), 1784–1792 (2016)
29. M.R. Moldover, J.P.M. Trusler, T.J. Edwards, J.B Mehl, R.S. Davis, Measurement of the universal gas constant $\Re$ using a spherical acoustic resonator. Phys. Rev. Lett. **60**(4), 249–252 (1988) and M.R. Moldover, et al, J. Res. Natl. Bur. Stand. **93**, 85–144 (1988)
30. L. Pitre, F. Sparasci, L. Risegari, C. Guianvarc'h, C. Martin, M.E. Himbert, M.D. Plimmer, A. Allard, B. Marty, P.A. Giuliano Albo, B. Gao, M.R. Moldover, J.B. Mehl, New measurement of the Boltzmann constant *k* by acoustic thermometry of helium-4 gas. Metrologia **54**, 856–873 (2017)
31. B.G. Schreger, Laennec's new system of diagnosis. Q. J. Foreign Med. Surg. **2**, 51–68 (1820)
32. K.U. Ingard, *Fundamentals of Waves and Oscillations* (Cambridge, 1988); ISBN 0 521 33957 X
33. C. M. Harris, *Noise Control in Buildings: A Practical Guide for Architects and Engineers* (McGraw-Hill, 1994); ISBN 0-07-028887-8

34. C.F. Eyring, Reverberation time in ‘dead’ rooms. J. Acoust. Soc. Am. **1**(1), 217–241 (1930)
35. E.A. Avallone, T. Baumeister II (eds), *Marks’ Standard Handbook for Mechanical Engineers*, 10th edn (McGraw-Hill, 1996). See Table 8.7.31, pp. 8–193; ISBN 0-07-004997-1
36. P.A. Nelson, S.J. Elliot, *Active Control of Sound* (Academic Press, 1993) ISBN 0-12-515426-7
37. S.L. Garrett, J.A. Smith, R.W.M. Smith, B.J. Heidrich, M.D. Heibel, Using the sound of nuclear energy. Nuc. Technol. **195**(3), 353–362 (2016)

Attenuation of Sound

14

Contents

There are four mechanisms that cause sound energy to be absorbed and sound waves to be attenuated as they propagate in a single-component, homogeneous fluid:

- Viscous (shear) effects in bulk fluids
- Thermal conduction in bulk fluids
- Molecular absorption in bulk fluids
- Thermoviscous boundary layer losses

The decrease in the amplitude of acoustical disturbances or in the amplitude of vibrational motion (due to dissipative mechanisms) has been a topic of interest throughout this textbook. In this chapter, we will capitalize on our investment in such analyses to develop an understanding of the attenuation of sound waves in fluids that are not influenced by proximity to solid surfaces. Such dissipation mechanisms are particularly important at very high frequencies and short distances or very low frequencies over geological distances.

The parallel addition of a mechanical resistance element to the stiffness and mass of a simple harmonic oscillator led to an exponential decay in the amplitude of vibration with time in Sect. 2.4. The

S. L. Garrett, *Understanding Acoustics*, Graduate Texts in Physics,
https://doi.org/10.1007/978-3-030-44787-8_14

(mechanically) series combination of a stiffness element and a mechanical resistance in the Maxwell model of Sect. 4.4.1, and in the Standard Linear Model of *viscoelasticity* in Sect. 4.4.2 introduced the concept of a relaxation time, τ_R, that had significant effects on the elastic (in-phase) and dissipative (quadrature) responses as a function of the nondimensional frequency, $\omega\tau_R$. Those response curves were "universal" in the sense that causality linked the elastic and dissipative responses through the Kramers-Kronig relations, as presented in Sect. 4.4.4.

That relaxation time perspective, along with its associated mathematical consequences, will be essential to the development of expressions for attenuation of sound in media that can be characterized by one or more relaxation times related to those internal degrees of freedom that make the equation of state a function of frequency. Examples of these relaxation time effects include the rate of collisions between different molecular species in a gas (e.g., nitrogen and water vapor in air), the pressure dependence of ionic association-dissociation of dissolved salts in seawater (e.g., $MgSO_4$ and H_3BO_3), and evaporation-condensation effects when a fluid is oscillating about equilibrium with its vapor (e.g., fog droplets in air or gas bubbles in liquids).

The *viscous drag* on a fluid oscillating within the neck of a Helmholtz resonator, combined with the *thermal relaxation* of adiabatic temperature changes at the (isothermal) surface of that resonator's compliance, led to energy dissipation in lumped-element fluidic oscillators in Sect. 9.4.4, producing damping that limited the quality factor of those resonances in exactly the same way as mechanical resistance limited the quality factor of a driven simple harmonic oscillator, which was first introduced as a consequence of similitude (i.e., dimensional analysis) in Sect. 1.7.1.

The *thermoviscous boundary layer* dissipation, summarized in Eq. (9.38), was used to calculate the attenuation of plane waves traveling in a waveguide in Sect. 13.5.5. As will be demonstrated explicitly in this chapter, thermoviscous boundary layer losses provide the dominant dissipation mechanism at low frequencies (i.e., lumped element systems and waveguides below cut-off) for most laboratory-sized objects (including the laboratory itself when treated as a three-dimensional enclosure). For fluid systems that are not dominated by dissipation on solid surfaces in close proximity to the fluids they contain, the dissipation due to losses within the fluid itself (i.e., bulk losses) can be calculated directly from the hydrodynamic equations of Sect. 7.3.

To reintroduce the concepts complex wavenumber or complex frequency that typically characterize the attenuation of sound over space or time, a simple solution of the Navier-Stokes equation will first be derived. That approach will not provide the correct results for attenuation of sound, even in the absence of relaxation effects, because it does not properly take into account the relationship between shear deformation and hydrostatic compression in fluids that are necessary to produce plane waves (see Fig. 14.1). That relationship was used to relate the modulus of unilateral compression for isotropic solids (aka the dilatational modulus) to other isotropic moduli in Sect. 4.2.2 and in Fig. 4.3. The complete solution for bulk losses due to a fluid's shear viscosity, μ; thermal conductivity, κ; and the relaxation of internal degrees of freedom (i.e., "bulk viscosity), ζ, will follow that nearly correct introductory treatment and will be based upon arguments related to entropy production, like the analysis in Sect. 9.3.3.

14.1 An Almost Correct Expression for Viscous Attenuation

Because we started with a complete hydrodynamic description of homogeneous, isotropic, single-component fluids using the Navier-Stokes equation, we are now well-prepared to investigate the dissipation mechanisms that attenuate the amplitude of sound waves propagating far from the influence of any solid boundaries. A one-dimensional linearized version of the Navier-Stokes equation (9.2) is reproduced below:

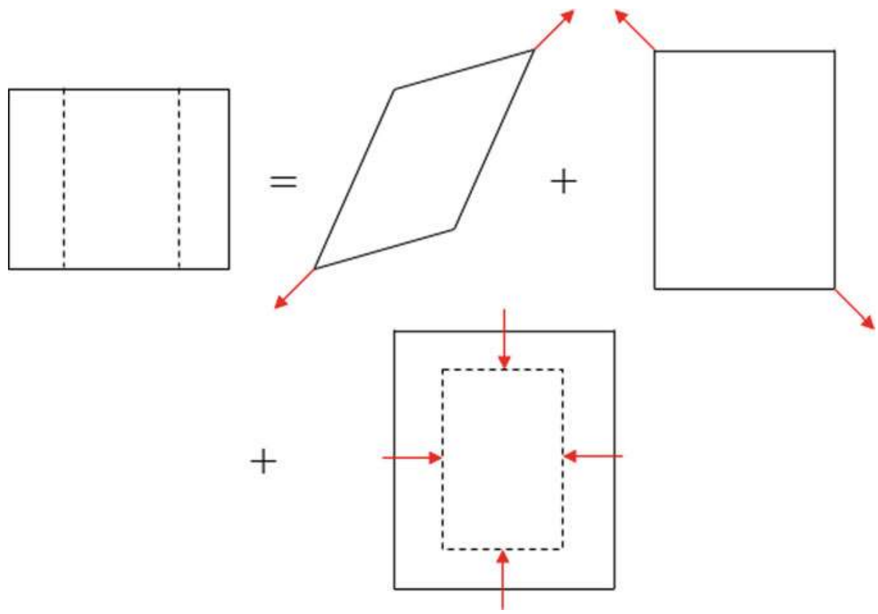

Fig. 14.1 Schematic two-dimensional representation of the combination of shear and hydrostatic deformations necessary to produce the unilateral compression of a fluid element, corresponding to a plane wave, shown at the *upper left*. If the original fluid parcel at the *upper left* is a square, shown by the *solid lines*, then the compression accompanying a plane wave does not change the upper and lower boundaries, but would require that the two vertical boundary lines contract to the positions indicated by the two *dashed lines*. This deformation can be accomplished by first shearing the square fluid element along one diagonal and then shearing it again along the other diagonal, as indicated by the *arrows*. Those two deformations result in making the square into a rectangle. When the rectangle is subjected to a hydrostatic compression, that rectangle is compressed into the required shape

$$\rho_m \frac{\partial v_1(x,t)}{\partial t} + \frac{\partial p_1(x,t)}{\partial x} - \mu \frac{\partial^2 v_1(x,t)}{\partial x^2} = 0 \tag{14.1}$$

The linearized, one-dimensional continuity equation (10.1) is not affected by the inclusion of viscosity in the Navier-Stokes equation.

$$\frac{\partial \rho_1(x,t)}{\partial t} + \rho_m \frac{\partial v_1(x,t)}{\partial x} = 0 \tag{14.2}$$

Since the thermal conductivity of the fluid is ignored, $\kappa = 0$, the linearized version of the adiabatic equation of state can still be invoked to eliminate $\rho_1(x, t)$ in favor of $p_1(x, t)$, allowing expression of the continuity equation in terms of the same variables used in Eq. (14.1).

$$\begin{aligned} \rho_1(x,t) &= \left(\frac{\partial \rho}{\partial p}\right)_s p_1(x,t) = \frac{p_1(x,t)}{c^2} \\ \Rightarrow \quad \frac{1}{\rho_m c^2} \frac{\partial p_1(x,t)}{\partial t} &+ \frac{\partial v_1(x,t)}{\partial x} = 0 \end{aligned} \tag{14.3}$$

As done so many times before, the dispersion relation, $\omega(k)$, will be calculated by assuming a right-going traveling wave to convert the homogeneous partial differential equations (14.1) and (14.3) to coupled algebraic equations.

$$\begin{aligned} -jkp_1 + (j\omega\rho_m + k^2\mu)v_1 &= 0 \\ j\omega\frac{p_1}{\rho_m c^2} - jkv_1 &= 0 \end{aligned} \tag{14.4}$$

There are now both real and imaginary terms in the coupled algebraic equations, unlike their nondissipative equivalents, such as Eqs. (10.16) and (10.17). The existence of a nontrivial solution to Eq. (14.4) requires that the determinant of the coefficients vanish.

$$\begin{vmatrix} \dfrac{j\omega}{\rho_m c^2} & -jk \\ -jk & (j\omega\rho_m + k^2\mu) \end{vmatrix} = 0 \tag{14.5}$$

The evaluation of this determinant leads to the secular equation that will specify the complex wavenumber, $\boldsymbol{k}$, in terms of the angular frequency,[1] ω.

$$\left(\frac{\omega}{c}\right)^2 = k^2\left(1 + \frac{j\omega\mu}{\rho_m c^2}\right) \tag{14.6}$$

If $\omega\mu/\rho_m c^2 << 1$, the binomial expansion can be used twice to approximate the *spatial attenuation coefficient*, α.

$$\mathbf{k} \cong \frac{\omega}{c} - j\frac{\omega^2\mu}{2\rho_m c^3} = k - j\alpha_{almost} \tag{14.7}$$

To remind ourselves that this result is not completely correct, this spatial attenuation coefficient has been designated $\alpha_{almost} = \omega^2(\mu/2\rho_m c^3)$. The form of this result, specifically the fact that the attenuation is proportional to ω^2/ρ_m, suggests that experimental results could be plotted as a function of the square of frequency divided by mean pressure, as shown in Fig. 14.4.

It is also useful to notice that $\mu/\rho_m c^2$ in Eq. (14.6) has the units of time, so the "small parameter" in those binominal expansions of Eq. (14.6) is of the form $j\omega\tau_{\bar{\ell}}$. Equally important is the recognition that such a *relaxation time*, $\tau_{\bar{\ell}}$, is on the order of the *collision time* in a gas, based on the *mean free path*, $\bar{\ell}$, derived from simple *kinetic theory* of gases in Sect. 9.5.1 [1].

$$\tau_{\bar{\ell}} = \frac{\bar{\ell}}{c} \cong \frac{3\mu_{gas}}{\rho_m c^2} = \frac{3}{\gamma}\frac{\mu_{gas}}{p_m} \tag{14.8}$$

This is different from the relaxation times, τ_R, which can characterize the time dependence of the equation of state or the response of a viscoelastic medium described in Sect. 4.4, where $\omega\tau_R \gtreqless 1$. At frequencies above $\omega_{\bar{\ell}} \cong \left(\tau_{\bar{\ell}}\right)^{-1}$, the assumptions that underlie the hydrodynamic approach are no longer valid (see Chap. 7, Problem 1). For air near room temperature and at atmospheric pressure, $\tau_{\bar{\ell}} \cong$ 400 ps, so $f = \omega/2\pi \cong 400$ MHz. This is identical with the result obtained in Eq. (9.24) for the critical frequency, ω_{crit}, at which sound propagation in air transitions from adiabatic at low frequencies to isothermal at high frequencies. The regime where $\omega\tau_{\bar{\ell}} > 1$ becomes questionable within the context of a (phenomenological) hydrodynamic theory [1].

[1] The decision to treat ω as a real number, thus forcing the wavenumber, $\boldsymbol{k}$, to become a convenience (complex) number, is arbitrary. It leads to a spatial attenuation coefficient that is related to the imaginary component of the wavenumber. Treating the wavelength, $\lambda = 2\pi/k$, as a real number forces the frequency, $\boldsymbol{\omega}$, to be a convenience number, thus producing a temporal attenuation coefficient. Of course, spatial-to-temporal conversions can be accomplished using the sound speed, as shown in Eq. (14.10).

Unlike the complex wavenumbers of exponentially decaying thermal and viscous waves near boundaries, examined in Sects. 9.3.1 and 9.4.2, where $\Re e[\boldsymbol{k}] = \Im m[\boldsymbol{k}]$, most attenuation mechanisms in bulk fluids far from boundaries have $\Re e[\boldsymbol{k}] \gg \Im m[\boldsymbol{k}]$ or $|\boldsymbol{k}| \gg \alpha$. If $\boldsymbol{k}$ is substituted into the expression for the pressure associated with a single-frequency one-dimensional plane wave traveling in the $+x$ direction, $p_1\,(x, t)$, it is easy to see that α leads to an exponential decay in the amplitude with propagation distance for the sound wave.

$$p_1(x,t) = \Re e\left[\widehat{\mathbf{p}} e^{\,j(\omega t - \mathbf{k}x)}\right] = \Re e\left[\widehat{\mathbf{p}} e^{\,j[\omega t - (k - j\alpha)x]}\right] = e^{-\alpha x}\Re e\left[\widehat{\mathbf{p}} e^{\,j(\omega t - kx)}\right] \tag{14.9}$$

Since space and time can be transformed by the sound speed, a real *temporal attenuation coefficient* can be defined, $\beta = \alpha\, c$, to describe the rate at which the amplitude of the plane wave decays in time.

$$p_1(x,t) = e^{-\beta t}\Re e\left[\widehat{\mathbf{p}} e^{\,j(\omega t - kx)}\right] \quad \text{where} \quad \beta = \alpha c \tag{14.10}$$

Although the result for α_{almost} is not exactly correct, it does exhibit a feature of the correct result for the spatial attenuation coefficient that includes thermoviscous dissipation that is given by $\alpha_{classical}$ in Eq. (14.31) where internal relaxation effects are discussed in Sect. 14.5.[2]

Unlike the spatial attenuation coefficient for dissipation of plane waves in a waveguide, given in Eq. (13.78), which is proportional to $\sqrt{\omega}$, Eq. (14.7) shows that α_{almost} is proportional to the square of the frequency, as is $\alpha_{classical}$.

14.2 Bulk Thermoviscous Attenuation in Fluids

Although the previous results for α_{almost} are incomplete, it both has provided an introduction to the complex wavenumber, $\mathbf{k}$, that determines the attenuation distance and has introduced a relaxation time, $\tau_{\overline{\ell}}$, that sets an upper limit to the frequencies above which the continuum model of a fluid is not appropriate. One reason that previous result for the viscous attenuation is not complete is that we have ignored the fact that the fluid deformation corresponding to the passage of a plane wave requires the superposition of two shear deformations and a hydrostatic compression. This superposition of *shear strain* and *hydrostatic strain* is illustrated schematically in Fig. 14.1. Of course, the result for the attenuation coefficient, α_{almost}, in Sect. 14.1, also does not yet include the thermal conductivity, κ, of the fluid.

To incorporate all of the dissipative effects in a fluid, it is necessary to start from the complete expression for entropy production in a single-component homogeneous fluid. The mechanical energy dissipation, E_{mech}, is the maximum amount of work that can be done in going from a given non-equilibrium state of energy, E_o, back to equilibrium, $E(S)$, which occurs when the transition is reversible (i.e., without a change in entropy) [2]. $\dot{E}_{mech}$ is the rate at which the mechanical energy is dissipated by the periodic transitions from the non-equilibrium state to the equilibrium state as orchestrated by the wave motion.

$$\dot{\Pi}_{mech} = -\dot{E}(S) = -\left(\frac{\partial E}{\partial S}\right)\dot{S} = T_m\dot{S} \tag{14.11}$$

The right-most expression in Eq. (14.11) uses the fact that the derivative of the energy with respect to the entropy is the equilibrium value of the mean absolute temperature, T_m. The entropy equation

[2] Since inert gases have no internal degrees of freedom, $\alpha_{classical}$ provides their entire attenuation constant.

(7.43) can be written so that the shear stresses and the hydrostatic stresses can be expressed symmetrically in Cartesian components.[3]

$$\rho T\left(\frac{\partial s}{\partial t}+\vec{v}\cdot\vec{\nabla}s\right)=\nabla\cdot\left(\kappa\vec{\nabla}T\right)+\frac{1}{2}\mu\left(\frac{\partial v_i}{\partial x_k}+\frac{\partial v_k}{\partial x_i}-\frac{2}{3}\frac{\partial v_i}{\partial x_i}\right)^2+\zeta\left(\nabla\cdot\vec{v}\right)^2 \tag{14.12}$$

The two cross derivatives, $(\partial v_i/\partial x_k)$ and $(\partial v_k/\partial x_i)$, represent the two shear deformations with the hydrostatic component removed: $2/3\left(\partial v_i/\partial x_i\right)$ [3]. The square of the hydrostatic deformation is represented by $\left(\nabla\cdot\vec{v}\right)^2$. The hydrostatic deformation is multiplied by a new positive scalar coefficient, ζ, that must have the same units as the shear viscosity [Pa-s].

Having the form of a conservation equation (see Sect. 10.5), the right-hand side of Eq. (14.12) represents the rate of entropy production, $\dot{S}$, caused by thermal conduction, viscous shear, and some possible entropy production mechanism (unspecified at this point but eventually related to the time dependence of the equation of state) associated with the hydrostatic deformation. Using Eq. (14.12), the dissipated mechanical power, Π_{mech}, can be evaluated by integrating over a volume element that includes the plane wave disturbance, dV.

$$\Pi_{mech}=-\frac{\kappa}{T_m}\int(\nabla T)^2dV-\frac{\mu}{2}\int\left(\frac{\partial v_i}{\partial x_k}+\frac{\partial v_k}{\partial x_i}-\frac{2}{3}\frac{\partial v_i}{\partial x_i}\right)^2dV-\zeta\int\left(\nabla\cdot\vec{v}\right)^2dV \tag{14.13}$$

Since we are still attempting a solution in the linear limit, the lowest-order contribution to the power dissipation must be second order in the wave's displacement from equilibrium; in this case, T_1^2 and $\left|\vec{v}_1\right|^2$, hence it is positive definite (see Sect. 10.5). For that reason, the absolute temperature, T, can be taken outside the integral and represented by T_m, since allowing for acoustical variation of that temperature term would add a correction to the thermal conduction loss that is third order in displacements from equilibrium.

For a plane wave propagating in the x direction, it is convenient to express $v_x = v_1 \sin(\omega t - kx)$, setting $v_y = v_z = 0$. Substitution into the last two terms of Eq. (14.13) produces the (nonthermal) mechanical dissipation.

$$-\left(\frac{4}{3}\mu+\zeta\right)\int\left(\frac{\partial v_1}{\partial x}\right)^2dV=-k^2\left(\frac{4}{3}\mu+\zeta\right)v_1^2\int\cos^2(\omega t-kx)\,dV \tag{14.14}$$

Since we are only interested in the time-averaged power dissipation, the contributions from the nonthermal terms in Eq. (14.13) is $-\left(k^2/2\right)[(4\mu/3)+\zeta]v_1^2V_o$, where V_o is the volume of the fluid under consideration through which the plane wave is propagating.

It is worth comparing the appearance of the factor, 4/3, that multiplies the shear viscosity, μ, with the corresponding expression for the modulus of unilateral compression, D (aka the dilatational modulus), introduced in Sect. 4.2.2, to the shear modulus, G, and bulk modulus, B, in Table 4.1: $D = (4G/3) + B$. Again, this is a direct consequence of the fact that the distortion produced by a plane wave can be decomposed into two shears (related to G) and a hydrostatic compression (related to B).

The result in Eq. (14.14), without ζ, was first produced by Stokes who expressed the result as the temporal attenuation coefficient [4]. The lack of agreement between his theoretical predictions and experimental measurements provided the starting point for the modern attempts to account for

[3] The component form assumes that the equation is summed over the repeated indices, i and k. This is known as the "Einstein summation convention."

attenuation in terms of molecular relaxation [5]. The spatial attenuation coefficient, due to viscous dissipation, was first introduced by Stefan in 1866[4] [6]. The first calculation to include both the effects of thermal conductivity and shear viscosity on the absorption of sound was published by Kirchhoff in 1868 [7].

To evaluate the contribution of thermal conduction to the mechanical dissipation in Eq. (14.13), the temperature change needs to be related to the pressure change to evaluate the one-dimensional temperature gradient, $(\partial T/\partial x)$. For an ideal gas, this relation should be familiar, having been derived in Eqs. (1.21) and (7.25).

$$\left(\frac{\partial T}{\partial p}\right)_s = \left(\frac{\gamma - 1}{\gamma}\right)\frac{T_m}{p_m} \tag{14.15}$$

Since we seek an attenuation coefficient that would be applicable to all fluids, a more general expression for $(\partial T/\partial p)_s$ needs to be calculated to evaluate $(\partial T/\partial x)$.

$$\left(\frac{\partial T}{\partial x}\right)_s = \left(\frac{\partial T}{\partial p}\right)_s \left(\frac{\partial p}{\partial v}\right)_s \left(\frac{\partial v}{\partial x}\right)_s = -\rho_m c \left(\frac{\partial T}{\partial p}\right)_s k v_1 \cos\left(\omega t - kx\right) \tag{14.16}$$

The derivative of pressure with respect to velocity for a nearly adiabatic plane wave is a direct consequence of the Euler equation: $p_1 = \rho_m c v_1$.

The derivative of temperature with respect to density can be evaluated using the *enthalpy function*, $H(S, p) = U + pV$, that sums the internal energy, U, introduced in Sect. 7.1.2 to calculate heat capacities, with the mechanical work, $W = pV$. From Eqs. (7.8, 7.9, and 7.10), the internal energy, $U(S, V)$, can be transformed into the enthalpy, $H(S, p)$, using the product rule for differentiation. In thermodynamics, this operation is known as a *Legendre transformation* [8].

$$\begin{gathered} dU = TdS - pdV = TdS - d(pV) + Vdp \\ \Rightarrow d(U + pV) \equiv dH = TdS + Vdp \end{gathered} \tag{14.17}$$

The change in enthalpy, $dH(S, p)$, can be expanded in a Taylor series, retaining only the linear terms.

$$dH = \left(\frac{\partial H}{\partial S}\right)_p dS + \left(\frac{\partial H}{\partial p}\right)_S dp \tag{14.18}$$

Comparison of Eqs. (14.17) and (14.18) can be used to evaluate those derivatives.

$$\left(\frac{\partial H}{\partial S}\right)_p = T \quad \text{and} \quad \left(\frac{\partial H}{\partial p}\right)_S = V \tag{14.19}$$

Since the order of differentiation is irrelevant, the mixed partial derivatives must be equal.

$$\frac{\partial^2 H}{\partial p \partial S} = \frac{\partial^2 H}{\partial S \partial p} \quad \Rightarrow \quad \left(\frac{\partial T}{\partial p}\right)_S = \left(\frac{\partial V}{\partial S}\right)_p \tag{14.20}$$

This result is one of several thermodynamic identities known as the *Maxwell relations* [9].

[4] Stefan was the thesis advisor of Boltzmann, who was the advisor of Ehrenfest, who was the advisor of Uhlenbeck, who was the advisor of Putterman, who was my advisor, along with Isadore Rudnick, when I was a graduate student at UCLA.

$$\left(\frac{\partial V}{\partial S}\right)_p = \left(\frac{\partial V}{\partial T}\right)_p \left(\frac{\partial T}{\partial S}\right)_p \tag{14.21}$$

The result in Eq. (14.21) can be expressed in terms of tabulated material properties [10] using the definition of the (extensive) heat capacity at constant pressure, C_p, or the (intensive) specific heat (per unit mass) at constant pressure, c_p, from Eq. (7.14), and the definition of the isobaric (constant pressure) volume coefficient of thermal expansion, β_p.

$$C_p = T\left(\frac{\partial S}{\partial T}\right)_p \quad \text{or} \quad c_p = T\left(\frac{\partial s}{\partial T}\right)_p \quad \text{and} \quad \beta_p = \frac{1}{V}\left(\frac{\partial V}{\partial T}\right)_p = -\frac{1}{\rho_m}\left(\frac{\partial \rho}{\partial T}\right)_p \tag{14.22}$$

These results can be combined to produce an expression for the temperature gradient required to evaluate the thermal conduction integral in Eq. (14.13) using Eq. (14.16).

$$\frac{\partial T}{\partial x} = c\frac{\beta_p T_m}{c_p}\frac{\partial v_1}{\partial x} = -c\frac{\beta_p T_m}{c_p} v_1 k \cos(\omega t - kx) \tag{14.23}$$

As before, our interest will be in the time-averaged value for evaluation of the thermal conduction term in the integral expression for Π_{mech} in Eq. (14.12).

$$\left\langle -\frac{\kappa}{T_m}\int (\nabla T)^2 dV \right\rangle_t = \frac{-\kappa c^2 \beta_p^2 v_1^2 k^2}{2c_p^2} V_o \tag{14.24}$$

This result can be evaluated in terms of the difference in the specific heats that was shown by thermodynamic arguments to be $C_P - C_V = \Re$, in Eq. (7.14), for an ideal gas, or $c_p - c_v = \Re/M$, where $\Re$ is the universal gas constant and M is the mean molecular or atomic mass of the ideal gas or ideal gas mixture. By the same thermodynamic arguments, the general result for the specific heat difference can be expressed in terms of the fluid parameters in Eq. (14.22) [11].

$$c_p - c_v = T\beta_p^2\left(\frac{\partial p}{\partial \rho}\right)_T = T\beta_p^2\left(\frac{c_v}{c_p}\right)\left(\frac{\partial p}{\partial \rho}\right)_s = T\beta_p^2 c^2\left(\frac{c_v}{c_p}\right) \tag{14.25}$$

The relationship between the square of the isothermal sound speed, $(\partial p/\partial \rho)_T$, and the square of the adiabatic sound speed, $(\partial p/\partial \rho)_s = c^2$, should be familiar since $(c_v/c_p) \equiv \gamma^{-1}$.

Substitution of Eq. (14.25) into Eq. (14.24) provides a compact expression for the time-averaged power dissipation that is valid for ideal gases as well as for all other homogeneous fluids.

$$\left\langle -\frac{\kappa}{T_m}\int (\nabla T)^2 dV \right\rangle_t = -(½)\kappa k^2 v_1^2 V_o\left(\frac{1}{c_v} - \frac{1}{c_p}\right) \tag{14.26}$$

Combining Eq. (14.26) with Eq. (14.14) provides an expression for the time-averaged mechanical power dissipation due to all of the irreversible dissipation mechanisms.

$$\langle \Pi_{mech} \rangle_t = -(½)k^2 v_1^2 V_o\left[\left(\frac{4}{3}\mu + \zeta\right) + \kappa\left(\frac{1}{c_v} - \frac{1}{c_p}\right)\right] \tag{14.27}$$

The total energy, E, of the plane wave occupying the volume, V_o, can be expressed in terms of the maximum kinetic energy density, $(\mathrm{KE})_{\max}$.

$$E = (\mathrm{KE})_{\max} V_o = (½)\rho_m v_1^2 V_o \tag{14.28}$$

Since the decay rate of the energy is twice that of the amplitude decay rate, the spatial attenuation constant that reflects thermoviscous losses (and whatever ζ represents!), $\alpha_{T\text{-}V}$, can be written in terms of the time-averaged power dissipation, $\langle \Pi_{mech} \rangle_t$, in Eq. (14.27), and the average total energy, E, in Eq. (14.28).

$$\alpha_{T-V} = \frac{\left| \langle \Pi_{mech} \rangle_t \right|}{2cE} = \frac{\omega^2}{2\rho_m c^3} \left[\left(\frac{4}{3}\mu + \zeta \right) + \kappa \left(\frac{1}{c_v} - \frac{1}{c_p} \right) \right] \tag{14.29}$$

This final result for $\alpha_{T\text{-}V}$ is valid for all fluids as long as the decrease in the sound wave's amplitude over the distance of a single wavelength is relatively small, $\alpha_{T-V}\lambda \ll 1$, since the stored energy was calculated for an undamped sound wave.

We also see that this result is similar to the "almost correct" result, α_{almost}, calculated from the Navier-Stokes equation in Sect. 14.1. The dependence on frequency, ω; mass density, ρ_m; and sound speed, c, is identical, but the shear viscosity, μ, is no longer the only transport property of the medium that contributes to attenuation of the sound wave; in Eq. (14.29), μ has been replaced by the term within the square bracket.

As demonstrated earlier in Eq. (14.8), the expression for attenuation given in Eq. (14.29) will always be valid for sound in gases, since the kinematic viscosity, $\nu_{gas} = \mu_{gas}/\rho_m$, is on the order of the product of the mean free path, $\overline{\ell}$, times the mean thermal velocity of the gas molecules or the sound speed.

$$\frac{\nu_{gas}\omega}{c^2} \cong \overline{\ell}\frac{\omega}{c} \cong \frac{\overline{\ell}}{\lambda} \ll 1 \tag{14.30}$$

14.3 Classical Thermoviscous Attenuation

Before the role of molecular relaxation was appreciated and the associated dissipative coefficient, ζ, was introduced, attenuation of sound due to thermoviscous losses was calculated by Kirchhoff [7]. That result is often called the classical absorption coefficient, $\alpha_{classical}$.

$$\alpha_{classical} = \frac{\omega^2}{2\rho_m c^3} \left[\frac{4}{3}\mu + \kappa \left(\frac{1}{c_v} - \frac{1}{c_p} \right) \right] = \frac{\omega^2}{2c^3} \left[\frac{4}{3} \frac{\mu}{\rho_m} + \frac{\kappa}{\rho_m c_p} \left(\frac{c_p}{c_v} - 1 \right) \right] \tag{14.31}$$

For an ideal gas, the classical attenuation coefficient can be expressed more transparently in terms of the kinematic viscosity, $\nu = \mu/\rho_m$; the polytropic coefficient, $\gamma = c_p/c_v$; and the dimensionless ratio of the thermal and viscous diffusion constants, known as the Prandtl number, $\mathrm{Pr} \equiv (\mu/c_p\kappa) = (\delta_\nu/\delta_\kappa)^2$, that was introduced in Sect. 9.5.4.

$$\alpha_{classical} = \frac{\omega^2 \nu}{2c^3} \left[\frac{4}{3} + \frac{(\gamma - 1)}{\mathrm{Pr}} \right] \quad \Rightarrow \quad \frac{\alpha_{classical}}{f^2} = \frac{2\pi^2 \nu}{c^3} \left[\frac{4}{3} + \frac{(\gamma - 1)}{\mathrm{Pr}} \right] \tag{14.32}$$

Most single-component gases and many gas mixtures have $\mathrm{Pr} \cong {}^2/_3$. For air at atmospheric pressure and 20 °C, $\nu = 1.51 \times 10^{-5}$ m²/s, $\mathrm{Pr} = 0.709$, $\gamma = 1.402$, and $c = 343.2$ m/s. Under those conditions, $\alpha_{classical} / f^2 = 1.40 \times 10^{-11}$ s²/m. The accepted value of α/f^2 in the high-frequency limit is 1.84×10^{-11} s²/m. This discrepancy is due to the absence of ζ in Eq. (14.32) [12].

Since the difference between the specific heats at constant pressure and constant volume is small for liquids, the viscous contribution to the classical attenuation constant is dominant. For pure water at 280 K, $\nu_{H_2O} = 1.44 \times 10^{-6}$ m^2/s and$\Pr_{H_2O} = 10.4$, [13] with $c_{H_2O} = 1500$ m/s, making $\alpha_{classical}/f^2 = 1.1 \times 10^{-14}$ s^2/m for freshwater. The accepted value of α/f^2 in the high-frequency limit is 2.5×10^{-14} s^2/m, again due to the absence of ζ in Eq. (14.32) [14].

14.4 The Time-Dependent Equation of State

The distortion of a fluid element caused by passage of a plane wave was decomposed into shear deformations, which changed the shape of the element, and a hydrostatic deformation, which changed the volume of the element, as diagrammed schematically in Fig. 14.1. Each of those deformations introduced irreversibility that increased entropy as expressed in Eq. (14.12), leading to energy dissipation as expressed in Eq. (14.13). Based on the discussion in Sect. 9.4, the shear viscosity, μ, was introduced to relate the shear deformations to the dissipative shear stresses.

Another coefficient, ζ, was introduced to relate entropy production to the divergence of the fluid's velocity field, $\nabla \cdot \vec{v}$. The continuity equation requires that when $\nabla \cdot \vec{v} \neq 0$, the density of the fluid must also be changing: $(\partial \rho / \partial t) \neq 0$. Why should a change in the fluid's density be related to irreversible entropy production?

When the phenomenological model was introduced, it was assumed that only five variables were required to completely specify the state of a homogeneous, isotropic, single-component fluid: one mechanical variable (p or ρ) and one thermal variable (s or T), along with the three components of velocity (e.g., v_x, v_y, and v_z). For a static fluid, $|v| = 0$, only two variables were required, resulting in the laws of equilibrium thermodynamics (i.e., energy conservation and entropy increase) rather than the laws of hydrodynamics (that also incorporate thermodynamics). The evolution of those variables was determined by the imposition of five conservation equations (i.e., mass, entropy, and vector momentum). That assertion included an implicit assumption that an equation of state existed and it could be used to relate the thermodynamic variables (mechanical and thermal) to each other *instantaneously*.

For some fluids, the assumption of an instantaneous response of the density to changes in the pressure is not valid. (Noble gases are one notable exception, since they do not have any rotational degrees of freedom.) The microscopic models of gases that were based on the kinetic theory introduced the concept of collision times between the constituent particles (atoms and/or molecules) and the Equipartition Theorem in Eq. (7.2) that stated that through these collisions, an equilibrium could be established that distributed the total thermal energy of the system equitably (on average) among all of the available degrees of freedom. What has been neglected (to this point) was the fact that the collisions take a non-zero time to establish this equilibrium; if the conditions of the fluid element are changing during this time, the system might never reach equilibrium.

How did we get away with this "five-variable fraud" for so long? One answer is hidden in the transition from adiabatic sound speed in an ideal gas to the isothermal sound speed. Equation (9.24) defined a critical frequency, ω_{crit}, at which the speed of thermal diffusion was equal to the speed of sound propagation. At that frequency, the wavelength of sound corresponded to a distance, which was about 20 times the average spacing between particles, known as the mean free path between collisions, $\bar{\ell}$. Since that collision frequency was so much higher than our frequencies of interest, the equilibration between translational and rotational degrees of freedom in gases of polyatomic molecules occurred so quickly that the equation of state appeared to act instantaneously [15]. Even though a vibrating object couples to the translational degrees of freedom in a gas, the translational and rotational degrees of freedom came into equilibrium in much less time than the period of the vibrating object's oscillations.

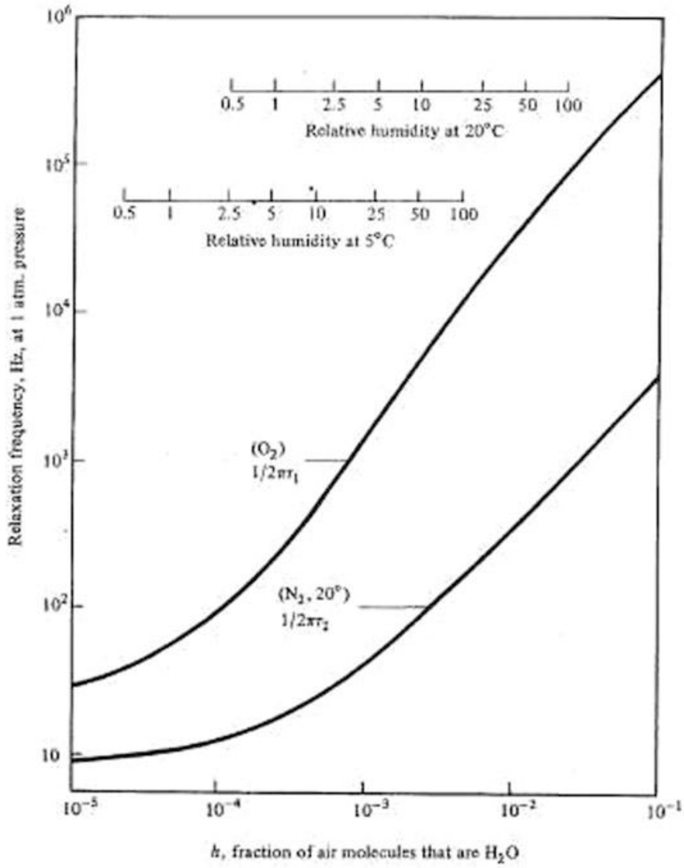

Fig. 14.2 Relaxation frequencies, $f_R = (2\pi\tau_R)^{-1}$, for equilibration between O_2 or N_2 and water vapor (H_2O) as a function of the mole fraction of water vapor in air, h, at $p_m = 1$ atmosphere. At the top of the graph are scales that can be used to relate the mole fraction of H_2O on the x axis to the more popular designation of percent "relative humidity" at 5 °C and 20 °C [16]

That "fraud" was obscured by our use of $\gamma = 7/5$ in the expression for sound speed which treated the air as instantly sharing energy between the internal translational and rotational degrees of freedom.

When there are other components in a gas or liquid, they may have relaxation times that are sufficiently close to the acoustic periods of interest that their "equilibration" to the acoustically induced changes cannot be considered to occur instantaneously. In air, for example, if there is water vapor present, it will equilibrate with the O_2 and N_2 over times that are comparable to the periods of sound waves of interest for human perception (i.e., 20 Hz $\lesssim f \lesssim$ 20 kHz). Figure 14.2 shows the relaxation frequencies as a function of the mole fraction, h, of H_2O and also relative humidity as a percentage [16].

Those equilibration times are dependent upon the gas mixture's temperature, pressure, and mixture concentration (i.e., mole fraction of water vapor, h, or relative humidity, RH) [17]. It is apparent that the relaxation frequencies in Fig. 14.2 are in the audio range for ordinary values of temperature and humidity [17].

$$
\begin{aligned}
f_{rO} &= \frac{p_m}{p_{ref}}\left\{24 + \left[\frac{\left(4.04x10^4 h\right)(0.02+h)}{0.391+h}\right]\right\} \\
f_{rN} &= \frac{p_m}{p_{ref}}\left(\frac{T}{T_{ref}}\right)^{-½}\left(9 + 280h \ \exp\left\{-4.170\left[\left(\frac{T}{T_{ref}}\right)^{-1/3} - 1\right]\right\}\right)
\end{aligned}
\tag{14.33}
$$

The relaxation frequencies for water vapor and nitrogen, f_{rN}, and for water vapor and oxygen, f_{rO}, assume a standard atmospheric composition with 78.1% nitrogen, 20.9% oxygen, and 314 ppm carbon dioxide at a reference pressure, $p_{ref} = 101{,}325$ Pa, and reference temperature, $T_{ref} = 293.15\ \text{K} = 20.0\ °\text{C}$. In Eq. (14.33), the molar concentration of water vapor, h, is expressed in percent. For ordinary atmospheric conditions near sea level, $0.2\% \lesssim h \lesssim 2.0\%$.

To relate RH to h (both in %), it is first necessary to calculate the saturated vapor pressure of water in air, p_{sat}, relative to ambient pressure, $p_{ref} = 101.325$ kPa, using the triple-point isotherm temperature, $T_{01} = 273.16\ \text{K} = +0.01\ °\text{C}$.

$$\frac{p_{sat}}{p_{ref}} = 10^C; \quad C = -6.8346\left(\frac{T_{01}}{T}\right)^{1.261} + 4.6151 \tag{14.34}$$

The molar concentration of water vapor, h, in percent, can then be expressed in terms of the relative humidity, RH, also in percent [17].

$$h = RH\left(\frac{p_{sat}}{p_m}\right) \tag{14.35}$$

A similar effect is observed in seawater where boric acid, $B(OH)_3$, and magnesium sulfate, $MgSO_4$, have relaxation frequencies of 1.18 kHz and 145 kHz, respectively, at 20 °C [18]. In the case of these salts, the relaxation time represents the pressure-dependent association-dissociation reaction between the dissolved salts and their ions.

14.5 Attenuation due to Internal Relaxation Times

> *"If a system is in stable equilibrium, then any spontaneous change of its parameters must bring about processes which tend to restore the system to equilibrium."* H. L. Le Châtelier[5]

A new positive scalar coefficient, ζ, was introduced in the entropy conservation Eq. (14.12) to scale the irreversibility of hydrostatic fluid deformations. It has the same units as the shear viscosity [Pa-s][6] and is usually of about the same magnitude. If the medium does not possess any additional internal degrees of freedom that have to be brought into equilibrium, then its value can be identically zero. That constant is zero for the noble gases (He, Ne, Ar, Kr, Xe, and Rn) that are intrinsically monatomic with atoms that are spherically symmetrical, thus lacking rotational degrees of freedom (see Sect. 7.2). On the other hand, as suggested in Fig. 14.2, if there are processes with relaxation times that are near the frequencies of interest, the value of ζ can be orders of magnitude greater than μ near those frequencies.

With acoustical compressions or expansions, as in any rapid change of state, the fluid cannot remain in thermodynamic equilibrium. Following *Le Châtlier's Principle*,[5] the system will attempt to return to a new equilibrium state that is consistent with the new parameter values that moved it away from its

[5] Henry Louis Le Châtelier (1850–1936) was a Parisian chemist. This principle is sometimes also attributed to German physicist Karl Ferdinand Braun (1850–1918), the inventor of the cathode-ray tube and the oscilloscope.

[6] Because ζ has the same units as shear viscosity, it is commonly called *bulk viscosity* or *second viscosity*, even though its effects are entirely unrelated to shear strains. I find both terms misleading and attempt to avoid their use in this textbook, although acousticians have to be aware that they represent the common nomenclature used to identify losses related to the relaxation of internal degrees of freedom within fluids.

previous state of equilibrium. In some cases, this equilibration takes place very quickly so that the medium behaves as though it were in equilibrium at all times. In other cases, the equilibration is slow, and the medium never catches up. In either case, the processes that attempt to reestablish equilibrium are irreversible and therefore create entropy and dissipate energy.

If ξ represents some physical parameter of the fluid and ξ_o represents the value of ξ at equilibrium, then if the fluid is not in equilibrium, ξ will vary with time. If the fluid is not too far from equilibrium, so the difference, $\xi - \xi_o$, is small (i.e., $|\xi - \xi_o|/\xi_o \ll 1$), and then the rate of change of that parameter, $\dot{\xi}$, can be expanded in a Taylor series retaining only the first term and recognizing that any zero-order contribution to $\dot{\xi}$ must vanish since $\xi = \xi_o$ at equilibrium.

$$\dot{\xi} = -\frac{(\xi - \xi_o)}{\tau_R} \tag{14.36}$$

This suggests an exponential relaxation of the system toward its new equilibrium state. Le Châtelier's Principle requires that the rate must be negative and that the relaxation time, τ_R, must be positive.

For acoustically induced sinusoidal variations in the parameter, ξ, at frequency, ω, the sound speed will depend upon the relative values of the period of the sound, $T = 2\pi/\omega$, and the relaxation time, τ_R. If the period of the disturbance is long compared to the exponential equilibration time, τ_R, so that $\omega\tau_R = 2\pi\tau_R/T \ll 1$, then the fluid will remain nearly in equilibrium at all times during the acoustic disturbance. In that limit, the sound speed will be the equilibrium sound speed, c_o. In the opposite limit, $\omega\tau_R = 2\pi\tau_R/T \gg 1$, the medium's sound speed, $c_\infty > c_o$, will be determined by the fluid's elastic response if the internal degrees of freedom cannot be excited by the disturbance. Said another way, the internal degrees of freedom are "frozen out" in that limit; they simply do not have enough time to participate before the state of the system has changed.

One way to think about this effect is to consider the sound speed in a gas of diatomic molecules that possess three translational degrees of freedom and two rotational degrees of freedom. The specific heats of monatomic and polyatomic gases were discussed in Sect. 7.2, and the relationship between the sound speed in such gases and the specific heat ratio, $\gamma = c_p/c_v$, is provided in Eq. (10.22). If the rotational degrees of freedom are not excited, then the gas behaves as though it were monatomic, so $\gamma = 5/3$. If the rotational and translational degrees of freedom are always in equilibrium, then $\gamma = 7/5 < 5/3$, so $c_\infty = \sqrt{25/21}\ c_o$.

The mathematical "machinery" needed to represent the attenuation and dispersion of sound waves in a homogeneous medium with an internal degree of freedom, or a "relaxing sixth variable," has already been developed to describe viscoelastic solids in Sect. 4.4.2. Figure 4.25 could just as well describe the propagation speed (solid line) as a function of the *nondimensional frequency*, $\omega\tau_R$, with c_o being the limiting sound speed for $\omega\tau_R = 2\pi\tau_R/T \ll 1$ and c_∞ being the sound speed for $\omega\tau_R = 2\pi\tau_R/T \gg 1$. In addition, the *Kramers-Kronig relations* of Sect. 4.4.4 would still apply; the variation in sound speed with frequency requires a frequency-dependent attenuation, shown in Fig. 4.25 as the dashed line, and vice versa.

The transformation of the results derived for the stiffness and damping of a viscoelastic medium simply requires that the sound speed is proportional to the square root of the elastic modulus (i.e., stiffness) as expressed in Eq. (10.21). That substitution allows Eq. (4.67) to produce the propagation speed as a function of the nondimensional frequency, $\omega\tau_R$.

$$c^2 = c_o^2 + \left(c_\infty^2 - c_o^2\right)\frac{(\omega\tau_R)^2}{1 + (\omega\tau_R)^2} \tag{14.37}$$

The same approach applied to Eq. (4.70) provides the attenuation per wavelength, $\alpha\lambda$, as function of the dimensionless frequency, $\omega\tau_R$.

$$(\alpha\lambda) = 2\pi \frac{\left(c_\infty^2 - c_o^2\right)(\omega\tau_R)}{c_o^2\left[1 + (\omega\tau_R)^2\right] + \left(c_\infty^2 - c_o^2\right)(\omega\tau_R)^2} \tag{14.38}$$

Following Eq. (4.71) or Eq. (4.89), the maximum value of attenuation per wavelength in Eq. (14.38) will occur at a unique value of the nondimensional frequency, $(\omega\tau_R)_{\max}$.

$$(\omega\tau_R)_{\max} = \frac{c_o}{c_\infty} \quad \text{and} \quad (\alpha\lambda)_{\max} = \pi\frac{\left(c_\infty^2 - c_o^2\right)}{c_\infty c_o} \tag{14.39}$$

The consequence of the Kramers-Kronig relations for such single relaxation time phenomena, as emphasized in Sect. 4.4.2, is that the attenuation is entirely determined by the dispersion, and vice versa.

Using these results, it is possible to write simple universal expressions for attenuation due to excitation of internal degrees of freedom in terms of the relaxation frequency, $f_R = (2\pi\tau_R)^{-1}$.

$$\frac{\alpha\lambda}{(\alpha\lambda)_{\max}} = \frac{2}{\frac{f}{f} + \frac{f}{f_R}} \quad \Rightarrow \quad \alpha(f) = \left[\frac{2(\alpha\lambda)_{\max}}{cf_R}\right]\frac{f^2}{1 + \left(\frac{f}{f_R}\right)^2} \tag{14.40}$$

The variation in the attenuation per wavelength, $\alpha\lambda$, and the propagation speed, c, as a function of nondimensional frequency, $\omega\tau_R$, is plotted in Fig. 14.3 and should be compared to the plot for a viscoelastic solid in Fig. 4.25, which exhibits identical behavior. For relaxation frequencies, f_R, that are much higher than the frequency of interest, f, the attenuation constant's quadratic frequency dependence is recovered, as was derived in Eq. (14.7) for α_{almost} and in Eq. (14.29) for $\alpha_{T\text{-}V}$.

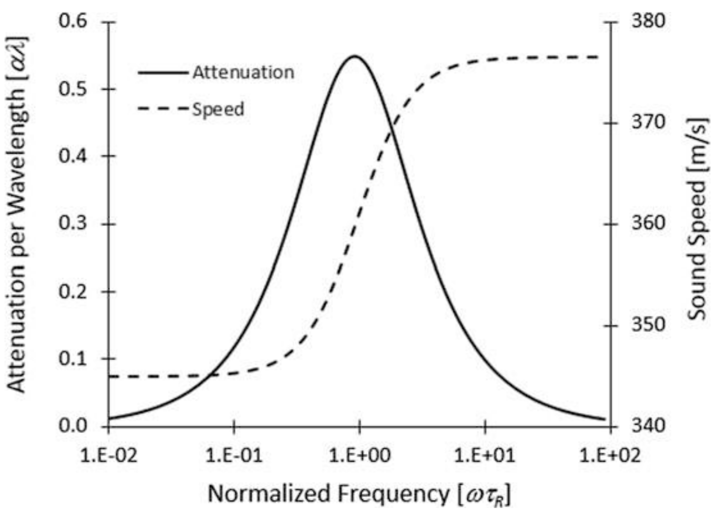

Fig. 14.3 The attenuation and dispersion for a fluid with $c_\infty = c_o\sqrt{25/21}$, where $c_o = 345$ m/s, as a function of the nondimensional frequency, $\omega\tau_R$. Values for the attenuation per wavelength (*solid line*), $\alpha\lambda$, should be read from the left-hand vertical axis, and the values of sound speed (*dashed line*) should be read from the right-hand axis. This behavior is identical to that of a viscoelastic solid that is shown in Fig. 4.25 since the Kramers-Kronig relations dictate the relationship between the real and imaginary parts of the linear response

14.5.1 Relaxation Attenuation in Gases and Gas Mixtures

The first example of the effects of the relaxation of an internal degree of freedom on sound speed and attenuation in gas is taken from the measurements of Shields in fluorine [19]. Halogen vapors (e.g., chlorine, fluorine, bromine, iodine) are unique in that they consist of homonuclear diatomic molecules that have appreciable vibrational energy, $E_V = (n + 1/2)\,\hbar\omega_V$, at room temperature (see Sect. 7.2.2). Because the diatomic molecules behave as simple (quantum mechanical) harmonic oscillators, that internal degree of freedom can be characterized by a single relaxation time corresponding to the radian period of their harmonic oscillations.

Figure 14.4 shows the measured values of attenuation per wavelength, $\alpha\lambda$, and sound speed, c, as a function of frequency (also normalized by pressure), in units of kHz/atm., for fluorine gas

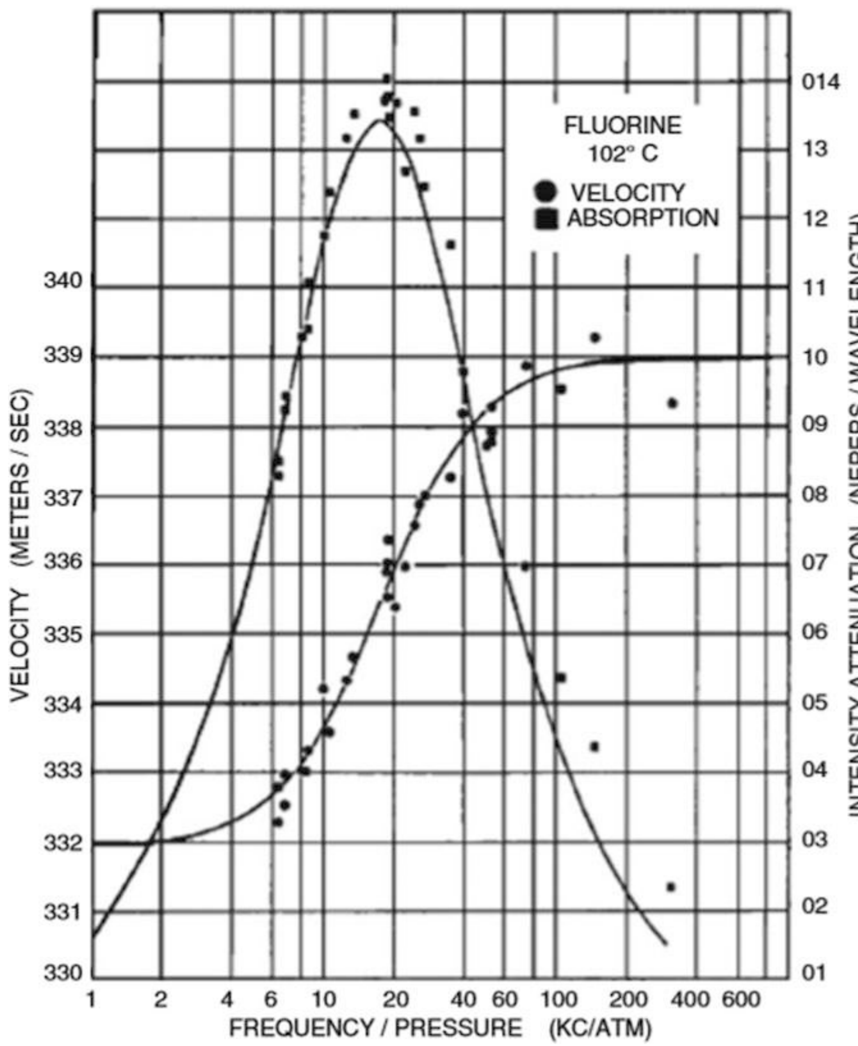

Fig. 14.4 Measured data for attenuation per wavelength and dispersion (sound speed) in fluorine gas at 102 ± 2 °C [19]. The sound speed should be read from the left-hand vertical axis, and the attenuation per wavelength, $\alpha\lambda$, should be read from the right-hand axis that is labeled "Intensity Attenuation (Nepers/Wavelength)." Nepers is an archaic dimensionless unit that was in common usage at the time this data was published to designate α in Np/m. It simply refers to the spatial attenuation coefficient, named after John Napier, the inventor of logarithms. 1 Np = 8.69 dB. The solid lines are fits to the data points that are based on expressions like Eqs. (14.37) and (14.38)

at 102 ± 2 °C, after correction for boundary layer losses at the surface of the tube containing the gas [20].

The *vibrational relaxation time* for diatomic fluorine at 102 °C is $\tau_R = 10.7$ μs, corresponding to a relaxation frequency, $f_R = (2\pi\tau_R)^{-1} = 14.9$ kHz. Based on the fit to the sound speed, the limiting speeds are $c_o = 332$ m/s and $c_\infty = 339$ m/s. The peak in the attenuation per wavelength, $(\alpha\lambda)_{\max} = 0.13$, occurs at $(\omega\tau_R)_{\max} = 0.98$, based on Eq. (14.39), in excellent agreement with the data in Fig. 14.4.

The relaxation attenuation in humid air is more complicated since the two relaxation frequencies for equilibration of the water vapor with the nitrogen and with the oxygen are different, as expressed in Eq. (14.33) and plotted in Fig. 14.2. Since energy loss is cumulative, it is possible to express the attenuation constant, α_{tot}, as the sum of the attenuation caused by the classical value, $\alpha_{classical}$, and the contributions from the two relaxation processes.

$$\alpha_{tot} = \alpha_{classical} + \alpha_{O_2} + \alpha_{N_2} \tag{14.41}$$

The pressure, frequency, and temperature dependence for the total attenuation coefficient is provided in combination with the relaxation times of Eq. (14.33) and plotted as a function of the frequency/pressure ratio for various values of the relative humidity in Fig. 14.5 [21].

$$\begin{aligned}\frac{\alpha_{Air}}{f^2} &= 1.84 \times 10^{-11}\left(\frac{p_m}{p_{ref}}\right)^{-1}\left(\frac{T}{T_{ref}}\right)^{½} + \left(\frac{T}{T_{ref}}\right)^{-5/2} \\ &\times\left\{0.01275\ e^{-2{,}239/T}\left[\frac{f_{rO}}{f_{rO}^2 + f^2}\right] + 0.1068e^{-3{,}352/T}\left[\frac{f_{rN}}{f_{rN}^2 + f^2}\right]\right\}\end{aligned} \tag{14.42}$$

The difference between the classical attenuation constant and the total is clearly very large. At 2 kHz and 1 atm., $\alpha_{classical} = 0.02$ dB/m, but with 10% relative humidity, the attenuation is $\alpha_{tot} = 0.80$ dB/m.

Values for the attenuation in dB/km are tabulated in a standard for different values of temperature from −25 °C to +50 °C and $10\% \le RH \le 100\%$ for pure tones with frequencies from 50 Hz to 10 kHz in ⅓ -octave increments [17]. A small subset of that data are presented in Table 14.1.

14.5.2 Relaxation Attenuation in Fresh and Salt Water

As earlier noted in Sect. 14.3, the measured attenuation of sound in water is greater than $\alpha_{classical}/f^2$ based on the shear viscosity by more than a factor of two. In the calculation of $\alpha_{classical}$ for water, the thermal conductivity was neglected. It can be shown that neglect of the thermal conductivity is not the cause of this discrepancy. Measurements of attenuation at 4 °C, where water has its density maximum and the thermal expansion coefficient vanishes, mean that $c_p = c_v$, so according to Eq. (14.25), there are no temperature changes associated with the acoustical pressure changes [22].

The excess attenuation has been ascribed to a *structural relaxation* process wherein a molecular rearrangement is caused by the acoustically produced pressure changes. During acoustic compression, the water molecules are brought closer together and are rearranged by being repacked more closely. This repacking takes a non-zero amount of time and leads to relaxational attenuation that makes $\zeta \neq 0$ [23]. The relaxation time as a function of water temperature for this process, τ_R, is on the order of picoseconds and is plotted as a function of temperature in Fig. 14.6.

At 4 °C, $\tau_R \cong 3.5$ ps, corresponding to a relaxation frequency, $f_R = (2\pi\tau_R)^{-1} = 45$ GHz, well above experimentally accessible frequencies. For that reason, there are no "relaxation bumps" in the attenuation vs. frequency, as seen in Fig. 14.7. Nonetheless, this structural relaxation makes $\zeta > \mu$, accounting for the excess attenuation in pure water.

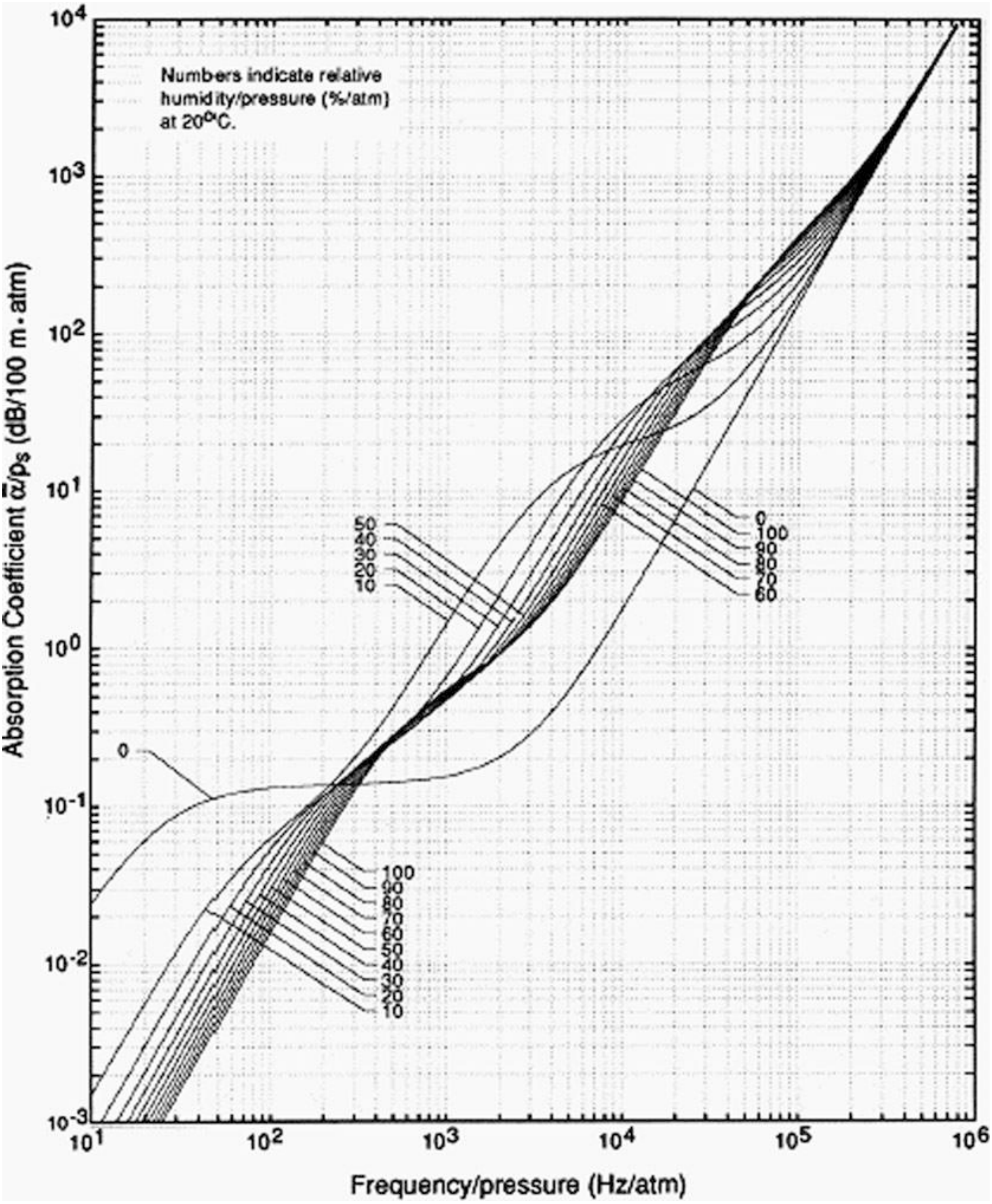

Fig. 14.5 Sound absorption coefficient per atmosphere in air at 20 °C. The parameter labeling the individual curves is the relative humidity from 0% to 100%. [21] The additional attenuation for dry air ($RH = 0$) is due to collisions between N_2 and CO_2

The attenuation of sound in seawater is similar to that in humid air where the relaxation frequencies are within a frequency range of interest. In seawater, there are two pressure-dependent ionic *association-dissociation reactions* due to the dissolved boric acid, $B(OH)_3$, and the dissolved magnesium sulfate, $MgSO_4$. Their contributions to the attenuation have the generic form introduced in Eq. (14.40).

Table 14.1 (*Left*) Attenuation in dB/km for air at 20 °C with $RH = 50\%$, as a function of frequency. (*Right*) Attenuation in dB/km at 4.0 kHz, for air at 20 °C, in the relative humidity range of $20\% \leq RH \leq 70\%$ [17]

Freq. [kHz]	[dB/km]	RH(%)	[dB/km]
1.60	7.37	20	74.4
2.00	9.85	30	48.5
2.50	13.7	40	36.1
3.15	19.8	50	29.4
4.00	29.4	60	25.4
5.00	44.4	70	22.9
6.30	67.8		
8.00	104		
10.00	159		

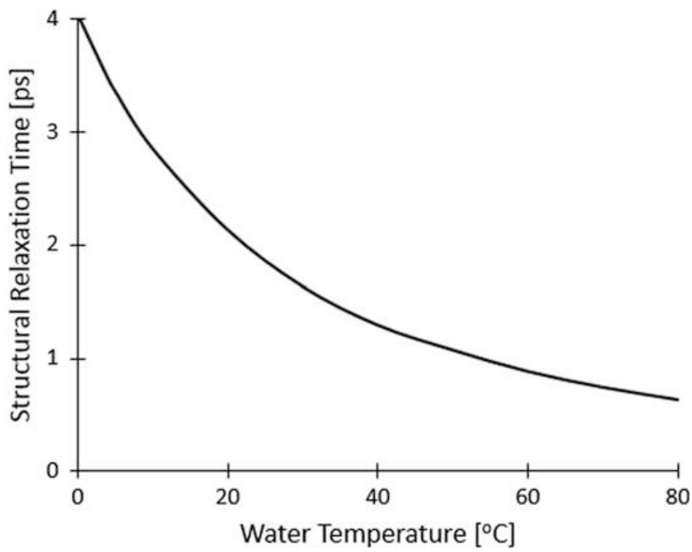

Fig. 14.6 Structural relaxation time for the repacking of water molecules caused by acoustical pressure changes [23]

$$\begin{aligned} MgSO_4 + H_2O \leftrightarrow Mg^{+3} + SO_4^{-2} + H_2O;\ \ \alpha_{MgSO_4} &\cong \frac{4.6 \times 10^{-3} (\text{kHz})^2}{4100 + (\text{kHz})^2} \\ B(OH)_3 + (OH)^{-1} \leftrightarrow B(OH)_4^{-1};\ \ \alpha_{B(OH)_3} &\cong \frac{1.2 \times 10^{-5} (\text{kHz})^2}{1 + (\text{kHz})^2} \end{aligned} \tag{14.43}$$

The approximate attenuation values, α_{MgSO_4} and $\alpha_{B(OH)_3}$, in Eq. (14.43) are in units of [m^{-1}] when the frequency is expressed in kHz.

Those reactions that have relaxation frequencies that depend upon absolute temperature, T, and salinity, S, that is expressed in parts per thousand, ‰, and those relaxation frequencies, $f_{rBH_3O_3}$ and f_{rMgSO_4}, are in hertz [24, 25].

$$\begin{aligned} f_{rBH_3O_3} &= 2,800\sqrt{S/35} \times 10^{[4-(1,245/T)]} \\ f_{rMfSO_4} &= \frac{8,170 \times 10^{[8-(1,990/T)]}}{1 + 0.008(S - 35)} \end{aligned} \tag{14.44}$$

For salinity, S = 35‰, and $T = 293$ K, $f_{rB(OH)_3} = 1.58$ kHz and $f_{rMgSO_4} = 132$ kHz.

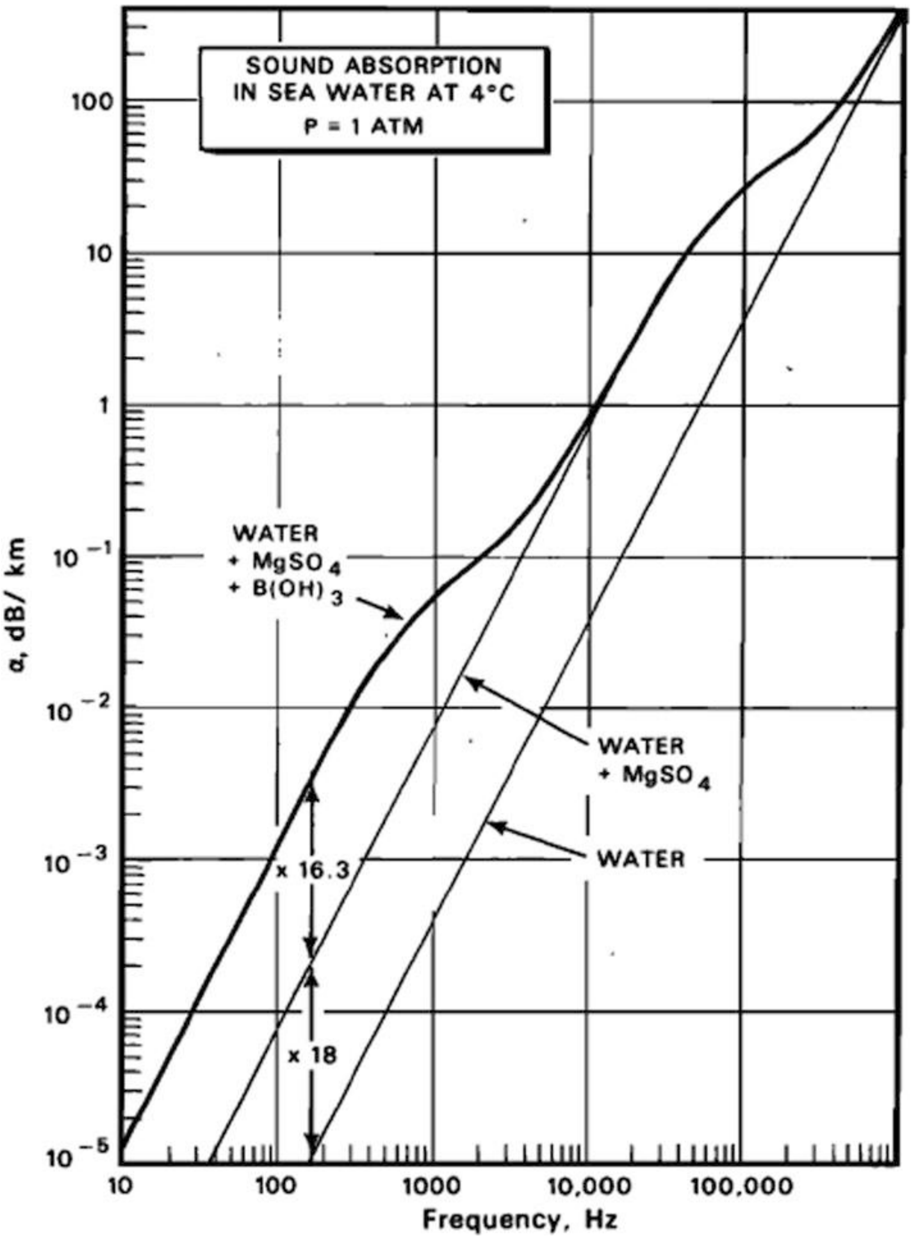

Fig. 14.7 Attenuation of sound in "standard" seawater [26] with salinity of 3.5% and pH = 8.0 at 4 °C [18]. Below 1 MHz, relaxation attenuation due to association-dissociation of boric acid, $B(OH)_3$, and magnesium sulfate, $MgSO_4$, dominates the "classical" contributions

The attenuation coefficient has the expected form, based on Eq. (14.40), and is plotted as a function of frequency in Fig. 14.7.

$$\frac{\alpha}{f^2} = \frac{A_{B(OH)_3} f_{B(OH)_3}}{f^2 + f_{B(OH)_3}^2} + \frac{P_{MgSO_4} A_{MgSO_4} f_{MgSO_4}}{f^2 + f_{MgSO_4}^2} + A_o P_o \tag{14.45}$$

Approximate expressions for the coefficients representing the relaxation strengths, A, and pressure correction factors, P, are provided by Fisher and Simmons [18] with more accurate values provided by François and Garrison [24, 25].

14.6 Transmission Loss

The fact that the bulk attenuation of sound in fluids is quadratic in the frequency has important consequences for ultrasonics ($f > 20$ kHz) and for long-range sound propagation. At the extremely low frequencies, infrasound in the Earth's atmosphere can propagate around the entire globe, and the sound of breaking waves generated by a storm on the Pacific coast of the United States has been detected by a low-frequency microphone at the Bureau of Standards in Washington, DC. An International Monitoring System with 60 infrasound monitoring stations has been deployed globally to detect violations of the Comprehensive Nuclear-Test-Ban Treaty [27].

14.6.1 Short and Very Short Wavelengths

As discussed in Sect. 12.8.1, the Rayleigh resolution criterion implies that the smallest feature that can be resolved in an ultrasonic image will be limited by the wavelength of the sound used to produce the image. Since many ultrasonic imaging systems are used in biomedical applications, we can assume a speed of sound in biological tissue that is approximately equal to the speed of sound in water, $c_{H_2O} =$ 1500 m/s [28]. To resolve an object that is about a millimeter would then require sound at a frequency, $f = c/\lambda \cong 1.5$ MHz. At that frequency, the attenuation of sound in liver tissue is over 2 dB/cm, so a roundtrip transmission loss to go to a depth of 10 cm is 40 dB.

Because the speed of sound in liquids is typically 200,000 times slower than the speed of light, it is possible to achieve optical wavelength resolution of about 5000 Å $=$ 0.5 μm using sound at a frequency of 3 GHz. In addition, acoustical microscopy produces image "contrast" due to variation in the acoustic absorption of the specimens and scattering that arises from the acoustic impedance mismatch between the specimen and the surrounding material due density and compressibility differences (see Sects. 12.6.1 and 12.6.2). Such sources of contrast will reveal completely different information about a specimen than can be deduced due to changes in optical index of refraction or optical reflectance. In addition, sound can penetrate an optically opaque object, and staining is not required for contrast enhancement.[7]

As mentioned, acoustic microscopy is limited by the fact that attenuation is such a strong function of frequency. At 1.0 GHz, the attenuation of sound in water is 200 dB/mm [29]. Despite the high attenuation loss, acoustic microscopes can image red blood cells acoustically at 1.1 GHz with a resolution equivalent to an oil-immersion optical microscope at a magnification of 1000 [30]. Subcellular details as small as 0.1–0.2 μm (e.g., nuclei, nucleoli, mitochondria, and actin cables) have been resolved due to the extraordinary contrast that can differentiate various cytoplasmic organelles [31].

The greatest resolution that has been achieved using acoustical microscopy has been accomplished in superfluid helium at temperatures near absolute zero, which has a sound speed, $c_1 \cong 240$ m/s, a speed that is even lower than the speed of sound in air. Since the dynamics of liquid helium at temperatures below $T_\lambda = 2.17$ K are determined by quantum mechanics, the attenuation mechanisms

[7] Encapsulated microbubbles are used occasionally to provide the ultrasonic image enhancement equivalent of "staining" in optical imaging.

are different than those for classical fluids, which also gives it a much smaller attenuation. At low temperatures, $T < 0.5$ K, the phonon mean free path is controlled by scattering from "rotons," which are quantized collective excitation of the superfluid [32]. Sound wavelengths in liquid helium shorter than 2000 Å = 0.2 μm, in a non-imaging experiment, at frequencies of 1.0 GHz, had been studied before 1970 by Imai and Rudnick [33].

14.6.2 Very Long Wavelengths

At the opposite extreme, at much lower frequencies, the absorption can be quite small. Although the worldwide network of infrasound monitoring sites, using electronic pressure sensors and sophisticated signal processing, that is being used to assure compliance with the Comprehensive Nuclear-Test-Ban Treaty has already been mentioned [27], the most famous measurement of long-distance infrasound propagation was made using barometers.

On 27 August 1883, the island of Krakatoa, in Indonesia east of Java, was destroyed by an immense volcanic explosion. The resulting pressure wave was recorded for days afterward at more than 50 weather stations worldwide. Several of those stations recorded as many as seven passages of the wave as it circled the globe:

> *"The barograph in Glasgow recorded seven passages: at 11 hours, 25 hours, 48 hours, 59 hours, 84 hours, 94 hours, and 121 hours (5 days) after the eruption."* [34]

About 4 h after the explosion, the pressure pulse appeared on a barograph in Calcutta. In 6 h, the pulse reached Tokyo; in 10 h, Vienna; and in 15 h, New York. The period of the pulse was between 100 and 200 s corresponding to a fundamental frequency of about 7 mHz. Its propagation velocity was between 300 and 325 m/s [35]. Although that is close to the speed of sound in air near room temperature, the wave was similar to a shallow water gravity wave in which the height of the atmosphere rose and fell with the passage of the wave [36].

14.7 Quantum Mechanical Manifestations in Classical Mechanics

> *"The major role of microscopic theory is to derive phenomenological theory."* G. E. Uhlenbeck[8]

Although acoustics is justifiably identified as a field of classical phenomenology, there are many acoustical effects that have their origin in the microscopic theory of atoms and therefore manifest macroscopic behaviors that can only be explained in terms of quantum mechanics. The effects of these "hidden variables" have been manifest throughout this textbook starting with the damping of simple harmonic oscillators that connects the "system" to the environment, thus producing Brownian motion [37], which was related to the more general theory coupling fluctuations and dissipation [38] in Chap. 2.[9]

This theme recurred in Chap. 7 when the quantization of energy levels for molecular vibration and rotation influenced the specific heat of gases and in Chap. 9 where a simple kinetic theory of gases was used to determine the pressure and temperature variation of viscosity and thermal conductivity. Now we see in this chapter how structural relaxations in water [23], like those in Fig. 5.23 for the four

[8] George Eugène Uhlenbeck (1900–1988) was a Dutch theoretical physicist who, with fellow Dutchman, Samuel Goudsmit (1902–1978), first proposed quantized "spin" as the internal degree of freedom for electrons.

[9] Lars Onsager (1903–1976) was the Norwegian-born physical chemist and theoretical physicist who received the Nobel Prize in chemistry, in 1968, for the reciprocal relations between fluctuations and dissipation that are now referred to as "Onsager reciprocity."

crystalline structures of plutonium [39], scattering of phonons and rotons in superfluids [32], or molecular vibrations in F_2 [19] and collision times in gas mixtures [15], or chemical reactions [24, 25], manifest themselves in the attenuation of sound.

These internal relaxation effects have been incorporated into our phenomenological theory through the introduction of an additional dissipative process that has been quantified by the introduction of a frequency-dependent parameter, ζ, that shares the same units with the coefficient of shear viscosity, μ. That coincidence has led to this new parameter being called the coefficient of "bulk viscosity" (or sometimes "second viscosity"), even though it is independent of the shear deformation of the fluid and is not the source of momentum transport.

Talk Like an Acoustician

Viscoelasticity	Mean free path
Viscous drag	Kinetic theory
Thermal relaxation	Einstein summation convention
Thermoviscous boundary layer	Bulk viscosity
Spatial attenuation coefficient	Second viscosity
Temporal attenuation coefficient	Le Châtelier's principle
Shear strain	Nondimensional frequency
Hydrostatic strain	Vibrational relaxation time
Collision time	Structural relaxation
Enthalpy function	Association-dissociation reactions
Legendre transformation	Kramers-Kronig relations
Maxwell relations	
Relaxation time	

Exercises

1. **Bulk attenuation and reverberation time**. An expression was provided in Eq. (13.29) to incorporate the attenuation in air contained within an enclosure into the expression for reverberation time. A "useful correlation" was provided in Eq. (13.30) that was applicable for 1500 Hz $\leq f \leq$ 10,000 Hz and for relative humidity in the range 20% $\leq RH \leq$ 70%.
   (a) *Average frequency dependence*. Table 14.1 (left) provides the attenuation in dB/km from the ANSI/ASA standard for the frequencies within the range specified at 20 °C for $RH = 50\%$ [17]. Plot the $\log_{10}$ of the spatial attenuation, α, in m^{-1} vs. the $\log_{10}$ of frequency, f, in kHz, to determine the power law dependence on frequency (see Sect. 1.9.3). Is your result proportional to $f^{1.7}$ to within the statistical uncertainty of your least-squares fit? Keep in mind that attenuation expressed in [dB/m] must be multiplied by $0.1151 \cong [10\log_{10}(e^2)]^{-1}$ to convert to m^{-1} (sometimes including the dimensionless "Nepers" to report results in Nepers/m).
   (b) *Humidity dependence*. Table 14.1 (right) also includes the attenuation in dB/km at 4.0 kHz and 20 °C for 20% $\leq RH \leq$ 70%. The "useful correlation" claims that the correction to frequency dependence for variations in relative humidity should be linear in (50%/RH). How close is that presumed humidity dependence to values in the table for variation in relative humidity at 4.0 kHz?
2. **The mother of all PA systems**. Shown in Fig. 14.8 is a loudspeaker that can produce 30,000 watts of acoustic power by modulating a pressurized air stream (like a siren) using a cylindrical "valve" mounted on a voice coil, like that used for an electrodynamic loudspeaker. That sound source, located at the apex of the horn, is called a "modulated airstream loudspeaker." [40]

Fig. 14.8 A very large horn loudspeaker mounted on an 18-wheel tractor-trailer. (Photo courtesy of Wiley Labs)

Such a public address system was developed to tell illiterate enemy combatants, in their native language, to put down their weapons and surrender from a distance that is greater than the distance that could be traversed by artillery shells. Although the bandwidth of telephone speech for very good intelligibility is generally 300 Hz to 3.4 kHz, for this problem, we will focus on the propagation of a 1 kHz pure tone. Since this system was deployed in desert terrain, assume that $RH = 10\%$, $T_m = +50\ °\text{C} = 122\ °\text{F}$, and $p_m = 100$ kPa.

(a) *Sound level at 100 m*. Assuming hemispherical spreading and no sound absorption, what is the root-mean-square acoustic pressure amplitude if the source produces 30 kW of acoustic power and any nonlinear effects that might cause harmonic distortion (see Sect. 15.2.3) can be neglected? Also neglect any refractive effects due to sound speed gradients caused by temperature or wind as discussed in Sect. 11.3. Report your results as both in r.m.s. pressure amplitude and in dB *re:* 20 $\mu\text{Pa}_{\text{rms}}$.

(b) *Greater distances*. Repeat part *a*, but determine the sound pressure at 1.0 km and 3.0 km, again neglecting attenuation.

(c) *Include attenuation*. Determine the spatial attenuation coefficient under these conditions at 1.0 kHz and use it to reduce the sound pressure at 0.1 km, 1.0 km, and 3.0 km below that obtained due only to hemispherical spreading.

3. **Pump wave attenuation for a parametric array**. The generation of highly directional sound beams from the nonlinear acoustical interaction of two colinear high-frequency sound beams will be discussed in Sect. 15.3.3. Calculate the exponential attenuation length, $\ell = \alpha^{-1}$, of a typical 40 kHz beam in dry air, $RH = 0\%$, and moist air with $RH = 60\%$ using the graph in Fig. 14.5.

4. **Siren**. The siren shown in Fig. 14.9 consumed 2500 ft^3/min of air at a pressure of 5 psi above ambient to produce 50 horsepower of acoustic power at 500 Hz, and did so with 72% efficiency [41].

(a) *Hydraulic power*. How much time-averaged power, $\langle \Pi_{hy} \rangle_t = (\Delta p)|U|$, is available, in watts and in horsepower, from the specified volume flow rate, U, and the available pressure drop, Δp?

(b) *Hemispherical spreading*. Assuming the mean temperature during the measurement was $T_m = 20\ °\text{C}$ and $p_m = 100$ kPa, what would be the root-mean-square pressure a distance of

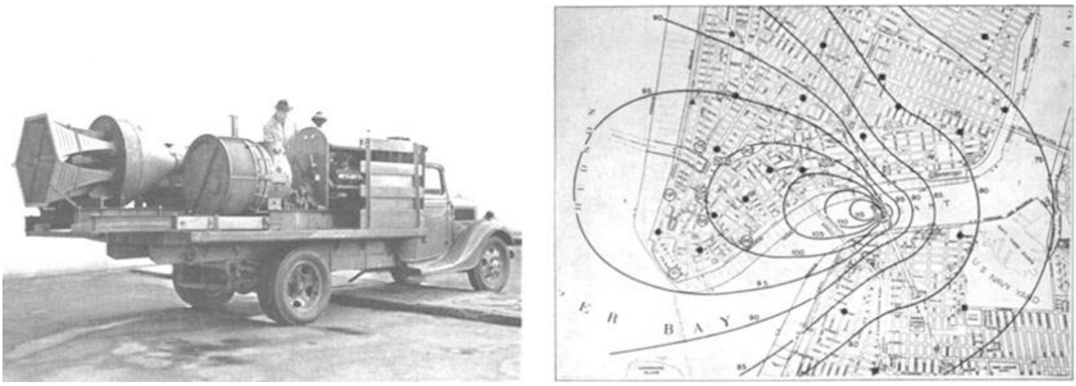

Fig. 14.9 (*Left*) Photograph of a 50-horsepower siren and compressor mounted on a truck. The intake filter and compressor are on the near side, and the exponential horn is farther away. (*Right*) Equal loudness contours measured throughout lower Manhattan when the siren was placed on the Manhattan Bridge facing toward the Financial District. The siren's directivity index was 11.8 dB at 500 Hz (see Sect. 12.8.2) [41]

1000 ft. from the siren if it produced a sound power of 50 horsepower? Report your results both in pressure and dB *re:* 20 μPa$_{rms}$.

(c) *Include attenuation*. If $RH = 50\%$, how much additional loss, in dB, would be produced by absorption at the same distance?

5. **The SOFAR channel**. One method for locating pilots who crash over the ocean is to drop an explosive sound source that is set to detonate at a depth that is equal to the axis of the deep sound channel that is created by a sound speed profile like the one shown in Fig. 11.8. In that figure, the axis of the sound channel is 1112 m below the ocean's surface. Sound that is trapped in that channel will spread cylindrically, rather than spherically, beyond a transition distance that will be assumed to be much shorter than the distance of interest, so the sound amplitude will decrease in proportion to $\sqrt{R}$, where R is the distance between the source and the receiver.
   (a) *Cylindrical spreading*. What would be the loss, in dB, due to cylindrical spreading over 5000 km relative to the level 1 km from the source?
   (b) *Include attenuation*. Using the results for seawater in Fig. 14.7, what would be the spatial attenuation, in dB, that would have to multiply the cylindrical spreading loss over 5.0 km calculated in part (a) for sound with a frequency of 100 Hz? Repeat for the loss due to attenuation in seawater after 5000 km.
6. **High-frequency relaxational attenuation constant for air and water**.
   (a) *Limiting frequency dependence*. Using Eq. (14.40), show that for frequencies well above the highest relaxational frequency, f_R, the attenuation of sound is independent of frequency.
   (b) *Relaxational attenuation constant (bulk viscosity) of air*. In Eq. (14.42), the measured high-frequency limit of the spatial attenuation constant in air is $\alpha_{air}/f^2 = 1.84 \times 10^{-11}$ s^2/m. Calculate $\alpha_{classical}/f^2$ for air at atmospheric pressure and 20 °C, and use both high-frequency results (i.e., with and without relaxation effects) to determine the value for ζ_{air} in the high-frequency limit.
   (c) *Relaxational attenuation constant (bulk viscosity) of pure water*. The measured high-frequency limit of the spatial attenuation constant in pure water at 4 °C is $\lim_{f \gg f_R} \alpha_{H_2O}/f^2 = 2.5 \times 10^{-14}$ s^2/m. Based on $\alpha_{classical}/f^2$ for pure water at atmospheric pressure and 4 °C, determine the value for ζ_{H_2O} in the high-frequency limit.

References

1. M. Greenspan, Transmission of sound waves in gases at very low pressures, in *Physical Acoustics*, vol. 2A, (Academic Press, 1965), pp. 1–45
2. L.D. Landau, E.M. Lifshitz, *Fluid Mechanics*, 2nd edn (Butterworth-Heinemann, 1987). See §79; ISBN 0-7506-2767-0
3. H. Lamb, *Hydrodynamics*, 6th edn (Cambridge, 1932), reprinted (Dover, 1945). See §30; ISBN 0-486-60256-7
4. G.G. Stokes, On the theories of the internal friction of fluids in motion and the equilibrium and motion of elastic solids. Philos. Trans. (Cambridge) **8**, 287–302 (1845)
5. R. B. Lindsay, *Acoustics: Historical and Philosophical Development* (Dowden, Hutchinson & Ross, 1973). p. 261; ISBN 0-87933-015-5
6. M.J. Stefan, Über den Einfluss der inneren Reibung in der Luft auf die Schallbewegung. Sitzber. Akad. Wiss. Wein **53**, 526–537 (1866)
7. G. Krichhoff, Über den Einfluss der Warmeleitung in einen Gase auf die Schallbewegung. Ann. Phys. Chem. **134**, 177–193 (1868). English translation: On the influence of thermal conduction in a gas on sound propagation, in *Physical Acoustics*, ed. by R.B. Lindsay (Dowden, Hutchinson & Ross, 1974). pp. 7–19
8. A. Bejan, *Advanced Engineering Thermodynamics*, 2nd edn (Wiley, 1997). See §4.4; ISBN 0-471-14880-6
9. F. Reif, *Fundamentals of Statistical and Thermal Physics* (McGraw-Hill, 1965), See §5.5
10. *American Institute of Physics Handbook*, 3rd edn, ed. by D.W. Grey (McGraw-Hill, 1972). ISBN 07-001485-X
11. J.J. Markham, R.T. Beyer, R.B. Lindsay, Absorption of sound in fluids. Rev. Mod. Phys. **23**(4), 353–411 (1951). See Eq. (A-13)
12. H.E. Bass, L.C. Sutherland, A.J. Zuckerwar, D.T. Blackstock, D.M. Hester, Erratum: Atmospheric absorption of sound: Further developments. J. Acoust. Soc. Am. **97**, 680–683 (1995), J. Acoust. Soc. Am. **99**(2), 1259 (1996)
13. J.T.R. Watson, R.S. Basu, J.V. Sengers, An improved representative equation for the dynamic viscosity of water substance. J. Phys. Chem. Ref. Prop. **9**(4), 1255–1290 (1980)
14. J.M.M. Pinkerton, A pulse method for the measurement of ultrasonic absorption in liquid: Results for water. Nature **160**, 128–129 (1947)
15. M. Greenspan, Rotational relaxation in nitrogen, oxygen, and air. J. Acoust. Soc. Am. **31**(2), 155–160 (1959)
16. A.D. Pierce, *Acoustics: An Introduction to its Physical Principles and Applications*, 2nd edn (Acoustical Society of America, 1989). ISBN 0-88318-612-8, pp 554
17. R.J. Peppin, A. Scharine, *Methods for Calculation of the Absorption of Sound in the Atmosphere*, Am. Nat. Standard ANSI/ASA S1.26-2014. See §5.2.1
18. F.H. Fisher, V.P. Simmons, Sound absorption in sea water. J. Acoust. Soc. Am. **62**(3), 558–564 (1977)
19. F.D. Shields, Thermal relaxation in fluorine. J. Acoust. Soc. Am. **34**(3), 271–274 (1962)
20. F.D. Shields, R.T. Lagemann, Tube corrections in the study of sound absorption. J. Acoust. Soc. Am. **29**(4), 470–475 (1957)
21. H. E. Bass, L. C. Sutherland, A. J. Zuckerwar, D. T. Blackstock, and D. M. Hester, Atmospheric absorption of sound: Further developments. J. Acoust. Soc. Am. **97**(1), 680–683 (1995), as corrected in the erratum, J. Acoust. Soc. Am. **99**(2), 1259 (1996)
22. F.E. Fox, G.D. Rock, Compressional viscosity and sound absorption in water at different temperatures. Phys. Rev. **70** (1/2), 68–73 (1946)
23. L. Hall, The origin of ultrasonic absorption in water. Phys. Rev. **73**(7), 775–781 (1948)
24. R.E. François, G.R. Garrison, Sound absorption based on ocean measurements. Part I: Pure water and magnesium sulfate contributions. J. Acoust. Soc. Am. **72**(3), 896–907 (1982)
25. R.E. François, G.R. Garrison, Sound absorption based on ocean measurements: Part II – Boric acid contribution and equation for total absorption. J. Acoust. Soc. Am. **72**(6), 1879–1890 (1982)
26. J. Lyman, R.H. Fleming, Composition of sea water. J. Mar. Res. **3**, 134–146 (1940)
27. H.E. Bass, J. Bhattacharyya, M.A. Garcés, M. Hedlin, J.V. Olson, R.L. Woodward, Infrasound. Acoust. Today **2**(1), 9–19 (2006)
28. J.C. Bamber, Speed of sound, in *Principles of Medical Ultrasonics*, 2nd edn, ed. by C.R. Hill, J.C. Bamber, G.R. ter Haar (Wiley, 2005). See Fig. 5.3, pg. 178; ISBN 0-470-09396-X
29. R.A. Lemons, C.F. Quate, Acoustic microscopy: Biomedical application. Science **181**(4191), 905–911 (1975)
30. C.F. Quate, A. Atalar, H.K. Wickramasinghe, Acoustic microscopy with mechanical scanning – A review. Proc. IEEE **67**(8), 1092–1114 (1975)
31. R.A. Johnston, A. Atalar, J. Heiserman, V. Jipson, C.F. Quate, Acoustic microscopy: Resolution of subcellular detail. Proc. Natl. Acad. Sci. U.S.A. **76**(7), 3325–3329 (1979)
32. I.M. Khalatnikov, D.M. Chernikova, Zh. Eksperim. i Teor. Fiz. **49**, 1957 (1965), **50**, 411 (1966). Translation: Sov. Phys.-JETP **22**, 1336 (1966), **23**, 274 (1966)
33. J.S. Imai, I. Rudnick, Ultrasonic attenuation in liquid helium at 1 GHz. Phys. Rev. Lett. **22**(14), 694–697 (1969)

34. G.J. Symons (ed.), *The Eruption of Krakatoa and Subsequent Phenomena*. Report of the Krakatoa Committee of the Royal Society (Trübner & Co., London, 1888)
35. T.B. Gabrielson, Krakatoa and the Royal Society: The Krakatoa explosion of 1883. Acoust. Today **6**(2), 14–18 (2010)
36. G.I. Taylor, Waves and tides in the atmosphere. Proc. R. Soc. **A126**(800), 169–183 (1929)
37. G.E. Uhlenbeck, S. Goudsmit, A problem in Brownian motion. Phys. Rev. **34**, 145–151 (1929)
38. C.W. McCombie, Fluctuation theory in physical measurements. Rep. Prog. Phys. **16**, 266–319 (1953)
39. Y. Suzuki, V.R. Fanelli, J.B. Betts, F.J. Freibert, C.H. Mielke, J.N. Mitchell, M. Ramos, T.A. Saleh, A. Migliori, Temperature dependence of elastic moduli of polycrystalline β plutonium. Phys. Rev. B **84**, 064105 (2011)
40. V. Salmon, J.C. Burgess, Modulated airstream loudspeaker. J. Acoust. Soc. Am. **29**, 767 (1957)
41. R.C. Jones, A fifty horsepower siren. J. Acoust. Soc. Am. **18**(2), 371–387 (1946)

Part III

Extensions

Nonlinear Acoustics

15

Contents

The goal of this chapter is to raise awareness of the limitation of linear analysis, not to create professional expertise in nonlinear acoustics. A fundamental assumption of linear acoustics is that the presence of a wave does not have an effect on the properties of the medium through which it propagates. Under that assumption, two sound waves can be superimposed when they occupy the same space at the same time, but one wave will have no effect on the other wave and once they part company there will be no evidence of their previous interaction. This is illustrated in Fig. 15.1. By extension, the

S. L. Garrett, *Understanding Acoustics*, Graduate Texts in Physics,
https://doi.org/10.1007/978-3-030-44787-8_15

Fig. 15.1 Two wave packets pass through each other. (*Left*) The two wave packets are approaching each other. (*Center*) When those wave packets overlap, the disturbances superimpose. (*Right*) After their superposition, they continue their propagation with no evidence of their previous interaction

assumption of linearity also means that a waveform is stable since any individual wave does not interact with itself.[1]

We already know that this assumption of the wave having no influence on the properties of the propagation medium cannot be strictly correct. The wave imparts a small particle velocity, v_1, to the fluid that adds to the sound speed when that velocity is in the direction of propagation and subtracts from the sound speed when the particle velocity is opposite to the direction of propagation. The local value of the sound speed, $c(x, t)$, will vary in time and space due to the wave's convective contribution so that $c_o + v_1(x, t) \geq c(x, t) \geq c_o - v_1(x, t)$, where c_o is the equilibrium (thermodynamic) sound speed: $c_o = \sqrt{(\partial p/\partial \rho)_s}$.

The wave also modulates the medium's thermodynamic sound speed. For the case of an ideal gas undergoing adiabatic compressions and expansions, there is an accompanying temperature change of amplitude, T_1, given by Eq. (7.25), that is related to the amplitude of the pressure change, $p_1(x, t)$: $(\partial T/\partial p)_s = [(\gamma - 1)/\gamma](T_m/p_m)$. Since the sound speed in an ideal gas is dependent upon the temperature of the gas through Eq. (10.23), this implies that the change in sound speed, δc, due to a temperature change is given by $(\delta c/c_o) = ½(T_1/T_m)$. In an ideal gas, the local sound speed is slightly faster than c_o when the acoustic pressure is positive since the gas is warmer and slightly slower than c_o when the acoustic pressure is negative since the gas is cooler.

As will be demonstrated, these small modifications in the sound speed due to wave-induced fluid convection and to the wave's effect on sound speed through the equation of state can lead to interesting effects that could not be predicted within the limitations imposed by the assumption of linearity. Although their influence on the sound speed may be small, those effects are cumulative. These are called nonlinear effects because the magnitude of the nonlinearity's influence is related to the square of an individual wave's amplitude (*self-interaction*) or the product of the amplitudes of two interacting waves (*intermodulation distortion*).

An additional consequence of the inclusion of nonlinearity is that the time-average of an acoustically induced disturbance may not be zero. In the linear case, the measure of a wave's amplitude will be equally positive and negative around its undisturbed equilibrium value, so that the time-average of the wave's influence will be zero. When the hydrodynamic equations and the equation of state were linearized, the terms in those equations that were discarded could lead to non-zero time-averaged effects. For the linearized continuity equation, the $\rho_1 v_1$ term was discarded since Eq. (8.19) demonstrated that it was smaller than the $\rho_m v_1$ term for small values of the acoustic Mach number, $M_{ac} \ll 1$. A similar choice was made for the linearization of the Euler equation. The convective portion of the total derivative, $\left(\vec{v}_1 \cdot \nabla\right)\vec{v}_1$, was discarded when compared to $\partial \vec{v}_1/\partial t$in Eq. (8.38) under the

[1] Although instability requires nonlinearity, nonlinearity does not necessarily always result in instability. Solitons are waveforms that remain stable due to the compensatory influences of nonlinearity and dispersion.

same assumption of small acoustic Mach number. To complete the overall linearization, the Taylor series expansion of the equation of state in Eq. (10.3) was truncated after the first-derivative term.

In this chapter we will recover some of the interesting acoustical phenomena that were lost to the linearization of the phenomenological equations that describe both the dynamics and the medium itself.

15.1 Surf's Up

When most people hear the term "wave," it is likely that word will conjure mental images of surf breaking along a beach. (It is a most pleasant image!) The breaking of waves in shallow water is a dramatic nonlinear effect that is due to both the *convective nonlinearity* and the fact that the height of the wave modulates the propagation speed of a shallow-water gravity wave. The speed of a shallow-water gravity wave represents the competition between the water's inertia and the restoring force of gravity. Figure 15.2 is a schematic representation of one cycle of such a wave on a fluid of equilibrium depth, h_o, with a peak wave height of magnitude $|h_1| \ll h_o$.

The assumption that the fluid is "shallow" implies that the mean depth of the fluid, h_o, is much smaller than the wavelength of the disturbance, λ.

$$h_1(x,t) = \Re\mathrm{e}\left[\widehat{\mathbf{h}} e^{\,j(\omega t - kx)}\right] \tag{15.1}$$

Since there is a free surface, we will assume that the fluid is incompressible. It is much more favorable (energetically) for the free surface to move up than it is for a pressure increase to increase the fluid's density. The continuity equation can be written by recognizing that the rate-of-change of the fluid's height, $\dot{h}_1(x,t)$, is determined by the difference in the amount of fluid that enters and leaves a "slab" of infinitesimal thickness, dx, shown in Fig. 15.2.

$$\frac{\partial h}{\partial t} + h_o \frac{\partial v_x}{\partial x} = 0 \quad \Rightarrow \quad \dot{h}_1 = jkh_o v_x \quad \Rightarrow \quad \left|\frac{\dot{h}_1}{v_x}\right| = \frac{2\pi h_o}{\lambda} \tag{15.2}$$

For a shallow-water gravity wave, the fluid's particle velocity in the direction of propagation, v_x, is greater than the rate-of-change of height of the free surface if $h_o \ll \lambda$. This is an effect most of us have experienced while frolicking in the surf near the ocean's shore—it is usually the "surge" that knocks us over, not $\dot{h}_1$.

Since gravity (not compressibility) provides the restoring force, Euler's Eq. (7.34) relates the fluid's velocity in the direction of propagation, v_x, to the gravitational pressure gradient.

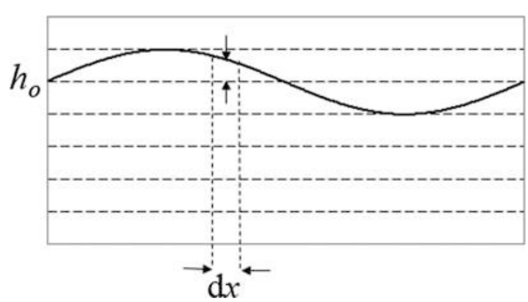

Fig. 15.2 Schematic representation of a sinusoidal disturbance on the free surface of a liquid that has a mean depth, h_o. The wave on the surface has an amplitude, $|h_1| \ll h_o$, but with a wavelength $\lambda \gg h_o$

$$\frac{\partial v_x}{\partial t} = -\frac{1}{\rho}\frac{\partial(\rho g h_1)}{\partial x} = -g\frac{\partial h_1}{\partial x} \tag{15.3}$$

The combination of Eqs. (15.2) and (15.3), with the assumption of a rightward traveling wave in Eq. (15.1), leads to a dispersion relation that generates the equilibrium values for propagation speed, c_{grav}, of a shallow-water gravity wave.[2]

$$\begin{vmatrix} +j\omega & -jh_o k \\ -jgk & +j\omega \end{vmatrix} = 0 \quad \Rightarrow \quad c_{grav} = \frac{\omega}{k} = \sqrt{gh_o} \;\text{ for }\; kh_o \ll 1 \tag{15.4}$$

Logarithmic differentiation of Eq. (15.4) provides the relationship between the local wave speed and the instantaneous depth of the fluid.

$$\frac{\delta c_{grav}}{c_{grav}} = \frac{1}{2}\frac{\delta h}{h_o} \quad \Rightarrow \quad \frac{\partial\, c_{grav}}{\partial\, h} = \frac{1}{2}\frac{c_{grav}}{h_o} \tag{15.5}$$

We would like to combine the effects of changing depth on the sound speed with the convective contribution to the local sound speed produced by v_x. The continuity Eq. (15.2) provides that necessary conversion.

$$j\omega h_1 = jkh_o v_x \quad \Rightarrow \quad \frac{h_1}{h_o} = \frac{v_x}{c_{grav}} \equiv M_{ac} \quad \Rightarrow \quad \frac{\partial h}{\partial v_x} = \frac{h_o}{c_{grav}} \tag{15.6}$$

The convective contribution to the local wave speed, $c(v_x)$, can be combined with the change in local wave speed due to the changing fluid depth.

$$c(v_x) = c_{grav} + v_x + \left(\frac{\partial c_{grav}}{\partial h}\right)\left(\frac{\partial h}{\partial v_x}\right)v_x = c_{grav} + \frac{3v_x}{2} \tag{15.7}$$

Both convection and the speed's change with depth conspire to increase the local wave speed when $h_1(x, t) > 0$ and reduce the local wave speed when $h_1(x, t) < 0$. The wave's crests travel faster than the zero-crossings (i.e., $h_1(x, t) = 0$) and its troughs travel slower than the zero-crossings. Figure 15.3 shows the cumulative consequences of the wave's influence on its own local propagation speed. As the wave progresses, the crests will start to overtake the troughs.

In Fig. 15.3, the coordinate system was chosen to move with the equilibrium wave speed, c_{grav}, so that the distortion becomes evident. At the instant captured in Fig. 15.3, the slope of the zero-crossing has become vertical. To reach that condition, the crest of a sinusoidal waveform must have advanced by one radian length toward the zero-crossing, $k^{-1} = \lambda/2\pi$ (see Prob. 1), and the trough must have lagged behind by the same amount. The time, T_S, it takes for the crest to advance by k^{-1} is given by the speed excess, $3v_x/2$, calculated in Eq. (15.7). The distance traveled by the wave once the slope first becomes infinite is known as the *shock inception distance*, D_S.

[2] The exact result for the propagation speed at all depths reduces to c_{grav} in Eq. (15.4) in the limit that $kh_o \to 0$. Since this result depends upon k, it is dispersive, so the phase speed, c_{grav}, will not be equal to the group speed except in the "shallow water" $kh_o \to 0$ limit.

$$c_{grav} = \frac{\omega}{k} = \sqrt{\frac{g}{k}\tanh kh_o}$$

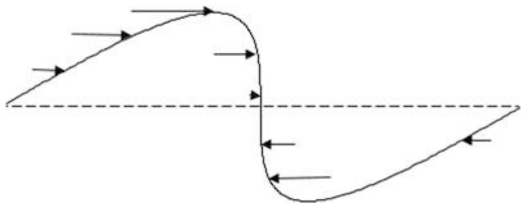

Fig. 15.3 The local propagation speed of a shallow-water gravity wave depends upon the amplitude, $|\hat{\mathbf{h}}| \equiv h_1$, of the wave. As shown by arrows, an initially sinusoidal wave will change shape because the crests are moving faster than the troughs. As shown, this distortion has made the slope at the zero-crossing infinite

$$D_S = c_{grav}T_S = c_{grav}\frac{\lambda/2\pi}{3v_x/2} = \frac{\lambda}{3\pi M_{ac}} \tag{15.8}$$

For surf, the wave can continue beyond D_S. Since surf has free surface, h_1 can actually become multivalued and will eventually "break," sometimes with a spectacularly powerful display of sound and foaminess. Stokes was the first to recognize in 1848 that viscosity is the physical mechanism that prevents a sound wave from becoming multivalued. Stokes was also the first to draw a distorted waveform, like the one in Fig. 15.3, which he did in that same paper where he talked about the essential role of viscosity[3] [1].

15.1.1 The Grüneisen Parameter

The principles introduced to describe waveform distortion and the creation of a shock front for shallow-water gravity waves are common to all sound waves in fluids. A sound wave will influence the propagation speed of the medium due to a combination of the convective contribution and the fact that the wave's amplitude also influences the propagation speed. Of course, the nature of that contribution and the relative importance of the convective and equation of state contributions will be differ depending upon the medium. The convenience of representing both contributions in terms of the local fluid particle velocity was demonstrated in the analysis of surf that produced Eq. (15.7). The strength of nonlinear distortion in any medium that supports a plane progressive wave will now be generalized by the introduction of the *Grüneisen parameter*, Γ.

$$c(v) = c_o + \left[1 + \frac{\partial c}{\partial y}\frac{\partial y}{\partial v}\right]v \equiv c_o + \Gamma v \quad \text{and} \quad D_S = \frac{\lambda}{2\pi\Gamma M_{ac}} \tag{15.9}$$

The Grüneisen parameter is a designation taken from solid-state physics where it represents the nonlinearity of a solid's elasticity that is responsible for the non-zero value of a solid's thermal expansion coefficient.[4] The reader should be cautioned that calling this nonlinear distortion parameter

[3] An excellent history of the early development of nonlinear acoustics is provided by D. T. Blackstock, "History of Nonlinear Acoustics: 1750s–1930s," as Chap. 1 in *Nonlinear Acoustics*, 2nd ed. (Acoust. Soc. Am., 2008), M. F. Hamilton and D. T. Blackstock, editors; ISBN 0–9,744,067–5-9.

[4] If the elastic potential of a solid depended on only the parabolic potential energy contribution (see Sect. 1.2.1), then as a solid heated up, the amplitude of the motion of the point particles (molecules) would increase, but their equilibrium position would remain unchanged. If there is a cubic contribution to the interparticle potential energy, then as the amplitude of the molecular vibrations increased (with increasing temperature), the equilibrium position would shift causing thermal expansion or contraction of the solid.

the "Grüneisen parameter" and designating it as Γ is not a common choice in other treatments of nonlinear acoustics. For example, in a recent paper by Hamilton [2], Γ represents the Gol'dberg number that is abbreviated as G in this textbook (see Sect. 15.1.4). In Eq. (15.9), the general amplitude variable is simply written as "y," and the equilibrium sound speed is designated c_o to distinguish it from the local amplitude-dependent sound speed, $c(v) = c_o + \Gamma v$.

If a medium's sound speed depended upon the density of the medium, ρ, which obeyed the linear continuity equation, the Grüneisen parameter would be expressed in terms of the sound speed's variation with density.

$$\frac{\partial \rho}{\partial t} + \nabla \bullet (\rho v) = 0 \quad \Rightarrow \quad \frac{\rho_1}{\rho_m} = \frac{v_1}{c_o} \quad \Rightarrow \quad \Gamma = 1 + \frac{\partial c}{\partial \rho}\frac{\partial \rho}{\partial v} = 1 + \frac{\rho_m}{c_o}\frac{\partial c}{\partial \rho} \tag{15.10}$$

For an ideal gas, the sound speed depends upon the mean absolute temperature, T_m. As before, δc represents the change in the sound speed due to the change in local temperature.

$$c_o^2 = \frac{\gamma \Re T_m}{M} \quad \Rightarrow \quad \frac{\delta c}{c_o} = \frac{1}{2}\frac{T_1}{T_m} \quad \Rightarrow \quad \left(\frac{\partial c}{\partial T}\right)_s = \frac{1}{2}\frac{c_o}{T_m} \tag{15.11}$$

The Grüneisen parameter for an ideal gas can be expressed in terms of the change in the speed of sound with temperature, the change in temperature with pressure, and the particle velocity amplitude, v_1, associated with the acoustic pressure amplitude, p_1, as related by the Euler equation for progressive plane wave propagation: $p_1 = (\rho_m c_o) v_1$.

$$c(v) = c_o + v_1 + \left(\frac{\partial c}{\partial T}\right)_s \left(\frac{\partial T}{\partial p}\right)_s \left(\frac{\partial p}{\partial v}\right)_s v_1 \tag{15.12}$$

Using the relationship between temperature and pressure for an adiabatic sound wave in Eq. (7.25), the Grüneisen parameter for an ideal gas can be calculated.

$$\Gamma_{gas} = \left(1 + \frac{\gamma - 1}{2}\right) = \frac{1 + \gamma}{2} \tag{15.13}$$

For noble gases, $\gamma = 5/3$ so $\Gamma = 4/3$. For diatomic gases and primarily diatomic gas mixtures like air, $\gamma = 7/5$, so $\Gamma_{air} = 6/5$. In both cases, it is the convective contribution that is most significant contributor for nonlinear distortion in a gas.

To start developing intuition regarding the formation of a shock wave, consider a sound wave in air that has an amplitude at the "threshold of feeling," 120 dB_{SPL}, so $p_1 = 28$ Pa. If the frequency of the sound wave is 1.0 kHz and the mean gas pressure is 100 kPa, then the acoustic Mach number for such a loud sound can be evaluated using the Euler equation.

$$M_{ac} = \frac{v_1}{c_o} = \frac{p_1}{\rho_m c_o^2} = \frac{p_1}{\gamma p_m} = 2\times 10^{-4} = 200 \ \text{ppm} \tag{15.14}$$

When such a wave propagates down a duct of constant cross-section, the shock inception distance, D_S, can be expressed in terms of the wavelength of sound using Eq. (15.9).

$$D_S = \frac{\lambda}{2\pi \Gamma_{air} M_{ac}} = \frac{5\lambda}{12\pi M_{ac}} \cong 460 \ \text{m} \tag{15.15}$$

At ten times that amplitude (140 $dB_{SPL,}$ the "threshold of pain") and for a frequency of 10 kHz, the shock inception distance would be 4.6 m. In the throat of the horn, for a horn-loaded compression driver [3] or in a brass musical instrument (e.g., trumpet or trombone), the amplitude can be still larger by a factor of ten [4].

15.1.2 The Virial Expansion and *B*/2*A*

For the characterization of nonlinear behavior of sound waves in liquids, it is common to expand the equation of state in a Taylor series, known as a *virial expansion*, in powers of the relative deviation of the density from its equilibrium value, $(\delta\rho/\rho_m) = (\rho - \rho_m)/\rho_m$.

$$p = p_m + A\left(\frac{\delta\rho}{\rho_m}\right) + \frac{B}{2!}\left(\frac{\delta\rho}{\rho_m}\right)^2 + \frac{C}{3!}\left(\frac{\delta\rho}{\rho_m}\right)^3 + \cdots \tag{15.16}$$

The coefficients in that expansion, A, B, C, etc. are called the virial coefficients and have the units of pressure. For an adiabatic process, they can be expressed in terms of progressively higher-order thermodynamic derivatives of pressure with respect to density.

$$A = \rho_m\left(\frac{\partial p}{\partial \rho}\right)_{s,\rho_m} = \rho_m c_o^2 \tag{15.17}$$

$$\begin{aligned} B &= \rho_m^2\left(\frac{\partial^2 p}{\partial \rho^2}\right)_{s,\rho_m} = \rho_m^2\left(\frac{\partial c^2}{\partial \rho}\right)_{s,\rho_m} = 2\rho_m^2 c_o^3\left(\frac{\partial c}{\partial p}\right)_{s,\rho_m} \\ \text{or}\quad \frac{B}{A} &= 2\rho_m c_o\left(\frac{\partial c}{\partial p}\right)_{s,\rho_m} = 2\rho_m c_o\left(\frac{\partial c}{\partial p}\right)_{T,\rho_m} + \frac{2\beta_p T_m c_o}{\rho_m c_P}\left(\frac{\partial c}{\partial T}\right)_{p_m,\rho_m} \end{aligned} \tag{15.18}$$

It is useful to notice that B can be expressed in terms of the derivative of the sound speed with respect to density, which was related to the non-convective contribution to the Grüneisen parameter in Eq. (15.10). The final form for B/A follows from the expansion of the sound speed derivative with respect to pressure, $(\partial c/\partial p)_s = (\partial c/\partial p)_T + (\partial T/\partial p)_s(\partial c/\partial T)_p$, and temperature, $(\partial p/\partial T)_s = (\partial \rho^{-1}/\partial s)_p = (\partial \rho^{-1}/\partial T)_p/(\partial s/\partial T)_p$, along with the introduction of the isobaric coefficient of thermal expansion, $\beta_p = (1/V)(\partial V/\partial T)_p = \rho_m(\partial \rho^{-1}/\partial T)_p$, and the introduction of the specific heat at constant pressure, $c_P = (1/T_m)(\partial s/\partial T)_p$ [5].

$$C = \rho_m^3\left(\frac{\partial^3 p}{\partial \rho^2}\right)_{s,\rho_m} \quad \text{or} \quad \frac{C}{A} = \frac{3}{2}\left(\frac{B}{A}\right)^2 + 2\rho_m^2 c_o^3\left(\frac{\partial^2 c}{\partial p^2}\right)_{s,\rho_m} \tag{15.19}$$

The sound speed can also be expressed in terms of these virial coefficients [6].

$$\frac{c^2}{c_o^2} = \frac{1}{c_o^2}\left(\frac{\partial p}{\partial \rho}\right)_{s,\rho_m} = 1 + \frac{B}{A}\left(\frac{\delta\rho}{\rho_m}\right) + \frac{C}{2A}\left(\frac{\delta\rho}{\rho_m}\right)^2 + \ldots \tag{15.20}$$

This result allows the Grüneisen parameter for liquids to be expressed in terms of B/A.

$$\Gamma = 1 + \frac{B}{2A} \tag{15.21}$$

Some representative values of B/A for different substances is provided in Table 15.1. The values of B/A for liquids are generally greater than 2.0, which means that it is the equation of state's nonlinearity that dominates the convective nonlinearity. This is reasonable since Euler's equation implies that the particle velocity in a liquid is much less than that of a gas for equal pressure changes: $(\rho_m c)_{liquid} \gg (\rho_m c)_{gas}$.

Table 15.1 Some representative values of *B*/*A* for different media [7]

Material	T [°C]	B/A
Monatomic gases (e.g., He, Ne, Ar, Kr, Xe, Rn)		0.667
Diatomic gases (e.g., O_2, N_2, HCl)		0.40
Distilled water	0	4.2
	20	4.985 ± 0.063
	30	5.18 ± 0.033
	40	5.4
	60	5.7
Sea water (3.5% NaCl)	20	5.25
Saturated marine sediment	20	12–19
Isotonic saline	20	5.540 ± 0.032
Ethanol	20	10.52
Methanol	20	9.42
Acetone	20	9.23
Glycerol (4% in H_2O)	25	8.58 ± 0.34
Ethylene glycol	25	9.88 ± 0.40
Carbon tetrachloride	25	7.85 ± 0.31
Liquid argon	–183.2	5.67
Liquid nitrogen	–195.8	6.6
Liquid helium	–271.4	4.5
Mercury	30	7.8
Sodium	110	2.7
Bovine serum albumin (20 g/100 mL H_2O)	25	6.23 ± 0.25
Bovine serum albumin (38.8 g/100 mL H_2O)	30	6.68
Bovine whole blood	26	5.5
Bovine milk	26	5.1
Bovine liver	23	7.5–8.0
Bovine heart	30	5.5

15.1.3 Anomalous Distortion*

Before moving on, it is interesting to consider the role that a non-zero value of C implies for the formation of shock waves. The behavior that is represented by the Grüneisen parameter causes the sound speed to be increased when the amplitude of the wave is positive and decrease when the amplitude is negative. The C coefficient makes a contribution that either always increases the sound speed, irrespective of the sign of the wave's amplitude, or always decreases the sound speed, depending upon the sign of C.

Cormack and Hamilton have investigated shear waves with a cubic nonlinearity, $C \neq 0$, using numerical simulations [8]. Figure 15.4 shows two plane waveforms that were initially sinusoidal (dotted lines) that have produced both leading- and trailing-edge shocks (solid lines); two shock fronts per wavelength, unlike Figs. 15.3 and 15.7, where only a quadratic nonlinearity was operative (e.g., $1 + B/2A \neq 0$ but $C/A = 0$).

A situation where both the quadratic and cubic nonlinearity play a role in superfluid helium sound propagation near absolute zero was identified for shockwave formation of compressional plane waves where the superfluid component velocity, v_s, is non-zero, but the (viscous) normal fluid is immobilized, $v_n = 0$. That sound wave mode in superfluids is known as 4$^{\text{th}}$ sound (see Fig. 15.5). This creates a superfluid critical acoustic velocity amplitude, v_d, which can be defined in terms of the virial

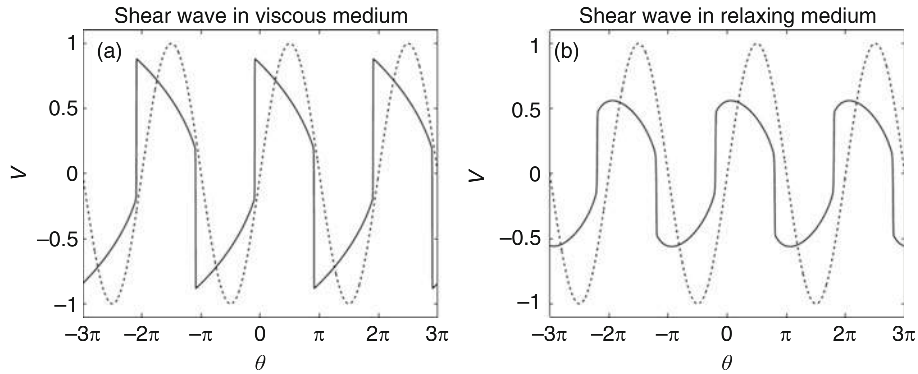

Fig. 15.4 Waveforms for an initially sinusoidal plane shear wave (dotted lines) in a medium that is dominated by a cubic nonlinearity disturbance far from the sound source with C < 0. (From [8])

Fig. 15.5 There are two different sound speeds in liquid ^{4}He below the superfluid transition temperature, $T_\lambda \cong 2.14$ K, at saturated vapor pressure. The ordinary bulk compressional wave speed, known as "first sound," is fairly constant. The speed of thermal waves, called "second sound," is generally an order of magnitude less than first sound and is a strong function of temperature, vanishing above the superfluid transition temperature, T_λ. Fourth sound is a compressional sound wave in a porous medium that immobilizes the normal fluid so that only the superfluid can oscillate

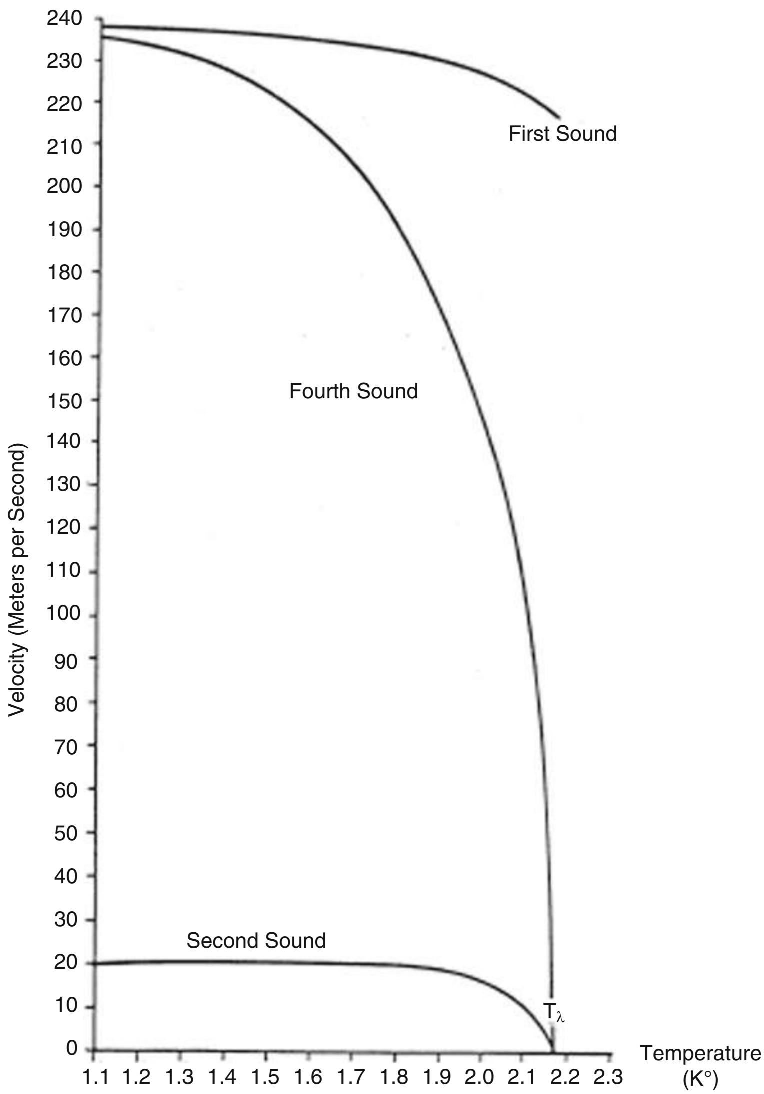

coefficients, to be the velocity amplitude where the contribution made by the wave distortion due to the ($B/2A$) term is equal to the influence of C/A [9].

$$\frac{v_d}{c_o} = \frac{4 + 2(B/A)}{(C/A) + (B/A)[1 - (B/A)]} \tag{15.22}$$

For negative values of C, the wave is slowed whether the amplitude of the wave is positive or negative.

This double-shock behavior, caused by $C \neq 0$, is rather rare for compressional waves. Using values for (B/A) and (C/A) for water [10], $v_d = 1.2c_o$, corresponding to acoustic pressure swings of 26,000 atmospheres, well over 100 times greater than the highest cavitation threshold ever measured for pure water [11]. This double-shock behavior has been observed for sound propagating through a liquid near its critical point [12].

In an ideal gas, the virial expansion can be expressed in terms of the ratio of specific heats, $\gamma = c_P / c_V$, also known as the polytropic coefficient.

$$\frac{p}{p_m} = 1 + \gamma\left(\frac{\delta\rho}{\rho_m}\right) + \frac{\gamma(\gamma-1)}{2}\left(\frac{\delta\rho}{\rho_m}\right)^2 + \frac{\gamma(\gamma-1)(\gamma-2)}{6}\left(\frac{\delta\rho}{\rho_m}\right)^3 + \cdots \tag{15.23}$$

For an ideal gas, $(B/A) = (\gamma-1)$ and $(C/A) = (\gamma-1)(\gamma-2)$ so the denominator of Eq. (15.22) vanishes making $v_d/c_o = \infty$; double shocks are an impossibility in gases.

Two other unusual results for the Grüneisen parameter arise from the propagation of sound in superfluid helium [13]. Superfluids are analogous to superconductors in that superfluids can flow without viscosity, just like electrical currents flowing without electrical resistance in superconductors. In addition, the superfluid component has both an elastic and a thermal "restoring force" [14]. In superfluid helium, there is a thermal sound mode, known as *second sound*, that is propagating, not diffusive, like the response governed by the Fourier heat diffusion Eq. (9.4) for classical liquids (see Sect. 9.3.1).[5] The temperature dependence of both second sound and the ordinary compressional wave speed (called first sound) are plotted in Fig. 15.5.

It is clear from the speed of second sound vs. temperature that there is a region where the second sound speed decreases with increasing temperature, behavior that is opposite to that of an ideal gas in Eq. (15.11). In that case, the convective contribution to the nonlinearity is opposite to the equation of state's contribution. At $T = 1.884$ K, the two contributions cancel each other, and a large amplitude second sound wave can propagate without distortion [15].

A final anomalous example is provided by third sound in superfluid helium. Because the superfluid can flow without resistance, sound waves can propagate in adsorbed films as thin as two atomic layers of helium.[6] In very thin films, the dominant restoring force is the van der Waals attraction which varies inversely with the fourth power of the distance: $f = \alpha/h^4$. Substituting the van der Waals force for the gravitational force in Eq. (15.4) and providing a correction for the thickness-averaged mass density of the superfluid component, $\langle\rho_s\rangle$, unlike the surf, the speed of third sound, c_3, is inversely proportional to the film thickness, h_o.

[5] In 1962, Lev Landau won the Nobel Prize in Physics for his prediction of the temperature dependence of second sound using his two-fluid theory of superfluid hydrodynamics after the speed of second sound was first measured by Pyotr Kapitza. Kapitza won the Nobel Prize in Physics in 1978 for his measurement of the speed of second sound in superfluid helium.

[6] Prof. I. Rudnick has pointed out that superfluids are interesting because they obey the laws of hydrodynamics on the microscopic scale and obey the laws of quantum mechanics on the macroscopic scale.

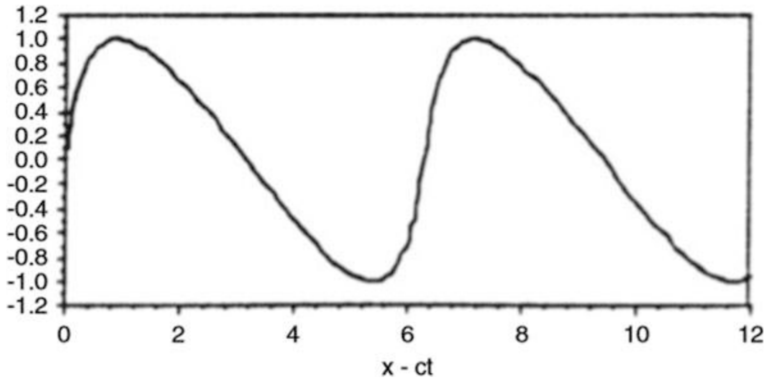

Fig. 15.6 Very thin films of superfluid helium can support surface waves that are restored by the van der Waals attraction between the fluid and the substrate on which the fluid is adsorbed. For films less than 10 Å thick (about three atomic layers), the troughs travel faster than the crests, and the wave bends backward

$$c_3 = \sqrt{\frac{\langle\rho_s\rangle}{\rho} f h_o} = \sqrt{\frac{\langle\rho_s\rangle}{\rho}\frac{3\alpha}{h_o^3}} \tag{15.24}$$

For superfluid films that are less than 10 Å $= 10^{-9}$ m thick or about three atomic layers of helium, the equation of state produces troughs that travel faster than the crests so the waves distort backward, as shown in Fig. 15.6, compared to ordinary distortion shown in Fig. 15.3.

15.1.4 The Gol'dberg Number

A wave of arbitrary amplitude will not necessarily form a shock. If the sound is attenuated, then the amplitude will decrease with distance, and the tendency to distort will be reduced, since the distortion is amplitude dependent. A dimensionless metric, known as the *Gol'dberg number*, G, compares the shock inception distance, D_S, to the exponential attenuation length, $\ell = \alpha^{-1}$, where α is the amplitude exponential attenuation constant that was examined in Chap. 14 [16].

$$G = \frac{\ell}{D_S} = (\alpha D_S)^{-1} \tag{15.25}$$

As an example, the Gol'dberg number can be evaluated for a 2 kHz sound wave with pressure amplitude of $|\hat{\mathbf{p}}| = 900$ Pa (150 dB *re:* 20 μPa$_{\text{rms}}$) in dry air that propagates down a cylindrical waveguide with an inside diameter of 10.0 cm. For dry air at mean pressure, $p_m = 100$ kPa and $T_m = 23$ °C, $c_o = 345$ m/s with $\delta_\nu = 50$ μm and $\delta_\kappa = 59$ μm. Using Eq. (15.15), with $M_{ac} = |\hat{\mathbf{p}}|/\gamma p_m = 0.64\%$ and $\lambda = 17.3$ cm, $D_S = 3.6$ m. Using Eq. (13.78), the attenuation length in that waveguide is $\ell = \alpha_{tv}{}^{-1} = 20.6$ m. The Gol'dberg number, given in Eq. (15.25), is $G = 5.7 > 1$. In this example, the wave will shock before the wave of that initial amplitude suffers sufficient attenuation.

For an initially sinusoidal plane wave in free space, far from any solid boundaries (i.e., not confined within a 10 cm diameter waveguide!), the attenuation length due to classical thermoviscous dissipation, including "bulk viscosity," at 2 kHz in dry air at one atmosphere would be about 1.2 dB/km $\cong 1.4 \times 10^{-4}$m (see Fig. 14.5), resulting in an exponential attenuation distance of about 7 km making $G \cong 200$. For a plane wave in free space with $G = 5.7$, there would be significant distortion, but a fully developed sawtooth shock would not be created. This is because the classical attenuation coefficient is proportional to frequency squared (see Sect. 14.3), so the attenuation of the second harmonic is four times that of the fundamental, rather than just $\sqrt{2}$ larger for the waveguide, where the attenuation depends upon the square root of the frequency. Mark Hamilton has provided numerical

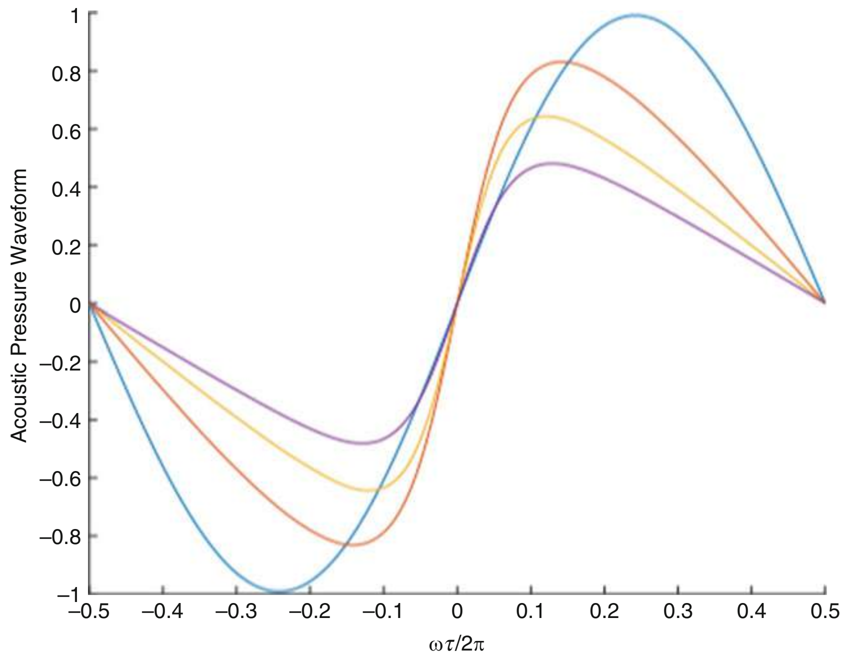

Fig. 15.7 Numerical simulation of an initially sinusoidal plane wave in free space with Gol'dberg number, $G = 5.7$, is shown as the blue sinusoid. As the wave progresses, nonlinear effects cause it to distort, and classical attenuation mechanisms reduce its amplitude. A sawtooth waveform, shown in Fig. 15.8, is not produced. (Figure courtesy of Mark Hamilton)

simulations of the waveforms of such a plane progressive wave in free space for $G = 5.7$ that are shown in Fig. 15.7.

The Gol'dberg number is a dimensionless measure of the importance of nonlinearity relative to dissipation. In some circumstance, dissipation can be entirely ignored. For deepwater gravity waves, the primary source of dissipation is viscosity, and the Gol'dberg number is on the order of one million [17].

15.1.5 Stable Sawtooth Waveform Attenuation

For large values of the Gol'dberg number, an initially sinusoidal sound wave propagating in one dimension (i.e., ignoring spherical spreading) will steepen and ultimately become a repeated sawtooth waveform. At sufficiently high Gol'dberg numbers, even spherically spreading waveforms that are initially sinusoidal can form shocks [2]. In fact, any periodic waveform will steepen and ultimately form a repeated sawtooth shape, shown in Fig. 15.8, when the Gol'dberg number is sufficiently large and the wave has propagated well past the shock inception distance.

Once the sawtooth waveform has developed, the shock front produces a gradient in the temperature, particle velocity, and pressure that is very large. Such gradients produce large dissipation due to thermal conduction across the shock front and viscous shear. The amplitude of the sawtooth waveform must decrease due to the resulting energy dissipation. Calculation of the shock wave's attenuation can be made by expressing the discontinuity of the entropy across the shock that is cubic in the pressure discontinuity [18]. For an ideal gas, the difference in entropy across the shock is expressed in terms of

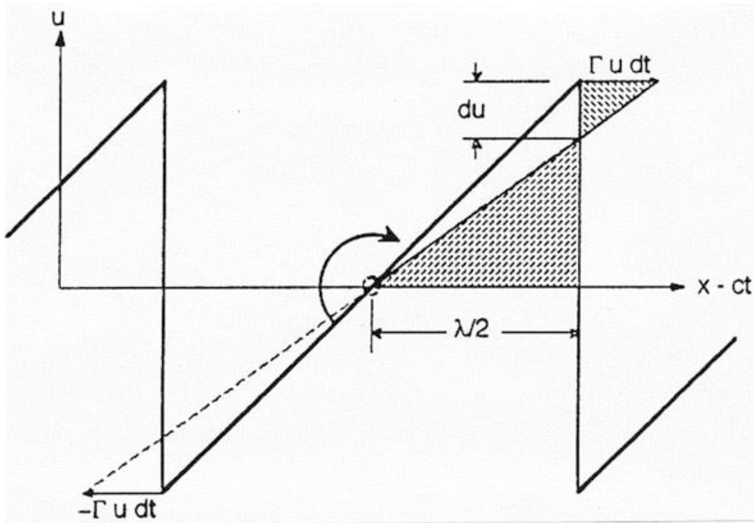

Fig. 15.8 Any periodic wave of sufficient Gol'dberg number will distort into the sawtooth waveform shown in a coordinate system that is moving along with the wave at the thermodynamic sound speed, c_o. The "excess velocity" produced by the Grüneisen parameter is proportional to the velocity amplitude, u, of the wave. The sloping "back" of the sawtooth must then experience solid body rotation since the excess velocity is proportional to the amplitude above its zero-crossing

the universal gas constant, $\Re$, and the mean molecular mass of the gas, M, by use of the Rankine-Hugoniot shock relations [19].

$$s_+ - s_- = \frac{\Re}{M}\frac{(\gamma+1)}{12\gamma^2}\left|\frac{p_+ - p_-}{p_-}\right|^3 \tag{15.26}$$

Inspection of Fig. 15.8 suggests a simpler geometric approach [20]. If the particle velocity amplitude for the sawtooth waveform is u, then by Eq. (15.9), each portion of the waveform must advance, relative to the zero-crossing, by (Γu dt) during a time interval, dt. The coordinate system, as shown in Fig. 15.8, moves with c_o, by making the x axis be $(x - c_o t)$. In that frame of reference, the fact that the back of the shock is a straight line, representing a linear increase in u, requires that the unshocked portion of the waveform undergo solid body rotation, as indicated by the curved arrow in Fig. 15.8.

Since the wave must remain single-valued, the shock front must dissipate sufficient energy to keep the waveform from becoming multiple-valued. The two hashed triangles shown in Fig. 15.8 are similar triangles by Garrett's First Law of Geometry, so the ratio of their heights to their bases must be equal.

$$\frac{du}{\Gamma u(dt)} = \frac{u}{\lambda/2} \tag{15.27}$$

Setting $dt = dx/c_o$, Eq. (15.27) can be integrated from a reference location, x_o, at which the acoustic Mach number is M_o, out to some arbitrary distance, x, from that reference location.

$$c_o\int_{u_o}^{u}\frac{du}{u^2} = \frac{2\Gamma}{\lambda}\int_{x_o}^{x}dx \quad \Rightarrow \quad \frac{1}{M} - \frac{1}{M_o} = 2\Gamma\frac{x - x_o}{\lambda} \tag{15.28}$$

This result is both interesting and distinctly different from previous expressions for attenuation. First, the amplitude of the shock does not decay exponentially with distance. Second, although the dissipation is due to thermoviscous losses produced by the steep gradients across the shock front, the attenuation is independent of both the fluid's shear viscosity, μ, and its thermal conductivity, κ, and depends instead upon the Grüneisen parameter.

This sawtooth waveform does not persist. Eventually, it "unshocks," as shown in Fig. 15.30, as its amplitude decreases to the level where classical attenuation mechanisms are dominant [21].

15.2 Weak Shock Theory and Harmonic Distortion

In most fluids, the nonlinearity in the equation of state and the nonlinearity introduced by the acoustically induced convection conspire to cause waves to distort. That distortion increases with the propagation distance, if the amplitude of the wave is sufficient for such nonlinear effects to dominate thermoviscous attenuation (i.e., $G \gg 1$). For waves of sufficiently large amplitude, this process will turn any periodic wave into a sawtooth wave. In this section, the focus will be on the initial stages of this distortion process.

If a wave is initially a sinusoidal "pure tone," it will only contain a single Fourier component. That fundamental frequency can be designated f_I. The distortion will change the wave shape, but the wave will still be periodic with a period, $T = (f_I)^{-1}$. The description of the distorted waveform will necessarily require additional Fourier components at harmonic multiples of the fundamental frequency, $f_n = nf_I$, with $n = 2, 3, 4$, etc. This section will focus on the growth of those harmonic components with distance and their dependence on the initial amplitude of the wave.

15.2.1 The Order Expansion

When linear acoustics was first developed in Chap. 8, the parameters that described the acoustic fields were expressed as the sum of an equilibrium value plus a first-order deviation from equilibrium. Equation (8.1) expressed the pressure as $p\left(\vec{x}, t\right) = p_m\left(\vec{x}\right) + p_1\left(\vec{x}, t\right)$. Similar expansions were made for the mass density, $\rho\left(\vec{x}, t\right)$, in Eq. (8.2), temperature, $T\left(\vec{x}, t\right)$, in Eq. (8.3), and (specific) entropy per unit mass, $s\left(\vec{x}, t\right)$, in Eq. (8.4). In all cases, the first-order deviations from equilibrium were assumed to be much smaller than the equilibrium values (e.g., $p_I \ll p_m$).

This *order expansion* will now be extended to keep track of the effects of nonlinearity on propagation. For example, the particle velocity will be represented as the sum of the fluid's mean equilibrium velocity, v_m, and the deviations from equilibrium that are proportional to successively higher powers of such deviations. These deviations will be subscripted to indicate their dependence on the amplitude of the disturbance. A subscript of "1" will indicate a first-order contribution that is linear in the amplitude of the disturbance. A subscript of "2" will indicate a second-order contribution that is quadratic in the amplitude of the disturbance or is the product of two first-order contributions, possibly produced by the interaction of two different waves.

$$v(x,t) = v_m(x) + v_1(x,t) + v_2(x,t) + v_3(x,t) + \cdots \tag{15.29}$$

Since our attention will be focused on one-dimensional propagation, x does not need to be a vector and because the fluids will not be subjected to any externally imposed mean flow, $v_m(x) = 0$. As was the case for linear acoustics, the first-order contribution to the acoustical deviation from equilibrium, $v_1(x, t)$, will be proportional to the amplitude of the disturbance from equilibrium. The second-order contribution, $v_2(x, t)$, will be proportional to the square of the amplitude of the disturbance from equilibrium or to the product of two first-order disturbances, etc.

It will also be assumed that these individual contributions are "well ordered," in that each successive higher-order contribution will be smaller than its lower-ordered neighbor. In the case of particle velocity, all contributions will also be significantly smaller than the thermodynamic sound speed, c_o, in the weak shock limit.

$$c_o \gg |v_1| > |v_2| > |v_3| > \cdots \tag{15.30}$$

15.2.2 Trigonometric Expansion of the Earnshaw Solution

The analysis of the distortion of an initially sinusoidal sound wave can generate a second-order correction by allowing the speed of sound to be dependent upon the amplitude of the disturbance. This result was first exploited by Earnshaw (1805–1888) and was published in 1860 [22].

$$\phi = t - \frac{x - X(\phi)}{\Gamma u(\phi) \pm c_o} \tag{15.31}$$

Here, Earnshaw solved the for a wave launched by a piston located at $x = 0$ that has a displacement, $X(t)$, and velocity $u(t) = \mathrm{d}X/\mathrm{d}t$. The parameter, ϕ, represents the time a given point on a waveform left the piston's face. Earnshaw was also the first to show that $\Gamma_{gas} = (\gamma + 1)/2$, for a sound wave in an gas obeying the Adiabatic Gas Law, as we did in Eq. (15.13).

We can exploit Earnshaw's insight to calculate the growth of the second harmonic by successive approximation [23] if the initial disturbance is assumed to be a single-frequency, rightward traveling wave with an initial particle velocity amplitude, v'.

$$v_1(x,t) = v' \cos(\omega t - kx) = v' \cos\omega\left(t - \frac{x}{c_o}\right) \tag{15.32}$$

A second-order contribution will be generated by substitution of the "local" sound speed, as expressed in Eq. (15.9), for the thermodynamic sound speed that appears in Eq. (15.32), as was expressed by Earnshaw in Eq. (15.31).

$$v_1(x,t) + v_2(x,t) = v' \cos\omega\left(t - \frac{x}{c_o + \Gamma v_1}\right) \tag{15.33}$$

In the weak shock limit, $M_{ac} = v_1/c_o \ll 1$, so the denominator of the argument of the cosine function can be approximated by its binominal expansion.

$$v_1(x,t) + v_2(x,t) \cong v' \cos\omega\left[t - \frac{x}{c_o}\left(1 - \Gamma\frac{v_1}{c_o}\right)\right] \tag{15.34}$$

The trigonometric identity for the cosine of the sum of two angles, a and b, is $\cos\omega(a + b) = \cos(\omega a)\cos(\omega b) - \sin(\omega a)\sin(\omega b)$. That identity can be used to separate Eq. (15.34) into two terms.

$$v_1(x,t) + v_2(x,t) \cong v' \cos\omega\left(t - \frac{x}{c_o}\right) - \frac{\Gamma x \omega v_1}{c_o^2} v' \sin\omega\left(t - \frac{x}{c_o}\right) \tag{15.35}$$

Since $v_1(x, t)$ was defined in Eq. (15.32), the first-order terms on both sides of Eq. (15.35) can be eliminated so that only the second-order contribution remains. The first-order contribution can also be substituted into the second-order expression.

$$v_2(x,t) = -\frac{\Gamma x \omega}{c_o^2}(v')^2 \sin\omega\left(t - \frac{x}{c_o}\right)\cos\omega\left(t - \frac{x}{c_o}\right) \tag{15.36}$$

Using the double-angle sine identity, $\sin(2a) = 2\sin(a)\cos(a)$, it becomes clear that the trigonometric product introduces a second harmonic component that grows linearly with distance, x, scaled by the wavelength, λ, and is proportional to the square of the initial amplitude, $(v')^2$.

$$v_2(x,t) = -\frac{\Gamma x \omega}{2c_o^2}(v')^2 \sin 2\omega\left(t - \frac{x}{c_o}\right) = -\pi\Gamma M_{ac}\frac{x}{\lambda}v' \sin 2\omega\left(t - \frac{x}{c_o}\right) \tag{15.37}$$

The assumption regarding the relative amplitude of the terms in the order expansion, as asserted in Eq. (15.30), will be violated before $|v_2| = |v_1|$. To determine the limit of this solution's applicability, those amplitudes can be equated to determine a distance, $x_{1=2}$, before which this assumption would be violated.

$$x_{1=2} = \frac{\lambda}{\pi\Gamma M_{ac}} \tag{15.38}$$

It is not surprising that this approximation would fail at a distance that is less than twice the shock inception distance, D_S. It is also true that this solution assumes that energy is transferred to the second harmonic with no reduction in the amplitude of the fundamental. That is clearly not possible, since the energy that appears as the second harmonic contribution was provided by the energy in the fundamental. The subsequent analysis will correct that difficulty.

15.2.3 Higher Harmonic Generation

It would be possible to continue the successive approximation procedure to calculate successively higher harmonics, but that procedure would quickly become algebraically messy. A simple and more intuitive approach is to use Eq. (15.9) to incorporate the local sound speed to deform the wave, as was done initially for shallow-water gravity waves in Fig. 15.3, and then simply use Fourier analysis to extract the amplitudes of the harmonics [24].

An undistorted wave can be parameterized by making its amplitude, y, be a function of a parameter, θ: $y = \sin(\theta)$. To distort the wave, the plotted position can be advanced by an amount related to the propagation distance, d, scaled by the shock inception distance, D_S.

$$\sigma = \frac{d}{D_S} = 2\pi\Gamma M_{ac}\frac{d}{\lambda}; \quad 0 \le \sigma < 1 \tag{15.39}$$

In Fig. 15.9, one-half of a sine function has been plotted on the x axis at two different advanced locations in Eq. (15.40).

$$x = \theta + \sigma \sin\theta \tag{15.40}$$

There is no additional information provided by the negative half-cycle, so the harmonic content of the distorted waveform can be Fourier analyzed between $0 \le \theta < \pi$.

The Fourier coefficients can be projected to obtain the amplitudes of the harmonics using the same procedure as applied to vibrating strings in Sect. 3.5.

$$C_n = \frac{2}{\pi}\int_o^\pi y \sin(nx)\,dx = \frac{2}{\pi}\int_0^\pi \sin\theta \sin[n(\theta + \sigma\sin\theta)](1 + \sigma\cos\theta)\,d\theta \tag{15.41}$$

Using the integral definition of Bessel functions of the 1st kind in Eq. (C.26), Eq. (15.41) can be expressed as the sum of four Bessel functions.

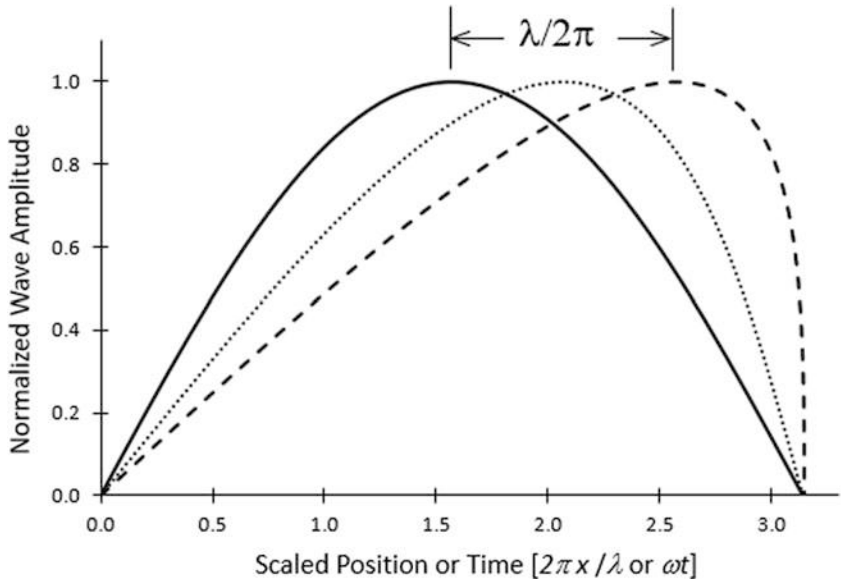

Fig. 15.9 One-half-cycle of nonlinear distortion. The solid line is the undistorted (sinusoidal) waveform. The dashed line represents the waveform that has propagated to the shock inception distance, $\sigma = x/D_S < 1$. The dotted line represents the waveform that has propagated to one-half the shock inception distance

Fig. 15.10 Fourier coefficients for a nonlinearly distorted sinusoidal wave as a function of the scaled propagation distance, $\sigma = x/D_S$. The solid line is the amplitude of the fundamental at f_1 that should be read from the left-hand axis. The long-dashed line is the second harmonic amplitude, C_2, at $f_2 = 2f_1$, the narrow-dashed line is the third harmonic amplitude, C_3, at $f_3 = 3f_1$, and the dotted line is the fourth harmonic amplitude, C_4, at $f_4 = 4f_1$. All C_n for $n > 1$ should be read from the right-hand axis

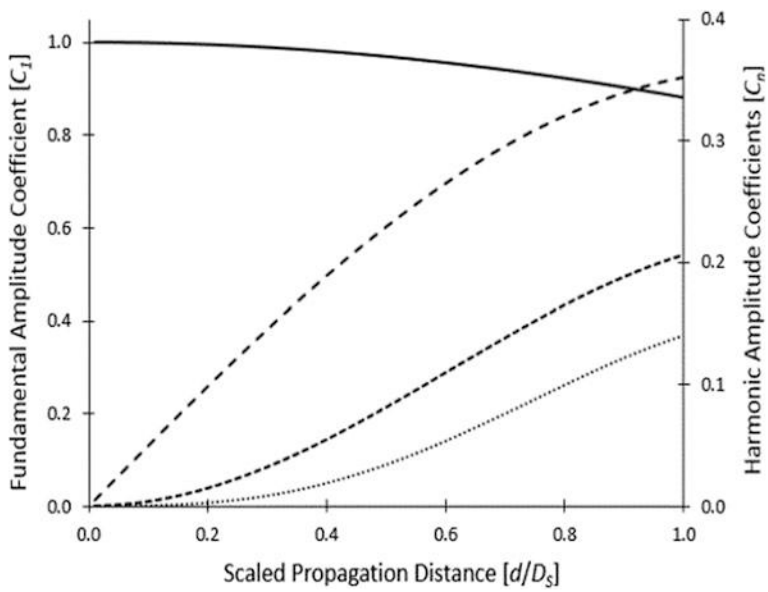

$$C_n = (-1)^{n+1}\{J_{n-1}(n\sigma) - J_{n+1}(n\sigma) - (\sigma/2)[J_{n-2}(n\sigma) - J_{n+2}(n\sigma)]\} \tag{15.42}$$

Two successive applications of the recurrence relations in Eqs. (C.27) and (C.28) reduce the expression for the harmonic amplitude coefficients, C_n, to the compact form in Eq. (15.43), which is plotted in Fig. 15.10.

$$|C_n| = \frac{2}{n\sigma} J_n(n\sigma) \quad \text{for} \quad \sigma < 1 \quad \text{and} \quad n = 1, 2, 3, \ldots \tag{15.43}$$

This result was originally obtained using algebraic methods by Fubini-Ghiron in 1935 [25].

The initial growth rate of the harmonics with propagation distance can be appreciated by expansion of the Bessel functions for small values of their arguments, $n\sigma$, as expressed in Eq. (C.12). As shown in Eq. (C.14), the $J_1(x)$ Bessel function increases linearly with $x = n\sigma$. By Eq. (15.43), $C_1 \propto J_1(\sigma)/(\sigma)$ so it is initially independent of distance. One nice feature of this solution is that as the higher harmonic amplitudes grow, the amplitude of the fundamental decreases. At $d = D_S$, the amplitude of the fundamental is only 88% of its original value.

The first terms in the expansion of the higher-order Bessel functions, $J_n(x)$, all are proportional to x^n. As per Eq. (15.43), each Bessel function is divided by $x = (n\sigma)$, so that each amplitude coefficient increases in proportion to the $(n-1)$ power of the scaled distance, $\sigma = x/D_S$. This behavior is evident in Fig. 15.10. The second harmonic amplitude, C_2, initially grows linearly with distance, just as predicted by Airy [23] in the solution by successive approximation that led to Eq. (15.37). The third harmonic amplitude, C_3, has an initially quadratic dependence on distance, and the fourth harmonic amplitude, C_4, has an initially cubic dependence on the propagation distance.

A calculation by Fay [26] that included dissipation also produced an expression for the harmonic amplitudes, B_n, that describe a stabilized waveform where the Gol'dberg number includes thermoviscous attenuation, $\alpha_{\text{T-V}}$, in Eq. (14.29).

$$B_n = \frac{2}{G \sinh\left[n(1+\sigma)/G\right]} \quad \text{for} \quad \sigma = \frac{x}{D_s} > 3 \tag{15.44}$$

Note that the Fay solution produces the (stable) sawtooth waveform of Fig. 15.8 for distances that satisfy $G \gg n(1 + \sigma)$, where the hyperbolic sine function can be replaced by its argument to produce the Fourier amplitude coefficients of a sawtooth waveform (see Fig. 1.22 and Chap. 1, Prob. 12), $B_n^{sawtooth} = 2/n(1+\sigma)$. As shown by Blackstock [27], the Fay result for the harmonic amplitudes does not reduce to those of Fubini in Eq. (15.43), in the limit of vanishing viscosity since the Fubini coefficients are valid near the source, $\sigma \leq 1$, and the Fay coefficients in Eq. (15.44) are valid in the sawtooth region, $\sigma \geq 3$. Blackstock provides a solution that connects those two regimes in his paper that has become known as the "*Blackstock bridging function*."

15.3 The Phenomenological Model

Hydrodynamics provides a complete description of the propagation of sound in fluids. All of the nonlinear behavior that has been introduced in this chapter thus far should be derivable from that hydrodynamic description. As will be demonstrated now, the hydrodynamic approach will also provide additional insights and motivate the description of additional nonlinear phenomena.

As discussed in Sect. 7.3, the dynamics of a single-component homogeneous fluid can be described by two thermodynamic variables (e.g., ρ and s or p and T) and the three components of the velocity field.

$$\vec{v} = v_x \hat{e}_x + v_y \hat{e}_y + v_z \hat{e}_z \tag{15.45}$$

As before, v_x is the x component of velocity, and $\hat{e}_x$ is the unit vector in the x direction. The "system" is "closed" if there are five independent conservation equations that relate the variables to each other. Those equations should be familiar by now and are reproduced below:

$$\frac{\partial \rho}{\partial t} + \nabla \cdot \left(\rho \vec{v}\right) = 0 \tag{15.46}$$

$$\begin{aligned} &\frac{\partial (\rho s)}{\partial t} + \nabla \cdot \left(\rho s \vec{v}\right) = \kappa \frac{(\nabla T)^2}{T} + \mu \Phi + \zeta \left(\nabla \cdot \vec{v}\right)^2 \\ &\Phi = \frac{1}{2} \sum_{i=x,y,z} \sum_{j=x,y,z} \left(\frac{\partial v_i}{\partial x_j} + \frac{\partial v_j}{\partial x_i} - \frac{2}{3}\delta_{ij} \nabla \cdot \vec{v}\right)^2 \end{aligned} \tag{15.47}$$

$$\frac{\partial \vec{v}}{\partial t} + \left(\vec{v} \cdot \nabla\right)\vec{v} = \frac{-\vec{\nabla} p}{\rho} + \mu \nabla^2 \vec{v} \tag{15.48}$$

The form of the entropy Eq. (15.47) is rather more general than will be required but includes the square of the viscous shear tensor, Φ, and the bulk viscosity, ζ, along with thermal conductivity, κ, all as potential sources of entropy production.

As before, those conservation laws contain both p and ρ as (mechanical) thermodynamic variables, so that an equation of state, $p = p(\rho, s)$, describing each individual fluid's properties, is required to "close" the set. In the absence of dissipation (i.e., $\kappa = \mu = \zeta = 0$), the equation of state can be combined with the continuity Eq. (15.46), and the entropy conservation Eq. (15.47) to demonstrate that the entropy will be conserved.

$$\frac{Ds}{Dt} = \frac{\partial s}{\partial t} + \vec{v} \cdot \vec{\nabla} s = 0 \tag{15.49}$$

This simplifies the expansion of the equation of state in terms of the density deviation, $\rho' = \rho - \rho_m$, since all of the derivatives can be evaluated at constant entropy.

$$p(\rho) = \left(\frac{\partial p}{\partial \rho}\right)_s \rho' + \left(\frac{\partial^2 p}{\partial \rho^2}\right)_s \frac{\rho'^2}{2} + \cdots \tag{15.50}$$

15.3.1 The (Nondissipative) Nonlinear Wave Equation

As with Earnshaw's solution and the calculation of the harmonic amplitude components in the weak shock limit, this analysis will be restricted to one-dimensional propagation (i.e., $v_y = v_z = 0$), but at this point, there is no penalty for retaining the vector velocity for evaluation of the hydrodynamic equations and the equation of state up to terms of second-order in the deviation from equilibrium.

$$\frac{\partial \rho_1}{\partial t} + \frac{\partial \rho_2}{\partial t} + \rho_m \nabla \cdot \vec{v}_1 + \rho_m \nabla \cdot \vec{v}_2 + \rho_1 \nabla \cdot \vec{v}_1 + \vec{v}_1 \cdot \vec{\nabla} \rho_1 = 0 \tag{15.51}$$

$$\rho_m \frac{\partial \vec{v}_1}{\partial t} + \rho_m \frac{\partial \vec{v}_2}{\partial t} + \rho_1 \frac{\partial \vec{v}_1}{\partial t} + \rho_m \left(\vec{v}_1 \cdot \vec{\nabla}\right) \vec{v}_1 = -\vec{\nabla} p_1 - \vec{\nabla} p_2 \tag{15.52}$$

$$p_2 = \left(\frac{\partial p}{\partial \rho}\right)_s \rho_2 + \left(\frac{\partial^2 p}{\partial \rho^2}\right)_s \frac{\rho_1^2}{2} \tag{15.53}$$

The first-order wave equation is homogeneous.

$$\frac{\partial^2 \rho_1}{\partial t^2} + \left(\frac{\partial p}{\partial \rho}\right)_s \nabla^2 \rho_1 = 0 \tag{15.54}$$

The first-order terms from Sect. 7.2 that were combined to produce that linear wave equation can be subtracted from the combination of Eqs. (15.51), (15.52), and (15.53) to leave a wave equation for the space-time evolution of the second-order sound fields.[7]

$$\frac{\partial^2 \rho_2}{\partial t^2} - c_o^2 \nabla^2 \rho_2 = \nabla^2 \left[\rho_m \vec{v}_1^{\,2} + \left(\frac{\partial^2 p}{\partial \rho^2}\right)_s \frac{\rho_1^2}{2} \right] \tag{15.55}$$

This wave equation for the second-order deviations of the density from equilibrium is not homogeneous; it has a source term that is driven by quadratic combinations of the first-order sound fields. Using the Euler relation for the first-order fields and Eq. (15.10), this second-order wave equation can be re-written in a more familiar form for plane progressive waves.

$$\frac{\partial^2 \rho_2}{\partial t^2} - c_o^2 \nabla^2 \rho_2 = \frac{c_o^2}{\rho_m} \left[1 + \frac{\rho_m}{c_o} \left(\frac{\partial c}{\partial \rho}\right)_s \right] \nabla^2 \rho_1^2 = \Gamma \frac{c_o^2}{\rho_m} \nabla^2 \rho_1^2 \tag{15.56}$$

Not surprisingly, the strength of this nonlinear source term is proportional to the Grüneisen parameter, Γ.

15.3.2 Geometrical Resonance (Phase Matching)

The second-order wave equation should reproduce the results obtained for second harmonic distortion in the weak shock limit that were generated by the trigonometric expansion of Earnshaw's solution. That result can be recaptured by squaring the right-going sinusoidal traveling wave, $\rho_1 = \rho' \cos(\omega t - kx)$, and then inserting it into the source term on the right-hand side of Eq. (15.56).

$$\Gamma \frac{c_o^2}{\rho_m} \nabla^2 \rho_1^2 = \Gamma \frac{c_o^2}{\rho_m} \frac{\rho'^2}{2} \nabla^2 [1 + \cos(2\omega t - 2kx)] \tag{15.57}$$

The constant will disappear upon operation by the Laplacian, but the $\cos 2(\omega\ t - kx)$ term will drive the second-order wave equation. What is crucially important is the recognition that the phase speed of the source term, $c_{ph} = 2\omega/2k$, is identical to the phase speed of the second-order density deviations, ρ_2, which propagates with speed, $c_o = \sqrt{(\partial p/\partial \rho)_s}$.

This correspondence between the phase speed of the source and the phase speed of the disturbance it creates is called *geometric resonance*. In this case, the wavevectors representing the first- and second-order fields, $\vec{k}_1$ and $\vec{k}_2$, are colinear. Considering this process as the first-order wave's interaction with itself, the geometric resonance for these colinear propagation directions can be expressed as a wavevector sum.

$$\vec{k}_2 = \vec{k}_1 + \vec{k}_1 \quad \text{where} \quad \left|\vec{k}_2\right| = 2\left|\vec{k}_1\right| \quad \text{and} \quad \omega_2 = 2\omega_1 \tag{15.58}$$

[7] Do not confuse the wave equation for the second-order deviations from equilibrium with the fact that both the first- and second-order wave equations are both second-order partial differential equations. For the classification of differential equations, second-order refers to the highest-order derivative that appears in the equation.

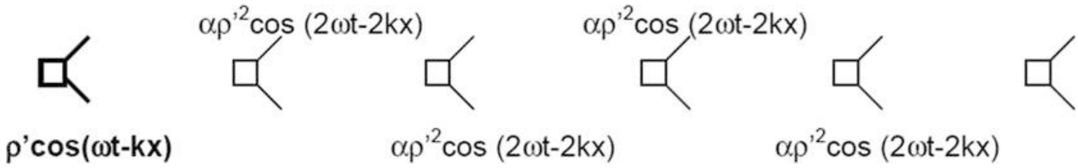

Fig. 15.11 Conceptual representation of the linear growth of the amplitude of the second harmonic with distance produced by the inhomogeneous source term that drives the wave equation for the second-order acoustic density deviations expressed in Eq. (15.56). The original pump-wave source "loudspeaker" is shown in *bold lines* and *bold fonts* at the far left of this figure

Each infinitesimal fluid volume that is excited by quadratic combinations of the first-order sound fields can be considered a source for the second-order sound field. In Fig. 15.11, those fluid volumes are represented by individual loudspeakers with amplitudes that are proportional to ρ'^2. Because the phase velocity is also the thermodynamic sound speed, c_o, each of those "virtual loudspeakers" produces sound that sums in just the same way as the discrete end-fire line array in Sect. 12.7.1. When the sound radiated by the first virtual loudspeaker propagates to the position of the second, the two will be in-phase, and their amplitudes will add coherently. The sum then propagates to the third location and adds in-phase and so on. This coherent addition along the direction of propagation produces the linear growth in the second harmonic's amplitude that was described in Eqs. (15.37) and (15.43), as well as in Fig. 15.10. It also demonstrates the corresponding quadratic dependence on the amplitude of the first-order field at any location.

15.3.3 Intermodulation Distortion and the Parametric End-Fire Array

The distortion of a single, initially sinusoidal plane wave is due to the wave's own influence on the medium through which it is propagating. The formalism of Eq. (15.56) makes it convenient to consider the nonlinear interaction of two plane waves propagating in the same direction but having different frequencies, $\omega_\downarrow$ and $\omega_\uparrow$. For simplicity, let both sound waves have equal amplitudes, ρ_1.

At the linear level, they create a sound field that is simply their superposition.

$$\rho'(x,t) = \rho_1\left[\cos\left(\omega_\downarrow t - k_\downarrow x\right) + \cos\left(\omega_\uparrow t - k_\uparrow x\right)\right] \tag{15.59}$$

The nonlinear source term in Eq. (15.56) is driven by the square of that linear superposition. Letting $a = (\omega_\downarrow t - k_\downarrow x)$ and $b = (\omega_\uparrow t - k_\uparrow x)$, the drive can be expressed as the sum of five contributions.

$$\rho'^2 = \left(\rho_1^2/2\right)[2 + \cos(2a) + \cos(2b) + \cos(a+b) + \cos(a-b)] \tag{15.60}$$

Again, the constant term in the square brackets will be eliminated from the driving term by the Laplacian in Eq. (15.56). The $(2a)$ and $(2b)$ terms represent the second harmonic distortion of the individual wave produced by their self-interaction. The sum and difference terms, $\cos(a + b)$ and $\cos(a - b)$, are called *intermodulation distortion* products and represent the effect that one wave has on the medium that the other wave is passing through.

Having already analyzed the self-distortion that creates the second harmonic distortion, our interest will now be focused on two interacting waves. Those interacting waves will be called the *pump waves* or *primary waves*. We will assume that their frequencies are closely spaced: $|\omega_\uparrow - \omega_\downarrow| \ll (\omega_\uparrow + \omega_\downarrow)/2$. These two colinear waves, as well as the products of their nonlinear interactions, are still all in geometric resonance.

$$c_{ph} = \frac{\omega_\uparrow}{\left|\vec{k}_\uparrow\right|} = \frac{\omega_\downarrow}{\left|\vec{k}_\downarrow\right|} = \frac{2\omega_\uparrow}{2\left|\vec{k}_\uparrow\right|} = \frac{2\omega_\downarrow}{2\left|\vec{k}_\downarrow\right|} = \frac{\omega_\uparrow + \omega_\downarrow}{\left|\vec{k}_\uparrow + \vec{k}_\downarrow\right|} = \frac{\left|\omega_\uparrow - \omega_\downarrow\right|}{\left|\vec{k}_\uparrow - \vec{k}_\downarrow\right|} = c_o \tag{15.61}$$

In the absence of dispersion, if the two waves are not colinear, then the *phase matching* that is the consequence of geometrical resonance does not occur, and the interaction does not produce waves that propagate beyond the interaction volume [28].

Since the two "pump" or "primary" waves are assumed to be close in frequency, they have about the same thermoviscous spatial attenuation coefficient, $\alpha_{T\text{-}V}$, resulting in a characteristic exponential decay distance, $\ell = (\alpha_{T\text{-}V})^{-1}$, as identified before in Sect. 15.1.3 for definition of the Gol'dberg number. Since the bulk attenuation coefficient is proportional to the square of the frequency, the two self-distorted second harmonic components will suffer exponential decay over a distance that is only one-fourth of ℓ, as will the wave that is produced by the nonlinear interaction that creates a wave at the sum of the two pump frequencies. The exponential decay of either of the pump waves is represented symbolically in Fig. 10.12 (Left). The growth and subsequent exponential decay of the second harmonics and sum waves are represented symbolically in Fig. 10.12 (right).

Although the waveform instability caused by nonlinear distortion had been understood since the time of the American Civil War, it was not until 1963 that Peter Westervelt recognized that highly directional receivers and transmitters of sound may be constructed by use of the nonlinearity in the equations of hydrodynamics[8] [29]. Although it had been known, both theoretically [30] and experimentally [31], that two plane waves of different frequencies propagating in the same direction generate two new waves at the sum and difference frequencies, it was not until Westervelt's paper that the practical utility of that difference-frequency wave was recognized.

As we know from the analysis of the radiation from baffled circular pistons in Sect. 12.8, it is impossible to produce a narrow (i.e., directional) sound beam if the circumference of the radiating piston, $2\pi a$, is on the order of the wavelength, λ, of the sound being radiated, or smaller. This makes it impossible to produce a directional sound beam at low frequencies from small vibrating surfaces. On the other hand, if $2\pi a \gg \lambda$, then the radiated sound will be confined to a narrow beam as quantified in Eq. (12.108). Westervelt recognized that it was possible to use nonlinear acoustics to create a narrow low-frequency beam through the interaction of two narrow high-frequency, high-amplitude sound beams of slightly different frequencies. If the high-frequency beams interacted over a distance that was much longer than the difference frequency wavelength, $\lambda_{\text{diff}} = 2\pi c_o/(\omega_\uparrow - \omega_\downarrow)$, then the virtual array, like that depicted symbolically in Fig. 15.11, would produce a directional low-frequency sound beam.

As long as the attenuation distance for the pump waves is longer than the wavelength of the difference frequency wave, the difference frequency will be produced by the end-fire linear array from the nonlinear interaction of the two pump waves and will have the directionality characteristic of the pump wave's directionality (see Fig. 15.15). The growth of the difference frequency wave will initially be linear with distance (as it was for the second harmonic distortion derived in Sect. 15.2.2), but due to the attenuation of the higher-frequency pump waves, depicted symbolically in Fig. 15.12 (left), the difference wave will reach some limiting amplitude as shown in Fig. 15.13.

An array consisting of 30 40 kHz piezoelectric transducers, shown in Fig. 15.14, was built to demonstrate the directionality of the difference-frequency beam. Fifteen of the transducers were wired electrically in parallel and driven at $\omega_\downarrow/2\pi = 37.5$ kHz, and the other 15 were wired in parallel and driven at $\omega_\uparrow/2\pi = 39.5$ kHz to produce a parametric array that would create a difference wave at

[8] Westervelt first presented his parametric array at a meeting of the Acoustical Society of America in Providence, RI, in 1960, J. Acoust. Soc. Am. **32**, 934 (1960). The abstract for that presentation included an expression for the radiated intensity of the difference-frequency beam.

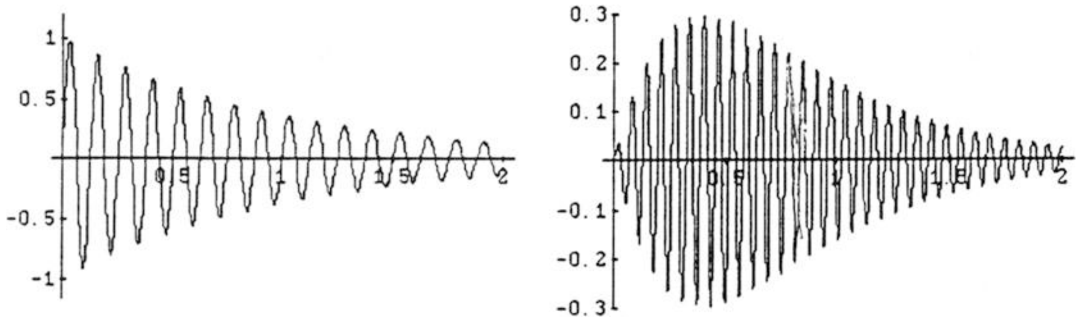

Fig. 15.12 (*Left*) Symbolic representation of the exponential decay of the one-dimensional pump wave due to thermoviscous attenuation. (*Right*) Symbolic representation of the growth and subsequent decay of the second harmonic and sum waves generated by nonlinear processes. Since the frequencies of the second harmonics and the sum wave are approximately twice that of the pump waves, the decay of these nonlinear products takes place over a characteristic exponential decay distance that is one-fourth of that for the pump waves

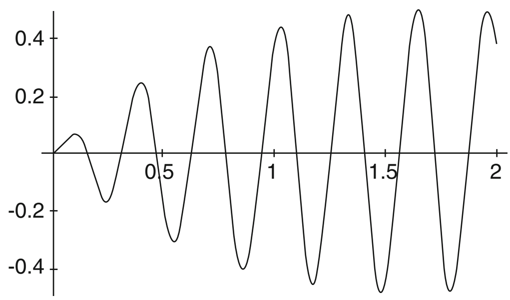

Fig. 15.13 A directional low-frequency "difference wave" can be created by the nonlinear interaction of two "pump" waves of slightly different frequency, like the wave shown in Fig. 15.12 (*left*). Since the pump wave attenuates with distance from the source, the difference-frequency wave amplitude initially increases linearly with distance from the source but eventually reaches a maximum amplitude before attenuating or spreading at greater distances

$(\omega_{\uparrow} - \omega_{\downarrow})/2\pi = 2.0$ kHz. These two sub-arrays were interlaced so that the nearest neighbors to any transducers driven at one of the frequencies would radiate at the other frequency.

That array is shown in Fig. 15.14. It has a height, $h = 5$ cm, and width, $w = 21$ cm. This produces a circular-equivalent effective radius, $a_{\text{eff}} = (h + w)/\pi \cong 8$ cm. At 40 kHz, the pump wavelength is $\lambda_{\text{pump}} \cong 0.9$ cm, so $ka_{\text{eff}} \cong 60$, making the pump waves very directional at that frequency. Using the directionality for a baffled piston in Eq. (12.108), the pump wave's major lobe is confined within about $\pm 3.6°$. Since the array is rectangular rather than circular, the 40 kHz beam will be wider than this circular approximation in the vertical direction and narrower in the horizontal direction.

The attenuation of a 40 kHz sound wave in air is strongly dependent upon humidity (see Fig. 14.5). In dry air, the exponential absorption length, ℓ (0% RH) = 23 m, while for a relative humidity of 60%, ℓ (60% RH) = 2 m. The pump amplitude, $p_1 \cong 20$ Pa, so by Eq. (15.15), the shock inception distance is $D_S = 8$ m, assuming no spreading. A conservative estimate of the effective low-frequency end-fire array length, d_{eff}, might be 2 m, making the virtual line array's value of $k_{diff}\, d_{eff} \cong 36$ for the 2.0 kHz difference-frequency wave.

Although the directionality that can be achieved by the parametric array in this example is impressive, the electroacoustic energy conversion efficiency is very poor. The difference-frequency acoustic pressure amplitude, measured at 4 m from the source, was $p_2 = 0.14$ Pa $\cong 74$ dB *re:* 20 $\mu\text{Pa}_{\text{rms}}$.

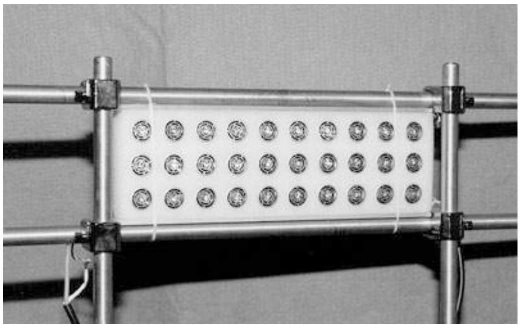

Fig. 15.14 Photograph of an array of 30 small piezoelectric transducers that is 5 cm tall and 21 cm wide. The array was wired as two interlaced 15-element sub-arrays. One sub-array was driven at $\omega_\downarrow/2\pi = 37.5$ kHz and the other at $\omega_\uparrow/2\pi = 39.5$ kHz to produce a difference-frequency wave at $(\omega_\uparrow - \omega_\downarrow)/2\pi = 2.0$ kHz. [Transducer and photo courtesy of T. B. Gabrielson]

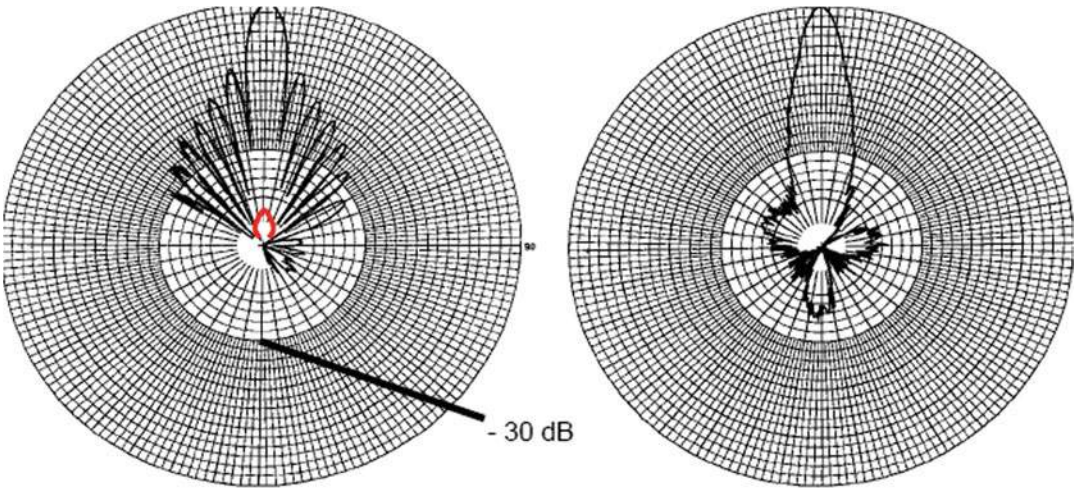

Fig. 15.15 (*Left*) The directionality of the pump and of the difference-frequency waves is plotted on the same scale. (*Right*) When the directionality of the difference-frequency wave is plotted by itself, it is clear that the directionality of the difference-frequency wave is only slightly broader than the directionality of the pump waves

At that distance, the beam's cross-section was about 1 m^2. The intensity corresponding to $p_2 = 0.14$ Pa is 22 μW/m^2. The electrical input power to the array was about 18 watts, so the net electroacoustic conversion efficiency is just about one-part-per-million or approximately 0.0001%.

This increase in difference-frequency directionality and the low conversion efficiency is illustrated in the directionality plots in Fig. 15.15 for a parametric end-fire array operating at pump frequencies of 22 kHz and 27 kHz to produce a 5 kHz difference-frequency wave in water. The efficiency is better than in air due to the higher value of Γ in water and the higher acoustic pressures that could be produced, but the ratio of the amplitude of the difference-frequency to the pump is quite low, as demonstrated when both the pump and the difference frequency waves are plotted together in Fig. 15.15 (left). The smaller-amplitude difference-frequency wave's directionality is plotted by itself in Fig. 15.15 (right). Comparison of the two graphs shows that the difference-frequency beam is only slightly wider than the pump frequency beams.

The low conversion efficiencies of the parametric array are deemed acceptable for some niche applications. Parametric arrays for use in air are being produced commercially, but I have some trepidation about the possibility of detrimental physiological effects due to the very high pump-wave amplitudes at frequencies that are above the normal range of human hearing. I'm not of the opinion that "what you can't hear, can't hurt you."

The ubiquity of such commercially available parametric arrays that are used to produce directional sound in air (i.e., "audio spotlights") has renewed interest in the potentially detrimental health effects of high-amplitude ultrasound exposure and led to the publication of a Special Issue of the *Journal of the Acoustical Society of America* that is focused on this subject [32].

We are currently in the undesirable situation where a member of the public can purchase a $20 device that can be used to expose another human to sound pressure levels that are > 50 dB in excess of the maximum permissible levels for public exposure.

Concern has been exacerbated by reports of the "weaponization" of high-amplitude ultrasound that may have been used to injure diplomats at the US Embassy in Havana, Cuba [33], and elsewhere [34].

When I make measurements near such an ultrasound source (e.g., Fig. 15.14), I wear ear plugs and place sound-attenuating earmuffs over my plugged ears. Other experimentalists who have not taken such precautions have exhibited symptoms like dizziness and nausea.

15.3.4 Resonant Mode Conversion

So far, the concept of geometrical resonance has restricted the evolution of harmonic distortion or the production of sum and difference waves to media that do not exhibit significant dispersion, as indicated by Eq. (15.61). If there is dispersion, so $dc_o/df \neq 0$, then the some portions of the virtual array will start to become out-of-phase with other portions, and the uniform linear increase in amplitude with distance will become instead a "beating" where the amplitude would start growing and then start diminishing, possibly repeating that alternation if the interaction length were sufficiently long, as some portions of the virtual array subtract from the growth produced by other portions.

In this sub-section, two beams that are not colinear are allowed to interact to produce another wave that travels at a different speed. That beating is illustrated by the measurements made in a waveguide of rectangular cross-section, made by Hamilton and TenCate [38], shown in Fig. 15.16.

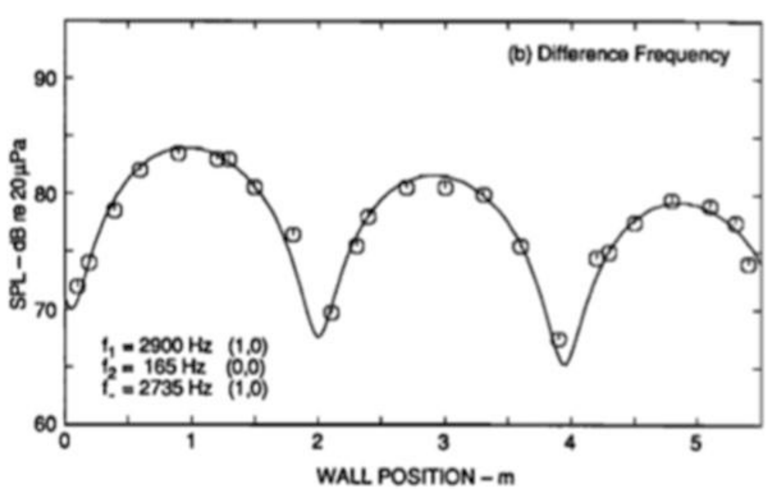

Fig. 15.16 The difference frequency amplitude vs. distance along a waveguide showing the "beating" created by the dispersion caused by the waveguide's frequency-dependent phase speed when the difference frequency, $f_2 = 165$ Hz, propagates as a plane wave and the two pump waves, at $f_1 = 2900$ Hz and $f_- = 2735$ Hz, propagate in the lowest-frequency non-plane wave mode [38]

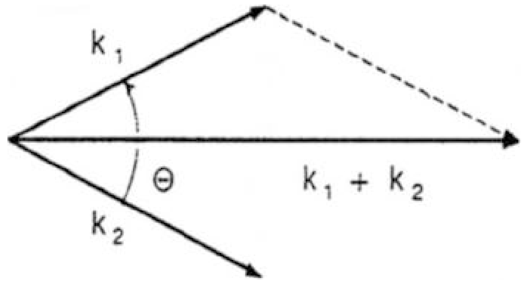

Fig. 15.17 Two pump waves of the same frequency interact at an angle, θ. If $\theta \neq 0°$, the vector sum of their wavevectors will be less than the sums of their wavenumbers

If the propagation speed of the nonlinear product is greater than the propagation speed of the pumps and if the pump wavevectors are not colinear, there can be geometrical resonance (i.e., phase matching) at a unique interaction angle. I like to call this a "scissors effect." If we assume that there are two waves of the same frequency, $\omega_\uparrow = \omega_\downarrow = \omega$, but their wavevectors make a relative angle, θ, with each other, then the phase speed of the "sum" wave will be higher than the phase speed of either pump (primary) wave. This simple geometry is illustrated in Fig. 15.17.

$$c_{ph} = \frac{\omega_\uparrow + \omega_\downarrow}{\left|\vec{k}_\uparrow + \vec{k}_\downarrow\right|} = \frac{2\omega}{2\left|\vec{k}\right| \cos\left(\theta/2\right)} = \frac{c_o}{\cos\left(\theta/2\right)} \geq c_o \tag{15.62}$$

This is similar to a scissors in that the speed of the intersection of the two blades moves faster than the speed at which the tips of the blades approach each other.

As introduced in Sect. 5.1.1, the speed of longitudinal waves in bulk solids is $c_L = \sqrt{D/\rho}$, where D is the dilatational modulus, also known as the modulus of unilateral compression (see Sect. 4.2.2). Shear waves in bulk isotropic solids propagate at the shear wave speed, $c_S = \sqrt{G/\rho}$, where G is the material's shear modulus (see Sect. 4.2.3). The relationship between the moduli of any isotropic solid, summarized in Table 4.1, allows the relationship between those two sound speeds to be expressed in terms of the solid's Poisson's ratio, ν, and its Young's modulus, E.

$$c_S^2 = \frac{G}{\rho} = \frac{E}{2\rho(1+\nu)} < c_L^2 = \frac{D}{\rho} = \frac{E(1-\nu)}{\rho(1+\nu)(1-2\nu)} \tag{15.63}$$

The stability criterion discussed in Sect. 4.2.3 restricts positive values of Poisson's ratio to $\nu < ½$, thus guaranteeing that $c_L > c_S$.

Based on the phase speed increase calculated for the interaction of two waves that are not colinear in Eq. (15.62) and the fact that $c_L > c_S$, it would be possible to have two shear waves interact though nonlinearity to produce the faster longitudinal wave where the mode-conversion interaction angle, θ_{mc}, is determined by the Poisson's ratio of the solid in which the two shear waves are interacting.

$$\cos\left(\frac{\theta_{mc}}{2}\right) = \frac{c_S}{c_L} = \sqrt{\frac{(1-2\nu)}{2(1-\nu)}} < 1 \tag{15.64}$$

For polycrystalline aluminum, $\nu_{Al} = 0.345$ [35], so $\cos\left(\theta_{mc}/2\right) = 0.486$. The required angle between the two shear wavevectors in aluminum must be $\theta_{mc} = 122°$ to make the interaction phase speed in Eq. (15.62) satisfies geometrical resonance for nonlinear mode conversion that couples two shear waves, each at frequency, ω, to a longitudinal wave with frequency 2ω.

Resonant mode conversion in solids was first described theoretically by Jones and Kobett [36] and observed experimentally shortly thereafter in aluminum, by Rollins, Taylor, and Todd, at the interaction angle predicted in Eq. (15.64) [37].

Another opportunity for resonant mode conversion is afforded by inspection of Fig. 15.5. From 1 K to 2 K, second (thermal) sound has a speed, c_2, of about 20 m/s, while the speed of first (compressional) sound, c_1, is around 230 m/s. Two second sound waves that are almost anti-colinear could have an interaction phase speed equal to that of first sound. Using the geometry of Fig. 15.16, the mode conversion half-angle, at temperatures below $T_\lambda = 2.172$ K, depends upon the velocity ratio.

$$\cos\left(\frac{\theta_{mc}}{2}\right) = \frac{c_2(T)}{c_1(T)} \leq 0.10 \tag{15.65}$$

This suggests that θ_{mc} will be close to 180°.

A waveguide of rectangular cross-section affords an ideal geometry to provide a long interaction length while also affording precise control of the mode conversion angle for two plane waves of second sound. In a waveguide, the interaction angle of the two traveling plane waves (see Fig. 13.23) is controlled by the ratio of the drive frequency to the cut-off frequency. From Fig. 15.17 and Eq. (13.69), the mode-conversion interaction half-angle, $\theta_{mc}/2$, is related to the ratio of the second sound drive frequency, ω, to the cut-off frequency of the waveguide's first non-plane wave mode, ω_{co}.

$$\cos\left(\frac{\theta_{mc}}{2}\right) = \frac{\left|\vec{k}\right|}{\sqrt{k^2 - k_z^2}} = \sqrt{1 - \frac{\omega_{co}^2}{\omega^2}} \tag{15.66}$$

As shown in Fig. 15.18, if the height of the waveguide is ℓ_z, then the cut-off frequency would correspond to a single half-wavelength of second sound being equal to the waveguide's height: $\omega_{co} = \pi c_2/\ell_z$. Substitution of Eq. (15.65) into Eq. (15.66) determines the ratio of the second sound frequency necessary for resonant mode conversion, ω_{mc}, to the waveguide's cut-off frequency, ω_{co}.

$$\frac{\omega_{co}}{\omega_{mc}} = \sqrt{1 - \frac{c_2^2}{c_1^2}} < 1 \tag{15.67}$$

Of course, it is necessary to do this experiment in superfluid helium at temperatures below T_λ, since second sound provides the pump (primary) waves, as well as to have an adequate nonlinear interaction

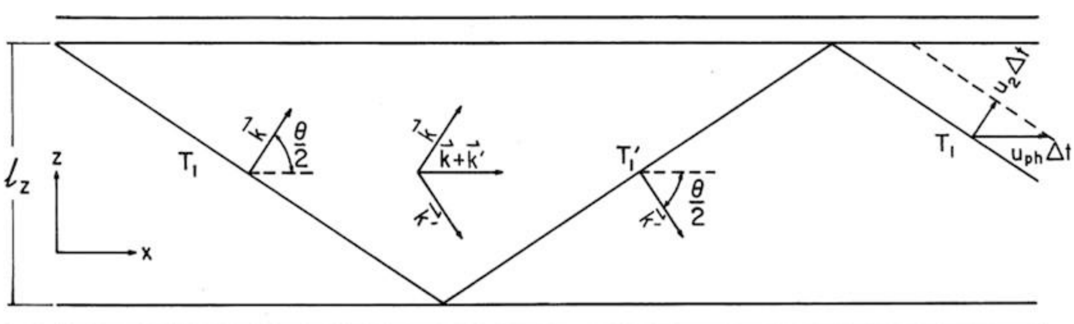

Fig. 15.18 A waveguide can provide precise control of the interaction angle, θ, of the two second sound traveling plane waves that satisfy the waveguide's boundary conditions, since the ratio of the frequency to the cut-off frequency controls the interaction angle

length to observe this resonant mode conversion of second sound to first sound. Those two constraints led to the use of a spiral waveguide shown in Fig. 15.18 (left). Sum and difference waves generated by non-colinear waves in an air-filled waveguide of rectangular cross-section that were not geometrically resonant are shown in Fig. 15.16 that were measured by Hamilton and TenCate [38].

Landau's two-fluid description of superfluid helium requires eight variables [39]. In addition to the two thermodynamic variables, two separate velocity fields are necessary to describe the motion of the superfluid component and of the normal fluid component, $\vec{v}_s$ and $\vec{v}_n$. This makes the second-order wave equation for the nonlinear acoustic interactions more complicated than Eq. (15.56), but the inhomogeneous form, which provides a wave Eq. (15.68) to describe the space-time evolution of the second-order pressure, p_2, is still driven by quadratic combinations of the first-order sound fields produced by first sound (v_1^2 and p_1^2), second sound(T_1^2 and w_1^2), or their interaction ($p_1 T_1$) [15].

$$\begin{aligned}\frac{\partial^2 p_2}{\partial t^2} - c_1^2 \nabla^2 p_2 = c_1^2 \bigg[&\frac{\partial^2}{\partial r_i \partial r_j} \left(\rho v_i v_j + \frac{\rho_n \rho_s}{\rho} w_i w_j \right) - \frac{1}{2} \left(\frac{\partial^2 \rho}{\partial p^2} \right) \frac{\partial^2 p_1^2}{\partial t^2} \\ &- \frac{1}{2} \left(\frac{\partial^2 \rho}{\partial T^2} \right) \frac{\partial^2 T_1^2}{\partial t^2} - \left(\frac{\partial^2 \rho}{\partial p \partial T} \right) \frac{\partial^2 (p_1 T_1)}{\partial t^2} - \left(\frac{\partial \rho}{\partial w^2} \right) \frac{\partial^2 (w^2)}{\partial t^2} \bigg] \end{aligned} \tag{15.68}$$

Since there are two velocity fields, Eq. (15.68) expresses the fluid's motion in terms of the center-of-mass velocity, $\vec{v}$, which is nearly zero for second sound and $\vec{w} = \vec{v}_n - \vec{v}_s$, which is nearly zero for first sound. Because w^2 is a Galilean invariant (i.e., its value is not dependent on the motion of the coordinate system), it is also a thermodynamic variable, as evidenced by the partial derivative in the final term in Eq. (15.68).

Resonant mode conversion of second sound to first sound was observed experimentally from 1.15 K < T_m < 2.0 K using the spiral waveguide and heater shown in Fig. 15.19 (Right) [40].

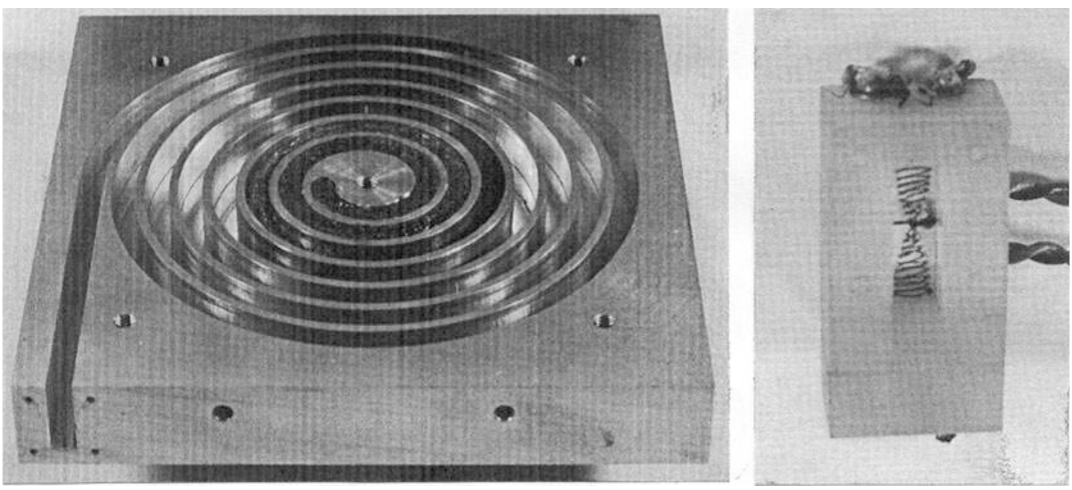

Fig. 15.19 (*Left*) A spiral waveguide shown with the lid that housed the first and second sound sensors (microphones) removed. The depth of the waveguide, $L_z = 14.73$ mm, and the width, $L_y = 4.8$ mm. The edge length of the square block into which the spiral groove was cut is 12.7 cm. The total length of the spiral is 150 cm, and a wedge absorber, visible near the waveguide's center, occupies the final 60 cm. (*Right*) Second sound is generated by periodically heating the superfluid. This heater consists of two individual NiCr resistance wire elements with a nearly sinusoidal profile to optimize coupling to the first non-plane waveguide (height) mode. Due to the frequency doubling produced when the heaters are driven with an AC current, the two heater halves were driven 90° out-of-phase (electrically) at one-half the mode conversion frequency

15.4 Non-zero Time-Averaged Effects

Nonlinear acoustical effects are driven by quadratic combinations of first-order sound fields. When the first-order sound field was squared to produce Eq. (15.57), the constant term was ignored because it was operated upon by a Laplacian to produce the virtual sources that drove the inhomogeneous wave equation for the propagation of the second-order sound field. In this sub-section, the effects of that constant term will be explored, first with a focus on the square of the first-order particle velocity, v_1, initially restricting our analysis to one-dimensional propagating plane waves.

$$v_1^2(x,t) = v'^2 \cos^2(\omega t - kx) = \frac{v'^2}{2}[1 + \cos 2(\omega t - kx)] \tag{15.69}$$

Since the first-order acoustic fields have a sinusoidal time dependence, their time-averaged values must vanish over times that are long compared to the periods of such disturbances, $T \gg 2\pi/\omega$.

$$\langle p_1 \rangle_t = \frac{1}{T}\int_0^T p_1 \ dt = 0 \tag{15.70}$$

The second-order terms, like the squared velocity in Eq. (15.69), that contain a constant term, will produce time-averaged second-order pressures that will not vanish: $\langle p_2 \rangle_t \neq 0$. These second-order non-zero time-averaged pressures can produce substantial forces [41] and torques [42] on objects that are within the sound field. As early as the 1940s, Hillary St. Clair was able to levitate copper pennies ($\rho_{Cu} = 8.9$ gm/cm^3) [43]. Using an intense sound field produced by a siren and a reflector, Allen and Rudnick were able to repeat St. Clair's demonstration:

> "*When a number of pennies are placed on a stretched silk screen, the parameters can be so adjusted that the pennies do somersaults with "Rockette"-like precision; or so that a penny can be made to rise slowly to a vertical position, appearing all the while to be supporting, acrobatically, another which finally assumes a horizontal position above the first penny touching rim to rim. Also, coins resting on the silk screen can be flipped a distance of a few feet by varying the frequency of the siren rapidly.*" [44]

15.4.1 The Second-Order Pressure in an Adiabatic Compression

Nonlinear distortion, the generation of harmonics, and the "scattering of sound by sound" were attributed to the fact that a wave will modify the properties of the medium through which it is propagating. To start our investigation of non-zero time-averaged effects, it will be instructive to consider the piston of area, A_{pist}, in a close-fitted cylinder that is filled with an ideal gas at equilibrium pressure, p_m. With the piston in its equilibrium position, designated as $x = 0$, the equilibrium volume of the gas in the cylinder will be $V_o = A_{pist} L$, where L is the length of the cylinder from the rigid end located at $x = L$ to the piston's equilibrium position. This arrangement is identical to that depicted schematically in Fig. 8.5.

If the gas inside the cylinder obeys the Adiabatic Gas Law and if the motion of the piston is sinusoidal, with the piston's position given by $x(t) = x_1 \sin(\omega t)$, then the pressure within the cylinder will be uniform throughout and given by the Adiabatic Gas Law as long as $\sqrt{A_{pist}} \ll \lambda/2\pi = c_o/\omega$ and $L \ll c_o/\omega$, so that the cylinder can be treated as a "lumped element," where $c_o = \sqrt{(\partial p/\partial \rho)_s}$ is the speed of sound under equilibrium conditions.

$$\begin{aligned} pV^{\gamma} = const. \quad &\Rightarrow \quad \frac{p_1(t)}{p_m} = -\gamma \frac{\delta V}{V_o} = -\gamma \frac{-A_{pist} x_1 \sin(\omega t)}{A_{pist} L} \\ &\Rightarrow \quad p_1(t) = \gamma p_m \frac{x_1 \sin(\omega t)}{L} \equiv p_1 \sin(\omega t) \end{aligned} \tag{15.71}$$

This is the familiar "linear" result; a sinusoidal variation in the piston's position leads to a sinusoidal variation of the pressure within the cylinder. Such a result assumes that $x_1/L \ll 1$, so the motion of the piston does not affect the volume, V_o, that appears in Eq. (15.71). Of course, that is not exactly true. As the ratio of x_1 to L increases, the importance of the piston's instantaneous position on the value of the volume of the gas becomes more influential. It is easy to take the change in the cylinder's volume into account. When the piston moves inward, it sweeps out a volume, $\delta V(t) = -A_{pist}\, x(t)$, which should be subtracted from the equilibrium volume, V_o.

$$p(t) = -\gamma p_m \frac{\delta V}{V_o\left(1 - \frac{\delta V}{V_o}\right)} \cong -\gamma p_m \frac{\delta V}{V_o}\left(1 + \frac{\delta V}{V_o}\right) = -\gamma p_m \left[\frac{\delta V}{V_o} + \left(\frac{\delta V}{V_o}\right)^2\right] \tag{15.72}$$

Taking the time-average of the pressure over a period, T, the linear term vanishes, but the quadratic term produces a non-zero time-averaged pressure, $\langle p_2 \rangle_t$, since $\sin^2(\omega\, t) = ½[1 - \sin(2\omega\, t)]$.

$$\langle p_2 \rangle_t = \frac{\gamma p_m}{2T}\left(\frac{x_1}{L}\right)^2 \int_0^T [1 - \cos(2\omega t)]\, dt = \frac{\gamma p_m}{2}\left(\frac{x_1}{L}\right)^2 \tag{15.73}$$

The integral over the component oscillating at 2ω will vanish but the constant component will not. That time-averaged excess pressure will tend to push the piston away from the closed end of the cylinder. This effect produces "piston walk" in Stirling cycle machines.

This time-averaged pressure can be expressed in terms of the first-order pressure calculated in Eq. (15.71): $x_1/L = p_1/\gamma p_m = p_1/\rho_m c_o^2$, if the cylinder contains an ideal gas.

$$\langle p_2 \rangle_t = \frac{p_1^2}{2\rho_m c_o^2} \tag{15.74}$$

In this form, it is clear that the non-zero time-averaged pressure is quadratic in the first-order pressure. It is also useful to recognize that this result is equal to the potential energy density as derived from the energy conservation Eq. (10.35).

As with the results of weak shock theory in Sect. 15.2, it is the effects of the piston's position on the volume that appears in the Adiabatic Gas Law of Eq. (15.72) that produces corrections to the linear result. The creation of a net second-order pressure is due to the asymmetry produced by the fact that the average volume on compression of a piston is smaller than the average volume during expansion.

Application of this result to a one-dimensional standing wave resonator is straightforward. Within the resonator, the first-order pressure can be written as $p_1(x,t) = \Re e[\widehat{\mathbf{p}} \cos(n\pi x/L) e^{j\omega t}]$. Close to the end at $x = 0$, the first-order acoustic pressure is nearly independent of position, just as it is in the piston and cylinder example. By the Euler equation, the longitudinal particle velocity can be written as $v_1(x,t) = \Re e[\, j(\widehat{\mathbf{p}}/\rho_m c_o) \sin(n\pi x/L) e^{j\omega t}] \equiv -v_1 \sin(n\pi x/L) \sin(\omega t + \varphi)$, so the particle velocity goes linearly to zero as x goes to L, just as it does in the piston and cylinder example. This situation near to the rigid end of the resonator (or close to any standing wave pressure anti-node) can be represented by an imaginary line (i.e., a Lagrangian marker) that moves with the gas, acting as the piston while neglecting the remaining gas in the resonator.

In a sealed resonator, the total mass of the gas cannot change. If the static pressure at the rigid ends (as well as at any pressure anti-node for higher-order longitudinal modes of the resonator, $n > 1$)

increases by the amount specified in Eq. (15.74), then the density of the gas must also increase in those locations. For that to happen in a sealed system, the gas density (and pressure) must decrease elsewhere.

In a standing wave, the amplitude of the gas particle velocity at a pressure node (velocity anti-node) is $v_1 = p_1/\rho_m c_o$, so if the total mass of the gas cannot change, then the non-zero, second-order, time-averaged pressure at the first-order pressure node must be equal and opposite to the value in Eq. (15.74) and can be re-written in terms of v_1.

$$\langle p_2 \rangle_t = -\frac{p_1^2}{2\rho_m c_o^2} = -(½)\rho_m v_1^2 \quad \text{at a pressure node} \tag{15.75}$$

In this form, it is clear that the non-zero time-averaged pressure is quadratic in the first-order velocity amplitude. It is also useful to recognize that this result is equal to the kinetic energy density at the velocity anti-node as derived from the energy conservation Eq. (10.35). It also has the functional form of the *Bernoulli pressure*.

The relationship between the second-order time-averaged pressure [45], also known as the *radiation pressure*, and the kinetic and potential energy densities will be derived from the hydrodynamic equations in Sect. 15.4.4 after examining a few examples of the acoustical consequences produced by the Bernoulli pressure in the following sub-section and in Sect. 15.4.3.

15.4.2 The Bernoulli Pressure

The first introduction in this textbook to the Bernoulli pressure[9] was provided in the analysis of the Venturi tube (see Sect. 8.4.1) that was intended to aid in the understanding of the convective term in the total hydrodynamic derivative in Eq. (8.33). This resulted in the introduction of a pressure gradient produced in the tube that was driven by the square of the fluid's velocity, v^2.

$$p = p_m - \frac{1}{2}\rho_m v^2 \tag{15.76}$$

Since the Bernoulli pressure is proportional to the square of the fluid's velocity, it is independent of the direction of flow. For the oscillatory velocities that are produced by sound waves, this means that the time-averaged Bernoulli pressure will be non-zero.

The effects of the Bernoulli pressure for oscillatory flows produced by sound waves were recognized and understood by Lord Rayleigh. The *Kundt's tube* was a popular piece of acoustic apparatus that produced high-amplitude standing waves by stroking a rod that would excite longitudinal vibrations and couple those vibrations to the air contained in a transparent glass tube [46]. Cork dust or lycopodium seeds were commonly used to visualize the sound field by "decorating" velocity anti-nodes. Figure 8.14 shows cork dust striations in the neck of a resonator that is excited in its Helmholtz mode, $f_o = 210$ Hz (left), and at a frequency, $f_1 = 1240$ Hz, that excited a half-wavelength standing wave in the neck (right) [47].

[9] Daniel Bernoulli (1700–1782) was a Dutch physicist and mathematician who published *Hydrodynamica* in 1738 that provided the basis of the kinetic theory of gases which he applied to explain Boyle's law. He was also well known for early development of elasticity theory with Leonard Euler, an effort recognized to this day by the fact that Eq. (5.36) is called Euler-Bernoulli beam equation.

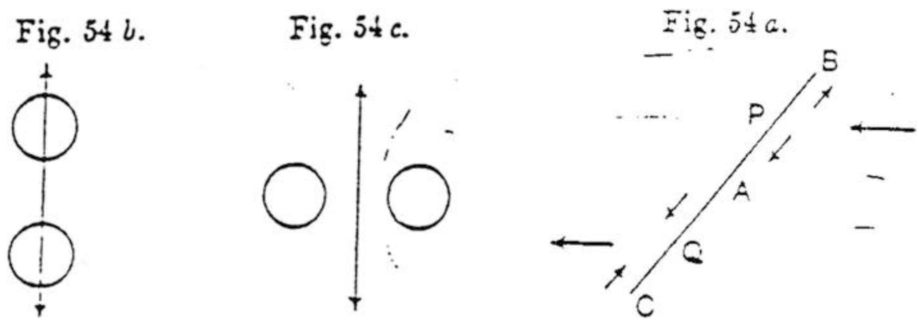

Fig. 15.20 Three figures taken from Rayleigh's *Theory of Sound*, Vol. II [50]. (*Left*) In Fig. 54b, two particles are oriented along the direction of oscillatory flow indicated by the double-headed arrow. Since the flow is occluded between the two spheres, the time-averaged pressure is greater between the particles causing them to repel. (*Center*) When the same two particles are oriented normal to the oscillatory flow in Fig. 54c, the increase in the velocity between the two produces a lower pressure that causes the two particles to attract each other. (*Right*) A rigid disk is placed at 45° with respect to the oscillatory flow

Rayleigh recognized that two small particles of sufficient mass to remain stationary within the oscillatory flow field, due to their inertia,[10] would be attracted to each other because the oscillatory air flow must accelerate as it passes between the constrictions produced by the adjacent particles. By Eq. (15.76), the increased fluid velocity between the particles results in a lower pressure so that the resultant pressure gradient would drive the particles together.

The figure taken from Rayleigh's *Theory of Sound* that diagrams this attraction is shown in Fig. 15.20 (center). This effect, known as acoustic agglomeration, has been used in several applications where removal of larger clusters of smaller particles from a fluid is easier than the removal of smaller individual particles [48]. More recently, "acoustic agglomeration" has been used for separation of biological cells grown in bioreactors from their nutrient liquid [49].

Rayleigh makes a similar argument, as also illustrated in Fig. 15.20 (left), to explain the striations of the dust particles agglomerated in planes that are normal to the oscillatory flow. When two particles (or planes of particles) are separated along the direction of the oscillatory flow, the stagnation of the fluid between them produces an increase in the time-averaged pressure that causes the particles (or planes of particles) to repel each other, as clearly visible in the striations seen in Fig. 8.14.

Another interesting manifestation of the Bernoulli pressure was mentioned by Rayleigh in regard to the forces on a Helmholtz resonator. The fluid's velocity in the neck of a Helmholtz resonator is high.

[10] The motion of a small particle in a sound field will depend upon the competition between the particle's inertia (mass), which tends to make it remain stationary in the laboratory frame of reference, and the Stokes drag due to the viscosity of the medium which tends to force the particle to move along with the acoustically oscillating fluid. The inertial force is given by Newton's Second Law, $F_{inertia} = m\ (dv_1/dt)$, and the Stokes drag force on a spherical particle of radius, a, (at sufficiently low Reynolds number) is $F_{drag} = 6\pi\mu a v_1$. Their dimensionless ratio will determine if the particle moves with the fluid or if the fluid moves around the particle. That ratio can be written for a spherical particle with mass density, ρ, and sound with frequency, f.

$$\frac{F_{inertia}}{F_{drag}} = \frac{4\pi}{9}\frac{a^2 f\rho}{\mu}$$

For a particle with the density of water ($\rho = 10^3$ kg/m^3), in air with $\mu \cong 1.8 \times 10^{-5}$ Pa-s, and then at 100 Hz, that ratio is one for a spherical particle with a radius of about 10 microns. A larger radius particle, like cork dust, coffee whitener, or a seed, will remain nearly stationary in the laboratory frame, and the fluid will oscillate around it, while a much smaller particle, like smoke, will move with the fluid.

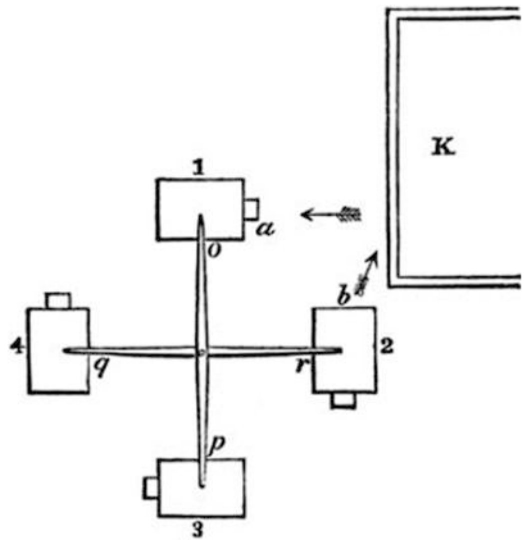

Fig. 15.21 Apparatus drawing, taken from Dvořák [52], showing "four very light paper or glass [Helmholtz] resonators upon two wooden rods, *o p*, *q r*, crossing at right angles, and balanced on a glass cap; all the openings of the resonators fronting one side in the direction of tangents. The whole apparatus is placed before the opening, K, of the resonating box and fork, in the manner indicated"

Based on Eq. (15.76), this suggests that the pressure in the neck must be reduced. Since the neck is in direct contact with an effectively infinite reservoir of atmospheric pressure, the only means by which the required pressure difference can be maintained is if the static time-averaged pressure within the compliance (volume) of the Helmholtz resonator is greater than atmospheric pressure.

This second-order, acoustically induced pressure difference, $\langle p_2 \rangle_t$, will lead to a net force on the Helmholtz resonator since the pressure on the surfaces of the volume are unbalanced over the cross-sectional area, πa_{neck}^2, of the neck:$F_{net} = \pi a_{neck}^2 \left\langle p_2\left(v_{neck}^2\right)\right\rangle_t$.

> "Among the phenomena of the second order which admit of a ready explanation, a prominent place must be assigned to the repulsion of resonators discovered independently by Dvořák [51] and Meyer [52]. These observers found that an air resonator of any kind when exposed to a powerful source experiences a force directed inwards from the mouth, somewhat after the manner of a rocket. A combination of four light resonators, mounted anemometer fashion upon a steel point, may be caused to revolve continuously." [53]

Apparently, an acoustical demonstration of the nonlinear force on a resonator that resembles a lawn sprinkler, shown in Fig. 15.21, from [52], was well known to RaylTheir dimensionless eigh.[11] This effect can be observed in a quantitative way by placing a Helmholtz resonator on a sensitive balance and producing a large amplitude sound field in the vicinity using a loudspeaker driven at the Helmholtz resonance frequency and then observing the increase in the resonator's apparent weight to do "the rocket."

15.4.3 The Rayleigh Disk

The Bernoulli pressure of Eq. (15.76) can also exert torques, $N\left(v_1^2\right)$, on an extended object placed in an oscillatory flow field. Rayleigh's diagram of such a disk that is aligned at about 45° with respect to the

[11] Video demonstrations of several of the non-zero, time-averaged effects in this section were recorded at the 100th meeting of the Acoustical Society of America held in Los Angeles, CA, in 1988. This video is included in the second disk of the *Collected Works of Distinguished Acousticians—Isadore Rudnick*, compiled by J. D. Maynard and S. L. Garrett (Acoust. Soc. Am., 2011); https://www.abdi-ecommerce10.com/ASA/p-230-collected-works-of-distinguished-acousticians.aspx.

flow field is shown in Fig. 15.20 (right). That figure captures the flow at an instant when it is moving from right to left, as indicated by the arrows. The approaching flow stagnates between A and B where it diverges, and the receding flow stagnates on the other side of the disk between C and Q where it rejoins. On the inflow side of the desk, the flow must accelerate along A-Q-C as the two flows converge on the outflow side at P. The stagnant flow between A and B on the inflow side and between C and Q on the outflow side has a higher pressure than the faster-moving flows at the same locations on the opposite sides of the disk. This produces a net torque that tends to orient the disk perpendicular to the flow, regardless of the flow direction.

An appreciation for the magnitude of this torque can be obtained by calculation of the moment of the Bernoulli pressure in Eq. (15.76) over both sides of a disk having radius, a, assuming the presence of the disk does not perturb the sound field.[12] The circle in Fig. 4.11 that was used to calculate the radius of gyration for beam flexure will provide the coordinate system for this integration.

$$\begin{aligned} N &= \int_0^a \langle p_2 \rangle_t r \; dS = 4\int_0^a \frac{\rho_m \langle v_1^2 \rangle_t}{2} h[2h\cos\theta] \; dh \\ &= 4\rho_m \langle v_1^2 \rangle_t \int_0^{\pi/2} (a\sin\theta)^2 a\cos\theta \; d\theta = \frac{4}{3}\rho_m \langle v_1^2 \rangle_t a^3 \end{aligned} \tag{15.77}$$

If the disk is assumed to be suspended by a torsion fiber in the oscillatory flow, then the torque will be zero when the surface of the disk is perpendicular to the flow or when the surface of the disk is aligned with the flow. If the angle between the normal to the disk's surface is designated θ, then the torque will be zero when $\theta = 0°$ (occluding the flow) or when $\theta = 90°$ (aligned with the flow), except that the $\theta = 90°$ orientation will be unstable. If the disk is aligned with the flow and its orientation deviates slightly from $\theta = 90°$, then the torque will cause the disk to seek the $\theta = 0°$ orientation. If the disk is in the $\theta = 0°$, any small deviation in θ will subject the disk to a torque that will tend to restore the $\theta = 0°$ orientation.

Based on the magnitude of the torque in Eq. (15.77) and the previous stability argument, the torque as a function of the square of the time-averaged oscillatory velocity amplitude, $\langle v_1^2 \rangle_t$, and the orientation angle can be written in the form that appears in *Theory of Sound*, which Rayleigh attributes to König [54].

$$N(\theta) = \frac{4}{3}\rho_m \langle v_1^2 \rangle_t a^3 \sin 2\theta \tag{15.78}$$

Rayleigh recognized that "Upon this principle an instrument may be constructed for measuring the intensities of aerial vibrations of selected pitch" and suggests that the disk be a mirror suspended by a silk thread so a light beam could be used as an optical lever (see Sect. 2.4.4) to determine the disk's orientation [55].

Prior to the introduction of the reciprocity method for calibration of reversible transducers (see Sect. 10.7.2, 10.7.3 and 10.7.4), the Rayleigh disk was a primary technique for determination of acoustic sound field amplitudes [56]. Due to its importance, a detailed analysis of the torque was made by King to include corrections produced by the disk's influence on the sound field [57]. The torque on a Rayleigh disk located at a velocity anti-node in a standing wave field included wavelength-dependent

[12] This assumption is not as bad as it seems since the Bernoulli pressure, as described in Eq. (15.76), is only valid along a streamline. The streamlines in Fig. 15.20 (right) will follow the contours of the disk accounting for the fact that simple results of Eqs. (15.77) and (15.78) are very nearly the correct result.

corrections for the disk's mass, m_1, as well as the disk's hydrodynamic (inertial) entrained mass, $m_o = (8/3)\rho_m a^3$, as calculated in Eq. (12.126).

$$N_{anti-node}(\theta) = \frac{4}{3}\rho_m \langle v_1^2 \rangle_t a^3 \sin 2\theta \left\{ \frac{m_1 \left[1 + \frac{2}{5}(ka)^2 \cos^2 2\theta\right]}{m_1 + m_o \left[1 + \frac{1}{5}(ka)^2\right]} \right\} \tag{15.79}$$

The indifference of the sign of the torque produced by flow in either direction was important in establishing the physical reality of Landau's two-fluid theory of superfluid hydrodynamics.[5] As mentioned briefly in Sects. 15.1.2 and 15.3.4, there are two velocity fields necessary to characterize the dynamics of superfluid flow, $\vec{v}_s$ and $\vec{v}_n$. In a thermally induced second sound wave, the superfluid's center-of-mass velocity is zero, but the counterflow of $\vec{v}_s$ and $\vec{v}_n$ is non-zero.

Since the Rayleigh disk responds to the torque of both flow fields without respect to their direction, Pellam and Hanson were able to establish the physical existence of both velocity fields and make the first mechanical measurement of second sound in superfluid helium [58]. Later, Koehler and Pellam were also able to measure the superfluid fraction, ρ_s/ρ, as a function of temperature using their Rayleigh disk [59]. Both measurements employed a mirror as the disk to detect the disk's deflection optically. Later measurements of torques in superfluids used a nonoptical method to determine the Rayleigh disk's orientation [60].

15.4.4 Radiation Pressure

Restricting attention to one dimension, the Bernoulli pressure can be derived from the Euler Eq. (15.48).

$$\frac{\partial v}{\partial t} + v\frac{\partial v}{\partial x} = -\frac{1}{\rho_m}\frac{\partial p}{\partial x} \tag{15.80}$$

The goal will be to express Eq. (15.80) entirely in terms of the gradient of a scalar, so it is useful to introduce the specific *enthalpy* (heat) function (see Sect. 14.2), $h = \varepsilon + pV$, where ε is the fluid's *internal energy* per unit volume (see Sect. 7.1.2): $d\varepsilon = dU/V$.

$$dh = d\varepsilon + p\ dV + V\ dp \tag{15.81}$$

Using the definition of the internal energy from Eq. (7.10), $d\varepsilon = T\,ds - p\,dV$, the pressure gradient can be expressed in terms of the specific enthalpy, $dh = dp/\rho_m$, and the product rule can be invoked to consolidate the convective contribution.

$$\frac{\partial v}{\partial t} + \frac{1}{2}\frac{\partial v^2}{\partial x} = -\frac{\partial h}{\partial x} \tag{15.82}$$

Having started with the Euler equation, the effects of viscosity have already been eliminated, so the Kelvin circulation theorem guarantees that the velocity field will be curl free; thus it can be expressed as the gradient of a scalar, ϕ, known as the *velocity potential*: $\vec{v} = \vec{\nabla}\phi$ [61].

$$\frac{\partial}{\partial x}\left(\frac{\partial \phi}{\partial t} + \frac{v^2}{2} + h\right) = 0 \tag{15.83}$$

Since the argument within the gradient in Eq. (15.83) is equal to zero, the function within the gradient must be a constant everywhere throughout the fluid.

$$\frac{\partial \phi}{\partial t} + \frac{v^2}{2} + h = \text{constant} \tag{15.84}$$

This is the "strong" form of Bernoulli's equation, since it is not restricted only to streamlines, as it was for the version introduced in Eq. (15.76).

To retain accuracy to second-order, the specific enthalpy must also be expanded to second-order.

$$h = h_o + \left(\frac{\partial h}{\partial p}\right)_s (p_1 + p_2) + \left(\frac{\partial^2 h}{\partial p^2}\right)_s \frac{p_1^2}{2} \tag{15.85}$$

These thermodynamic derivatives can be evaluated for adiabatic processes, $dS = 0$, from the differential form of the specific enthalpy: $dh = T\ dS - dp/\rho_m$.

$$\frac{\partial \phi}{\partial t} + \frac{v^2}{2} + h_o + \frac{(p_1 + p_2)}{\rho_m} - \frac{1}{2}\frac{p_1^2}{\rho_m^2 c_o^2} = \text{constant} \tag{15.86}$$

In this sub-section, we are only interested in the parts of Eq. (15.86) which produce a non-zero time-average. As in Eq. (15.70), the time-average of first-order variations will vanish: $\langle \partial \phi / \partial t \rangle_t = \langle p_1 \rangle_t = 0$.

$$\langle p_2 \rangle_t = \frac{1}{2}\frac{p_1^2}{\rho_m c_o^2} - \frac{1}{2}\rho_m v_1^2 + \text{constant} \tag{15.87}$$

The second-order time-averaged pressure is the difference between the potential and kinetic energy densities. In classical mechanics, that combination is known as the Lagrangian density [62].

For a collimated traveling wave of the usual form,[13] $p_1(x, t) = p_1 \cos(\omega t - kx)$, the linearized Euler's equation provides the ubiquitous relationship between the first-order acoustic field variables: $p_1 = \rho_m c_o v_1$. That relationship can then be substituted into Eq. (15.87).

$$\langle p_2 \rangle_t = \frac{1}{2}\frac{p_1^2}{\rho_m c_o^2} - \frac{1}{2}\frac{p_1^2}{\rho_m c_o^2} = 0 \tag{15.88}$$

This result is oddly both philosophically significant and trivially obvious. If there were an object in the traveling-wave field, it would scatter some portion of the sound (see Sects. 12.6.1 and 12.6.2), and the sum of the scattered and incident wave fields would produce a standing wave. If the field is entirely a traveling wave, then that wave field cannot include an "object" which would feel the force of a time-averaged second-order pressure based on the object's density and/or compressibility contrast.

15.4.5 Acoustic Levitation in Standing Waves

The result for the time-averaged second-order pressure in Eq. (15.87) can also be evaluated for a standing wave.

[13] For a plane wave of infinite extent, the constant in Eq. (15.87) cannot be set to zero as it has to produce Eq. (15.88). This is discussed in C. P. Lee and T. G. Wang, "Acoustic radiation pressure," J. Acoust. Soc. Am. **94**(2), 1099–1109 (1993).

$$p_1(x,t) = p' \cos(kx)\cos(\omega t) \text{ and } v_1(x,t) = \frac{p'}{\rho_m c_o}\sin(kx)\cos(\omega t) \tag{15.89}$$

Substitution of Eq. (15.89) into (15.87) produces the time-averaged second-order pressure distribution for a standing wave in an ideal gas where $\rho_m c_o^2 = \gamma p_m$.

$$\langle p_2(x,t)\rangle_t = \frac{1}{4}\frac{p'^2}{\rho_m c_o^2}\left[\cos^2(kx) - \sin^2(kx)\right] = \frac{1}{4}\frac{p'^2}{\gamma p_m}\cos(2kx) \tag{15.90}$$

A standing wave produces a time-averaged (i.e., static) second-order pressure distribution. Due to the spatial dependence on cos (2*kx*), there is a minimum in the second-order pressure at the location of each pressure node, thus at each velocity anti-node and a maximum one-quarter wavelength from that minimum. This is consistent with the second-order piston example used as an introduction to non-zero time-averaged effects in Sect. 15.4.1.

This second-order time-averaged pressure distribution produces pressure gradients that are fixed in space and time and will exert forces on solid objects of non-zero thickness. The force on an object at either the maximum or the minimum in $\langle p_2\rangle_t$ will be zero, but that equilibrium will be unstable at the maximum. If a levitated object is displaced slightly from the maximum, it will be forced toward the minimum in $\langle p_2\rangle_t$ that occurs at a first-order velocity anti-node which has the lowest pressure, due to Bernoulli.

The integrated pressure over a small sphere of radius, $a \ll \lambda$, will produce a force, F_{sphere}, that is, a function of the sphere's location in the standing wave field.

$$F_{\text{sphere}} = \frac{4\pi a^2}{3}\frac{p'^2}{\rho_m c_o^2}(ka)\sin(2kx) = kV_{\text{sphere}}\frac{(p')^2}{2\rho_m c_o^2}\sin(2kx) \tag{15.91}$$

Rudnick provided a clever confirmation of this result in a simple standing wave tube that measured the angle of displacement of small spheres suspended by "a hair" due to the standing wave [63]. The integrated pressure over a small disk of thickness, t, and radius, a, will produce a force, F_{disk}, that is, a function of the disk's location

$$F_{disk} = \frac{\pi a^2}{2}\frac{p'^2}{\rho_m c_o^2}(kt)\sin(2kx) = kV_{disk}\frac{(p')^2}{2\rho_m c_o^2}\sin(2kx) \tag{15.92}$$

To levitate a small sphere made of a material with a mass density, ρ_{sphere}, against the force of gravity, the weight of the sphere must be cancelled by the levitation force. This requires that the square of the first-order standing wave pressure field amplitude, p'^2, exceed a minimum value, p'^2_{min}.

$$p'^2_{\text{min}} > \gamma p_m \rho_{\text{sphere}}\frac{g\lambda}{\pi} \tag{15.93}$$

When this criterion is satisfied, then the position of the sphere will adjust itself within the (vertical) standing wave field to make the net force on the sphere be zero at some location below a velocity anti-node. The stability of that equilibrium will be the subject of Sect. 15.4.6.

Of course, the levitated object does not have to be either a sphere or a disk. As shown in Fig. 15.22, almost any small object can be suspended against the force of gravity if the amplitude of the standing wave sound field is sufficient.

Fig. 15.22 Clockwise from the top left are shown a ladybug, minnow, spider, and ant being levitated by intense standing waves in air. [Courtesy of Northwestern Polytechnical University in Xi'an, China]

15.4.6 Adiabatic Invariance and the Levitation Force

In the previous sub-section, the influence of the object being levitated by the standing wave on the response of the resonator was ignored. As will now be demonstrated, the perturbation of the resonator's normal mode frequency caused by an object will provide an alternative method to predict the levitation force by use of adiabatic invariance and without the necessity of integrating the pressure gradient around the object. In the subsequent sub-section, the feedback between the radiation force and the object's influence on the resonance frequency will also have significant impact on the stability of the levitated object in a resonator that is driven at a constant frequency.

Throughout this text, the concept of adiabatic invariance [64] has been utilized when it was convenient to relate changes in a system's constraints (e.g., boundary conditions) to one or more of that system's normal mode frequencies. Now adiabatic invariance will be applied in the same way (i.e., the "variable constraint" being the position of the object in the sound field) to a one-dimensional standing wave tube's resonance frequencies that are perturbed by an incompressible obstacle that can be placed anywhere within the resonator of length, L, and cross-sectional area, A.

It is assumed that the obstacle of volume, V, shown as a small cube in Fig. 15.23 (left), has dimensions that are all much smaller than the wavelength, λ_n, of any normal mode of interest: $\sqrt[3]{V} \ll \lambda_n$. Because the obstacle is located at a pressure anti-node (velocity node) in Fig. 15.23 (left), the excluded (incompressible) volume "stiffens" the gas springiness at that rigid end and raises the unperturbed (empty resonator) frequency, f_1, of the fundamental ($n = 1$) mode:$f_1 = c_o/2L$.

To estimate the increase in frequency caused by the obstacle when it is near a pressure anti-node (velocity node), we can use the same trick that simplified the calculation of the frequency shift caused by the deposition of a thin layer of gold that lowered the fundamental frequency of a quartz microbalance in Sect. 5.1.2 due to its additional mass loading. Let the cube be made of wax. If the wax were melted with the tube in the vertical orientation, then the volume of wax would remain unchanged, but it would be spread uniformly over the resonator's endcap as shown in Fig. 15.23 (right). Since the slope of the pressure at the endcap is zero, the cube and slab versions of the obstacle produce the same

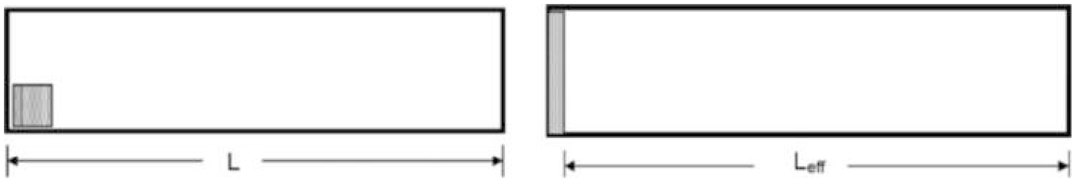

Fig. 15.23 (*Left*) A small rigid obstacle (*grey square*) is placed adjacent to the rigid end of a one-dimensional standing wave resonator of length, *L*. (*Right*) That obstacle has been "melted" so that its entire volume (*grey rectangle*) has been preserved but is now distributed uniformly over the resonator's cross-section, producing a decreased effective length, L_{eff}

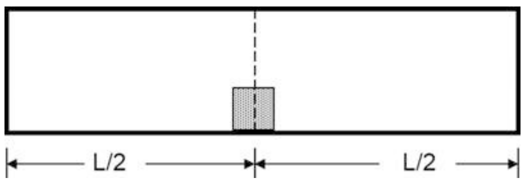

Fig. 15.24 The same obstacle that was shown in Fig. 15.23 is now located at the center of the resonator. In that position, it lowers the frequency of the fundamental ($n = 1$) normal mode but raises the frequency of the second normal mode ($n = 2$)

stiffening of the gas (i.e., exclude the same amount of resonator volume). The perturbed frequency, $f_1{}'$, is then that of the slightly shorter resonator shown in Fig. 15.23 (right): $f_1{}' = c_o/2L_{eff}$.

If the same obstacle was moved to the center of the resonator, as shown in Fig. 15.24, then it would lower the resonance frequency below the unperturbed frequency, f_1. This is because the obstacle has created a constriction in the resonator's cross-sectional area, A, at a position within the fundamental mode that is located at a velocity anti-node (pressure node). The high-speed gas near the resonator's midplane must accelerate to go around the obstacle, thus increasing the kinetic energy without affecting the potential energy stored at the ends of the resonator (see Sect. 13.3.4).

By Rayleigh's method (see Sect. 2.3.2), this means that the fundamental normal mode frequency must be reduced. The amount of that frequency reduction is dependent upon the shape of the obstacle, so it is not as easy to make a quantitative estimate of the frequency reduction as it was for the case where the incompressible obstacle was located at a pressure anti-node (velocity node). Fortunately, the use of adiabatic invariance provides a method to measure the effect of an obstacle of any shape and any location within the standing wave then relate that frequency shift produced to the levitation force, as described in the next sub-section.

For the resonator's second mode ($n = 2$), the obstacle is located at a pressure anti-node and thus raises the resonance frequency of that mode. Again, since the resonator's midplane contributes gas stiffness in the second mode (along with the gas stiffnesses at both ends), the volume exclusion produced by the obstacle increases the gas stiffness. The "melted wax" trick would work again by symmetry, treating the resonator as two half-resonators, each shortened by the appropriate amount: $L_{\text{eff}}/2 < L/2$.

It is worthwhile to notice that when this obstacle is located at the center of the resonator, it has ruined the harmonicity of the modes of the closed-closed resonator of uniform cross-section: $f_n \neq nf_1$. All of the $n =$ odd modes will be "flattened" (^{b}) (i.e., their normal mode frequencies will be lowered), and all of the $n =$ even modes will be sharpened ($^\#$), as long as the $\sqrt[3]{V} \ll \lambda_n$ constraint is satisfied so the obstacle can be consider to be "small." This strategy is regularly employed to suppress the formation of shock waves in standing wave resonators that are used in high-amplitude applications like thermoacoustic refrigerators [65] and sonic compressors [66].

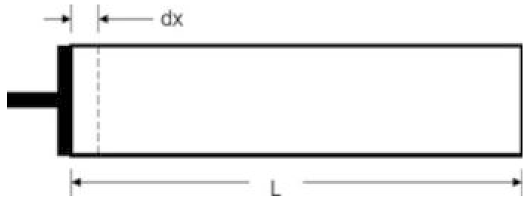

Fig. 15.25 A simple plane wave resonator with an adjustable left boundary position (piston)

In previous applications of adiabatic invariance, the work that was done against (or by) the radiation pressure was used to estimate normal mode frequencies of resonators with shapes that did not conform to the 11 separable geometries (see Sect. 13.1). It will now be easy, using Eq. (15.87), to demonstrate the connection between frequency changes and work done against the radiation force. If the resonator, shown schematically in Fig. 15.25, has an initial length, L, the standing wave pressure distribution is related to the velocity distribution that satisfied the rigid (impenetrable) boundary conditions as provided in Eq. (15.89). Here, we will focus on the fundamental mode, $n = 1$.

The time-averaged energy in the first mode, E_1, can be expressed as the time-average of the sum of the kinetic and potential energies, or by the virial theorem (Sect. 2.3.1), as the maximum potential energy,$(PE)_{\max}$, by integrating the potential energy density of Eq. (10.35) throughout the resonator's volume.

$$E_1 = \langle PE_{\max} \rangle_t = \int_0^L \frac{[p' \cos(\pi x/L)]^2}{2\rho_m c_o^2} A \ dx = \frac{(p')^2}{4\rho_m c_o^2} AL = \frac{(p')^2}{4\gamma p_m} AL \tag{15.94}$$

The rightmost result again assumes an ideal gas. The radiation force on the piston at the left of Fig. 15.23 is given by Eq. (15.90). The work increment, dW, done by the piston against the radiation force is just the force, $F_{rad} = \langle p_2 \rangle_t A$, times the displacement, dx.

$$dW = A \langle p_2 \rangle_t dx = A \frac{(p')^2}{4\gamma p_m} dx \tag{15.95}$$

Adiabatic invariance requires that the ratio of the energy in a mode to its frequency remains constant if the system's constraints are changed slowly (i.e., we don't "jerk" the piston).

$$\frac{E_n}{f_n} = \text{const.} \quad \Rightarrow \quad \frac{\delta E_n}{E_n} = \frac{dW}{E_1} = \frac{A \frac{(p')^2}{4\gamma p_m} dx}{\frac{(p')^2}{4\gamma p_m} AL} = \frac{dx}{L} = \frac{\delta f}{f_1} \tag{15.96}$$

This is exactly the frequency change that would be due to a decrease in the resonator's length by an amount, dx, based on the simplest result: $f_1 = c_o/2\ L$. In fact, the triviality of this result can be interpreted as a check on the expression (or a derivation) of the radiation pressure, $\langle p_2 \rangle_t$, in Eqs. (15.87) and (15.90).

It is now possible to combine adiabatic invariance and the normal mode frequency change, related to the change in an obstacle's position in a standing wave resonator, to calculate the levitation force from an alternative perspective [67]. A DeltaEC model of a resonator is provided in Fig. 15.26. The DeltaEC model makes use of a "Master-Slave Link" between Segments #2c and #6c that keeps the total length of the resonator fixed as the constriction, produced by Segments #3, #4, and #5, is moved from one end of the resonator to the other by changing the length of the DUCT in Seg. #2c from 0.0 m to 0.97 m.

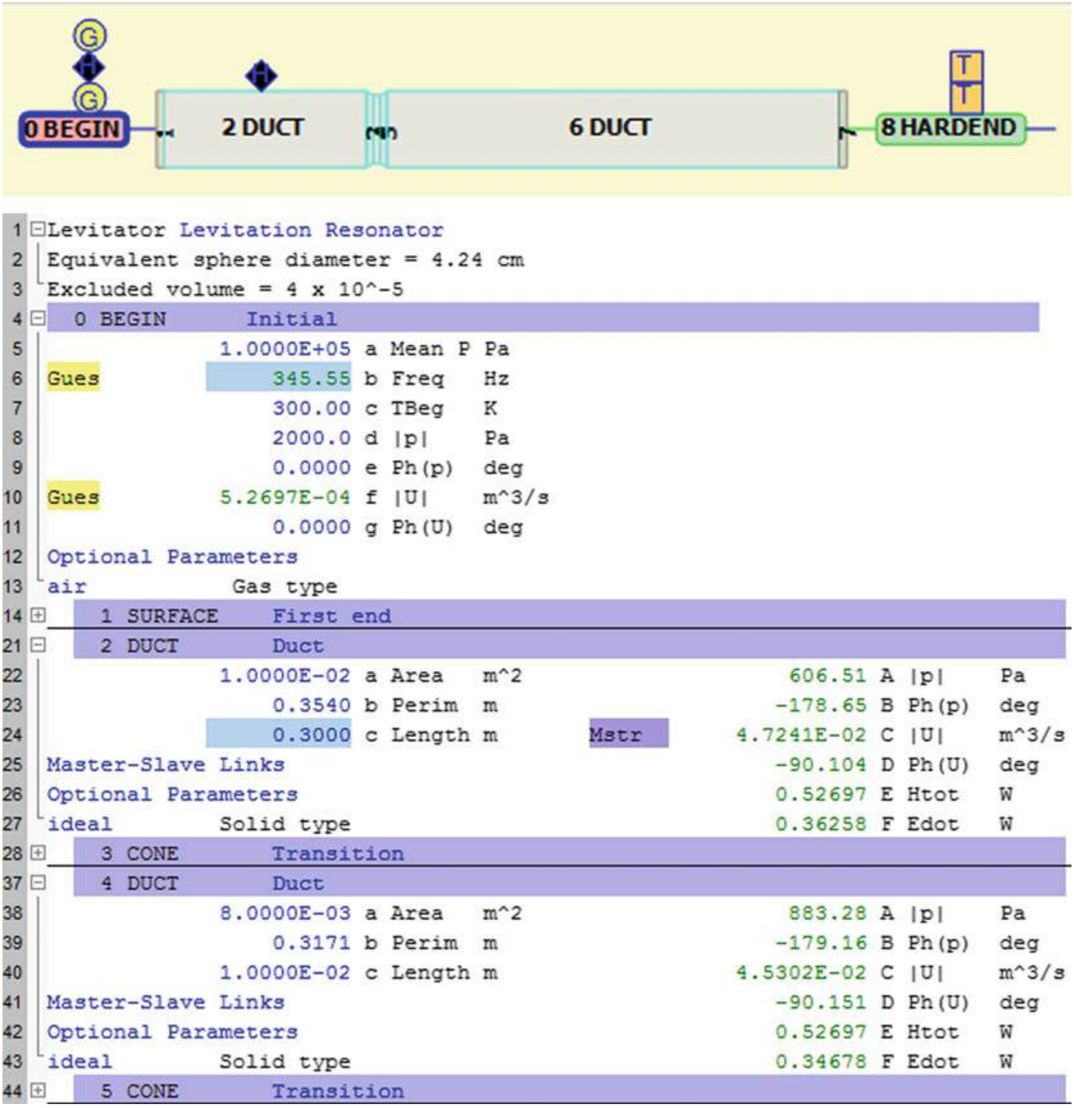

Fig. 15.26 Screenshot of a DeltaEC model of a resonator with cross-sectional area, $A = 1.0 \times 10^{-3}\,\mathrm{m}^2$, and length, $L = 1.0$ m, filled with dry air at 300 K and $p_m = 100$ kPa. There is a constriction that reduces the cross-sectional area to 8.0×10^{-3} $\mathbf{m}^2$ that is 1.0 cm long and two transitions using CONE segments, each 1.0 cm long. That combination of two CONE segments and the constrictive DUCT (Seg. #4) can be positioned anywhere within the resonator. The "Master-Slave Link" in Segments #2c and #6c maintain the total length as the position of the constriction is moved when the DUCT length in Seg. #2c is changed. The "schematic view" at the top of this figure shows the center of the tapered constriction positioned 31.5 cm from the driven end

The resonance frequencies of the first and second standing waves that are plotted in Fig. 15.27 as a function of the constriction's location were produced using DeltaEC's incremental plotting function (see Sect. 8.6.12). Plots of the normal mode frequency shifts, similar to those in Fig. 15.27, appeared in the literature for the fundamental mode and for the $n = 2$ mode [68], although it was not recognized at that time that those shifts were related to the levitation forces by adiabatic invariance.

The mobile constriction in the DeltaEC model removes 40 cm^3 of resonator's unperturbed 10 liter volume (10,000 cm^3). This is approximately equivalent to a resonator of uniform cross-sectional area,

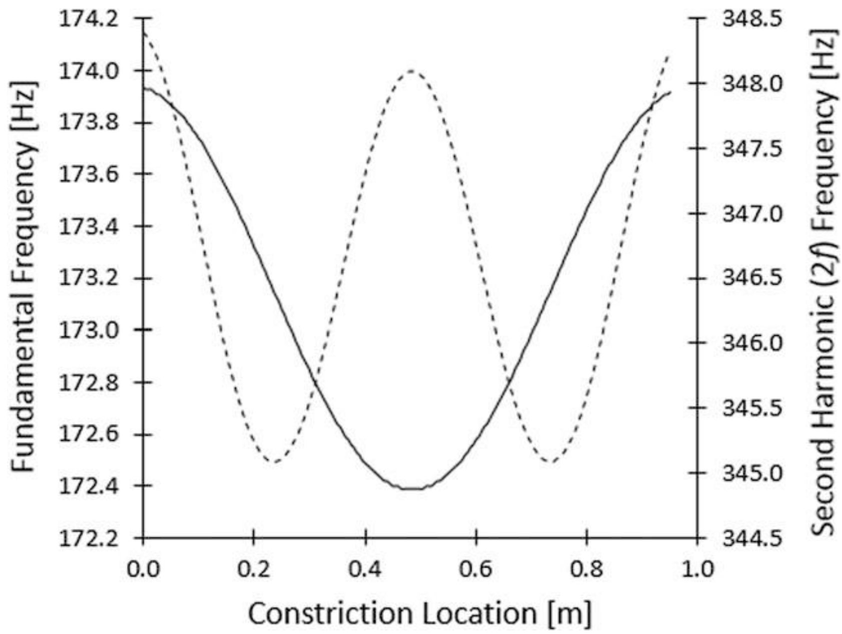

Fig. 15.27 Resonance frequency of the resonator modeled by DeltaEC in Fig. 15.26 as a function of the position of a constriction that could represent the location of an incompressible sphere or disk. The frequency of the fundamental ($n = 1$) mode is shown as the *solid line* with that frequency to be read from the left axis. The frequency of the second harmonic mode ($n = 2$) is shown as the *dashed line* to be read from the right axis

$A = 1.0 \times 10^{-2}$ m^2, that contains an incompressible sphere of radius, $a_{sphere} = 2.12$ cm, or to a disk of radius, $a_{disk} = 2.52$ cm and thickness, $t = 2.0$ cm. Again, the DeltaEC model will not be exact because the shift in the frequency due to a kinetic energy perturbation is shape dependent, even if the obstacle is small compared to the wavelength. Although the constriction in the DeltaEC model is trapezoidal and not a sphere or disk, it provides a plausible approximation of the change in the resonator's cross-sectional area that would be caused by the sphere or disk that provides the same volume exclusion.

Adiabatic invariance requires that the ratio of the modal energy to the modal frequency, E_n/f_n, be a constant as long as the motion of the obstacle is slow compared to the period of the standing wave, $T_n = (f_n)^{-1}$. As shown in Fig. 15.27, the resonance frequency is a function of the constriction's location within the resonator. The energy of the mode must also be a function of position so the radiation force on the sphere, F_{sphere}, or an obstacle of some other shape must be equal to the gradient in that energy (see Sect. 1.2.1).

$$\vec{F}_{sphere} = -\vec{\nabla} E_n \quad \Rightarrow \quad F_{sphere} = -\frac{dE_n}{dx} = -\frac{dE_n}{df_n}\frac{df_n}{dx} \tag{15.97}$$

Adiabatic invariance guarantees that $E_n/f_n = constant$, so by log differentiation (Sect. 1.1.3), $\mathrm{d}E_n/\mathrm{d}f_n = E_n/f_n = constant$.

The value of $\mathrm{d}f_n/\mathrm{d}x$ will depend upon the obstacle's position within the resonator. That slope will have its maximum value at locations equidistant between the nodes and the anti-nodes of the first-order standing wave fields. Using the results for the second standing wave mode produced by the DeltaEC model and plotted in Fig. 15.25, the maximum slope is just $\pi/2$ times the difference between the maximum frequency ($f_{2+} = 348.4$ Hz) and the minimum frequency ($f_{2-} = 345.09$ Hz), divided by the separation between the location of those two extrema, $\Delta x = 0.235$ m: $\mathrm{d}f_2/\mathrm{d}x = 21.1$ Hz/m.

For convenience, the constant, E_2/f_2, can be evaluated with the obstacle located at the driven end of resonator (i.e., Seg. #2c = 0.0 m), where E_2 is given by Eq. (15.94), with $p' = 2.0$ kPa (Seg. #0d), $p_m = 100$ kPa (Seg. #0a), $\gamma = (7/5)$, and $(AL) \cong 0.01\ \mathrm{m}^3$. At that location, $f_2 = f_{2+} = 348.4$ Hz, and $E_2 = 7.14 \times 10^{-2}$ J, so $E_2/f_2 = 2.05 \times 10^{-4}$ J/Hz. Substitution of these two results into Eq. (15.97) provides the radiation force due to the constriction, F_{rad}, at a position equidistant between the nodes and the anti-nodes of the first-order standing wave fields, which is a consequence of adiabatic invariance for a trapezoidal-shaped obstacle.

$$F_{\mathrm{rad}} = 2.05 \times 10^{-4}\ \frac{\mathrm{J}}{\mathrm{Hz}} \times 21.1 \frac{\mathrm{Hz}}{\mathrm{m}} = 4.3 \times 10^{-3}\mathrm{N} \tag{15.98}$$

This result can be compared to the radiation force at the same position for the $n = 2$ mode, under the same conditions, if the pressure at either anti-node (i.e., rigid end) is set to $p' = 2.0$ kPa, equivalent to 157 dB *re:* 20 μPa$_{\mathrm{rms}}$, for a sphere, F_{sphere}, in Eq. (15.91), or a disk, F_{disk}, in Eq. (15.92). To make a reasonable comparison, the volume of the sphere is set equal to the volume excluded by the trapezoidal constriction: $V = 40\ \mathrm{cm}^3$.

$$F_{\mathrm{sphere}} = V_{\mathrm{sphere}} \frac{(p')^2}{\gamma p_m} \frac{\pi f_2}{c_o} = 3.6 \times 10^{-3}\ \mathrm{N} \tag{15.99}$$

From Eq. (15.92), the result would be the same for a disk of the same volume.

Our estimate of the levitation force based on the DeltaEC model and adiabatic invariance is reasonably close to that result, given that the frequency shift computation was based on a constriction rather than an obstruction.

At this point, the serious reader will pause to marvel at the elegance and beauty that adiabatic invariance has demonstrated by its ability to circumvent the difficulties of integrals of second-order pressure fields over objects of arbitrary shape in favor of a simple measurement of the resonant frequency shift as a function of position of the object to be levitated within the resonator. Putterman claims that adiabatic invariance is “the cornerstone of modern physics” [69]. Similar results can be obtained for determination of the torque on a Rayleigh disk by measuring the shift in the resonance frequency as a function of the disk’s orientation [60].

15.4.7 Levitation Superstability (“Acoustic Molasses”)

Most acoustic levitation systems are driven at a fixed frequency [70]. Since the position of the levitated object can change, the ratio of the drive frequency to the resonator’s resonance frequency, ω/ω_o, will also change. That frequency shift at fixed drive frequency produces an effect referred to as “de-tuning” that is illustrated in Fig. 15.27. The frequency shift causes the amplitude of the standing wave to change resulting in a change in the radiation pressure acting on the levitated object. This modifies the Hooke’s law “stiffness” of the radiation force acting on the object. If the object did not influence the tuning, then the object would be levitated at the equilibrium position within the standing wave where the radiation force and the gravitational force would be equal and opposite. The fact that the object’s position also changes the tuning would change the trapping stiffness constant because its position influences the amplitude of the sound in the resonator when driven at fixed frequency.

This change in stiffness can be understood by examining the three shifted response curves illustrated in Fig. 15.28. All the resonance curves in Fig. 15.28 correspond to a quality factor of $Q = 10$. Assume that the resonator is driven at a fixed frequency that was 5% above the resonance frequency of the empty resonator so that $\omega/\omega_o = 1.05$. The value of v_1^2 would be 51.2% of the

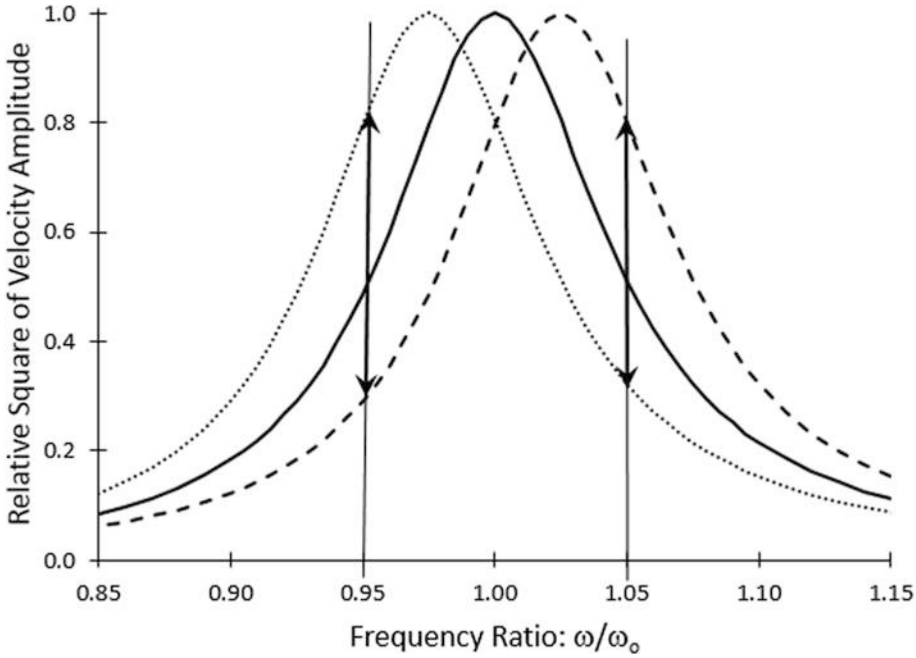

Fig. 15.28 The presence of the acoustically levitated object changes the resonance frequency of the resonator [68]. The *solid line* is the normalized value of the square of the peak velocity amplitude, v_1^2, produced when the resonator is driven a frequency relative to the resonance frequency of the empty resonator, $\omega/\omega_o = 1$. The *dotted line* corresponds to the resonator's frequency response when the levitated object is located closer to a velocity anti-node. The *dashed line* corresponds to the resonator's frequency response when the levitated object is located closer to a velocity node (i.e., a pressure anti-node)

maximum that occurs at $\omega/\omega_o = 1.00$, if the resonator was empty. If the object moved up from its equilibrium position (i.e., toward the closest velocity anti-node), then the resonator's resonance frequency would become lower, corresponding to the dotted resonance curve. The force on the object would decrease because the acoustic standing wave amplitude would decrease, since the value of v_1^2 would be 32.3% of the maximum that occurs at $\omega/\omega_o = 1.00$.

If the object moved down from its equilibrium position (i.e., toward the closest velocity node), then the resonator's resonance frequency would become higher, and the drive frequency would be closer to the resonance frequency. The value of v_1^2 in Fig. 15.28 would be 80.4% of the maximum that occurs at $\omega/\omega_o = 1.00$, if the resonator was empty. This corresponds to the dashed resonance curve in Fig. 15.28, and the force on the object would increase because the acoustic standing wave amplitude would have increased. The combined effect would be an increase in the stiffness.

If the empty resonator was initially tuned $\omega/\omega_o = 0.95$, then the effective stiffness would be less by the same argument except that the object's influence on the sound amplitude would be determined by its "motion" along the vertical line in Fig. 15.28 above $\omega/\omega_o = 0.95$, instead of the previous discussion that had the object's motion causing changes to the acoustic amplitude represented by "motion" along the vertical line above $\omega/\omega_o = 1.05$ in Fig. 15.28.

If this influence of the object's position on the effective stiffness of its capture around its equilibrium position in the standing wave occurred instantaneously in response to the object's change in position, then any displacement of the object would simply oscillate at a slightly different frequency about the equilibrium position than it would if the de-tuning was neglected. Viscous effects (i.e., Stokes drag) would eventually damp those oscillations, corresponding to a mechanical resistance, R_m, in the simple harmonic oscillator equation.

$$m\frac{d^2x}{dt^2} + R_m\frac{dx}{dt} + \mathrm{K}x = 0 \tag{15.100}$$

Because we are considering the standing wave resonator as a driven resonant system with $Q \neq 0$, the exponential relaxation time, τ, required for the resonator to achieve its steady-state response after its tuning is changed is non-zero (see Sect. 2.5.4): $Q = (½)\omega_o\tau$. The resonator's response time is much longer than the period, $T = 2\pi/\omega_o$, of the standing wave: $\tau = (Q/\pi)T$. That delay in the resonator's response to the position of the levitated object means that there will be a component of the force modulated by the object's position that will not be in-phase with the object's position but that will be in-phase or out-of-phase with the object's velocity. The influence of the de-tuning will be retarded by a time, τ, so the current radiation force acting on the object will depend upon the position of that object at an earlier time, $t - \tau$.

If this retardation produces a component of the excess (i.e., de-tuning) force that is out-of-phase with the velocity of the object's displacement from its equilibrium position, dx/dt, then this force will behave like mechanical damping in addition viscous "Stokes drag," in Eq. (15.100). If this retardation produces a component of the excess (i.e., de-tuning) force that is in-phase with the velocity of the object's displacement from its equilibrium position, dx/dt, then this force will behave like a negative mechanical resistance.

When the magnitude of that negative resistance is less than the ordinary viscous resistance, R_m, in Eq. (15.100), then oscillations will take longer to damp out. If the magnitude of that negative resistance is greater than R_m, then the amplitude of the object's oscillations will grow exponentially with time until some other effect limits the oscillation's amplitude. In some important cases this *de-tuning/de-phasing instability* will throw the levitated object out of the equilibrium position and possible propel the object against the resonator's boundaries [71].

The two possible scenarios are illustrated symbolically in Fig. 15.29. If the natural frequency of the resonator is lower than the drive frequency, $\omega/\omega_o > 1$ (sharp tuning), then motion of the levitated object

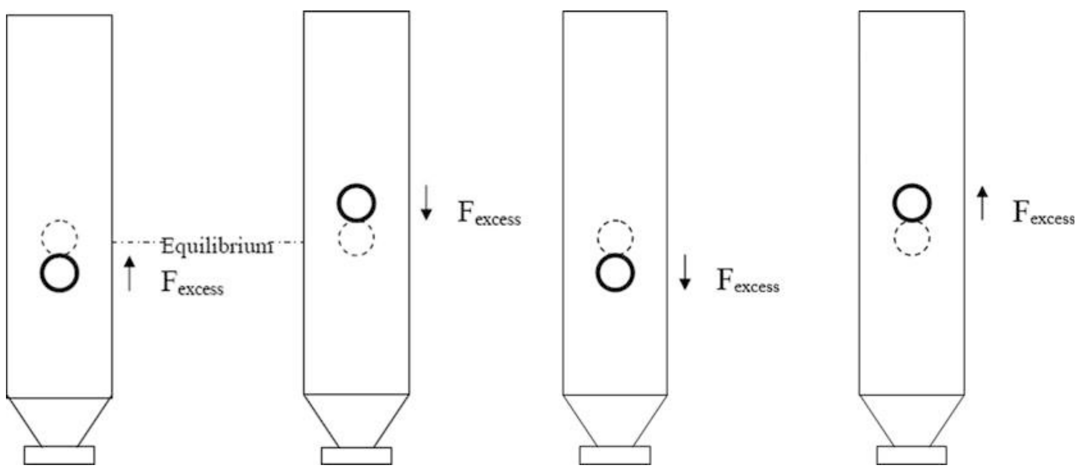

Fig. 15.29 The de-tuning/de-phasing instability (or superstability) for an acoustically levitated object depends upon whether the resonance frequency of the resonator is above or below the frequency of the sound produced by the loudspeaker. (*Left*) If the drive is tuned "sharp" (i.e., $\omega/\omega_o > 1$), then small displacements from equilibrium will increase, and the trapping will become unstable. (*Right*) If the drive is tuned "flat," (i.e., $\omega/\omega_o < 1$), then small displacements from equilibrium will damp out faster than if only viscous drag was providing the mechanical resistance making the trapping "superstable"

toward a pressure anti-node (i.e., away from a velocity anti-node) will raise ω_o and bring the drive frequency closer to the resonance frequency. This will produce an excess force, F_{excess}, that will be increased, thus in-phase with the velocity of the object as it is moving up from its lowest position, since the force will depend upon the previous position of the object at a time, τ, earlier. When the object reaches its maximum vertical position, the natural frequency of the standing wave resonator will be farther out-of-tune, and the radiation force is reduced, so gravity will provide an excess force. Again, due to the delay, that excess force will be acting in the downward direction and is again in-phase with the (now downward) velocity of the object. This scenario is depicted in Fig. 15.29 (left).

The net effect for the "sharp tuning" case has the excess force doing work on the object, thus increasing the amplitude of its oscillations during each cycle. If the effect is sufficiently large, it can overcome viscous damping making the amplitude of the object's oscillations grow linearly with time until some other effect limits the amplitude of the oscillations or the object is flung too far from the equilibrium position that it is no longer trapped or bangs against the walls or ends of the resonator.

If the natural frequency of the resonator is higher than the drive frequency, $\omega/\omega_o < 1$ (flat tuning), then motion of the levitated object toward a pressure anti-node (i.e., away from a velocity anti-node) will raise ω_o and bring the drive frequency farther from the resonance frequency. This will reduce the excess radiation force, F_{excess}, making the influence of gravity more important. That will produce an additional force that is out-of-phase with the velocity of the object as it is moving up from its lowest position, since the force depends upon the previous position of the object at a time, τ, earlier.

When the object reaches its maximum vertical position, the natural frequency of the standing wave resonator will be closer to the drive frequency, and the radiation force will be increased. Again, due to the delay, that excess force will be acting in the upward direction and is again out-of-phase with the velocity of the object which will be moving downward. This scenario is depicted in Fig. 15.29 (right).

The net effect for the "flat tuning" case has the excess force adding to the viscous resistance and thus increases the damping. The amplitude of the object's oscillations, if displaced from equilibrium, will decay more quickly than it would if the damping was due only to the Stokes drag. This additional damping causes superstability [72].

This same damping effect is observed in optics where it is known as "optical molasses" and was responsible for Stephen Chu sharing the Nobel Prize in Physics in 1997 with Claude Cohen-Tannoudji and William Phillips "for development of methods to cool and trap atoms with laser light" [73].

15.5 Beyond the Linear Approximation

Most ordinary acoustical phenomena can be analyzed from the linear perspective that has been the focus of every other chapter of this textbook. Linear acoustics and vibrations provide many useful and convenient simplifications. As we have seen, such simplifications are applicable to a large range of interesting problems. That said, this chapter has introduced a few interesting and useful phenomena that are not contained within a linear analysis. Waveform distortion, harmonic generation, shock wave formation and dissipation, parametric end-fire arrays, and mode conversion all rely upon incorporation of effects that a wave has on its propagation medium which are ignored in the linear limit. Inclusion of nonlinear effects leads to an interesting "life cycle" for a large amplitude acoustic disturbance: distortion → shocking → dissipation → classical attenuation [21]. That evolution in an ordinary fluid is depicted symbolically in Fig. 15.30.

By restricting the analysis to one-dimensional propagation of plane wave, many of the nonlinear behaviors have been demonstrated while avoiding more complicated mathematics and still being able to appreciate the cumulative influence of convection and of the medium's own nonlinearity.

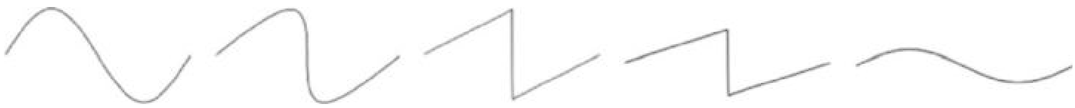

Fig. 15.30 The simplified life cycle of an initially sinusoidal large amplitude acoustic disturbance propagating as a plane wave in one dimension

The inclusion of nonlinear contributions also provided an introduction to the ability of a sound wave to exert non-zero time-averaged forces and torques on objects that are exposed to high-amplitude sound waves. Acoustic radiation forces are generally much larger than forces that can be exerted by electromagnetic radiation used for trapping atoms [73]. Much of our understanding of these effects can be attributed directly to the Bernoulli pressure that provides an intrinsically second-order contribution to the linear (first-order) pressure field. Once again, exploitation of adiabatic invariance provided a means of avoiding complicated mathematics while providing useful quantitative results.

Finally, it is important to recognize that this chapter was only the "tip of the iceberg." Many important nonlinear acoustical phenomena have not even been mentioned. Among the most significant are thermoacoustic engines, refrigerators [74], pulse-tube cryocoolers, and sonic mixture separators [75], as well as other important cases of acoustically driven mass streaming [76]. Another area that has been entirely ignored is nonlinear bubble oscillations that can be so violent that they convert sound into light by a process referred to as "sonoluminescence" [77]. The nonlinear distortion of pulses and the propagation of N-waves [78], like those which produce a "sonic boom" [79], are other important phenomena also worthy of investigation.

Topics in the area of nonlinear vibrations also abound. As mentioned in the beginning of this textbook, the inclusion of non-Hookean elasticity leads to the violation of Galilean isochronous independence of period and amplitude. Much like the harmonic distortion produced in high-amplitude wave propagation, a driven nonlinear oscillator will respond at frequencies that are not just the driving frequency. In fact, the response of a nonlinear oscillator can be at sub-harmonic frequencies or can become entirely chaotic rather than deterministic [80].

The purpose of this chapter was to raise awareness of the limitation of linear analysis, not to create professional expertise in nonlinear acoustics. If the reader can recognize the "symptoms" of nonlinear behavior and understand how they arise, then the goals of this final chapter will have been realized.

Talk Like an Acoustician

Convective nonlinearity	Phase matching
Self-interaction	Resonant mode conversion
Intermodulation distortion	Pump waves
Shock inception distance	Primary waves
Grüneisen parameter	Bernoulli pressure
Virial expansion	Radiation pressure
Second sound	Kundt's tube
Gol'dberg number	Internal energy
Order expansion	Enthalpy
Blackstock bridging function	Velocity potential
Geometric resonance	Acoustic levitation
Intermodulation distortion	De-tuning/de-phasing instability

Exercises

1. **Shock inception distance.** The derivation of Eq. (15.8) used the fact that the crest of a plane sinusoidal wave advances "by one radian length," k^{-1}, toward the zero-crossing when the slope of the zero-crossing, dv/dx, becomes infinite. By using the excess velocity, Γv, defined in Eq. (15.9), show this is true in the case where dissipation can be neglected, with an initial waveform, $v(x,t) = |\hat{\mathbf{v}}| \sin(\omega t - kx)$. For the waveform to become the fully developed sawtooth shock, the crest of the initially sinusoidal wave must advance by $\lambda/4$, placing the crest directly over the zero-crossing (see Fig. 15.6). Express that distance, D_{saw}, in terms of D_S, again for the case where dissipation can be neglected.
2. **Waveform distortion.** A 19.2 m long waveguide of circular cross-section with inside diameter, $D = 5.21$ cm, is shown in Fig. 15.31 and Fig. 15.32 (center). The waveguide is driven by two compression drivers, shown in Fig. 15.32 (left), which can produce large amplitude sound waves.[14] The waveguide is terminated by a porous anechoic cone.

   Three ¼" microphones are flush-mounted at three locations using the fixture that joins smoothly to the PVC pipe to eliminate reflections, shown in Fig. 15.32 (right). One microphone is located

Fig. 15.31 A U-shaped waveguide made from 2″ diameter (nominal) Schedule 40 PVC pipe is suspended from the ceiling to provide an overall propagation path of 19.2 m. At the far end are two compression drivers, and at the near end is a 1.05 m long porous wedge absorber to eliminate reflections. [Waveguide courtesy of Lauren Falco]

Fig. 15.32 (*Left*) Two compression drivers. (*Center*) U-shaped waveguide turn-around section. (*Right*) Microphone flush-mount holder

[14] The use of two drivers not only increases the achievable amplitudes but also facilitates measurements of the interaction of two waves of different frequencies.

very close to the drivers at a position designated $x = 0$. The second microphone is located at $x = 3.17$ m, and the third is located at $x = 17.9$ m.

Assume that the waveguide contains dry air at $p_m = 100$ kPa with a sound speed, $c_o = 345$ m/s, and it is driven sinusoidally at $f_1 = 880$ Hz.

(a) *Attenuation length*. Using the expression in Eq. (13.78), determine the exponential thermoviscous attenuation length, $\ell = \alpha_{T-V}^{-1}$, due to boundary layer dissipation at the fundamental frequency, f_1. Is that attenuation length shorter or longer for the higher harmonics?

(b) *Shock inception distance and Gol'dberg number*. Determine the shock inception distance, D_S, and using the result of part (*a*), determine the Gol'dberg number, G, if $p_1(0) = 100$ Pa (131 dB *re:* 20 μPa$_{rms}$), $p_1(0) = 300$ Pa (140.5 dB *re:* 20 μPa$_{rms}$), and $p_1(0) = 1000$ Pa (151 dB *re:* 20 μPa$_{rms}$).

(c) *Harmonic distortion*. Using Eq. (15.43) and neglecting attenuation, determine the amplitude of the fundamental, $f_1 = 880$ Hz, second harmonic, $f_2 = 1.76$ kHz, third harmonic, $f_3 = 2.64$ kHz, and forth harmonic, $f_4 = 3.52$ kHz, at $x = 3.17$ m and at $x = 17.9$ m, assuming $p_1(0) = 100$ Pa.

(d) *More harmonic distortion*. Repeat part (*c*) assuming $p_1(0) = 300$ Pa.

3. **Repeated shock**. Determine the ratio of the amplitudes of the harmonics to the amplitude of the fundamental, C_n/C_1, for a fully developed shock wavelike that shown in Fig. 15.8.

4. **Levitation demonstration resonator**. A ground-based levitator (i.e., $g = 9.8$ m/s^2) is being designed to demonstrate acoustic levitation by levitating the bottoms of Styrofoam coffee cups. Those disks have a diameter of 5.0 cm and a thickness of 1.5 mm, and each has a mass, $m_{disk} = 0.15$ gm. Assume that resonator will be constructed from a 1.5 m long, 6″ (nominal) diameter, optically clear cast acrylic tube with inside diameter, $D_{tube} = 14.0$ cm.

(a) *Levitation force*. If the resonator is operated in its $n = 3$ standing wave mode, $f_3 = 350$ Hz. Determine the pressure amplitude of the standing wave at the rigid end of the resonator so that the levitation force on the disk is three times its weight.

(b) *Equilibrium location*. If the tube is oriented so that the speaker is at the bottom and the rigid end is at the top (like those in Fig. 15.29), how far from the top end of the resonator will the disk be levitated at its highest stable location if the standing wave amplitude is that calculated in part (*a*)?

(c) *DeltaEC model*. Make a DeltaEC model of the resonator (without the levitated disk) to determine the volume velocity of a piston that has the same diameter as the tube, D_{tube}, which would be required to produce the standing wave pressure amplitude at the rigid end calculated in part (*a*) for the $n = 3$ mode. You may make a slight adjustment of the tube's length to force $f_3 = 350$ Hz. What are the frequencies of the f_1, f_2, and f_4 modes?

(d) *Adiabatic invariance*. Use your DeltaEC model in part (*a*) to estimate the frequency as a function of disk position by moving a constricted DUCT segment that is the same length as the disk (1.5 mm) and has a cross-sectional area equal to that of the empty tube minus the cross-sectional area of the disk. Move that constricted section from the rigid end to about 0.3 m from the driven end of the resonator. Plot f_3 vs. position to produce a graph similar to Fig. 15.27. Repeat for f_2 vs. position.

(e) *Advanced DeltaEC model*. Repeat part (*c*) but explicitly includes the loudspeaker in Fig. 2.43 using the following speaker parameters: $m_o = 12.0$ gm, $K = 1440$ N/m, $B\ell = 7.1$ N/A, $R_{dc} = 5.2\ \Omega$, $L = 0.1$ mH, $R_m = 1.9$ kg/s, and $A_{pist} = 98.5$ cm^2. The rear of the speaker is enclosed (to protect your hearing!) in a cylindrical enclosure that has an inside diameter of 6″ (15.2 cm) and a length of 8″ (20 cm). What is the electrical current that must be supplied to the voice coil to produce the $n = 3$ standing wave amplitude calculated

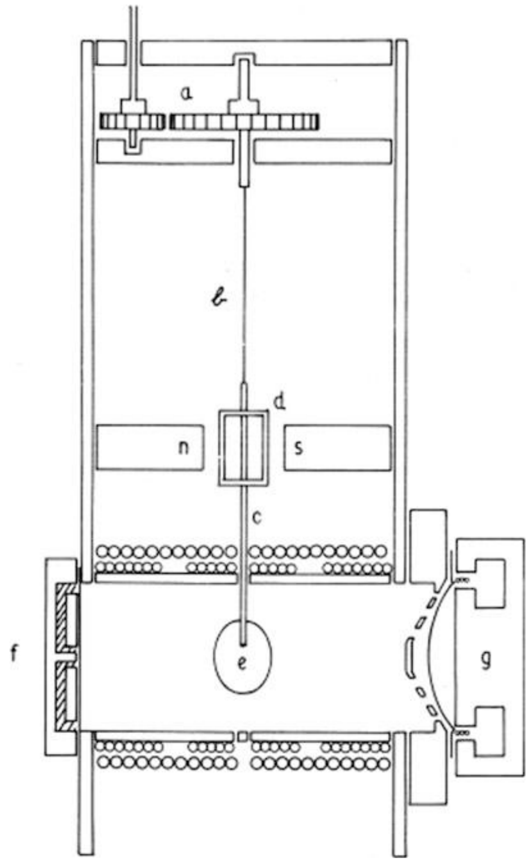

Fig. 15.33 Cross-sectional view of a "modern" Rayleigh disk apparatus. [60]

in part (a) at $f_3 = 350$ Hz? What are the frequencies of the f_1, f_2, and f_4 modes of the coupled speaker-resonator system (see Sect. 10.7.5)?

Hints: The DeltaEC model of the bass-reflex loudspeaker enclosure in Fig. 8.41 might provide a helpful starting point. An "enclosed current driven speaker" segment, IESPEAKER, will provide a way to incorporate the rear enclosure with the electrodynamic speaker's excitation of standing waves in the tube.

(5) **Rayleigh disk**. The apparatus in Fig. 15.33 shows a rigid disk (e) suspended at the midplane of a cylindrical resonator from a torsion fiber (b). The resonator has an electrodynamic dome tweeter (g) at one end and an electret microphone (see Sect. 6.3.3) providing a rigid termination at the other end (f). The disk's angular orientation is detected with the coils surrounding the resonator that incorporates a split-secondary astatic transformer [60]. A gearing system (a) and a coil (d) and magnet structure (n and s) from an analog meter movement can be used to adjust the equilibrium orientation, θ_o, of the disk or excite a free-decay oscillation. The maximum occlusion of the resonator occurs when $\theta_o = 0°$.

The resonator's inside diameter is 3.0 cm and its length, $L = 12.0$ cm. The diameter of the disk is $D_{disk} = 1.2$ cm. The disk has a mass, $m_1 = 0.80$ gm and a moment of inertia of about its diameter of $I_{disk} = 2.0 \text{ x } 10^{-8}$ kg-m^2

Assume the resonator contains dry air at 300 K with $p_m = 100$ kPa.

(a) *Fundamental resonance frequency*. What is the frequency of the fundamental half-wavelength mode of the resonator?
(b) *Torsional stiffness*. If the frequency of disk oscillations is 1.1 Hz, what is the torsional stiffness of the disk's suspension?
(c) *Standing wave pressure amplitude*. The disk's equilibrium position is adjusted so that $\theta_o = 45°$. What is the acoustic pressure amplitude, p_1, at the surface of the electret microphone if the standing wave causes the disk equilibrium orientation to be $\theta = 35°$ and the corrections in the curly brackets of Eq. (15.79) are ignored?
(d) *Scattering corrections*. How large is the correction provided by Eq. (15.79) relative to the simpler expression for the torque in Eq. (15.78)? Express your result as $N_{\text{antinode}}\ (35°)/N\ (35°)$.
(e) *Electret microphone sensitivity*. If the open-circuit output voltage of the electret microphone is 285 mV_{ac} under the conditions of part (*b*), what is the microphone's open-circuit sensitivity?

References

1. G.G. Stokes, On a difficulty in the theory of sound. Phil. Mag. (Series 3) 33, 349–356 (1848). Also available in R. T. Beyer, *Nonlinear Acoustics in Fluids* (Van Nostrand Reinhold, 1984)
2. M.F. Hamilton, Gol'dberg number for diverging waves. J. Acoust. Soc. Am. **104**(6), 4419–4427 (2016)
3. I. Rudnick, On the attenuation of high amplitude waves of stable saw-tooth form propagated in horns. J. Acoust. Soc. Am. **30**(4), 339–342 (1958)
4. A. Myers, R.W. Pyle Jr., J. Gilbert, D.M. Campbell, J.P. Chick, S. Logie, Effects of nonlinear sound propagation on the characteristic timbres of brass instruments. J. Acoust. Soc. Am. **131**(1, Pt. 2), 678–688 (2012)
5. R.T.Beyer, "The parameter B/A ", in *Nonlinear Acoustics*, M. F. Hamilton and D. T. Blackstock, eds. (Acoust. Soc. Am., 2008). Ch. 2; ISBN 0-9744067-5-9.
6. R. T. Beyer, *Nonlinear Acoustics* (Acoust. Soc. Am., 1997); ISBN 1-56396-724-3. §3.1.
7. EE.C. Everbach, Parameters of nonlinearity of acoustic media, in *Encyclopedia of Acoustics*, ed. by M. J. Crocker, (Wiley & Sons, 1997). Vol. I, Ch. 20; ISBN 0-471-17767-9
8. C.M. Cormack, M.F. Hamilton, Plane nonlinear shear waves in relaxing media. J. Acoust. Soc. Am. **143**(2), 1035–1048 (2018)
9. S.L. Garrett, Nonlinear distortion of 4^{th} sound in superfluid helium ^{3}He-B. J. Acoust. Soc. Am. **69**(1), 139–144 (1981)
10. R.T. Beyer, Nonlinear Acoustics (Experimental), in *American Institute of Physics Handbook*, ed. by D. E. Grey, 3rd edn., (McGraw-Hill, 1972). See Table 30-3, pg. 3–208
11. M. Greenspan, C.E. Tschiegg, Radiation-induced acoustic cavitation: apparatus and some results. J. Res. Nat'l. Bur. Standards, Sec. C **71**, 299–312 (1959)
12. M.S. Cramer, A. Kluwick, On the propagation of waves exhibiting both positive and negative nonlinearity. J. Fluid Mech. **142**(1), 9–37 (1984)
13. I. Rudnick, Physical Acoustics at UCLA in the Study of Superfluid Helium, in *New Directions in Physical Acoustics – Course LXIII, Varenna, Italy*, ed. by D. Sette, (Italian Physical Society and IOS Press, Amsterdam, 1974)
14. S. J. Putterman, *Superfluid Hydrodynamics* (North-Holland, 1974); ISBN 0 7204 030104.
15. S. Putterman, S. Garrett, Resonant mode conversion and other second-order effects in superfluid He-II. J. Low Temp. Phys. **27**(3/4), 543–559 (1977)
16. Z.A. Gol'dberg, Second approximation acoustic equations and the propagation of plane waves of finite amplitude. Soviet Phys. Akust. **2**, 346–350 (1956)
17. A. Larraza, S.L. Garrett, S. Putterman, Dispersion relations for gravity waves in a deep fluid: second sound in a stormy sea. Phys. Rev. A **41**(6), 3144–3155 (1990)
18. L.D. Landau, E.M. Lifshitz, *Fluid Mechanics*, 2nd edn. (Butterworth-Heinemann, 1987). See Eq. 86.1; ISBN 0 7506 2767 0
19. I. Rudnick, On the attenuation of a repeated sawtooth shock wave. J. Acoust. Soc. Am. **25**(5), 1010–1011 (1953)
20. I. Rudnick, On the attenuation of finite amplitude waves in a liquid. J. Acoust. Soc. Am. **30**(6), 564–567 (1958)
21. J.A. Shooter, T.G. Muir, D.T. Blackstock, Acoustic saturation of spherical waves in water. J. Acoust. Soc. Am. **55**(1), 54–62 (1974). See Fig. 1
22. S. Earnshaw, On the mathematical theory of sound. Phil. Tran. Roy. Soc. (London) **150**, 133–148 (1860)

23. G.B. Airy, On a difficulty in the problem of sound. Phil. Mag. (Series 3) **34**, 401–405 (1848). Also available in R. T. Beyer, *Nonlinear Acoustics in Fluids* (Van Nostrand Reinhold, 1984). pp. 37–41
24. L.E. Hargrove, Fourier series for the finite amplitude sound waveform in a dissipationless medium. J. Acoust. Soc. Am. **32**(4), 511–512 (1960)
25. E. Fubini-Ghiron, Anomalie nella propagazione di onde acustiche di grande ampiezza (Anomalies in acoustic wave propagation of large amplitude). Alta Frequenza **4**, 530–581 (1935)
26. R.D. Fay, Plane sound waves of finite amplitude. J. Acoust. Soc. Am. **3**(2A), 222–241 (1931)
27. D.T. Blackstock, Connection between the Fay and Fubini solution for a plane sound wave of finite amplitude. J. Acoust. Soc. Am. **39**(6), 1019–1026 (1966)
28. J.L.S. Bellin, R.T. Beyer, Scattering of sound by sound. J. Acoust. Soc. Am. **32**(3), 339–341 (1960)
29. P.J. Westervelt, Parametric acoustic array. J. Acoust. Soc. Am. **35**(4), 535–537 (1963)
30. H. Lamb, *Dynamical Theory of Sound*, 2nd edn. (E. Arnold & Co., 1931). See §63 and §95; reprinted (Dover, 1960)
31. A.L. Thuras, R.T. Jenkins, H.T. O'Neill, Extraneous frequencies generated in air carrying intense sound waves. J. Acoust. Soc. Am. **6**(3), 173–180 (1935)
32. T.G. Leighton, Ultrasound in air – Guidelines, applications, public exposure, and claims of attacks in Cuba and China. J. Acoust. Soc. Am. **144**(4), 2473–2489 (2018)
33. R.L. Swanson, S. Hampton, J. Green-McKenzie, R. Diaz-Arrastia, M.S. Grady, R. Verma, R. Biester, D. Duda, R.L. Wolf, D.H. Smith, Neurological manifestations among US Government personnel reporting directional audible and sensory phenomena in Havana, Cuba. J. Am. Med. Assoc. **319**(11), 1125–1133 (2018)
34. J. Perlez and S. L. Myers, "U.S. issues alert to Americans in China in wake of sonic attack fears," *New York Times* (June 8, 2018), https://www.nytimes.com/2018/06/08/world/asia/sonic-attack-china-guangzhouconsulate.html
35. *Metals Handbook (Desk Edition)*, H. E. Boyer and T. L. Gall, eds. (Am. Soc. for Metals, 1985); ISBN 0-87170-188-X. Table 1, pg. 2–16.
36. G.L. Jones, D.R. Kobett, Interaction of elastic waves in an isotropic solid. J. Acoust. Soc. Am. **35**(1), 5–10 (1963)
37. R.R. Rollins Jr., L.H. Taylor, P.H. Todd Jr., Ultrasonic study of three-phonon interactions. II. Experimental results. Phys. Rev. **136**(3A), 597–601 (1964)
38. M.F. Hamilton, J.A. TenCate, Sum and difference frequency generation due to noncollinear wave interactions in a rectangular duct. J. Acoust. Soc. Am. **81**(6), 1703–1712 (1987)
39. L.D. Landau, E.M. Lifshitz, *Fluid Mechanics*, 2nd edn. (Butterworth-Heinemann, 1987).; ISBN 0 7506 2767 0. §139
40. S. Garrett, S. Adams, S. Putterman, I. Rudnick, Resonant mode conversion in He II. Phys. Rev. Lett. **41**(6), 413–416 (1978)
41. P.M. Gammel, A.P. Croonquist, T.G. Wang, A high-powered siren for stable acoustic levitation of dense materials in the Earth's gravity. J. Acoust. Soc. Am. **83**(2), 496–501 (1988)
42. F.H. Busse, T.G. Wang, Torque generated by orthogonal acoustic waves – Theory. J. Acoust. Soc. Am. **69**(6), 1634–1638 (1981)
43. H.W.S. Clair, Electromagnetic sound generator for producing intense high frequency sound. Rev. Sci. Inst. **12**(5), 250–256 (1941)
44. C.H. Allen, I. Rudnick, A powerful high-frequency siren. J. Acoust. Soc. Am. **19**(5), 857–865 (1947)
45. B.L. Smith, G.W. Swift, Measuring second-order time-averaged pressure. J. Acoust. Soc. Am. **110**(2), 717–723 (2001)
46. J. W. Strutt (Lord Rayleigh), "On the circulation of air observed in Kundt's tubes, and on some allied acoustical problems," Phil. Trans. Roy. Soc. (London) **175**, 1-21 (1883); *Collected Works*, (Dover, 1964) Vol. II, §108.
47. H. Mukai, S. Sakamoto, H. Tachibana, Experimental study on the absorption characteristics of resonance-type brick/block walls. J. Acoust. Soc. Japan (E) **20**(6), 433–438 (1999)
48. M. B. Barmatz, "Acoustic agglomeration methods and apparatus," U.S. Pat. No. 4,475,921 (Oct. 9, 1984).
49. J.P. Dionne, B. Dutra, K.C. Chitale, G. Ghoshal, C. Leidel, B. Lipkens, A novel acoustic cell processing platform for cell concentration and washing. J. Acoust. Soc. Am. **141**(5), 3741 (2017)
50. J. W. Strutt (Lord Rayleigh), *Theory of Sound*, Vol. II (Macmillan, 1896); (Dover, 1945). §253b
51. V. Dvořák, Ueber die ackustiche Abstoggung. Ann. Physik **239**(3), 328–338 (1878)
52. V. Dvořák (with note by A. M. Mayer), "On acoustic repulsion," Phil. Mag. **6**, Series 5, 225-233 (1878); https://doi.org/10.1080/14786447808639500.
53. J. W. Strutt (Lord Rayleigh), *Theory of Sound*, Vol. II (Macmillan, 1896); (Dover, 1945). §253a.
54. W. König, Hydrodynamisch-akustische Untersuchungen. Wied. Ann. **43**, 51 (1891)
55. J. W. Strutt (Lord Rayleigh), "On an instrument capable of measuring the intensity of aerial vibrations," Phil. Mag. **14**, 186-187 (1882); *Collected Works* (Dover, 1964) Vol. II, §91.
56. L.L. Beranek, *Acoustic Measurements* (Wiley & Sons, 1949), pp. 148–158
57. L.V. King, On the theory of the inertia and diffraction corrections for the Rayleigh disk. Proc. Roy. Soc. (London) **A153**, 17–40 (1935)

58. J.R. Pellam, W.B. Hanson, Thermal Rayleigh disk measurements in liquid helium II. Phys. Rev. **85**(2), 216–225 (1952)
59. T.R. Koehler, J.R. Pellam, Observation of torque exerted by pure superflow. Phys. Rev. **125**(3), 791–794 (1962)
60. S.L. Garrett, Butterfly-valve inductive orientation detector. Rev. Sci. Inst. **51**(4), 427–430 (1980)
61. L.D. Landau, E.M. Lifshitz, *Fluid Mechanics*, 2nd edn. (Butterworth-Heinemann, 1987). §8; ISBN 0 7506 2767 0
62. L. D. Landau and E. M. Lifshitz, *Mechanics*, (Pergamon, 1960); See §1 – §5.
63. I. Rudnick, Measurements of the acoustic radiation pressure on a sphere in a standing wave field. J. Acoust. Soc. Am. **62**(1), 20–22 (1977)
64. L.D. Landau, E.M. Lifshitz, *Fluid Mechanics*, 2nd edn. (Butterworth-Heinemann, 1987). §49 ISBN 0 7506 2767 0
65. S. L. Garrett, R. W. M. Smith and M. E. Poese, "Eliminating nonlinear acoustical effects from thermoacoustic refrigeration systems," *Proc. 17th International Symposium on Nonlinear Acoustics* (ISNA 17), pg. 407-415 (Am. Inst. Physics, 2006); ISBN 0-7354-0330-9.
66. Y.A. Ilinskii, B. Lipkens, T.S. Lucas, T.W. Van Doren, E.A. Zabolotskaya, Nonlinear standing waves in an acoustical resonator. J. Acoust. Soc. Am. **104**(5), 2664–2674 (1998)
67. S. Putterman, J. Rudnick, M. Barmatz, Acoustic levitation and the Boltzmann-Ehrenfest principle. J. Acoust. Soc. Am. **85**(1), 68–71 (1989)
68. E. Leung, C.P. Lee, N. Jacobi, T.G. Wang, Resonance frequency shift of an acoustic chamber containing a rigid sphere. J. Acoust. Soc. Am. **72**(2), 615–620 (1980)
69. S.J. Putterman, Adiabatic invariance, the cornerstone of modern physics. J. Acoust. Soc. Am. **83**(1), S39 (1988)
70. M. Barmatz, Overview of containerless processing technologies, in *Materials Processing in the Reduced Gravity Environment of Space*, ed. by G. E. Rindone, (Elsevier, 1982), pp. 25–37
71. J. Rudnick, M. Barmatz, Oscillational instabilities in single-mode acoustic levitators. J. Acoust. Soc. Am. **87**(1), 81–92 (1990)
72. M. B. Barmatz and S. L. Garrett, "Stabilization and oscillation of an acoustically levitated object," U.S. Pat. No. 4,773,266 (Sep. 27, 1988).
73. S. Chu, Laser manipulation of atoms and particles. Science **253**(5022), 861–866 (1991)
74. S.L. Garrett, S. Backhaus, The power of sound. Am. Scientist **88**(6), 11–17 (2004)
75. G.W. Swift, Mixture separation, in *Handbook of Acoustics*, ed. by T. D. Rossing, (Springer, 2007). ISBN 978-0-387-30446-7. See §7.6
76. W.L. Nyborg, Acoustic streaming, in *Nonlinear Acoustics*, Acoust. Soc. Am, ed. by M. F. Hamilton, D. T. Blackstock, (2008). See Ch. 7; ISBN 978-0-123-21860-5
77. S.J. Putterman, Sonoluminescence: Sound into light. Scientific American **272**(2), 46–51 (1995)
78. R.T. Beyer, *Nonlinear Acoustics* (Acoust. Soc. Am., 1997). §4.7, ISBN 1-56396-724-3
79. D. J. Maglieri and K. J. Plotkin, *Sonic Boom*, NASA Tech. Report RP-1258 (1991).
80. A. B. Pippard, *The Physics of Vibration* (Cambridge, 1989). See Ch. 8, ISBN 0 521 37200 3

Appendices

Appendix A: Useful Physical Constants and Conversion Factors

$\Re = k_B N_A$	8.314462 J/mole-K
k_B	1.380649×10^{-23} J/K $= 8.617333 \times 10^{-5}$ eV/K
N_A	$6.02214076 \times 10^{23}$ mol^{-1}
V_{molar}	22.4141 l/mol @ 273.15 K, 101,325 Pa
M_{air}	28.9644 g/mol
e	$1.602176634 \times 10^{-19}$ C
g	9.80665 m/s^2
h	$6.62607015 \times 10^{-34}$ J-s $= 4.135667 \times 10^{-15}$ eV-s
$\hbar = h/2\pi$	$1.05457182 \times 10^{-34}$ J-s
$c = (\varepsilon_o \mu_o)^{-½}$	2.99792458×10^{8} m/s
ε_o	$8.8541878128 \times 10^{-12}$ F·m^{-1}
μ_o	$4\pi \times 10^{-7}$ H m^{-1}
$2e/h$	483.5978484 MHz/μV
σ	5.6697×10^{-8} W/m^2-K^4 $= [k_B{}^4\pi^2/60\hbar^3 c^2]$

As of 20 May 2019 (the 144th anniversary of the Metre Convention), the above values of k_B, N_A, c, e, h, μ_o ε_o, and $2e/h$ are taken to be exact.

1 psi	6894.8 Pa = 2.307 ft H_2O	1 psf = 47.88 Pa
1 torr	133.322 Pa = 1.0 mm Hg	
1 atm	101,325 Pa	1″ H_2O = 249.1 Pa
1 bar	100 kPa	
1 ft^3	28.317 l	
1 gal	3.785411784 l = 231in^3	
1 gpm	63.088 cm^3/s	1 cfm = 4.72×10^{-4} m^3/s
1 cal	4.184 J	
1 W	3.413 BTU/h	
1 ton	3517 W (≡ 12,000 BTU/h)	
1 hp	746 W	

S. L. Garrett, *Understanding Acoustics*, Graduate Texts in Physics,
https://doi.org/10.1007/978-3-030-44787-8

Appendix B: Resonator Quality Factor

"A man with one watch knows the time; a man with two is never sure."

The quality factor (Q) of a resonator is a dimensionless measure of the "sharpness" of a resonance. One of the greatest sources of its utility is that we have many equivalent ways of expressing the Q. This variety allows us to connect the most convenient experimental method to the parameter of interest and provides us with a "second watch" if we want to make a self-consistency check of our results, either theoretically or experimentally.

Caution The results summarized below assume that the resonance under consideration is "isolated," so there are no other resonances that might be sufficiently close in frequency that they would affect the amplitude or phase of the resonance being considered.

***Q*-Multiplier** For a given force, F, or pressure, p, the magnitude of the response at the resonance frequency of the ith mode, ω_i, $i = 0, 1, 2, 3, \ldots\infty$, will be "amplified" by the quality factor Q_i of that mode.

$$Q_i = \left|\frac{p(\omega_i)}{p(\omega = 0)}\right| \tag{B.1}$$

Energy Storage-to-Dissipation Ratio The time-averaged power dissipated is written as $\langle \Pi_{dissipated} \rangle_t$ below.

$$Q = 2\pi \frac{E_{stored}}{E_{dissipated/cycle}} = \frac{\omega E_{stored}}{\langle \Pi_{dissipated} \rangle_t} \tag{B.2}$$

Lumped-Element Storage-to-Loss Ratio For a mass-spring system with natural frequency, ω_o; mass, m; mechanical resistance, R_m; and stiffness K; or a similar electrical circuit with inductance, L; resistance, R_{dc}; and capacitance, C; or an acoustical compliance, C, and acoustical inertance, L

$$Q = \frac{\omega_o m}{R_m} = \frac{\mathrm{K}}{\omega_o R_m} = \frac{1}{\omega_o R_m C} = \frac{\omega_o L}{R_{dc}}$$

Half-Power Bandwidth If the frequencies of the –3 dB points are f_+ and f_-,, then the full –3 dB bandwidth of the resonance, $\Delta f = f_+ - f_-$, is related to the quality factor, Q, by the resonance frequency, $f_o = (f_+ f_-)^{1/2}$ as written below.

$$Q = \frac{f_o}{f_+ - f_-} = \frac{\omega_o}{\omega_+ - \omega_-} \quad \text{where} \quad f_o = \sqrt{f_+ f_-} = \frac{\sqrt{\omega_+ \omega_-}}{2\pi} \tag{B.3}$$

Rate of Phase Change with Frequency at Resonance If the phase shift between force (or pressure) and velocity (or volume flow rate) is expressed as ϕ in radians, or θ in degrees, then

$$Q = \frac{\omega_o}{2} \frac{d\phi}{d\omega}\bigg|_{\omega_o} = \frac{f_o}{2} \frac{d\phi}{df}\bigg|_{f_o} = f_o \frac{\pi}{360^\circ} \frac{d\theta}{df}\bigg|_{f_o} \cong \frac{f_o}{114.6^\circ} \frac{d\theta}{df}\bigg|_{f_o} \tag{B.4}$$

Free Decay Rate If the time required for the amplitude of the oscillations to decay to $e^{-1} \cong 0.368$ of their value is $\tau = \beta^{-1} = (2\,m)/R_m$, then

$$Q = \frac{1}{2}\omega_o \tau = \pi \tau f_o = \frac{1}{2}\frac{k}{\alpha} = \frac{\pi}{\alpha \lambda} \tag{B.5}$$

The exponential spatial attenuation constant, α, is related to the temporal decay rate, τ, by the sound speed, c, where k is the wavenumber and λ is the wavelength: $\alpha = \tau/c$.

Similarly, the Q is expressed as 2π times the number of cycles required for the ***energy*** to decay by e^{-1}, or π times the number of cycles required for the ***amplitude*** to decay by e^{-1}. More generally,

$$Q = \frac{\pi N}{\ln [x]} \tag{B.6}$$

N is the number of cycles for the amplitude to decay by a factor of x.

Reflection Coefficient In a standing wave resonator, the standing wave can be represented as the superposition of a right- and left-going traveling waves. If the left-going wave is reflected with an amplitude that is $R < 1$ times the right-going wave amplitude, the coefficient of the right-going wave would be given by the infinite geometric series $1 + R + R^2 + R^3 + \ldots$, and the left-going wave would have an amplitude that is R times that infinite sum. The resulting quality factor, Q_n, of the nth mode of the resonator can be expressed in terms of the reflection coefficient R and the mode number n.

$$Q_n = n\pi \frac{\sqrt{R}}{1 - R} \tag{B.7}$$

Pole-Zero Resonance Fit Many modern spectrum analyzers allow a resonance to be fit by a pole-zero function. A single resonance will have two complex poles that are complex conjugates, $a \pm jb$. The resonance frequency is $f = (a^2 + b^2)^{1/2} \cong b$, if the damping is small ($a \ll b$).

$$Q = \frac{-1}{2a}\sqrt{a^2 + b^2} \cong \frac{-b}{2a} \tag{B.8}$$

Loss Tangent and Damping Factor In the characterization of elastomers used as vibration isolators, it is common to define a frequency-dependent, complex elastic modulus E^*. The complex modulus has a real part, E', and an imaginary part, E'', such that $E^* = E' + jE'' \cong E\,(1 + j\delta)$, where we choose to define a "loss tangent," $\tan \delta$, that is the inverse of the quality factor.[1]

$$Q = \frac{1}{\tan \delta} = \frac{E'}{E''} = \frac{1}{2\zeta} \tag{B.9}$$

The damping factor, ζ, is the ratio of the mechanical resistance to the critical value of the mechanical resistance, $R_m^{crit} = 2(km)^{1/2} = 2m\omega_o$.[2]

[1] For example, see J. C. Snowdon, *Vibration and Shock in Damped Mechanical Systems* (Wiley, 1968).

[2] W. T. Thomson, *Theory of Vibration with Applications,* 2nd edn. (Prentice-Hall, 1981); ISBN 0-13-914,523-0

Appendix C: Bessel Functions of the First Kind

Bessel's equation

$$\frac{d^2 J_m(x)}{dx^2} + x\frac{dJ_m(x)}{dx} + \left(x^2 - m^2\right)J_m(x) = 0 \tag{C.1}$$

$$\frac{1}{x}\frac{d}{dx}\left(x\frac{dJ_m(x)}{dx}\right) + \left(1 - \frac{m^2}{x^2}\right)J_m(x) = 0 \tag{C.2}$$

Series expansions

$$J_m(x) = \frac{1}{m!}\left(\frac{x}{2}\right)^m - \frac{1}{1!(m+1)!}\left(\frac{x}{2}\right)^{m+2} + \frac{1}{2!(m+2)!}\left(\frac{x}{2}\right)^{m+4} - \cdots \tag{C.3}$$

$$J_0(x) = 1 - \frac{x^2}{2^2} + \frac{x^4}{2^2 \cdot 4^2} - \frac{x^6}{2^2 \cdot 4^2 \cdot 6^2} + \cdots \tag{C.4}$$

$$J_1(x) = \frac{x}{2} - \frac{2x^3}{2 \cdot 4^2} + \frac{3x^5}{2 \cdot 4^2 \cdot 6^2} - \cdots \tag{C.5}$$

$$J_2(x) = \frac{x^2}{2 \cdot 2^2} - \frac{x^4}{2 \cdot 3 \cdot 2^4} + \frac{x^6}{2 \cdot 3 \cdot 4 \cdot 2^6} - \cdots \tag{C.6}$$

Asymptotic forms for large argument

$$\lim_{x\to\infty}[J_m(x)] = \sqrt{\frac{2}{\pi x}}\cos\left(x - \frac{m\pi}{2} - \frac{\pi}{4}\right) \tag{C.7}$$

Addition theorem

$$1 = J_0(x) + 2J_2(x) + 2J_4(x) + 2J_6(x) + \cdots \tag{C.8}$$

Relationships to trigonometric functions

$$\sin x = 2J_1(x) - 2J_3(x) + 2J_5(x) - 2J_7(x) + \cdots \tag{C.9}$$

$$\cos x = J_0(x) - 2J_2(x) + 2J_4(x) - 2J_6(x) + \cdots \tag{C.10}$$

$$\cos(x\cos\theta) = J_0(x) + 2\sum_{k=1}^{\infty}(-1)^k J_{2k}(x)\cos(2k\theta) \tag{C.11}$$

$$\cos(x\sin\theta) = J_0(x) + 2\sum_{k=1}^{\infty} J_{2k}(x)\cos(2k\theta) \tag{C.12}$$

$$\sin(x\sin\theta) = 2\sum_{k=0}^{\infty} J_{2k+1}(x)\sin[(2k+1)\theta] \tag{C.13}$$

$$\sin(x\cos\theta) = 2\sum_{k=1}^{\infty}(-1)^k J_{2k+1}(x)\cos[(2k+1)\theta] \tag{C.14}$$

Integral representations

$$J_m(x) = \frac{(x/2)^m}{\sqrt{\pi}\ \Gamma(m+½)} \int_0^{\pi} \cos(x\cos\theta)\ d\theta \tag{C.15}$$

$$J_0(x) = \frac{1}{\pi}\int_0^{\pi} \cos(x\sin\theta)\ d\theta = \frac{1}{\pi}\int_0^{\pi} \cos(x \quad \cos \quad \theta)\ d\theta \tag{C.16}$$

$$J_m(x) = \frac{1}{\pi}\int_0^{\pi} \cos(x\sin\theta - m\theta)\ d\theta \tag{C.17}$$

Recurrence relations

$$J_{m-1}(x) + J_{m+1} = \frac{2m}{x} J_m(x) \tag{C.18}$$

$$J_{m-1}(x) - J_{m+1}(x) = 2\frac{dJ_m(x)}{dx} \tag{C.19}$$

$$\frac{dJ_m(x)}{dx} = J_{m-1}(x) - \frac{m}{x}J_m(x) \tag{C.20}$$

$$\frac{dJ_m(x)}{dx} = -J_{m+1}(x) + \frac{m}{x}J_m(x) \tag{C.21}$$

Derivatives

$$\frac{dJ_m(x)}{dx} = \frac{1}{2}[J_{m-1}(x) - J_{m+1}(x)] \tag{C.22}$$

$$\frac{dJ_0(x)}{dx} = -J_1(x) \tag{C.23}$$

$$\frac{d}{dx}[x^m J_m(x)] = x^m J_{m-1}(x) \tag{C.24}$$

$$\frac{d}{dx}[x^{-m} J_m(x)] = -x^{-m} J_{m+1}(x) \tag{C.25}$$

Integrals

$$\int J_1(x)\,dx = -J_0(x) \tag{C.26}$$

$$\int xJ_0(x)\,dx = xJ_1(x) \tag{C.27}$$

$$\int x^{p+1} J_p(x)\,dx = x^{p+1} J_{p+1}(x) \tag{C.28}$$

$$\int J_0^2(x)\,x\,dx = \frac{x^2}{2}\left[J_0^2(x) + J_1^2(x)\right] \tag{C.29}$$

$$\int J_m^2(x)\,x\,dx = \frac{x^2}{2}\left[J_m^2(x) - J_{m-1}(x)J_{m+1}(x)\right] \tag{C.30}$$

$$\int J_m(ax)J_m(bx)\,x\,dx = \frac{x}{a^2-b^2}[bJ_m(ax)J_{m-1}(bx) - aJ_m(bx)J_{m-1}(ax)] \tag{C.31}$$

Roots of Bessel Functions (15 Digits)

nth roots of Bessel functions,[3] $J_m(x) = 0$

m\n	n=1	n=2	n=3	n=4	n=5
m=0	2.40482555769577	5.52007811028631	8.65372791291101	11.7915344390142	14.9309177084877
m=1	3.83170597020751	7.01558666981561	10.1734681350627	13.3236919363142	16.4706300508776
m=2	5.13562230184068	8.41724414039986	11.6198411721490	14.7959517823512	17.9598194949878
m=3	6.38016189592398	9.76102312998166	13.0152007216984	16.2234661603187	19.4094152264350
m=4	7.58834243450380	11.0647094885011	14.3725366716175	17.6159660498048	20.8269329569623
m=5	8.77148381595995	12.3386041974669	15.7001740797116	18.9801338751799	22.2177998965612
m=6	9.93610952421768	13.5892901705412	17.0038196678160	20.3207892135665	23.5860844355813
m=7	11.0863700192450	14.8212687270131	18.2875828324817	21.6415410198484	24.9349278876730
m=8	12.2250922640046	16.0377741908877	19.5545364309970	22.9451731318746	26.2668146411766
m=9	13.3543004774353	17.2412203824891	20.8070477892641	24.2338852577505	27.5837489635730
m=10	14.4755006865545	18.4334636669665	22.0469853646978	25.5094505541828	28.8873750635304

nth roots of the derivatives of Bessel functions[3] $(dJ_m(x)/dx) = 0$

m\n	n=1	n=2	n=3	n=4	n=5
m=0	3.83170597020751	7.01558666981561	10.1734681350627	13.3236919363142	16.4706300508776
m=1	1.84118378134065	5.33144277352503	8.53631636634628	11.7060049025920	14.8635886339090
m=2	3.05423692822714	6.70613319415845	9.96946782308759	13.1703708560161	16.3475223183217
m=3	4.20118894121052	8.01523659837595	11.3459243107430	14.5858482861670	17.7887478660664
m=4	5.31755312608399	9.28239628524161	12.6819084426388	15.9641070377315	19.1960288000489
m=5	6.41561637570024	10.5198608737723	13.9871886301403	17.3128424878846	20.5755145213868
m=6	7.50126614468414	11.7349359530427	15.2681814610978	18.6374430096662	21.9317150178022
m=7	8.57783648971407	12.9323862370895	16.5293658843669	19.9418533665273	23.2680529264575
m=8	9.64742165199721	14.1155189078946	17.7740123669152	21.2290626228531	24.5871974863176
m=9	10.7114339706999	15.2867376673329	19.0045935379460	22.5013987267772	25.8912772768391
m=10	11.7708766749555	16.4478527484865	20.2230314126817	23.7607158603274	27.1820215271905

[3] http://wwwal.kuicr.kyoto-u.ac.jp/www/accelerator/a4/besselroot.htmlx

Appendix D: Trigonometric Functions

Euler's formula

$$e^{jx} = \cos x + j\sin x \tag{D.1}$$

$$\cos x = \frac{e^{jx} + e^{-jx}}{2}; \quad \sin x = \frac{e^{jx} - e^{-jx}}{2j}; \quad \tan x = \frac{1}{j}\frac{e^{jx} - e^{-jx}}{e^{jx} + e^{-jx}} \tag{D.2}$$

Addition and subtraction

$$\cos\alpha = \pm\sin\left(\alpha \pm \frac{\pi}{2}\right); \quad \sin\alpha = \pm\cos\left(\alpha \mp \frac{\pi}{2}\right) \tag{D.3}$$

$$\sin^2\alpha + \cos^2\alpha = 1 \tag{D.4}$$

$$\sin(\alpha \pm \beta) = \sin\alpha\cos\beta \pm \cos\alpha\sin\beta \tag{D.5}$$

$$\cos(\alpha + \beta) = \cos\alpha\cos\beta \mp \sin\alpha\sin\beta \tag{D.6}$$

$$\sin\alpha \pm \sin\beta = 2\sin\left(\frac{\alpha \pm \beta}{2}\right)\cos\left(\frac{\alpha \mp \beta}{2}\right) \tag{D.7}$$

$$\cos\alpha + \cos\beta = 2\cos\left(\frac{\alpha + \beta}{2}\right)\cos\left(\frac{\alpha - \beta}{2}\right) \tag{D.8}$$

$$\cos\alpha - \cos\beta = -2\sin\left(\frac{\alpha + \beta}{2}\right)\sin\left(\frac{\alpha - \beta}{2}\right) \tag{D.9}$$

Products and powers

$$\cos\alpha\cos\beta = ½[\cos(\alpha - \beta) + \cos(\alpha + \beta)] \tag{D.10}$$

$$\sin\alpha\sin\beta = -½[\cos(\alpha + \beta) - \cos(\alpha - \beta)] \tag{D.11}$$

$$\sin\alpha\cos\beta = ½[\sin(\alpha + \beta) + \sin(\alpha - \beta)] \tag{D.12}$$

$$\sin^2\alpha = ½(1 - \cos 2\alpha) \tag{D.13}$$

$$\sin^3\alpha = \frac{1}{4}(3\sin\alpha - \sin 3\alpha) \tag{D.14}$$

$$\cos^2\alpha = ½(1 + \cos 2\alpha) \tag{D.15}$$

$$\cos^3\alpha = \frac{1}{4}(3\cos\alpha + \cos 3\alpha) \tag{D.16}$$

Appendix E: Hyperbolic Functions

$$e^x = \cosh x + j\sinh x \tag{E.1}$$

$$\cosh x = \frac{e^x + e^{-x}}{2}; \quad \sinh x = \frac{e^x - e^{-x}}{2} \tag{E.2}$$

$$\tanh x = \frac{e^x - e^{-x}}{e^x + e^{-x}} = \frac{e^{2x} - 1}{e^{2x} + 1}; \quad \coth x = \frac{1}{\tanh x} \tag{E.3}$$

Series expansions

$$e^x = 1 + \frac{x}{1!} + \frac{x^2}{2!} + \frac{x^3}{3!} + \ldots \tag{E.4}$$

$$\sinh x = x + \frac{x^3}{3!} + \frac{x^5}{5!} + \frac{x^7}{7!} + \ldots \tag{E.5}$$

$$\cosh x = 1 + \frac{x^2}{2!} + \frac{x^4}{4!} + \frac{x^6}{6!} + \ldots \tag{E.6}$$

$$\tanh x = x - \frac{x^3}{3} + \frac{2x^5}{15} - \frac{17x^7}{315} + \ldots \quad \left(x^2 < \frac{\pi^2}{4}\right) \tag{E.7}$$

$$\sinh^{-1} x = x - \frac{x^3}{2\cdot 3} + \frac{1\cdot 3}{2\cdot 4}\frac{x^5}{5} - \frac{1\cdot 3\cdot 5}{2\cdot 4\cdot 6}\frac{x^7}{7} + \ldots \quad (x^2 < 1) \tag{E.8}$$

$$\cosh^{-1} x = \ln(2x) - \frac{1}{2}\frac{1}{2x^2} - \frac{1\cdot 3}{2\cdot 4}\frac{1}{4x^4} - \frac{1\cdot 3\cdot 5}{2\cdot 4\cdot 6}\frac{1}{6x^6} - \ldots \quad (x^2 < 1) \tag{E.9}$$

$$\tanh^{-1} x = x + \frac{x^3}{3} + \frac{x^5}{5} + \frac{x^7}{7} + \ldots \quad (x^2 < 1) \tag{E.10}$$

Addition and subtraction

$$\cosh^2\alpha - \sinh^2\alpha = 1 \tag{E.11}$$

$$\sinh(\alpha \pm \beta) = \sinh\alpha\cosh\beta \pm \cosh\alpha\sinh\beta \tag{E.12}$$

$$\cosh(\alpha \pm \beta) = \cosh\alpha\cosh\beta \pm \sinh\alpha\sinh\beta \tag{E.13}$$

$$\tanh(\alpha \pm \beta) = \frac{1 + \tanh\alpha\tanh\beta}{\tanh\alpha + \tanh\beta} = \frac{\sinh 2\alpha \pm \sinh 2\beta}{\cosh 2\alpha + \cosh 2\beta} \tag{E.14}$$

$$\sinh\alpha \pm \sinh\beta = 2\sinh\left(\frac{\alpha \pm \beta}{2}\right)\cosh\left(\frac{\alpha \mp \beta}{2}\right) \tag{E.15}$$

$$\cosh\alpha + \cosh\beta = 2\cosh\left(\frac{\alpha + \beta}{2}\right)\cosh\left(\frac{\alpha - \beta}{2}\right) \tag{E.16}$$

$$\cosh\alpha - \cosh\beta = 2\sinh\left(\frac{\alpha + \beta}{2}\right)\sinh\left(\frac{\alpha - \beta}{2}\right) \tag{E.17}$$

Products and powers

$$\sinh\alpha\sinh\beta = ½[\cosh(\alpha+\beta) - \cosh(\alpha-\beta)] \tag{E.18}$$

$$\cosh\alpha\cosh\beta = ½[\cosh(\alpha+\beta) + \cosh(\alpha-\beta)] \tag{E.19}$$

$$\sinh\alpha\cosh\beta = ½[\sinh(\alpha+\beta) + \sinh(\alpha-\beta)] \tag{E.20}$$

$$\sinh 2\alpha = 2\sinh\alpha\cosh\alpha \tag{E.21}$$

$$\sinh 3\alpha = 3\sinh\alpha + 4\sinh^3\alpha \tag{E.22}$$

$$\cosh 2\alpha = 2\cosh^2\alpha - 1 \tag{E.23}$$

$$\cosh 3\alpha = 4\cosh^3\alpha - 3\cosh\alpha \tag{E.24}$$

$$\sinh^2\alpha = ½(\cosh 2\alpha - 1) \tag{E.25}$$

$$\sinh^3\alpha = \frac{1}{4}(\sinh 3\alpha - 3\sinh\alpha) \tag{E.26}$$

$$\cosh^2\alpha = ½(\cosh 2\alpha - 1) \tag{E.27}$$

$$\cosh^3\alpha = \frac{1}{4}(\cosh 3\alpha + 3\cosh\alpha) \tag{E.28}$$

Functions of complex arguments

$$\begin{array}{ll} \sin jx = \cosh x & \sinh jx = j\sin x \\ \sin x = -j\sinh jx & \sinh x = -j\sin jx \end{array} \tag{E.29}$$

$$\begin{array}{ll} \cos jx = \cosh x & \cosh jx = \cos x \\ \cos x = \cosh jx & \cosh x = \cos jx \end{array} \tag{E.30}$$

$$\tan jx = -j\tanh jx \quad \tanh jx = -j\tan jx \tag{E.31}$$

Index

S. L. Garrett, *Understanding Acoustics*, Graduate Texts in Physics,
https://doi.org/10.1007/978-3-030-44787-8

F

Q

R